INVESTIGATING THE INFLUENCE OF NANOARCHITECTURE AND ATOMS / UNIT AREA ON CONSTITUENT STRUCTURE AND TRANSPORT PROPERTIES OF NANOLAMINATE HETEROSTRUCTURES.

by

DANIELLE M. HAMANN

A DISSERTATION

Presented to the Department of Chemistry and Biochemistry
and the Graduate School of the University of Oregon
in partial fulfillment of the requirements
for the degree of
Doctor of Philosophy

June 2020

DISSERTATION APPROVAL PAGE

Student: Danielle M. Hamann

Title: Investigating the Influence of Nanoarchitecture and Atoms / Unit Area on Constituent Structure and Transport Properties of Nanolaminate Heterostructures

This dissertation has been accepted and approved in partial fulfillment of the requirements for the Doctor of Philosophy degree in the Department of Chemistry and Biochemistry by:

Shannon W. Boettcher	Chairperson
David C. Johnson	Advisor
Cathy Y. Wong	Core Member
Thomas Giachetti	Institutional Representative

and

Kate Mondloch	Interim Vice Provost and Dean of the Graduate School

Original approval signatures are on file with the University of Oregon Graduate School.

Degree awarded June 2020

DISSERTATION ABSTRACT

Danielle M. Hamann

Doctor of Philosophy

Department of Chemistry and Biochemistry

June 2020

Title: Investigating the Influence of Nanoarchitecture and Atoms / Unit Area on Constituent Structure and Transport Properties of Nanolaminate Heterostructures

At the thin film limit, interface interactions between constituents become increasingly important. This dissertation focuses on exploring thin films with the goal of preparing novel compounds, understanding interactions between layers, and examining the formation mechanism of these materials. All of the materials in this work were prepared by the low temperature modulated elemental reactants (MER) synthesis method which enables the preparation of metastable compounds with unique nanoarchitectures via designed elemental precursors. Synthesis and characterization of heterostructures and single-phase compounds were facilitated by a unique XRF data treatment which related measured XRF signal to atoms/Å^2 with sub-monolayer sensitivity. The ability to precisely deposit elemental layers into specific sequences and measure the absolute amount of material in each layer was foundational for this work, which is split into two sections: 1. Investigating the influence of nanoarchitecture on properties and 2. Preparing novel compounds with targeted properties.

The influence of nanoarchitecture on observed properties was investigated by preparing series of compounds with systematic changes in the repeating unit structure (i.e. number of each constituent or arrangement of the constituent layers). Both $[(SnSe)_{1+\delta}]_m[TiSe_2]_n$ and $[(PbSe)_{1+\delta}]_m[TiSe_2]_n$ heterostructures were studied. There are strong interactions between the two constituents as a result of charge donation from the SnSe/PbSe layer to the $TiSe_2$ layer. The charge donation results in a novel conducting material at the interface, which can be composed of two or three layers depending on the nanoarchitecture and has transport properties that differ from the material's bulk counterparts. These materials demonstrate complex temperature dependent transport properties which are dominated by variable range hopping from the novel interfacial material at low temperatures and the non-interfacial layers at high temperatures.

A series of novel Mn- containing materials were prepared as a result of a synergistic theoretical and experimental collaboration. First, a DFT "island" based approach was used to predict kinetically stable heterostructures. After the identification of these potentially stable phases, heterostructures containing various layering schemes of these phases were prepared via the MER method. This symbiotic relationship lead to the synthesis of an interfacially-stabilized ferromagnetic $(Pb_2MnSe_3)_{0.6}VSe_2$ compound.

This dissertation includes previously published and unpublished coauthored material.

CURRICULUM VITAE

NAME OF AUTHOR: Danielle M. Hamann

GRADUATE AND UNDERGRADUATE SCHOOLS ATTENDED:

University of Oregon, Eugene, Oregon
Lake Superior State University, Sault Ste. Marie, Michigan

DEGREES AWARDED:

Doctor of Philosophy, Chemistry, 2020, University of Oregon
Bachelor of Science, Chemistry, 2015, Lake Superior State University

AREAS OF SPECIAL INTEREST:

Materials Chemistry

PROFESSIONAL EXPERIENCE:

Research Assistant, D. C. Johnson Research Group, University of Oregon, 2016-2020

Research Assistant, Iretski Research Group, Lake Superior State University, 2013-2015

Research Experience Undergraduate Intern, Lonergan Research Group, University of Oregon, 2014

Research Experience Undergraduate Intern, Ford Research Group, University of Oregon, 2013

GRANTS, AWARDS, AND HONORS:

National Science Foundation Graduate Research Fellowship, University of Oregon, 2017

Graduate Student Award for Excellence in the Teaching of Chemistry, University of Oregon, 2016

LSSU Board of Trustees Distinguished Scholarship, Lake Superior State University, 2011 -2015

PUBLICATIONS:

Hamann, D. M.; Bardgett, D.; Cordova, D. L. M.; Maynard, L. A.; Hadland, E. C.; Lygo, A. C.; Wood, S. R.; Esters, M.; Johnson, D. C. Sub-Monolayer Accuracy in Determining the Number of Atoms Per Unit Area in Ultrathin Films Using X-ray Fluorescence. *Chem. Mater.* **2018,** 30, 6209-6216.

Hamann, D. M.; Lygo, A. C.; Esters, M.; Merrill, D. R.; Ditto, J.; Sutherland, D. R.; Bauers, S. R.; Johnson, D. C. Structural Changes as a Function of Thickness in $[(SnSe)_{1+\delta}]_m TiSe_2$ Heterostructures. *ACS Nano.* **2018**, *12*, 1285–1295.

Hamann, D. M.; Hadland, E.C.; Johnson, D.C. Heterostructures Containing Dichalcognides- New Materials with Predictable Nanoarchitectures and Novel Emergent Properties. *Semicond. Sci. Tehcnol.* **2017,** *32*, 1-27.

Hamann, D. M.; Merrill, D. R.; Bauers, S. R.; Mitchson, G.; Ditto, J.; Rudin, S. P.; Johnson, D. C. Long-Range Order in $[(SnSe)_{1.2}]_1[TiSe_2]_1$ Prepared from Designed Precursors. *Inorg. Chem.* **2017**, *56* (6), 3499-3505.

Hamann, D. M.; Bardgett, D.; Bauers, S. R.; Mroz, A. M.; Hendon, C. H.; Medlin, D. L.; Johnson, D. J.; Influence of Nanoarchitecture and Charge Donation on Electrical Transport Properties in $[(SnSe)_{1+\delta}][TiSe_2]_q$ Heterostructures. *Submitted to JACS April 2020.*

Hamann, D. M.; Rudin, S. P.; Asaba, T.; Ronning, F.; Cordova, D. L. M.; Lu, P., Johnson, D. C. Emergent Structures and Properties in Interface Stabilized 2D-Layers. *Submitted to JACS May 2020.*

Göhler, F.; Hamann, D.M.; Rösch, N.; Wolff, S.; Logan, J.T.; Fischer, R.; Speck, F.; Johnson, D.C.; Seyller, T. Electronic Structure of Designed $[(SnSe)_{1+\delta}]_m[TiSe_2]_2$ Heterostructure Thin Films with Tunable Layering Sequence. *JMR.* **2019**, *34,* 1965-1975

Bauers, S. R.; Hamann, D. M.; Patterson, A.; Perkins, J.; Talley, K. R.; Zakutayev, A. Compostion, Structure, and Semiconducting Properties of $Mg_xZ_{2-x}N_2$ Thin Films. *JJAP.* **2019,** *58*, SC1015.

Choffel, M. A.; Hamann, D. M.; Joke, J.A.; Cordova, D. M. L.; Johnson, D. C. The Reaction between Mn and Se Layers. *ZAAC*. **2018,** *664,* 1875 – 1880.

Chen, J.; Hamann, D. M.; Choi, D.; Poudel, N.; Shen, L.; Shi, L.; Johnson, D. C.; Cronin, S. Enhanced Cross-Plane Thermoelectric Transport of Rotationally Disordered $SnSe_2$ via Se-Vapor Annealing. *Nano Lett.* **2018**, *18*, 6876 – 6881.

Lygo, A. C.; Hamann, D. M.; Moore, D. B.; Merrill, D. R.; Ditto, J.; Esters, M.; Orlowisz, J.; Wood, S. R.; Johnson, D. C. Formation and Decomposition of Kinetically Stable $[(BiSe)_{1+\delta}]_m[TiSe_n]$ Compounds. *J. Am. Chem. Soc.* **2018**, *140*, 3385–3393.

Woods, K. N.; Hamann, D. M.; Page, C. J. Composition-Property Relationships in High- κ La X Zr 1-X O Y Thin Films from Aqueous Solution. *Solid State Sci.* **2018**, *75*, 34–38.

Gunning, N.S.; Dankwort, T.; Falmbigl, M.; Ross, U.; Mitchson, G.; Hamann, D.M.; Lotnyk, A.; Kienle, L.; Johnson, D.C. Expanding the Concept of van der Waals Heterostructures to Interwoven 3D Structures. *Chem. Mater.* **2017** , *29*, 8292–8298.

Li, Z.; Bauers, S. R.; Poudel, N.; Hamann, D.; Wang, X.; Choi, D. S.; Esfarjani, K.; Shi, L.; Johnson, D. C.; Cronin, S. B. Cross-Plane Seebeck Coefficient Measurement of Misfit Layered Compounds $(SnSe)_N$ $(TiSe_2)_N$ (N = 1,3,4,5). *Nano Lett.* **2017**, *17*, 1978-1986.

Wood, S. R.; Merrill, D. R.; Mitchson, G.; Lygo, A. C.; Bauers, S. R.; Hamann, D. M.; Sutherland, D. R.; Ditto, J.; Johnson, D. C. Modulation Doping in Metastable Heterostructures via Kinetically Controlled Substitution. *Chem. Mater.* **2017**, *29* , 773-779.

Beekman, M.; Bauers, S. R.; Hamann, D. M.; Johnson, D. C. Charge Transfer in Thermoelectric Nanocomposites: Power Factor Enhancements and Model Systems. In Advanced Thermoelectric Materials.

ACKNOWLEDGMENTS

During my time at the University of Oregon I have had the distinct pleasure of working with a wide variety of scientist locally, nationally, and internationally. I would like to extend thanks to all of these researchers whose collaborations have allowed me to complete this work.

I would like to thank my advisor, Professor David C. Johnson for willingly accepting me into his group. Your continual patience, guidance, and encouragement has modeled me into the scientist I am today. Thank you- I can't imagine being as successful or productive without you. I would also like to extend a special thank you to my mentor Dr. Sage Bauers. Almost four years ago you passed the torch onto me. I hope I have kept it burning bright. I would now like to pass it on to Alex and Aaron. Your initial and continual teaching and encouragement has allowed me to achieve more than I ever expected possible. Thank you to the previous DCJ lab members Erik Hadland, Marco Esters, Devin Merrill, Jeffrey Ditto, Gavin Mitchson, Kyle Hite, and Suzannah Wood.

I had the distinct pleasure of mentoring and working with the next set of DCJ lab members: Marisa Choffel, Renae Gannon, Aaron Miller, and Alexander Skochko. You have all provided me with many laughs and emotional support. I would especially like to thank Aaron and Alex, I hope I have inspired you as much as you have inspired me.

I would like to thank the wonderful undergraduate students who I had the privilege of working with during my Ph.D. Alex Lygo, thank you

for training me. Jordan Joke, Jake Logan, and Dylan Bardgett, thank you for sticking with me as I learned, and we grew as scientists together.

I have had the honor of working with many collaborators from across the globe including Sven Rudin, Saskia Fischer, Steve Cronin, Filip Ronning, Dennice Roberts, Doug Medlin, and Jihan Chen. Thank you all for your scientific contributions and general encouragements.

I would like to acknowledge funding from the National Science Foundation under grant GRFP-1309047. The Advanced Photon Source at Argonne National Laboratory is a user facility under the Office of Science. It is supported by the DOE (contract no. DE-AC02-06CH11357). Electron microscopy facilities at PNNL are supported under DOE contract no. DE-AC05-76rL01830. I would like to thank the National Center for Electron Microscopy at Lawrence Berkley National Lab.

Thank you to CAMCOR and the UO machine shop including Clif Dax, Kris Johnson, and Jeffrey Garmin, for your extensive knowledge and support. Thank you to my class professors and committee.

Finally, I would like to thank my family, friends, and especially my partner Andy Hicks. Without all of your love and support I would not have been able to achieve this dream. Andy thank you for moving across the country to support me in this journey and for being my rock throughout this process. I'm so excited to see what our next adventure holds and thankful we are embarking on it together.

To my parents, who encouraged me to reach for the stars and never give up.

TABLE OF CONTENTS

Chapter Page

I. HETEROSTRUCTURES CONAINTING DICHALCOGENIDES-NEW MATERIALS WITH PREDICTABLE NANOARCHITECTURES AND NOVEL EMERGENT PROPERIES 1

1.1 Introduction 1

1.2 Origins of Emergent Properties 8

1.2.1 Changes in Band Structure Due to Removing Adjacent Layers 8

1.2.2 Finite Size Effects 10

1.2.3 Structural Changes with Layer Thickness 12

1.2.4 Strain 15

1.2.5 The Presence of Adjacent Layers 17

1.3 Heterostructures Containing Transition Metal Dichalcogenides 18

1.3.1 Synthesis 20

1.3.2 Characterization 23

1.4 Properties 34

1.4.1 Semiconducting Heterostructures 35

1.4.2 Metal Heterostructures 39

1.5 Summary 48

1.6 Dissertation Overview 50

1.7 Bridge 53

Chapter Page

II. SUB-MONOLAYER ACCURACY IN DETERMINING THE NUMBER OF ATOMS PER UNIT AREA IN ULTRATHIN FILMS USING X-RAY FLUORESCENCE 54

2.1 Introduction 54

2.2 Materials and Methods 57

2.3 Results and Discussion 58

2.4 Conclusion 71

2.5 Bridge 71

III. SYNTHESIS AND CHARACTERIZATION OF DESIGNED PRECUSORS PREPARED VIA THE MODULATED ELEMENTAL REACTANTS METHOD 72

3.1 Modulated Elemental Reactants Method Principle 72

3.2 Synthesizing Thin Films and Heterostructures Via MER 74

3.3 Informing MER Synthesis Via XRF 79

3.4 Structural and Compositional Characterization 83

3.5 Electrical Transport Property Characterization 84

3.6 Bridge 85

IV. ENHANCED CROSS-PLANE THERMOELECTRIC TRANSPORT OF ROTATIONALLY-DISORDERED SNSE2 VIA SE VAPOR ANNEALING 86

4.1 Introduction 86

4.2 Results and Discussion 88

Chapter Page

4.2.1 Thermoelectric Device Fabrication and Measurement 88

4.2.2 Film Composition and Thickness 92

4.2.3 Control Experiments 94

4.3 Conclusions 95

4.4 Materials and Methods 96

4.5 Bridge 97

V. INVESTIGATING THE FORMATION OF $MOSE_2$ AND $TiSe_2$ FILMS FROM ARTIFICALLY LAYERED PRECURSORS 99

5.1 Introduction 99

5.2 Materials and Methods 101

5.3 Results and Discussion 102

5.4 Conclusion 117

5.5 Bridge 118

VI. LONG RANGE ORDER IN $[(SNSE)_{1.2}]_1[TISE_2]_1$ PREPARED FROM DESIGNED PRECURSORS 119

6.1 Introduction 119

6.2 Materials and Methods 122

6.3 Results and Discussion 124

6.4 Conclusion 135

6.5 Bridge 136

VII. STRUCTURAL CHANGES AS A FUNCTION OF THICKNESS IN $[(SNSE)_{1+\delta}]_M TISE_2$ HETEROSTRUCTURES 137

Chapter ..... Page

7.1 Introduction 137

7.2 Results and Discussion 140

7.2.1 Synthesis 140

7.2.2 Structure 141

7.2.3 Calculations 150

7.2.4 Transport Properties 156

7.3 Conclusions 160

7.4 Materials and Methods 161

7.5 Bridge 164

VIII. INFLUENCE OF NANOARCHITECTURE ON CHARGE DONATION AND ELECTRICAL TRANSPORT PROPERTIES IN $[(SNSE)_{1+\delta}][TISE_2]_Q$ HETEROSTRUCTURES 165

8.1 Introduction 165

8.2 Materials and Methods 168

8.3 Results and Discussion 171

8.3.1 Synthesis 171

8.3.2 Structural Characterization 172

8.3.3 Electrical Transport Properties 179

8.3.4 Computational Calculations and Models 188

8.4 Conclusions 191

8.5 Bridge 192

Chapter Page

IX. INVESTIGATING SIZE EFFECTS IN $[(SNSE)_{1+\delta}]_M[TISE_2]_N$ HETEROSTRUCTURE COMPOUNDS 193

9.1 Introduction 193

9.2 Materials and Methods 194

9.3 Results and Discussion 197

9.3.1 Synthesis 197

9.3.2 Structure 198

9.3.3 Transport Properties 208

9.3.3 Temperature Dependent Diffraction 215

9.4 Conclusions 216

9.5 Bridge 217

X. ELECTRONIC STRUCTURE OF DESIGNED $[(SNSE)_{1+\delta}]_M[TISE_2]_2$ HETEROSTRUCTURE THIN FILMS WITH TUNABLE LAYERING SEQUENCES 219

10.1 Introduction 219

10.2 Results and Discussion 221

10.2.1 Synthesis and Structure 221

10.2.2 Characterization of Electronic Structure via XPS 228

10.2.3 Discussion of XPS Results 233

10.3 Conclusions 239

10.4 Materials and Methods 240

10.4.1 Synthesis 240

Chapter Page

10.4.2 Diffraction 241

10.4.3 HAADF-STEM 241

10.4.4 Photoelectron Spectroscopy 242

10.5 Bridge 243

XI. SYNTHESIS AND CHARACTERIZATION OF $[(PBSE)_{1+\delta}]_4[TISE_2]_4$ HETEROSTRUCTURE ISOMERS 244

11.1 Introduction 244

11.2 Materials and Methods 246

11.3 Results and Discussion 248

11.3.1 Structure 248

11.3.2 Formation Discussion 262

11.3.3 Electrical Transport Properties 265

11.4 Conclusions 269

11.5 Bridge 269

XII. THE REACTION BETWEEN MN AND SE LAYERS 271

12.1 Introduction 271

12.2 Results and Discussion 273

12.3 Conclusions 282

12.4 Materials and Methods 282

12.5 Bridge 283

XIII. EMERGENT STRUCTURES AND PROPERTIES IN INTERFACE STABILIZED 2D-LAYERS 285

Chapter Page

13.1 Introduction 285

13.2 Materials and Methods 287

13.2.1 Density Functional Theory 287

13.2.2 Materials 287

13.2.3 Heterostructure Synthesis via Modulated Elemental Reactants 288

13.2.4 Compositional and Structural Characterization 288

13.2.5 Transport Measurements 288

13.3 Results and Discussion 289

13.4 Conclusions 302

13.5 Bridge 303

XIV. CONCLUSIONS, SUMMARY, AND FUTURE OUTLOOK..... 304

APPENDICES 311

A. SUPPORTING INFORMATION FOR CHAPTER 2 311

B. SUPPORTING INFORMATION FOR CHAPTER 4..... 318

C. SUPPORTING INFORMATION FOR CHAPTER 5..... 324

D. SUPPORTING INFORMATION FOR CHAPTER 7 328

E. SUPPORTING INFORMATION FOR CHAPTER 8..... 335

F. SUPPORTING INFORMATION FOR CHAPTER 9 338

G. SUPPORTING INFORMATION FOR CHAPTER 11..... 341

H. SUPPORTING INFORMATION FOR CHAPTER 13..... 344

REFERENCES CITED 345

LIST OF FIGURES

Figure Page

1.1. Transition metal dichalcogenides are naturally occurring layered materials with highly anisotropic bonding. Weak van der Waals forces along the c axis enable them to be easily cleaved to obtain monolayer structures, while strong covalent bonds in the ab plane preserve the crystalline structure within a layer during cleaving. The schematic illustrates the structure of five layers (left), two layers (center) and a monolayer (right). The arrows represent the thinning of the sample via cleaving. 2

1.2 Heterostructures are local minima in the free energy Landscape and different stacking arrangements will have different energies. The kinetic barrier to forming the thermodynamic mixture of bulk constituents is a consequence of the activation energy for solid-state diffusion..... 3

1.3. Misfit layer compounds are thermodynamically stable heterostructures of alternating layers of rock salt and transition metal dichalcogenide. A defining feature of this class of materials is that they usually possess a single commensurate in-plane lattice parameter..... 6

1.4. Structural schematics of heterostructures composed of various 2D-materials. a. MoS_2 and WS_2 - yellow represents S, purple represents W and rose represents Mo. The constituent layers are held together by weak van der Waals interactions. b. SnSe and $TiSe_2$ - green represents Se, magenta represents Sn, and blue represents Ti. The SnSe layer does not have a layered structure but is a fragment of a distorted rock salt structure. c. PbSe and $TiSe_2$ (green represents Se, blue represents Ti, and maroon markers represent Pb)..... 7

1.5. Schematic of rotationally disordered constituent layers within a heterostructures. Lattice mismatch between constituent layers will increase the distribution of rotation angles between layers. 12

Figure Page

1.6. As rock salt bulk compounds are reduced to ultrathin dimensions, the lattice becomes increasingly “puckered” such that metal cations extend into the van der Waals gap while the chalcogens occupy atomic positions on the interior of the bilayer. (a) the bulk rock salt crystal structure (b) Two stacked bilayers of a puckered rock salt structured constituent (c) Structure of a single puckered 2D rock salt bilayer. The metal atoms are shown in red and the chalogen atoms are shown in yellow. 15

1.7. Synthesis of metastable heterostructures from a precursor with defined amounts of elements deposited the precursor is annealed at low temperatures to self-assemble the desired heterostructure..... 23

1.8. Calculated (blue) and experimental (red and yellow) XRR patterns for $MoSe_2$ films containing 8 layers..... 26

1.9. Locked-coupled theta-2theta X-ray diffraction used to understand the layer thickness of stacked unit cells of a PbSe-$MoSe_2$ heterostructure. A Rietveld refinement was conducted to optimize the structure to understand where planes of atoms are located. The inset shows a schematic of the structure of the compound with parameters that can be determined using Rietveld refinement. 27

1.10. In-plane diffraction of $MoSe_2$ films with 4, 8, and 24 layers (blue, red, and yellow, respectively). All maxima can be indexed as (hk0) reflections of hexagonal $MoSe_2$ to determine the basal plane lattice parameter. 28

1.11. The in-plane diffraction pattern of a 24-layer $MoSe_2$ film is shown in blue. The yellow pattern is an in-plane scan of a $MoSe_2$- SnSe- $NbSe_2$ heterostructure. The additional maxima can be indexed as SnSe and $NbSe_2$ reflections, enabling the lattice parameters of all three constituent structures to be determined. 29

1.12. Reciprocal space map of a PbSe WSe_2 heterostructure. For both PbSe and WSe_2 there are no distinct reflections that correspond to the super-lattice period, only streaking indicating extensive rotational disorder between constituents.... 30

Figure Page

1.13. Schematic illustrations of the 6 possible sequences of layers requiring 4 dichalcogenide and 4 rock salt bilayers without repeating a portion of the sequence. Repeating one layer of each structure 4 times or two layers of each structure twice create an eight-layer repeat pattern with four layers of each structure, but segments are repeated..... 31

1.14 Band alignments in semiconducting heterostructures fall into one of the three categories depicted. In type I heterostructures, the band gap of one material falls entirely within the band gap of the other material. In type II heterostructures, the two band gaps are staggered such that $CB_2 < CB_1$ and $VB_2 < VB_1 < CB_2$. In type III, the band gap of one material falls entirely within The valence band of the other material..... 36

1.15. In type one alignment of the bands, photons can be absorbed if the energy of the incident light is above the respective band gaps, forming excitons. The kinetics of charge transfer between the constituents (labeled 2) and the ratio of initial absorption between the two constituents will determine the relative intensities of light emitted at the different band gap energies. In type II alignment, formation of the exciton occurs in one constituent layer and electrons will transfer into the adjacent material to achieve a lower energy state, resulting in an interlayer exciton. Since the constituents are separated only by the small van der Waals gap, the two charges remain bound..... 39

2.1. The change in the XRF intensity as a function of the thickness of material deposited as measured by quartz crystal monitors for a variety of different elements (shown with different colors and symbols). The error in the amount of material deposited for each element is shown for a single data point and when error bars are absent the error is the size of the marker. The lines are fits assuming that the XRF intensity is directly proportional to the amount of material deposited. Slopes for each line can be found in Table 2.1..... 60

Figure Page

2.2. Three different diffraction scans of a $[(PbSe)_{1+\delta}]_1$ $[NbSe_2]_1$ film. (a) XRR scan. (b) Specular XRD scan. (c) Grazing incidence in-plane XRD scan. The crystallographic indices are given above each reflection and were used to determine the total film thickness from (a), the c-axis unit cell parameter from (b) and the in-plane unit cell parameters from (c). 64

2.3. Graphs of the XRF intensity versus the number of atoms per unit area of several elements calculated from diffraction information such as that shown in Figure 2.2 for a number of different films..... 67

2.4. XRF intensity versus the total number of Se atoms per unit area determined from diffraction information (black), from films of $SnSe_2$ (red) and from films of $TiSe_2$ (blue). For the $SnSe_2$ and $TiSe_2$ films, the information in Figure 2.3 was used to determine the number of cation atoms in these films from the measured Sn and Ti XRF intensities. These values were then used to calculate the number of Se atoms in each of the films..... 68

2.5. The Sn-La emission intensity from a film with 0.11 Sn/Å^2 and the blank Si substrate before deposition of Sn. 69

2.6. Measured and calculated XRR patterns of an 8-layer $MoSe_2$ film showing the application of this XRF method to prepare films containing a finite number of layers. The inset HAADF-STEM image shows further evidence of the formation of 8 $MoSe_2$ layers..... 70

3.1. Schematic demonstrating the influence of having the correct precursor stoichiometry of A and B, but the wrong layer thickness to prepare a compound AB (a.) and the both the correct stoichiometry and layer thickness of A and B to prepare a layered compound of AB (b.)..... 73

3.2. A schematic of the physical vapor deposition chamber used to prepare MER precursor thin films. Under high vacuum conditions, pneumatic shutters open and close to deposit the vaporized material into a targeted structure. The inset at the right shows a depiction of building up the atomic elemental layers for a binary film. 76

Figure Page

3.3. A schematic of a designed elemental precursor prepares by MER whose structure mimics the pattern for the desired heterostructure being converted to the desired heterostructure via “gentle annealing”..... 76

3.4. Annealing study data of a two constituent heterostructure material composed of SnSe and $TiSe_2$ demonstrating the evolution of the film as a function of annealing temperature where ‘AD’ is the sample as-deposited before annealing. Specular x-ray diffraction is shown in (a.) and In-plane x-ray diffraction is shown in (b.)..... 77

3.5. Schematic showing the stacking nature of the heterostructure, the individual constituent basal plane structures, and the observed rotational disorder between constituents for a material self-assemble upon heating form a designed precursor made my MER. 78

3.6. Structural schematic demonstrating the various series of heterostructure materials that can be achieved by modifying the precursor nanoarchitecture using the MER method. In this example MX is a rocksalt, TX_2 is a dichalcogenide, and $1+\delta$ represents the different in-plane area between the two constituents..... 79

3.7. Schematic demonstrating using elemental ratios determined by XRF and *c* – axis lattice parameters determined from specular X-ray Diffraction to systematically calibrated the correct about of material needed per layer in the designed precursor to prepare the targeted heterostructure..... 81

3.8. Measured XRF counts normalized to the amount of each element deposited in a thin film elemental precursor for Se (a.) and Ti (b.) demonstrating the deposition behavior observed for the system 83

4.1. (a-d) Schematic diagrams of the device fabrication process and (e) optical image of the completed device..... 89

Figure Page

4.2. Schematic illustration of a precursor designed to form a layered structure of SnSe when annealed in an inert atmosphere under optimized conditions. Upon heating in Se-vapor for 30 minutes at 300 °C, the layered SnSe converts to $SnSe_2$. Se and Sn atoms are represented in orange and blue, respectively..... 90

4.3. Temperature calibration of the bottom RTD of a 50 nm $SnSe_2$ film after Se-vapor annealing. (a) The resistance of the RTD measured at different temperatures. (b) Normalized resistance (R/R_0, where R_0 is the resistance at 300 K) plotted as a function of temperature. (c) The resistance changes of the RTD under various heating currents. (d) Temperature change of the metal RTD plotted as a function of heating power 90

4.4. Cross-plane Seebeck coefficient of the 50 nm SnSe film before Se-vapor annealing. 91

4.5. Cross-plane Seebeck coefficient of the 50 nm SnSe2 after Se-vapor annealing 92

4.6. Specular X-ray diffraction (XRD) patterns of SnSe films. Both samples were annealed in a nitrogen atmosphere and one was subsequently annealed in a selenium atmosphere (the blue pattern) resulting in a conversation to $SnSe_2$. Miller indices are provided for select reflections. The intensity was plotted on a log scale to enhance weak reflections. 93

4.7. In-plane X-ray diffraction (XRD) patterns for targeted SnSe samples. Both samples were annealed in a nitrogen atmosphere and one was subsequently annealed in a selenium atmosphere (the blue pattern) resulting in a conversation to $SnSe_2$. The reflections are indexed to SnSe and $SnSe_2$ with one substrate peak (marked with the asterisk) in the Se-vapor annealed sample..... 94

5.1. XRD patterns from an annealing study of an as-deposited Mo|Se precursor. The annealing temperatures are presented above the scans. For the scan at 650°C, X-ray reflectivity is also included. Indices are provided above the observed reflections. 104

5.2. Grazing incidence in-plane diffraction of the $MoSe_2$ precursor after annealing at 650°C. The Miller indices are shown above the reflections. 105

Figure Page

5.3. $MoSe_2$ crystal quality as determined by specular diffraction reflection intensity and peak width shown as a function of Mo|Se precursor composition. 106

5.4. XRD diffraction data of a Ti|Se sample with a starting composition of 1:2.24 (Ti:Se) annealed for 30 minutes in an inert N_2 atmosphere at the indicated temperatures. Indexes are shown above the observed reflections and the scan with the highest intensity and lowest linewidths is shown in red..... 109

5.5. Representative specular (a.) and in-plane (b.) x-ray diffraction patterns of Ti|Se thin films with various compositions. All observed reflections that correspond to the $TiSe_2$ crystal structure are indexed in black. Reflections marked with an asterisk observed in the specular pattern are attributed to the Si substrate. Reflections for the observed Ti_2Se impurity phase are indexed in blue. Black curves show the diffraction pattern of the precursor, while red curves show the pattern for the films annealed at 350 °C. Additional diffraction patterns can be found in SI Figure C.2., more closely matching the expected positions for $TiSe_2$ shown as vertical lines..... 112

5.6. In-plane and *c*-axis crystallite size determined from the x-ray diffraction patterns as a function of Ti|Se composition. As-deposited parameters are shown in black and annealed parameters are shown in red. The diffraction patterns used to determine these parameters are found in Figure 5.5 and Figure C.2..... 113

5.7. Experimental specular XRD pattern (red) and the theoretical Laue oscillations expected for 81-unit cells of $TiSe_2$ (black)..... 115

5.8. Proposed atomic level pictures for the evolution of Mo|Se (a) and Ti|Se (b) precursors as they are annealed to form crystalline $MoSe_2$ and $TiSe_2$. There is much more interdiffusion during deposition of the lighter Ti atoms, resulting in larger crystalline domains in the as-deposited $TiSe_2$ precursor relative to the Mo|Se precursor..... 116

Figure Page

6.1. In-plane diffraction data for two $(SnSe)_{1.2}TiSe_2$ samples. The reflections originating from SnSe are marked in bold, and those from $TiSe_2$ in italics. The inset in the top right corner of the figure emphasizes the splitting of the SnSe reflections, indicating the existence of a rectangular basal plane 125

6.2. Representative HAADF-STEM image of a $(SnSe)_{1.2}TiSe_2$ heterostructure. The layers of SnSe are marked with pink boxes and layers of $TiSe_2$ are marked with blue boxes. The labels on the right side of the image reflect the primary plane-normal orientation, if resolved, of that layer 126

6.3. FFT of HAADF STEM image shown in Figure 6.1. The (00*l*) and $TiSe_2$ (11*l*) intensity profiles are plotted in the inset with the y-axis corresponding to the location in the FTT of HAADF STEM image. 128

6.4. Top) Reciprocal space map from a $(SnSe)_{1.2}TiSe_2$ compound at two different constant *hk* postions with a varying *l* position. The bright regions indicate coherence between layers. (Bottom) A line profile extracted from the reciprocal space map along the (22*l*) SnSe direction is overlaid onto the (00*l*) diffraction pattern. The presence of coincident maxima in the overlaid scans suggests long range ordering within the sample 129

6.5. The top and bottom left schematics depict a top down view of the SnSe and $TiSe_2$ basal plane. The schematics on the right show SnSe and $TiSe_2$ layer structures when looking down different zone axes. Gold markers indicate Se, pink represent Sn, and blue represents Ti. 131

6.6. (left) Schematic showing a DFT unit cell with islands of SnSe in two different orientations between layers of $TiSe_2$ with two different "leanings." The red balls represent Ti, the gray represent tin and selenium is represented by the green balls. (right) Plan view of the $(SnSe)_{1.2}TiSe_2$ layered compound with a rotational angle of 0° between layers (bottom) and a 15° rotation between layers (top). 134

6.7. Schematic showing the top down view of the stacking between the SnSe rock rocksalt (represented by pink atoms connected by black bonds) and the $TiSe_2$ dichalcogenide (structure with green bonds connecting the yellow Se atoms and blue Ti atoms) layers which is consistent with the theoretical and experimental data collected. 135

7.1. Specular X-ray diffraction scans of $[(SnSe)_{1+\delta}]_mTiSe_2$ compounds (m = 1-4). The intensity is plotted on a log scale to enhance weak reflections. Miller indices are provided for select reflections and asterisks indicate reflections from the Si substrate 143

7.2. (a) In-plane diffraction pattern of the $[(SnSe)_{1+\delta}]_mTiSe_2$ compounds where $1 \leq m \leq 4$. The reflections are indexed to either SnSe or $TiSe_2$, with a single impurity peak being indexed to $SnSe_2$ (denoted with a + symbol). (b) Expansion of the high-angle region emphasizing the change in the SnSe reflections at approximately 61° and 69° that occurs as m is increased from 1 to 4. (c) Expansion of a higher angle region that highlights the reflection differences between the m = 1 and $m \geq 2$ in-plane diffraction patterns..... 145

7.3. Schematic of shifting atomic positions of the SnSe constituent of $[(SnSe)_{1+\delta}]_mTiSe_2$ causing a redefinition of the in-plane unit cell from the m = 1 compound to the $m \geq 2$ compounds. 147

7.4. HAADF-STEM images of $[(SnSe)_{1+\delta}]_mTiSe_2$ compounds ($m \leq 3$). (a) An image of $(SnSe)_{1.20}TiSe_2$ showing the consistent alternation of the two constituent structures throughout the entire film. The bright layers correspond to SnSe while the darker layers correspond to $TiSe_2$. (b) Enlarged image of $[(SnSe)_{1.20}]_1TiSe_2$ showing the local atomic structure. Repeating orientations in some areas of the film support previous reports of regions of long-range coherence. (c) A magnified image of $[(SnSe)_{1.24}]_2TiSe_2$ showing the pairing of the SnSe layers. Multiple orientations for the same constituent are observed throughout the film demonstrating the turbostratic disorder present in all compounds. (d) An expanded image of $[(SnSe)_{1.20}]_3TiSe_2$ showing the disorder between the different bilayers of SnSe 148

Figure Page

7.5. An expanded HAADF-STEM image showing two different SnSe orientations within the same layer of $[(SnSe)_{1+\delta}]_mTiSe_2$ 150

7.6. Relaxed structures of two SnSe bilayers for the different polytypes used in the DFT calculations viewed along the [010] axis. Sn atoms are blue and Se atoms are red 152

7.7. In-plane lattice parameters for the *a*-axis (a), (b) and the *b*-axis (c), (d) of the different SnSe polymorphs as a function of the number of bilayers. (a) and (c) were calculated without a van der Waals functional. (b) and (d) were calculated with the DFT-D2 van der Waals functional. Including the DFT-D2 van der Waal's functional does not change the trends in lattice parameters of the polymorphs as the number of bilayers is increased. The lattice parameters for the NaCl and staggered structures are given in their primitive lattices. The experimental lattice parameters for $m = 1$ were normalized to give a better comparison to the lattice parameters for $m > 1$ 153

7.8. Temperature dependent resistivity measurements of the $[(SnSe)_{1+\delta}]_mTiSe_2$ compounds with $m = 1$-4. Measurements of two different $m = 1$ samples are plotted to show reproducibility of their behavior..... 157

7.9. Temperature dependent Hall coefficients for $[(SnSe)_{1+\delta}]_mTiSe_2$ compounds. 159

8.1. XRR patterns of representative $[(SnSe)_{1+\delta}][TiSe_2]_q$ heterostructures after low temperature annealing. The (00*l*) Bragg reflections are indexed and are different from the low intensity maxima between the Bragg reflections known as Kiessig fringes that are due to the finite thickness of the films 173

8.2. Specular diffraction patterns of the $[(SnSe)_{1+\delta}][TiSe_2]_q$ heterostructures. All reflections can be indexed as (00*l*) Bragg reflections and indices for select reflections are indicated in the pattern. The asterisk marks a Si reflection from the substrate present in particular patterns..... 174

Figure Page

8.3. In-plane diffraction patterns of $[(SnSe)_{1+\delta}][TiSe_2]_q$ heterostructures. All reflections can be indexed to (hk0) planes of either $TiSe_2$ or distorted SnSe, with the relative intensities of $TiSe_2$ reflections increasing with increasing q. 176

8.4. HAADF-STEM images and FFT's of the $[(SnSe)_{1+\delta}]_1[TiSe_2]_3$ (a and b), $[(SnSe)_{1+\delta}]_1[TiSe_2]_4$ (c and d), and $[(SnSe)_{1+\delta}]_1[TiSe_2]_8$ (e and f) respectively, and a higher magnification HAADF-STEM image of a region of the $[(SnSe)_{1+\delta}]_1[TiSe_2]_4$ sample (g). 178

8.5. Seebeck coefficients for $[(SnSe)_{1+\delta}]_1[TiSe_2]_q$ heterostructures plotted as a function of the number of $TiSe_2$ layers in the unit cell, q (a.). Temperature-dependent Hall coefficients (b.) and resistivity data for the $[(SnSe)_{1+\delta}][TiSe_2]_q$ heterostructures. The resistivity data are plotted on two different resistivity Scales (c. q = 1 - 6 and d. q = 8 - 15) so the temperature dependence in samples with thinner $TiSe_2$ layer blocks can be observed. The solid lines in b. are models calculated from a two-carrier model with variable range hopping at low temperatures as discussed in the text which describes the entire temperature regime. The dashed lines in b., c., and d. show the fits to a VRH mechanism, which describes the Hall coefficient and resistivity at low temperatures 181

8.6. The values of the number of carriers that can become mobile for the low temperature activated process, n_o, plotted as a function of the number of $TiSe_2$ layers in the sample. n_o values were obtained by fitting the low temperature transport data using a single band, variable range hopping model. The dashed line assumes that n_o should vary as $n_{SnSe \rightarrow TiSe2} / q + 1$, where q is the number of $TiSe_2$ layers in the heterostructures and use the $n_{SnSe \rightarrow TiSe2}$ obtained from the $[(SnSe)_{1+\delta}]_1[TiSe_2]_1$ compound..... 184

8.7. Vacuum aligned Density of States for SnSe and $TiSe_2$ slab models. The frontier valence of SnSe is ~1.2 eV above that of $TiSe_2$, indicating that charge transfer from SnSe to $TiSe_2$ would occur at the interface between them..... 189

9.1. X-ray reflectivity patterns of the series of layered compounds, $[(SnSe)_{1+\delta}]_m[TiSe_2]_n$, $m = n$, after annealing at 350°C for 30 minutes in a N_2 environment..... 199

Figure Page

9.2. XRF data was collected from the annealed heterostructures and is plotted in atoms / Å^2, normalized to the total number of crystallized SnSe and $TiSe_2$ layers that make up each nanoarchitecture. The integrated and background corrected values normalized for the number of crystallized repeat units for each element are shown with a symbol (red circle – Se, blue square – Sn, green triangle – Ti) and the targeted value for each element is shown as a dotted line. 201

9.3. Specular X-ray diffraction patterns of annealed $[(SnSe)_{1+\delta}]_m[TiSe_2]_n$ heterostructures (a.) and a linear regression of the *c*-lattice parameter vs. the number of SnSe and $TiSe_2$ layers in each repeating unit (b.). 202

9.4. Specular X-ray diffraction patterns of annealed $[(SnSe)_{1+\delta}]_m[TiSe_2]_n$ heterostructures (a.) and a linear regression of the *c*-lattice parameter vs. the number of SnSe and $TiSe_2$ layers in each repeating unit (b.). 205

9.5. HAADF-STEM images of $[(SnSe)_{1+\delta}]_m[TiSe_2]_n$,($m$ = n = 1, 2, 3) nanolaminates showing templated interfaces for m=n=1 and several stabilized structures for m=n=2. 208

9.6. Temperature dependent Hall coefficient measurements for $[(SnSe)_{1+\delta}]_m[TiSe_2]_n$ heterostructures with m, n = 1 – 8. 212

9.7. Temperature dependent resistivity measurements of $[(SnSe)_{1+\delta}]_m[TiSe_2]_n$ heterostructures with m, n = 1 – 8. 213

9.8. Temperature-dependence of *a*- and *b*-axis lattice parameters of an $[(SnSe)_{1+\delta}]_m[TiSe_2]_n$, m, n = 4 heterostructure. 216

10.1 XRR (a), Specular XRD (b), and in-plane XRD (c) of the representative $[(SnSe)_{1+\delta}]_m[TiSe_2]_2$ sample with m = 3 as deposited (AD) and annealed at various temperatures. The diffraction pattern of the sample annealed at 350 °C and studied by HAADF-STEM and XPS is highlighted. Dashed lines indicate the position of the Bragg reflections expected for a well crystalized sample. 225

10.2. Representative HAADF-STEM images of a $[(SnSe)_{1+\delta}]_m[TiSe_2]_2$ sample showing the entire thickness of the film (a), a region with a pristine (3, 2) layering structure (b), and a region where layering defects occur (c). A step fault is marked with a solid purple line demonstrating the bottom border of the $TiSe_2$ layer and a dashed yellow line demonstrating the top of the SnSe layer. There is a layer of mixing between the two layers that is outlined by the two borders of the SnSe and $TiSe_2$ layer, respectively. 226

10.3. Specular (a) and in-plane (b) XRD patterns of the SnSe, $TiSe_2$, and $[(SnSe)_{1+\delta}]_m[TiSe_2]_2$ heterostructures with m = 1, 2, 3, and 7. 227

10.4. Normalized XPS Sn3*d* (a), Ti2*p* (b), and Se3d (c) core-level spectra as well as valence band (d) spectra of binary SnSe (bottom row), binary $TiSe_2$ (top row), and $[(SnSe)_{1+\delta}]_m[TiSe_2]_2$ heterostructures with m = 1, 2, 3, and 7. Dashed lines are added as a guide to the eye, indicating the position of the Sn3*d* and Ti2*p* core levels in the heterostructure. 229

10.5. Fit of the Se3*d* (a) and valence band (b) spectra using superpositions of the SnSe and TiSe2 components, shown exemplarily for $[(SnSe)_{1+\delta}]_2[TiSe_2]_2$. For the Se3*d* fit, the ratio of the two components was constrained using composition data. The inset in (b) shows the ratio of $SnSe/TiSe_2$ needed to adequately fit the data, showing a linear increase with m. 232

10.6. Energy diagram of the experimental binding energies of core levels and valence band maximum (VBM) in SnSe (left), $[(SnSe)_{1+\delta}]_m[TiSe_2]_2$ (middle), and $TiSe_2$ (right). The Sn3*d*, Se3*d*, and VBM show an energy shift in the heterostructure compared to the binary compound. 235

10.7. Energy diagram of the experimental binding energies of core levels and valence band maximum (VBM) in SnSe (left), $[(SnSe)_{1+\delta}]_m[TiSe_2]_2$ (middle), and $TiSe_2$ (right). The Sn3*d*, Se3*d*, and VBM show an energy shift in the heterostructure compared to the binary compound. 237

Figure Page

10.8. Valence bands of TiSe2 and $[(SnSe)_{1+\delta}]_3[TiSe_2]_2$ measured with UPS at different polar angles between sample surface and analyzer. Especially for larger angles, the Ti3*d* state at EF can be observed. In the heterostructure, the intensity of this Ti3*d* peak is increased, confirming a higher electron population in this state. 239

11.1. As-deposited XRR and XRD for a 2**1**1**2**1**1** isomer providing representative behavior observed in all of the $[(PbSe)_{1+\delta}]_4(TiSe_2)_4$ isomer heterostructures. 00*l* reflections, corresponding to the artificial layering, the crystalized $[(PbSe)_{1+\delta}]_4(TiSe_2)_4$ isomer heterostructure, and the impurity Ti_2S phase, are indexed in black, blue, and green, respectively. Additional as-deposited XRR patterns can be found in the supporting information Figure G.1..... 251

11.2. Experimental and simulated XRR patterns for the 3**2**1**2** structural isomer. The upper left panel focuses on the Kiessig fringes, indicating that the total film thickness is 491.4 Å. The upper right panel emphasizes the Laue oscillations, showing that 9-unit cells are present, not the 11 expected from the deposition sequence. The bottom panel compares the simulated and experimental patterns based on the complete model described in the text 252

11.3. Schematic representation of the variation of electron density through a unit cell for each of the $[(PbSe)_{1+\delta}]_4[TiSe_2]_4$ isomers 254

11.4. X-ray reflectivity patterns (in color) shown against simulated patterns created using models of the targeted isomers (in black) described in Figure 11.3. 256

11.5. Specular (a.) and in-plane (b.) XRD patterns of the $[(PbSe)_{1+\delta}]_4[TiSe_2]_4$ structural isomers. The indices of the observed reflections are shown above each reflection in the in-plane pattern and representative indices are indicated in the specular pattern..... 259

11.6. HAADF-STEM image of the 4**4** $[(PbSe)_{1+\delta}]_4[TiSe_2]_4$ structural isomer showing the entire film from substrate to surface..... 260

11.7. HAADF-STEM images of each isomer heterostructure highlighting the formation of the targeted nanoarchitecture, sharp interfaces between constituents, and rotational misregistration between layers. 261

11.8. Atomistic picture demonstrating the initial crystallization occurring in the material (a.) and a snapshot showing the movement of atoms and further growth of the crystals upon annealing (b.) The arrows demonstrate the concentration gradient of the metals and point to where the metals are diffusing. Upon deposition a layer of Ti_2Se forms and persists even after annealing. 264

11.9. Temperature dependent resistivity of 6 $[(PbSe)_{1+\delta}]_4(TiSe_2)_4$ isomer heterostructures, both measured (a.) and normalized (b.) values. 265

11.10. Temperature dependent carrier concentration (a.) and mobility (b.) of 6 $[(PbSe)_{1+\delta}]_4(TiSe_2)_4$ isomer heterostructures. Values are calculated assuming a single n-type band 267

11.11. Room-temperature Seebeck coefficients for each of the $[(PbSe)_{1+\delta}]_4(TiSe_2)_4$ isomer heterostructures. Colors correspond to nanoarchitecture and symbols correspond to precursor parameters. 268

11.12. Schematic demonstrating charge donation occurring in isomers containing different numbers of buried interfaces, the 4**4** (a.) and the 2**2**1**1**1**1** (b.). The SnSe layers are shown in red, the $TiSe_2$ is shown in blue, and purple arrows depict the charge donation from the SnSe to the $TiSe_2$ layers. The purple boxes indicter a single isomer repeating unit. 268

12.1. Summary of the composition and thickness of the prepared precursors. 274

12.2. Grazing incidence diffraction scans of the eight precursors before any annealing (a. films A1-D1 and b. films A2-D2). The dashed vertical lines at 32.9, 47.2, and 58.7° mark the locations of the (200), (220), and (222) reflections of the α-MnSe. 275

12.3. Grazing incidence diffraction scans collected for samples A1(a) and A2(b) as a function of annealing temperature. The (111) reflection of α-MnSe has been marked by an asterisk 277

12.4. Grazing incidence diffraction scans of samples B1 (a) and B2 (b) as a function of annealing temperature. 278

12.5. Grazing incidence diffraction scans collected from samples C1 (a) and C2 (b) as a function of annealing temperature. 279

12.6. Grazing incidence diffraction scans of samples D1 (a) and D2 (b) as a function of annealing temperature. 281

13.1. A schematic of the theoretical approach used to examine the kinetic stability of constituent compound candidates. A candidate model structure of an AB compound with a rock salt structure that remains intact when relaxed (a.). Also included is the top-down view of the promising system after relaxation, which emphasizes the recognizable structure as well as the systematic distortions from the initial model. A candidate model structure of an AB_2 compound which forms a fragment without long-range ordering when allowed to relax and its top down view (b.). 291

13.2. Example of an island structure before (a) and after (b) optimization. Sandwiched between a complete VSe_2 layer (only V shown in purple), the structure of nine Mn (red) and 24 Se (yellow) dramatically changes its bonding structure, enabled by the island structure..... 292

13.3. The grey plane in the quaternary phase diagram was explored for synthesizable heterostructures. There are no known ternary or higher order compounds in this phase diagram. The circles indicate systems that were computationally explored as described in the text. Systems that relaxed to ill-formed fragments that lack a recognizable pattern have red circles and systems that formed fragments with recognizable periodic structures have green circles. The results of synthetic attempts are shown as filled symbols. Red indicates that the nanoarchitecture of the MER precursor is destroyed during annealing. Green symbols indicate that the targeted heterostructure formed. Orange indicates that a heterostructure formed with a structure close to that of the computational search. Yellow indicates that the nanoarchitecture is enhanced on annealing, but the processing conditions have yet to be optimized. Representative HAADF-STEM images and their respective structure schematics are shown for the $(PbSe)_{1.1}VSe_2$ and $(Pb_2MnSe_3)_{0.6}VSe_2$ heterostructures. A diffraction pattern and structure schematic are included for synthetic attempts at the $(Pb_3Mn_2Se_5)_{1+\delta}VSe_2$ heterostructure 294

13.4. Structural characterization of the $(Pb_2MnSe_3)_{0.6}VSe_2$ heterostructure. The specular diffraction pattern contains only reflections that can be indexed to the same *d*-spacing (a.). Reflections in the in-plane diffraction pattern can be indexed to either hk0 reflections for a hexagonal or cubic unit cell which correspond to either VSe_2 or Pb_2MnSe_3, respectively(b.). EDS map (c.) and intensity profile (d.) of the STEM-EDS map clearly show V between planes of Se alternating with a Mn/Se plane between Pb/Se planes. This structure is shown as a schematic with Se atoms shown in yellow, V atoms in purple, Mn atoms in red and Pb atoms in blue (e.) 298

13.5. Resistivity and hall coefficient plots of $(Pb_2MnSe_3)_{0.6}VSe_2$ and $(PbSe)_{1.1}VSe_2$ heterostructures. Both heterostructures have an upturn in the temperature dependent resistivity (a.) at ~100 K, consistent with the VSe_2 charge density wave, though the $(Pb_2MnSe_3)_{0.6}VSe_2$ turn on appears to be smeared out. The $(PbSe)_{1.1}VSe_2$ Hall coefficient as a function of temperature (b.) has a similar upturn at about 100 K at different fields and linear resistivity measurements as a function of field supporting that there is not a magnetic moment (inset). The $(Pb_2MnSe_3)_{0.6}VSe_2$ temperature dependent Hall coefficient (c.) has a slight kink at 100 K, but also has a field dependent upturn that occurs around 50 K. The inset shows field dependent resistivity that goes from linearly to sigmoidal as temperature is decreased. The transition from linear to sigmoidal appears to occur between 30 K and 10 K. This switch as well as the hysteresis observed in Fig. H.1 indicates a magnetic moment is occurring..... 301

A.1. Graph of intensity (arbitrary units) versus film thickness (nm) according to Equation 2.1 (red diamonds) and Equation 2.2 (blue triangles). The error in intensity of assuming film thickness is small is less than 5% for thicknesses below 100 nm. For this plot, the mass absorption coefficient $\mu_T(\lambda_i)$ of the wavelength of interest and film density ρ were chosen to be 1000 cm^2/g and 7 g/cm^3, respectively. The values of each were chosen to be representative of typical films with a Lα emission lines 311

A.2. XRF intensity as a function of the amount of molybdenum deposited from an electron beam gun. Mo was deposited using a different physical vapor deposition system and a different XRF diaphragm was used to define an area during the XRF experiments, so there is a different metric for the arbitrary units of the amount of material deposited and in the XRF intensity in Figure A.2 versus the films shown in Figure 2.1..... 312

A.3. X-ray emission lines for the (a) Lα, (b) $L\beta_1$, and (c) Mα of Pb were tested to determine the best parameters for measuring the amount of Pb in each sample. The Mα line was chosen as it showed the largest difference in intensity between the sample containing Pb and the blank substrate..... 313

Figure Page

A.4. Calculated X-ray emission intensities for the (a) Kα, (b) Lα, and (c) Mα lines of Bi in a film of Bi_2Se_3. The values inserted into Equations 2.1 and 2.2 are: ρ = 7.71 g/cm^3, μ(Mα) = 1300 cm^2/g, μ(Lα) = 100 cm^2/g, and μ(Kα) = 2.0 cm^2/g. The total mass attenuation coefficient μ is calculated form the weighted average of the individual attenuation coefficients of each element present in the film. Equation 2.2 yields the blue dashed line and the values from Equation 2.1 are given by the red continuous line. 314

A.5. Calculated X-ray emission intensities for the (a) Kα, (b) Lα, and (c) Mα lines of Pb in a film of PbSe. The values inserted into Equations 2.1 and 2.2 are: ρ = 8.29 g/cm^3, μ(Mα) = 1600 cm^2/g, μ(Lα) = 100 cm^2/g, and μ(Kα) = 2.0 cm^2/g. The total mass attenuation coefficient μ is calculated form the weighted average of the individual attenuation coefficients of each element present in the film. Equation 2.2 yields the blue dashed line and the values from Equation 2.1 are given by the red continuous line. 315

A.6. Calculated X-ray emission intensities for the (a) Kα and (b) Lα lines of Se in a film of PbSe. The values inserted into Equations 2.1 and 2.2 are: ρ = 8.29 g/cm^3, μ(Lα) = 2000 cm^2/g, and μ(Kα) = 100 cm^2/g. The total mass attenuation coefficient μ is calculated form the weighted average of the individual attenuation coefficients of each element present in the film. Equation 2.2 yields the blue dashed line and the values from Equation 2.1 are given by the red continuous line. 316

A.7. A graph of intensity versus atoms per Å^2 for the elements (a) Bi, (b) Nb, (c) Pb, and (d) V found in a variety of samples, each consisting of a different element matrix. This shows the versatility of using XRF to probe various elements in a variety of samples. 317

B.1. Temperature calibration of the top resistive temperature detector (RTD) of 50nm SnSe film without Se-vapor annealing. (a) The resistance of the RTD measured at different temperatures. (b) Normalized resistance (R/R_0, where R_0 is the resistance at 300 K) plotted as a function of T. (c) The resistance change of the RTD under various heating currents. (d) Temperature change of the metal RTD plotted as a function of heating power. 318

Figure Page

B.2. Temperature calibration of the bottom RTD of 50nm SnSe film without Se-vapor annealing. (a) The resistance of the RTD measured at different temperatures. (b) Normalized resistance (R/R_0, where R_0 is the resistance at 300K) plotted as a function of T. (c) The resistance change of the RTD under various heating currents. (d) Temperature change of the metal RTD plotted as a function of heating power. 319

B.3. Temperature calibration of the top RTD of 50nm $SnSe_2$ film after Se-vapor annealing. (a) The resistance of the RTD measured at different temperatures. (b) Normalized resistance (R/R_0, where R_0 is the resistance at 300K) plotted as a function of T. (c) The resistance change of the RTD under various heating currents. (d) Temperature change of the metal RTD plotted as a function of heating power. 320

B.4. Leakage current measurement through the atomic layer deposition layer..... 321

B.5. Cross-plane Seebeck coefficient of a (a) 50nm-thick and (b) 100nm-thick SnSe film (without Se annealing). 321

B.6. Cross-plane electrical resistances of (a) 50nm-thick and (b) 100nm-thick SnSe film (without Se annealing), respectively. 322

B.7. Seebeck coefficient as a function of Fermi energy for SnSe and $SnSe_2$, respectively. 322

B.8. Calculated range of errors that correspond to the expected range of interface conductance values found in the literature. ... 323

C.1. XRR of Ti|Se annealing study showing evolution of film thickness and roughness as energy is applied to the system..... 324

C.2. Specular (a.) and in-plane (b.) XRD patterns for additional Ti|Se precursors annealed at 350°C showing the influence of precursor composition on structure. 325

C.3. XRR patterns for various Ti|Se precursors annealed at 350 °C showing the variation in roughness and loss of layers as a function of stoichiometry 326

Figure Page

C.4. Experimental (red) and simulated (black) XRR patterns demonstrating effect of oxide growth. Based on the amount of excess material in each film, the annealed films developed either a thin (~9 Å) or thick (~60 Å) oxide layer 327

D.1. Le Bail fit of the in-plane diffraction pattern for m = 1. Blue tick marks indicate the position of SnSe reflections and red tick marks indicate the position of $TiSe_2$ reflections 328

D.2. Le Bail fit of the in-plane diffraction pattern for m = 2. Blue tick marks indicate the position of SnSe reflections and red tick marks indicate the position of $TiSe_2$ reflections. The reflection at approximately 47° is the (110) reflection of $SnSe_2$..... 329

D.3. Le Bail fit of the in-plane diffraction pattern for m = 3. Blue tick marks indicate the position of SnSe reflections and red tick marks indicate the position of $TiSe_2$ reflections. The reflection at approximately 47° is the (110) reflection of $SnSe_2$..... 329

D.4. Le Bail fit of the in-plane diffraction pattern for m = 4. Blue tick marks indicate the position of SnSe reflections and red tick marks indicate the position of $TiSe_2$ reflections. The reflection at approximately 47° is the (110) reflection of $SnSe_2$..... 330

D.5. HAADF-STEM of $(SnSe)_{1.2}TiSe_2$ showing $SnSe_2$ on the surface, outlined in red 331

D.6. Relaxed structures of an (010) slab of SnSe with three bilayers in the TlI structure and its distorted relatives (see text) as viewed along (a) the [100] axis and (b) the [010] axis. Sn atoms are blue and Se atoms are red. 333

E.1. X-ray reflectivity patterns of representative, as-deposited (AD) heterostructure precursors and their annealed (AN) counterparts. This data demonstrates the changes in the entire film that occur when the samples undergo heating at 350 °C for 30 minutes in an inert atmosphere 335

Figure Page

E.2. Temperature dependent resistivity curves of the $[(SnSe)_{1+\delta}][TiSe_2]_3$ layered heterostructures (a) and the $[(SnSe)_{1+\delta}][TiSe_2]_{11}$ layered heterostructure (b.) plotted with the exponential equations $y = 50\ e^{(-0.03)} + 23$ and $y = 1200\ e^{(-0.07)} + 100$, respectively. This data emphasizes the deviation at low temperatures from exponential behavior and the constant offset that is required. 336

E.3. In-plane lattice parameters determined from in-plane grazing incidence diffraction collected at various temperatures for a $[(SnSe)_{1+\delta}][TiSe_2]_8$ heterostructure. There is no significant change in the basal plane structure of either constituent upon cooling. This indicates that the unique transport behavior is not the result of a structure change. This data was collected at the advanced photon source using beamline 33 BM. 337

F.1. Annealing study for *m, n* = 3 sample to study the formation and subsequent decomposition of the superlattice structure as seen with XRR (a.) specular XRD (b.) and in-plane XRD (c.) From this data, 350 °C was determined to be the optimal annealing temperature for the system and was subsequently used to crystallize the remaining samples. 338

G.1. Representative as-deposited XRR patterns demonstrating the initial layering and rearrangement occurring in the sample before annealing occurs 341

G.2. Representative grazing incidence in-plane diffraction of an as-deposited $[(PbSe)_{1+\delta}]_1[TiSe_2]_1$ heterostructure demonstrating the initial nucleation of both PbSe and TiSe2 crystallites before annealing. 343

G.3. STEM-EDS showing the relative intensity of characteristic X-ray signals from Pb and Ti when moving down the *k*=2**3**2**1** structure. 343

Figure Page

H.1. Field dependent resistivity measured at various temperatures emphasizing the hysteresis. Hysteresis appears at 30 K and continues are lower temperatures which is in the region where the non-linearity occurs in the magnetoresistance measurements. This is also where the low temperature discontinuity in the temperature dependent resistivity occurs. The hysteresis supports that ferromagnetic ordering is occurring in the samples as a result of the Mn constituent and is not the result of multi-band physics. 344

LIST OF TABLES

Table Page

2.1. The slopes of the lines in Figure 1 for each element along with the fluorescence line used. The maximum film thickness is the thickness where absorption reduces the intensity of fluorescence of the given element by 5%. 61

2.2. Sensitivity of the XRF measurement for a series of elements as a percent of a monolayer of the compound in parenthesis 69

4.1. XRF integrated counts and counts per layer for both SnSe targeted films annealed under different conditions. 92

5.1. A summary of the structure and composition of the as-deposited Ti|Se precursors 108

5.2. Compositions and lattice parameters for annealed Ti|Se films as determined from full pattern XRD Le Bail fits. 111

6.1. DFT calculated energy differences between four configurations with differing relative orientations of SnSe layers and leanings of $TiSe_2$ layers. 134

7.1. Lattice parameters, and misfit parameters for $[(SnSe)_{1+\delta}]_mTiSe_2$ compounds. 144

7.2. Total energy differences per formula unit ΔE_{GeS} of the polymorphs with respect to the GeS (α-SnSe) structure as a function of the number of bilayers. Values in parentheses represent values obtained using DFT-D2. 155

7.3. Room temperature transport properties for $[(SnSe)_{1+\delta}]_mTiSe_2$ compounds. 159

8.1. Lattice and misfit parameters for the $[(SnSe)_{1+\delta}]_1[TiSe_2]_q$ heterostructures determined from x-ray diffraction patterns 176

Table Page

8.2. Parameters obtained for fits of the temperature dependent Hall coefficient and resistivity transport data. Parameters we determined assuming charge transfer from SnSe to $TiSe_2$ results in carriers that are localized at low temperature due to variable range hopping and at high temperatures holes and additional electrons are created due to activation of carrier across a band gap requiring a 2-carrier model. The low temperature parameters were used to fit the VRH model and the 2-carrier model with VRH at low temperatures. 185

8.3. Average atomic charge of bulk SnSe, bulk $TiSe_2$, and the average charge transfer between them in the heterojunction 191

9.1. Comparison of Deposited vs. Crystallized Repeating Units (RU's) for the $[(SnSe)_{1+\delta}]_m[TiSe_2]_n$ series 199

9.2. Heterostructure *c*-axis lattice parameter and in-plane lattice parameters for SnSe and $TiSe_2$ of $[(SnSe)_{1+\delta}]_m[TiSe_2]_n$ heterostructures determined from Le Bail fits..... 204

9.3. Room temperature electrical transport properties 210

11.1. Total Atoms / $Å^2$ in each of the annealed $[(PbSe)_{1+\delta}]_4[TiSe_2]_4$ isomer films. The error in the conversion factor between XRF intensity and number of atoms per unit area is 2-3%..... 251

11.2. Calculated number of atoms / $Å^2$ for each element for the $[(PbSe)_{1+\delta}]_4(TiSe_2)_4$ isomers for different film thicknesses..... 252

11.3. Parameters extracted from the XRR patterns as described in the text. Not shown in the table are parameters that do not vary the calculated patterns significantly. These parameters (the bottom impurity roughness (5Å), and the roughness of the Si substrate (5Å)) were held constant in all of the models 257

11.4. Lattice parameters for the $[(PbSe)_{1+\delta}]_4[TiSe_2]_4$ structural isomers determined from the annealed diffraction patterns 260

Table Page

D.1. In-plane lattice parameters a and b of the structures shown in Figure D6, and the energy differences per formula unit between these structures and the undistorted slab in the TlI structure ΔE_{TlI}. The energy difference per formula unit to a (001) slab of three bilayers in the GeS structure ΔE_{GeS} is added for comparison. 334

E.1. Calculated electronic band gaps of the explored alternative crystal polymorphs are presented. These electronic band gaps were obtained using the procedure outlined in the Materials and Methods section. The computational models were prepared from the computationally ready structures from Materials Project. 337

F.1. Temperature Dependence in Lattice Parameters for the $[(SnSe)_{1+\delta}]_m[TiSe_2]_n$, m, n = 4 heterostructure. 340

G.1. Total Film thickness and repeat layer thickness for representative $[(PbSe)_{1+\delta}]_4[TiSe_2]_4$ isomer heterostructures. AD total thickness obtained from BedeREFS by assuming an 11-layer isomer block with no impurities and varying the c-lattice parameter of the isomer block until the simulated Kiessig fringes between θ_c and the 001 reflection maxima matched those of the experimental XRR pattern. The simulated electron density was scaled by a factor of 0.9 – 0.95 to get a precise match for the experimental θ_c. The as-deposited repeat unit thickness was calculated using a modified version of Bragg's Law, which corrected for refraction, and the first two Bragg reflections observed in the low angle diffraction patterns. 342

CHAPTER I

HETEROSTRUCTURES CONTAINING DICHALCOGENIDES – NEW MATERIALS WITH PREDICTABLE NANOARCHITECTURES AND NOVEL EMERGENT PROPERTIES

1.0. AUTHORSHIP STATEMENT

This chapter was formatted from a manuscript with the same name, that was published as an invited review article in the IOP journal Semiconductor Science and Technology (DOI: 10.1088/131-6641/aa7785.) on August 17, 2017. This review was co-authored by myself, Erik C. Hadland, and David C. Johnson. All three authors contribute in the literature search that makes up the review article. The three authors also all contributed to writing the manuscript. I was primarily responsible for the literature survey and writing of the sections focusing on material heterostructures and sample characterization. I responsible for compiling, formatting, and editing all parts of the manuscript. I was the primary author on this article. David C. Johnson is my advisor.

1.1. INTRODUCTION

For at least the past half century scientists have been curious about how material properties change as thicknesses are reduced to the atomic scale.[1–4] In the era before scanning tunneling microscopies, there were significant challenges in directly determining the thickness of the samples being studied. Instead indirect methods such as sheet resistance, absorbance or shadowing effects were used to infer thicknesses. Researchers reported very early that naturally anisotropic compounds, such as the transition metal dichalcogenides or graphite, with easily cleavable van der Waals planes were ideally suited to these investigations.[1,3,4] As early as 1966, the "scotch tape" method of cleaving van der Waals solids and isolating finite layers was reported.[1] As

dimensions were reduced towards single layers (Figure 1.1), anomalies in exciton binding energy[2] and systematic changes in superconducting properties[3,4] were discovered. Although novel properties were reported, the analytical challenges in determining thickness and recognizing large domains of constant thickness prevented researchers from discovering that the anomalous properties of materials such as graphene or MoS_2 were intrinsic to single layer thick two-dimensional (2D) planes.

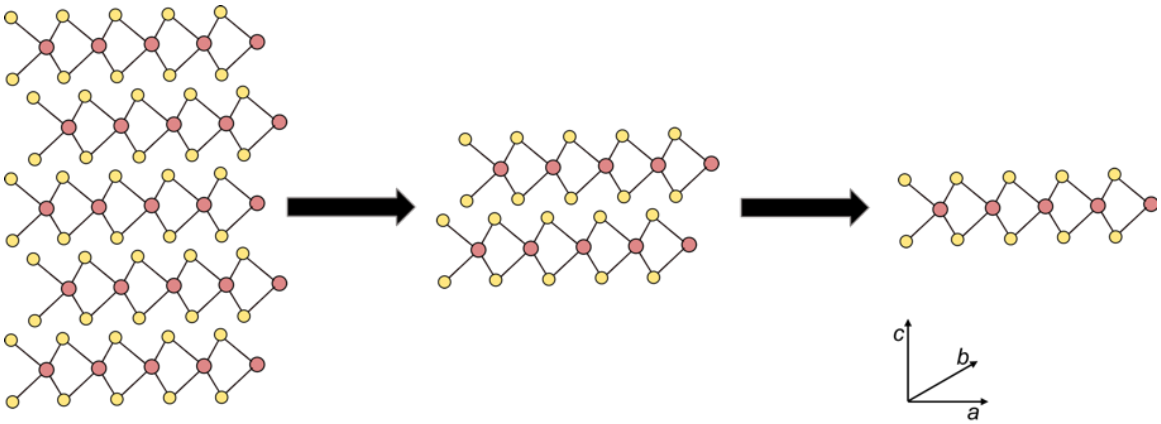

Figure 1.1. Transition metal dichalcogenides are naturally occurring layered materials with highly anisotropic bonding. Weak van der Waals forces along the c axis enable them to be easily cleaved to obtain monolayer structures, while strong covalent bonds in the ab plane preserve the crystalline structure within a layer during cleaving. The schematic illustrates the structure of five layers (left), two layers (center) and a monolayer (right). The arrows represent the thinning of the sample via cleaving.

During this same era, Arthur and Choi developed molecular beam epitaxy (MBE) at Bell Labs.[5] The ability to use epitaxial interfaces to grow designed sequences of layers of materials with known thicknesses and structure dramatically increased the repertoire of potentially available functional materials.[6] The ability to imagine sequences of structures that could actually be prepared resulted in increased theoretical activity predicting properties and potential devices from proposed nanoarchitectures. Although the compositional sequences produced by

MBE are typically not the thermodynamic ground state of the system, they are often sufficiently kinetically stable at normal operating conditions to be used in devices. Figure 1.2 shows a schematic energy landscape of kinetically stable heterostructures where the thermodynamic ground state is a physical mixture of the constituents. Just as in MBE, kinetic stability results from sufficiently high inter-diffusion barriers (the energy maxima in the lines connecting the heterostructures with the ground state) that prevent the layers from interdiffusing. Preparation of artificially layered materials with designed nanoarchitectures via MBE has led to fundamental discoveries in physics, including the quantum Hall effect.[7] Control of the nanoarchitecture has provided access to electronic and transport properties not available in the bulk form, and has led to many critical technology-enabling discoveries such as 2D electron gas,[8] modulation doping,[9] light emitting diodes,[10] and quantum cascade lasers.[11]

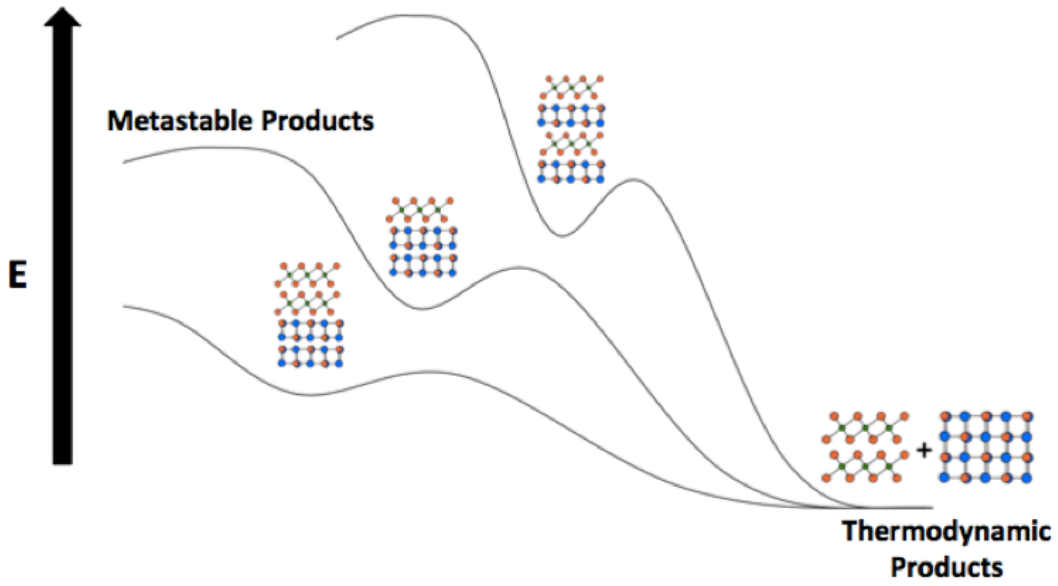

Figure 1.2. Heterostructures are local minima in the free energy landscape and different stacking arrangements will have different energies. The kinetic barrier to forming the thermodynamic mixture of bulk constituents is a consequence of the activation energy for solid-state diffusion.

The development of MBE was a tremendous advance, but is a technically challenging growth technique. Constituents need to have structures and unit cell parameters with close lattice matches between them for epitaxial growth to occur. If the two constituents do not have a close lattice match, then the interfaces will contain a large concentration of dislocations and other defects necessary to reduce the lattice strain. Besides the lattice match requirement, there are also significant challenges associated with finding deposition conditions where material A can be grown on material B and material B can be grown on material A. Finally, the growth of distinct layers at the 2-D limit is exceedingly challenging due to mixing that occurs during growth and the competition between completing the first layer and nucleating the next layer.

While MBE research focused mainly on intergrowths of semiconductors with diamond-based lattices, other researchers discovered ways to prepare new materials containing intergrowths of constituents with a variety of different structures. In the early 1980's, Koma, et al. showed that it was possible to grow single layers of compounds containing van der Waals interactions between building units - molecules such as C_{60}, 1D chains such as Se or Te, and/or 2D layers such as the transition metal dichalcogenides - on substrates terminated with a van der Waals surface. [12,13] They demonstrated that the weak van der Waals interaction between constituents drastically relaxed the lattice matching condition usually required in heteroepitaxial growth. The lack of dangling bonds at the van der Waals surfaces resulted in very abrupt interfaces with small defect levels even with lattice mismatches of up to 50%.[14] The removal of epitaxial constraints dramatically increased the number of combinations of constituents that could be utilized in the preparation of heterostructures. "van der Waals epitaxy" provided the first synthesis route to heterostructures containing ultrathin superconducting, metallic, semiconducting or insulating

monolayer dichalcogenides as constituents with controlled and designed nanoarchitecture. [12,13, 14]

Van der Waals epitaxy is an innovative technique that allowed preparation of novel heterostructures, however it is still technically very demanding and the challenges of finding growth conditions compatible with growing material A on material B and B on A are similar to those experienced with epitaxial growth techniques. Around this same time period, chemists discovered thermodynamically stable materials, called misfit layer compounds (Figure 1.3), that contained interwoven monolayers of constituents that in the bulk are superconducting, metallic, semiconducting, magnetic or insulating.[15] These compounds are typically prepared directly from the elements at high temperature and single crystals are prepared via vapor transport.[16] The atomic abruptness of the interfaces in misfit layer compounds results from the distinctly different crystal structures of the constituents. Unfortunately, there is essentially no ability to prepare compounds with different constituent layer thicknesses or nanoarchitectures by changing the synthesis conditions.[15] It is also not possible to prepare isolated monolayers or heterostructured bilayers utilizing these high temperature synthesis approaches. The growth of research in the field of 2D materials and novel heterostructures did not accelerate at this time due to the technical challenges of the available growth techniques and the limited analytical tools available to characterize the resulting materials.

The activity level in the field of 2D materials has exploded in the last decade fueled by the discovery of novel properties in graphene by Novoselov, Geim and coworkers that resulted in their sharing of the Nobel prize in Physics in 2010.[17–19] This growth in activity is a consequence of analytical advances (scanning probe microscopy, aberration corrected electron microscopes), the rediscovery of the scotch tape approach to cleave van der Waals compounds, and a breakthrough

in the use of optical microscopy to rapidly identify crystals of different thickness.[20] The "Scotch-tape method", mentioned earlier, is simple, effective and does not require either a large investment or complicated equipment. The optical contrast mechanism of ultrathin layers on a silicon wafer coated with SiO_2 is now well understood. [21,22] This technique permits the rapid scanning of large areas to identify optimal crystals using a light microscope, which is neither expensive nor complicated. The resulting literature on graphene alone is enormous, with estimates of over 10,000 papers a year being published.[23] The second wave of research in this area has focused on related materials whose bulk structure contains strongly bonded layers separated by weak van der

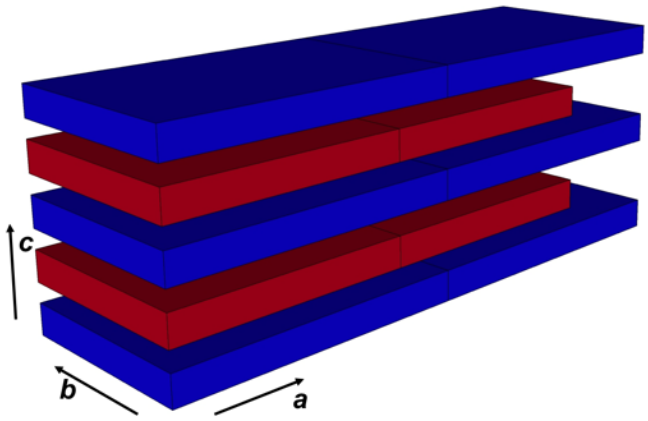

Figure 1.3. Misfit layer compounds are thermodynamically stable heterostructures of alternating layers of rock salt and transition metal dichalcogenide. A defining feature of this class of materials is that they usually possess a single commensurate in-plane lattice parameter.

Waals forces, including diverse materials such as hexagonal boron nitride,[24,25] transition metal dichalcogenides,[26–32] fluorographene,[33] and new elemental analogs of graphene - germanane,[34–36] silicene,[37] and phosphorene.[38,39] There are already multiple reviews available on these materials, and the sheer number of papers published makes a comprehensive review daunting. Due to the large amount of literature on the various 2D-materials this review will focus on the emerging field of

heterostructures containing dichalcogenide layers. A schematic of various heterostructures is shown in Figure 1.4. Since there are already excellent reviews that focus on emergent properties and devices,[40,41] this review focuses on the synthesis and characterization of heterostructures.

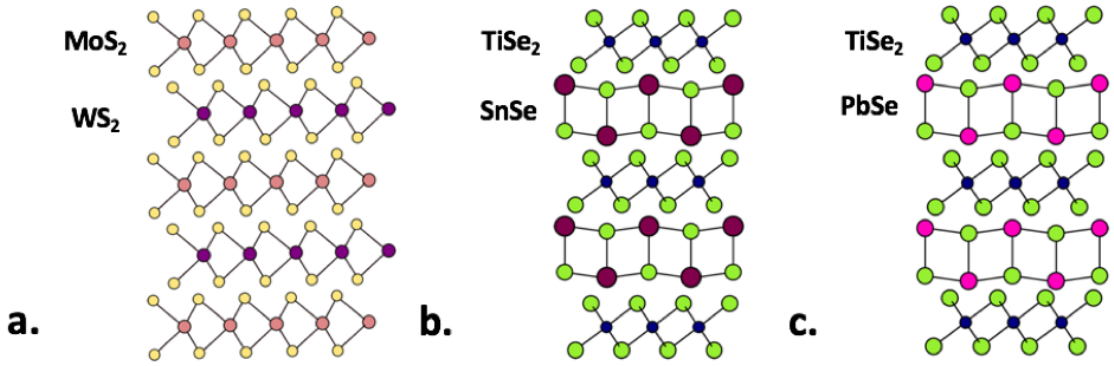

Figure 1.4. Structural schematics of heterostructures composed of various 2D materials. a. MoS_2 and WS_2 - yellow represents S, purple represents W and rose represents Mo. The constituent layers are held together by weak van der Waals interactions. b. SnSe and $TiSe_2$ - green represents Se, magenta represents Sn, and blue represents Ti. The SnSe layer does not have a layered structure but is a fragment of a distorted rock salt structure. c. PbSe and $TiSe_2$ (green represents Se, blue represents Ti, and maroon markers represent Pb).

Researchers have discovered that the properties of monolayer materials depend on the substrate they are attached to, and that the properties can be emergent - ie. not found in either the monolayer or the substrate.[42,43] This has spawned investigations into heterostructures containing two or more 2D materials combined into a composite, and there have been considerable efforts made to understand the origin of emergent properties.[42–57] Several origins have been proposed for different emergent properties, including changes in band structure due to removing adjacent layers, finite size effects, structural changes with layer thickness, strain, and the presence of adjacent layers as discussed in the following section. We will also discuss the synthesis and characterization of dichalcogenide containing heterostructures.

1.2. Origins of Emergent Properties

In the context of 2D materials, an emergent property is a property that does not exist in a bulk compound but occurs as the material becomes increasingly thinner. Frequently, the emergent property only occurs when thickness has been reduced to a monolayer.[17,26,27] In heterostructures, emergent properties arise when adjacent layers interact with one another. These properties are not present in the individual constituent compounds.[58] Harnessing the power of heterostructure systems for a variety of uses — optoelectronic, thermoelectric, magnetic, etc. — depends on developing a set of design principles to understand how to optimize emergent properties. For synthetic groups, the ability to precisely control thicknesses and sequences of layers in a heterostructures is a critical task that is necessary for the systematic study of structure/property relationships. For theoretical groups, identifying the combination of layers and their structural characteristics that give rise to a specific set of properties is a challenge. The need is to inform what parameter spaces and nanoarchitectures must be explored to optimize desirable properties. In the following paragraphs, we discuss the underpinnings behind categories of emergent properties, highlighting the discussion with representative examples.

1.2.1. Changes in Band Structure Due to Removing Adjacent Layers

Perhaps the most obvious cause for emergent properties in single-layer systems is the removal of electronic interactions between adjacent layers. The loss of orbital overlap changes the band structure and, consequently, gives rise to new properties. Graphene is the prototypic example. Each carbon is sp^2 hybridized, leaving the p_z orbitals—oriented perpendicular to each hexagonal layer—half empty. In graphite, the p_z orbitals in adjacent layers interact to create a filled orbital from the bonding interaction and an empty antibonding orbital. Overlap of these bands causes graphite to be a semimetal. In a single sheet of graphene,

this orbital remains half-filled leading to a zero-gap semiconductor with a linear Dirac-like spectrum around the Fermi energy,[59] resulting in the emergent properties discovered by Novoselov, Geim and coworkers.[17] The semiconducting dichalcogenides with trigonal prismatic coordination of the transition metal (MoS_2, $MoSe_2$, WS_2, WSe_2) are a second example wherein emergent properties result from a loss of interlayer interactions.[26,27] In 2010, two independent studies were published that showed MoS_2 transitions from an indirect to direct band gap material in going from a bilayer to a monolayer. [26,27] In 2013, Komsa et al. showed that wave functions at the Γ point extend from the chalcogen atoms into the Van der Waals gap, leading to strong interactions with the d_z^2 orbitals of the transition metal in the adjacent layers (for a 2H polytype).[60] The highest energy position of the valence band in the bulk is at the Γ point. This band rises in energy due to an antibonding interaction between the layers. In the monolayer, this antibonding interaction is removed, decreasing the energy of this band as it approaches the Γ point, resulting in it being below the energy at the K point. The energy of the conduction band and its general shape do not change significantly with thickness, so the lowest energy point in the conduction band stays at the K point.[61,62] The net result is that the monolayer has a direct band gap.

Since the impact of changing coordination at interfaces is apparent even in systems with weak van der Waals interactions between layers, more significant changes are observed in heterostructures with constituent layers that are more three dimensional. Constituents that in the bulk have a rock salt structure, for example PbSe, distort significantly when they are present as a bilayer in a heterostructures adjacent to a dichalcogenide. The Pb and Se atoms that are in the same (001) plane in the bulk are puckered in the bilayer, with the Pb and Se planes displaced from one another by over 0.2 Å in $(PbSe)_1(MoSe2)_1$.[63]

This distortion results from the termination of the rock salt structure and the interaction between the constituent layers. This has significant consequences for the band structure, but also impacts a range of other properties. An example is the surface segregation of alloys. There is a different chemical composition at the surface of an alloy from that in the bulk,[64] because surface energies depend strongly on the crystal structure of the alloy components.[65] Another example is changes in solubility in alloy systems. Sn and Pb are miscible in bilayers of PbSe-SnSe alloys across the entire solid solution, but the bulk phase diagram shows a large miscibility gap.[66] Changes in bonding at interfaces and between constituents at interfaces are likely to become valuable tools used to tune and control properties as they become better understood.

1.2.2. Finite Size Effects

As the thickness of a layer is reduced below the de Broglie wavelength of the electron wave function, there is a transition from continuous to discrete energy levels.[67] In 1993, Hicks and Dresselhaus described how changes in the density of states due to localization within a layer could greatly enhance the Seebeck coefficient in heterostructures, specifically calculating potential enhancements in thermoelectric performance for Bi_2Te_3 containing superlattices.[68] They considered the Bi_2Te_3 layer as a two-dimensional quantum well with potential barriers formed by the physical boundaries of the layer. The calculated band structures showed sharp features in the density of states that were predicted to enhance the thermoelectric power factor.[69] The emergent properties found in graphene were also initially thought to result from changes in electronic structure due to quantum size effects. The discovery of strong photoluminenescence in transition-metal dichalcogenides and the crossover from an indirect and direct band gap as thickness is reduced to a monolayer initially lead to speculation that quantum size effects might be a general phenomenon in 2-D

monolayers.[26,27] Since these initial reports, MX_2 monolayers, where M (Mo, W) and X (S, Se), have been found to have other novel excitonic properties, including efficient control of valley and spin occupation by optical helicity. [28,29,70–73] Additional studies focused on the fundamental excitonic physics of low- dimensional materials and potential technological applications are being rapidly reported. [73–82]

There has also been considerable effort aimed at distinguishing between properties that emerge in ultrathin materials due to unusual features in their band structure (for example, interactions between layers in the bulk) and features that result specifically from the quantization and changes in energy that result from finite size effects.[62] One strategy for attributing particular emergent properties to either of these two effects is to study properties as a function of relative angle between monolayers or between monolayers and substrate. Figure 1.5 shows a schematic of a rotationally disordered heterostructure. If the phenomena are dominated by a finite thickness phenomena, then the effect of relative rotation angle will be relatively small.[83] If the phenomena are due to interlayer interactions or their removal, then rotation angle will have a pronounced effect.[83] First principle calculations of these systems as a function of rotation angle are challenging, because the size of the supercell varies considerably and is always considerably larger than the primitive unit cell of either a single layer or the stable bulk polymorph. Consequently, atomistic simulations are limited to special twist angles with manageable supercell sizes instead of random orientations. Simpler models that attempt to captures the essential physics are often used. There were extensive studies investigating the properties of bilayers of graphene with rotation angle soon after the novel properties of monolayer graphene were reported, showing that the interlayer interaction changes dramatically as the angle is changed. [59,84–92] These studies suggest that interlayer interactions, rather than finite size effects, dictate the

difference in properties between monolayer and bilayer graphene. Initial studies exploring the effect of rotation angle in bilayers or bilayer heterostructures of Mo and W containing dichalcogenides also show a strong dependence of properties on stacking sequence or rotation angle.[83,93–101] This supports the conclusion that the lack of interlayer bonding is an important factor in the direct band gap and novel optical properties of monolayers of these compounds. [62]

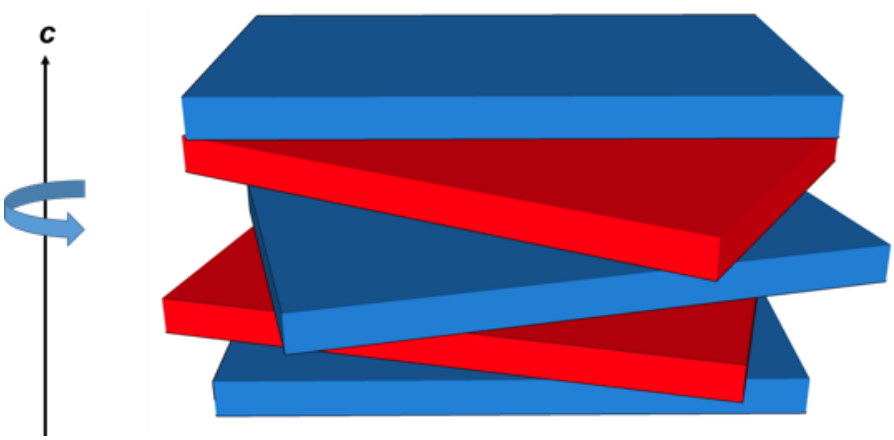

Figure 1.5. Schematic of rotationally disordered constituent layers within a heterostructures. Lattice mismatch between constituent layers will increase the distribution of rotation angles between layers.

1.2.3. Structural Changes with Layer Thickness

As suggested in section 3a, the most salient feature of monolayers relative to their bulk counterparts is the removal of the electronic interaction between adjacent layers. For very anisotropic compounds—those with strong bonding within layers and weak van der Waals interactions between layers—the structure of free monolayers has been calculated or assumed to be quite similar to constituent monolayers in the corresponding bulk solid,[102,103] in agreement with many transition electron microscopy images.[104–107] For less anisotropic bulk solids, however, more extensive structural changes might be expected at lower dimensions due to the increased influence of surface energy that results from the removal of adjacent layers. In an infinite crystal, the forces

exerted by all the other atoms in the crystal determine the position of each individual atom. At a surface, these forces are altered, and surface atoms experience more asymmetric inter-atomic forces. Consequently, the positions of the surface atoms change from the equilibrium in the bulk, assuming distinct spacing and/or symmetry. Indeed, surface reconstructions are a common feature of crystalline solids, with specific distortions depending on the crystal face and atoms at the surface.[108] Surface reconstructions can extend into the bulk, with the extent of distortion decreasing as distance from the surface increases. Hence, structural distortions might be expected to change as a function of layer thickness, due to the relative importance of surface and volume free energies.

There is limited data available on the atomic structure of 2D layers, as most analytical techniques give only information about the symmetry of the layer or perhaps only one or two of the three atomic coordinates of the atoms in the 2D layer. Raman and other optical spectroscopies provide information about changes in symmetry and the stacking sequences of layers (i.e. polytypism).[109] A review article was recently written that describes the evolution in Raman modes and lattice vibrations in monolayer, few-layer, and bulk systems.[110] Transmission electron microscopy and scanning probe microscopies provide low resolution information about the in-plane coordinates of the atoms in 2-D layers. In-plane x-ray diffraction provides information about symmetry and the in-plane lattice parameters. The intensities can be used to refine the in plane atomic coordinates if the data is of high enough quality.[111] Partially due to the challenges in obtaining quantitative information about the structure, the majority of studies on mono- and few-layer anisotropic compounds that can be prepared using the "scotch tape" synthesis approach have assumed that the bulk structure is preserved in the monolayer. There are a few studies of heterostructures containing 3-

D solids. There is a report of the structure of PbSe layers, which has a cubic rock salt structure in the bulk, as a function of thickness. A bilayer orientated with the (100) planes is the thinnest layer reported, and it has a square in plane lattice but each of the (100) planes distort such that the Pb atoms sit in a plane extending slightly into the van der Waals gap, and the Se atoms are in a plane slightly interior.[112] This puckering distortion is significant, on the order of 0.2 Å. As the PbSe layer is increased, the magnitude of this puckering distortion decreases. The structure of a four-plane PbSe layer distorts to form two bilayers, with a larger distance between the bilayers. The structure of a six-plane PbSe layer distorts to form three bilayers, with the distortion in the center bilayer different than the outer bilayers. By the time the PbSe layer reaches ten planes, the structure looks like the bulk structure with a surface distortion. This puckering phenomenon and its comparison to the bulk PbSe structure (a) is depicted in figure 1.6, below. It was suggested that these distortions result from the interplay between surface and volume free energies.[112]

Similar changes in structure with thickness was reported for SnSe layers sandwiched between dichalcogenide layers.[113–118] Bulk SnSe possess an orthorhombic unit cell. However, a bilayer of SnSe was found to have a square basal plane when interleaved between either $MoSe_2$ or $TaSe_2$ layers.[113,114] Interestingly, the SnSe lattice was found to have a rectangular basal plane when interleaved with $NbSe_2$,[115] showing the importance of adjacent layers. The in-plane lattice parameters in this heterostructure became increasingly different as the thickness of the SnSe layer increased.[116] Around 40 planes of SnSe are required before the lattice parameters resemble the bulk compound. Similar changes in structure are anticipated as other 3D solids are prepared as 2D layers. The changes in the structure of 2D layers of 3D solids with thickness reflects the changes in the bonding at the internal surfaces, which

provides an additional mechanism to tune properties. The unique environment between 2D layers may also make it possible to prepare structures as 2D layers that are not stable as 3D solids.[117,118]

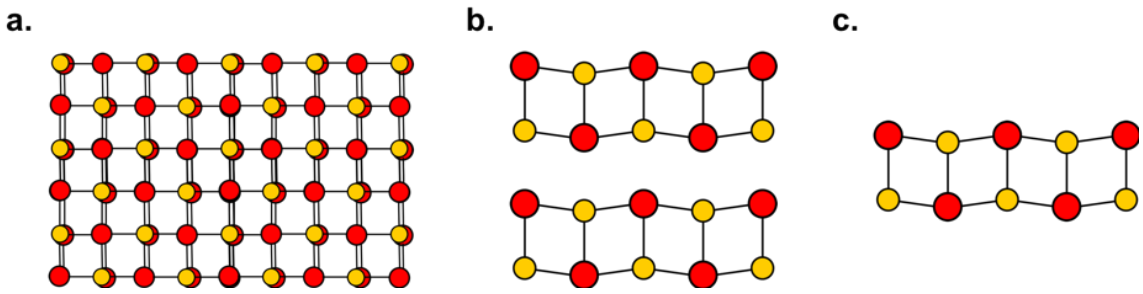

Figure 1.6. As rock salt bulk compounds are reduced to ultrathin dimensions, the lattice becomes increasingly "puckered" such that metal cations extend into the van der Waals gap while the chalcogens occupy atomic positions on the interior of the bilayer. (a) the bulk rock salt crystal structure (b) Two stacked bilayers of a puckered rock salt structured constituent (c) Structure of a single puckered 2D rock salt bilayer. The metal atoms are shown in red and the chalogen atoms are shown in yellow.

1.2.4. Strain

Strain has historically been a valuable tool used in semiconductor technology to optimize properties and performance in today's microelectronics devices.[119] In traditional semiconductor devices, strain is typically created during epitaxial growth through lattice mismatch at interfaces. For fundamental studies of strain, external forces can be applied in a variety of ways to plastically deform the material in question. These studies have a long history, with the first report of strain-enhanced mobility in *n* and *p* type bulk Si and Ge occurring in 1954.[120] Many papers have explored the effect of strain on bulk materials, thin films, and epitaxially grown layers, including superlattices.[121,122] It is not surprising that soon after the discovery of the remarkable properties of graphene, strain was theoretically and experimentally explored as a tool to modify properties. [123]The effect of strain on graphene has been recently reviewed.[123]

Researchers have explored the effect of strain on properties of novel 2D materials using various approaches.[60,123–126] Theoretically changing the lattice parameters is relatively easy, and it is common, for example, to create supercells with varying degrees of strain to approximate rotational angles between layers. As Komsa and Krasheninnikov have pointed out, however, it is difficult to distinguish which features originate from the monolayer or stacking of the monolayers and which are due to the strain artificially introduced into the system to make the calculations easier.[60] Experimentally straining graphene and other 2D materials is challenging because the weak interlayer van der Waal forces that make these materials cleavable and chemically stable as monolayers also make them resilient to deformations induced by epitaxy. Indeed, dichalcogenide heterostructures epitaxially grown by Koma and coworkers[124] and epitaxial growth of TMD mono- layers on graphene[125] both resulted in layers with lattice constants very close to those of the bulk and the isolated monolayers. This is a consequence of the energy cost for straining the lattice and exceeding the incremental bonding energy between layers. van der Waal forces are significantly weaker than the covalent bonds found at the interfaces of epitaxial III-V heterostructures. The weak interlayer bonding in van der Waals heterostructures does not provide a sufficient energy barrier to trap growing layers in their strained state during growth.[60]

Researchers have been clever in using a variety of approaches to strain 2D monolayers, and the large volume of research published in this area has recently been reviewed.[126] Monolayers have been placed on substrates that have different thermal expansion coefficients, resulting in increasing strain as a function of temperature. Two-dimensional materials have also been placed on flexible substrates, which, when bent create a tensile strain on the top of the substrate and a compressive

strain on the bottom. This strain can also arise if a 2D material is placed on an elastic substrate. Compressive stress is created if the substrate is elongated before the 2D material is applied, while tensile strain occurs if the 2D layer is placed on the substrate and is subsequently elongated. In a similar manner, the piezoelectric effect can be used to stretch or compress a 2D layer on top of a suitable substrate. The van der Waals bonding between the monolayer and a substrate can maintain approximately 1% strain before releasing. A monolayer can be tacked in place by an edge coating of metal, increasing the magnitude of achievable strain. Releasing strain on a monolayer can produce layers with controlled wrinkling. This is typically accomplished by positioning a 2D layer on a stretched substrate and then releasing the tensile strain on the substrate. Micro Raman spectroscopy is a valuable tool to investigate local strain in 2D materials and heterostructures and this technique will be discussed in more detail later in this review.[127–129] Strain will continue to be a valuable tool in the pursuit to tune the properties of monolayers to both understand fundamental interactions and create devices.

1.2.5. The Presence of Adjacent Layers.

Monolayers may be thought of as one-dimensional "particle in a box" situations, with the electrons of the layer confined to that layer. Because the potential barriers at the walls of the box are not infinite, the wave functions extend outside of the box for a couple of angstroms, decaying exponentially. These extended wave functions interact with adjacent layers or surfaces causing the layer properties to be modified.[42] This interaction with adjacent layers can significantly modify the band structures of the individual 2D layer, even though no real chemical bonds are formed between them.[43] The resulting properties of the 2D layer depends on the alignment of bands between that 2D layer and the substrate, the density of states of each material, and the extent of charge transfer due to electrons having different chemical potentials in the

various constituents. In semiconducting 2D layers, for example, the exciton binding energy and the quasiparticle band gap are influenced by the choice of substrate material and also by excited electrons within the 2D layer.[44–47] When a semiconducting single layer transition metal dichalcogenide is placed on a metallic substrate, a strong band gap renormalization is observed.[48,49] Interactions between monolayers and a substrate can be strong enough to modulate electronic properties even if the interface is not epitaxial.[50,51] The number of papers describing different behaviors of monolayers on various substrates is rapidly expanding and researchers are investigating a wide range of monolayers and substrates both theoretically and experimentally.[52–57] Theoretical predictions about non-lattice matched monolayers are complicated by the large unit cells required to avoid introducing significant strain into the constituents and by the difficulties in treating the van der Waals interactions and charge transfer at interfaces.[60,130] Experimentally, applying a gate voltage to a substrate or changing the Fermi level by chemical doping are both being used to discover new phenomena in 2D monolayers.[131,132] The dependence of properties of monolayers on changes in chemical potential provide a mechanism to create novel sensors.[133,134]

1.3. HETEROSTRUCTURES CONTAINING TRANSITION METAL DICHALCOGENIDES

Adding an additional layer (or layers) on top of a monolayer on a substrate, creating a three-component sandwich, produces additional complexity. Since many potential devices will use monolayers that are buried as part of an overall architecture, research in this area will expand considerably as the ease of both manipulating monolayers and directly growing different monolayers on top of one another increases. We will refer to these composites as heterostructures, and heterostructures of transition metal dichalcogenides are the topic of the rest of this review article.

Heterostructures will grow in importance as a research field for a variety of significant reasons. First, devices will require additional layers (top and bottom) to provide electrical contacts, protect the monolayers from damage, and to generate emergent properties through the interaction between layers. By judiciously choosing adjacent top and bottom layers, existing properties can be modified, and novel properties can be created. The ability to predict the structures and properties of heterostructures that have not yet been created provides an opportunity for theorists to create models to probe for unique effects in systems that have not been experimentally prepared.[135] These predictions will provide significant motivation to prepare the identified systems. The resulting differences in properties from those predicted and their dependence on nanoarchitecture will lead to a greater understanding of structure-property relationships.

There is already an impressive number of papers that describe the properties of heterostructures containing graphene,[55,136–158]and a growing number of papers that describe heterostructures containing one or more dichalcogenide and the properties that arise from the interaction between constituents.[159–162] In the future, new constituent layers will be prepared and assembled with control of both thickness and the sequence of layers. Researchers will have a set of building blocks to create new materials where the nanoarchitecture and resulting interaction between constituents provide the tools to discover novel and optimize known properties. Perhaps, much like a building is designed using optimally designed composites of concrete and steel, new materials will be designed by creating nanocomposites with specific architectures to optimize emergent properties for targeted applications. This will require the development of an understanding of how emergent properties of 2D layers arise and how 2D layers interact to form composites that outperform individual materials.

1.3.1. Synthesis.

Due to their promising applications in a wide variety of devices, [163] researchers have devoted considerable effort to discovering efficient means of synthesizing monolayers and heterostructures, with ongoing efforts aimed at producing uniform structures over large areas. The "scotch tape" method enables the preparation of heterostructures composed of different monolayers, but the micromechanical manipulations require considerable skill and patience. There are also concerns about surface contamination that can affect the properties of the resulting heterostructures and the technique is limited to constituents that can be isolated and stabilized as monolayers.[137,141,164,165] However, micromechanical exfoliation is a surprisingly robust approach and there are many reports of new combinations of constituents and novel device structures being prepared using this technique.

While most of the initial work has been based on monolayers cleaved from single crystal materials, there has been substantial interest in developing approaches that provide monolayers over sizeable areas. A number of transition metal dichalcogenides have been prepared on a variety of substrates using chemical vapor deposition, sputtering and other vacuum deposition approaches where the chemical fluxes and substrate temperatures are controlled to grow a defined number of layers of a desired material. [166–171] When the layers are parallel to the substrate, the challenge in these growth techniques is controlling the conditions to completely grow each layer before nucleating the following layer. This challenge arises from the limited number of variables that can be easily controlled, including the mass flow of reactants and temperature profiles. The synthesis of vertically oriented layers, needed for catalytically active samples, is more challenging, typically requiring a template layer.[172,173] The nucleation and growth issue is addressed by Koma's van der Waals

epitaxy growth technique,[12–14] which has grown in use all over the world. A wide variety of new systems prepared using this approach are reported every year.[138,171,174–179] The in-situ monitoring of growth using low energy electron diffraction enables the growth conditions to be systematically optimized but achieving layer-by-layer growth is challenging. A third approach to prepare a defined number of layers is to deposit a limited amount of the metal and then react this metal layer at low temperatures with chalcogen containing reactants. Both ALD[136,180–182] and physical deposition approaches[183] have been used to deposit a defined amounts of metal, however confirming that exactly a monolayer has been deposited is challenging. In a related approach, it has been shown that exchange reactions can be used to change oxide films into chalcogenide films while preserving the structure and thickness of the original film. [184]

In parallel with these layer-by-layer vacuum based growth techniques discussed briefly above, there has been a significant effort to develop low cost solution processing approaches to 2D materials.[140,184–191] Many compounds with layered structures can be exfoliated in solutions using a variety of approaches (ion intercalation, ion exchange, sonication) as summarized in several reviews.[192–194] The key to exfoliation is finding a combination of solvent and starting layered material such that the interaction of the layers and ions within the solvent is larger than the interaction between the layers of the starting layered material. For neutral systems such as graphene, the solvent-graphene interaction needs to be large to compensate for the loss of bonding between the graphene layers. For starting materials containing ions, the enthalpy of solvation of the cations needs to overcome the bonding between layers and the entropy loss associated with organizing solvent molecules around the ions. Exfoliated layered materials, which have been used for centuries in a variety of applications, continue to grow in importance. Researchers have discovered applications ranging from catalysts and

sensors, which take advantage of both unusual properties and large surface areas,[187] to polymer-exfoliated clay composites used as gas diffusion barriers.[195] Assembly of the 2D sheets created by exfoliation into heterostructures range from a sheet-by-sheet assembly of specific stacking sequences to self-assembly of sequences from solutions.[186] Groups are beginning to use liquid phase printing and spin coating techniques to make simple devices from solution precursors.[139] The scalability of solution processing and its low intrinsic cost relative to vacuum processing approaches gives solution processing a unique niche that will continue to expand.

The challenges involved in the synthesis of heterostructures with targeted nanoarchitecture are different than those in the traditional synthesis of new alloys or compounds. Since most targeted heterostructures will be metastable, the traditional high temperature or fluid phase mediated synthesis approaches that mostly yield thermodynamic products will not work. It has been recognized that approaches that control kinetics and reaction intermediates, such as molecular beam epitaxy, are required. A number of interesting approaches to dichalcogenide-containing heterostructures are being developed that rely on preparing a precursor containing some of the structure of the targeted heterostructure, which is then further processed using approaches that preserve the structure of the precursor (Figure 1.7).[66,183,196–201] The appeal of these approaches is that they avoid the challenges of finding suitable growth conditions as needed for van der Waals epitaxy, so several different constituents can be prepared on top of one another (ie A on B or C, B on A or C, and C on A or B) which is required to prepare complex layer sequences with multiple constituents. Encouragingly, theory groups are beginning to explore the growth process, which can provide insights into why some approaches work and also potential new approaches to try.[202,203]

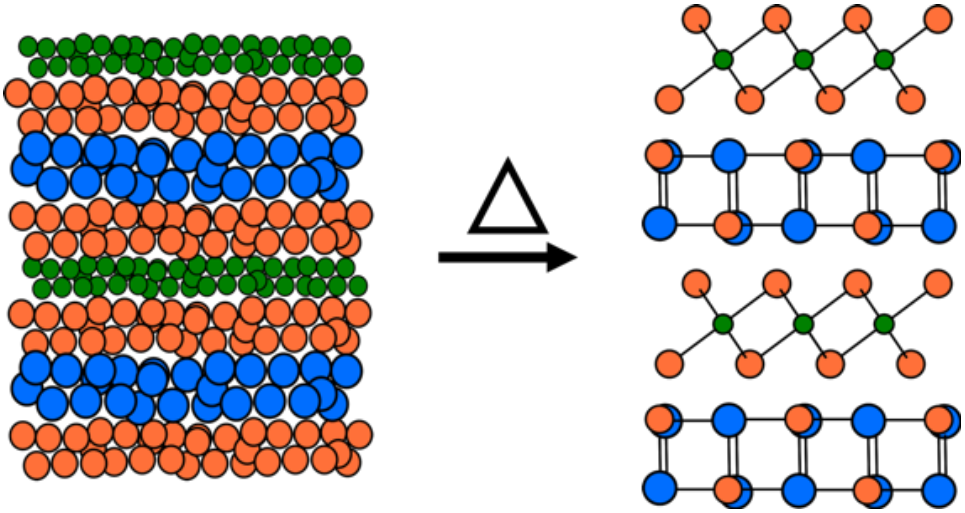

Figure 1.7. Synthesis of metastable heterostructures from a precursor with defined amounts of elements deposited The precursor is annealed at low temperatures to self-assemble the desired heterostructure.[205]

The fundamental underpinning of the post processing of designed precursors is surprisingly similar to that involved in traditional organic synthesis. In both cases precursors are designed and then reacted to obtain desired products, with the reaction conditions and or design of the precursor used to favor the formation of targeted products. Diffusion constraints (temperature and/or protecting groups) are used to direct the system towards desired products. The concept of energy landscapes[204] provides a valuable framework to potentially understand how the structure of the precursor and/or the reaction conditions enables the synthesis of metastable heterostructures.[205]

1.3.2. Characterization.

Characterizing the structure of constituent layers within heterostructures is critical, as most emergent properties will be intimately connected with structural changes at the interfaces or throughout the thin layers. These structural changes may be due to the large surface to volume ratios in the individual constituents and/or due to interactions between the constituents. Understanding the interplay

between synthesis conditions and the structure as well as the density of defects present in the heterostructures is very important, and it is limited by the ability to characterize the samples. Characterizing even the average structure of a 2D monolayers or heterostructures is, however, a major challenge due to the small amounts of material present. Determining parameters such as local and average layer thickness, bond lengths and average composition are significant analytical challenges. The development of new analytical tools, for example the easily observed optical interference pattern differences between graphene and SiO_2 as a function of the number of layers,[21,22] has been and will continue to be critical as this field advances. Numerous techniques have already been used to determine different structural features of heterostructures as discussed in the following paragraphs.

Measuring thickness of layers, both locally and over larger areas, has been a known challenge in this field. Historically, thickness was estimated through resistivity[4] or electron microscopy measurements.[1] In the resistivity measurements, researchers assumed a constant resistivity and used the resistance per square to determine thickness.[4] The electron microscopy experiments used both cross sections and the extent of shadowing to measure thickness. [1] Both optical interference[21,22] and scanning tunneling microscopy measurements were critical new tools used by Geim[19] and Novoselov[18] to determine the thickness of different regions as they probed the properties of graphene as a function of layer thickness. Additional tools need to be developed to speed the selection of heterostructured samples and preparation conditions.

Several different x-ray techniques have been used to determine the thickness and structure of thin film samples. X-ray reflectivity (XRR), an in-FAB metrology tool in the semiconductor industry, is very sensitive approach to measuring thickness.[206] Figure 1.8 shows a calculated reflectivity pattern (middle blue trace) for a heterostructure containing 8

$MoSe_2$ trilayers and two experimental attempts to prepare an 8 layer $MoSe_2$ film. The XRR pattern represents the sum of the intensities gathered over a relatively large, cm^2 sample area. The top pattern clearly deviates from that calculated for the ideal sample, with the low angle portion of the scan, which is dominated by front surface and back surface interference, having a different period than the higher angle portion of the scan (10-13°), which is dominated by the incomplete destructive interference of the $MoSe_2$ trilayers. This suggests that while the sample contains regions with the targeted 8 trilayers of $MoSe_2$, other regions are thinner than targeted. The bottom experimental pattern closely resembles the calculated pattern, indicating that the majority of the sample contains the targeted 8 trilayers. One challenge in interpreting XRR data remains determining which interfaces in a sample dominate the intensity pattern. Ellipsometry is a complementary tool that can be used to determine film thickness. Extracting thicknesses from ellipsometry data requires assumptions about the index of refraction at the wavelengths used. Resonant X-ray reflectometry (RXRR) is a developing tool that is, in principle, capable of determining complex chemical composition profiles in a non-destructive manner, as data collected at different energies greatly constrains potential structures.[207] A challenge in extracting detailed, quantitative information from XRR, elipsometry and RXRR data is the needed to construct models. While software exists to optimize models to fit experimental data, it is possible for incorrect models to do reasonably well in fitting limited data sets, so complementary information from other analytical techniques that can be used to develop initial models is very valuable.

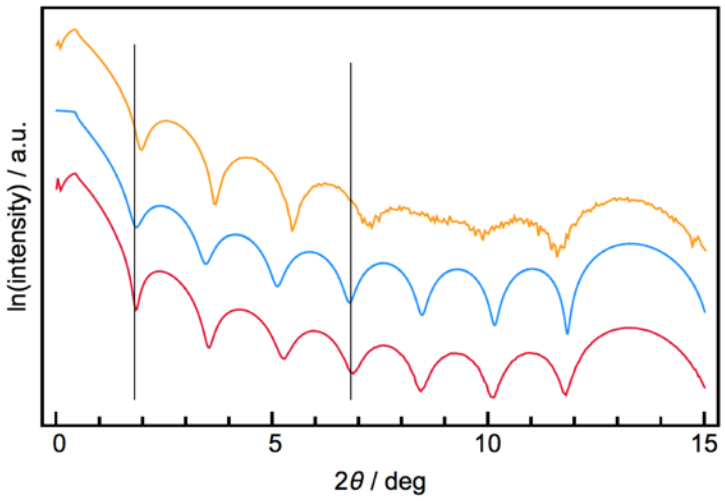

Figure 1.8. Calculated (blue) and experimental (red and yellow) XRR patterns for $MoSe_2$ films containing 8 layers.

For heterostructures containing more than one repeating layer sequence, specular x-ray diffraction provides a convenient tool to quantitatively determine the average position of atomic planes within the repeating layer sequence. There are relatively few examples in the literature where specular x-ray diffraction and subsequent refinement are used to determine the location of atomic planes.[208–210] Figure 1.9 contains the specular diffraction pattern of $(PbSe)_1(MoSe_2)_1$ along with a calculated pattern and the difference between them, where Rietveld refinement was used to optimize a model for the structure. The optimized structure is shown in the inset of Figure 1.9, with the inter plane distances from the model graphically displayed by the layer separation. Due to the alignment of constituents parallel to the substrate, only the *c*-lattice parameter can be extracted from the specular diffraction pattern and the refinement provides the location of the individual planes of atoms in the *c*-direction, as well. From the arbitrary locations of the atomic planes, the interplanar distances can be determined and any deviations from the bulk structure will be observed. From this model the Mo-Se intra unit distance was found to be 0.151 nm and places the Mo

plane of atoms symetrically between the two Se layers.[63] The metal layer in the dichalcogenide might not always be centered, however, as asymetric heterostructures might cause planes of atoms to shift due to the forces caused by the presence of different neighboring layers. In the PbSe consituent, there is a disortion of the rock salt layer due to the termination of the rock salt structure and the attraction and repulsion of the cations and anions respectively to the neighboring dichalcogenide layers. The distance between the $MoSe_2$ and PbSe layers was calculated to be 0.331 nm, which is longer than the van der Waal's gaps in pure dichalcogenides, presumably due to the layers having incommensurate structures.[63] The use of Rietveld refinement with models informed by complimentary techniques allows for fairly accurate determination of constituent layer crystal structures within layered materials.

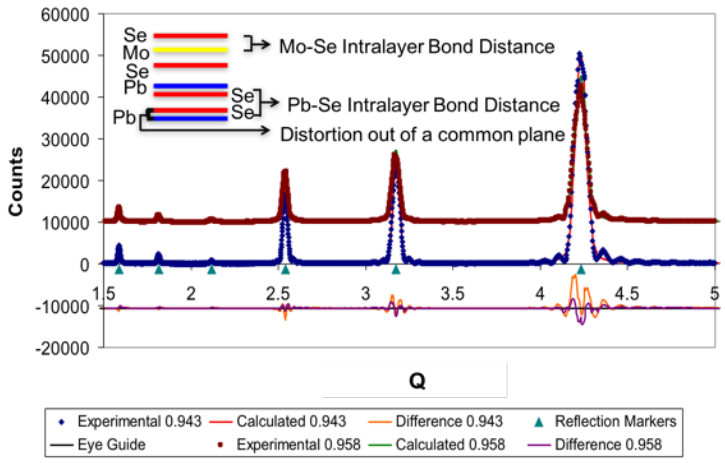

Figure 1.9. Locked-coupled theta-2theta X-ray diffraction used to understand the layer thickness of stacked unit cells of a PbSe-$MoSe_2$ heterostructure. A Rietveld refinement was conducted to optimize the structure to understand where planes of atoms are located. The inset shows a schematic of the structure of the compound with parameters that can be determined using Rietveld refinement.[63]

In-plane diffraction patterns can be used to obtain the in-plane symmetry and lattice parameters as well as additional information about

the basal plane structure of the film's constituents. Figure 1.10 contains the in-plane diffraction patterns of a 4-layer, 8-layer, and 24-layer $MoSe_2$ film. The reflections in the patterns can be indexed assuming a hexagonal unit cell and the indices are shown on top of each diffraction maximum. Since all expected (*hk*0) reflections are observed with the anticipated relative intensities, the sample consists of randomly oriented domains within the large (cm^2) analytical area. The change in intensity of the reflections between patterns correlates to the difference of the thickness of material in the beam. If the sample were to contain only a single orientation, then rotating the film would result in a set of maxima corresponding to the symmetry of the crystal system—i.e. a "pole figure" scan. If there is a second constituent in the heterostructures, the in-plane diffraction pattern would contain additional reflections, as shown in Figure 1.11 for a SnSe-$NbSe_2$-$MoSe_2$ heterostructure. The observation of all expected (*hk*0) reflections again indicates that the sample consists of domains of all orientations.

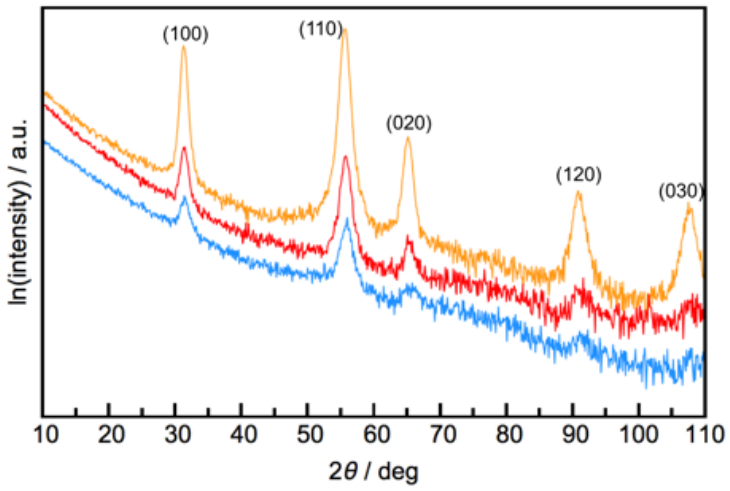

Figure 1.10. In-plane diffraction of $MoSe_2$ films with 4, 8, and 24 layers (blue, red, and yellow, respectively). All maxima can be indexed as (hk0) reflections of hexagonal $MoSe_2$ to determine the basal plane lattice parameter.

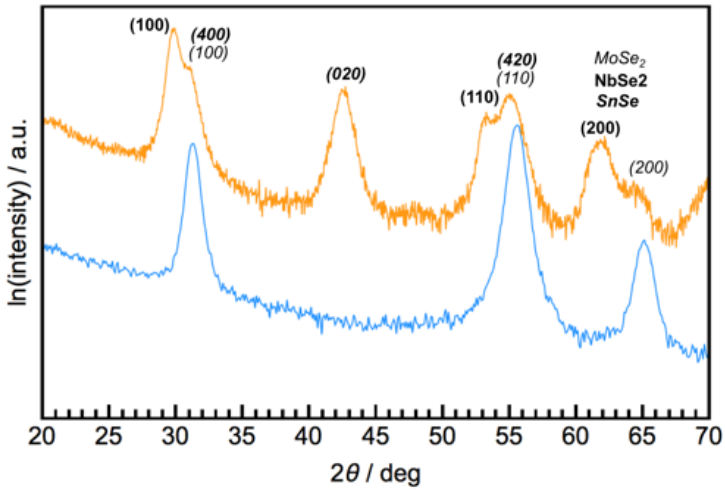

Figure 1.11. The in-plane diffraction pattern of a 24-layer $MoSe_2$ film is shown in blue. The yellow pattern is an in-plane scan of a $MoSe_2$- SnSe- $NbSe_2$ heterostructure. The additional maxima can be indexed as SnSe and $NbSe_2$ reflections, enabling the lattice parameters of all three constituent structures to be determined.[200]

Reciprocal space maps can be used to elucidate the extent of interlayer ordering. Figure 1.12 shows the reciprocal space map of $(PbSe)_1(WSe_2)_1$.[63] In this map, there are no distinct (hkl) reflections expected from the super lattice. Only broad maxima from the PbSe and WSe_2 are observed. This is consistent with extensive, random rotational disorder between constituents. Rotational disorder is not surprising in heterostructures due to the strong in-plane bonding in constituent layers. Even when one system is chemically "soft" due to a more three-dimensional structure, such as the SnSe containing heterostructures shown in the diffraction figures, the small energy difference between different stacking configurations and the kinetically controlled synthesis approaches used to make them will both likely prevent the system from finding a distinct, low energy, long range stacking arrangement. The rotational disorder and resultant lack of (hkl) diffraction maxima limits the ability to determine average bond lengths both within and between constituent layers.

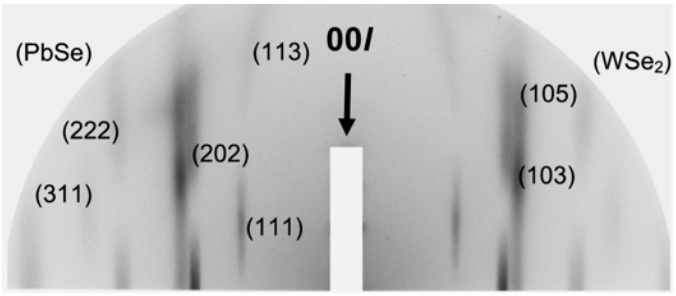

Figure 1.12. Reciprocal space map of a PbSe WSe_2 heterostructure. For both PbSe and WSe_2 there are no distinct reflections that correspond to the super-lattice period, only streaking indicating extensive rotational disorder between constituents.[63]

Transmission electron microscopy has been an indispensable tool for obtaining structural information about constituent layers and the relative orientation between them. [20,111,211–216] For example, plan view HAADF-STEM images of monolayer MoS_2 show that the molybdenum and sulfur atoms are arranged in a hexagonal configuration with Mo-S and Mo-Mo separations of ~0.19 and ~0.33 nm respectively.[211] This is consistent, within error, to the bulk structure which contains Mo trigonal prismatically coordinated by S.[211] Cross section HAADF-STEM images also corroborated trigonal prismatic coordination of Mo by S. Cross section HAADF-STEM images of all six possible heterostructure isomers containing 4 bilayers of SnSe and 4 $MoSe_2$ trilayers in the repeating unit showed that the Mo is trigonal prismatically coordinated by Se, but that there was extensive rotational disorder between adjacent $MoSe_2$ layers and between $MoSe_2$ and SnSe layers.[212] A schematic illustration of these isomers is shown in Figure 1.13. It is also possible to use HAADF-STEM images to obtain the average separation between atomic planes as demonstrated by Mitchison, et al.[111] The interplanar distances from these experiments can be used to create initial models for Rietveld analysis of x-ray diffraction data. The location of specific atoms within monolayers and the distribution of elements between layers in heterostructures can be determined using HAADF-STEM contrast or

EDX-STEM data.[213,214] These examples demonstrate how various STEM analytical techniques provide direct structural information. This insight is valuable for heterostructures both at a local level and to provide structural models for the interpretation of more global analysis techniques. Determining fine scale information, such as interlayer and interatomic distances, will become increasingly important to explain changes in properties.

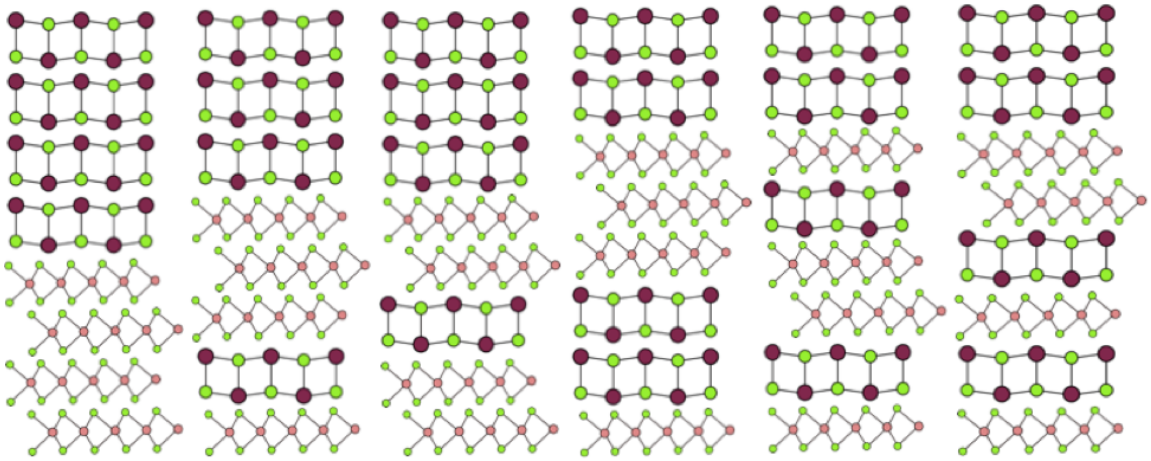

Figure 1.13. Schematic illustrations of the 6 possible sequences of layers requiring 4 dichalcogenide and 4 rock salt bilayers without repeating a portion of the sequence. Repeating one layer of each structure 4 times or two layers of each structure twice create an eight-layer repeat pattern with four layers of each structure, but segments are repeated.

Scanning probe techniques offer another route to determine the structural arrangement of atoms in both monolayers and the top layers of heterostructures.[217–220] A particularly valuable use of scanning tunneling microscopy/spectroscopy has been to examine the effect of synthesis parameters on the structure and defect levels of the resulting samples.[217] Scanning probe microscopy provides the ability to map electronic states and correlate them to topographical features and specific arrangement of surface atoms.[218] Probing changes to surface structure and electronic states as a function of exposure to atmosphere or different gases is particularly important to understanding the

differences in properties of samples prepared in various environments.[219] Scanning probe microscopy is a critical tool to determine changes in thickness of layers transferred using the scotch tape approach.

Measuring composition is a significant challenge in heterostructures due to the small amount of material, small probe sizes, and resulting small analytical volumes present in many common approaches. Electron or ion beam techniques are particularly challenging due to the small analytical volumes of the probe beam in the layer of interest relative to the analytical volume buried in the substrate. While the substrate signal can be reduced by changing the accelerating energy of the beam, this also affects the excitation probabilities for different transitions in the layer being probed. Energy dispersive spectroscopic (EDS) techniques suffer from the need to subtract relatively large background signals, whereas wavelength dispersive spectroscopic techniques (WDS) have a significantly smaller background signal. This makes WDS more appropriate for trace element analysis. Instrumentation improvements are required to increase the signal level necessary to obtain both relative composition and absolute quantitative amounts. Ion beam approaches, such as time of flight secondary ion mass spectroscopy (tof-SIMS), have the sensitivity to detect monolayers, but rigorously quantifying the ion yields has also proven difficult.[221] For large area samples, techniques such as x-ray fluorescence might provide enough signals, due to the increased area probed, to quantify the extent of fractional layers, but quantifying the geometric factors affecting the signal is challenging. Atom probe tomography is another approach to determine both composition and structure, and has been shown to be particularly useful to determine local occupancies of dopant atoms in 2D heterostructures.[222]

Raman spectroscopy is the most common analytical tool used to probe 2D materials,[109,223–228] because characteristic vibrational modes

can be used to identify specific monolayer materials and polytypes.[229] It is a quick, non-destructive probe of small areas and does not require complicated sample preparation. The high frequency intralayer vibrational modes of different dichalcogenides each have characteristic frequencies. These high frequency interlayer modes do not shift much in energy or intensity from the bulk dichalcogenide with the same local coordination of the transition metal (octahedral or trigonal prismatic).[229] The low-frequency breathing and shear modes, however are different for each polytype.[109] Once vibrational modes for different materials are tabulated, the Raman spectra of monolayer samples can be used to determine the local coordination and stacking motif of the layers. In few layer dichalcogenides and in heterostructures stacks, the changes in local symmetry due to the limited number of layers results in new Raman active modes.[230] For heterostructures or multilayer samples where the layers are not rotationally aligned, the interlayer breathing and shear modes can be highly sensitive to variation of the twist angle.[231] This complicates the Raman analysis of heterostructures and multilayers with random twist angles, and complementary techniques that more directly probe structure, such as electron or scanning probe microscopies, are frequently used in parallel.

Raman spectroscopy has become one of the first tools used for probing the properties of layered dichalcogenides and therefore has been the subject of multiple reviews. We refer interested readers to these excellent reviews. Zhang, et al. has discussed changes in Raman of transition metal dichalcogenides as a function of thickness, from monolayer to bulk. [110] A review by Saito, et al. covers the fundamentals of the polarization dependence of the Raman intensity and the Raman tensor. Zhang, et al. provide a more comprehensive review of different types of layered chalcogenides.[232] They demonstrate how low frequency modes can be used to probe the rotational angle between layers in a

bilayer and to investigate the interlayer coupling of vertically stacked dichalcogenides in heterostructures.[229] Puretzky, et al. beautifully illustrate this point, using complementary electron microscopy data to demonstrate how low frequency Raman modes due to interlayer vibrations serve as fingerprints to characterize the number of layers and their stacking configurations.[233] These papers and the references they contain provide valuable insight into the importance of Raman spectroscopy as a quick initial probe of heterostructures.

1.4. PROPERTIES

An iterative relationship between theory and experimental probing of physical properties, particularly in the nascent stages of discovery, greatly accelerates advancing a field. Optimizing the properties of dichalcogenide-based heterostructures through rational design is in an early stage and the number of potential heterostructures is enormous even if confined to those containing dichalcogenides.[214] The more theory can be informed by experimental data and vice versa, the faster progress there will be in predicting and engineering the properties of particular heterostructures.

An advantage of transition metal dichalcogenides as constituents of heterostructures is the wide range of properties that are known in the bulk compounds. Layered dichalcogenides can be metallic, superconducting, semiconducting, semimetallic, catalytically useful, and potential photocatalysts. A wide range of 2D magnetic properties can be found in closely related MPX_3 compounds where a phosphorus dimer substitutes for a transition metal in the hexagonal metal layer.[234–244] Transition metal dichalcogenide containing heterostructures provide an entire new set of parameters, including but not limited to - modulation doping via charge transfer between constituents, layer specific alloying, stacking sequence, rotation angle, and non-periodic graded structures - to combine, tune and/or optimize properties. Relative to more traditional

tetrahedral semiconductor-based layered architectures, the chalcogenide surface layers of dichalcogenides provide the ability to abruptly change both structure and composition. The lack of covalent bonding between layers allows for a range of rotation angles between the constituent layers and for their structures to be independent of one another. This field is just beginning and the following sections review recent progress with the discussion grouped around common properties or materials.

1.4.1. Semiconducting Heterostructures

Emergent phenomena in dichalcogenide monolayers were first discovered in semiconducting group 6b (Mo, W) dichalcogenides. MoS_2,[26,27] $MoSe_2$,[70] WS_2,[245] and WSe_2[31] have all been reported to transition from an indirect to a direct band gap as thickness is reduced to a single monolayer. Since monolayers of these compounds are relatively easy to isolate and are stable in ambient conditions, these systems and their emergent properties have proven amenable to extensive investigation. The group 6b dichalcogenides all contain a central plane of trigonal prismatically coordinated transition metal atoms, while the tin atoms of the semiconducting SnS_2 and $SnSe_2$ compounds, which adopt TMD-like layered structures, are all octahedrally coordinated. It is interesting to note that bulk tin dichalcogenides, like the group 6b analogues, are indirect band gap semiconductors, yet at the monolayer limit, tin dichalcogenides have both have been reported to maintain the indirect band gap.[246]

In heterostructures containing these and other semiconducting dichalcogenides, the band alignment between the constituents is critically important in determining properties (see Figure 1.14). In so-called type I band alignment, the band gap of one material falls entirely within the bandgap of the other material. In type II band alignment, the two band gaps are offset from each other such that $EVB_{,1} < E_{VB,2} < E_{CB,1}$ and $E_{CB,1} < E_{CB,2.}$ In type III ("broken") band alignment, the band gap of

one material falls entirely within the valence band of the other material. The first reference to heterostructures of semiconducting dichalcogenides we could find in the literature was on $SnS_2/SnSe_2/SnS_2$ heterostructures published in 1999. Van der Waals epitaxy[12] was used to prepared these heterostructures and a series of measurements were done to determine band offsets.[247] The recent interest in 2D materials has resulted in several papers reporting band offsets of heterostructures as a function of twist angle between bilayers,[93] and between different dichalcogenides that are stacked on top of one another.[248,249] There has also been considerable interest in lateral heterostructures – i.e. the in-plane junction of two different dichalcogenides.[250] Both calculations and scanning tunneling experiments examining lateral 2D heterostructures have been reported.[157,251]

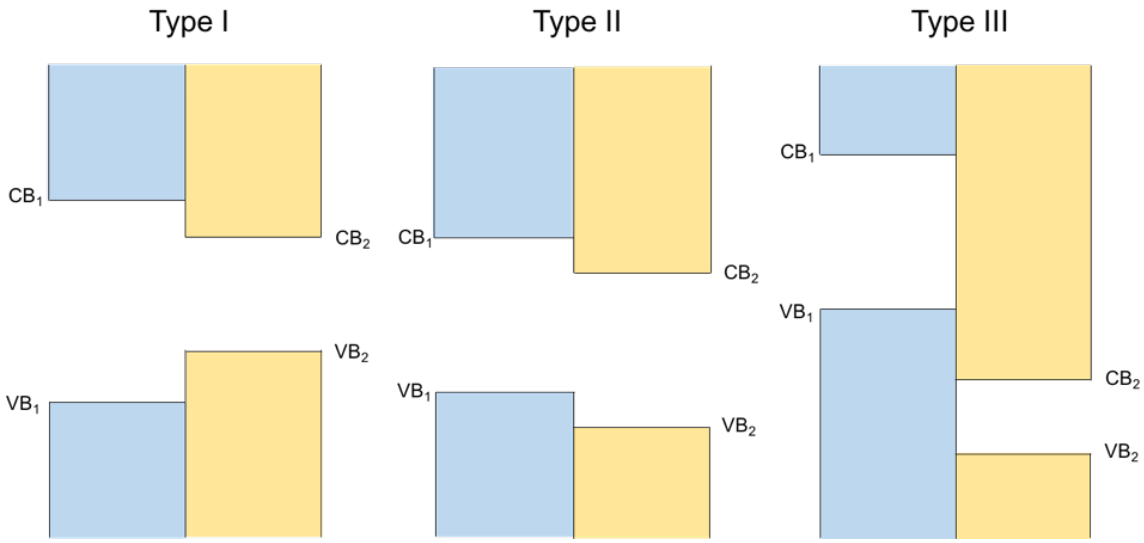

Figure 1.14. Band alignments in semiconducting heterostructures fall into one of the three categories depicted. In type I heterostructures, the band gap of one material falls entirely within the band gap of the other material. In type II heterostructures, the two band gaps are staggered such that $CB_2 < CB_1$ and $VB_2 < VB_1 < CB_2$. In type III, the band gap of one material falls entirely within the valence band of the other material.

The band alignment has an important influence on the carrier dynamics of electron-hole pairs created when light is absorbed (i.e. "excitons"). If a heterostructure has type II alignment, for example, the electron-hole pair created by the absorption of a photon in one layer can reduce its energy by transferring either the electron or hole to the adjacent constituent. In MoS_2-WS_2 heterostructures the holes can substantially reduce their energy by transferring from the MoS_2 to WS_2 and vice versa for electrons.[252,253] Significantly, the transfer of the hole between layers does not depend on the orientation of the layers, so epitaxy is not required, and this result implies that lattice mismatch should not affect the transfer rate.[253] This has been confirmed by subsequent reports showing ultrafast charge transfer in MoS_2-WSe_2,[254] $MoTe_2$-MoS_2[255] and $MoSe_2$–WSe_2[256] heterostructures. Since an electron-hole pair is tightly bound in 2D monolayers and there is a momentum mismatch between randomly rotated layers, the efficient and ultrafast charge transfer between layers has significant implications for devices prepared from heterostructures. Consequently, various aspects of the charge transfer mechanism have been explored both theoretically[257–259] and experimentally.[159] Figure 1.15 summarizes the optical transitions expected for heterostructures with type I and type II band alignments.

The discovery that monolayers of the group 6b dichalcogenides have direct band gaps and the discovery of fast charge transfer in heterostructures containing them has spawned research into the electronic properties of these systems and their derivatives. These dichalcogenides interact strongly with light at the ultimate monolayer limit[260] and host highly stable excitons (i.e. high binding energies, extended lifetimes),[56,261,262] which has resulted in exciting studies that either probe or exploit these properties. The substrate influences the excitons[154] but some properties, such as the conservation of spin-valley polarization during charge transfer between two monolayers, have been

found to be only weakly dependent on the twist angle between layers.[161] The unique properties of dichalcogenide monolayers and the heterostructures built from them provides a promising platform for light–matter interaction experiments[260,263] and has resulted in a continuing stream of papers building devices to take advantage of these properties. The devices include light emitting tunneling diodes,[150] floating gate memory,[156] photovoltaic devices,[160,264] and high sensitivity,[151] broadband,[153] and large area detectors.[265] Dichalcogenide nanosheets are also being explored as efficient photocatalysts and electrocatalysts for the production of hydrogen.[187,266,267] There has been considerable interest in the growth and properties of lateral heterostructures – in-plane junctions of two different dichalcogenides.[250,268] Alloying either the transition metal[269] or the chalcogen[270] can be used to tune most of the important properties of these dichalcogenides, including structural phase transitions,[271] band offsets,[272] band gaps,[273] and resulting device properties.[68,274] This field is rapidly advancing, and ultimately the emergent properties of semiconducting TMD monolayers and heterostructures may find practical applications in lasers, light-emitting diodes, detectors, and photovoltaics. The next decade will see a significant growth in our understanding of the relationship between the structural nuances of TMD's in heterostructures, such as the importance of the interactions between layers, between constituents and substrates, between the active and protecting layers, and the resulting optoelectronic properties. This understanding will be of paramount importance for the efficient optimization of the emergent properties. The ability to construct novel heterostructures with reasonable assurance that they can be made provides value to predicting their properties. These predictions will significantly speed the development of this area.

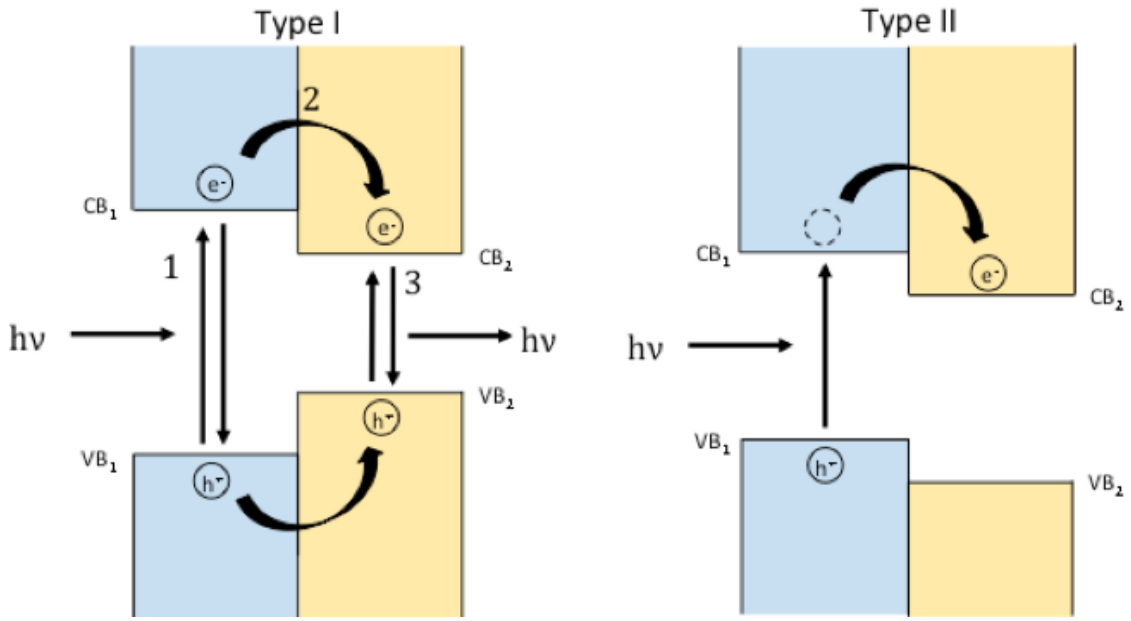

Figure 1.15. In type one alignment of the bands, photons can be absorbed if the energy of the incident light is above the respective band gaps, forming excitons. The kinetics of charge transfer between the constituents (labeled 2) and the ratio of initial absorption between the two constituents will determine the relative intensities of light emitted at the different band gap energies. In type II alignment, formation of the exciton occurs in one constituent layer and electrons will transfer into the adjacent material to achieve a lower energy state, resulting in an interlayer exciton. Since the constituents are separated only by the small van der Waals gap, the two charges remain bound.

1.4.2. Metallic Heterostructures

The transition metal dichalcogenides, structurally related compounds, and other compounds that are potential heterostructure constituents offer a wide array of interesting properties that should, in principle, change as a function of thickness. While most of the early work has been on semiconducting monolayers, due to their novel emergent properties, the group IV and V group transition metal dichalcogenides offer additional and distinctly different opportunities. The group IV and group V transition metal dichalcogenides are semimetallic or metallic. There have been extensive studies aimed at understanding superconductivity, charge

density waves, catalyst activity, and intercalation phenomena in the bulk group IV and V dichalcogenides.[275–277] The nanoscale thickness and monolayer properties of the metallic and semimetal compounds are less explored because they are typically less stable in normal atmospheric conditions than the semiconducting systems. For example, atomically thin $NbSe_2$[278] and TaS_2[279] have been reported to be unstable under ambient conditions. These stability challenges have been overcome by covering the sample with a protective layer[280] or by preparing a heterostructure containing the dichalcogenide layer of interest sandwiched between protective layers that are more stable under normal atmospheric conditions.[281,282] Properties such as superconductivity and charge density waves have been shown to be thickness dependent, but as discussed below there are often considerable differences between literature reports.

There is an earlier body of literature that provides important structural data and ideas for the current interest in heterostructures containing isolated single nanosheets of layered group IV and V dichalcogenide compounds. Thermodynamically stable heterostructures of Ti, Cr and the group V dichalcogenides were prepared starting in the late 1980's by the groups of Wiegers,[283] Meerschaut,[284] Onoda[285] and Gotoh[286]. The properties of these compounds provide valuable insights for heterostructures being pursued today. These compounds were prepared by a direct reaction of the elements at high temperature, and are thermodynamically stable compounds. Single crystals can be grown using vapor transport reactions. As an example, combining Pb, Nb and Se and heating the elements to ~1000°C results in a so called misfit layered compound containing single $NbSe_2$ layers separated by a unit cell thick layer of distorted PbSe.[287] The fact that this is stable relative to a mixture of PbSe and $NbSe_2$ indicates that the interaction between the layers is strong, even though there is not an epitaxial relationship between the constituents. It has been suggested that charge transfer

between constituents creates a significant electrostatic bond between the layers that stabilizes these compounds,[288] although there is still considerable debate.[289] The physical properties change considerably as constituent layers are altered, and there are several extensive reviews reflecting significant interest in the structure and physical properties of these unusual compounds.[15,290] None of these compounds have charge density wave transitions, but many of them are superconducting. Compounds with atoms containing magnetic moments, such as rare earth atoms, displayed magnetic order.[15] In these misfit layered compounds, the structure of each layer typically distorts to create one common in plane lattice parameter while the other axis is incommensurate.[290]

Analogs of the crystalline misfit compounds can be prepared via low temperature synthesis routes. Compounds prepared by this route contain a random twist angle between layers, which, in the clay literature, is called turbostratic disorder.[291] These turbostratically disordered polymorphs, called ferecrystals, have been shown to have charge density waves, different superconducting properties than their analogous crystalline properties, and extraordinarily small thermal conductivities.[292] The variation of heterostructure properties as a function of constituent pairings and the rotation angle between them shows the importance of layer interaction in property determination. By extension, the surface on which a heterostructures is placed will also impact property measurements. The existence of thermodynamically stable misfit compounds - monolayers of dichalcogenides with a fragment of a 3D structure between them - suggests that there are many other heterostructures, combinations of 2D layers and 3D fragments of structures, that should be, at a minimum, kinetically stable.

The ability to predict the structures of layers and their potential combinations has already resulted in a significant theoretical effort

exploring potential constituents, combinations of constituents, and their potential properties. The electronic structure and band alignment of monolayers of transition metal dichalcogenides in heterostructures has been systematically investigated, exploring interfacial charge polarization and redistribution.[248] Due to both the random twist angles between layers and the different lattice parameters for various constituents, the charge polarization and redistribution both deviate from conventional epitaxial semiconducting heterostructures based on tetrahedral semiconductors. Researchers have investigated structural and charge density wave phase transitions by probing how substrates, charge transfer between constituents, and electrostatic gating impact physical properties.[293,294] Researchers have begun to explore the properties of 2D fragments of 3D structures, for example a unit cell (or two atomic planes) of the group IV monochalcogenides, in searching for potential emergent properties.[295,296] The stability of CuS 2D layers as a function of thickness was recently reported.[297] The impact of the twist angle between ultrathin layers of Bi_2Se_3[298] and the specific arrangement of different cations within a dichalcogenide layer[299] on potential topological states has been explored, as well. Extending these studies to probe potential heterostructures would be useful for experimentalists, and the misfit layer compounds provide an opportunity to compare predictions with experimental data. One aspect yet to be explored are the energy differences between different 2D slices of a 3D structure.

Experimentalists have also been exploring both new compounds and composites to probe for emergent properties. Research has explored doping known compounds with structures that appear to consist of interleaved 2d layers to create emergent properties that might be replicated in designed heterostructures. Knowing the distribution of the doping atoms between the layers is important for understanding the origin of superconductivity[222] and is important in determining the

amount of modulation doping required to induce superconductivity in a heterostructure. Alemayheu, et al. showed that it is possible to prepare heterostructures containing fragments of 3D structures by preparing several new VSe_2-$GeSe_2$ heterostructures. In this report the thickness of the VSe_2 block was varied while a monolayer of $GeSe_2$ was maintained.[197]

There has been considerable interest in finding a magnetic layer that could be used in the construction of heterostructures to probe topological properties and potential devices. One approach has been to create an interface between a magnetic insulator and a 2D layer to create a strong interfacial exchange field.[158] A second approach has been to find compounds containing magnetic ordering in layers that have strong bonding in a 2D layer separated by van der Waals bonding. The MPX_3 family of compounds, where M is Mn, Cu, Fe, In, … and X = S, Se, are semiconducting compounds due to strong electron correlation between the layers, but result in magnetic ordering within each layer of magnetic ions.[226] Ultrathin flakes of non-magnetic members of this same family have also been explored as ferroelectrics.[300] Heterostructures containing different thicknesses of SnSe and PbSe alternating with blocks of MSe_2 trilayers (M=V, Nb, Ta) show systematic changes to the structure of the SnSe or PbSe block with thickness, and also display systematic changes in Hall coefficient and resistivity.[112,116,282,301,302] These results, while not inclusive of all that has been reported, illustrate the large number of potential heterostructures that can be prepared and several different approaches to discover emergent properties or optimize them for potential device applications.

A relatively general phenomenon that has been observed in both metallic monolayers and metallic heterostructures is an upturn in the resistivity as the temperature is lowered below approximately 30K. This has been observed in NbS_2 as the thickness is decreased[303] and also in a number of heterostructures.[201,281,304] In both the pure dichalcogenide

and the heterostructures, the upturn becomes more pronounced as the thickness of the metallic layer is decreased. In the heterostructures, the upturn becomes more pronounced as increasing thickness of a semiconducting constituent separates the metallic dichalcogenide layer. The upturn in resistivity is not observed in crystalline metallic misfit layer compounds with identical composition and sequential layers as found in the ferecrystals, suggesting that the upturn is related to the disorder.[305]

Charge density wave (CDW) transitions have been extensively explored in both heterostructures and as a function of thickness of dichalcogenide layers. This interest stems from the fundamental interest in the effect of dimensionality on the CDW[165,306–310] and the potential use of CDW materials in optoelectronic devices[311] and quantum information processing.[312] Controlling the thickness of a dichalcogenide layer or the layer sequence and thickness in a heterostructures might potentially enable the CDW transition to be tuned to an optimal temperature or enable it to be controlled by an electric field.[167,313,314] A relatively large spread of reported CDW transition temperatures have been reported for nominally the same compound. For instance, an ordering temperature above 100K was reported for atomically thin $NbSe_2$,[165] while a lower ordering temperature CDW order (~ 25 K) was reported for a monolayer $NbSe_2$ grown on graphene.[315] There are several different reports on how the CDW changes as the number of VSe_2 layers are reduced. VSe_2 exhibits a CDW transition at 100K in the bulk.[316] The onset of the CDW in thin layers of VSe_2, prepared via liquid exfoliation, is 135 K as thickness is reduced to 4-8 trilayers.[317] Micromechanically exfoliated nanoflakes have lower onset temperatures which decrease to 81K at the lowest thickness.[307] Studies of $[(SnSe)_{1.15}]_m(VSe_2)_n$ prepared by annealing designed precursors have shown that compounds with a single layer of VSe_2 separated by *m* layers of SnSe are p-type metals with a CDW that

depends on the thickness of SnSe.[302] Increasing the VSe_2 layer thickness to two or more layers results in low temperature n-type metals and the suppression of the pronounced effect in transport properties at the CDW transition temperature is similar to bulk VSe_2.[318] The influence of surface contaminations, the effect of different constituents, and/or the substrate on the charge density wave transition are only beginning to be explored or discussed in the literature. Encapsulation of the dichalcogenide layer of interest has been shown to enhance the CDW order in $TiSe_2$.[319] Similarly, TaS_2 layers were encapsulated by covering them with boron nitride.[279] VSe_2 layers prepared in situ from designed precursors have shown reproducible CDW transition temperatures and systematic changes as the thickness of either the VSe_2 block or SnSe has been changed.[302,318] These results suggest that much of the observed variability of results is a consequence of the instability of monolayers of the metallic dichalcogenides under ambient conditions. It might be possible to systematically control the CDW transition temperature of heterostructures through the choice of constituents and/or controlling the position of the Fermi level through modulation doping.

Given that some of the earliest investigations of ultrathin dichalcogenides by Frindt investigated superconductivity as a function of thickness, it is surprising that until recently there has been little attention directed in this area. This seems to have changed in 2016, with several high profile reports of well-defined 2D superconducting states in atomically thin $NbSe_2$,[320] TaS_2[321] and doped MoS_2[322]. It is important to note that there were earlier reports of superconductivity in atomically thin flakes of $NbSe_2$ prepared by mechanical exfoliation which demonstrated that the carrier density in these 2D layers could be changed by an electric field. [323] While traditionally carrier concentration is altered by chemical doping via atom substitutions, changing carrier density with an electric field minimizes potential complications such as

impurity scattering. There have been several papers that show enhancement of the effective electron–phonon coupling constant, due to the change in phonon modes in monolayers.[165,278,315] All studies show a decreasing superconducting critical temperature as the thickness of the layers is decreased, although the values reported for samples of the same dichalcogenide with nominally the same thickness are different.[131,165,278,279,305,315,320] The variations may be due to different doping levels caused by neighboring layers or substrates, as Alemayheu reported a systematic increase in the Hall coefficient of $(SnSe)_1(NbSe2)_n$ heterostructures as n was decreased to 1.[324] A similar trend was observed in $(PbSe)_1(NbSe_2)_n$ layered structures,[305] although the amount of charge transfer was different due to changes in the band alignment as SnSe[281] was replaced by PbSe.[325] Researchers exploring the superconducting and structural properties of FeSe layers on a variety of substrates have reported similar modulation doping effects.[52,132,216,326–333] Adjacent layers or adsorbed surface species have begun to be used to investigate the interaction between two phenomena, for example superconductivity and ferromagnetism.[334] Monolayers are particularly sensitive to modulation doping, and phase transitions can be controlled by changing the Fermi level of adjacent layers through doping.[51] The investigation of superconductivity in 2D material is poised to see dramatic growth, as the ability to prepare stacks of constituents with different intrinsic properties will enable the interaction between phenomena to be investigated systematically.

The thermal conductivity of monolayer dichalcogenides and the heterostructures built from them has intrigued researchers since the first report, in 2007, of ultra-low thermal conductivity in heterostructures containing dichalcogenides.[335] Subsequent reports have reinforced the idea that the ultra-low thermal conductivity in the stacking direction of the turbostratically disordered heterostructures results from the random

twist angles between adjacent dichalcogenide layers and between the various constituent layers.[212,336–338] Low thermal conductivity of thermodynamically stable misfit layer compounds have been correlated with the density of stacking faults between adjacent layers.[339] The in-plane thermal conductivity of the heterostructures is a factor of 3 to 5 higher in the systems that have been measured, with the absolute value probably correlated with the in-plane grain size of the constituent layers.[340] The thermal conductivity of a monolayer has been calculated to also be anisotropic.[341] The ultra-low thermal conductivity of heterostructures provides opportunities to control the temporal features of heat pulses, which might be useful in designing phase change memory devices.

The very low thermal conductivity of heterostructures containing dichalcogenides has led to heterostructures being investigated as potential thermoelectric materials. Promising thermoelectric performance in dichalcogenide based materials have been reported for intercalates, due to the lowering of thermal conductivity and the ability to optimize carrier concentration.[342,343] Low lattice thermal conductivity and promising un-optimized power factors have been reported for dichalcogenide monolayers.[344,345] The thermodynamically stable misfit layered compounds have also been investigated as thermoelectric materials, with promising un-optimized figures of merit.[346,347] The ability to prepare heterostructures of dichalcogenides with desired thicknesses of various constituents and targeted layer sequences provides an opportunity to optimize performance while gaining a better understanding of interactions and bonding between different constituent layers.[348] The ability to prepare heterostructures with junctions between constituents that have very different properties provides an avenue to increase efficiencies[349] and discover novel phenomena.

Topological phases, including topological insulators and Weyl semimetals have been the focus of recent attention, including the 2016 Nobel Prize in Physics to David Thouless, Duncan Haldane, and Michael Kosterlitz. Many of the most common materials studied for the topological properties consist of strongly bonded layers weakly connected by van der Waals bonding. For example, $HfTe_2$, $MoTe_2$ and WTe_2 have all been reported to be topological Weyl semimetals[178,350–353] while bismuth chalcogenides, Bi_2Te_3, Bi_2Se_3 and their alloys, are the prototypic topological insulators.[354–367] Both absolute size of the particles being investigated[368] and chemical doping have been used to produce new phenomena.[369] From a materials perspective, heterostructures containing very thin constituent layers might be useful in reducing contributions from the bulk, enabling exotic topological states to be both easier to study and utilize. Heterostructures also potentially provide an avenue to prepare materials with different properties adjacent to one another,[370] for example a ferromagnetic layer adjacent to a superconducting layer, with a defined interface between them. The use of heterostructures to probe topological properties is just beginning.

1.5. SUMMARY

The ability to prepare and manipulate monolayers of dichalcogenides and other 2D materials as building blocks for heterostructures provides scientific challenges and opens new opportunities. Challenges include:

- Developing approaches to synthesize heterostructures over large areas with control of individual constituent layer thicknesses and the sequence of layers.
- Advancing measurement techniques to characterize the local composition and structure of each constituent layer.

- Developing theoretical approaches to predict band alignments, the extent of charge transfer between constituents, structural distortions and properties of heterostructures with incommensurate interfaces.

The new opportunities include:

- Predicting the structure of an essentially infinite number of new heterostructures, enabling theorists to predict the properties of compounds yet to be made.
- Creating interfaces where atoms are in unusual coordination environments, potentially leading to the discovery of more emergent properties.
- Designing heterostructures that combine multiple technologically desirable functionalities in adjacent constituent layers that tend not to co-exist.
- Using the concept of an energy landscape to develop synthetic routes to the infinite number of potential metastable heterostructures.

Tremendous progress has been made in the past decade developing approaches to make monolayers of specific compounds, understanding the origin of emergent properties at the monolayer limit, and identifying how properties change as monolayers are placed on different substrates. Understanding how incommensurate layers interact, how different combinations of constituents lead to emergent properties, and how to utilize new properties in devices are likely to dominate this field of research in the coming decade. The potential outcome of these efforts will be materials by design, with constituents and nanoarchitecture of heterostructures optimized for predicted emergent properties and the desired function of the total material in a specific device.

1.6. Dissertation Overview

The comprehensive goal of this work is to investigate how nanoarchitecture, amount of material per layer, and constituent type influence constituent structure, sample formation mechanism, and transport properties in multilayer heterostructures. The results of this work can be used to recognize trends in families of compounds with systematic changes in nanoarchitecture and provide a platform for the synthesis and characterization of novel building block materials with unique properties for use in nanolaminate heterostructures. This work is divided into 3 sections, each one investigating a different aspect of the overarching theme.

The first section is comprised of Chapters 2 and 3, which focuses on the general methods and experiments used to prepare and characterize the materials investigated in this work. Chapter 2 was previously published in ACS *Chemistry of Materials* in 2018 and I am the primary author. This was a collaborative effort between Dylan Bardgett, Dmitri Cordova, Liese Maynard, Alexander Lygo, Suzannah Wood, Marco Esters, and David Johnson. This investigation demonstrates sub-monolayer sensitivity for X-ray Fluorescence (XRF) measurements within the thin film limit and shows that this technique can be used to measure the absolute amount of material in a film, as opposed to simply determining relative compositions. This method is the basis for determining what synthesis conditions are needed to prepare the desired heterostructures. Chapter 3 provides an overview of the synthetic method used to prepare the various thin film materials, including an in-depth explanation of how XRF data is used to inform heterostructure preparation. Lastly, a brief description of the characterization techniques used to analyze the films is discussed.

Section 2, which is composed of Chapters 4 – 11, focuses on investigating interactions in $[(MSe)_{1+\delta}]_m[TiSe_2]_n$ (M = Sn or Pb) families of

compounds and how the amount of material, constituent type, and nanoarchitecture influences these properties. The main goal of this section is to investigate interlayer interactions and formation mechanisms to understand the properties that are observed for families of compounds with systematic changes. Chapters 4 - 5 concentrate on the individual properties of binary SnSe and $TiSe_2$ films. Chapters 6 – 10 center around investigating the role of nanoarchitecture on constituent structure properties, charge donation between layers, and carrier transport properties in $[(SnSe)_{1+\delta}]_m[TiSe_2]_n$ heterostructure compounds. Chapter 11 investigates the influence of the amount of material per unit area and nanoarchitecture on $[(PbSe)_{1+\delta}]_m[TiSe_2]_n$ heterostructures thin films.

Chapter 4 was published in ACS *Nano Letters* in 2019 as a collaborative work between myself, Jihan Chen (primary author), David Choi, Niraker Poudel, Lang Shen, Li Shi, David Johnson, and Stephen Cronin. This study focuses on the thermoelectric and transport measurements of SnSe and $SnSe_2$ thin films, providing insight into the inherent properties of these materials. The work in Chapter 5 investigates the formation mechanism of $TiSe_2$ thin films and the influence that the amount of material per unit area has on the structure of the crystalized material. This is unpublished work that is written in collaboration with Aaron Miller and David Johnson.

Chapter 6 was published in 2017 in the ACS journal *Inorganic Chemistry* and was co-authored by myself, Devin Merrill, Sage Bauers, Gavin Mitchson, Jeffrey Ditto, Sven Rudin, and David Johnson. This chapter discusses in-plane preferential aligned between SnSe and $TiSe_2$ in a $[(SnSe)_{1+\delta}]_1[TiSe_2]_1$ heterostructure as a result of an accidental lattice match caused by lowering of the systems total free energy. Chapter 7 was coauthored by myself, Alexander Lygo, Marco Esters, Devin Merrill, Jeffrey Ditto, Duncan Sutherland, Sage Bauers, and David Johnson and

was published in *ACS Nano* in 2018. This work investigates the inflence of nanoarchitecture on constituent in-plane structure and transport properties in a $[(SnSe)_{1+\delta}]_m[TiSe_2]$ series of heterostructures. Chapter 8 focuses on charge donation between layers and how it is modified by nanoarchitecture in a $[(SnSe)_{1+\delta}][TiSe_2]_n$ series of compounds. This is unpublished work that is submitted to *Chemistry of Materials* and coauthored with Dylan Bardgett, Austin Mroz, Thomas Kasel, Chris Hendon, Doug Medlin, and David Johnson. Chapter 9 is unpublished work that investigates how transport properties change in $[(SnSe)_{1+\delta}]_m[TiSe_2]_n$ polymorphs with the same composition ratio but different nanoarchitectures. This work is cowritten with Dylan Bardgett, Sage Bauers, Jeffrey Ditto, and David Johnson. Chapter 10 investigates the bonding and charge donation in the $[(SnSe)_{1+\delta}]_m[TiSe_2]_2$ via XPS and informs on the band structure that might occur in the materials. This work was previously published in the MRS *Journal of Materials Research* in 2019 and is coauthored with Fabian Göhler, Niels Rösch, Susanne Wolff, Jacob Logan, Robert Fischer, Florian Speck, David Johnson, and Thomas Seyller.

The influence of amount of material per unit area on the formation mechanisms of $[(PbSe)_{1+\delta}][TiSe_2]_n$ heterostructures as well as the influence of nanoarchitecture on properties was the focus of Chapter 11. This is unpublished work that is coauthored with Sage Bauers, Tara Clayton, Jeffrey Ditto, Daniel Moore, and David Johnson. It reports on the role of buried interfaces on the transport properties of $[(SnSe)_{1+\delta}]_4[TiSe_2]_4$ isomer heterostructures, as well as how precursor's nanoarchitecture drives the crystallization process even when the amount of material required is insufficient.

The last section focuses on preparing novel Mn-containing magnetic materials by controlling the amount of material deposited and the heterostructures nanoarchitecture, which includes Chapters 12 and

13. Chapter 12 focuses on the interaction of Mn and Se in the thin film limit and the different conditions required to allow for various materials to form. This article was a collaborative work with Marisa Choffel (primary author), Jordan Joke, Dmitri Cordova, and David Johnson that was published in *Zeitschrift für anorganische und allegemeine chemie* in 2018 and laid the groundwork for the synthesis of future Mn containing materials. Chapter 13 describes the preparation, characterization, and properties of novel Mn containing compounds as well as the computational and experimental path taken to achieving the synthesis of these novel materials. This chapter is currently unpublished; however, a manuscript is in preparation and is coauthored by Sven Rudin, Tomoya Asaba, Filip Ronning, Dmitri Cordova, Ping Lu, and David Johnson. Chapter 16 provides conclusions and summary of this work as well as discusses next steps including work towards other novel heterostructure building blocks.

1.7. BRIDGE

Chapter 1 provided a general overview of the synthesis, characterization, and properties of dichalcogenide containing thin film heterostructures. The vast amount of literature on thin film heterostructures demonstrates that nanoarchitecture, amount of material per unit area, and interfaces all play a large role in the resultant structure and properties. The next chapter will focus on the use of XRF to quantify material at the sub-monolayer limit in thin film heterostructures. By relating the intensity of signal measured to the amount of material in each sample, new heterostructures can be made quickly and efficiently by calculating and targeting specific amounts of material.

CHAPTER II

SUB-MONOLAYER ACCURACY IN DETERMINING THE NUMBER OF ATOMS PER UNIT AREA IN ULTRATHIN FILMS USING X-RAY FLUORESCENCE.

2.0. AUTHORSHIP STATEMENT

The work in this chapter was published August 16, 2018 in Chemistry of Materials (DOI: 10.1021/acs.chemmater.8b02591). I am the primary author on this work. Dylan Bardgett, Dmitri Leo M. Cordova, Liese A. Maynard, Erik C. Hadland, Alexander C. Lygo, Suzannah R. Wood, Marco Esters, and David C. Johnson were co-authors on this work. This manuscript uses data provided by all of the co-authors. I helped develop the idea, compiled and analyzed the data, as well as wrote the manuscript. David C. Johnson is my advisor.

2.1. INTRODUCTION

The discovery that isolated two-dimensional layers have extraordinary properties that are not found in their bulk counterparts has resulted in intense experimental and theoretical interest in these materials.[1–12] A distinct challenge towards the future use of these materials in new technologies is developing techniques to grow single layers of various 2D solids over large areas. While a variety of techniques have been explored to prepare monolayers, chemical vapor deposition involving a volatile metal source has become increasingly popular.[13–26] Typically, "about a monolayer" of a metal is deposited on a surface and treated at high temperatures with a second reagent to form domains of the desired monolayer on substrates.[27–29] Since the deposited metal species is typically not volatile once the precursor has reacted on the surface, time is the parameter tuned to get close to monolayer coverage. This type of monolayer synthesis creates an analytical need to be able to quickly measure fractional monolayer amounts of elements on a substrate, ideally without significant sample preparation.

More generally, measuring the number of atoms per unit area of each element in a thin film is a challenging analytical problem and critically important in many situations. Physical properties depend on both composition and thickness of constituent layers in devices, and the properties of compound films are a sensitive function of composition. A variety of approaches have been used to determine composition, including Rutherford backscattering, electron probe microanalysis, particle-induced X-ray emission, X-ray photoelectron spectroscopy, time of flight secondary ion mass spectrometry, and a variety of electron microscopy techniques.[27–30] Most of these techniques involve expensive instrumentation and several also require significant sample preparation. Sensitivity and converting the signal to the number of atoms of each element per unit area can also be very challenging, particularly if the signal is sensitive to the matrix. Typically, only a composition ratio is determined, as taking the ratio of two different elements eliminates several difficult to determine proportionality factors that depend on geometry, other instrument dependent factors, and the sample itself.

X-ray fluorescence (XRF) is a metrology method that can determine both composition and thickness of thin films and has several advantages. While it requires the use of standards to obtain instrument parameters and absorption corrections need to be made (via standards with similar matrices or modeling), it is quick and precise. Early work on the XRF analysis of thin films focused on using a variety of different methods to correct for absorption effects in the thin film geometry.[31,32] This lead to the development of XRF as a tool to characterize relatively simple multilayer films in the advance of materials for a variety of applications, including memory devices and optical recording.[33,34] More recent reports have shown that XRF is also a useful approach to characterize patterned thin films, with intensity differences before and after patterning proportional to the amount of material removed during the patterning

process.[35] While a significant challenge has been to accurately correct the XRF data for absorption effects, there is at least one report where XRF using wavelength-dispersive X-ray detection was used to examine films that are thin enough that absorption can be ignored.[36] This study showed that a resolvable composition difference of 0.025 atomic percent could be obtained with relatively short counting times in a series of chalcopyrite solar cells.

In this paper, we present data showing that XRF intensity is proportional to the number of atoms per unit area in ultrathin films and the intensity is relatively insensitive to the matrix. The number of atoms per unit area for a subset of exceptionally smooth films was calculated using data from a combination of x-ray reflectivity, specular diffraction, and in-plane diffraction scans. Calculating the proportionality constant between XRF intensity and the number of atoms per unit area simply requires division of the measured XRF intensity by the calculated number of atoms per unit area. The proportionality constant in over 20 samples with a range of thicknesses is consistent for the elements examined, indicating this is a valid approach. Once the proportionality constant is known for an element, preparing films of known compounds with defined atomic ratios between the previously studied element and other elements enables the determination of the proportionality constant for previously unstudied elements without the need for exceptionally smooth films. The consistency of results for films containing a wide range of different matrix constituents makes this a simple, relatively inexpensive, nondestructive, and fast method to measure the number of atoms in an ultrathin film. This study demonstrates that XRF is capable of detecting changes in the amounts of an element equivalent to a fraction of a monolayer for all elements examined, and less than 1% of a monolayer for some elements. For films with thicknesses around a monolayer, the XRF intensity of the substrate before the film is deposited

needs to be subtracted from the total signal of the film plus substrate to achieve this accuracy.

2.2. Materials and Methods

Precursors were synthesized in a high-vacuum physical vapor deposition system, with depositions occurring at pressures below 5×10^{-7} Torr. Metals were deposited using electron beam guns, and selenium was deposited using an effusion cell. A computer controlled pneumatic shutter system was used to control the sequence and thickness of the elemental layers.[37,38] The rate of deposition and the thickness of each of the elemental layers deposited were measured and controlled using quartz crystal microbalances, with rates maintained at 0.1 - 0.3 Å/s at the substrate.

X-ray fluorescence data was collected using a Rigaku ZSX Primus II wavelength dispersive X-ray fluorescence spectrometer with a rhodium X-ray source. This instrument measures intensities of characteristic X-ray emission lines as a function of crystal angle. Samples were loaded onto a small metal puck with either a 30 mm, 20 mm, or 10 mm diameter masking-frame. Incident X-rays were passed through either a 10 mm or 20 mm diaphragm before contacting the spinning sample in a vacuum. Fluoresced X-rays were reflected off selected crystals into a detector. Intensity was measured by integrating the area under the entire peak measured in intensity as a function of two-theta using MATLAB's cubic smoothing spline function (csaps) with the smoothing parameter set to zero smoothing (function value 1). The two-theta limits of integration were held constant. Data were also collected for substrates without any deposited film, referred to as blanks. The intensity data measured for the blanks was treated in the same manner as the deposited samples. The resulting integrated counts were subtracted from the integrated intensity of the coated substrates to correct for the background signal and any signal from the substrate itself.

X-ray diffraction (XRD) was used to characterize the structure of the samples that were subsequently analyzed by XRF. Low angle and specular XRD scans were collected using a Bruker d8-discover diffractometer. Grazing incidence in-plane XRD scans were collected on a Rigaku Smartlab diffractometer. All diffraction patterns were collected with Cu Kα radiation.

2.3. Results and Discussion

The intensity of the XRF signal I_{ij} for a particular element i of interest in a film with a characteristic line j at wavelength λ_{ij} is given by:[36,39]

$$I_{ij} = \{ K_j(\lambda_s)\, C_i \,/\, \mu_T(\lambda_{ij}) \} \{ 1 - exp [-\mu_T(\lambda_{ij})\rho d] \}. \qquad \text{(Equation 2.1)}$$

In Equation 2.1, C_i is the mass fraction of element i in the film, ρ is the average film density, d is the film thickness, and $\mu_T(\lambda_{ij})$ is the total mass absorption coefficient at λ_{ij}. $K_j(\lambda_s)$ is a product of many constants, including a constant representing the spectrometer geometry, the intensity of the excitation X-ray source, and the excitation probability for the characteristic line j under the spectrum of intensities of the excitation source. If the thickness of the analyzed film is thin enough, $\mu_T(\lambda_{ij})\rho d$ becomes small, and for films within this thickness regime (defined in more detail later), the exponential can be expanded as a power series. If only the leading terms are kept, Equation 2.1 simplifies to:

$$I_{ij} = C_i\, K_j(\lambda_s)\, \rho d. \qquad \text{(Equation 2.2)}$$

For such thin films the intensity of the XRF signal is thus expected to be directly proportional to the product of C_i, ρ, and d, which is the number of atoms of element i in the area of the film probed. The deviation between equation 2.1 and equation 2.2 as a function of film thickness for a representative film is shown in Figure A.1 in the supporting information.

To test the applicability of this approximation, a series of films with thicknesses below 120 nm containing a variety of elements with different elemental ratios were prepared using physical vapor deposition. Quartz crystal microbalances were used to measure the amount of material deposited onto the silicon substrates. Figure 2.1a and Figure 2.1b and Figure A.2 in the supplemental information each contain a graph of the background corrected intensity of the XRF signal as a function of the thickness of each element deposited. The intensity data for each element was found to be proportional to the amount of the element in the film. The linear relationship between intensity and amount of material indicates that the absorption of both the incident and fluorescence X-rays are negligible in these films. The greater the slope of the line, the more sensitivity there is to small changes in the amount of the element in the film. Table 2.1 summarizes the slopes and associated errors as well as the X-ray absorption line used for all of elements that were studied. Figure A.3 in the Supporting information explains how each line was chosen for each element in question.

The spread of the data points about the linear relationship in Figure 2.1 results from several potential sources, including the limits of the reproducibility of the deposition process itself (for example the shape of the deposition plumes), limits to resolution of the quartz crystal monitors, and limits to the reproducibility of the XRF measurements. To assess the reproducibility of the XRF measurements, the XRF intensity of the same sample was measured repeatedly over a time period of 6 months, using a variety of sample masks of nominally the same size that define the sample size analyzed. The intensities for most elements studied were constant to less than a third of a percent. This suggests that the majority of the deviation in the plotted intensity versus amount deposited plots is due to errors in the amount of material deposited from either the crystal monitors or the deposition process itself.

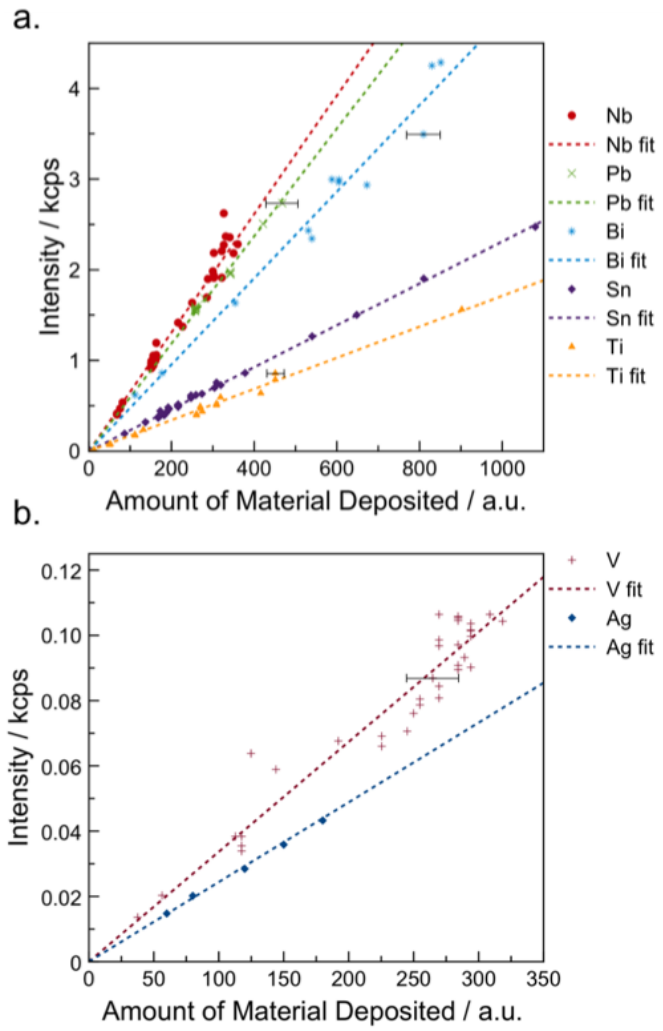

Figure 2.1. The change in the XRF intensity as a function of the thickness of material deposited as measured by quartz crystal monitors for a variety of different elements (shown with different colors and symbols). The error in the amount of material deposited for each element is shown for a single data point and when error bars are absent the error is the size of the marker. The lines are fits assuming that the XRF intensity is directly proportional to the amount of material deposited. Slopes for each line can be found in Table 2.1.

The sensitivity of the XRF intensity to the amount of material deposited makes it a valuable tool to improve deposition reproducibility. For example, the amount of Se deposited on a sample was found to systematically increase with time when high melting point metals were evaporated in the same deposition even though the thicknesses deposited

onto the quartz crystal microbalance was kept constant. The excess Se resulted from Se evaporating from chamber walls as they were heated by infrared radiation from the electron beam deposition. The sensitivity of the XRF data combined with tracking the data as a function of time and experimental conditions is a powerful tool to improve deposition processes.

Table 2.1. The slopes of the lines in Figure 1 for each element along with the fluorescence line used. The maximum film thickness is the thickness where absorption reduces the intensity of fluorescence of the given element by 5%.

Element	Line Used	Slope	Maximum Film Thickness (nm)
Ag	Lα	0.00024(1)	150
Bi	Lα	0.00477(9)	1300
Mo	Lα	0.03019(9)	100
Nb	Lα	0.00653(6)	100
Pb	Mα	0.00592(4)	100
Se	Lα	0.00319(3)	50
Sn	Lα	0.00231(1)	200
Ti	Kα	0.00171(3)	200
V	Kα	0.000337(5)	250

The approximation that $\mu_T(\lambda_i)\rho d$ is small neglects absorption corrections to the measured fluorescence intensity. When $\mu_T(\lambda_i)\rho d = 0.1$, the difference between the intensities calculated with and without absorption corrections yields an error of ~5%. Absorption corrections become more important as the energy of the x-ray fluorescence line decreases as show in figures A.4, A.5, and A.6 in the supporting information.[40,41] Table 2.1 contains estimates of the thickness where the error in neglecting absorption becomes 5%, assuming a film with a total

mass absorption coefficient of ~10^3 cm^2/g and a density of ~10 g/cm^3. For most elements, this corresponds to a film that is more than a hundred nanometers thick. While the exact thickness depends on the element being probed, the mass absorption coefficient of the matrix, and the density of the film, the approximation that $\mu_T(\lambda_i)\rho d$ is small is a conservative approximation for thicknesses less than 50 nm for most elements. Films below this thickness are common in many research projects and in many devices prepared by sequential deposition of layers. The supporting information contains calculations of the thickness value when the calculated intensity of the given material using Equation 2.2 is 5% higher than the intensity calculated for Equation 2.1 for samples containing Bi, Pb, or Se in their matrix using Kα, Lα, and Mα lines.

While quantifying the relative amount of an element in a film is valuable when monitoring a process, determining the number of atoms per unit area is significantly more valuable in many research applications. Unfortunately, $K(\lambda_s)$ is a product of many constants that are difficult to quantify or calculate and both the average film density and thickness are generally difficult to experimentally determine. Our approach to quantifying the amount of material in a film per unit area is to synthesize standards where the number of atoms of each element per unit area can be calculated from diffraction data. Figure 2.2 contains representative X-ray reflectivity (XRR), specular XRD and in-plane XRD scans of one of these films, a sample of $[(PbSe)_{1.12}]_1[NbSe_2]_1$. The Kiessig fringes in the XRR scan provide a measure of the smoothness of the film and allow the total thickness and the total number of repeats of the film to be calculated. The number of repeat units in the film is equal to the number of Kiessig fringes plus 2. The specular diffraction scan shows that the film is crystallographically aligned with the substrate and enables the *c*-axis lattice parameter to be determined. The value of the *c*-lattice parameter informs on how many of each layer type are in the

repeat unit. The total thickness of the film divided by the *c*-axis lattice parameter yields an integer, indicating that all of the film thickness comes from the crystalline material. Assuming there are no impurity phases present that are not evident in the diffraction scans, for example an amorphous phase, this allows us to calculate the number of atoms of each element per unit area as the product of the number of crystallographically aligned unit cells obtained from the specular diffraction information times the number of atoms per unit cell from the structure solution divided by the area per unit cell obtained from the in-plane lattice parameters.

As an example, using the data in Figure 2, the formula to calculate atoms per unit area is given by:

$$\text{Total } \frac{\text{atoms}}{\text{Å}^2} = \sum_{\text{Constituent Layers}} \left(\frac{\text{\# of atoms per unit cell in basal plane}}{\text{area of the basal plane per unit cell}} \right) (\text{\# of layers}).$$

(Equation 2.3)

In Figure 2.2, the XRR pattern of $[(PbSe)_{1.12}]_1[NbSe_2]_1$ has 20 Kiessig fringes present between the critical angle and the first Bragg reflection, indicating that there are 22 repeat units of the $[(PbSe)_{1.12}]_1[NbSe_2]_1$ structure in the film. The total thickness of the film is obtained from the spacing between the Kiessig fringes. The specular diffraction pattern shown in Figure 2b results in yields a *c*-axis lattice parameter of 12.39(2) Å which matches the targeted *c*-axis lattice parameter for a $[(PbSe)_{1.12}]_1[NbSe_2]_1$ heterostructure.[42] Dividing the total thickness by the *c*-axis lattice parameter yields the number of repeating layers in the film, which in this case is 22, agreeing with the number of layers determined from the number of Kiessig fringes. Since the repeating unit contains one layer of PbSe and one layer of $NbSe_2$, the number of layers in Equation 2.3 is 22 for both constituents.

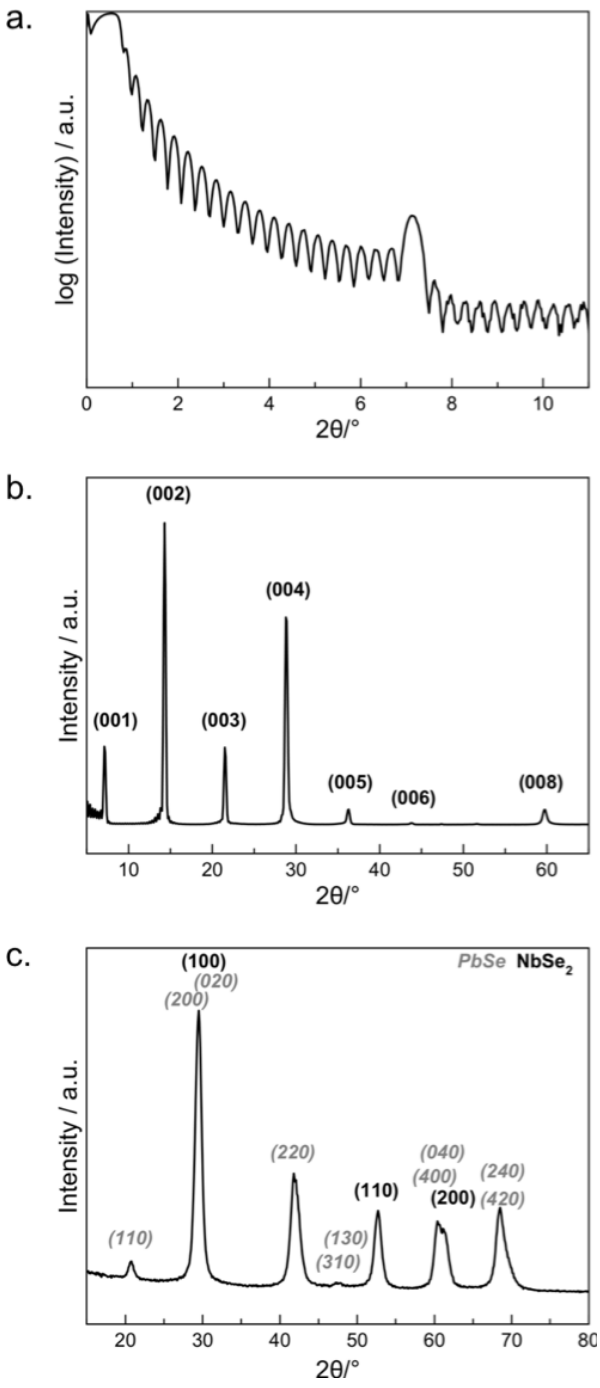

Figure 2.2. Three different diffraction scans of a $[(PbSe)_{1+\delta}]_1$ $[NbSe_2]_1$ film. (a) XRR scan. (b) Specular XRD scan. (c) Grazing incidence in-plane XRD scan. The crystallographic indices are given above each reflection and were used to determine the total film thickness from (a), the c-axis unit cell parameter from (b) and the in-plane unit cell parameters from (c).

In-plane XRD is used to determine the number of atoms and the area of the basal planes in each unit cell. All the reflections in the in-plane diffraction pattern (Figure 2.2c) can be indexed as hk*0* reflections for PbSe and $NbSe_2$, consistent with the formation of a $[(PbSe)_{1.12}]_1[NbSe_2]_1$ heterostructure.[42] The indices are consistent with a rectangular basal plane for PbSe (distorted rock-salt structure) and a hexagonal basal plane for $NbSe_2$. The number of atoms per unit cell in the basal plane follow from the crystal structure of each constituent (4 Pb and 4 Se for PbSe and 1 Nb and 2 Se for $NbSe_2$). The indexed patterns are then used to calculate the *a*-lattice and *b*-lattice parameters for the PbSe constituent (6.06 Å and 6.14 Å, respectively) and the *a*-lattice parameter for the $NbSe_2$ constituent (3.47 Å). The resulting basal plane areas for each constituent, assuming that they are stoichiometric, are 12.5 $Å^2$ for PbSe and 9.47 $Å^2$ for $NbSe_2$. Using this information, we calculate that the $[(PbSe)_{1.12}]_1[NbSe_2]_1$ film contains 2.37 Pb atoms/$Å^2$, 2.11 Nb atoms/$Å^2$ and 6.58 Se atoms/$Å^2$.

Figure 2.3 shows the XRF intensity for a number of different elements versus the calculated number of atoms of each element in a number of films containing a variety of different rock salt structured constituents and transition metal dichalcogenides that have diffraction data similar to that displayed in Figure 2.2. The data for each element is well described by straight lines through the origin, where the slopes provide the conversion factor between intensity and atoms per unit area. The supporting information contains data for other elements (Figure A.7), reinforcing that this is a reasonable approach to obtain the proportionality constant between the XRF intensity and number of atoms in the analytical volume. The largest error in this approach is the assumption that the films do not contain either significant defect densities or amorphous phases that are not evident in the diffraction scans. The observed linear behavior for films containing a variety of

different constituents suggests that the approximation is valid and using the slope averages this error over many samples. The graph for selenium (Figure 2.4) has the largest deviations. We believe points above the line are the result of small amounts of amorphous Se in grain boundaries, inclusions, and on the surface of the films, which could be removed by additional annealing time. Points below the line are likely the result of Se loss due to annealing the samples for too long in an open system. The ability to accurately and non-destructively measure Se content will aid researchers to adjust the annealing temperatures and times to obtain stoichiometric Se content.

Once the conversion factor is known for a particular element, the conversion factor for other elements can be determined by measuring XRF intensities of stoichiometric compounds that contain elements with known and unknown conversion factors. For example, to obtain the conversion factor for Se, XRF measurements on thin films with stoichiometric $SnSe_2$ can be used. The conversion factor of Se is then determined using the XRF intensities of Sn and Se, the known conversion factor of Sn (Figure 2.3), and the stoichiometry of the crystal. Figure 2.4 illustrates this process for three $SnSe_2$ and two $TiSe_2$ films, where the validity of this approach is confirmed by the consistency of the calculated conversion factor with that determined from crystal structure information as presented in Figure 2.3 for other elements.

While the number of atoms per unit area in a thin film via XRF can be determined with less than 1% error, the error increases as the amount of an element approaches zero as subtracting the background signal becomes more significant. Figure 2.5 shows the signal from the Sn Lα emission line for a silicon substrate and the substrate with 0.11 atoms of $Sn/Å^2$ (~140% of the amount of Sn in a single layer of $SnSe_2$)). The background intensity constitutes roughly 20% of the total intensity under the Sn Lα background intensity correctly. For Sn films deposited

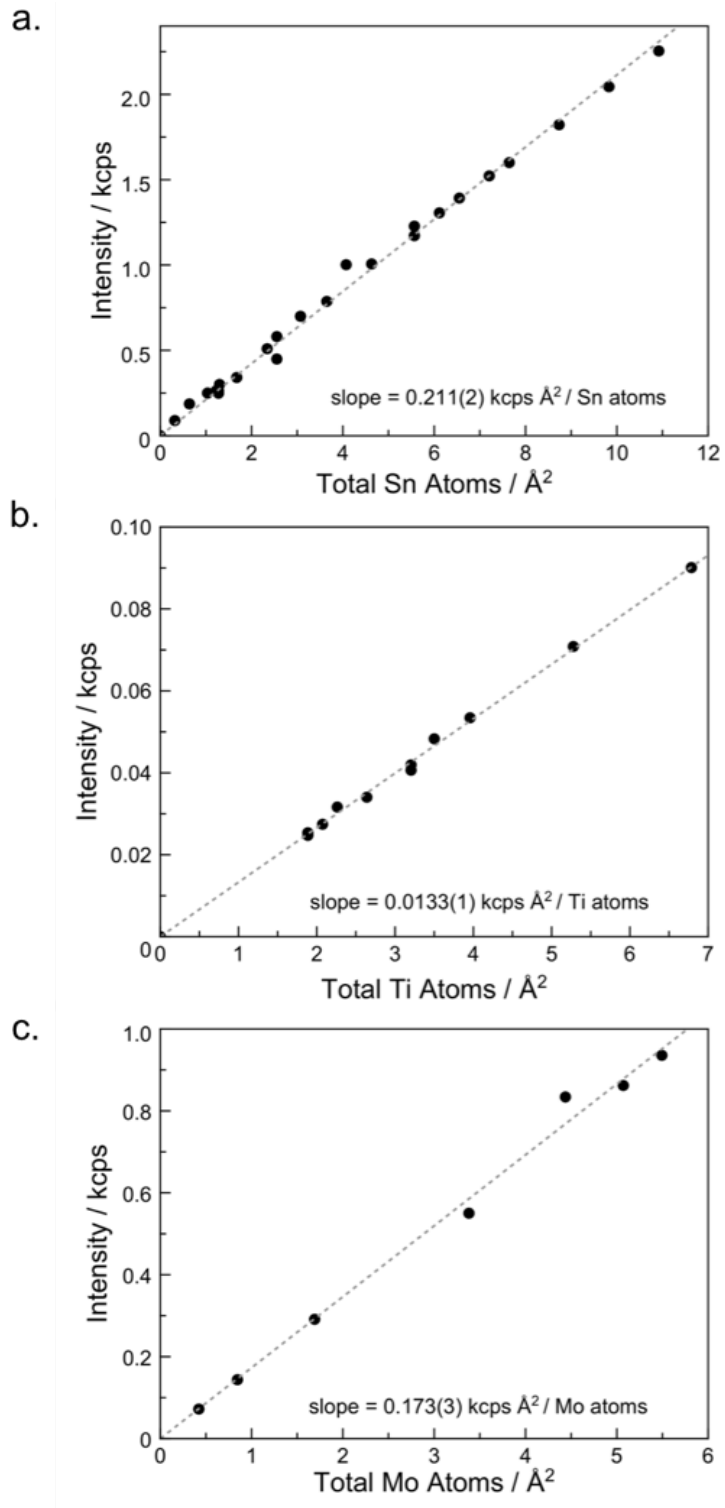

Figure 2.3. Graphs of the XRF intensity versus the number of atoms per unit area of several elements calculated from diffraction information such as that shown in Figure 2.2 for a number of different films.

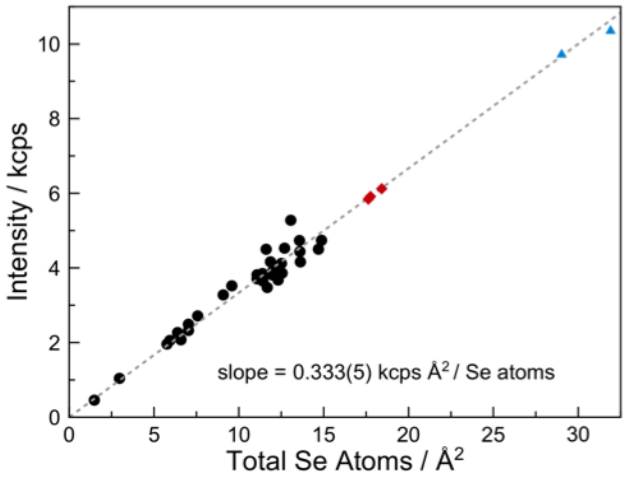

Figure 2.4. XRF intensity versus the total number of Se atoms per unit area determined from diffraction information (black), from films of $SnSe_2$ (red) and from films of $TiSe_2$ (blue). For the $SnSe_2$ and $TiSe_2$ films, the information in Figure 2.3 was used to determine the number of cation atoms in these films from the measured Sn and Ti XRF intensities. These values were then used to calculate the number of Se atoms in each of the films.

on silicon substrates under these data collection times and conditions (less than an hour total scan time for both film and blank substrate), the error of the net intensity measurements in our instruments indicates that changes of less than 1 % of a monolayer film of $SnSe_2$ can be detected. The sensitivity of detecting small changes of an element depends on the change in intensity of the XRF signal for that element, which is proportional to the slope of the lines in Figure 2.1, and on the specific diffracting crystals and detectors used. For example, the intensity of the Pb emission from the Mα line is about 10 times more intense per atom than the intensity of the Ti emission from the Kα line in our instrument. Therefore, we can detect smaller changes in Pb atoms/Å^2 than Ti atoms/Å^2. Sensitivities for several elements based on the data collected in this study are given in Table 2.

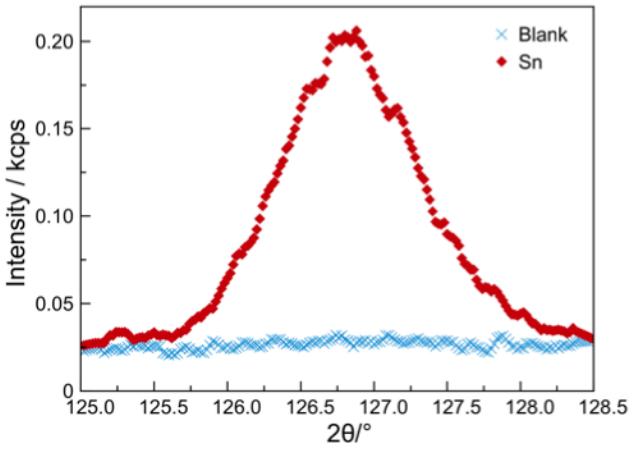

Figure 2.5. The Sn-La emission intensity from a film with 0.11 Sn/Å^2 and the blank Si substrate before deposition of Sn.

For ultra-thin films (a monolayer or less), the ability to subtract the background intensity accurately and reproducibly is obviously critical, making the choice of the emission line an important factor. Figure A.3 in the supporting information illustrates this point, showing the measured intensity of a Pb-containing sample and its blank substrate for three different emission lines, the Lα, the Lβ$_1$, and Mα. While the signal intensity is largest for the Lα emission line, the low and constant intensity measured on the blank substrate for the Mα line makes it the preferred emission line.

Table 2.2. Sensitivity of the XRF measurement for a series of elements as a percent of a monolayer of the compound in parenthesis.

Element	Sensitivity
Sn (SnSe)	> 1%
Pb (PbSe)	> 1%
Nb ($NbSe_2$)	> 1%
Mo ($MoSe_2$)	2%
V (VSe_2)	7 %
Ti ($TiSe_2$)	10 %

The ability to quickly measure the number of atoms per unit area of each element in a film enables films to be prepared with a precise number of unit cells such as that shown in Figure 2.2. To demonstrate this, a film where eight elemental Mo and Se layers were sequentially deposited onto a room temperature silicon substrate, with each pair containing the appropriate amount of these elements per unit area to form a single crystalline $MoSe_2$ layer. After annealing at 650°C, a variety of diffraction and reflectivity scans were collected. The XRR scan in Figure 2.6 is that expected for a film containing 8 identical layers, with a thickness consistent with 8 MoSe2 trilayers. The high angle annular dark field scanning transmission electron microscopy (HAADF-STEM) cross-section image of this sample, also shown in Figure 2.6, is consistent with the XRR scan. The specular diffraction pattern contains only four broad 00*l* reflections, indicating that the $MoSe_2$ is crystallographically aligned with the substrate yielding a *c*-axis lattice parameter of 6.53(1) Å, consistent with the literature value of 6.46 Å.[43] The in-plane diffraction pattern contains only *hk*0 reflections, from which an *a*-axis lattice parameter of 3.27(3) Å was calculated. This is in good agreement with that previously reported for $MoSe_2$ (3.31 Å).[43]

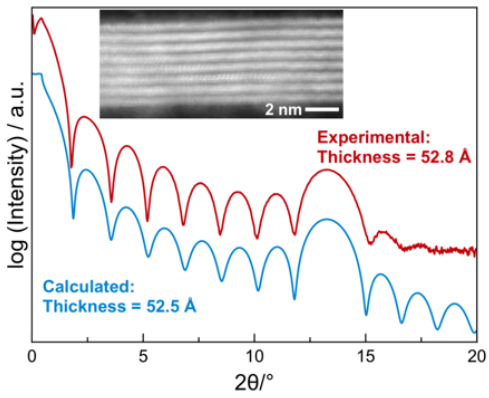

Figure 2.6. Measured and calculated XRR patterns of an 8-layer $MoSe_2$ film showing the application of this XRF method to prepare films containing a finite number of layers. The inset HAADF-STEM image shows further evidence of the formation of 8 $MoSe_2$ layers.

2.4. Conclusion

XRF is a sensitive and precise probe of the number of atoms per unit area of select elements in thin film samples. If films are thin enough, absorption corrections can be ignored, and the matrix has minimal impact on fluorescence intensity. The proportionality factor between intensity and the number of atoms of each element per unit area was determined using diffraction data from smooth, crystallographically aligned thin films that are an integral number of unit cells in thickness. The sensitivity of this approach enables less than 1% of a monolayer to be quantified.

2.5. Bridge

Chapter 2 focused on the precise measurement of atoms per unit area in thin films samples using XRF. This method provides a direct measure of the amount of material in a sample by relating XRF intensity to number of atoms per unit area and no longer relies on relative amounts of materials, which is necessary for other elemental analysis techniques. This analysis technique provides the ability to more accurately target novel materials and nanoarchitecture and is essential for a more successful and efficient heterostructure synthesis. This approach is successful, as demonstrated by the synthesis of the materials discussed in Chapters 4 – 13. Chapter 3 discussed the use of this technique in preparing families of heterostructures with systematic changes in nanoarchitecture and novel building block for heterostructures as well as the general synthesis, structural characterization, and electrical characterization methods used throughout the rest of this work.

CHAPTER III

SYNTHESIS AND CHARACTERIZATION OF DESIGNED PRECURSORS PREPARED VIA THE MODULATED ELEMENTAL REACTANTS METHOD.

3.0. Authorship Statement

This chapter was written for this work alone and will not be published elsewhere. I am the primary author of this chapter. David C. Johnson is my advisor and consulted on the material discussed.

3.1. Modulated Elemental Reactants Method Principle

The compounds discussed in this body of work were prepared via the Modulated Elemental Reactants (MER) synthesis method. This method relies on physical vapor deposition to prepare elemental precursors that are subsequently heat treated to facilitate their transformation into the targeted crystalline structure.[1,2] While this work focuses on thin films composed of single-phase compounds and heterostructures, the motivation for this synthesis method stems from limitations in traditional solid-state synthesis routes. Traditional solid-state synthesis, or 'heat and beat' reactions are typically used to prepare bulk, thermodynamically stable compounds. For the 'heat and beat' method, stoichiometric amounts of reactants are heated at high temperatures to allow for diffusion, which is slow in solids. High temperatures are required to move reactant atoms to the nucleation front where the reaction is occurring. Even when the correct amount of starting material is mixed, the final product can exist with a concentration gradient and impurities as a result of incomplete diffusion. These necessary high temperatures limit the ability to modify local coordination in materials, so the resulting products are global minima in the free energy landscape.[3,4] Solid-state chemists have developed methods to prepare different phases by manipulating temperature,

pressure, and starting composition, but they are still diffusion limited and dominated by the lowest energy structure.

To overcome limitations typically observed in solid-state reactions, the MER method deposits elemental layers next to each other in such a way that diffusion is no longer the limiting step.[5,6] Instead, the system is limited by its ability to nucleate and grow the material. In order to do so, the elemental layers must contain both the correct thickness to prepare a single layer of the targeted material as well as the correct stoichiometry to crystalize the correct phase. If both the thickness and composition are incorrect, the wrong phase will form. If the layers have the targeted composition but are too thick, the system is limited by diffusion of material A to material B and vice versa, resulting in a series of materials related by a concentration gradient as depicted in Figure 3.1a. When both the stoichiometry and layer thickness are representative of the desired targeted material there is little diffusion that is required to obtain mixing between the two constituents, facilitating nucleation, as shown in figure 3.1b. Though these rules are not obeyed every time, they can be reliably used when preparing materials by MER.

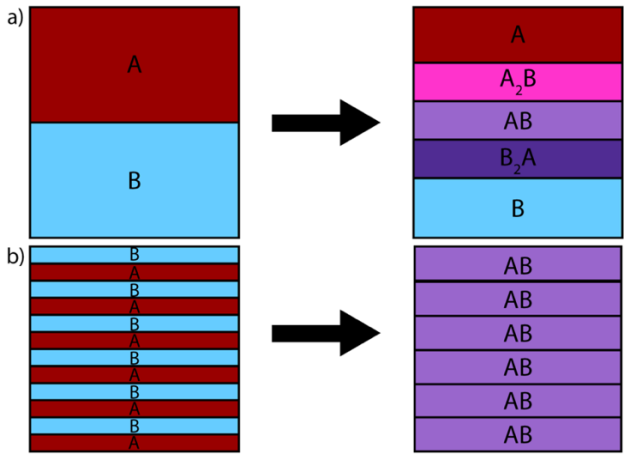

Figure 3.1. Schematic demonstrating the influence of having the correct precursor stoichiometry of A and B, but the wrong layer thickness to prepare a compound AB (a.) and the both the correct stoichiometry and layer thickness of A and B to prepare a layered compound of AB (b.).

3.2. Synthesizing Thin Films and Heterostructures Via MER

MER precursors were prepared via physical vapor deposition using a high vacuum deposition system.[7] A schematic of the home-built deposition chamber is shown in Figure 3.2. The elemental precursors are deposited at pressures less than 1 x 10^{-6} Torr. These pressures are achieved by way of an oil sealed rough pump, a turbomolecular pump, and a cryogenic pump to get down from atmospheric pressure. The system, equipped with 4 ports at the bottom, allows for the deposition of up to 4 different elemental sources, either by electron beam gun or Knudson effusion cells. The elemental sources are evaporated at rates of less than 1 Å/sec which vary depending on the element. Elements deposited by an electron beam gun that melt tend to be deposited at lower rates (~0.4 Å/sec) than elements that sublime (~0.6 Å/sec). Elements deposited with a Knudson effusion cell (specifically Se) were deposited at a rate of ~0.9 Å/sec. Quartz crystal microbalances located halfway between the source and the substrate (which are not denoted in the schematic) are used to monitor the deposition rate and amount of material deposited. Custom LabVIEW software was used to set the rate, layering scheme, and layer thickness for each element to be deposited.[8] This program controls pneumatic shutters which open and close to deposit precursor material in a specific sequence. The films are deposited on substrates located at the top of the chamber on a rotating stage. The inset on the right side of Figure 3.2 shows plumes of material being deposited on the substrate, building up layers for a binary compound.

A wide variety of constituents can be prepared via MER since the elements, deposition order, and processing conditions can be readily changed. Not only can single phase compounds be prepared, but unique heterostructures consisting of 2 or more constituents can be prepared. Figure 3.3 shows a schematic of a deposited precursors being converted to a crystalline product. The correct amount of material to form

compound AC and compound BC is deposited in each layer. The layering scheme is repeated to build up the total precursor film. The precursor is annealed by heating the sample on a hot-plate at low temperatures in an inert atmosphere to provide the atoms with enough energy to diffuse and start nucleation and growth of crystalline layers. The low temperatures and short diffusion length required to crystalize the layers allows metastable products to be trapped in local energy minima instead of diffusing all the way to the lowest energy, thermodynamic product. The appropriate annealing temperature is determined through an x-ray diffraction study in which a sample, with approximately the correct amount of material deposited, is annealed at various temperatures. An example of an annealing study for a heterostructure material is shown in Figure 3.4. The temperature at which the highest quality diffraction pattern is observed is considered to be the appropriate annealing temperature for the system.

Typically, the materials prepared using this method are heterostructures composed of a metal chalcogenide rock salt constituent (MX) and a transition metal dichalcogenide constituent (TX_2) in various stacking sequences as depicted in Figures 3.4, 3.5, and 3.6. This is not as a result of limitations to the synthesis, but instead as a result of their thermodynamic misfit layer compounds counterparts. Future chapters will focus on other materials that have more complex structures, but a description of the materials formed will be given here using an MX and TX_2 heterostructure as an example.

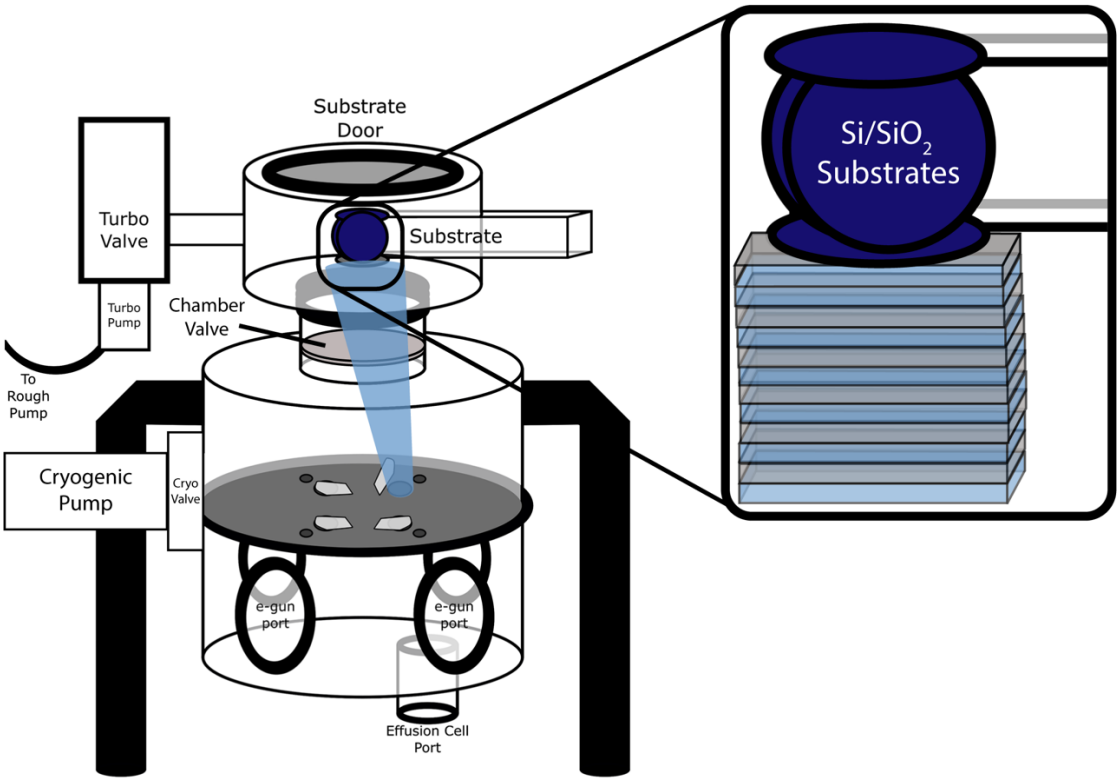

Figure 3.2. A schematic of the physical vapor deposition chamber used to prepare MER precursor thin films. Under high vacuum conditions, pneumatic shutters open and close to deposit the vaporized material into a targeted structure. The inset at the right shows a depiction of building up the atomic elemental layers for a binary film.

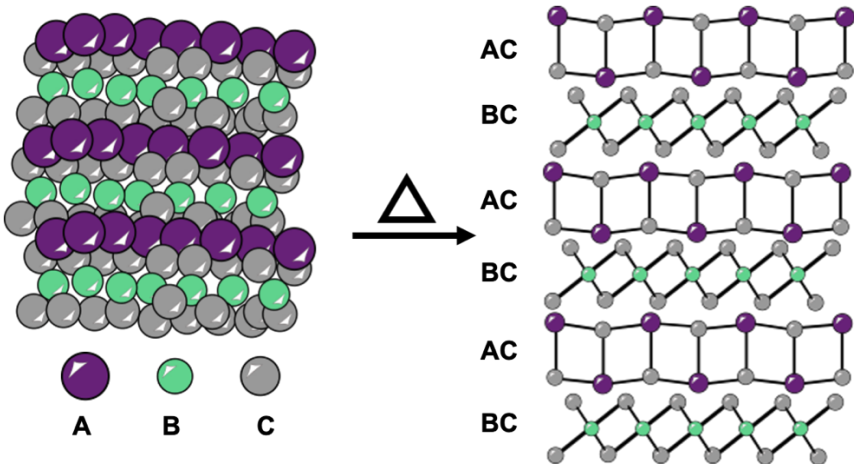

Figure 3.3. A schematic of a designed elemental precursor prepares by MER whose structure mimics the pattern for the desired heterostructure being converted to the desired heterostructure via “gentle annealing”.

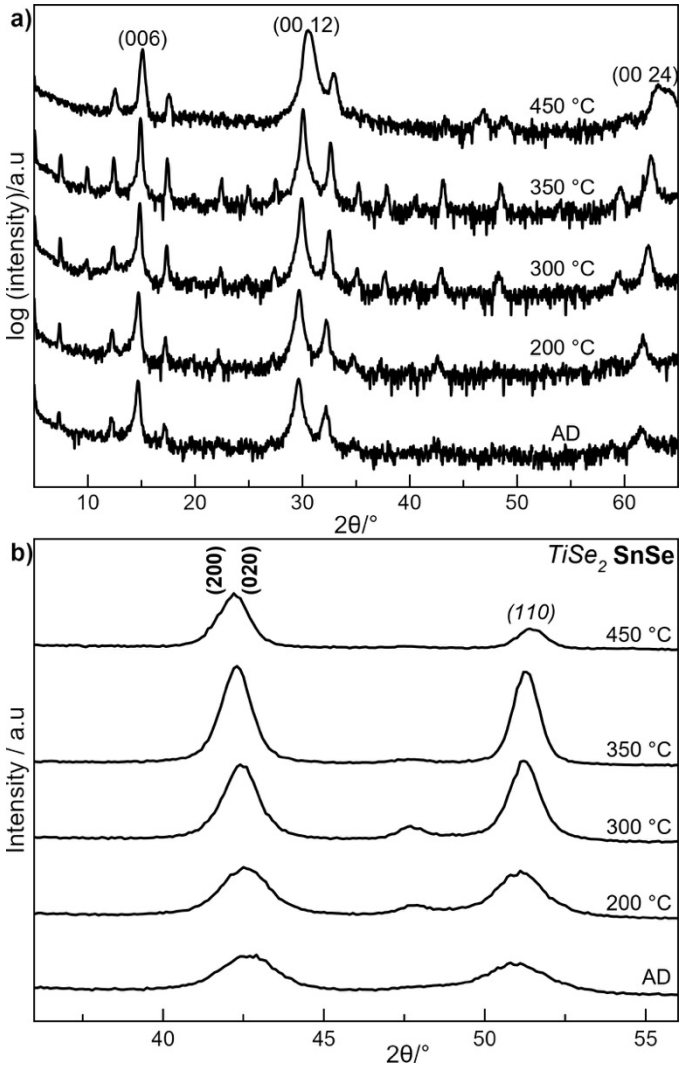

Figure 3.4. Annealing study data of a two constituent heterostructure material composed of SnSe and $TiSe_2$ demonstrating the evolution of the film as a function of annealing temperature where 'AD' is the sample as-deposited before annealing. Specular x-ray diffraction is shown in (a.) and In-plane x-ray diffraction is shown in (b.)

As a result of the self-assembly of the elemental layers into the designed heterostructure upon annealing, the materials have distinct structural features. When the material crystalizes, the layers are typically stacked in such a way that they are crystalline out of plane with the repeating unit structure's *c*-axis lattice parameters aligned perpendicular

to the substrate as observed in the left side of Figure 3.5. The in-plane structure of the material is a 2D random powder where the two individual constituent basal plane structures are distinguishable. This is depicted in the middle panel of Figure 3.5 showing the hexagonal and rectangular in-plane structure for the two different constituents. Because of the alignment in the *c*-axis direction and the random in-plane crystallization, there is apparent rotational disorder that occurs between the two constituents, which is shown in the right side of Figure 3.5.

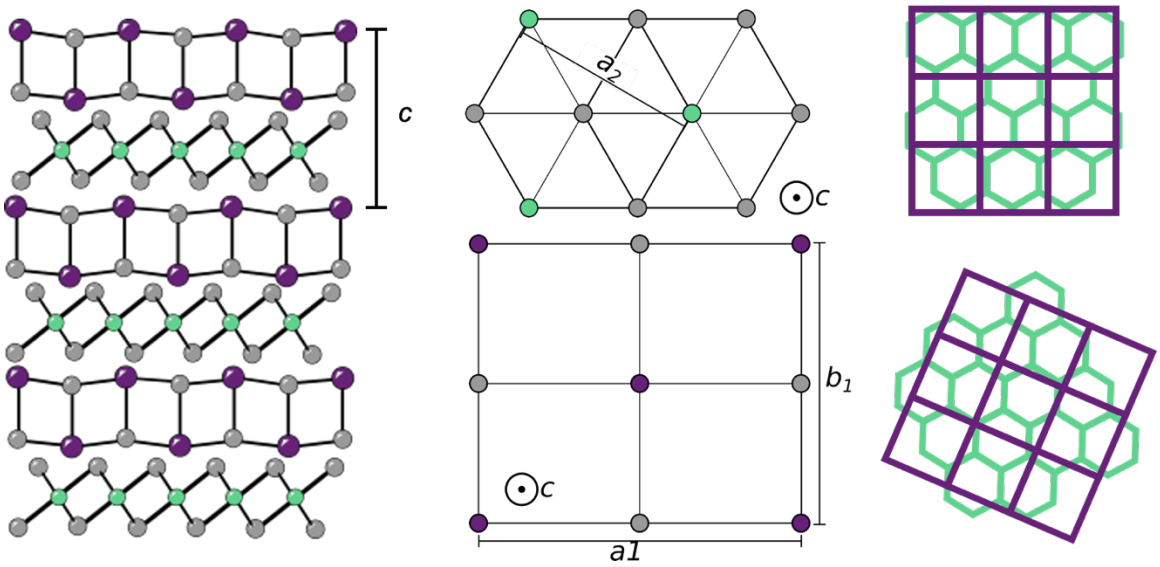

Figure 3.5. Schematic showing the stacking nature of the heterostructure, the individual constituent basal plane structures, and the observed rotational disorder between constituents for a material self-assemble upon heating form a designed precursor made my MER.

The low temperature annealing, and the designed nature of the precursors has facilitated the synthesis of many new single phase compounds as well as a variety of novel heterostructures composed of various constituent materials.[9,10,19,20,11–18] By changing the nanoarchitecture of the designed precursor's repeating unit, which builds up the film, a series of compounds composed of the same two single phase materials can be made. A schematic of the various series of compounds that can be made from two constituent materials is shown in

Figure 3.6. Different nanoarchitectures are achieved by changing the stacking sequence in the deigned precursor to mimic that of the targeted material. The possibilities for more complex and novel heterostructures are nearly unlimited, restricted only by one's ability to deposit a finite number of elements within a single deposition sequence.[21] Since this method is not depended on formation of the thermodynamic product, it allows for new material phases to be prepared as well as novel heterostructures.

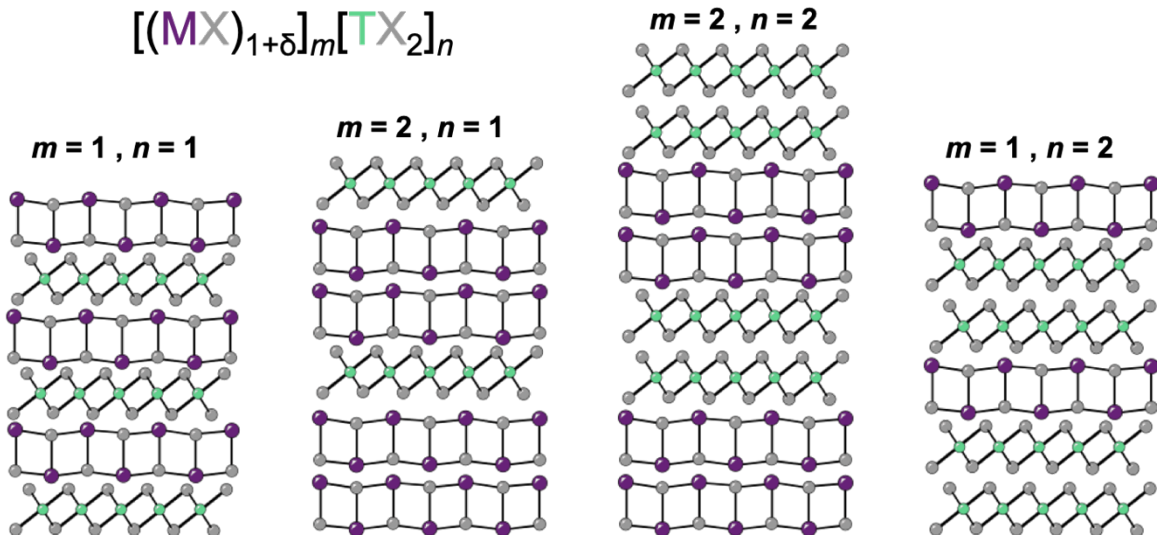

Figure 3.6. Structural schematic demonstrating the various series of heterostructure materials that can be achieved by modifying the precursor nanoarchitecture using the MER method. In this example MX is a rocksalt, TX_2 is a dichalcogenide, and $1+\delta$ represents the different in-plane area between the two constituents.

3.3. Informing MER Synthesis Via XRF

To prepare unique stacking sequences within heterostructures it is necessary to control the nanoarchitecture, but also requires fine control over the amount of material within each deposited layer. A precise amount of material is required in order to crystalize the targeted product to limit the amount of diffusion that must occur and help to trap the metastable product. Two different methods were used to target the

correct amount of material necessary to prepare the compounds discussed in this work. The first method relied on the ratio between the elements and then second relied on the precise measurement of the amount of material per unit area as discussed in Chapter 2. The following paragraphs will discuss how both methods were used to calibrate deposition parameters for preparing compounds by MER as well as the added benefits of measuring the actual amount of material per unit area in the sample opposed to relative amounts.

Prior to the calibration of the XRF to measure the amount of material per unit area for an element,[22] calibration of the deposition relied on relative ratios of the elements needed to prepare a heterostructure material. Figure 3.7 depicts the systematic method that was used to calibrate a two constituent heterostructure composed of layers of MX and TX. The first step was to calibrate the deposition parameters for the two constituents, MX and TX, individually to get the correct ratio of metal to Se. A series of precursors were made for each constituent in which the amount of Se deposited was help constant while the amount of metal, M or T, deposited was varied. By sweeping over the composition space in a systematic fashion for each of the two constituents the correct ratio between metal and Se was determined. After the ratio of metal to Se for each constituent was determined, the correct ratio between the two constituent precursor layers, MX and TX was investigated. A similar systematic series of precursors was prepared in which the composition and thickness of the T-X precursor layers was help constant and the composition ratio in the M-X precursors layer was held constant, but the thickness of the M-X precursor layer was systematically varied. This allowed for the variation of the M:T ratio while the M:X and M:T ratios were held constant. Once viable MX:TX ratios were determined, the thickness of the targeted structure was used to inform the total amount of material deposited. This was done by keeping

the M-X-T-X precursor ratio constant while systematically scaling the thickness of the precursor unit, tracked by x-ray reflectivity and x-ray diffraction.

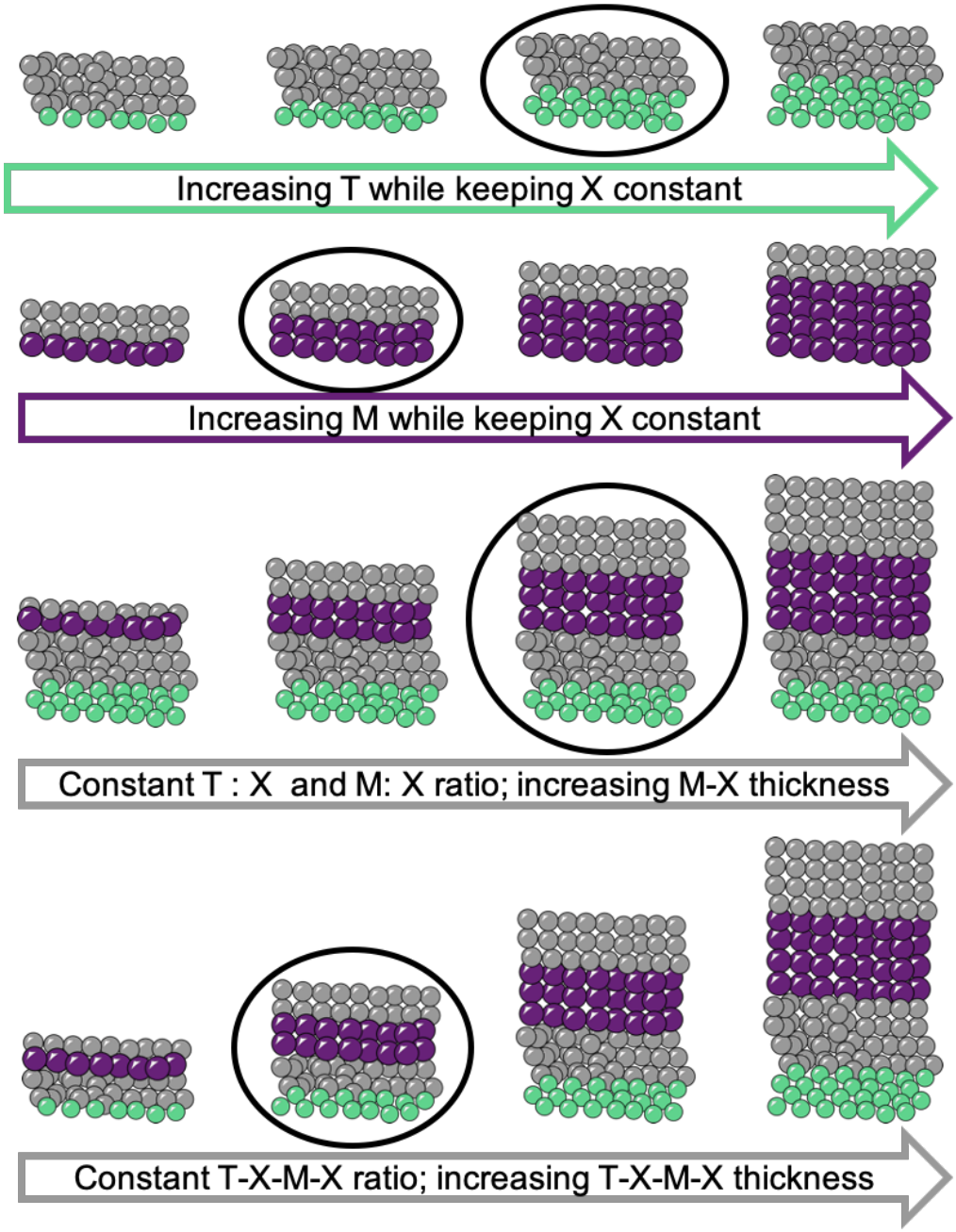

Figure 3.7. Schematic demonstrating using elemental ratios determined by XRF and *c* – axis lattice parameters determined from specular X-ray Diffraction to systematically calibrated the correct about of material needed per layer in the designed precursor to prepare the targeted heterostructure.

Though this was an effective method, it required many series of samples to be prepared and analyzed in order to calibrate the deposition system and determine the deposition parameters for a single sample. This process took months for known systems and even longer for novel systems. This method also did not provide a means of tracking variations in the deposition system, making it very easy to stray from the targeted system. By determining there was a direct relationship between the amount of material deposited and the XRF intensity, absolute material amounts could be determined. Chapter 2 focused on how the XRF measurements are sensitive to a monolayer of material and how the intensity can be related to the amount of material per unit are in the sample. Here we discuss how the calibration curves can be used to target novel materials and diagnose issues in the deposition chamber.

First, the atoms per unit area in a layer of material from either experimental or literature values must be calculated, as discussed in chapter 2. A series of samples are made with different deposition parameters to examine the XRF response to the changes in deposition, which is related to the amount of material present in the film. Once the relationship is known, the deposition parameters are scaled to achieve the targeted amount of material. This should not vary deposition to deposition, unless there are issues with the chamber. Figure 3.8 shows normalized counts, as determined using equation 3.1., which are used to related deposition parameters to the amount of material deposited. The left panel shows an issue with the system and the right shows consistent normalized values which are expected for a working system. There is a correlation between decreasing value with time, so deposition parameters need to be scaled appropriately to ensure that the correct amount of material is still being deposited. For example, the Se normalized counts decrease as a function of time, so the amount of material that needs to be deposited goes up as a result of dampening in the crystal monitor. It

is important to not change parameters based on small oscillations in normalized counts because those are a result of noise and not actual physical system changes. Using targeted atoms/Å^2 and normalized counts has expedited the synthesis of novel thin film.

$$\text{Normalized Counts} = \frac{\text{Intensity /CPS}}{\text{Material Desposited /fÅ}} \qquad \text{(equation 3.1)}$$

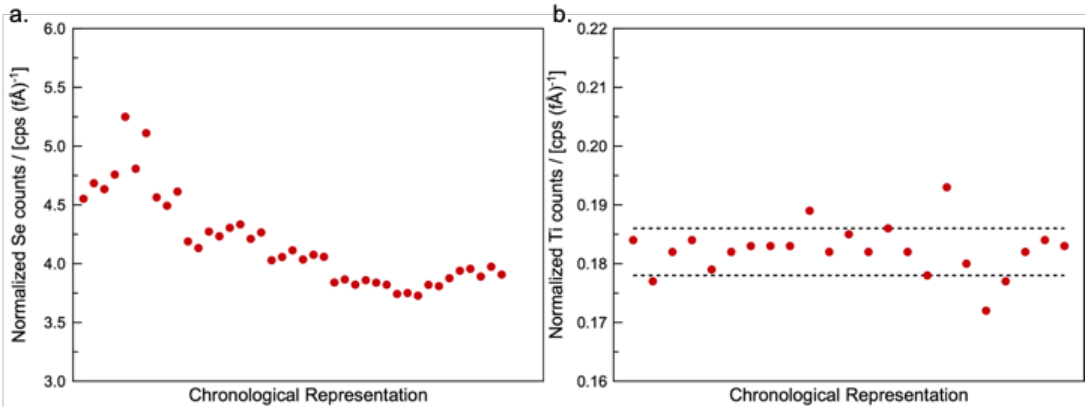

Figure 3.8. Measured XRF counts normalized to the amount of each element deposited in a thin film elemental precursor for Se (a.) and Ti (b.) demonstrating the deposition behavior observed for the system.

3.4. Structural and Compositional Characterization

As stated above, the amount of material in the sample was measured using XRF and was presented either as relative atomic ratios or measured atoms per unit area of each element. The XRF data was collected using a using a Rigaku Primus Z XRF with a rhodium tube. Previously determined calibration curves were used to convert integrated signal into atoms / Å^2 for each element. Si substrates were analyzed prior to being deposited on to be used for a background correction.

A combination of x-ray diffraction techniques were used to characterize the global structure of the materials. X-ray reflectivity and specular x-ray diffraction patterns were collected using a Bruker D8 Discover with a Cu-Kα source. The x-ray reflectivity data was collected to determine total film thickness, film roughness, number of repeating units

and portion of the entire film that was composed of the repeating unit structure. Specular x-ray diffraction was collected to characterize the repeating unit structure of the material and to determine if any other phases were present. The position of the reflections in the specular x-ray diffraction patterns were used to determine the size of the repeating unit structure. In-plane x-ray diffraction patterns were collected using a Rigaku SmartLab with a Cu-Kα source. This data was used to determine the phase of the constituents that made up the repeating unit structure as well as its basal plane structure. The positions of the observed reflections were used to determine the in-plane lattice parameters for the observed phases.

Local structure and composition were analyzed by High-Angle Annular Dark Field Scanning Transmission Electron Microscopy (HAADF-STEM) and Energy Dispersive X-ray Spectroscopy (EDS) profiles. Electron transparent cross sections (lamellae) were prepared from the single phase and heterostructure materials. HAADF-STEM images and STEM-EDS provide real space atomic images of the film structure and composition, where the contrast in HAADF-STEM depends on the atomic number Z. All of the techniques discussed in this section are used together to provide a comprehensive representation of the materials structure.

3.5. Electrical Transport Property Characterization

Electrical transport measurements, collected on a variety of different single phase and heterostructure compounds, included temperature dependent Hall Coefficient and resistivity measurements. as well as room temperature Seebeck coefficient measurements. The two systems used to collect these data were home built and controlled through a custom LabVIEW program to communicate with various Keithley instruments. All transport measurements were collected on compounds deposited onto an insulating quartz substrate through a

shadow mask. The temperature dependent measurements were collected using a closed-cycle He cooled cryostat system with temperatures ranging from ~300 K down to ~20 K. The samples measured in this system were deposited in a Hall cross to utilize the van der Pauw geometry for measurements. Copper wires connected to the sample holder were connected to the sample surface using indium contacts. Room temperature Seebeck measurements were collected on a rectangular bar of the sample using a tabletop measurement system. Contacts were pressed into the bar and half of the sample was cooled. The voltage and temperature difference were measured for the cooled sample using Type T thermocouples. Specifics on the measurement details can be found in the following chapters.

3.6. Bridge

Chapter 3 provided the foundation for both the synthetic and characterization methods used to investigate the formation mechanism, structure, and transport properties of binary compounds and novel heterostructure materials. The ability to measure amounts of material with sub-monolayer precision and control the nanoarchitecture of material with monolayer accuracy allows for novel materials to be prepared that are not accessible by other synthesis methods. The rest of this work will focus specifically on various binary compounds and heterostructures that were prepared by the Modulated Elemental Reactants synthesis method and the unique properties that were observed.

CHAPTER IV

ENHANCED CROSS-PLANE THERMOELECTRIC TRANSPORT OF ROTATIONALLY-DISORDERED $SnSe_2$ VIA SE VAPOR ANNEALING.

4.0. Authorship Statement

This chapter was formatted from a manuscript with the same name, that was published by Nano Letters (DOI: 10.1021/acs.nanolett.8b02744) on October 19, 2018, and was co-authored by myself, Jihan Chen, David Choi, Nirakar Poudel, Lang Shen, Li Shi, David C. Johnson and Stephen Cronin. Jihan Chen is the primary author on this paper and he, David Choi, Nirakar Poudel, Lang Shen, Li Shi, and Stephen Cronin made the substrates, prepared the devices, collected the cross-plane measurements on the samples, analyzed the cross-plane data, and contributed to the writing on the manuscript. David Johnson is my advisor and consulted in the preparation of this publication. I prepared the films that were studied, characterized their structure and composition, collected in-plane transport measurement data and contributed to the writing of the manuscript.

4.1. Introduction

Over the past two decades, significant improvements in thermoelectric efficiencies have been achieved through a reduction of lattice thermal conductivity while maintaining good electrical conductivity.[1] Highly anisotropic materials with weak van der Waals bonding across incoherent interfaces gives rise to exceptionally low cross-plane thermal conductance. Cahill and Johnson have shown that WSe_2 “disordered layered crystals" (i.e., solids that combine order and disorder in the random stacking of two-dimensional crystalline sheets) have a thermal conductivity that is only a factor of 2 larger than air.[2] Subsequent investigations have shown that ultralow thermal conductivity is a general feature of disordered layered crystals,

$(MSe)_m(TSe_2)_n$, $(T'Se_2)_m(TSe_2)_n$, (where M = Sn, Pb, Bi, La,…; T' and T = Ti, V, Cr, Nb, Mo, Ta, W and Sn) and related materials with rotational disorder between the layers.[3-6] The cause of this low thermal conductivity is explained by the large anisotropy in elastic constants that suppresses the density of phonon modes propagating along the soft direction.

Over the past several years, the Johnson group has developed a controlled synthesis route that enables the preparation of interdigitated layers of two or more constituents that do not have an epitaxial relationship between their structures.[7] Within the planes, the constituent layers are crystalline. From plane to plane, the layers are randomly misregistered in *x* and *y* and rotated relative to each other. To date, the constituent 2D layers include transition metal dichalcogenides, rock salt structured layers (e.g., SnSe, PbSe, BiSe, LaSe), Bi_2Se_3 and related compounds, more exotic layered structures including $V_{n+1}Se_{2n+2}$, and alloys of these constituents.[8-13] These materials are intermediate between crystalline and amorphous and have been called *ferecrystals* (from Latin *fere*, meaning almost). They are closely related to misfit layered structures, which contain two constituent layers with an epitaxial relationship along one of the in-plane axes and no systematic rotational order.[14] These disordered layered crystals have been found to have extremely low cross-plane thermal conductivity, with total thermal conductivity values less than 0.10 $Wm^{-1}K^{-1}$ for a large number of different constituents ($MoSe_2$, WSe_2, PbSe, SnSe, and $SnSe_2$) in a variety of different configurations.[6] While cross-plane thermal conductivities have been measured, the cross-plane electrical and thermoelectric properties have not been reported for any of these compounds.

In the work presented here, cross-plane thermoelectric devices based on SnSe and $SnSe_2$ are fabricated on a Si wafer with a 300nm insulating oxide. One set of samples was annealed in an open system (i.e., flowing N_2 gas environment), resulting in the formation of SnSe with

some $SnSe_2$ present (referred to as "SnSe" in the following description). This first sample likely has some Se vacancies due to the annealing in an open N_2 atmosphere. A second set of samples was annealed in a fixed partial pressure of Se vapor after the initial annealing in an open system, resulting in the formation of $SnSe_2$ (referred to as "$SnSe_2$" henceforth).

4.2. Results and Discussion

4.2.1. Thermoelectric Device Fabrication and Measurement

To fabricate the cross-plane thermoelectric device, a bottom metal 4-probe resistance temperature detector (RTD) is patterned using electron beam lithography followed by metal deposition of Ti/Au, as illustrated in Figure 4.1. Following this, a layer of PMMA is spin-coated on the substrate, and an 12 μm×12 μm window is opened on the bottom RTD. The SnSe material is then deposited on the substrate by physical vapor deposition followed by a lift-off process and annealing in an inert N_2 environment at 350°C for 30 min to form the crystalline layered structure, as illustrated in Figure 4.2. After annealing in a N_2 environment, $SnSe_2$ is obtained by annealing in Se vapor at a fixed Se partial pressure, which transitions the SnSe into $SnSe_2$ (see Methods section). The top metal RTD is patterned in the same fashion as the bottom metal RTD. The samples are then capped with a 50nm insulating film of Al_2O_3 deposited by atomic layer deposition (ALD) at 200°C using trimethylaluminum (TMAl) and water as precursors. Lastly, a serpentine metal heater with 5 nm Ti and 35 nm Pd is patterned on top of the Al_2O_3 layer. The heater also contains four probes in order to measure the heating power precisely. The device fabrication process and an optical microscope image of a completed device are shown in Figure 4.1.

Once the thermoelectric device is fabricated, the top and bottom RTDs are calibrated in a vacuum, temperature-controlled stage, as shown in Figure 4.3. First, the resistance of the RTD is measured from 300 to 330 K in increments of 5 K. To anneal out any strain induced in

the samples due to thermal expansion, several thermal cycles are performed until the resistance becomes stabilized. The resistance is normalized with respect to the room temperature resistance (i.e., R/R_0, where R_0 is the resistance at 300 K) and fitted to a linear function of the temperature (see Figure 4.3b). The RTDs' resistance measurement is performed as a function of the heater current (see Figure 4.3c). Based on this relation and the data in Figure 4.3b, we establish the relation between the temperature change and applied heater power, as shown in Figure 4.3d. A similar temperature calibration is carried out for the top RTD, as shown in Figure B.1 – B.3 of the Supplemental Document.

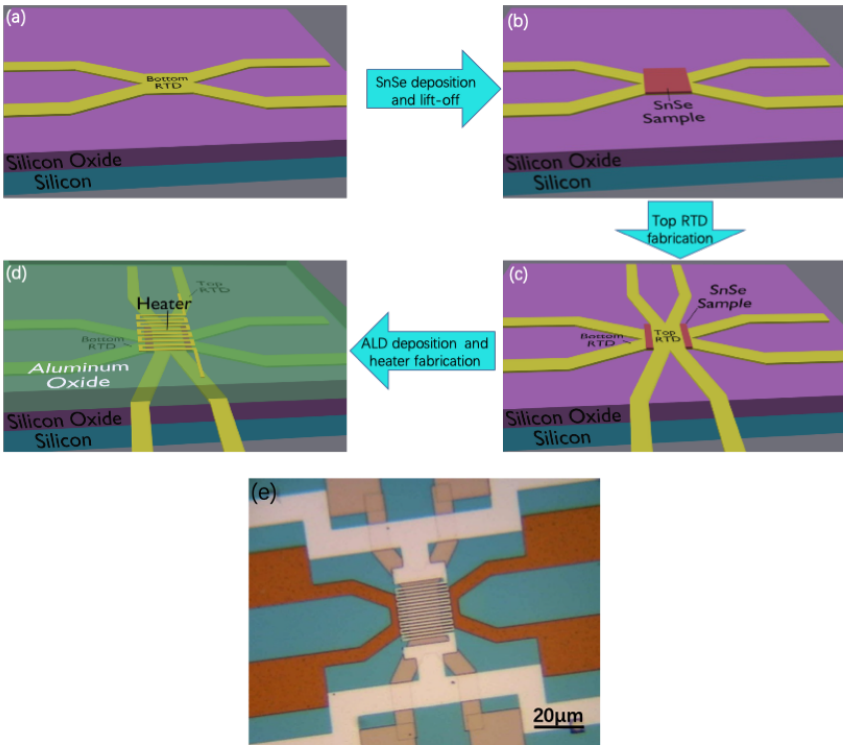

Figure 4.1. (a-d) Schematic diagrams of the device fabrication process and (e) optical image of the completed device.

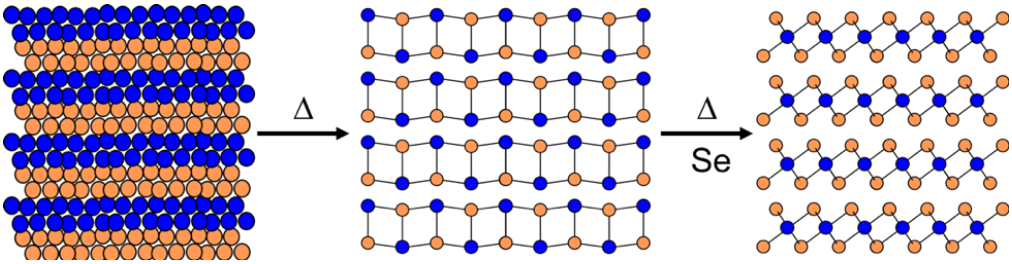

Figure 4.2. Schematic illustration of a precursor designed to form a layered structure of SnSe when annealed in an inert atmosphere under optimized conditions. Upon heating in Se-vapor for 30 minutes at 300 °C, the layered SnSe converts to $SnSe_2$. Se and Sn atoms are represented in orange and blue, respectively.

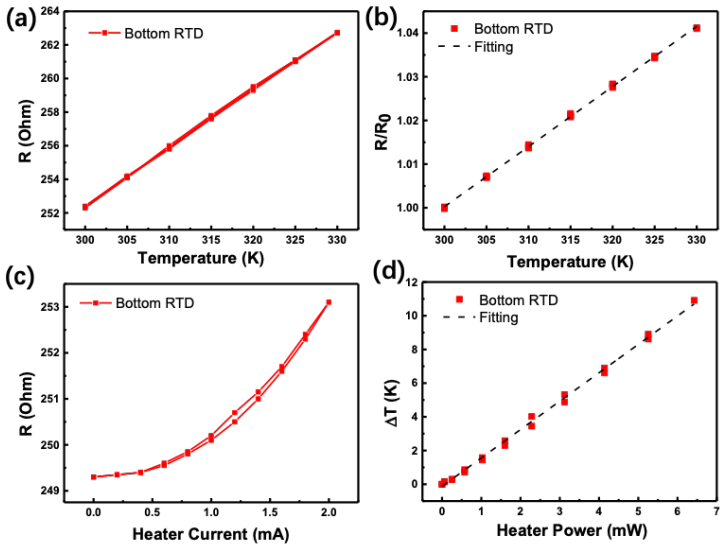

Figure 4.3. Temperature calibration of the bottom RTD of a 50 nm $SnSe_2$ film after Se-vapor annealing. (a) The resistance of the RTD measured at different temperatures. (b) Normalized resistance (R/R_0, where R_0 is the resistance at 300 K) plotted as a function of temperature. (c) The resistance changes of the RTD under various heating currents. (d) Temperature change of the metal RTD plotted as a function of heating power.

The thermoelectric voltage (ΔV) is then measured as a function of the temperature difference between the top and bottom RTDs (ΔT), and the Seebeck coefficient is obtained from the slope of this data. Figure 4.4 shows the thermoelectric voltage plotted as a function of the temperature

difference across the as-grown SnSe device (without Se-vapor annealing). The thermoelectric voltage measurement was performed with both positive and negative heating voltages, which provide nearly the same result, indicating that the voltage drop across the device is in fact a thermoelectric effect rather than a potential difference induced by the heater voltage. Also, the leakage currents between the Pd heater and the top RTD is less than 50 pA for applied bias voltages up to 5 V (>GΩ), as shown in Figure B.4 of the Supplemental Document. All data sets were fit to linear functions with the slope corresponding to the Seebeck coefficient (*S*), as indicated in the Figure 4.4. Here, the cross-plane Seebeck coefficient of the SnSe film without Se-vapor annealing is -38.6 μV/K and the electrical conductivity is 3 S/m.

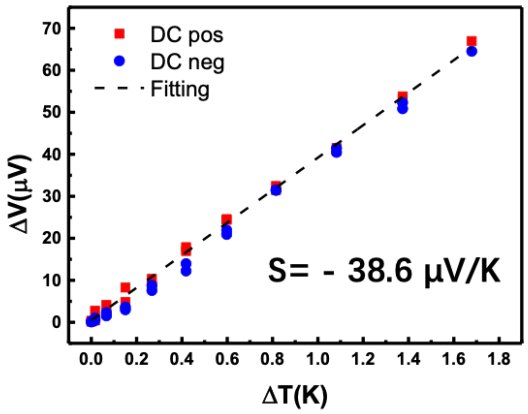

Figure 4.4. Cross-plane Seebeck coefficient of the 50 nm SnSe film before Se-vapor annealing.

Figure 4.5 shows the cross-plane Seebeck coefficient of the $SnSe_2$ film after Se-vapor annealing at a fixed Se partial pressure at 300°C for 30 minutes. The cross-plane Seebeck coefficient (Figure 4.5) of the $SnSe_2$ device after Se-vapor annealing is -630.8 μV/K, and the electrical conductivity is 0.5 S/m. This corresponds to a factor of 16X improvement in the Seebeck coefficient, reflecting the transition from SnSe to $SnSe_2$ and the mitigation of unintentional doping caused by Se vacancies.

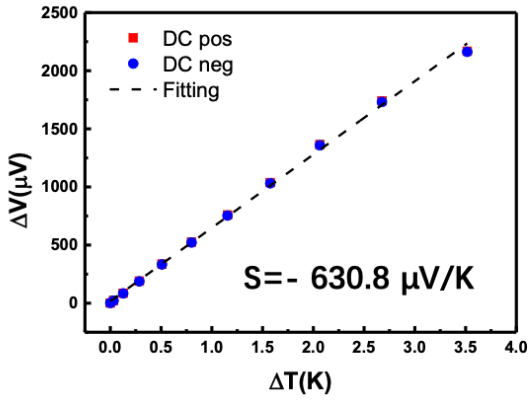

Figure 4.5. Cross-plane Seebeck coefficient of the 50 nm $SnSe_2$ after Se-vapor annealing.

4.2.2. Film Composition and Thickness

X-ray fluorescence (XRF) measurements were collected to monitor the amount of each elemental species (including oxygen) present in each sample under the two annealing conditions (see Table 4.1). Here, the Sn counts are roughly the same for both annealing conditions, as expected. The oxygen counts are negligible, indicating that the films are not degraded upon annealing, and annealing under different conditions does not cause excessive oxidation. After annealing in Se vapor, we observe an approximate doubling in the total Se counts measured. This data further suggests that Se vapor annealing results in a conversion from SnSe to $SnSe_2$.

Table 4.1. XRF integrated counts and counts per layer for both SnSe targeted films annealed under different conditions.

	Sn counts	Se counts	O counts	Sn counts/layer	Se counts/layer
N_2 anneal	1.975	2.912	0.007	0.23	0.035
N_2 & Se anneal	1.946	5.908	0.006	0.23	0.071

Specular XRD patterns for the nitrogen-annealed and Se vapor-annealed samples are shown in Figure 4.6. In the N_2 annealed sample,

only (00*l*) reflections are observed, which correspond to the *c* axis lattice constant of the SnSe structure. This results from an alignment of the material with the substrate in the *c* axis direction while remaining randomly oriented in the *ab*-plane.[15] After Se annealing, the reflections shift to lower 2θ angles, and can be indexed to the $SnSe_2$ structure. This change is consistent with the doubling of Se counts measured with XRF (see Table 4.1). Reflections that do not correspond to the (00*l*) were also observed for the Se-annealed film, which is indicative of a lower degree of alignment with the substrate.

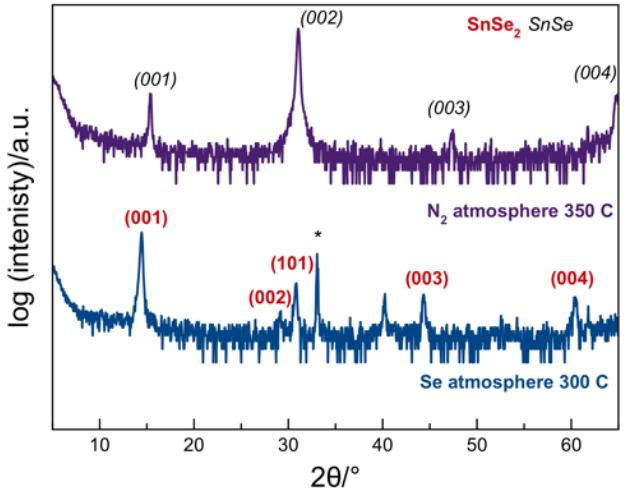

Figure 4.6. Specular X-ray diffraction (XRD) patterns of SnSe films. Both samples were annealed in a nitrogen atmosphere and one was subsequently annealed in a selenium atmosphere (the blue pattern) resulting in a conversation to $SnSe_2$. Miller indices are provided for select reflections. The intensity was plotted on a log scale to enhance weak reflections.

In-plane XRD measurements were collected for films annealed under both conditions, as shown in Figure 4.7, in order to study the structure of the compound in the *ab*-plane. Here, the reflections for both patterns are indexed to either SnSe or $SnSe_2$, with the underlying substrate peak identified with an asterisk. For the SnSe film annealed in a N_2 atmosphere, all the reflections are indexed to (*hk*0) reflections of either SnSe or $SnSe_2$. Here, reflections for both constituents have nearly

equal intensities, indicating that there are nearly equal amounts of both crystallinities present. The lack of (00*l*) reflections for the $SnSe_2$ film is likely the result of the preferred alignment of the SnSe constituent obscuring the $SnSe_2$ constituent from specular diffraction.[15] The presence of $SnSe_2$ in the N_2-annealed sample indicates that there is extra Se present and that longer annealing times are required to form only the monoselenide. The film annealed in Se vapor shows only reflections corresponding to $SnSe_2$, but also contains non-(*hk*0) reflections. The presence of these extra reflections along with the 00*l* axis supports the fact that the sample loses a considerable degree of alignment upon converting from the monoselenide to the diselenide.

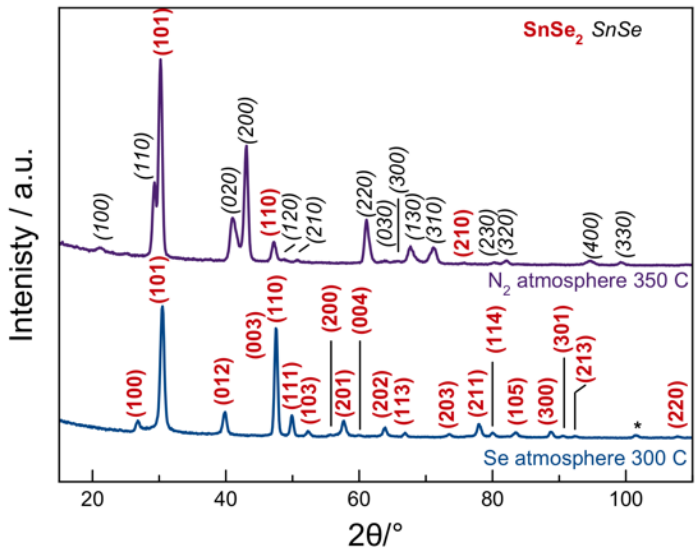

Figure 4.7. In-plane X-ray diffraction (XRD) patterns for targeted SnSe samples. Both samples were annealed in a nitrogen atmosphere and one was subsequently annealed in a selenium atmosphere (the blue pattern) resulting in a conversation to $SnSe_2$. The reflections are indexed to SnSe and $SnSe_2$ with one substrate peak (marked with the asterisk) in the Se-vapor annealed sample.

4.2.3. Control Experiments

One potential concern in the measurement of these extremely thin films (~50 nm), which are on the same order as the thickness of the metal RTDs (30 nm), is that the temperature and voltage drops at the

contacts would significantly affect the measurement, resulting in substantially underestimated values of the Seebeck coefficient. In order to verify the validity of this measurement technique, we measured samples with different thicknesses. Figure B.5 of the Supplemental Document shows the Seebeck measurements of 50 nm-thick and 100 nm-thick SnSe films grown in the Johnson lab. Other than the thickness, these films were prepared under identical conditions. Both samples show nearly the same Seebeck coefficient (differing by <3 %), which verifies the validity of the measurement and indicates that the effect of the contacts is negligible for this material system. That is, the voltage and temperature drop across the contacts seem to have a negligible effect on the measurement. This is an important result, which indicates that the relatively low Seebeck coefficients observed in Figures 4.4 and B.5 are not simply due to the measurement technique and instead reflect the true nature of the material composition. Another important consideration in this general measurement approach is the relative resistance of the RTDs and the heterostructure structure itself. If the resistance of the heterostructure is smaller than that of the RTDs, there will be electrical shorting of the RTD through the thin film of interest material, rendering the RTDs ineffective. Typically, the RTD resistance is approximately 4 Ω and the cross-plane resistance of these samples is around 120 Ω, which is well within the reliable range of operation. We estimate that reliable results can be obtained below a ratio R_{RTD}/R_{film} of approximately 10%.

4.3. Conclusion

In conclusion, we report an enhancement in the cross-plane thermoelectric properties of SnSe films due to Se vapor annealing, which induces a SnSe-to-$SnSe_2$ (i.e., monoselenide-to-diselenide) transition and mitigates the effects of unintentional doping. This results in an extremely high Seebeck coefficient (-631 μV/K), and increased power factor (0.2

$\mu W/m \cdot K^2$). Our XRF measurements show a doubling in the total Se counts, which is consistent with a transition from SnSe to $SnSe_2$, stoichiometrically. This SnSe-to-$SnSe_2$ transition is corroborated by specular and in-plane XRD measurements. After the Se vapor annealing, the diffraction peaks can be indexed to the $SnSe_2$ structure. By conducting post-growth Se annealing at a fixed Se partial pressure, the compound changes to $SnSe_2$ and alleviates unintentional doping due to Se-vacancies that resulted in the relatively low Seebeck coefficients observed in our previous work on disordered layered SnSe-based materials. As a result, we observe a 16-fold increase in the cross-plane Seebeck coefficient (from -38.6 to -631μV/K), and a 44-fold increase in power factor (from 4.5 $nW/m \cdot K^2$ to 0.2 $\mu W/m \cdot K^2$). A corresponding 6-fold drop in the electrical conductivity is observed, which is consistent with the drop in the free carrier concentration.

4.4. Materials and Methods

The targeted SnSe films were crystalized by heating designed precursors prepared by high vacuum physical vapor deposition. The films were prepared using a modified method of that described by Fister *et al.*[16] Sn was deposited with an electron beam gun and Se was deposited with a Knudson effusion cell. Elemental layers were deposited sequentially to obtain a precursor with compositional modulation that mimics the desired final product. A quartz crystal microbalance was used to monitor the deposition rates and pneumatic shutters positioned above the sources controlled the flux of material to the substrate. The deposition parameters were calibrated using X-ray fluorescence (XRF), X-ray reflectivity (XRR), and X-ray diffraction (XRD) to ensure that the amount of material deposited in each layer was correct for crystallization of the desired product. The films were deposited on Si with a native SiO_2 layer for structure and composition characterization, as well as patterned substrates for cross-plane transport measurements as well as fused

silica for in-plane transport measurements. After deposition, all films were annealed on a hotplate at 350 °C for 30 minutes in a nitrogen environment to facilitate crystallization of the desired materials. Some films were subsequently annealed in a sealed quartz tube with a Se vapor pressure provided by powdered $SnSe_2$.[17] The tubes were heated in a single zone Carbolite tube furnace at 300 °C for 3 hours.

X-Ray fluorescence spectra were collected using a Rigaku ZSX Primus II with a rhodium source. Counts were determined by integrating the area under the intensity line at the °θ range where a fluorescence peak is expected for each element in question. The integrated area is proportional to the atom/area for the element in question. X-ray reflectivity and specular X-ray diffraction patterns were collected using a Bruker D-8 Discover diffractometer in a locked-coupled θ-2θ geometry. In-plane X-ray diffraction spectra were collected with a Rigaku Smartlab diffractometer using an in-plane gracing incidence geometry. All diffraction experiments were conducted using Cu Kα radiation.

4.5. BRIDGE

Chapter 4 provided insight into the structure and properties of SnSe films prepared from the Modulated Elemental Reactants method and discussed the effects of post treatment on the entire nature of the film which resulted in a second compound with subsequently different properties. Elucidating the inherent nature of the SnSe constituent is necessary to understand how it contributes to the properties of a heterostructure when it is incorporated. The ability to modify the material properties with processing provides another means with which heterostructures composed of various constituents and nanoarchitectures can be modified and manipulated to obtain desired properties. Chapter 5 will provide information about the inherent

properties of $TiSe_2$, the second constituent used in preparing the SnSe heterostructures discussed in the following chapters.

CHAPTER V

INVESTIGATING THE FORMATION OF $MoSe_2$ AND $TiSe_2$ FILMS FROM ARTIFICIALLY LAYERED PRECURSORS.

5.0. Authorship Statement

At this time, this work is an unpublished manuscript that will published in the future. This work is coauthored with to Aaron Miller, Dylan Bardgett, Erik Hadland and David Johnson. I developed the project, prepared and characterized samples, and wrote and edited the manuscript. Aaron Miller, Erik Hadland, and Dylan Bardgett assisted with the sample preparation and characterization as well as contributed to manuscript preparation. David Johnson is my advisor who assisted in the experimental design, analysis of data, and writing of the manuscript.

5.1. Introduction

In the 1980's and 1990's, the sequence of solid-state reactions between transition metals deposited on silicon substrates were intensively investigated because transition metal silicides were desired as low resistance replacements for heavily doped polysilicon contacts to transistors in integrated circuits.[1–3] A key aspect of this research was understanding the evolution of the reaction of metals on silicon surfaces, as it was crucial to control the first phase formed in developing the self-aligned silicide or "salicide" process. [4] The first step in the reaction is the formation of an amorphous layer at the interface between the metal and silicon, driven by the enthalpy of mixing of the elements. Since diffusion rates roughly scale with melting temperatures, the amorphous phase takes the composition of the lowest melting eutectic in the phase diagram. The compound that is easiest to nucleate from this eutectic will form first, although the literature offers various definitions of "easiest". Walser and Bene suggested that the congruently melting compound with the highest melting point adjacent to the lowest melting eutectic would

form first.[4] A second proposal suggested that the compound with the largest effective heat of formation at the eutectic composition would form first. Over time, the concepts developed in the study of metal-silicon reactions were applied to a broad range of systems, from the formation of amorphous metallic alloys[5] to the sequence of intermetallic phase formation at reacting metal interfaces.[6]

Recent interest in preparing monolayers of compounds, either alone or as constituents in heterostructures, has focused attention on understanding the formation of ultrathin crystalline layers. Key goals include developing an approach that is scalable to wafer-scale synthesis, capable of controlling thickness to a precise number of unit cells, and able to control defect levels. Thin film transition metal dichalcogenides (TMD's) and other layered chalcogenides provide a promising platform towards achieving these requirements due to their diverse and exotic physical properties that can be manipulated by varying the thickness, substrate, or adjacent layers in heterostructures.[7–12] While thickness-dependent properties were initially discovered by cleaving bulk samples, subsequent research focused on developing wafer-scale preparation techniques such as chemical vapor deposition.[13–15] More recently, atomic layer deposition,[16–18] metal-organic-CVD,[19–21] and direct deposition methods (sputtering, pulsed laser deposition, e-beam)[22–24] have been used to make high quality layered TMD's.[25] These approaches use elevated temperatures or light to increase reaction rates, but the quality of the product remains dependent on the temperature and the pressure of the carrier gas and reactants, the substrate, and/or the photon energy utilized. The formation process for 2D materials also depends on the lattice parameter of substrates, reaction temperature, and atomic gas flux. While plausible chemical reactions have been proposed for many of these systems, there is little reported data of intermediate states and no

overarching understanding of how changing reaction parameters impacts the formation mechanism.

In this report we present x-ray reflectivity (XRR) and x-ray diffraction (XRD) data on the reaction between ultra-thin layers of two different metals, Mo and Ti, with amorphous Se. Multiple repeating M|Se layers were deposited on nominally room temperature substrates to increase the intensity of the diffraction signals. For Mo|Se precursors, nucleation but little crystal growth occurred during deposition. However, for the Ti|Se precursors, nucleation of both Ti_2Se and $TiSe_2$ occurred during deposition, and the $TiSe_2$ grains grew significantly during deposition of subsequent layers. Annealing precursors for both systems resulted in the formation of well-defined layered dichalcogenide films. It was experimentally determined that depositing about 10% excess Se in the precursors results in the largest grain sizes for the annealed films. It is likely that the excess Se not only compensates for the loss of Se to the open system during annealing, but also acts as a flux to help facilitate diffusion of metal atoms during crystallization of the layers. Laue oscillations present in the specular diffraction patterns of optimized samples indicate that most crystalline domains in the films have the same number of unit cells.

5.2. Materials and Methods

$TiSe_2$ and $MoSe_2$ films were prepared by repeatedly depositing elemental bilayers of Ti|Se or Mo|Se to form an artificially layered precursor. The Mo and Ti layers were deposited using an electron beam gun and Se was deposited use a Knudsen effusion cell. Elemental precursors were deposited onto silicon substrates with a native oxide layer while maintaining a vacuum of $<10^{-7}$ Torr during the deposition. The thickness of the Ti and Mo elemental layers were held constant at the thickness required to provide enough metal to form a single Se-M-Se dichalcogenide trilayer. The thickness of the Se layer was varied to probe

the influence of composition and excess Se on nucleation and growth of the respective dichalcogenides. In-house deposition software were used to control and monitor the amount of material deposited in each layer via quartz crystal microbalances and pneumatic controlled shutters.[24–27] The designed precursors were heated in an N_2 environment with <1 ppm O_2 present to crystallize the deposited elemental layers.

Structure and composition were studied via a suite of x-ray techniques. The film structures were characterized by XRD and x-ray reflectivity XRR while the sample composition was determined using x-ray fluorescence (XRF). XRR and specular XRD were collected on a Bruker D-8 Discover diffractometer. In-plane diffraction was collected on a Rigaku SmartLab diffractometer. All diffraction measurements utilized a copper Ka radiation source. The absolute amount of each element deposited was determined using XRF data collected on a Rigaku ZSX Primus II with a Rhodium tube. Previously published calibration curves were used to related the background corrected integrated raw intensity to the atoms/Å^2 of each element.[28]

5.3. Results and Discussion

The initial structure and evolution of the $MoSe_2$ precursors during annealing were investigated using XRR and specular XRD. The as-deposited XRR pattern, shown in Figure 5.1, contains Kiessig fringes, reflecting the total thickness of the deposited films, and two additional reflections. The first narrow reflection at around 10.9° 2θ is caused by the artificial layering of the Mo|Se precursor, yielding a Mo|Se thickness of 8.1 Å using Bragg's law. The total thickness calculated from the Kiessig fringes, 194 Å, is within error of what is expected for a film composed of twenty-four 8.1 Å layers. The broad reflection at 13.4° 2θ indicates that nucleation and growth of $MoSe_2$ grains perpendicular to the substrate has occurred during deposition. A potential second order reflection of this broad reflection maybe present at higher angles but is

very weak. This suggests that there is significant variation in the distance between crystalized $MoSe_2$ layers within the grains. Together, the XRR and specular XRD indicate that the precursor consists of twenty-four layers containing Mo-rich and Se-rich regions relative to the average composition that are each 8.1 Å thick. Within these layers are small regions that consist of several irregularly stacked $MoSe_2$ layers forming barely coherent grains of $MoSe_2$.

The specular XRD patterns evolve gradually as the annealing temperature is increased (Figure 5.1) and a very crystalline $MoSe_2$ 00*l* diffraction pattern is obtained after annealing at 650°C. The reflection from the artificial layering moves to higher angle indicating that the period of the artificial layering is becoming smaller as annealing temperature is increased. The broad reflection at 13.4 2θ moves to higher angle and becomes narrower and more intense as annealing temperature is increased indicating that the $MoSe_2$ layers within the grains are becoming closer together, there is a smaller spread in the interlayer distances within each grain, there are more $MoSe_2$ layers within each coherent domain, and there are more $MoSe_2$ domains present in the film. After the 300°C annealing, second, third, and fourth order reflections from the $MoSe_2$ grains are observed, reflecting the increased order and larger size of the grains. These higher order reflections also increase in intensity and become narrower as annealing temperature is increased, reflecting the growing order and increased size of the $MoSe_2$ domains. There is a considerable growth in intensity and narrowing of diffraction line widths due to the $MoSe_2$ grains between the 500°C and the 650°C anneals. The *c*-axis lattice parameter calculated from the position of the Bragg reflections is 6.52 Å. This is slightly larger than previously reported for $MoSe_2$ (6.460(1) Å).[29] After annealing at 650°C, the low angle reflection from the artificial layering is no longer visible. Kiessig fringes observed in the XRR scan after annealing 650°C are well resolved and

decay in intensity as expected for a film of uniform thickness and electron density. The total film thickness calculated from the positions of the Kiessig fringes is 158Å, which is within error of that calculated for 24 layers of $MoSe_2$ having a *c*-axis lattice parameter of 6.52Å. Between the first and second Bragg reflections, Laue oscillations are present. Laue fringes result from the incomplete destructive interference between Bragg reflections due to a finite number of unit cells. Their presence indicates that a significant portion of the film consists of the same number of $MoSe_2$ layers coherently diffracting. Analysis of the spacing of the Laue fringes indicate that the coherent domains contain 24 $MoSe_2$ layers, consistent with the number of Mo|Se bilayers deposited in the precursor.

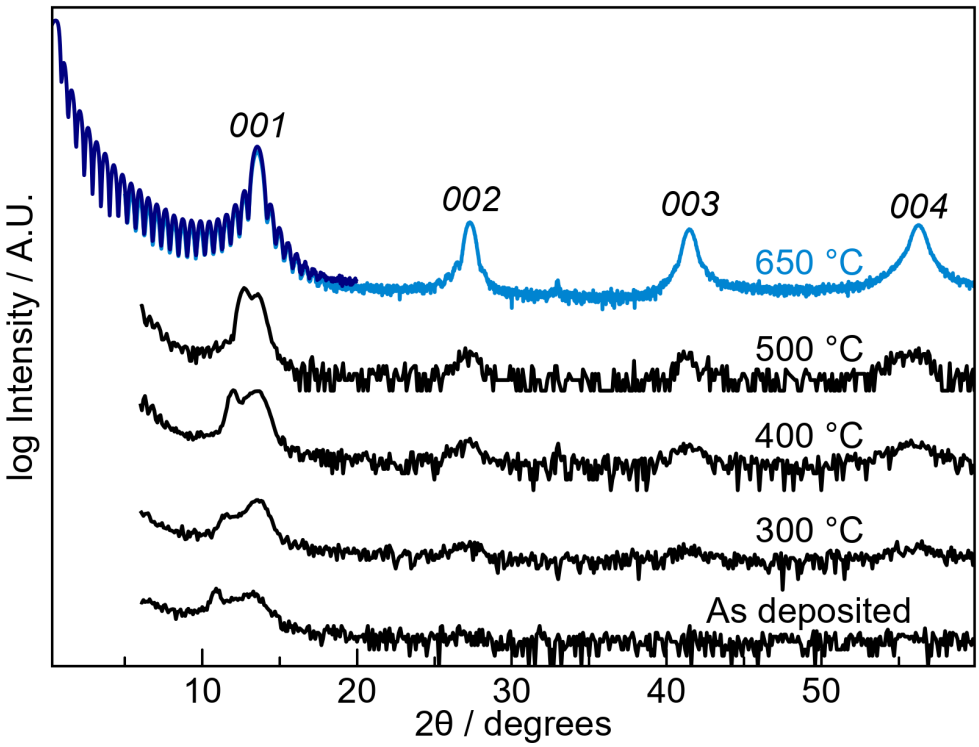

Figure 5.1. XRD patterns from an annealing study of an as-deposited Mo|Se precursor. The annealing temperatures are presented above the scans. For the scan at 650°C, X-ray reflectivity is also included. Indices are provided above the observed reflections.

In-plane diffraction data was collected for the Mo|Se film annealed at 650 °C and is shown in Figure 5.2. All of the reflections can be indexed to a hexagonal unit cell with an *a*-axis lattice parameter of 3.31(1) Å. This lattice parameter is consistent what has been previously reported for both bulk $MoSe_2$ *a*-axis lattice parameters (3.289(1) Å)[29] and lattice parameters previously published for $MoSe_2$ thin films (3.246 Å).[30] The composition of the films and both the specular and in-plane diffraction data provide consistent evidence that the crystalized material is $MoSe_2$.

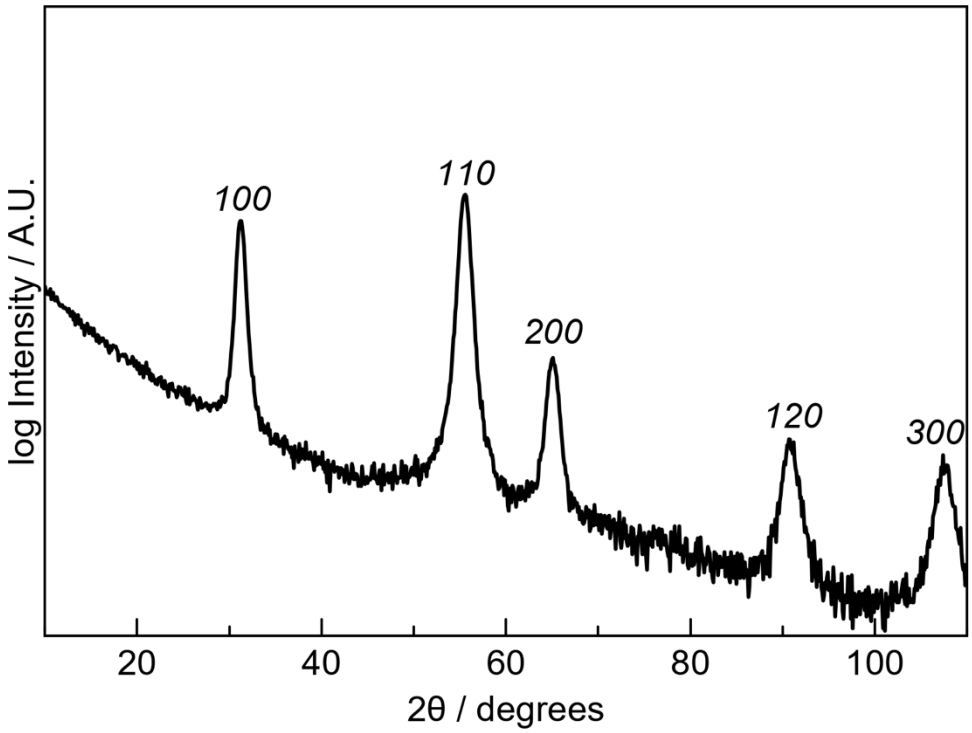

Figure 5.2. Grazing incidence in-plane diffraction of the $MoSe_2$ precursor after annealing at 650°C. The Miller indices are shown above the reflections.

A series of Mo|Se films with varying amount of Se were prepared, annealed at 650°C, and characterized by XRD to probe the influence of composition on the growth and crystallinity of the final product. Figure 5.3 graphs the intensity and peak width of the *002* reflection of $MoSe_2$ as a function of the Se content of the as-deposited sample. The peak width

of the 00*l* reflections depends on the size and coherence of the $MoSe_2$ layers along the *c*-axis, with a minimum peak width occurring when the entire film thickness consists of a single coherent domain. Data in Figure 5.3 demonstrates that an excess of Se is required to obtain the narrowest linewidths, but too much Se increases the linewidth. The intensity of the 00l reflections is proportional to the number of $MoSe_2$ domains that are aligned parallel to the substrate and a maximum in the intensity is observed with 10-15% excess of Se. Rocking curves taken on these samples are narrowest for those with the highest intensity of the 002 reflection, suggesting that the intensity maximum is due to the percentage of the sample that is crystallographically aligned. The variation of crystalline quality with Se concentration is probably caused by the excess Se acting as a flux, increasing the mobility of the Mo cations. Too much Se, however, results in the nucleation of grains of $MoSe_2$ that are not orientated with the basal plane perpendicular to the substrate. This prevents the entire film thickness from becoming a single coherent domain.

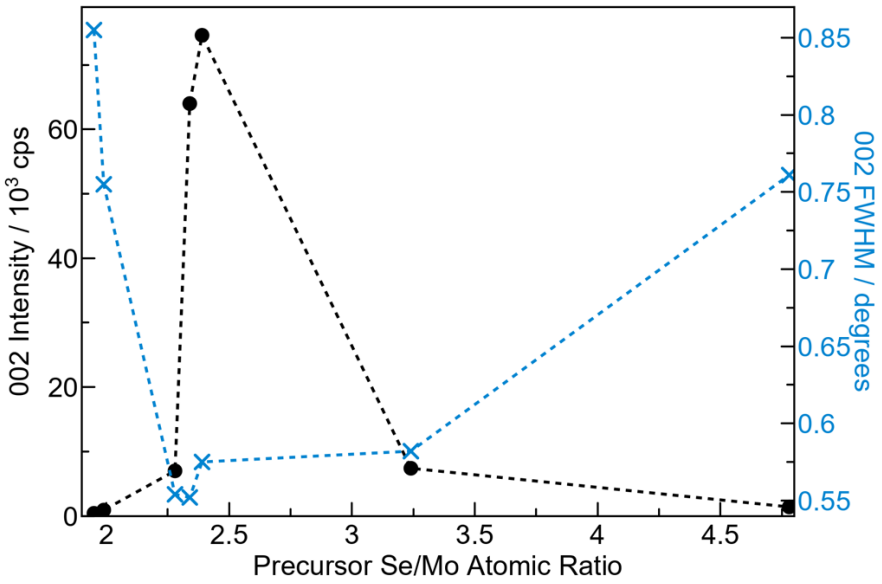

Figure 5.3. $MoSe_2$ crystal quality as determined by specular diffraction reflection intensity and peak width shown as a function of Mo|Se precursor composition.

A series of Ti|Se precursors with various Se: Ti ratios were prepared to investigate if their evolution to form $TiSe_2$ is similar to that of $MoSe_2$. Table 5.1 summarizes information obtained on each of the Ti|Se precursors. The XRF data indicated that all of the precursors were Se rich as deposited, and the number of Ti atoms/$Å^2$ deposited per Ti|Se bilayer ranged above and below the number required for a single crystalline $TiSe_2$ trilayer (0.092 Ti/$Å^2$). The as-deposited XRR patterns (See SI Figure C.1) contained Kiessig fringes, reflecting the total thickness of the deposited films, and a strong 001 reflection from crystalline $TiSe_2$. No reflection was observed that could be attributed to the artificial layering of the Ti|Se precursors. The total thicknesses for the samples were calculated from the Kiessig fringes and divided by the number of Ti|Se bilayers that were deposited to obtain the average Ti|Se thicknesses in the various samples (see Table 5.1). The thicknesses are consistent with the number of atoms deposited calculated from the XRF intensities (see table 5.1) and are close to the *c*-axis lattice parameter of $TISe_2$. The specular diffraction patterns of the as-deposited precursors all contain two to four 00*l* reflections of crystalline $TiSe_2$ domains (see Figure 5.4), indicating that the as-deposited films are much more crystalline that the corresponding Mo|Se films. The *c*-axis lattice parameters were all larger than those previously reported for $TiSe_2$, reflecting the high defect levels resulting from the low ambient temperature during the deposition. There is a systematic increase in the *c* – axis lattice parameter as a function of the amount of Se deposited in the sample, suggesting that interstitial Se atoms may be present. No evidence for artificial layering remains in any of the as deposited Ti|Se precursors, in contrast to what was observed for Mo|Se films. The in-plane diffraction pattern (see SI Figure C.2, SI) also reflects the more crystalline nature of the as-deposited Ti|Se films, containing reflections that can be indexed as $TiSe_2$ as well as broad reflections consistent with the presence of Ti_2Se.

Table 5.1. A summary of the structure and composition of the as-deposited Ti|Se precursors.

# Ti|Se layers deposited	Total Film Thickness (Å, ±0.5)	Average bilayer thickness (Å)	Average Ti atoms/Å^2 per bilayer (±0.07)	Average Se atoms/Å^2 per bilayer (±0.04)	Ti:Se	As-deposited $TiSe_2$ *c*-axis lattice parameter (Å, ±0.01)
83	478	5.8	0.092	0.185	1:2.01	6.14
83	487	5.9	0.092	0.188	1:2.05	6.17
83	507	6.1	0.094	0.198	1:2.11	6.16
84	509	6.1	0.089	0.192	1:2.14	6.17
83	524	6.3	0.092	0.198	1:2.16	6.19
84	527	6.3	0.089	0.197	1:2.22	6.19
82	482	5.8	0.084	0.188	1:2.24	6.18
83	532	6.4	0.090	0.204	1:2.26	6.20
84	564	6.7	0.082	0.210	1:2.57	6.27

The diffraction data taken together indicate that the Ti|Se samples substantially interdiffuse and react during the deposition. Since the film's overall compositions are Se-rich, we suspect that the observed Ti_2Se is formed during the deposition when Se is deposited on top of the initial Ti layer. After the first Ti|Se bilayer is deposited, the film consists of Se on top of a Ti_2Se layer. Ti deposited on top of the Se layer nucleates $TiSe_2$, either at the surface or at the Ti_2Se surface below by diffusing through the amorphous Se layer. When the next Ti layer is deposited, Ti must diffuse through the Se layer to the growth fronts of the existing $TiSe_2$ crystallites. If the diffusion length through the Se-rich amorphous layers becomes sufficiently large, new crystalline layers of $TiSe_2$ may nucleate near the surface of the sample as Ti is deposited. These reactions during the deposition result in regions of large crystalline $TiSe_2$ surrounded by a Se-rich matrix, with a Ti_2Se layer adjacent to the Si substrate.

Figure 5.4 contains a series of XRD patterns collected as a function of annealing temperature for a representative Ti|Se precursor with an initial composition Ti:Se of 1:2.24. The 00*l* reflections of the $TiSe_2$

crystallites move noticeably to higher angle as annealing temperature is increased, indicating a decrease in *c*-axis lattice parameter. Intensities of the reflections increase, and the line widths decrease as annealing temperature increases. This suggests that the registration between the $TiSe_2$ planes increases as excess atoms between layers and at grain boundaries are either incorporated into the growing crystals or diffuse to the surface. In Se rich films, the in-plane reflections of Ti_2Se become unobservable. Ti_2Se in-plane reflections remain after annealing in the most Ti rich film studied. Films annealed at 350 °C have the greatest reflection intensity and narrowest peak widths. Annealing above 350 °C results in a decrease in intensity and an increase in peak width of the 00*l* reflections. Based on the above observations, the optimal annealing temperature for the Ti|Se precursors was determined to be 350 °C.

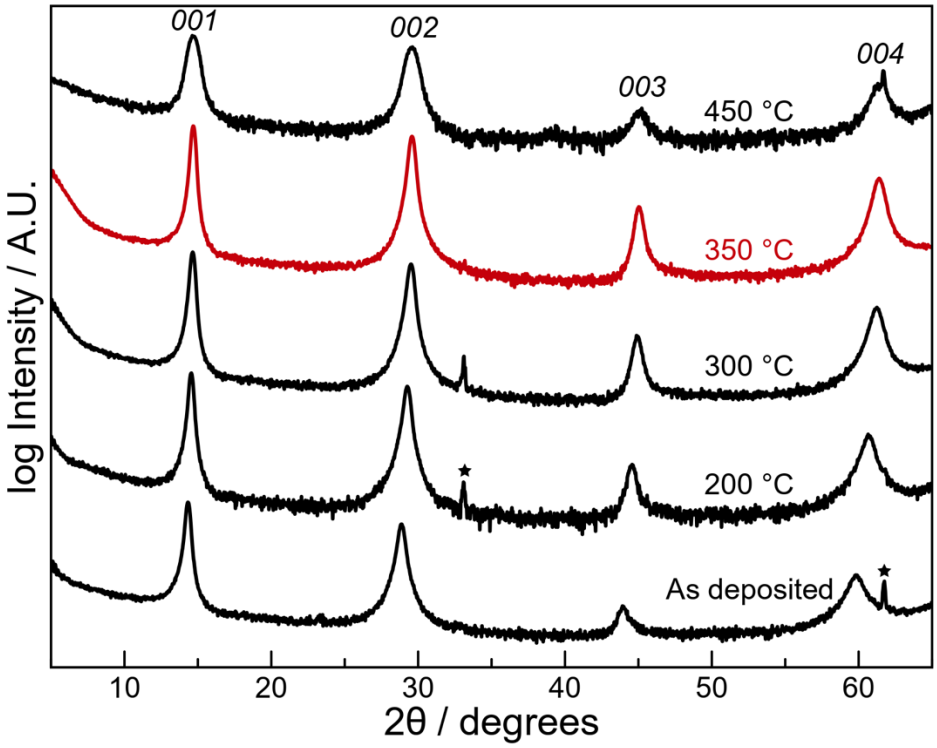

Figure 5.4. XRD diffraction data of a Ti|Se sample with a starting composition of 1:2.24 (Ti:Se) annealed for 30 minutes in an inert N_2 atmosphere at the indicated temperatures. Indexes are shown above the observed reflections and the scan with the highest intensity and lowest linewidths is shown in red.

As was done in the Mo|Se system, the precursor films with various as-deposited Ti:Se ratios were annealed under the same conditions (350°C for 30 minutes) to study the effects of precursor composition on film quality. XRF data collected on the annealed films show that they all lose Se during the annealing as summarized in Table 5.2. XRR patterns, shown in Figures C.1 and C.3, all contain Kiessig fringes from the interference of the front and back of the film. The thicknesses of the annealed films (see Table 5.2) are all thinner than the as-deposited films due to the loss of Se during the annealing. There are oscillations in the intensity of the Kiessig fringes in all of the samples that indicate that a surface layer has formed that has a different electron density than the rest of the sample, probably resulting from the formation of a surface layer of amorphous TiO_2. The XRR patterns fall into two general categories- those with a thicker (~50 Å) TiO_2 layer and those with a thinner (~10 Å) TiO_2 layer on the top of the film, SI Figure C.4. The specular diffraction patterns are shown in Figure 5.5a and C.2a and all of them contain 00*l* reflections from crystalline $TiSe_2$.The observed reflections are more intense, narrower and occur at higher 2θ angles than those in the as deposited precursors, indicating that there are more 00l planes aligned with the substrate, the $TiSe_2$ crystalline domains are thicker and that the *c*-axis lattice parameters are smaller. The *c*-axis lattice parameters obtained from full pattern Le Bail fits are shown in Table 5.2. Samples that have a slight excess of Se, in the composition range of $TiSe_{1.14}$ and $TiSe_{2.22}$ on deposition, have *c*-axis lattice parameters that match the reported values for $TiSe_2$. The films with initial compositions on either side of this regime have *c*-axis lattice parameters that are slightly larger than the literature value. Representative in-plane x-ray diffraction patterns are shown in Figure 5.5b and C.2b. The annealed patterns have narrower reflections than found in the as deposited samples, indicating a significant increase in the in-plane domain size. All of the reflections in the annealed samples can be

indexed to a hexagonal unit cell with lattice parameters that are similar to reported values for $TiSe_2$, see Table 5.2, except for broad reflections for Ti_2Se found in the pattern for the $TiSe_{2.01}$ sample.[31] These reflections can be indexed as reflections from Ti_2Se. This phase also appears to be present in all films to some extent before annealing. The *a*-axis lattice parameters for all of the Ti|Se films, determined from the Le Bail fits of the in-plane diffraction patterns found in Figure 5.5b, are very similar to previously determined values for $TiSe_2$.[31] Unlike the *c*-axis lattice parameters, which were significantly influenced by the amount of Se present in the precursor sample, the *a*-axis lattice parameter for the annealed $TiSe_2$ films do not depend on the composition of the precursors.

Table 5.2. Compositions and lattice parameters for annealed Ti|Se films as determined from full pattern XRD Le Bail fits.

AD (Ti:Se)	Total Film Thickness	*c*-lattice parameter (Å)	*a*-lattice parameter (Å)	Annealed Expt. Ti Atoms/Å^2 (±0.08)	Annealed Expt. Se Atoms/Å^2 (±0.02)	Annealed (Ti:Se)
1:2.01	479	6.053(1)	3.551(1)	7.54	15.05	1:2.00
1:2.05	479	6.051(1)	3.558(1)	7.57	15.21	1:2.01
1:2.11	503	6.050(1)	3.559(1)	7.86	15.46	1:1.97
1:2.14	483	6.034(1)	3.558(1)	7.70	14.41	1:1.87
1:2.16	501	6.037(1)	3.560(1)	7.70	15.49	1:2.01
1:2.22	503	6.043(1)	3.553(1)	7.70	15.35	1:1.99
1:2.24	450	6.066(1)	3.549(1)	6.86	12.85	1:1.87
1:2.26	496	6.058(1)	3.554(1)	7.50	15.10	1:2.01
1:2.57	505	6.096(1)	--	6.80	13.80	1:2.03

The change in the crystallinity of the $TiSe_2$ films as a function of precursor composition was estimated by using the line widths of the specular and in-plane reflections in the diffraction patterns of the annealed precursors. In-plane and *c*-axis crystallite size were determined from the line widths via Scherrer analysis and are plotted in Figure 5.6 as a function of as-deposited Se:Ti ratio. In the as deposited films, the crystallite size along the *c*-axis has a maxima at a Se:Ti ratio of ~ 2.15-2.2 while the all the films have a very similar in-plane crystallite sizes.

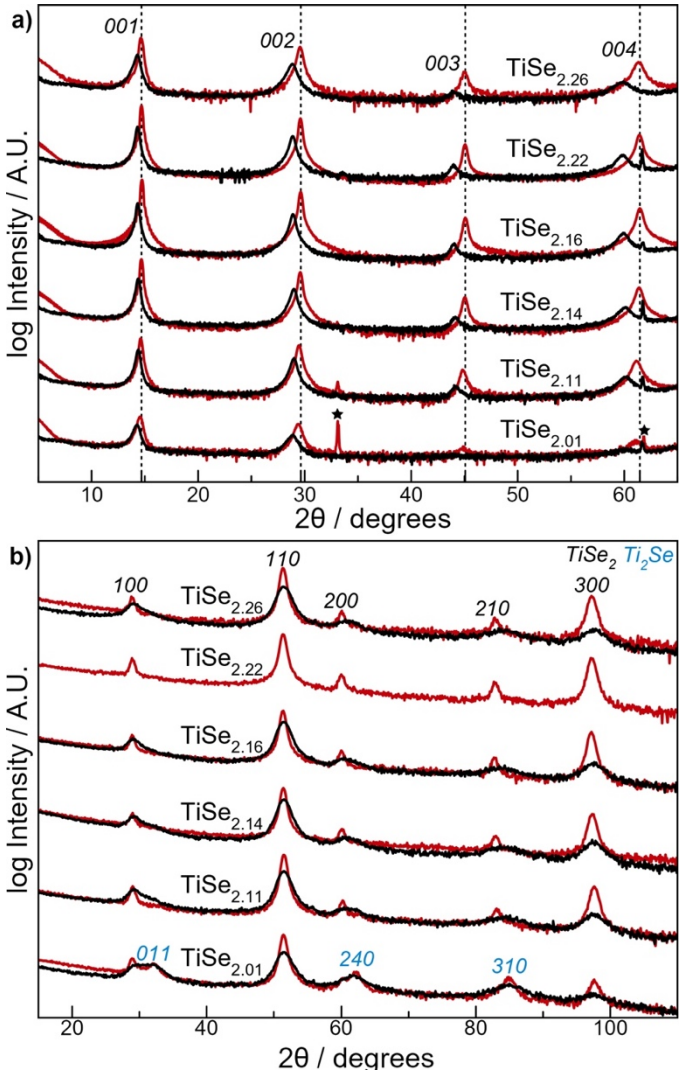

Figure 5.5. Representative specular (a.) and in-plane (b.) x-ray diffraction patterns of Ti|Se thin films with various compositions. All observed reflections that correspond to the $TiSe_2$ crystal structure are indexed in black. Reflections marked with an asterisk observed in the specular pattern are attributed to the Si substrate. Reflections for the observed Ti_2Se impurity phase are indexed in blue. Black curves show the diffraction pattern of the precursor, while red curves show the pattern for the films annealed at 350 °C. Additional diffraction patterns can be found in SI Figure C.2., more closely matching the expected positions for $TiSe_2$ shown as vertical lines.

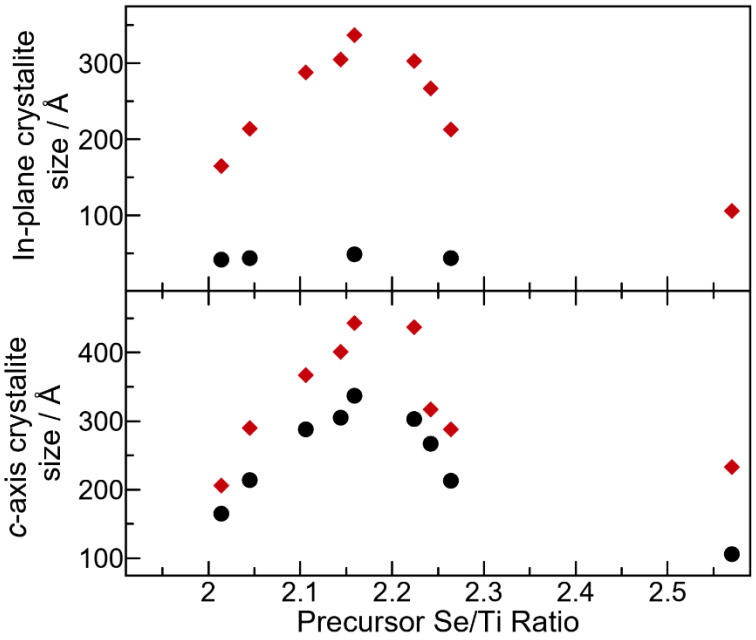

Figure 5.6. In-plane and *c*-axis crystallite size determined from the x-ray diffraction patterns as a function of Ti|Se composition. As-deposited parameters are shown in black and annealed parameters are shown in red. The diffraction patterns used to determine these parameters are found in Figure 5.5 and Figure C.2.

After annealing, both the in-plane and specular have the smallest linewidths (and largest crystallite sizes) at a Se:Ti ratio of ~ 2.15-2.2. The slight excess of Se may act as a flux to assist the transport of Ti atoms to the growth fronts, very similar to what was observed in the Mo-Se system.

For the three $TiSe_2$ samples with the optimal amount of excess Se, Laue oscillations are visible surrounding the first Bragg reflection. Laue oscillations occur due to the incomplete destructive interference of a finite number of unit cells in a crystal. For a small number of unit cells, N, the Laue function, sin(Nx)/sin(x), results in a principle intensity maximum whose position is determined by the lattice parameters of the diffracting crystal and a series of evenly spaced maxima on either side whose spacing is determined by the number of unit cells in the crystal.

To observe Laue oscillations, the majority of a film must consist of crystallites that have exactly the same number of unit cells, because crystallites with different numbers of unit cells would contribute Laue intensities at different angles, destroying the expected interference pattern. Figure 5.7 shows the measured diffraction pattern of the annealed sample with the as-deposited composition of $TiSe_{2.16}$. The position of the highest intensity maxima is consistent with a c-axis lattice parameter of 6.037(1) Å. The spacing of the Laue oscillations is consistent with the diffracting crystallites having 81-unit cells, as shown by the simulated pattern in Figure 5.7. The total film thickness of this sample is larger than 81 times the *c*-axis lattice parameter. Since 83 Ti|Se bilayers were deposited in this precursor and the amount of Ti in each bilayer equaled the amount required for a single $TiSe_2$ trilayer, this suggests that two Ti|Se bilayers were either oxidized, formed Ti_2Se, and/or reacted with the substrate. The precursors for the other two samples whose annealed diffraction patterns contained Laue oscillations, samples with the as-deposited composition of $TiSe_{2.14}$ and $TiSe_{2.22}$, had 84 Ti|Se bilayers deposited, but each bilayer was ~ 4 +/- 2 percent Ti deficient. Consequently, the $TiSe_{2.14}$ sample had Laue oscillations consistent with only 73 layers in the diffracting crystal and the $TiSe_{2.22}$ sample had 77 layers. In both of these samples, two or more of the initial bilayers did not contribute to the coherent crystal causing the Laue oscillations.

The combination of XRF, XRR, and XRD data enable us to speculate on an atomic level picture of the structure of the as deposited Mo|Se and Ti|Se precursors and how they evolve during annealing. Analysis of the diffraction data clearly indicates that the structure of the as-deposited Mo and Ti precursors are very different, and we illustrate these differences schematically in Figure 5.8. The Mo|Se precursor, Figure 5.8a, has a composition modulation from the sequence of as-

deposited layers with small crystallites of $MoSe_2$ several layers thick distributed throughout the film. Figure 5.8b demonstrates that the Ti|Se precursor has reacted much more during the deposition than the Mo|Se precursor. In the Ti|Se precursors, there is no evidence of compositional modulation, Ti_2Se forms during the deposition of Se on the first layer of Ti deposited, and thick domains of poorly stacked $TiSe_2$ layers grow during the deposition. In both the Mo|Se and Ti|Se precursors, there is a gradient in metal concentration as it is depleted at the growth front of the crystallites. For the Mo|Se precursor, the concentration gradient is not enough to induce diffusion during the deposition. However, in Ti|Se precursors, Ti must diffuse significantly during the deposition to form the thick $TiSe_2$ domains. In both systems, annealing at elevated

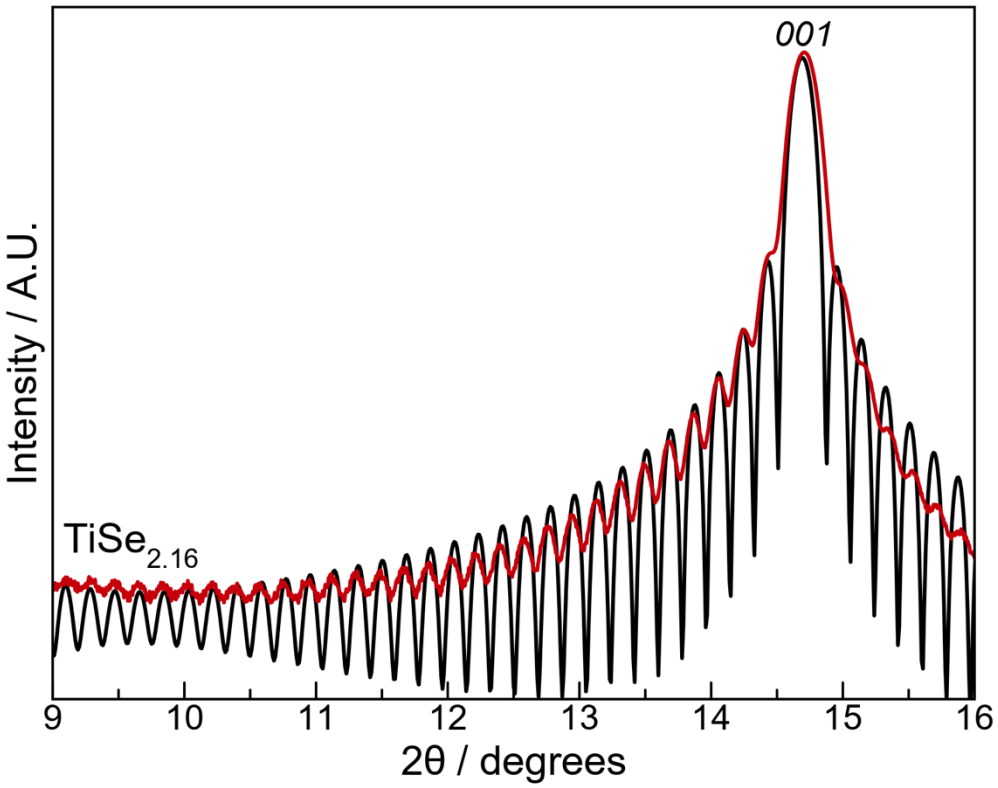

Figure 5.7. Experimental specular XRD pattern (red) and the theoretical Laue oscillations expected for 81-unit cells of $TiSe_2$ (black).

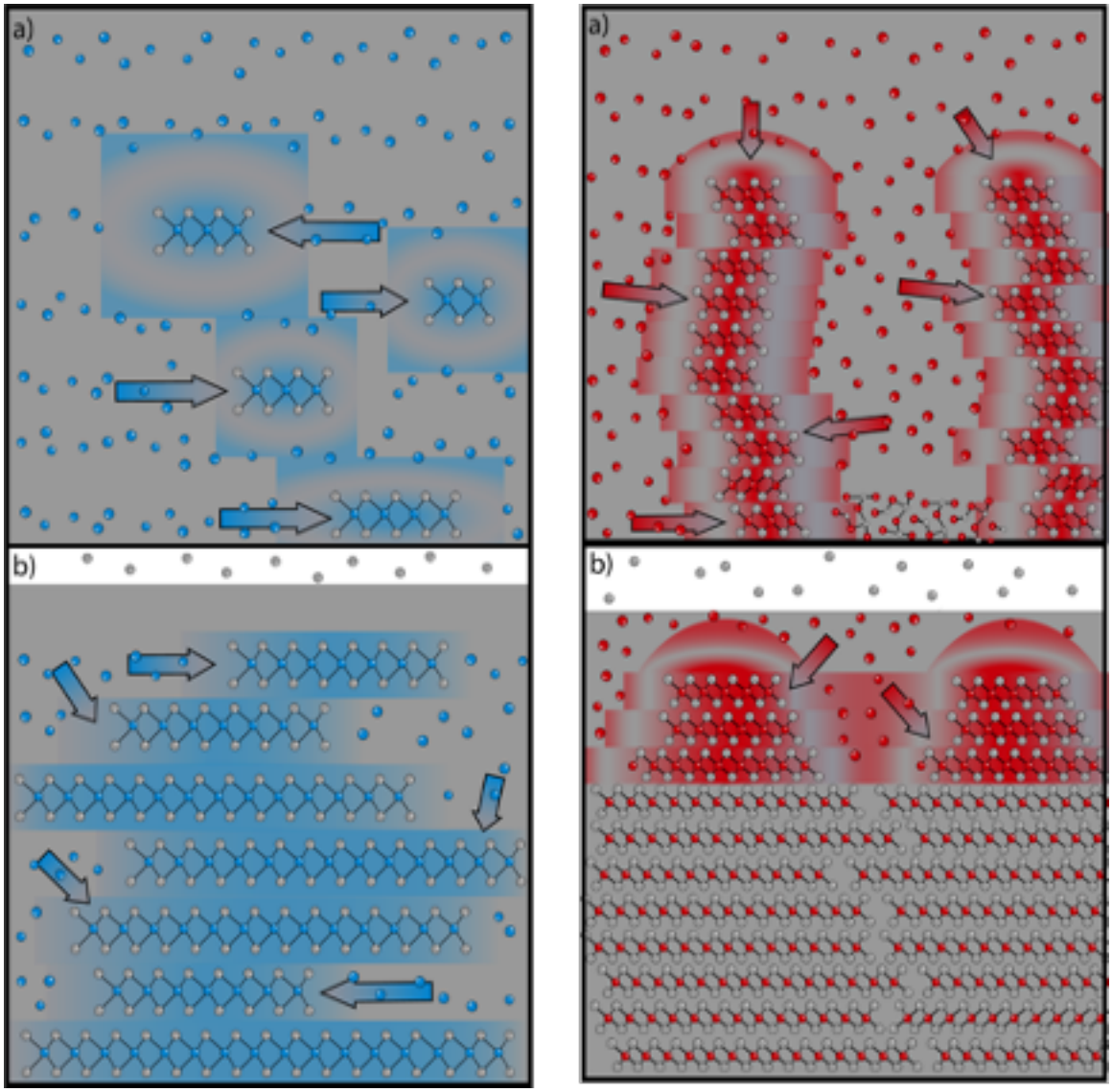

Figure 5.8. Proposed atomic level pictures for the evolution of Mo|Se (a) and Ti|Se (b) precursors as they are annealed to form crystalline $MoSe_2$ and $TiSe_2$. There is much more interdiffusion during deposition of the lighter Ti atoms, resulting in larger crystalline domains in the as-deposited $TiSe_2$ precursor relative to the Mo|Se precursor.

temperatures causes more diffusion to occur, leading to the growth of well-organized crystallites. A small amount of excess Se (10%) results in the formation of larger coherent domains of dichalcogenide in both systems, presumably acting as a flux to increase the rate of diffusion of the metal cations. Too much excess Se results in less crystallographically

aligned layers and smaller grain sizes. In both systems, optimized precursor structure and annealing temperatures resulted in the formation of films that contained the same thickness dichalcogenide layers with a precise number of dichalcogenide planes. For Mo|Se films with the correct amount of Mo per Mo|Se bilayer in the precursor, each Mo|Se layer evolved into a single $MoSe_2$ trilayer plane in the coherent domain. In analogous Ti|Se films, all of the Ti|Se layers evolved into $TiSe_2$ except for a couple of layers at the surface of the film that oxidized, forming a TiO_2 surface layer.

5.4. Conclusions

Highly crystalline diselenide films can be prepared by depositing alternating layers of the metal and selenium. With the correct amount of metal and a slight excess of Se deposited per M|Se bilayer, each M|Se layer deposited will evolve into a dichalcogenide plane. This enables the thickness of the dichalcogenide film to be controlled to a specified number of unit cells over large areas. While a precise number of dichalcogenide planes was obtained in both the Ti-Se and Mo-Se systems, the reaction pathways were very different. $TiSe_2$ mostly self-assembles during the deposition process while $MoSe_2$ mostly self assembles during annealing. In both systems, concentration gradients drive the diffusion of metals to the growth front, and process is aided by the short diffusion distances in the precursor or during the deposition. The diffraction data gathered on the as-deposited films and during annealing enabled us to create and compare atomistic pictures for the self-assembly of $MoSe_2$ and $TiSe_2$ from their respective precursors. By understanding the formation of these films and developing control over the composition and morphology of the precursors, we show that we can control growth of dichalcogenides to achieve uniform thicknesses over large areas.

5.5. BRIDGE

This chapter provided an in-depth investigation on the role that the amount of material within a layered precursor will have on the quality of the layers that form. Specifically, $TiSe_2$ will form over a large composition range, but there is a narrow window of excess Se that provides the highest quality samples. This not only informs on the formation of $TiSe_2$ but also provides information about way in which precursors prepared by the Modulated Elemental Reactants method transform into crystalized products. The next chapter will combine SnSe and $TiSe_2$ layers into a heterostructure material prepared via the Modulated Elemental Reactants method and investigate the resulting structure that forms.

CHAPTER VI

LONG RANGE ORDER IN $[(SNSE)_{1.2}]_1[TISE_2]_1$ PREPARED FROM DESIGNED PRECURSORS

6.0. AUTHORSHIP STATEMENT

The work in this chapter was published March 9, 2017 in Inorganic Chemistry (DOI: 10.1021/acs.inorgchem.6b03063). I am the primary author on this work. Devin R. Merrill, Sage R. Bauers, Gavin Mitchson, Jeffrey Ditto, Sven P Rudin, and David C. Johnson were co-authors on this work. Devin R. Merill contributed to the preparation and characterization of the samples. Sage R. Bauers assisted in with data analysis and writing of this manuscript. Gavin Mitchson analyzed the HAADF STEM data as well as aided in the writing of this manuscript. Jeffrey Ditto collected HAADF STEM data. David C. Johnson is my advisor.

6.1. INTRODUCTION

The development of epitaxial deposition techniques in the late 1960's ignited significant interest in materials containing two or more interleaved compounds as crystalline superlattices. The ability to synthesize high quality superlattices resulted in new discoveries in condensed matter physics and new technologies including light emitting diodes and quantum cascade lasers.[1–5] Recent work demonstrates that materials prepared with incommensurate interfaces result in unique and altered properties relative to superlattices. This has created new excitement, in part because potential structures can be imagined and properties predicted.[6–12] Synthesizing repeat structures containing non-epitaxial intergrowths of two or more constituents results in emergent properties, i.e. properties not found in the bulk constituents, including ultra-low thermal conductivity, charge density waves in intergrowths containing single layers of VSe_2, direct band gaps and long lived excited states due to charge separation between constituents.[13–16]

Intergrowths without epitaxial relationships between constituents are usually metastable relative to a mixture of the bulk constituents and their preparation requires a kinetically controlled growth technique. The four most common techniques are: the "Scotch^{tm} Tape" approach, mostly used for a small number of constituents;[17] chemical vapor deposition, limited to materials with similar in-plane lattice parameters;[18] van der Waals epitaxy useful for constituents with 2D structures and monolayers;[19] and the modulated elemental reactant (MER) approach,[20] which uses designed, layered amorphous precursors to kinetically trap designed sequences of constituents.[7] MER has enabled preparation of a wide variety of compounds consisting of interleaved layers of rock-salt chalcogenides, MX, and transition metal dichalcogenides, TX_2, which form a nanolaminate $([MX]_{1+\delta})_m(TX_2)_n$.[20, 21] The *a-b* planes of the MX and TX_2 structures are square or rectangular and hexagonal, respectively, making epitaxial relationships in multiple directions at the interfaces geometrically challenging. The 1+δ term in the chemical formula accommodates the mismatch in formula units per area.

Structures prepared using the MER synthesis route have specific crystallographic surfaces of each constituent adjacent to one another, but the layers are rotationally disordered with respect to one another.[22,23] This disorder presumably arises from the 2-D constrained nucleation kinetics.[24] Crystalline layers' form from multiple nucleation points as the precursors self-assemble balancing various volume, surface, and diffusive energetic terms within a complex multidimensional energy landscape. The system lowers its free energy as quickly as possible within this landscape, which contains multiple phases. This approach kinetically traps products with architectures close to that of the precursor due to the use of low temperatures, which limit diffusion rates and prevent the system from exploring more of the energy landscape.

We have been able to prepare SnSe rock salt-like layers paired with various transition metal dichalcogenide layers. The SnSe layers undergo structural distortions, varying between the high-temperature β-SnSe and low-temperature α-SnSe phases. As the size of the SnSe layers is increased, surface and volume free energy terms are minimized.[25–27] The trade-off between volume and surface energies results in distortions driven more by size than by the interfacial interactions with the dichalcogenide layers.[25] During the self-assembly, the already crystalline layers provide nucleation sites for adjacent amorphous layers, further complicating the crystallization process.[23,28] The extent of this interfacial nucleation likely depends on the specific constituents and their sequence in the repeating superstructure. High temperature solid state synthesis techniques yield analogous compounds containing a single bilayer of SnSe combined with a range of different dichalcogenides, but these compounds form crystals in which the structures of both constituents distort to typically become commensurate along one in- plane direction requiring higher dimensional crystallography to solve the structures. [29]

Recently it was noted that $([SnSe]_{1.2})_1(TiSe_2)_1$, referred to as $(SnSe)_{1.2}TiSe_2$ in the remainder of this manuscript, contained regions ordered over several periods of the heterostructure.[30,31] This behavior has not been observed in other heterostructures prepared using the MER approach. Here, we investigate this phenomenon in greater detail, as this exception provides insight to the growth process in this approach. In-plane X-ray diffraction (XRD) patterns indicate a √3 ratio in *a*-axis lattice parameters between the two constituents, suggesting a potential commensurate interface along the <100> (SnSe) and <110> ($TiSe_2$) directions. High angle annular dark field scanning transmission electron microscopy (HAADF STEM) data confirms the formation of an ordered structure with this commensurate interface. X-ray reciprocal space maps collected at the European Synchrotron Radiation Facility indicate that

significant regions of long-range 3-D order exist within these samples. Calculations show that different orientations of SnSe relative to the $TiSe_2$ layer have different energies, with the lowest energy consistent with the formation of a commensurate interface along the <100> (SnSe) and <110> ($TiSe_2$) directions. The longer-range order results from the near lattice match of the constituents. While regions of order exist, rotational disorder is still present. This suggests long-range order is not normally seen in materials prepared by MER because the energy penalty for distortion of the rock salt constituent is not offset by a higher bonding energy between the constituents. The extent of rotational disorder at the interfaces between constituents and structural distortion of the constituents both affect transport properties. Rotational disorder has been shown to result in extraordinarily small thermal conductivity. The accidental lattice match between SnSe and $TiSe_2$ provides potential opportunities to examine the interplay between rotational disorder and both thermal and electrical transport properties in other members of the $[(SnSe)_{1.2}]_m[TiSe_2]_n$ family of compounds.

6.2. Materials and Methods

Merrill et al.[32] previously described in detail the synthesis procedure for $(SnSe)_{1.2}TiSe_2$. We briefly review the procedure here. Precursor films were deposited from elemental sources by electron beam guns (Sn and Ti) or a Knudson effusion cell (Se) in a high vacuum (10^{-7} Torr) chamber. Single element layers were deposited one after another in a pattern mimicking the nanoarchitecture of the targeted compound, with the thickness of each layer chosen to yield the stoichiometry of the target compound. The thickness of each elemental layer was monitored in real-time by quartz crystal microbalances. Pneumatic shutters controlled the amount of each element that was deposited onto SiO_2 native oxide/silicon substrates. The pattern of elemental layers was repeated until a desired total film thickness was reached, typically 50

nm. The layered amorphous precursors were gently heated on a hotplate (350 °C) in an N_2 atmosphere ([O_2] < 1 ppm) to induce layer crystallization.

After annealing the precursors, specular locked-coupled θ-2θ X-ray diffraction (XRD) patterns were acquired using a Bruker D8 Discover diffractometer (Cu Kα radiation). In-plane XRD patterns and reciprocal space maps were collected at the European Synchrotron Radiation Facility (ESRF).

Focused Ga+ ion beam (FIB) milling, lift out, and thinning were used to prepare electron-transparent cross-sectional specimens of the annealed compounds. A procedure similar to the Wedge Pre-milling method described by Schaffer *et al.* was employed,[33] with the final polishing step using 2 keV FIB acceleration voltage to minimize residual amorphous surface layers on the thinned lamellae. Immediately prior to insertion into the transmission electron microscope, the samples were cleaned for 20 seconds in an argon/oxygen gas plasma.

High angle annular dark field scanning transmission electron microscopy (HAADF STEM) images were collected using a Cs-corrected FEI Titan 80-300 S/TEM, operating at 300 keV, at the Environmental Molecular Science Facility (EMSL) at Pacific Northwest National Laboratory (PNNL).

The density functional theory (DFT) calculations employ the PAW method in the generalized gradient approximation (GGA) of Perdew, Burke, and Ernzerhof (PBE) implemented in the electronic structure code VASP.[34–37] Evaluation of the electronic structure involves first-order Methfessel-Paxton smearing with σ = 27 meV and a convergence criteria of 10^{-5} eV; optimization of the structures uses a convergence criteria of 10^{-4} eV.[38] The calculations rely on periodic boundary conditions and hence deal with the incommensurate nature of $(SnSe)_{1.2}TiSe_2$ by

employing the island approximation, wherein the periodically repeated $TiSe_2$ layers are interleaved with finite SnSe islands surrounded by vacuum.[8] Energy differences between different orientations of the SnSe structure relative to the $TiSe_2$ layers are converged to less than 1 meV with a 1•1•8 k-point mesh. Total energies are also well converged with the 1•1•8 k-point mesh, differing from those with a 1•1•4 k-point mesh by less than 1 meV. The in-plane coordinates of the k-points are zero (i.e., a 1•1 mesh) because we approximate each SnSe layer as decoupled, finite island structures. The van der Waals interactions are treated using the method of Tkatchenko-Scheffler.[39]

6.3. Results and Discussion

In-plane (*hk*0) diffraction patterns for two different $(SnSe)_{1.2}TiSe_2$ samples (Figure 6.1) provide insight into the in-plane structures of the two constituents. The in-plane lattice parameter of the $TiSe_2$ layers, 0.354(3) nm, and symmetry is consistent with all previous reports for $TiSe_2$-containing misfit compounds and with bulk CdI_2-type $TiSe_2$.[31,40–42] Previous work on other compounds containing SnSe prepared using modulated elemental reactants have displayed either a square basal plane for a single bilayer or a rectangular basal plane that approaches the orthorhombic bulk structure α-SnSe when the layer thickness is increased.[30] In $(SnSe)_{1.2}TiSe_2$, the SnSe reflections cannot be indexed using either of these space groups. Splitting of distinct SnSe reflections with $h \neq k$ are observed (inset of Figure 6.1), ruling out the square basal plane structure, while the splitting of reflections does not match the reduced symmetry of α-SnSe. The reflections can be fit using the 2-D space group p2gg, which yields *a*- and *b*-axis lattice parameters of 0.6094(3) and 0.5974(4) nm, respectively.[31]

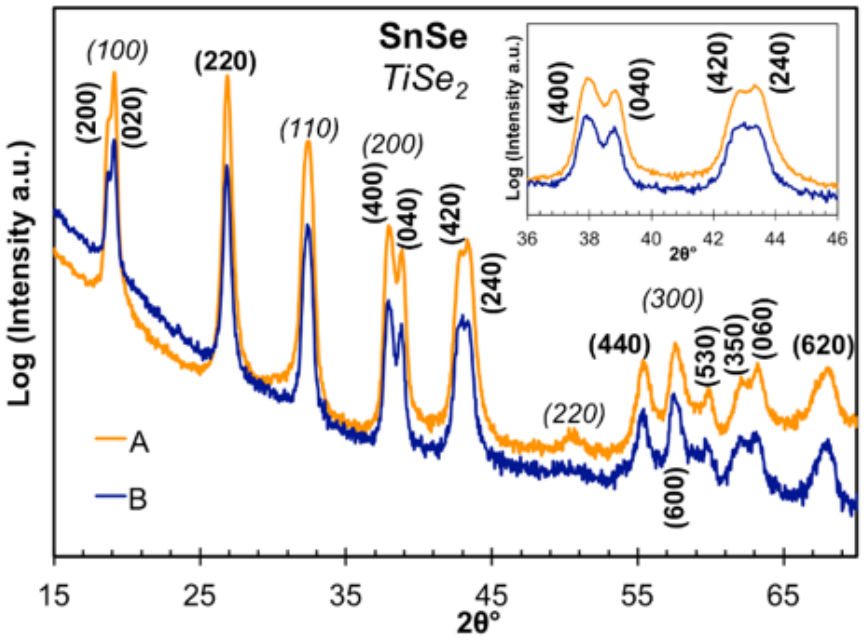

Figure 6.1. In-plane diffraction data for two $(SnSe)_{1.2}TiSe_2$ samples. The reflections originating from SnSe are marked in bold, and those from $TiSe_2$ in italics. The inset in the top right corner of the figure emphasizes the splitting of the SnSe reflections, indicating the existence of a rectangular basal plane.

HAADF-STEM images were collected from several $(SnSe)_{1.2}TiSe_2$ samples to determine the orientation between the constituent layers and a representative image is shown in Figure 6.2. Since the contrast mechanism in HAADF STEM imaging is the atomic number,[43] SnSe layers are bright and $TiSe_2$ are dark, confirming that the basic structural motif of $(SnSe)_{1.2}TiSe_2$ contains alternating layers of each structure crystallographically aligned with the substrate. Immediately apparent in Figure 6.2 is a large region in the bottom half of the image where both constituents have resolved atomic columns. In the SnSe layers, this orientation corresponds to (100) SnSe planes. The $TiSe_2$ layers are oriented with either $(\bar{1}\bar{1}0)$, $(\bar{1}20)$, or $(2\bar{1}0)$ (right-leaning) or (110), $(1\bar{2}0)$, or $(\bar{2}10)$ (left-leaning) planes normal to the microscope optical axis. The statistical improbability of seeing repetitious adjacent layers oriented in a

consistent manner across several samples suggests that these regions are not the result of random chance.

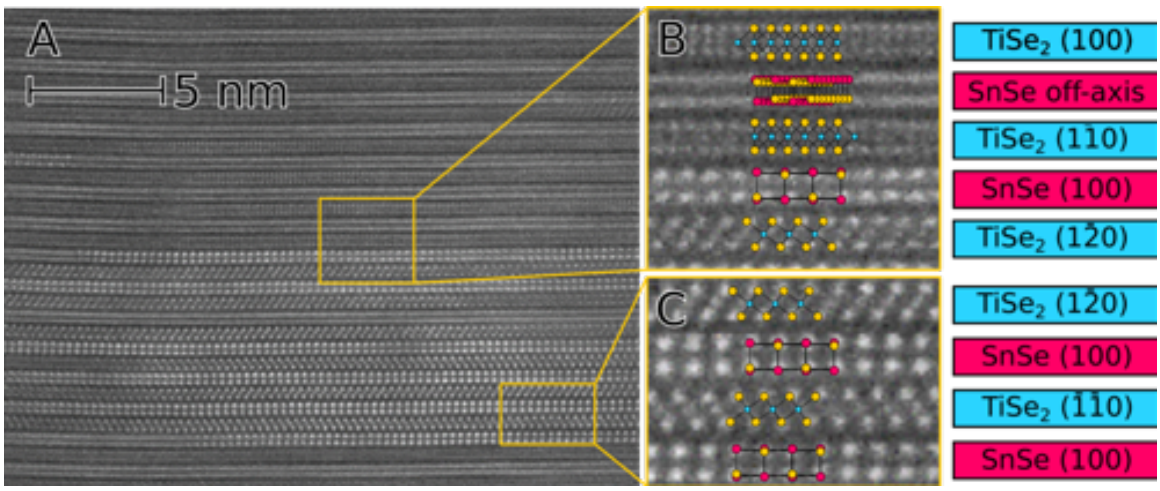

Figure 6.2. Representative HAADF-STEM image of a $(SnSe)_{1.2}TiSe_2$ heterostructure. The layers of SnSe are marked with pink boxes and layers of $TiSe_2$ are marked with blue boxes. The labels on the right side of the image reflect the primary plane-normal orientation, if resolved, of that layer.

The observed alignment suggests formation of a commensurate interface along the <100> direction of SnSe and <110> direction of $TiSe_2$. Rotation from the alignment in this region results in distinct differences in visible atomic columns in the various layers. For example, assuming a preferred orientation exists between the two constituents, a 30° rotation from SnSe (100) would result in no observable atomic columns for the SnSe layer, but atomic columns corresponding to the (100), (010), or $(\bar{1}10)$ planes for the $TiSe_2$ layer would be observed. This is consistent with the region in the upper half of Figure 6.2, where atomic columns in the $TiSe_2$ layers corresponding to the (100), (010), or $(\bar{1}10)$ planes are visible, but no atomic columns are visible in the adjacent SnSe layers. Furthermore, if there is a preferred orientation along the <100> direction of SnSe and <110> direction of $TiSe_2$, regions with (110) planes of SnSe visible should not be observed in regions where atomic columns are present in the $TiSe_2$ layers. This is consistent with the image in Figure

6.2 and all but one of the HAADF STEM images collected from many areas of several different samples. Globally, different zone axes present throughout the cross-sectional images still exhibit turbostratic disorder, commonly found in similar intergrowth materials, but with a finite number of registrations between constituents. We infer that interface interactions between the SnSe and $TiSe_2$ are likely the cause of the regions with long-range order.

The presence of long-range order in the sample is confirmed by FFT analysis (Figure 6.3) of the HAADF STEM image shown in Figure 6.2. Compounds prepared from modulated elemental reactants exhibit sharp 00*l* diffraction peaks due to precise layering and crystallographic alignment to the substrate. However, they typically display streaking along the *l* direction for each family of *hkl* ($h,k \neq 0$) reflections due to the incoherence in the structure from the layer-to-layer rotational disorder.[20] For $(SnSe)_{1.2}TiSe_2$, the 00*l* family of reflections have sharp intensity maxima, consistent with the superlattice structure and the specular XRD pattern previously reported.[32] In contrast to other compounds prepared from modulated elemental reactants there is a considerable degree of order present in the *hkl* families with $h, k \neq 0$. The (20*l*) SnSe and (10*l*) $TiSe_2$ reflections overlap, but clear intensity maxima are present along *l* for the (11*l*) family of $TiSe_2$ reflections. The correlation of the (11*l*) $TiSe_2$ reflections with the (00*l*) superlattice reflections is highlighted in the inset of Figure 6.3, which shows that the intensity maxima occur with a regular periodicity on the same order as the superlattice periodicity. The HAADF STEM images show ordering over longer distances than have been observed previously for other compounds prepared using this synthesis method, but only gives insight into the compound's structure at a local level due to the small volume of sample observed.

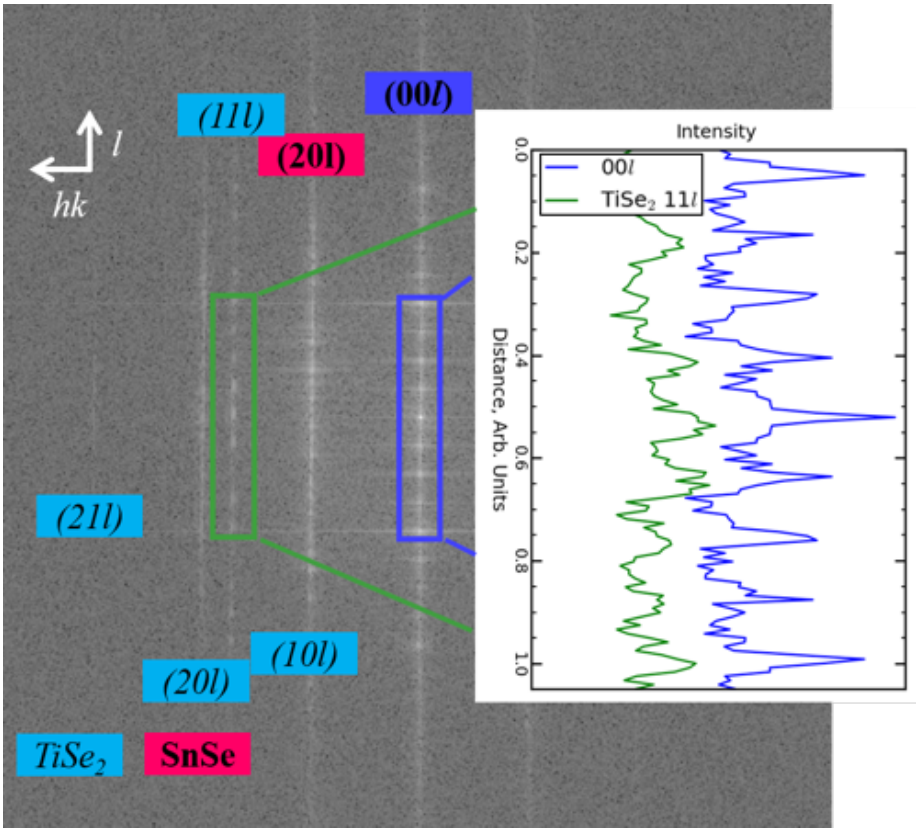

Figure 6.3. FFT of HAADF STEM image shown in Figure 6.1. The (00*l*) and $TiSe_2$ (11*l*) intensity profiles are plotted in the inset with the y-axis corresponding to the location in the FTT of HAADF STEM image.

A reciprocal space map was collected at the ESRF to determine if long-range order exists over a significant percentage of the sample area. Figure 6.4 contains the reciprocal space map along with the expected positions of the l = 1,4 peaks based on the known *c*-axis lattice parameter given for reference. The reciprocal space map displays broad maxima in the l direction in both the (22*l*) SnSe and (11*l*) $TiSe_2$ families of reflections. The positions of the maxima correlate with the *c*-axis lattice parameter determined from the (00*l*) reflections, which is highlighted in the lower panel of Figure 6.4 containing integrated intensities along the (00*l*) and SnSe (22*l*) families of reflections. The presence of discreet maxima that correspond to the *c*-axis lattice parameter suggests that a significant volume of the film consists of regions that show greater

coherence than observed for other compounds prepared using this growth technique. The X-ray data is consistent with the preferred orientation observed in the HAADF STEM data; both indicate increased coherence across multiple adjacent unit cells.

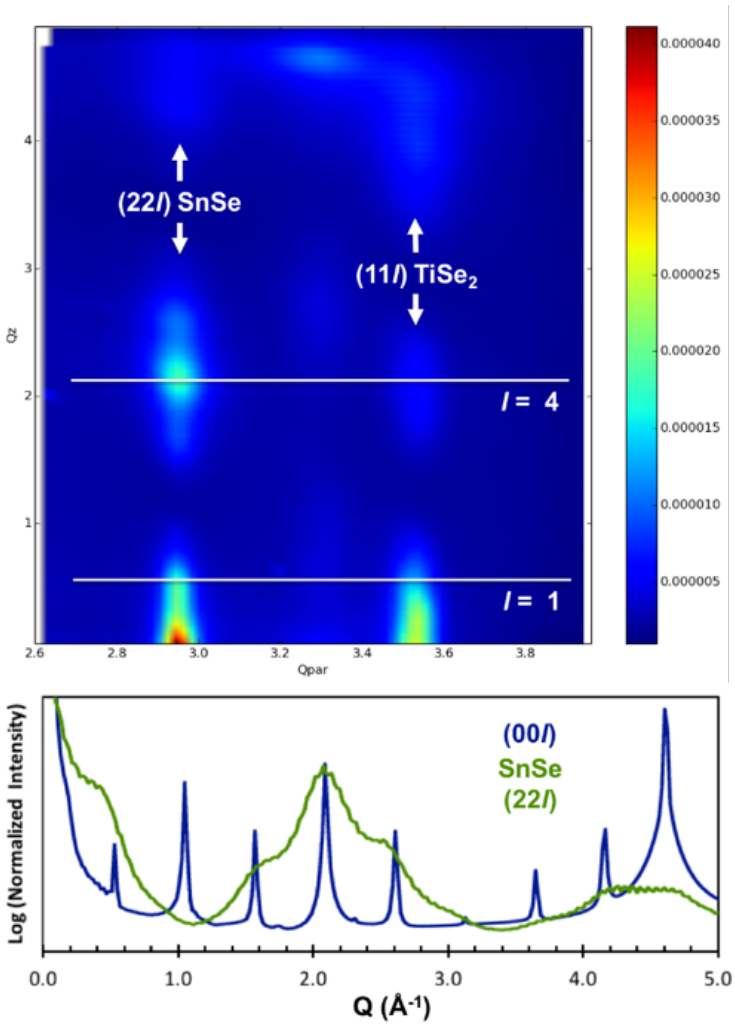

Figure 6.4. Top) Reciprocal space map from a $(SnSe)_{1.2}TiSe_2$ compound at two different constant *hk* postions with a varying *l* position. The bright regions indicate coherence between layers. (Bottom) A line profile extracted from the reciprocal space map along the (22*l*) SnSe direction is overlaid onto the (00*l*) diffraction pattern. The presence of coincident maxima in the overlaid scans suggests long range ordering within the sample.

HAADF STEM and reciprocal space map diffraction both support the formation of long range coherence across layers of $(SnSe)_{1.2}TiSe_2$.

However, a commensurate interface can only form along one direction when stacking a cubic structure with a hexagonal structure. This suggests that any distortion in the basal plane that might be made to accommodate the regular interface would likely be anisotropic. The establishment of long-range order and any distortions necessary to accommodate it are likely due to minimizing the energy by varying parameters in this complex energy landscape. Because the film consists of purely interfacial layers, increasing the thickness of either constituent will introduce interior atoms into the unit cell and add an internal volume term to the stabilization. This perhaps explains why an ordered structure has only been observed for $(SnSe)_{1.2}TiSe_2$, with thicker SnSe layers having structures in between the bulk polymorphs α-SnSe and β-SnSe.

HAADF STEM and XRD data both indicate that $(SnSe)_{1.2}TiSe_2$ consists of interleaved layers of SnSe bilayers and $TiSe_2$ monolayers, with each constituent oriented with the (00*l*) planes parallel to the substrate. Figure 6.5 shows the constituent SnSe and $TiSe_2$ structures. The larger structures on the left of Figure 6.5 show a plan-view representation of the two constituents with Se in gold, Sn in pink, and Ti in blue. One unit cell of SnSe is shown and the dashed diamond illustrates one unit cell of $TiSe_2$. The basal plane of the SnSe constituent has a much larger tetragonal lattice relative to the bulk SnSe phases, whereas the $TiSe_2$ basal plane is similar to bulk values.[32] The right shows different plane-normal orientations of the structure as they would appear in cross-sectional STEM images. We illustrate two orientations of SnSe that might be observed: (1) One corresponding to (100) or (010), where every atomic column appears identical due to atomic columns containing overlapping Sn and Se atoms; or (2) One corresponding to the (110) planes, where the individual Sn and Se columns can be resolved by Z contrast as they do not overlap. The puckering previously quantified by Rietveld analysis of

(00*l*) diffraction data can be observed in this orientation.[32] For $TiSe_2$, there are three possible sets of planes that might be observed: (1) Closely-spaced, vertically stacked Se – Ti – Se atomic columns, corresponding to the (100), (010), or $(\bar{1}10)$ planes; (2) Diagonally stacked Se – Ti – Se atomic columns that lean right, corresponding to the (110), $(1\bar{2}0)$, or $(\bar{2}10)$ planes; or finally (3) Diagonally stacked Se – Ti – Se atomic columns that lean left, corresponding to the $(\bar{1}\bar{1}0)$, $(\bar{1}20)$, or $(2\bar{1}0)$ planes.

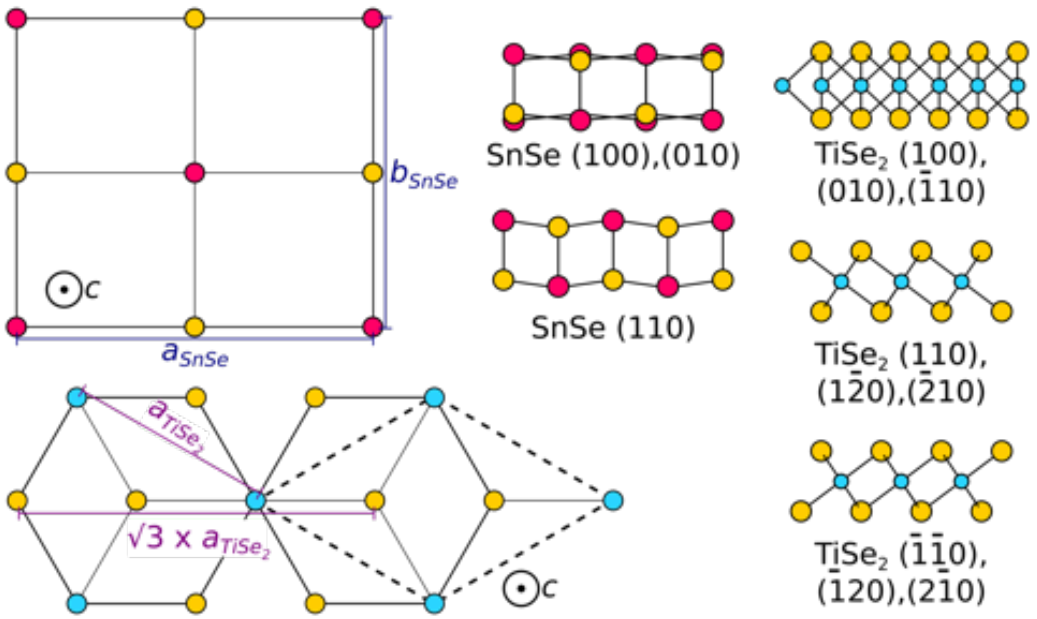

Figure 6.5. The top and bottom left schematics depict a top down view of the SnSe and $TiSe_2$ basal plane. The schematics on the right show SnSe and $TiSe_2$ layer structures when looking down different zone axes. Gold markers indicate Se, pink represent Sn, and blue represents Ti.

As suggested in Figure 6.5, $\sqrt{3} \times a_{TiSe2}$ = 0.613(5) nm is within error equal to a_{SnSe}, 0.6094(3) nm, suggesting that lattice matching of the two constituents may occur along the <100> SnSe and the <110> $TiSe_2$ directions. This alignment of axes of SnSe and $TiSe_2$ is consistent with the HAADF-STEM observations of alignment. Further evidence for lattice

matching comes from measuring interplanar distances in the HAADF STEM images. In (110)-oriented $TiSe_2$ layers, the horizontal Se-Se spacing is 0.310(4) nm. The adjacent (100)-oriented SnSe layers have average horizontal Sn/Se-Sn/Se column spacing that are the same within error, 0.3087(7) nm. These experimental observations of lattice-matching behavior provide further support that there is a preferred alignment between the SnSe and $TiSe_2$ layers. The quality of the diffraction data, however, is insufficient to refine the three dimensional structure as was done by Ren et al. for $(SbS)_{1.15}TiS_2$ using a superspace approach.[44] The observation of a common in- plane axis between SnSe and $TiSe_2$ indicates that a (3 + 1) dimensional superspace would be required, rather than the (3+2) superspace used for $(SbS)_{1.15}TiS_2$. In this regard, the structure of $(SnSe)_{1.2}TiSe_2$ is more similar to that of $(SnSe)_{1.18}(TiSe_2)_2$, for which the unit cell parameters but not the refined structure was reported.[45] The observed crystallographic alignment between layers and the extended order implies that the structures template off of one another during the crystallization. It is apparently lower energy for the chemically softer SnSe to distort than $TiSe_2$.

DFT calculations were performed to determine the energies of forming various interfaces between the two structures as well as the establishment of interlayer registration. Figure 6.6 shows the basic approach for the calculations, with two islands of bilayer SnSe in the rock salt crystal structure surrounded by dichalcogenide layers that are octahedrally coordinated to the center atom and stacked in a 1T-polytype. The islands were placed in two combinations of locations between the dichalcogenide layers, which were arranged either leaning in the same direction or opposite. Table 6.1 shows the results of the calculations, with the most stable configuration occurring for both SnSe islands at a $\delta=15^{\circ}$ rotation and with one $TiSe_2$ layer leaning left while the other $TiSe_2$ layer leans right. Within the limitations of the observable

plane-normals, these orientations match those observed in STEM. From these calculations, the energy is clearly lowered by establishing a repeating structure with the SnSe rotated at a 15° angle with respect to the $TiSe_2$. Furthermore, they predict that in the most stable configuration $TiSe_2$ surrounds islands of SnSe where both $TiSe_2$ layers lean in alternating directions, while in the STEM, observed regions typically contained alternating layers of left- and right-leaning $TiSe_2$ between SnSe layers. In contrast, calculations layering SnSe with VSe_2 show only a slight preference for VSe_2 leaning in the same direction, in agreement with no experimental observation of alternating layers of left- and right-leaning VSe_2 between SnSe layers. Calculations to establish a commensurate lattice failed to energetically describe the basal plane distortion that occurs in the SnSe layer – possibly because the SnSe island used in the calculation was too small to capture the penalties in energy that occur for slightly mismatched lattices. Based on the relative orientations surmised by both STEM observations and DFT calculations, it is somewhat surprising that no instances are observed in STEM with (100) SnSe layered upon (100) $TiSe_2$, which would be expected in 1/3 of the regions exhibiting long range order.

Both the theoretical and experimental data support a heterostructure of SnSe and $TiSe_2$ that has some form of long-range coherence as depicted in figure 6.7. The rectangular basal plane in the SnSe structure is supported by the in-plane diffraction data. The HAADF-STEM images, FFT plot, reciprocal space map, and DFT calculations support an alignment of the crystal structure in one direction. With respect to figure 6.7, the alignment in the horizontal direction is known, but in the vertical direction information about the crystal structure alignment is absent. The alignment that is observed is likely due to interfacial interactions and lattice matching between the two constituents resulting in a lowering of the overall energy. This

understanding of the distortion in $(SnSe)_{1.2}TiSe_2$ provides insight into the rotational disorder that is normally seen in heterostructures prepared by MER.

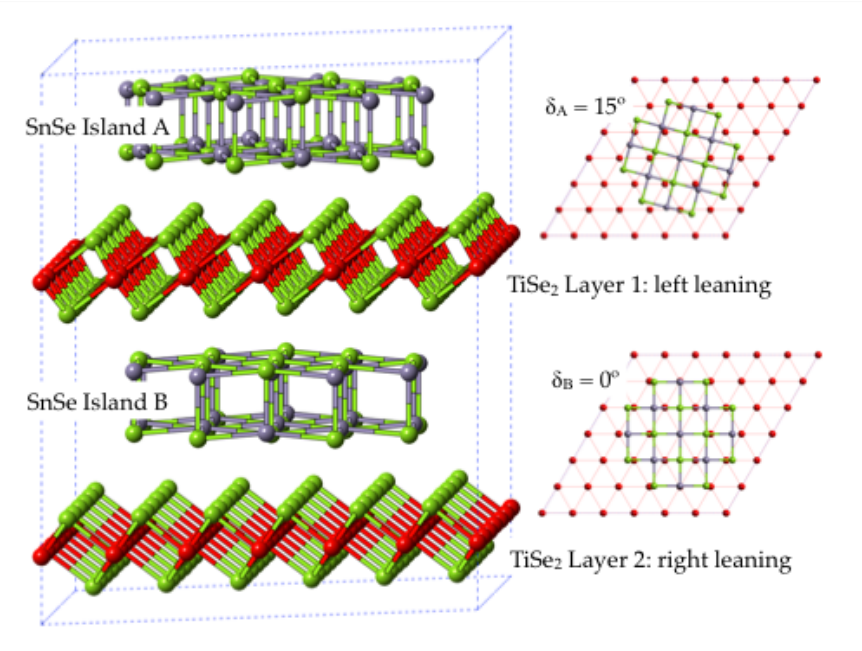

Figure 6.6. (left) Schematic showing a DFT unit cell with islands of SnSe in two different orientations between layers of $TiSe_2$ with two different "leanings." The red balls represent Ti, the gray represent tin and selenium is represented by the green balls. (right) Plan view of the $(SnSe)_{1.2}TiSe_2$ layered compound with a rotational angle of 0° between layers (bottom) and a 15° rotation between layers (top).

Table 6.1. DFT calculated energy differences between four configurations with differing relative orientations of SnSe layers and leanings of $TiSe_2$ layers.

δ_A	δ_B	$TiSe_2$ layer 1	$TiSe_2$ layer 2	ΔE (meV)
0°	15°	Right	Right	60
0°	15°	Right	Left	39
15°	15°	Right	Right	16
15°	15°	Right	Left	0

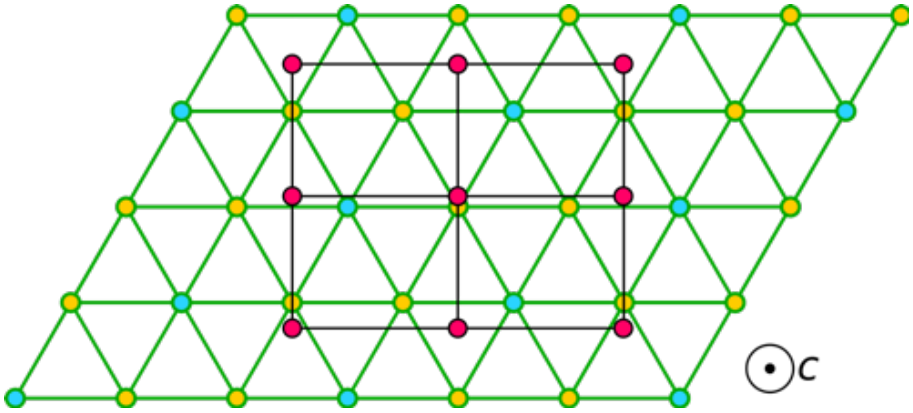

Figure 6.7. Schematic showing the top down view of the stacking between the SnSe rock rocksalt (represented by pink atoms connected by black bonds) and the $TiSe_2$ dichalcogenide (structure with green bonds connecting the yellow Se atoms and blue Ti atoms) layers which is consistent with the theoretical and experimental data collected.

6.4. Conclusion

The coincidental similarities in in-plane lattice parameters of SnSe and $TiSe_2$ results in a quasi-epitaxial relationship between the constituents in $(SnSe)_{1.2}TiSe_2$. Long-range order across several unit cells is observed and results in distortions previously unseen in other SnSe-containing intergrowths prepared using the MER technique. In light of the present study, preparing SnSe-$TiSe_2$ intergrowth compounds with thicker SnSe and/or $TiSe_2$ layers may provide opportunities to unravel the interplay between transport properties (thermal and electrical) and rotational disorder. One might expect intergrowths with thicker $TiSe_2$ layers to maintain the crystallographically aligned interfaces. The lack of long-range order in compounds with larger thicknesses of SnSe and $TiSe_2$ highlight the interplay between the volume free energy of each constituent and the interface energy between them. $(SnSe)_{1.2}TiSe_2$ is the first compound prepared using modulated elemental reactants that exhibits long range order, which suggests that this kinetically controlled

synthesis approach is dominated by maximizing the rate of reduction in the free energy during self-assembly. The accidental coincidence of the in-plane lattice parameters along the *a*-axis of SnSe and the <110> direction in $TiSe_2$ leads to preferential nucleation and layer alignment during growth of adjacent layers.

6.5. BRIDGE

Chapter 6 combined the two binary constituents discussed in Chapters 4 and 5 into a heterostructure material to investigate structural information. While most heterostructures prepared via the Modulated Elemental Reactants method result in materials displaying complete rotational disorder, the $(SnSe)_{1.2}TiSe_2$ heterostructure is better described as a misfit layer compound with regions of rotational disorder. This is the result of an in-plane distortion occurring in SnSe that results in an accidental lattice match between the two constituents. The next chapter will investigate the occurrence of this distortion and accidental lattice match in $[(SnSe)_{1+\delta}]_m[TiSe_2]$ heterostructures with increasing number of SnSe layers in the repeating unit structure, as well as the influence it has on transport properties.

CHAPTER VII

STRUCTURAL CHANGES AS A FUNCTION OF THICKNESS IN $[(SNSE)_{1+\delta}]_M TISE_2$ HETEROSTRUCTURES.

7.0. AUTHORSHIP STATEMENT

The work in this chapter was published February 9, 2018 in ACS Nano (DOI: 10.1021/acsnano.7b07506). I am the primary author on this work. Alexander C. Lygo, Marco Esters, Devin R. Merrill, Jeffrey Ditto, Duncan R. Sutherland, Sage R. Bauers, and David C. Johnson were co-authors on this work. Alexander C. Lygo assisted with the data fitting of the diffraction and writing of the manuscript. Marco Esters completed the computation analysis. Devin R. Merrill and Duncan R. Sutherland contributed to the preparation and characterization of the samples. Sage R. Bauers assisted in with data analysis and writing of this manuscript. Jeffrey Ditto collected HAADF STEM data. Sage R. Bauers assisted in with data analysis and writing of this manuscript. David C. Johnson is my advisor.

7.1. INTRODUCTION

Two-dimensional (2D) materials continue to attract increasing attention as researchers discover emergent electronic properties in monolayers and heterostructures.[1–5] For example, transitions from an indirect to a direct band gap have been discovered in semiconducting TX_2 (T = Mo, W; X = S, Se) compounds in going from a bilayer to a monolayer as interactions with the neighboring TX_2 layer are eliminated.[6–8] The properties of single layers are impacted by interactions with the substrate and/or adjacent layers, with the overlap of states and the band offsets suggested as being important factors.[9–12] This has led to the concept of 2D layers acting as building blocks that can be stacked in specific sequences, yielding heterostructures with desired properties.[13] Understanding how layers interact with one another to yield emergent

properties is critical to enable materials design for specific applications and is a current focus of the materials community.

Less well investigated are structural modifications associated with changes in electronic structure as these heterostructures are created. There are several reasons for this, including challenges in obtaining direct structural information on ultrathin layers, lack of structural information from common analytical techniques used to confirm layering, and the initial systems investigated being rigid layers with van der Waals gaps on both sides in the bulk (graphene, HBN, transition metal dichalcogenides, etc.) where only small distortions might be expected. Since there are a limited number of rigid structures with a narrow subset of properties, researchers have begun to explore 2D layers of compounds with 3D structures. Structural changes are more pronounced in 2D layers of materials with bulk 3D structures as the layers distort to stabilize dangling bonds at the interfaces. For example, bilayers of bulk rock salt structured constituents between dichalcogenide layers distort significantly, with the cations moving as much as 0.2 Å towards the anion layers in the dichalcogenide.[14,15] As the thickness of rock salt structured layers is increased, the distortions evolve towards a bulk structure with a surface distortion at the interface.[14,16] These structural distortions reflect changes in the free energy landscape as the ratio of atoms at the interface relative to those interior decreases. The properties of these heterostructures have been observed to systematically change as layer thicknesses are varied, reflecting the interactions between the layers.[17–19] Understanding how structural distortions in 3D materials change as their thickness approaches the 2D limit and how these distortions impact their properties is necessary to design heterostructures with specific properties.

This paper investigates structural transitions in SnSe as a function of layer thickness in heterostructures also containing a $TiSe_2$ monolayer.

The naming convention for these structures is $[(SnSe)_{1+\delta}]_m[TiSe_2]_1$ where m is the number of SnSe bilayers between the single layers of $TiSe_2$ and the $1+\delta$ term accounts for the difference in basal plane area between the two constituents. SnSe was chosen because bulk SnSe undergoes a structural transition from the room temperature phase, α-SnSe (GeS structure, *Pcmn*), to the high temperature β-SnSe (TlI structure, *Cmcm*) structure.[20] Von Schnering and coworkers investigated this phase transition in detail as a model system to test Landau theory predictions about symmetry-breaking changes in solids.[21–23] They found that the distortion is second order, with the Sn and Se *x*-coordinates changing continuously between the distorted α-SnSe structure and the undistorted β-SnSe structure. This investigation probes how the SnSe structure is impacted by layer thickness when stacked in a heterostructure. SnSe has been incorporated into heterostructures with several TX_2 layers, where T = V, Nb, Mo, and Ta.[19,24–27] In this work $TiSe_2$ was chosen as a second constituent because $(SnSe)_{1.21}(TiSe_2)$ prepared from modulated reactants is unique in having long range order, where the SnSe structure distorts to obtain an epitaxial relationship with $TiSe_2$.[28] Increasing the thickness of the SnSe constituent will create a competition between the surface free energy, which favors the formation of an epitaxial relationship, and the bulk free energy, which would be expected to result in a bulk structure for a sufficiently thick SnSe layer. In-plane X-ray diffraction (XRD) revealed that as the thickness of the SnSe layer is increased, the structure distorts significantly from a rectangular in-plane unit cell when $m = 1$ to a different rectangular unit cell that is related to the bulk α-SnSe orthorhombic structure for $m = 4$. High angle annular dark field scanning transmission electron microscopy (HAADF-STEM) images reveal a variety of stacking sequences of the SnSe bilayers as the SnSe thickness increases. Density functional theory (DFT) calculations suggest that the structural changes cannot be explained by

isolated SnSe layers but are impacted by interactions between the constituent layers. Electrical transport measurements reveal independent changes in the signs of the Hall coefficient and Seebeck coefficient with increasing *m* and changes in temperature, reflecting the complex interactions between the layers. This is the first time p-type behavior has been observed in $(MSe)_m(TiSe_2)_n$ compounds. The interplay between constituent layers provides an opportunity to customize desired properties by adjusting the identity, thickness and/or stacking sequence of 2D layers.

7.2. Results and Discussion

7.2.1. Synthesis

The modulated elemental reactants (MER) approach was used to prepare the targeted $[(SnSe)_{1+\delta}]_mTiSe_2$ ferecrystaline compounds (turbostratically disordered polymorphs of misfit layer compounds).[29,30] The deposition parameters required to prepare layered amorphous precursors that closely resemble the targeted structure in both local composition and layer thickness were determined using an iterative approach. This involved preparing a series of precursors of the sequence {1 × [Ti|Se] + *m* × [Sn|Se]} with varying *m* and *n* values, measuring their compositions *via* electron probe microanalysis (EPMA), measuring the thickness of the repeating amorphous sequence *via* X-ray reflectivity (XRR), and interpolating to obtain desired compositions and thicknesses as described previously.[24] Once the deposition was calibrated, precursors for each of the targeted $[(SnSe)_{1+\delta}]_mTiSe_2$ compounds were prepared by depositing the {[Ti|Se] + *m* × [Sn|Se]} sequence the required number of times to obtain the desired total thickness. An annealing study was conducted to determine optimum annealing temperatures and times to transform the designed precursors into the targeted compounds. The line widths and intensities of the reflections in specular XRD were used to assess the quality of the samples. A temperature of 350 °C for 30

minutes was selected as the optimum annealing conditions to crystallize the desired products. These conditions were the same as those used previously to prepare $(SnSe)_{1.2}TiSe_2$.[31]

7.2.2. Structure

The specular XRD patterns of the annealed precursors are shown in Figure 7.1. Only (00*l*) reflections are observed in the patterns, indicating that the *c*-axis of the targeted compounds is perpendicular to the Si substrate. All reflections are narrow, sharp, and can be indexed to a single family of planes suggesting that a single repeating structure is formed. The calculated *c*-axis lattice parameters for the products are summarized in Table 7.1. As the number of SnSe bilayers deposited in the precursor increases, there is a systematic increase in the *c*-axis lattice parameter of 5.79(1) Å per bilayer of SnSe in $[(SnSe)_{1+\delta}]_mTiSe_2$. This result is consistent with the 5.77(5) Å and 5.806(2) Å increase in the *c*-axis lattice parameter per SnSe bilayer reported for $[(SnSe)_{1+\delta}]_m[NbSe_2]_n$ and $[(SnSe)_{1+\delta}]_m[MoSe_2]_n$ based compounds, respectively.[17,32] Extrapolating this relationship to $m = 0$, the thickness of the single $TiSe_2$ layer is 6.25(3) Å in each compound, which is thicker than the *c*-axis lattice parameter of bulk $TiSe_2$ (6.008 Å)[33] and the thickness per $TiSe_2$ layer in $(PbSe)_{1+\delta}[TiSe_2]_n$ (6.03 – 6.04 Å) obtained from the change in *c*-axis lattice parameter as *n* is varied.[18,34,35] The larger value reflects the different species interacting across the van der Waals interface. A single $TiSe_2$ layer has two $TiSe_2$-SnSe interfaces that are mismatched and hence cannot nest together. The extrapolated $TiSe_2$ thickness in the $[(SnSe)_{1+\delta}]_mTiSe_2$ compounds also reflects other interactions between the constituents, such as charge transfer.

In-plane diffraction patterns were collected to characterize the basal plane structures of the constituent layers and are shown in Figure 7.2a. All observed reflections can be indexed to either a hexagonal unit cell for $TiSe_2$ or a rectangular unit cell for SnSe, except for reflections

marked with a cross. The extra reflections at 48° in the m = 2-4 patterns and at 90° for m = 2, 4 patterns are consistent with (110) and (300) $SnSe_2$ reflections and are likely the result of a slight excess of Sn and Se in the precursor. The in-plane lattice parameters for each constituent were refined using a full pattern Le Bail[36] fit and are summarized in Table 7.1. The results of the fits can be found in Figures D.1-D.4 in the Supporting Information. The larger errors in the $TiSe_2$ lattice parameters relative to the SnSe lattice parameters result from overlapping reflections, with only the (110) reflection of $TiSe_2$ being distinct from reflections of SnSe. The hexagonal $TiSe_2$ reflections yield a-axis lattice parameters of 3.56(1) Å, except for the m = 2 compound which has an a-axis lattice parameter of 3.60(5) Å. The larger error for the m = 2 compound is a consequence of the overlap of the $TiSe_2$ (110) reflection with the (110) $SnSe_2$ reflection (Figure 7.2a). These a-axis lattice parameters are within error of each other and are consistent with those previously reported for other ferecrystals containing $TiSe_2$ layers and the binary $TiSe_2$ compound.[18,34,35,37–39] This suggests, the in-plane structure of $TiSe_2$ is independent of the SnSe layer thickness.

Surprisingly, the in-plane diffraction patterns for SnSe change considerably as m increases. Splitting, merging, and shifting of reflections indicate that the symmetry and lattice parameters change substantially as m is varied. Figure 7.2b contains an expanded view of a high angle region containing several reflections to highlight the changes in the in-plane unit cell of SnSe as m is increased. The m = 1 compound has two reflections occurring at 60.6° and 62.2° that can be indexed as the (400) and (040) reflections in a distorted rock salt structure. In contrast, the m = 4 compound has a single reflection at 61.3° that can be indexed as a (220) reflection of a rectangular basal plane unit cell, which is consistent with either a distorted α-SnSe or β-SnSe structure. The shifts in reflection positions for the m = 1 and m = 4 patterns require

different unit cells and indexing. This is most visible at higher angles (Figure 7.2c). At higher angles between 85° and 110°, the patterns for the m = 2 and m = 3 compounds have reflections at the same angles as for m = 4. Because of the similarity in the diffraction patterns, the m = 2 and 3 compounds can be indexed in the same manner as the m = 4 compounds. When looking at the reflection around 69°, the m = 1 and 4 compounds are clearly rectangular as indicated by the splitting of the peak. Although no splitting is observed for the m = 2 and 3 compounds, a line width broadening of the $h \neq k$ reflections compared to the $h = k$ reflections is present suggesting the basal plane is rectangular for these compounds as well.

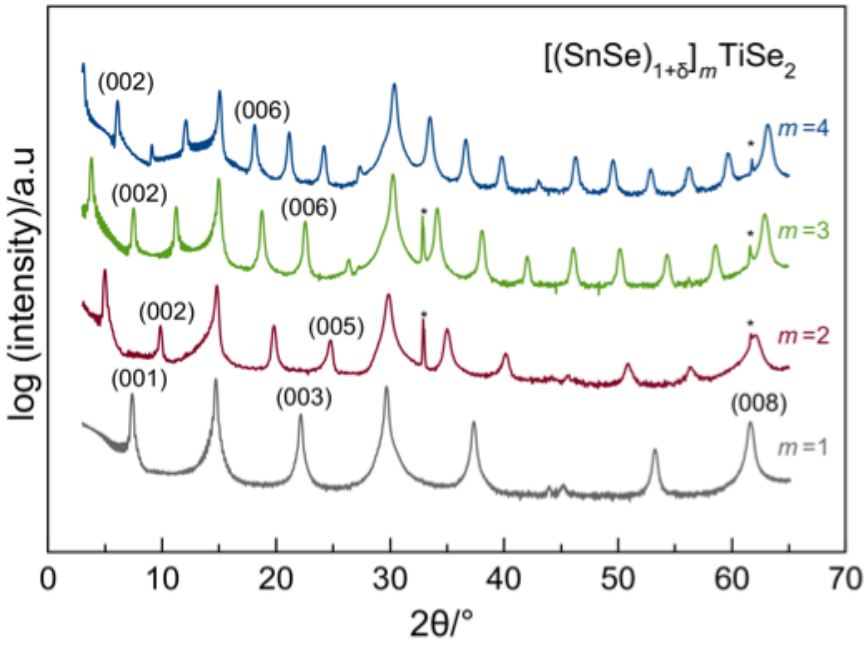

Figure 7.1. Specular X-ray diffraction scans of $[(SnSe)_{1+\delta}]_mTiSe_2$ compounds (m = 1-4). The intensity is plotted on a log scale to enhance weak reflections. Miller indices are provided for select reflections and asterisks indicate reflections from the Si substrate.

Table 7.1. Lattice parameters, and misfit parameters for $[(SnSe)_{1+\delta}]_mTiSe_2$ compounds.

	SnSe	SnSe	$TiSe_2$		$([SnSe]_{1+\delta})_m(TiSe_2)_n$
m	a (Å)	b (Å)	a (Å)	1 + δ	c (Å)
1	6.1036(6)	5.9787(4)	3.56(1)	1.203(9)	12.04(1)
2	4.2320(7)	4.2887(7)	3.60(5)	1.24(7)	17.84(1)
3	4.2487(4)	4.3126(4)	3.56(1)	1.198(7)	23.64(1)
4	4.2401(4)	4.3196(5)	3.56(1)	1.196(8)	29.42(2)

Changes in the structure of SnSe layers with thickness have previously been reported for both misfit layer compounds and ferecrystals. In misfit layer compounds, bilayers of SnSe adopt a distorted NaCl structure, where the Sn atoms move towards the dichalcogenide and the Se atoms are displaced away from it.[35] There are additional distortions due to the structures adopting a common in-plane lattice parameter in one direction. In ferecrystals, the Sn atoms also move towards the dichalcogenide and the Se atoms are displaced away from it. However, the in-plane structure of the SnSe layer changes with thickness while the dichalcogenide unit cell does not vary. In compounds with a single SnSe bilayer (m = 1), the basal plane unit cell of the SnSe is typically square or very close to square. Thicker SnSe layers have rectangular in-plane unit cells that approach the bulk low temperature structure (α -SnSe) as m increases. This trend is observed for the $m \geq 2$ compounds reported herein, with m = 1 deviating significantly. As reported previously, however, $(SnSe)_{1.21}TiSe_2$ is the only example of a compound that forms large domains with ordering between the constituent layers when prepared via the low temperature self-assembly of a layered precursor. It is thought that the epitaxial relationship results from a coincidental lattice match between SnSe and $TiSe_2$.[28] The m = n =

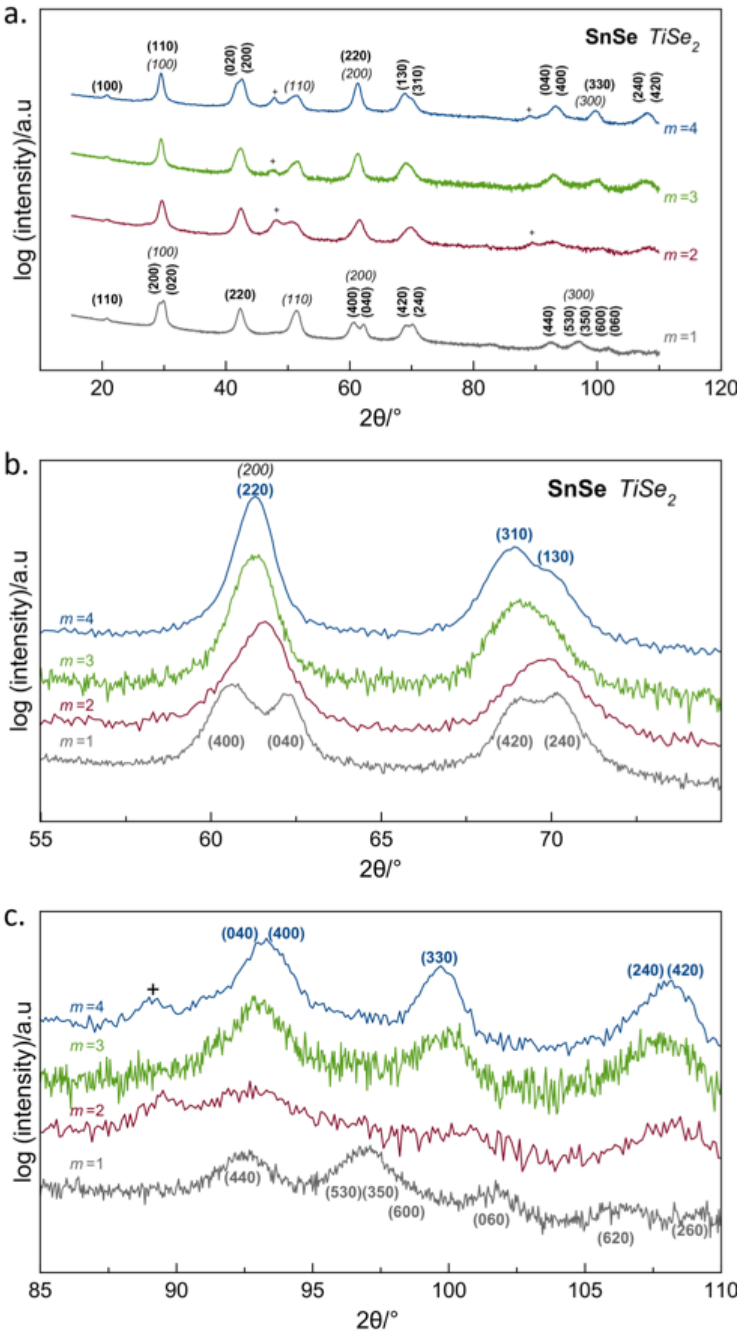

Figure 7.2. (a) In-plane diffraction pattern of the $[(SnSe)_{1+\delta}]_mTiSe_2$ compounds where $1 \leq m \leq 4$. The reflections are indexed to either SnSe or $TiSe_2$, with a single impurity peak being indexed to $SnSe_2$ (denoted with a + symbol). (b) Expansion of the high-angle region emphasizing the change in the SnSe reflections at approximately 61° and 69° that occurs as m is increased from 1 to 4. (c) Expansion of a higher angle region that highlights the reflection differences between the $m = 1$ and $m \geq 2$ in-plane diffraction patterns.

1 compound is best described as a misfit layer compound with a large number of rotational defects present. The significant changes in structure as m is increased reflect the decreased importance of surface free energy as the thickness of the SnSe layer is increased.

In contrast to the m = 1 compound, the SnSe layer in the m = 4 compound has an in-plane structure that is closest to the bulk, reflecting a decrease in the surface to volume ratio of the SnSe layer. The structure is indexed to a rectangular in-plane unit cell and the a and b lattice parameters are similar to those measured for the bulk at a temperature of approximately 700 K as it transforms between the α-SnSe and β-SnSe structures. Similar changes in the basal plane structure as a function of m have been previously observed in the $[(SnSe)_{1+\delta}]_m[TaSe_2]_n$ and $[(SnSe)_{1+\delta}]_m[MoSe_2]_n$ systems[24,25] The lattice parameters for the compounds with m = 2 and 3 are similar to the in plane lattice parameters of either the α-SnSe structure at 800 K or the β-SnSe structure at 825 K. The lattice parameters, however, are smaller than those reported for β-SnSe. If the $m \geq 2$ compounds possessed either the GeS or TlI SnSe bulk structure, the (100) reflection would be extinct. Its presence indicates the existence of small distortions that change the atomic positions within the ab-plane. The large difference between the lattice parameters for m = 1 and $m \geq 2$ results from redefining the unit cell from a face centered unit cell to a primitive unit cell to be consistent with von Schnering and coworkers,[21–23] The relationship between the two different unit cells and the shift in atomic positions that require this re-indexing is shown in Figure 7.3. The redefinition of the unit cell results in a change in the formula units per cell from 4 to 2. Despite the change in lattice parameters, the misfit parameters 1+ δ (the ratio of the in-plane packing density between the two constituents) only range from 1.20 to 1.24, which are within error of one other. The change in SnSe structure with thickness suggests that the energetic cost of distorting the

interior of the SnSe layer to achieve a lattice match is higher than the energy gain resulting from a more coherent interface with $TiSe_2$. In the m = 1 case, however, there are no interior atoms to compete with the surface stabilization gained by the tetragonal distortion.

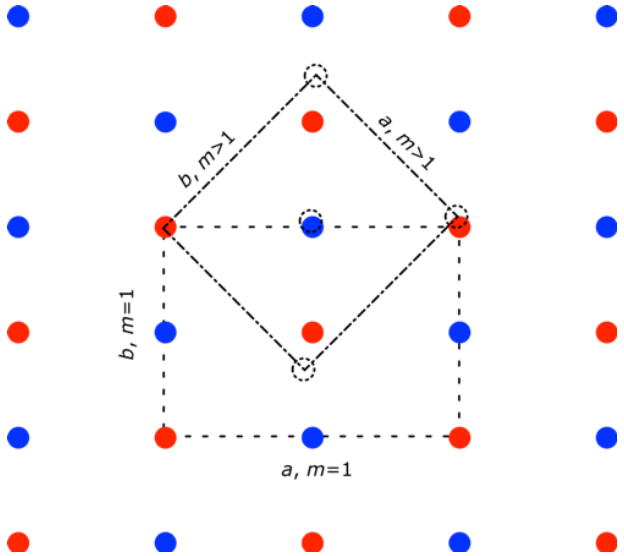

Figure 7.3. Schematic of shifting atomic positions of the SnSe constituent of $[(SnSe)_{1+\delta}]_mTiSe_2$ causing a redefinition of the in-plane unit cell from the m = 1 compound to the $m \geq 2$ compounds.

HAADF-STEM was collected to further probe the layering, in-plane structure, and connectivity between the layers of the compounds. Representative images are shown in Figure 7.4. The two constituents are distinguished by the different contrasts in the image, with the SnSe layers appearing brighter and the $TiSe_2$ appearing darker. The interfaces between the different constituents in all images are atomically abrupt and smooth, reflecting diffusion during the self-assembly process, which corrects for local variations in either thickness or composition. Where zone axes are observed for the darker $TiSe_2$ layers, they are those expected for a CdI_2-structured $TiSe_2$ with octahedrally coordinated Ti. The SnSe layers are consistent with the in-plane diffraction data. Figure 7.4a shows that the sequence of layers is consistently repeated throughout the entire film in agreement with the diffraction data.

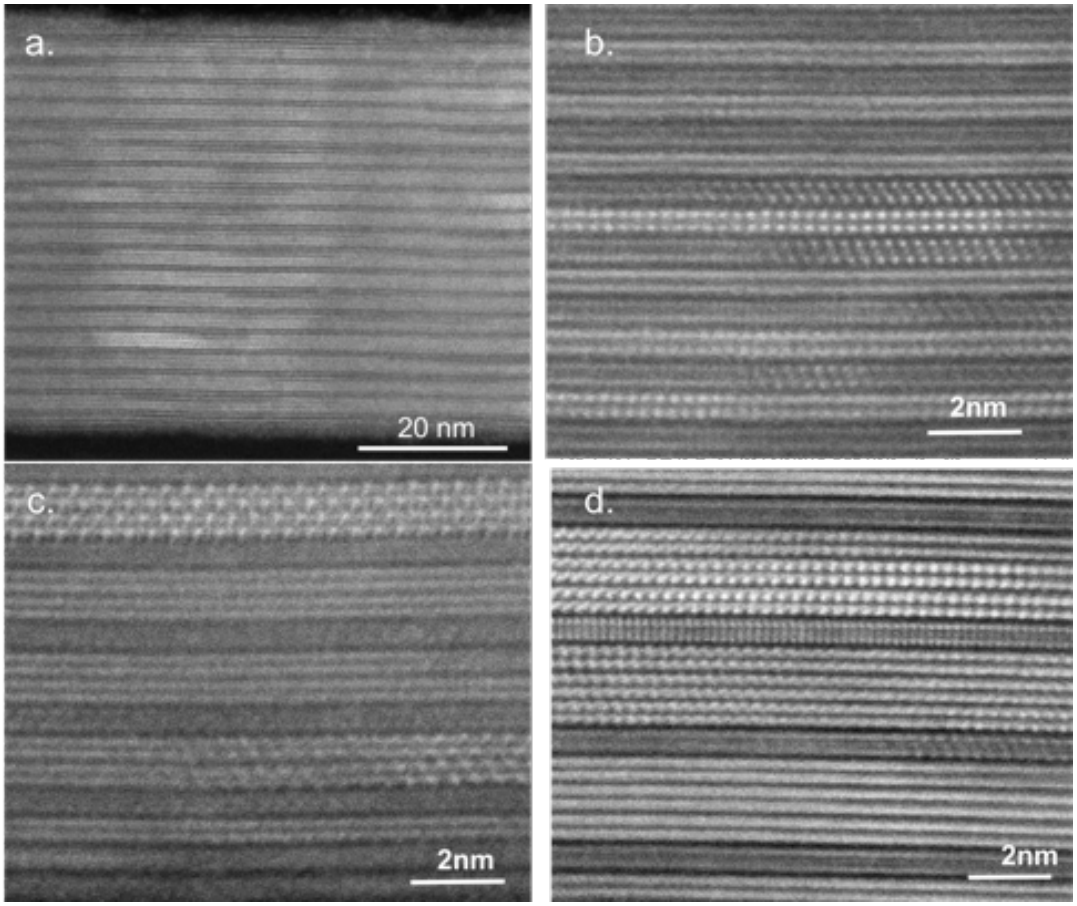

Figure 7.4. HAADF-STEM images of $[(SnSe)_{1+\delta}]_mTiSe_2$ compounds ($m \leq 3$). (a) An image of $(SnSe)_{1.20}TiSe_2$ showing the consistent alternation of the two constituent structures throughout the entire film. The bright layers correspond to SnSe while the darker layers correspond to $TiSe_2$. (b) Enlarged image of $[(SnSe)_{1.20}]_1TiSe_2$ showing the local atomic structure. Repeating orientations in some areas of the film support previous reports of regions of long range coherence. (c) A magnified image of $[(SnSe)_{1.24}]_2TiSe_2$ showing the pairing of the SnSe layers. Multiple orientations for the same constituent are observed throughout the film demonstrating the turbostratic disorder present in all compounds. (d) An expanded image of $[(SnSe)_{1.20}]_3TiSe_2$ showing the disorder between the different bilayers of SnSe.

The images of the $m = 1$, $m = 2$, and $m = 3$ compounds, Figures 7.4b, 7.4c, and 7.4d, respectively, show that the targeted structures were prepared. Small regions with substitutional defects, where $TiSe_2$ replaces

a portion of an SnSe bilayer, can occasionally be found when surveying all of the images.[40] These types of substitutional defects that have been observed previously in ferecrystalline compounds are an artifact of the self-assembly and correlated with small deviations in precursor composition from that of the targeted compound.[41,42] Small regions of $SnSe_2$ are also observed at the surface and the film/substrate interface in some films (Figure D.5 in the Supporting Information), explaining the low intensity $SnSe_2$ reflection observed in the in-plane diffraction. This surface $SnSe_2$ is postulated to form as excess Sn and Se migrate out of the sample as the superstructure self-assembles.

The HAADF-STEM images provide information about the alignment between constituent layers at the atomic level that is absent from the diffraction data due to the preferred alignment and turbostratic disorder. Regions with long range order and regions of rotational disorder are observed in the $m = 1$ compound (Figure 7.4b).[28] In the $m \geq 2$ images no long-range order between the constituent layers is observed. The extensive rotational disorder between SnSe and $TiSe_2$ layers is consistent with the independent in-plane lattice parameters determined from the X-ray diffraction patterns. The rotational disorder in the $m \geq 2$ compounds is consistent with previous reports of $[(SnSe)_{1+\delta}]_m[TSe_2]_n$ compounds synthesized using the modulated elemental reactants approach.[24,25]

The STEM images reveal several structural changes and stacking sequences in SnSe layers that are not expected from the bulk structure. The SnSe layers in compounds with $m \geq 2$ distort, forming pairs of atomic planes referred to in the following as bilayers. A similar distortion into pairs of layers was observed for thin PbSe layers and rationalized as an interplay between volume and surface free energy.[14] The spacing between bilayers is larger than the spacing within them, consistent with distorted α-SnSe (GeS structure) or β -SnSe (TlI structure) and in contrast to the equally spaced atomic planes in a rock salt structure

(Figures 7.4c and 7.4d). Where zone axes are observed for the SnSe layers, most of the layers stack on top of one another with the cations alternating with the anions in a face centered arrangement, which is consistent with a distorted rock salt structure, but also with the (100) zone axis of α -SnSe and β -SnSe. Occasionally, the bilayers stack with the cations aligned above each other as found along the (010) axis of the bulk α -SnSe structure and the (001) axis of the bulk β -SnSe structure, sometimes even within the same layer, as evident in areas highlighted in Figure 7.5. These unexpected stacking arrangements may reflect either the mechanism of formation,[43] or the competition between the different SnSe structures.

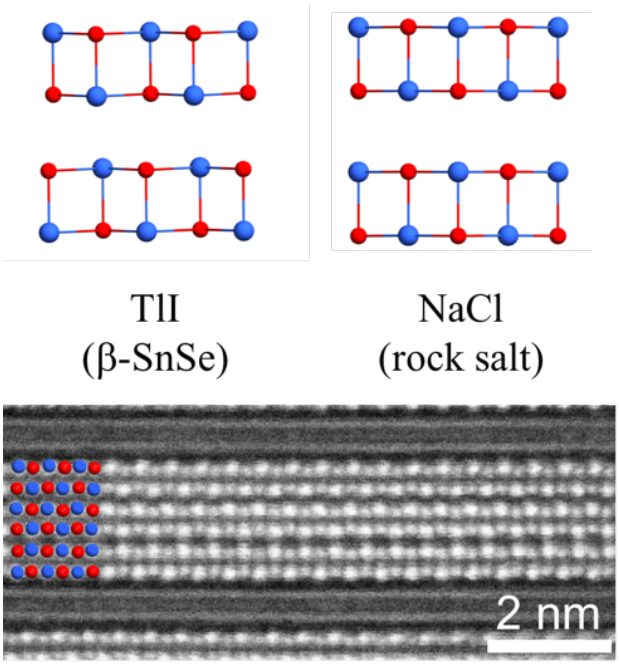

Figure 7.5. An expanded HAADF-STEM image showing two different SnSe orientations within the same layer of $[(SnSe)_{1+\delta}]_mTiSe_2$.

7.2.3. Calculations

Density functional theory (DFT) calculations were undertaken to understand the changes in structure of the SnSe layer with thickness and the shift in the location of different bilayers with respect to one another. In doing these calculations, there were two approximations to

choose between. One option would be to create a supercell and distort the structure of both constituents. Since the observed structures are not distorted and the layer orientation in the m = 2 - 4 compounds is random from layer to layer, this is a significant approximation. The other choice was to calculate the energy of isolated layers of each constituent, focusing on the energy differences between different constituents as a function of the thickness of the layer. Since creating a supercell would force a distortion in the structure of the layer whose structure we are trying to understand, we limited our calculations to vacuum isolated SnSe layers of different thickness.

DFT calculations were carried out on isolated multi-layers ($1 \leq m \leq 4$) using four different SnSe structures, as shown in Figure 7.6, to probe the observed structure changes as m is increased. Figure 7.7 shows the evolution of the lattice parameters as a function of the number of bilayers. The GeS structure is the only structure type where the lattice parameters change significantly with thickness. The lattice parameters trend towards the calculated lattice parameters of the bulk structure at room temperature (a = 4.56 Å, b = 4.21 Å) as thickness is increased. This is consistent with DFT calculations using the optB88 functional published elsewhere,[44] and with the experimental data for SnSe layers as a function of thickness in ferecrystals with a variety of dichalcogenide layers.[27] The lattice parameters for the GeS and NaCl-structured bulk structures are larger than the experimental bulk and thin film lattice parameters (GeS: a = 4.450 Å, b = 4.153 Å[21]; NaCl: a = 5.99 Å[45]) as expected from GGA. The calculated bulk TlI structure, on the other hand, has smaller lattice parameters (a = 4.301 Å, b = 11.808 Å, c = 4.293 Å) than experimentally determined in bulk β-SnSe at 825 K (a = 4.310 Å, b = 11.705 Å, c = 4.318 Å,).[21] The staggered structure converges to a rectangular basal plane, even when started as a square lattice. To account for possible van der Waals interactions, we also included

dispersion corrections using Grimme's DFT-D2 method.[46] Including these corrections results in improved bulk lattice parameters for α -SnSe (a = 4.407 Å, b = 4.185 Å, c = 11.626 Å) and NaCl-structured SnSe (a = 5.949 Å). For β-SnSe, the lattice parameters are further decreased (a = 4.218 Å, b = 11.675 Å, c = 4.245 Å). The lattice parameters obtained with DFT-D2 follow the same trend for isolated layers as when using the uncorrected PBE, albeit with smaller lattice parameters and a/b ratios. The structures of the isolated layers distort along the c-axis where the Se atoms are distorted into the vacuum region with respect to the Sn atoms, except for the single bilayer where the Sn atoms are distorted into the vacuum region. The degree of distortion increases with increasing number of bilayers from 0.01 Å to 0.04 Å (0.02 Å to 0.09 Å for DFT-D2). Layers adjacent to the vacuum region show larger distortions than layers adjacent to other SnSe layers. The trends of the distortion with m are consistent with structural refinements of SnSe layers observed in $[(SnSe)_{1+\delta}]_m[(NbSe_2)]_n$ and $[(SnSe_{1+\delta})]_m[(MoSe_2)]_n$,[25,47] although the magnitude is smaller than observed experimentally.

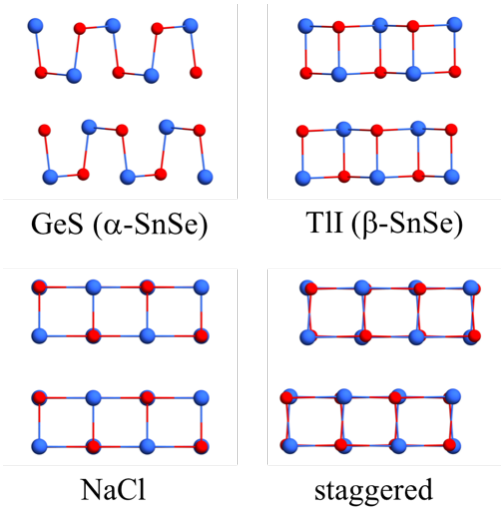

Figure 7.6. Relaxed structures of two SnSe bilayers for the different polytypes used in the DFT calculations viewed along the [010] axis. Sn atoms are blue and Se atoms are red.

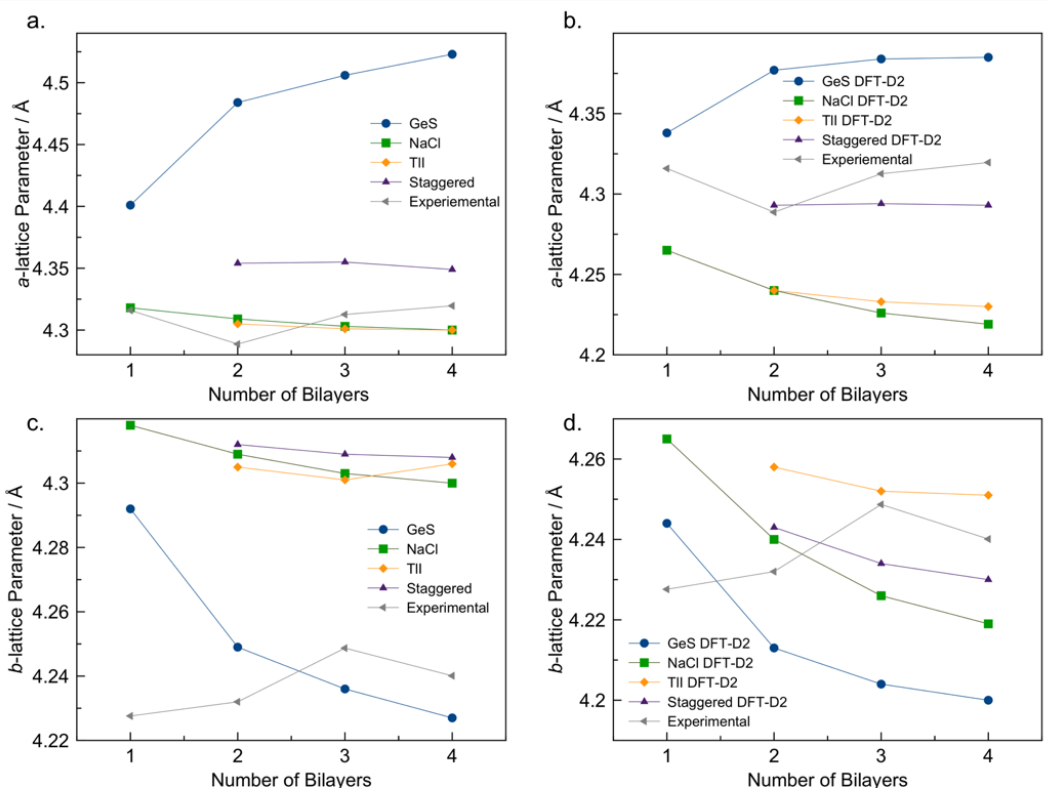

Figure 7.7. In-plane lattice parameters for the *a*-axis (a), (b) and the *b*-axis (c), (d) of the different SnSe polymorphs as a function of the number of bilayers. (a) and (c) were calculated without a van der Waals functional. (b) and (d) were calculated with the DFT-D2 van der Waals functional. Including the DFT-D2 van der Waal's functional does not change the trends in lattice parameters of the polymorphs as the number of bilayers is increased. The lattice parameters for the NaCl and staggered structures are given in their primitive lattices. The experimental lattice parameters for $m = 1$ were normalized to give a better comparison to the lattice parameters for $m > 1$.

Total energies were calculated for each of the structures for different thicknesses as shown in Table 7.2. The GeS structure has the lowest total energy per formula unit (f.u.) for all investigated numbers of bilayers. The TlI structure is 15 – 17 meV/f.u. higher in energy than GeS, and this energy difference is nearly independent of the thickness of SnSe. The energy differences to the NaCl structure and its staggered derivative systematically increase relative to the GeS structure as the SnSe

thickness is increased. While the trends are similar when dispersion corrections are included, the magnitude of the energy differences change significantly for $m \geq 2$. Using DFT-D2, the TlI structure is much closer in energy to the GeS structure (< 5 meV/f.u.) and the NaCl structure is much higher in energy (> 50 meV/f.u.). This suggests that there are significant van der Waals interactions in the GeS and TlI structures that stabilize them compared to the rock-salt type structures. For one bilayer, however, the energy difference between the GeS and the NaCl structure is only 3 meV/f.u. (2 meV/f.u. using DFT-D2), indicating that both structures are almost equally stable. This also suggest that van der Waals interactions primarily occur between and not within the bilayers. It is known that in ferecrystals, compounds with SnSe monolayers can, depending on the adjacent transition metal dichalcogenide, adopt square (V, Mo, Ta) or rectangular (Ti, Nb) basal planes.[27] To probe the energy penalty for creating the rectangularly distorted NaCl lattice, additional calculations were performed. Calculations with a rectangular NaCl starting structure lattice converged to a square structure. However, relaxing only the atomic positions and the in-plane lattice parameters while keeping the a/b ratio fixed at the experimentally determined ratio yields a rectangular structure with a total energy that is only 3 meV/f.u. larger than the undistorted NaCl structure. The relaxed lattice parameters, 6.169 Å and 6.047 Å (6.094 Å and 5.974 Å using DFT-D2) for the *a*-axis and the *b*-axis, respectively, are in good agreement with the experimental lattice parameters for $(SnSe)_{1.20}TiSe_2$. Any surface stabilization by forming a commensurate interface with the $TiSe_2$ layers is not included in these calculations, so the small energy difference in our calculations suggest that a single SnSe bilayer can easily distort to form a commensurate lattice with $TiSe_2$. However, additional interactions must be present that raise the energy of the GeS structure above the energy of the NaCl structure.

Table 7.2. Total energy differences per formula unit ΔE_{GeS} of the polymorphs with respect to the GeS (α-SnSe) structure as a function of the number of bilayers. Values in parentheses represent values obtained using DFT-D2.

	Energy of Various Structure Types (meV) Referenced to that of GeS		
Layers	TlI	NaCl	Staggered
1	-	3 (2)	-
2	15 (3)	11 (51)	12 (35)
3	16 (4)	15 (60)	17 (45)
4	15 (4)	17 (62)	19 (51)

For $m > 1$, the energy of the NaCl structure per formula unit increases significantly relative to GeS and TlI due to the stabilizing effect of van der Waals interactions in the GeS and TlI structures. Hence, it is not energetically favorable to maintain a lattice match with the $TiSe_2$ layers Instead, the symmetry of the in-plane lattice is consistent with the GeS or TlI structure with a steadily increasing *a*-axis lattice parameter and a nearly constant *b*-axis lattice parameter. This behavior is consistent with the DFT results of GeS-structured SnSe layers, albeit with a much smaller slope. The values of the experimental lattice parameters on the other hand are more consistent with the TlI structure. The transition from the GeS to the TlI structure is second order, and the observed (100) reflection in the in-plane diffraction pattern should be extinctin either structure, suggesting that neither structure describes the in-plane symmetry completely. The interactions with the $TiSe_2$ layers that raise the energy of the GeS structure above the energy of the NaCl structure for $m = 1$ could also raise the energy of the GeS structure to a value similar to the energy of the TlI structure for $m > 1$, resulting in a competition between these two structure types. It is thus plausible that the actual structure is an interpolation between the GeS and the TlI

structure, which cannot be determined conclusively without including the interactions between the $TiSe_2$ and SnSe layers. More experimental evidence is needed to determine the exact structure (or structures) the SnSe layers adopt for m = 2 and 3. These results, in combination with experimental data, suggest that the van der Waals interactions inside the SnSe layers significantly stabilize the GeS and the TlI structures, resulting in a competition between these two structures during growth.

The HAADF-STEM image of $[(SnSe)_{1.20}]_3TiSe_2$ (Figure 7.4d) shows SnSe layers that are inconsistent with any zone axis of a single SnSe structure, but instead show a single β-SnSe unit cell with half of another β-SnSe unit cell shifted by half a lattice constant. DFT calculations on these shifted unit cells show only a small energy difference between them and undistorted β-SnSe with three bilayers (see Supporting Information Figure D.6 and Table D.1). Since Sn(II) has a lone pair, we calculated the electron localization functions (ELFs) for the different structures and layer thicknesses. For the GeS structure, the Sn atoms in the surface layer have prominent ELFs that project out into the vacuum. The Sn atoms in the inner layer have less pronounced lone pairs again pointed outward towards the adjacent bilayer. Thus, the interface consists of lone pair electrons of Sn and Se in each bilayer projected towards each other. This suggests that there is little penalty to grow these layers with or without this defect, so the structure of SnSe with three bilayers may depend entirely on nucleation and growth kinetics.

7.2.4. Transport Properties

The structural changes with thickness also result in changes in the electronic structure, which will impact the trends in transport properties of these compounds. Temperature dependent resistivity data collected on the title compounds are shown in Figure 7.8. The resistivity of the m = 2, 3 and 4 compounds are all larger than the previously reported m = 1 compound.[31] The highest resistivity measured is for the m

= 2 compound, with subsequent increases in *m* resulting in lower resistivity. This behavior is opposite to that observed previously for $[(SnSe)_{1+\delta}]_mNbSe_2$, where an increase in the thickness of SnSe resulted in a systematic increase in resistivity.[44] This difference reflects the impact of structural changes with thickness of the SnSe layer and interactions between the layers on the electronic properties of these materials. At low temperatures, the resistivity increases as temperature is decreased for all compounds, where the overall magnitude of this upturn decreases with increasing *m*. The increase in resistivity is not exponential as expected for a traditional semiconductor and is not pronounced enough to suggest a metal-insulator transition.[48] The much weaker temperature dependence is consistent with a metal or heavily doped semiconductor where carrier localization is occurring at low temperatures, but the possibility of the upturn being the result of a charge density wave in the $TiSe_2$ layer cannot be excluded.[49,50] Similar upturns in resistivity are observed at low temperatures in $[(PbSe)_{1+\delta}]_m[TiSe_2]_n$ compounds. In the $[(PbSe)_{1+\delta}]_m[TiSe_2]_n$ compounds, however, there is a decrease in resistivity as temperature is decreased prior to the upturn.

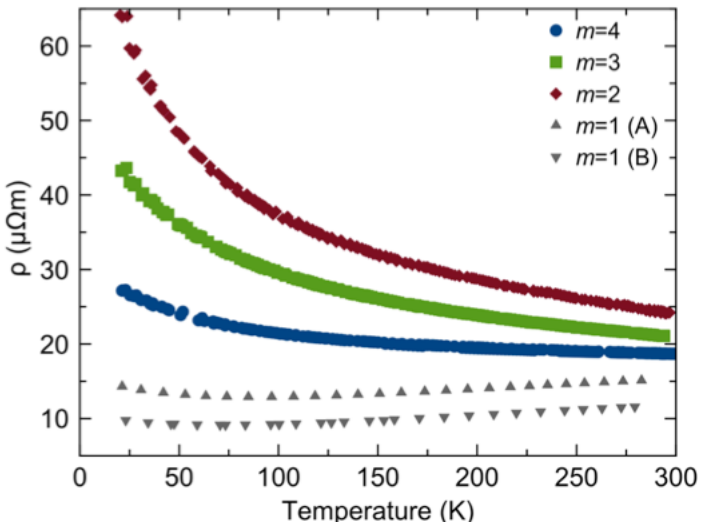

Figure 7.8. Temperature dependent resistivity measurements of the $[(SnSe)_{1+\delta}]_mTiSe_2$ compounds with *m* = 1-4. Measurements of two different *m* = 1 samples are plotted to show reproducibility of their behavior.

Hall effect measurements (Figure 7.9) were collected to provide additional information about the electronic properties. For all compounds, the Hall coefficient changes only slightly with temperature in an approximately linear fashion, which is inconsistent with semiconducting behavior. This suggests the low temperature upturns in resistivity are caused by a change in mobility with temperature or a more complex two-carrier behavior. The Hall coefficient varies systematically with m and changes sign as m is increased. The Hall coefficient for the m = 1 compound is negative and stays constant with temperature, as expected for a simple metal, indicating electrons are the majority carrier. The Hall coefficient for the m = 2 compound decreases as the temperature is lowered, switching sign at approximately 160 K, indicating a change in the majority carrier type from holes to electrons. The m = 3 compound has a positive Hall coefficient at all temperatures and the m = 4 compound has a larger positive Hall coefficient at all temperatures. The positive room temperature Hall coefficients suggest holes are the majority carrier. The changes in the magnitude of the Hall coefficient as m increases and the positive signs are not consistent with prior models where transport properties were assumed to be dominated by electrons in $TiSe_2$ resulting from charge donation from SnSe to $TiSe_2$. The magnitude of the Hall coefficients as m increases and as temperature is decreased, combined with the resistivity data discussed previously, also suggests that the average carrier mobility significantly increases as m is increased and varies with temperature.

Room temperature Seebeck coefficients (α) were measured for all the compounds to gain more information about the change of carrier type as m and temperature are varied. The results are summarized in Table 7.3. Like the Hall coefficient, the Seebeck coefficient also changes sign as m is increased. The sign of the Seebeck coefficient agrees with the sign of the Hall coefficient for m = 1, 3, 4, indicating agreement in majority

carrier type. The m = 2 compound, however, displays a positive Hall coefficient and a negative Seebeck coefficient, which indicates that both carrier types contribute to the observed conductivity. This is consistent with the change in the Hall coefficient as a function of temperature.

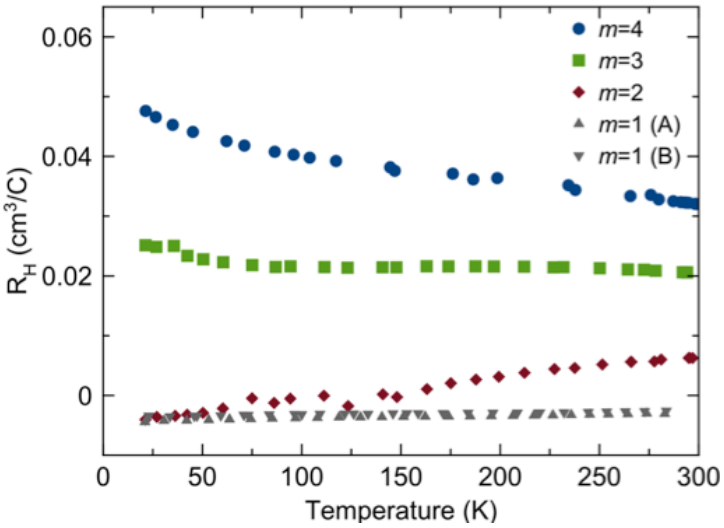

Figure 7.9. Temperature dependent Hall coefficients for $[(SnSe)_{1+\delta}]_mTiSe_2$ compounds.

Table 7.3. Room temperature transport properties for $[(SnSe)_{1+\delta}]_mTiSe_2$ compounds.

m	ρ (T = 295 K) (μΩm)	R_H (cm^3/C)	α (μV/K)
1 (A)	15(1)	-0.0044(1)	-75(3)
1 (B)	12(1)	-0.0034(1)	-77(3)
2	24(1)	0.0064(1)	-29(1)
3	21(1)	0.021(1)	2(1)
4	19(1)	0.032(1)	22(1)

Historically, the band structures of both misfit layer compounds and ferecrystals have been discussed using a rigid band approximation,

with MX bands and TX_2 bands only slightly perturbed by the interface and the charge transfer between them.[51] For most misfit layer compounds and ferecrystals containing $TiSe_2$ it appears that the rock salt layers "dope" the dichalcogenides to which then dominate transport. For example in the analogous $[(PbSe)_{1+\delta}]_m[TiSe_2]_n$ compounds where $m = n$,[52] a donor-acceptor behavior between the PbSe and $TiSe_2$ layers was suggested and the establishment of a space-charge region near the interface was used to describe the transport. The data is consistent with the relative position of the Fermi level remaining unchanged as m and n are simultaneously increased. The trends in the transport properties as m is varied in $[(SnSe)_{1+\delta}]_mTiSe_2$ are more complicated as the band structure is being altered due to structural distortions within the SnSe constituent and the ratio of m to n is also being changed.

The complex variation of the structure and electrical properties indicate that these compounds cannot be thought of as simple composites where the properties of the individual constituents can be summed to obtain the properties of the intergrowth. DFT, XRD, and STEM data all indicate that the structure of the SnSe constituent is changing with thickness and that the interactions between the SnSe and $TiSe_2$ are important. Charge transfer is likely a function of structure, the m/n ratio, and the interaction between the constituents. The changes in transport properties reflect the change in SnSe structure with thickness. Given the 2nd order phase transition in bulk SnSe with temperature, it is likely that the changes in the temperature dependence of the electrical data could result from structural transitions with temperature.

7.3. Conclusion

Three new $[(SnSe)_{1+\delta}]_mTiSe_2$ compounds were synthesized using modulated elemental reactants as precursors. Control of the nanoarchitecture was achieved by systematically increasing the number of SnSe layers in the repeating unit of the precursor. As the SnSe block

thickness is increased, the basal plane structure of SnSe evolves from rectangular (m = 1) to an orthorhombic GeS related structure (m = 4) with the m = 2, 3 compounds having related distorted structures. This evolution indicates that the energetic cost of distorting to form an epitaxial interface with $TiSe_2$ increases as the number of interior layers increases. This is consistent with DFT calculations and can be attributed to stabilizing van der Waals interactions. For SnSe blocks with m = 3, shear defects are observed within the same repeating unit. DFT calculations showed that the different shear structures and the undistorted structure of β-SnSe are very close in energy, suggesting that the existence of these defects depend on nucleation and growth kinetics. The compounds also display unexpectedly complex electrical properties, with resistivity decreasing as the thickness of the SnSe layer is increased, and the carrier type changing as m and temperature are varied. The evolving structure and electrical properties suggest the interactions between constituents are complicated and the previously used simple models based on rigid bands and charge transfer between the constituents is not appropriate for these compounds. Further investigations into this behavior are necessary to fully understand the cause of the upturn at low temperatures in the resistivity and the change in carrier type with increasing number of SnSe layers.

7.4. Materials and Methods

Precursors were synthesized in a high-vacuum physical vapor deposition system, with depositions occurring at pressures below 5×10^{-7} Torr. Tin (Alfa Aesar, 99.98%) and titanium (Alfa Aesar, 99.99%) metals were deposited using electron beam guns, and selenium was deposited using an effusion cell. A computer controlled pneumatic shutter system was used to control the sequence and thickness of the elemental layers.[53] The rate of deposition and the thickness of the elemental layers were measured using quartz crystal microbalances, with rates maintained at

0.1 - 0.3 Å/s at the substrate. The elemental layers were deposited in a {Ti-Se-(Sn-Se)$_m$} sequence, with the number of sequential Sn|Se repeats, m, equal to the number of Sn-Se bilayers desired in the targeted compounds. The {Ti-Se-(Sn-Se)$_m$} sequence was repeated to get a total film thickness of approximately 500 Å, a thickness convenient for thin film diffraction and electrical property measurements. Samples were prepared on either *(100)* Si with a SiO_2 native oxide layer for structural and compositional characterization or fused silica for electrical characterization. Composition measurements used for the calibration of deposition parameters was performed using EPMA using a method described by Donovan *et al.*[54] The precursors were annealed in an inert nitrogen environment ($p[O_2] \leq 0.8$ ppm) at 350 °C for 30 minutes to self-assemble the mostly amorphous precursors into the desired products.

The structure of the precursors and products were determined using XRD and electron microscopy studies. Specular XRD and XRR were used to determine the compound's superstructure and the total film thickness, respectively, using a Bruker D8 Discover. Constituent in-plane structures were characterized using an in-plane diffraction geometry on a Rigaku SmartLab diffractometer. All diffraction experiments were conducted using a Cu K_β radiation source with a nickel filter used to remove any Cu K_β radiation. In-plane lattice parameters were refined with the Le Bail Method[36] using the FullProf suite which takes into account both signal from both the Cu Kα(1) and Cu Kα(2) radiation.[55,56]

High angle annular dark field scanning transmission electron microscopy (HAADF-STEM) data was collected at Pacific Northwest National Laboratory using a probe aberration-corrected FEI Titan 80-300 STEM. Electron-transparent cross-sectional lamellae of the samples were prepared using an FEI Helios 600 Ga^+ focused ion beam. A procedure

was employed similar to the Wedge Prep method described by Schaffer[57] with final thinning and polishing performed using 2 keV ions.

Electrical resistivity and Hall effect measurements were conducted using the van der Pauw geometry on a home-made closed-cycle helium low temperature system using samples deposited on fused silica. Magnetic fields ranging from 0 kG to 16 kG were applied to the sample during the van der Paaw Hall measurement. The magnetic field was increased in steps, so 5 data points were taken for each of the four lead configurations. A straight line was fit to the change in Hall voltage as a function of field to obtain the Hall coefficient. Seebeck measurements were made on bar shaped samples with copper-constantan thermocouples. In this experiment, one end of the sample was cooled and the voltage between the same material thermocouple leads was measured.

DFT calculations were performed using the Vienna *ab initio* simulation (vasp) package.[58–60] The projector augmented wave (PAW)[61,62] method was used to describe the interactions between the core and the valence electrons. Exchange and correlation were described using Perdew-Burke-Ernzerhof (PBE) functionals in the generalized-gradient approximation (GGA).[63] A cut-off energy of 500 eV was used for all calculations. Calculations were carried out on isolated multilayers using a 15 × 15 × 1 Monkhorst-Pack[64] grid for GeS- and TlI-structured layers, and a 11 × 11 × 1 Monkhorst-Pack grid for the other layers. To minimize interactions between periodic images, vacuum spacing of at least 20 Å was included between each multilayer. For bulk calculations, Monkhorst-Pack grids of 15 × 15 × 5, 15 × 5 × 15, and 11 × 11 × 11 were used for the GeS structure, the TlI structure, and the NaCl structure, respectively. Self-consistency was achieved with an energy convergence of 10^{-6} eV. Atomic positions and in-plane lattice parameters were allowed to relax until the forces were smaller than 0.005 Å/eV and the stresses

were smaller than 0.01 GPa. For α-SnSe, rock salt (NaCl structure, $Fm\bar{3}m$), and a staggered rock salt-related structure, (001) slabs of the bulk structures were used, and a (010) slab for β-SnSe. The calculations were carried out on two, three, and four bilayers of each polytype, and additionally on a single bilayer for the GeS and NaCl structures. Dispersion corrections were included using Grimme's DFT-D2 functional.[46] We chose this functional because it gave the best agreement with the bulk SnSe structure.

7.5. BRIDGE

Chapter 6 provided an in-depth investigation into the in-plane structure of $[(SnSe)_{1.2}]_1[TiSe_2]_1$ compound and identified a distortion that occurs in the SnSe constituent to provided and accidental lattice match with the $TiSe_2$ constituent in order to lower the overall free energy of the system. Chapter 7 discussed the realization that when the number of SnSe layer within a repeating unit of a $[(SnSe)_{1+\delta}]_mTiSe_2$ heterostructure is greater than 1, the SnSe basal plane structure can be re-indexed to a smaller unit cell that approaches the bulk structure of SnSe as the number of SnSe layers increases. This behavior and observed structural distortion as a function of nanoarchitecture greatly influences the observed transport behavior. As the number of SnSe layers increases there is a change in carrier type from holes to electrons which indicates that there is complex layer interaction occurring within these materials. To further probe this layer interaction without the influence of the structural distortion, a series of $[(SnSe)_{1+\delta}]_1[TiSe_2]_q$ heterostructures were prepared and characterized. In this series, the number of $TiSe_2$ layers within the unit cell was increased while holding the number of SnSe layers constant at one layer. Chapter 8 provides a detailed study of the charge donation and layer interactions that occurs in this family of compounds.

CHAPTER VIII

INFLUENCE OF NANOARCHITECTURE ON CHARGE DONATION AND ELECTRICAL TRANSPORT PROPERTIES IN $[(SNSE)_{1+\delta}][TISE_2]_Q$ HETEROSTRUCTURES

8.0. AUTHORSHIP STATEMENT

The manuscript that composes this chapter is currently under review to be published in JACS. Coauthors of this work include Dylan Bardgett, Sage Bauers, Thomas Kasel, Austin Mroz, Chris Hendon, Doug Medlin, and David Johnson. I am the primary author on this work. Dylan Bardgett aided in the data collection and analysis. Sage Bauers synthesized and characterized the samples. Thomas Kasel, Austhin Mroz, and Chris Hendon completed the computational work included in this manuscript. Doug Medlin collected and analyzed the HAADF-STEM images presented in this paper as well as contributed to writing the manuscript. David Johnson is my advisor who assisted in the experimental design, analysis of data, and writing of the manuscript.

8.1. INTRODUCTION

While the ability to isolate graphene and other 2D materials has been known since the 1970's, the discovery of an easy optical method to determine the thickness of these thin materials has facilitated an explosion of research activity.[1] Researchers have discovered a number of unusual emergent properties, especially at the monolayer limit, including the conversion of indirect to direct band gaps,[2,3] the observation of the fractional quantum Hall effect,[4] the realization of Hofstadter's butterfly,[5–7] and advances in valleytronics.[8] Researchers also discovered that "artificial" materials created by stacking different 2D layers in designed sequences have emergent properties and provide many experimental parameters (identity, properties, thickness, and sequence of layers) that can be used to modify and manipulate these properties.[9–12] The

interaction between a 2D layer and a substrate or a neighboring 2D layers in heterostructures has been found to strongly impact the emergent electronic properties.[13,14] The atomically flat interfaces between adjacent surfaces provides a large area where the orbitals extending from each layer overlap and interact, resulting in a significant renormalization of the electronic states. Due to the easy cleaving of the bulk materials along these crystal planes, the interactions between the layers have typically been described as weak van der Waals interactions, but the substrate dependent properties suggest stronger interactions are present. Understanding the interaction between layers and the impact of these interactions on the near Fermi energy electronic structure is critical to understand the evolution of emergent properties – a critical step in designing heterostructures for next generation devices.

There is significant evidence indicating the common assumption of weak van der Waals bonding between layers in a heterostructure is incorrect. Perhaps, the strongest piece of evidence for stronger interactions between layers in a heterostructure is the thermodynamic stability of the misfit layer compounds, compounds which contain alternating bilayers of a rock salt structure and a monolayer or bilayer of a transition metal dichalcogenide. These compounds are formed via direct reaction of the elements, such as Ti, Se, and Sn, at high temperatures for long time periods.[15] The literature describes the bonding between the layers in these compounds as weak when the cation in the rock salt layer is divalent.[16–18] For these compounds to be thermodynamically stable, however, the bonding between the rock salt structured bilayer and the dichalcogenide layer must be stronger than the sum of the ionic interaction within the bulk rock salt structure and the bonding between layers in the bulk dichalcogenide. A significant interaction between the layers of a heterostructure that is often ignored is charge transfer. Since the chemical potential and dielectric constants

of the various constituent layers will be dissimilar, the spatial extent, energies, and occupancy of these wavefunctions will be different in the heterostructure compared to their isolated layers. The resulting charge transfer, a fraction of an electron per formula unit of the constituents, can create a strong "ionic bond" across the interface that stabilizes these compounds.[19] This charge transfer can have a dramatic effect on properties, such as emergent superconductivity of $(SnSe)_{1.18}(TiSe_2)_2$.[15]

In this paper, a series of $[(SnSe)_{1+\delta}][TiSe_2]_q$ heterostructures are synthesized to quantify the amount of charge transfer and probe the importance of charge transfer on the evolution of electrical properties as a function of layer thickness. This system was chosen because the electrical properties of $TiSe_2$ and misfit compounds containing $TiSe_2$ layers are well studied and known to be very sensitive to variations in carrier concentration, specific dopants, defect concentrations, and constituent structures.[15,20–24] $TiSe_2$ has been reported to have a charge density wave, to be a heavily doped semiconductor, and is theoretically calculated to be a semiconductor with a small band gap if made defect free.[20,25–27] SnSe has been reported to be a semiconductor, a promising thermoelectric material, and a topological crystalline material.[28–30] The 1-1 misfit compound has regions of rotational disorder and is a normal metal, while the 1-2 misfit layer compound is superconducting.[15,23,31] In the $[(SnSe)_{1+\delta}]_m[TiSe_2]_1$ homologous series of compounds an unusual change in electronic properties were reported.[24] Here, we prepared and structurally characterized the q = 1,2,3,4, 6, 8, 11 and 15 heterostructures, which all contain a single SnSe layer separated by q layers of $TiSe_2$. Though varying from their bulk counterparts, the constituent crystal structures do not change with nanoarchitecture. The electrical properties systematically evolve as q increases. The changes were successfully modeled based on a $[(SnSe)_{1+\delta}][TiSe_2]_2$ conducting unit that becomes increasingly isolated by $TiSe_2$ layers as q becomes larger.

As the number of $TiSe_2$ layers increase the average carrier concentration decreases, and there is increasing localization of the carriers in the $[(SnSe)_{1+\delta}][TiSe_2]_2$ at low temperatures consistent with Anderson localization. In heterostructures with large *q* values, additional carriers (electrons and holes) are created by thermal excitation at higher temperatures. Density functional theory (DFT) calculations and the modeling of electrical data both indicate charge transfer of approximately 0.1 electron per SnSe to $TiSe_2$. Quantifying the charge transfer between layers and understanding how it changes with nanoarchitecture is important for future design of thin film materials with targeted properties.

8.2. Methods and Materials

Samples were prepared via the MER method as described previously by Atkins and coworkers.[32,33] Elemental layers were deposited onto Si with a native SiO_2 layer and quartz substrate for structural and electrical characterization, respectively. Titanium and tin (Alfa Aeser, 99.99% and 99.98%, respectively) were deposited using electron beam guns while selenium (Alfa Aeser, 99.999%) was deposited using a Knudson effusion cell. Quartz crystal microbalances, located between the source and the substrate, were used to monitor the deposition rate and thickness of each element. Custom software which communicated with the crystals and controlled the pneumatic shutters, assembled the precursor with the designed architecture and number of atoms per elemental layer calculated to produce the targeted product.[34]

Samples were annealed on a hotplate at 350 °C for 30 minutes in a nitrogen atmosphere with less than 1 ppm oxygen. This temperature was determined in a previous study of $[(SnSe)_{1.2}]_1[TiSe_2]_1$ samples and assumed to be the optimal annealing temperature for these $[(SnSe)_{1+\delta}]_1[TiSe_2]_q$ heterostructures.[31] The annealed structures were

determined via x-ray diffraction (XRD) using Cu-Kα radiation (λ = 0.15418 nm). Total film and repeating unit (c-axis lattice parameter) thicknesses were gathered from low angle x-ray reflectivity (XRR) and specular diffraction data, respectively. The reflectivity and specular diffraction data were collected on a Bruker D8-discover diffractometer using a locked couple scan type and (θ-2θ) ranges of 0-10° and 5-65° respectively. The in-plane diffraction scans were collected using a Rigaku Smartlab diffractometer with a (θ-2θ) range of 15-110°.

Ultrathin cross-sections were prepared using a FEI Helios Nanolab 600i focused ion beam scanning electron microscope (FIB-SEM) for electron microscopy investigations. As the lamellae approached electron transparency, low energy 2kV milling was used to avoid damaging the crystallinity of the sample while thinning the sample to the targeted thickness. The prepared samples were imaged in high angle annular dark field scanning transmission electron microscopy (HAADF-STEM) mode at 300kV using a Thermofisher Themis TEM located at Sandia National Laboratory in Livermore, CA.

Temperature-dependent transport measurements were collected on a home-built measurement system that uses a closed-cycle helium cryostat to obtain low temperatures. Resistivity measurements were conducted using the van der Pauw technique. Films were deposited onto a masked quartz substrate to create 1 cm x 1 cm samples with a cross-arm geometry. Indium contacts were pressed onto each of the four points of the cross. Resistivity measurements were taken periodically at temperatures ranging from 20 to 295 K. Hall measurements were done with magnetic fields ranging from 0 to 16 kG also using the van der Pauw technique. At 4 kG increments, a constant current of 0.100 A was sequentially applied to each of the four lead configurations. The Hall Coefficient was determined from the slope of a linear fit of the Hall voltage as a function of magnetic field. Seebeck measurements were

performed on a rectangular sample deposited onto a quartz substrate. One end of the sample was cooled, and the temperature difference measured using independent thermocouples. The voltage difference between either end of the sample was measured and divided by the temperature difference to obtain the Seebeck coefficient.

Computational models of bulk SnSe and $TiSe_2$ were prepared from the computationally ready structures from the Materials Project.[35] Prior to generation of slab and heterojunction models, bulk structures were geometrically optimized. All calculations utilized the PBEsol functional[36,37] with Tkatchenko-Scheffler dispersion corrections[38] and a scaling factor of 0.94 alongside a projector-augmented-wave (PAW) basis[39] and a 500 eV plane-wave cutoff as implemented in the Vienna *ab initio* Simulation Package (VASP).[40–43] All structures were considered geometrically optimized when forces were below 0.005 eV/Å^2 and electronically optimized when the total energy was below 10^{-6} eV. A 10 x 10 x 4 Γ-centered k-grid were used for both bulk SnSe and bulk $TiSe_2$. Once bulk models were geometrically optimized, slab models were generated containing 7 layers and ~20 Å of vacuum space with a Γ-centered k-mesh of 10 x 10 x 1 for both SnSe and $TiSe_2$. Density of States plots of slab models were calculated from a minimized wave function using the same electronic convergence criteria as above and Gaussian smearing with σ = 0.3 eV with a 10 x 10 x 1 and a 6 x 6 x 1 Γ-centered k-grid for SnSe and $TiSe_2$, respectively. The valence band maximum eigenvalue was aligned to vacuum utilizing the MacroDensity code.[44,45] While a previous report on the SnSe-$TiSe_2$ heterojunction utilized an island-based modeling approach,[23] here we elected to utilize supercell expansions of bulk models to maintain the *ab* plane connectivity as to not artificially confine SnSe. This was done by first generating a 6 x 7 x 2 supercell of $TiSe_2$ followed by removal of one of the two $TiSe_2$ sheets to create a cavity for SnSe insertion. SnSe was

expanded to a 5 x 6 x 1 supercell and a single layer was inserted into the $TiSe_2$ cavity. The SnSe layer was subsequently rotated about the normal of the *ab* plane by hand to minimize lattice mismatch. Following rotation excess atoms were removed. The resulting heterojunction was geometrically minimized using the criteria above in a spin polarized scheme with a 2 x 2 x 2 Γ-centered k-grid. After geometric optimization, Bader charge analysis was performed on both the heterojunction and bulk models using the Bader code and the charge density was sampled with 150% of the default resolution in all directions.[46–48]

8.3. Results and Discussion

8.3.1. Synthesis

A series of $[(SnSe)_{1+\delta}]_1[TiSe_2]_q$ heterostructures with an increasing number of $TiSe_2$ layers per repeat unit ($1 \leq q \leq 15$) were prepared from precursors with composition profiles designed to mimic the desired final product. Each precursor was made by depositing elemental layers in a repeating sequence containing a single Sn|Se bilayer and q Ti|Se bilayers. The deposition parameters for the Sn|Se bilayer were adjusted to obtain a one to one atomic ratio of Sn to Se and the required number of atoms such that two 001 planes of rock salt structured SnSe formed from the deposited bilayers when annealed. The deposition parameters for the Ti|Se bilayer were adjusted to obtain a one to two ratio of Ti to Se and a thickness such that a single $TiSe_2$ layer with a CdI_2 structure formed upon annealing. Heterostructures with q = 1, 2, 3, 4, 6, 8, 11, and 15 were targeted by changing the number of Ti|Se bilayers within the repeating unit. The Sn|Se + q[Ti|Se] sequence of layers was repeated 41, 28, 21, 17, 12, 9, 7, and 5 times, respectively, to form precursor films that were approximately 50 nm thick. Annealing at 350°C for 30 minutes converted the designed precursors into the targeted heterostructures, as reported previously for $[(SnSe)_{1+\delta}]_1[TiSe_2]_1$ and $[(SnSe)_{1+\delta}]_m[TiSe_2]_1$ compounds.[24,31]

8.3.2. Structural Characterization

Figure 8.1 contains X-ray reflectivity (XRR) patterns of the annealed q = 1, 2, 4, and 6 samples. The patterns contain Kiessig fringes from the interference between the front and the back of the samples and Bragg reflections from the repeating layer sequence. The angle of the first order Bragg reflection systematically decreases as the number of $TiSe_2$ layers increases, consistent with an increasing c-axis lattice parameter. The q = 1, 2, 4, and 6 compounds have 38, 24, 14, and 10 Kiessig fringes between Bragg reflections respectively, indicating the total thickness contains 40, 26, 16, and 12-unit cells in the final product. The number of unit cells in the q = 6 sample matches the number of layers that were deposited in the precursor. The number of unit cells for the q = 1 and q = 4 samples are one less than deposited in the precursor. For the q = 2, there are two fewer unit cells in the annealed sample than deposited in the precursor. The variations in the XRR patterns demonstrating the change in the total number of layers can be observed in figure E.1. The decrease in the number of unit cells relative to the number of layers deposited in the precursor for these samples results from deviation in the amount of material deposited compared to the target amount of material needed in each repeating unit, the reaction of the first layer(s) with the substrate, and/or surface oxidation of the film during annealing. The angle where the Kiessig fringes disappear is related to the roughness of the films via the Parratt equation.[49] Most of the fringes can no longer be resolved at ~ 6° degrees 2θ for all of the samples, indicating a roughness less than ~ 0.4 nm. The presence of Bragg reflections in the XRR patterns of the annealed samples parallels those observed in the as-deposited samples indicates that the nanoarchitecture of the precursors are preserved as the desired heterostructures self-assemble (Figure E.1).

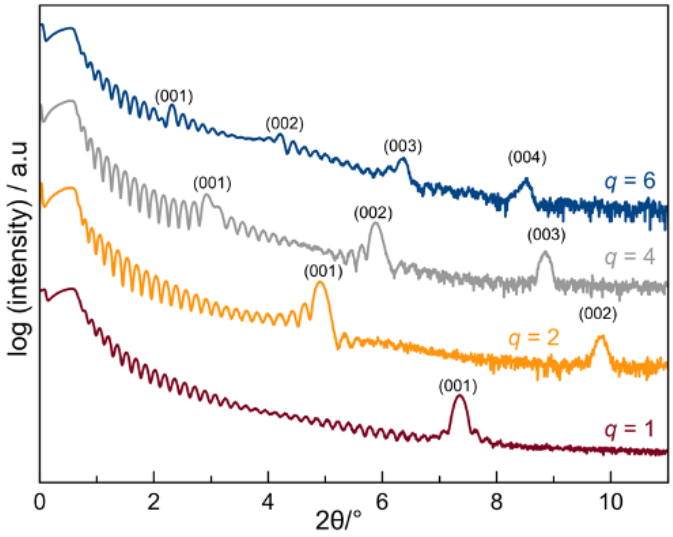

Figure 8.1. XRR patterns of representative $[(SnSe)_{1+\delta}][TiSe_2]_q$ heterostructures after low temperature annealing. The (00*l*) Bragg reflections are indexed and are different from the low intensity maxima between the Bragg reflections known as Kiessig fringes that are due to the finite thickness of the films.

Specular X-ray diffraction scans were collected on each of the $[(SnSe)_{1+\delta}]_1[TiSe_2]_q$ heterostructures and are shown in Figure 8.2. The intensity maxima in each pattern can all be indexed as (00*l*) reflections, indicating that the heterostructures are crystallographically aligned to the substrate. With increasing *q*, the spacing between observed Bragg reflections decreases as the c-axis lattice parameter increases. The intensities of most reflections diminish as *q* increases except for the reflections at approximately 14°, 30°, and 62° 2θ, which become more intense. More of the Fourier terms are needed to describe the structure as the number of ~ 0.6 nm thick $TiSe_2$ layers is increased. The calculated *c* - axis lattice parameters for the $[(SnSe)_{1+\delta}]_1[TiSe_2]_q$ compounds are given in Table 8.1. The *c* - axis lattice parameter of $[(SnSe)_{1.2}]_1[TiSe_2]_1$ is 1.204(1) nm, which is in good agreement with that reported previously for similar compounds.[24,31] The *c* - axis lattice parameter increases linearly as *q* increases, with a slope of 0.602(1) nm per $TiSe_2$ layer. This thickness increase per $TiSe_2$ bilayer is consistent with values reported for

$[(PbSe)_{1+\delta}]_1[TiSe_2]_q$ compounds.[50–52] The change per $TiSe_2$ layer is also consistent with the *c* - axis lattice parameter of 1T-$TiSe_2$ (0.6004 nm).[53] Extrapolating the *c*-axis lattice parameter to $q = 0$ yields an intercept of 0.600(8) nm, which corresponds to the thickness of the SnSe bilayer and the associated incommensurate interface thickness between the different structures. This thickness is larger than both the bulk SnSe *c* - axis lattice parameter of 0.5751(1) nm[54] and the change in *c* - axis lattice parameter as the SnSe constituent is increased in thickness while the TSe_2 thickness is kept constant in $[(SnSe)_{1+\delta}]_q[TSe_2]_q$ (T = Ti, V, Nb or Ta) heterostructures (0.5775 nm – 0.5806 nm).[24,32,55–57] The added thickness due to the interfaces on either side of SnSe is also similar to the difference between the extrapolated $TiSe_2$ trilayer thickness in the series $[(SnSe)_{1+\delta}]_m[TiSe_2]_1$ relative to the thickness of a $TiSe_2$ layer in 1T -$TiSe_2$.[24] The added thickness is probably due to the structural mismatch at the incommensurate interface between SnSe and $TiSe_2$.

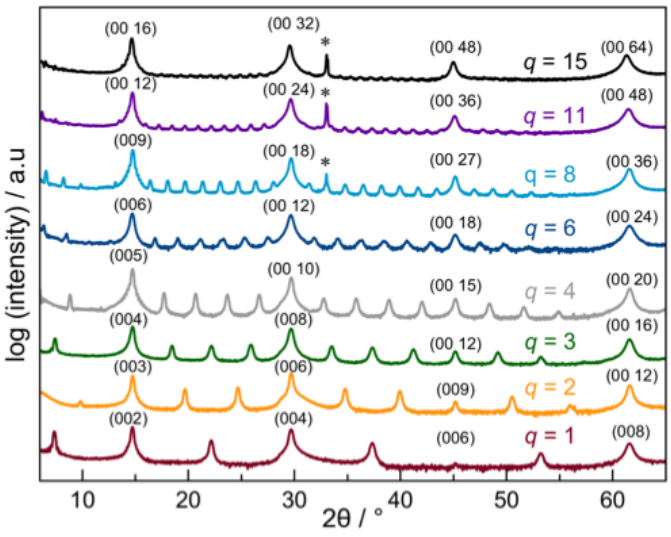

Figure 8.2. Specular diffraction patterns of the $[(SnSe)_{1+\delta}][TiSe_2]_q$ heterostructures. All reflections can be indexed as (00*l*) Bragg reflections and indices for select reflections are indicated in the pattern. The asterisk marks a Si reflection from the substrate present in particular patterns.

In-plane diffraction was collected to provide information about the *a*-*b*- plane crystal structures of the two constituents. All reflections in these scans can be indexed as (*hk*0) reflections of either a hexagonal or a rectangular unit cell. The intensity of the rectangular unit cell decreases and that of the hexagonal cell increases as *q* increases. This indicates that the rectangular unit cell is from the SnSe constituent and the hexagonal unit cell is from the $TiSe_2$ constituent. The position of the reflections remains approximately the same for all *q* values indicating that the in-plane structures of the two constituents do not changing significantly with increasing $TiSe_2$ thickness.

The in-plane lattice parameters for each heterostructures are summarized in Table 8.1. The *a*-axis lattice parameter for the $TiSe_2$ constituent varies only slightly as *q* is increased, with an average value of 0.356(1) nm. This agrees with values previously reported for $TiSe_2$ in both $[(SnSe)_{1+\delta}]_1[TiSe_2]_1$ and $[(SnSe)_{1+\delta}]_m[TiSe_2]_1$,[23,24] as well as other $TiSe_2$ containing heterostructures.[58–63] Bulk $TiSe_2$ has an *a* - axis lattice parameter of 0.354 nm, which is slightly smaller than the values found in Table 8.1, reflecting the interaction with the SnSe layer. The SnSe rectangular basal plane unit cell does not change drastically as the thickness of the $TISe_2$ constituent is increased. This is not surprising, as the SnSe layer has the same environment, with $TiSe_2$ interfaces present on both sides of the single SnSe layer, in all of the heterostructures. The average lattice parameters for the SnSe basal plane summarized in Table 8.1 are 0.596(1) nm and 0.610(2) nm for the *a* - axis and *b* - axis lattice parameters, respectively. These are consistent with the values of 0.597(1) nm and 0.610(1) nm previously reported for the $[(SnSe)_{1+\delta}]_1[TiSe_2]_1$ heterostucture.[23,24] The in-plane lattice parameters of SnSe can vary considerably in a heterostructure depending on the dichalcogenide with which it is layered.[64] The lattice parameters reflect the interactions between SnSe and the dichalcogenide, demonstrating the resulting

tradeoffs in surface and volume free energy. The basal plane areas of SnSe and $TiSe_2$ remain relatively constant as q is increased, resulting in an average misfit parameter $(1+\delta)$ of 1.207(3) (Table 8.1). This misfit parameter is similar to what was previously reported for $[(SnSe)_{1+\delta}]_1[TiSe_2]_1$ and $[(SnSe)_{1+\delta}]_m[TiSe_2]_1$.[23,24,31]

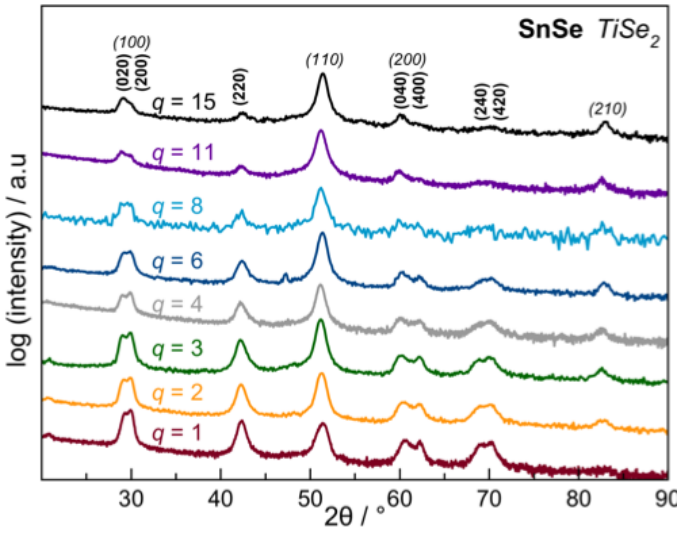

Figure 8.3. In-plane diffraction patterns of $[(SnSe)_{1+\delta}][TiSe_2]_q$ heterostructures. All reflections can be indexed to (hk0) planes of either $TiSe_2$ or distorted SnSe, with the relative intensities of $TiSe_2$ reflections increasing with increasing q.

Table 8.1. Lattice and misfit parameters for the $[(SnSe)_{1+\delta}]_1[TiSe_2]_q$ heterostructures determined from x-ray diffraction patterns.

q	$[(SnSe)_{1+\delta}][TiSe_2]_q$ c – axis lattice parameter / nm	SnSe a–axis lattice parameter / nm	SnSe b–axis lattice parameter / nm	$TiSe_2$ a–axis lattice parameter / nm	1 + δ
1	1.204 (1)	0.597 (1)	0.609 (1)	0.355 (1)	1.202 (1)
2	1.805 (1)	0.597 (1)	0.605 (1)	0.355 (1)	1.210 (1)
3	2.408 (1)	0.597 (1)	0.612 (1)	0.357 (1)	1.206 (1)
4	3.001 (1)	0.598 (1)	0.611 (1)	0.357 (1)	1.207 (1)
6	4.212 (1)	0.595 (1)	0.611 (1)	0.356 (1)	1.207 (1)
8	5.418 (1)	0.595 (1)	0.613 (1)	0.356 (1)	1.203 (1)
11	7.231 (3)	0.597 (1)	0.610 (1)	0.357 (1)	1.209 (1)
15	9.665 (3)	0.595 (1)	0.607 (5)	0.355 (1)	1.210 (1)

HAADF-STEM was collected to provide local information about the heterostructures including layer stacking arrangement, constituent structures, extent of rotational disorder between constituent layers, and amount of disproportionation. Representative HAADF-STEM images of $[(SnSe)_{1+\delta}]_1[TiSe_2]_q$, with q = 3, 4 and 8, spanning the entire film thickness are shown in Figure 8.4. The two different constituent layers are distinguished by their *z* contrast, with SnSe layers appearing brighter and $TiSe_2$ layers appearing darker. In the SnSe layers the Sn atoms are brighter than the Se atoms. In all images the targeted layering scheme is observed, indicating that the desired heterostructures were formed. Some damage from the focused ion beam sample preparation is visible, and the image for q = 8 has regions where the SnSe bilayer is missing. To further probe the global layering of the heterostructures Fast Fourier transforms (FFT), Figure 8.4, were taken from the representative HAADF-STEM images. The expected Fourier components for each of the targeted compounds are observed and the spacing between the Fourier components is consistent with the period measured in the specular diffraction pattern. The full thickness HAADF-STEM images and their FFT indicate that the desired layering scheme makes up the majority of the films, which is consistent with the diffraction data discussed previously.

To probe the layer arrangement and zone axis stacking a representative area from the $[(SnSe)_{1+\delta}]_1[TiSe_2]_4$ sample is magnified and shown in Figure 4g. In this image, various zone axis and rotations off zone axis can be observed for both constituent layers. This demonstrates the rotational disorder that occurs in the *a*-*b*-plane of the heterostructures. For SnSe the (100) and (110) zones axes are observed, while for $TiSe_2$ the (100) and (110) zone axes are present. Various layering defects are present in the film, but the majority of the area imaged is that of the targeted layering sequence. For example, the bottom

SnSe layer in Figure 4g stops while a $TiSe_2$ continues from that space. In the thicker block of $TiSe_2$ there are some unique stacking sequences where there is either twinning of the $TiSe_2$ layers or places where two different nucleation sites grew together. These layering defects and stacking sequences perhaps provide an opportunity to understand how the precursors self-assemble into the $[(SnSe)_{1+\delta}]_1[TiSe_2]_q$ compounds, however a more thorough investigation is required.

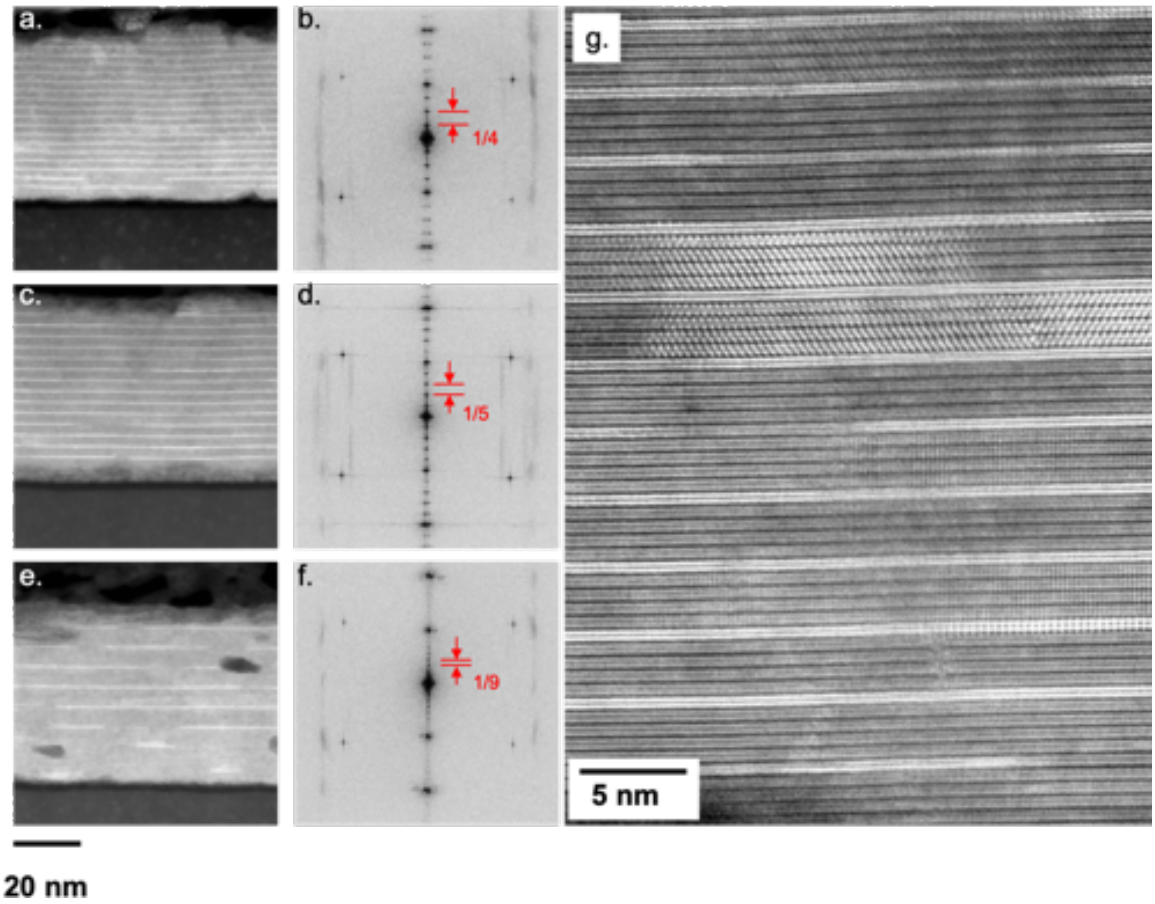

Figure 8.4. HAADF-STEM images and FFT's of the $[(SnSe)_{1+\delta}]_1[TiSe_2]_3$ (a and b), $[(SnSe)_{1+\delta}]_1[TiSe_2]_4$ (c and d), and $[(SnSe)_{1+\delta}]_1[TiSe_2]_8$ (e and f) respectively, and a higher magnification HAADF-STEM image of a region of the $[(SnSe)_{1+\delta}]_1[TiSe_2]_4$ sample (g).

8.3.3. Electronic Transport Properties

Room temperature Seebeck coefficients collected from the $[(SnSe)_{1+\delta}]_1[TiSe_2]_q$ heterostructures (Figure 8.5a.) are all negative, suggesting that electrons are the majority carrier. The magnitude of the Seebeck coefficient becomes systematically larger with increasing q indicating that the carrier concentration decreases as the number of $TiSe_2$ layers is increased.[65,66] Koumoto suggested that charge carriers in $[SnSe]_1TiSe_2$ result from the SnSe layer donating electrons to the $TiSe_2$ layer, which dominate the conduction.[16] If the amount of charge donated by the SnSe layer is constant, then the average electron concentration in the $TiSe_2$ layers would decrease as q increases, which is consistent with the data and prior reports of $(MX)_1(TiX_2)$ (M = Pb or Sn and X = S or Se) compounds.[51,52,65] The q- dependency of the Seebeck coefficient, however, has a much steeper negative slope for the $q \leq 3$ heterostructures than for $q \geq 3$ heterostructures, suggesting that there are two regimes dominated by different phenomena.

Variable temperature resistivity data collected from $[(SnSe)_{1+\delta}]_1[TiSe_2]_q$ heterostructures are shown in Figure 8.5c and 8.5d. The temperature-dependent resistivity generally increases with more $TiSe_2$ layers present in the repeating unit (the q = 6 and 15 samples are exceptions). Samples q = 6 and q = 15 deviate from the trend, presumably due to different defect concentrations impacting carrier concentrations and/or mobility values. All samples have resistivity upturns as temperature is lowered, with the temperature where the upturn begins increasing as q gets larger. For samples with the largest number of $TiSe_2$ layers in the repeating unit, the resistivity continually goes up with decreasing temperature over the entire temperature regime. The samples with smaller q have a decrease in the resistivity with decreasing temperature from room temperature. Below a certain sample dependent temperature, the resistivity increases as temperature is

decreased. The initial decrease in resistivity for the q = 1, 2, 3, 4, and 6 heterostructures is consistent with decreased electron-phonon scattering with lowering of temperature, as expected for a metal. Overall, the rate of resistivity increase at low temperatures for all of the samples is not as large as would be expected for semiconducting behavior. For samples with more $TiSe_2$ layers in the repeating unit, the upturn in the temperature dependent resistivity is similar to previous reports on $TiSe_2$ where the samples were reported to have low defect concentrations.[20]

To further probe the transport behavior, Hall coefficients were measured for the $[(SnSe)_{1+\delta}]_1[TiSe_2]_q$ heterostructures as a function of temperature (Figure 5b). Each heterostructure exhibits a negative Hall coefficient throughout the entire temperature range, which is consistent with the negative room temperature Seebeck coefficients (Figure 5a). However, it appears as if the samples with $q \geq 8$ will have positive Hall coefficients at temperatures slightly above the range measured (above ~300 K). At low temperatures, the negative Hall coefficient with decreasing temperature suggests that electrons dominate the transport properties in this regime. The increase in the magnitude of the Hall coefficient with decreasing temperature, which systematically increases as q gets larger, implies that the carrier concentration decreases as temperature is decreased, and decreases more in high q heterostructures. The temperature dependence of the samples with larger q values also suggests that there are two different phenomena present, one that dominates at low temperature and one that dominates at high temperatures.

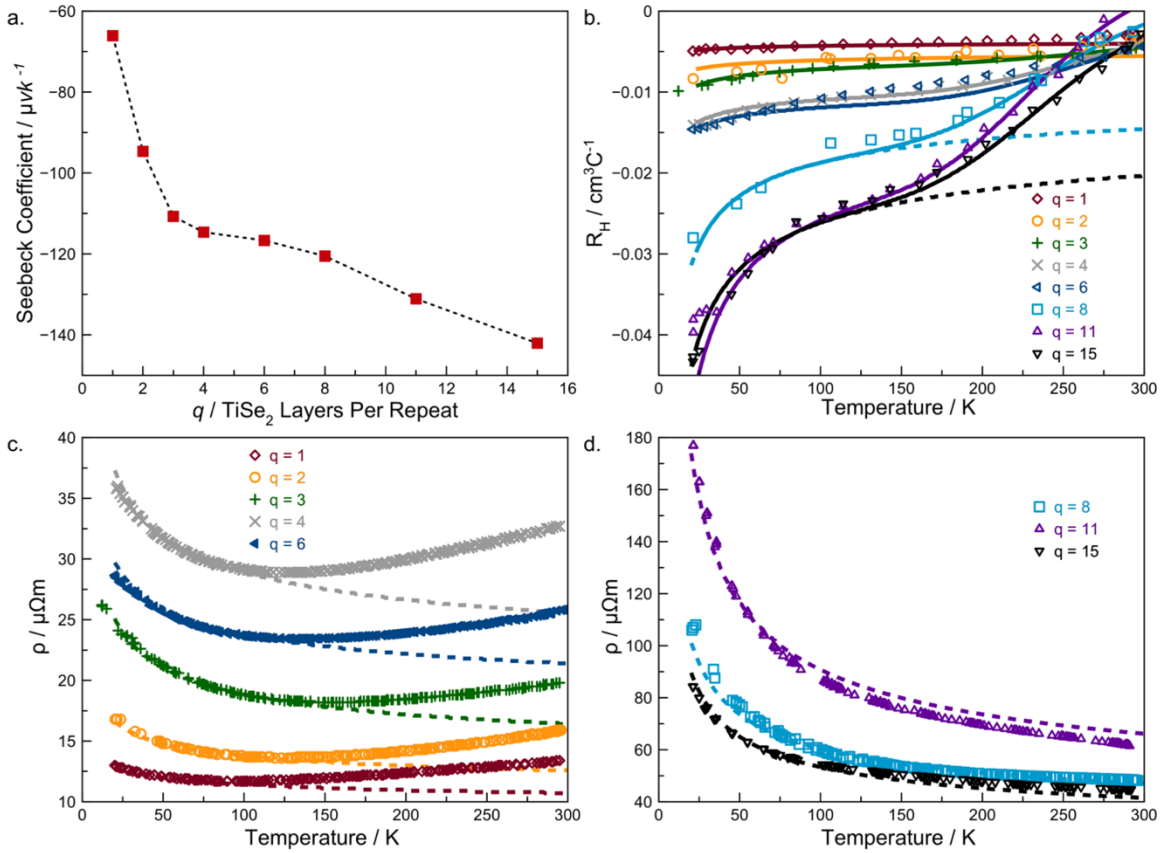

Figure 8.5. Seebeck coefficients for $[(SnSe)_{1+\delta}]_1[TiSe_2]_q$ heterostructures plotted as a function of the number of $TiSe_2$ layers in the unit cell, q (a.). Temperature-dependent Hall coefficients (b.) and resistivity data for the $[(SnSe)_{1+\delta}][TiSe_2]_q$ heterostructures. The resistivity data are plotted on two different resistivity scales (c. q = 1 - 6 and d. q = 8 - 15) so the temperature dependence in samples with thinner $TiSe_2$ layer blocks can be observed. The solid lines in b. are models calculated from a two-carrier model with variable range hopping at low temperatures as discussed in the text which describes the entire temperature regime. The dashed lines in b., c., and d. show the fits to a VRH mechanism, which describes the Hall coefficient and resistivity at low temperatures.

The transport properties of all samples in the low temperature regime suggest that the carrier concentration decreases as temperature declines. As q, the number of $TiSe_2$ layers in the repeating unit gets bigger, both the upturns in resistivity and the systematic increase in the absolute magnitude of the Hall coefficient get larger. The temperature

dependence of the resistivity at low temperatures cannot be fit to an exponential for any of the samples (see Figure E.2). This suggests that the decrease in resistivity as temperature is increased does not result from excitation across a band gap. A charge or spin density wave would be consistent with a decrease in carriers as temperature is lowered, however we did not find any discontinuities in lattice parameters as a function of temperature. (see Figure E.3). Similar non-exponential temperature dependence in resistivity and Hall coefficient data has been seen observed in other materials and attributed to variable range hopping (VRH). VRH is commonly observed in disordered systems and is identified by its characteristic ln resistivity vs $T^{-1/4}$ temperature dependency.[67–72]

The low temperature transport data from all heterostructures was fit with a VRH model assuming that a single band approximation at low temperatures. The resistivity data was fit to equation 1:

$$\rho(T) = \rho_o \exp[(T_M / T)^{1/4}] \qquad \text{(equation 8.1)}$$

where $\rho(T)$ is the resistivity as a function of temperature, ρ_o is the resistivity when all of the carriers are mobile, T is the temperature, and T_M is a characteristic temperature related to the energy needed for hopping to occur.[70] The temperature dependence of the Hall coefficients was fit to equation 8.2:

$$R_H = \frac{-1}{|e|\, n(T)} = -\left(\frac{\exp\left[\left(\frac{T_M}{T}\right)^{\frac{1}{4}}\right]}{|e|\, n_0} \right) \qquad \text{(equation 8.2)}$$

where n(T) is the number of mobile carriers and n_o is the total number of carriers that can become mobile. $n_o = 1/\rho_o e\mu$ where μ is the mobility. These equations fit the transport data below 150 K for all values of q well (Figure 8.5b, 8.5c, 8.5d).

As shown in Figure 8.6, the fitted n_o values generally decrease as the number of $TiSe_2$ layers in the unit cell increases. The carriers

donated by SnSe to adjacent $TiSe_2$ layers ($n_{SnSe \rightarrow TiSe2}$) are diluted by additional $TiSe_2$ layers as q increases. If the amount of charge donated is constant in this family of compounds, an estimate for $n_{SnSe \rightarrow TiSe2}$ would be the value of n_o in the $[(SnSe)_{1+\delta}]_1[TiSe_2]_1$ compound. This value is consistent with previous estimates of the amount of charge donated from SnSe or PbSe layers to $TiSe_2$ layers.[51,52,65] The amount of charge donated is about $^1/_{10}$ of an electron per SnSe bilayer, which suggests that there is a significant electrostatic interaction between the constituent layers that helps to stabilize these compounds. n_o would vary as $n_{SnSe \rightarrow TiSe2}/\ q+1$, where q is the number of $TiSe_2$ layers in the heterostructures if the amount of charge donated was constant. The calculated values from this simple model consistently underestimate the n_o values derived from the fits to the data, suggesting that the amount of charge donation increases as q increases (see Figure 8.6). Defects in $TiSe_2$ layers also become an increasingly important source of potential carriers as q increases. The values of T_M obtained from the fits increase systematically as q increases (see table 8.2). The increase in T_M values correlates with a decrease in the average carrier concentration, suggesting that decreased screening causes an increase in localization. Edwards and Sienko correlated the behavior of many systems that undergo a metal to non-metal transition,[73] showing that carriers become localized when the product of the carrier concentration and the effective Bohr radius reaches a critical value. The behavior observed here suggests that a metal to non-metal transition is occurring, in part driven by disorder, as carrier concentration is decreased. Further analysis looking at the derivatives of conductivity has been proposed by Mobius to determine the origin of the metal to non-metal transition but requires careful temperature equilibration before transport properties are measured.[74]

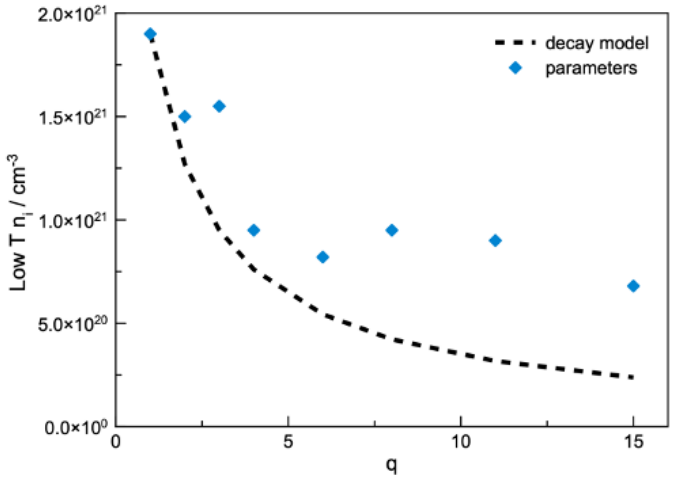

Figure 8.6. The values of the number of carriers that can become mobile for the low temperature activated process, n_o, plotted as a function of the number of $TiSe_2$ layers in the sample. n_o values were obtained by fitting the low temperature transport data using a single band, variable range hopping model. The dashed line assumes that n_o should vary as $n_{SnSe \rightarrow TiSe2} / q + 1$, where q is the number of $TiSe_2$ layers in the heterostructures and use the $n_{SnSe \rightarrow TiSe2}$ obtained from the $[(SnSe)_{1+\delta}]_1[TiSe_2]_1$ compound.

Mobility values were calculated directly from the resistivity and Hall data at low temperatures where electrons dominate the transport behavior. The average mobility values in the low temperature regime are given in Table 8.2. Values range from 2.85 $cm^2v^{-1}s^{-1}$ to 5.0 $cm^2v^{-1}s^{-1}$ with an average value of 4.0(8) $cm^2v^{-1}s^{-1}$ and do not systematically change as the number of $TiSe_2$ layers is varied. These mobility values are similar to those reported previously for $[(SnSe)_{1+\delta}]_m[TiSe_2]_q$ misfit layer compounds and low compared to values previously reported for bulk and thin film $TiSe_2$.[26,31,75]

Table 8.2. Parameters obtained for fits of the temperature dependent Hall coefficient and resistivity transport data. Parameters we determined assuming charge transfer from SnSe to $TiSe_2$ results in carriers that are localized at low temperature due to variable range hopping and at high temperatures holes and additional electrons are created due to activation of carrier across a band gap requiring a 2-carrier model. The low temperature parameters were used to fit the VRH model and the 2-carrier model with VRH at low temperatures.

q	μ_h / $cm^2\ v^{-1}\ s^{-1}$	μ_e / $cm^2\ v^{-1}\ s^{-1}$		n_i / cm^{-3}		E_a / meV	T_m / K
	High T	High T	Low T	High T	Low T		
1	NA	NA	3.75	NA	1.9×10^{21}	NA	0.5
2	NA	NA	4.4	NA	1.5×10^{21}	NA	2
3	5	1	3.8	3.70×10^{21}	1.55×10^{21}	110	11
4	6	1	3.8	5.92×10^{21}	9.5×10^{20}	107	7
6	6.5	1	5.0	8.46×10^{21}	8.2×10^{20}	107	4
8	5	1	3.1	9.87×10^{21}	9.5×10^{20}	113	120
11	5.5	1	2.85	1.11×10^{22}	9.0×10^{20}	115	300
15	5.4	1	4.9	1.20×10^{22}	6.8×10^{20}	113	120

The Hall coefficient data above 150 K for samples with a large number of $TiSe_2$ layers in the repeating unit cell suggests that there is another process that results in the activation of additional carriers. Recently, Watson et al. suggested that the electrical properties of $TiSe_2$ are dominated by either electrons or holes depending on the temperature regime. At low temperatures the transport behavior of $TiSe_2$ is dominated by electrons from defects, but above 150 K activation of intrinsic carriers occurs, and holes become increasingly important in the transport. The influence of the activated holes becomes more pronounced due to their higher mobility relative to their electron counterparts.[76] We fit our transport data to the two-carrier model suggested by Watson et al., with an additional term for the electrons donated from SnSe to the $TiSe_2$ layers at low temperature:

$$R_H = \frac{[\mu_h{}^2 n_h - \mu_{e(highT)}{}^2 n_{e(highT)} - \mu_{e(lowT)}{}^2 n_{e(lowT)}}{\{|e|[\mu_h n_h + \mu_{e(highT)} n_{e(highT)} + \mu_{e(lowT)} n_{e(lowT)}]^2\}}$$

(equation 8.3).

In equation 8.3, μ_h, $\mu_{e(highT)}$ and $\mu_{e(lowT)}$ are the hole and electron mobilities, and n_h, $n_{e(lowT)}$, and $n_{e(lowT)}$ are the hole and electron carrier concentrations, respectively.[76] The mobility values were assumed to be temperature independent. This model is not sensitive to the mobility of the electrons created from the high temperature process because the larger number of electrons from the low temperature process dominate the average electron mobility. We assumed that the mobility values for the holes dominate the high temperature process due to their higher mobility, as suggested by Watson, and set μ_{elowT} = 1 $cm^2\ v^{-1}\ s^{-1}$. The hole concentration was assumed to come only from activation at high temperatures (equation 8.4),

$$n_h = n_{i(high\ T)}\ e^{[-Ea\ /kT]} \qquad \text{(equation 8.4).}$$

The electron concentration was assumed to be the sum of the low and high temperature carriers (equation 8.5):

$$n_e = n_{e(low\ T)} + n_{e(high\ T)} \qquad \text{(equation 8.5)}$$

where:

$$n_{e(low\ T)} = n_{i(low\ T)}/\exp[(T/T_M)^{1/4}] \qquad \text{(equation 8.6)}$$

$$n_{e(high\ T)} = n_{i(high\ T)}\ e^{[-Ea\ /kT]}. \qquad \text{(equation 8.7).}$$

The fits are not very sensitive to the value of $n_{i(high\ T)}$ due to the small temperature range for which there is data. We set $n_{i(high\ T)}$ to be close to the density of Se atoms in $TiSe_2$ (n_{TiSe2}). Since charge transfer between SnSe and $TiSe_2$ will modify the electronic structure of layers close to the interface, the fraction of bulk-like $TiSe_2$ in each unit cell varies as

$$[(q - x)/(q + 1)] \qquad \text{(equation 8.8)}$$

where q is the number of $TiSe_2$ layers in the unit cell, $q + 1$ is the total number of layers (SnSe + $TiSe_2$) in the unit cell, and x is the number of layers near the interface that do not behave as bulk $TiSe_2$ due to the charge transfer. Therefore,

$$n_{i(high\ T)} = n_{TiSe2}\,[(q - x)/(q + 1)]. \qquad \text{(equation 8.9)}$$

The high temperature carrier concentration, $n_{i(high\ T)}$, calculated with x = 2 gave the most constant values for the hole mobilities and high temperature activation energy (E_a) across all samples. This is reasonable since there are two $TiSe_2$ layers adjacent to SnSe which will be most impacted by the charge donated by SnSe to $TiSe_2$.

The model does reasonably well at fitting the temperature dependence of the Hall coefficients, with the solid lines in Figure 8.5b demonstrating the result of the fits for each sample. The low temperature fitted values for the low temperature T_M (Table 8.2), and the low temperature carrier concentration ($n_{i(low\ T)}$) (Figure 8.6) were used in these fits. The values for the hole mobilities and high temperature activation energy (E_a) are similar for all of the samples. The average activation energy for the high temperature carriers, ~ 0.11(1) eV, is similar to values previously reported for bulk $TiSe_2$.[77] The average hole mobility value, μ_h, is 5.4(1) $cm^2\ v^{-1}\ s^{-1}$, which is higher than values previously reported for the $[(SnSe)_{1+\delta}]_m[TiSe_2]_q$ misfit layer compounds[31] and lower than the range reported previously for $TiSe_2$.[26,75] The hole mobility needs to be higher than the mobility of the electrons created by excitation across the gap to reproduce the decreasing absolute value of the Hall coefficient observed as temperature increases.[76]

The resistivity is given by equation 8.10:

$$\rho\frac{1}{\sigma} = \frac{1}{[|e|(\mu_h n_h + \mu_{e(highT)} n_{e(highT)} + \mu_{e(lowT)} n_{e(lowT)})]} \qquad \text{(equation 8.10)}$$

where μ_h, n_h, μ_e and n_e are defined as described above. The values obtained for the carrier concentration, mobility, activation energy and characteristic hopping energy from fitting the Hall coefficient data to the two-carrier model (table 8.2) reproduce the low temperature resistivity data reasonable for all of the samples (Figure 8.5). This suggests that the resistivity can be described by a single carrier model in this temperature range. The agreement at high temperature is not good, as the model underestimates the resistivity. This suggest that the assumption of a temperature independent mobility is not valid.

8.3.4. Computational Calculations and Models

DFT was used to model the electronic structure of bulk SnSe, $TiSe_2$, the surfaces of each, and a large-scale epitaxial model of the $q = 1$ system to further understand the properties observed in the heterostructures. Following the computational procedure detailed in the materials and methods section, three key properties were obtained; i) the electronic band gaps of both bulk materials, ii) the work functions for slab models thereof, and iii) representative charge densities in both the slab and epitaxial models. Together, these properties provide additional and complimentary insights into the mechanism of charge donation in $[(SnSe)_{1+\delta}]_1[TiSe_2]_q$ heterostructures. The electronic band gaps of bulk SnSe and $TiSe_2$ were computed using the hybrid GGA functional, HSE06,[78] known to perform well for narrow gap semiconductors. As informed by the crystallography, SnSe is modeled as face-centered cubic, whose band gap is predicted to be 0.5 eV. Other crystal polymorphs were also explored, and their band gaps are presented in the Supporting Information Table E.1. The workfunction (Φ = 4.3 eV) was recovered using a surface slab model and permits the alignment of the valence band energy, and therefore computational Fermi level, to the vacuum (Figure 8.7). A seven layer slab was used to sufficiently account for the bulk, as well as its surface, and was aligned using a method previously

described.[44] A similar procedure was performed for $TiSe_2$, however, both GGA and hybrid GGA approaches are known to predict bulk metallicity in $TiSe_2$,[79,80] despite experimental evidence for a thermally activated transport mechanism. Indeed, a narrow band gap (200-300 meV) is recovered using a GW approach,[81] but the procedure does not significantly augment the workfunction. Here, the nature of the gap is less important that the workfunction. Hence, $TiSe_2$ is presented as a bulk metal with a workfunction of 5.5 eV (Figure 8.7). A comparison of these computed workfunctions suggests that spontaneous charge transfer should occur between SnSe and $TiSe_2$, as the valence band of the former lays above the conduction band of the latter.

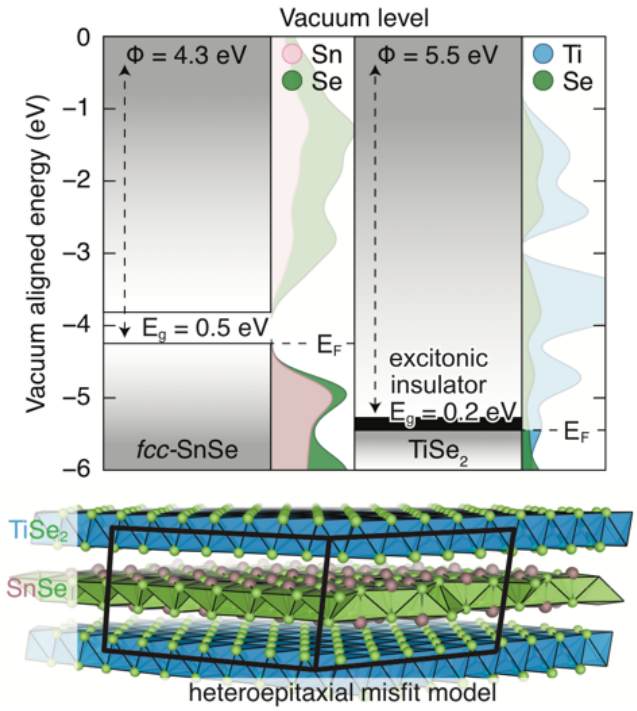

Figure 8.7. Vacuum aligned Density of States for SnSe and $TiSe_2$ slab models. The frontier valence of SnSe is ~1.2 eV above that of $TiSe_2$, indicating that charge transfer from SnSe to $TiSe_2$ would occur at the interface between them.

To test this hypothesis, a lattice matched $[(SnSe)_{1+\delta}]_1[TiSe_2]_1$ model was constructed, minimizing the lattice mismatch by expanding the unit in the a-b plane to a 6 x 7 supercell as shown in Figure 7. A Bader

charge analysis[46] was done on bulk SnSe and $TiSe_2$ and the lattice matched $[(SnSe)_{1+\delta}]_1[TiSe_2]_1$ to provides a quantitative estimate of the extent of charge transfer between the materials. In the bulk structures, positive charges are observed on the cations and negative charges are observed on the anions. The smaller negative charge on the Se in $TiSe_2$ reflects the covalent hybridization of the Ti and Se orbitals in this compound. By comparing the charges in the bulk structures with the charges calculated for the lattice matched heterostructure, a charge transfer from SnSe to $TiSe_2$ is observed in the heterostructure (Table 3). The magnitude of the electron transfer from SnSe to $TiSe_2$ is approximately 10%, in excellent agreement with the experimental observation of $1/10^{th}$ of an electron per formula unit. Interestingly, the added charge in $TiSe_2$ is localized on the Se rather than the Ti, reflecting the extent of covalent character in the bonding of this compound. There is a net "ionic" bond between the layers of SnSe and $TiSe_2$, with higher electron density in the lone pair of the Se atoms in $TiSe_2$ and a positive charge in the SnSe planes. This picture agrees well with the analysis of the transport properties, which suggests that the two $TiSe_2$ layers adjacent to SnSe have different transport properties than those not adjacent to SnSe. The added charge to the conduction band indicated in the calculation agrees well with the metallic like conductivities observed for the small *q* heterostructures above the hopping temperature. The calculation also provides a basis for the model shown in Figure 8.7. A calculation of the stabilization energy of the ionic "bond" between the layers is surprisingly high, 3.6 eV, suggesting that this interaction is a key factor in stabilizing the heterostructures. This ionic interaction between layers makes $[(SnSe)_{1+\delta}]_1[TiSe_2]_1$ more stable than a physical mixture of SnSe and $TiSe_2$ by ~ 0.09 eV, consistent with the thermodynamic stability of the known misfit layer compound.[15]

Table 8.3. Average atomic charge of bulk SnSe, bulk $TiSe_2$, and the average charge transfer between them in the heterojunction.

	Avg. Charge in Bulk / $Bohr^{-3}$	Avg. Charge in Heterostructure / $Bohr^{-3}$	Avg. Charge Transfer / $Bohr^{-3}$
Sn	0.777	0.860	0.083
Ti	1.341	1.345	0.004
Se in SnSe	-0.777	-0.729	0.048
Se in $TiSe_2$	-0.671	-0.747	-0.076

8.4. CONCLUSION

A series of compounds $[(SnSe)_{1+\delta}]_1[TiSe_2]_q$ were prepared and the structural data indicates that the structure of the constituent layers are similar in all of the heterostructures. The electrical properties suggest that charge donation from the SnSe to the $TiSe_2$ layers occurs, resulting in metallic behavior for samples with a low number of $TiSe_2$ layers. The carrier concentration decreases as the number of $TiSe_2$ layers increase. Localization of the carriers occurs at low temperature, with the temperature required to activate the hopping of these carriers increasing as the $TiSe_2$ layer thickness is increased. DFT calculations show that the valence band of SnSe is higher in energy than the conduction band of $TiSe_2$, supporting the experimentally suggested charge transfer from SnSe to $TiSe_2$. The calculations suggest that the charge transfer between the constituents contributes a significant “ionic” stabilization of these heterostructures, which may be the key factor in their kinetic stability. Similar charge transfer effects will be present in all heterostructures to equalize the chemical potential and understanding how they modify properties is necessary for the synthesis of novel materials with designer properties.

8.5. BRIDGE

Chapter 8 explored the interaction and charge donation between adjacent layers and the influence it has on the heterostructure's transport properties. It was found that charge donation occurs from SnSe to the $TiSe_2$ blocks adjacent to it, creating a three-layer conductive material. This material is inherently different from the remaining $TiSe_2$ layers that exist depending on the nanoarchitecture of the $[(SnSe)_{1+\delta}]_1[TiSe_2]_q$ heterostructure in question. At low temperatures the transport behavior is dominated by variable range hopping as a result of the charge donation. At high temperatures the transport is dominated by the remaining $TiSe_2$ that retains its inherent properties. This influence of the charge donation was further investigated in Chapter 9 by increasing the number of SnSe and $TiSe_2$ layers in the repeating unit at the same time. By keeping the stoichiometry constant, it allows the experiments to solely probe the influence of layer size effects in heterostructures.

CHAPTER IX

INVESTIGATING SIZE EFFECTS IN $[(SNSE)_{1+\delta}]_M[TISE_2]_N$ HETEROSTRUCTURE COMPOUNDS

9.0. AUTHORSHIP STATEMENT

At this time, the work in this chapter is unpublished, but a manuscript is in preparation. Coauthors of this work include Aaron Miller, Dylan Bardgett, Sage Bauers, Jeffrey Ditto, and David Johnson. I am the primary author on this work. Aaron Miller assisted in the data analysis and manuscript preparation. Dylan Bardgett aided in the data collection and analysis. Sage Bauers aided in the synthesis, characterization, and data collection of the samples. Jeffrey Ditto prepared the lamella and collected the HAADF-STEM images. David Johnson is my advisor who contributed to the data analysis and manuscript preparation.

9.1. INTRODUCTION

The ability to systematically tune properties in materials has been a long sought-after objective in materials science.[1] Altering the properties of a molecule in traditional organic synthesis is a matter of restricting the ways reactants may combine; whether by concentration, reagent choice, or reaction condition, these experimental parameters are manipulated to push the reaction towards the desired product.[2–9] However, for an inorganic synthesis of a layered material composed of a small number of elements, many of those parameters are invariant during synthesis. One method by which inorganic synthesis has adapted to these limitations is the exploration of size dependent properties. Quantum dots,[10–12] nanostructures,[13] and alloys[14–16] are well known examples of how changing the size and interfacial properties of a material can influence the observed properties. The idea of manipulating properties in thin film materials has recently been realized with the isolation of graphene and

subsequent 2D materials. Because of the importance of interlayer interactions in these systems, removing abutting layers can greatly influence the observed electronic,[17,18] optical,[19,20] or magnetic properties.[21,22] The influence of this removal is magnified at the monolayer limit.

In this investigation, the influence of size and interface was investigated for a series of $[(SnSe)_{1+\delta}]_m[TiSe_2]_n$ heterostructures. In this series the ratio of SnSe to $TiSe_2$ layers was held constant, but the total number of layers in the repeating unit was systematically increased. This system was chosen due to the previously reported strong interfacial interaction between SnSe and $TiSe_2$.[23–27] It was found that when the repeating unit size is small, the interface interaction dominates both the structure and the transport behavior of the material, creating a novel, conductive material "block". As the repeating unit size increases and there is more non-interfacial SnSe and $TiSe_2$ present in the sample, the heterostructure begins to act as a composite of SnSe, $Tise_2$ and the novel conductive block. Both the constituent structure of SnSe and the transport behavior are influenced by the unit cell size. Temperature-dependent measurements confirm this complex behavior in both structure and transport. For small repeating units, electrons are the dominant carrier at all temperatures measured, but as the unit cell size increases, the dominant carrier type begins to vary with temperature. Finally, films with the largest unit cells are dominated by holes over the entire temperature regime. While more studies are required to fully understand the origin of this complex behavior, this series of compounds demonstrates the ability to manipulate electrical transport properties with heterostructure nanoarchitecture.

9.2. MATERIALS AND METHODS

$([SnSe]_{1+\delta})_m(TiSe_2)_n$ heterostructures with $m = n = 1$ - 5, 6, 8 were formed from layered amorphous precursor samples that were prepared

via the Modulated Elemental Reactants (MER) method on a custom-built, high vacuum (10^{-7} torr) physical vapor deposition chamber as described previously.[28,29] The precursors were deposited with a layer structure mimicking that of the desired isomer. Desired sample layer architectures were achieved by alternating the elements deposited via pneumatic shutters controlled by an IC6 deposition controller directed by customized LabVIEW program.[30] Electron beam guns were used to vaporize Sn and Ti from elemental sources. A Knudson effusion cell was used to deposit Se. Quartz crystal microbalances were used to monitor the deposition rates and the relative amount of material deposited. The amount of material required to crystallize a single layer of either SnSe or $TiSe_2$ was calibrated using a combination of X-ray fluorescence (XRF), X-ray reflectivity (XRR), specular and in-plane X-ray diffraction (XRD). Samples characterized via diffraction were deposited onto Si wafers with a native SiO_2 layer, while samples for electrical transport measurements were deposited onto fused silica substrates. Once deposited, samples were annealed in a N_2 atmosphere to promote crystallization of the desired product.

X-ray techniques were used to structurally characterize the $([SnSe]_{1+\delta})_m(TiSe_2)_n$ heterostructures with $m = n$, study the structural evolution of the films upon annealing, and determine the relative composition of the samples. The superstructures of the various compounds were monitored via specular XRD and the thickness and roughness of the films were observed via XRR. Both XRR and XRD were collected on a Bruker D8-Discover diffractometer using Cu-K_a radiation (λ = 0.15418 nm). Total film thickness was calculated by applying modified Braggs law to the data extracted from the XRR pattern. The *c*-axis lattice parameters were determined from applying Bragg's law to Bragg reflections in the specular diffraction pattern. Constituent crystal structures were characterized with in-plane XRD on a Rigaku SmartLab

diffractometer (Cu-K*a* radiation) using the in-plane general resolution with parallel beam optics. The in-plane lattice parameters (*a* and *b*) were determined from constituent reflection position in the in-plane diffraction pattern and full pattern fitting using the Fullprof suite.[31] Chemical composition was monitored with XRF by comparing relative intensities of elemental signals. XRF measurements were collected in-house on a Rigaku ZSX Primus II wavelength dispersive X-ray fluorescence spectrometer with a Rhodium X-ray source. The data was analyzed using both the ZSX- analyzed results software that was originally calibrated with data collected from electron microprobe analysis and a house developed method to convert XRF intensity to the number of atoms per unit area of an element.[32,33]

Real space images with atomic resolution of the crystallized $([SnSe]_{1+\delta})_m(TiSe_2)_n$ heterostructures were collected by high angle annular dark field scanning transmission electron microscopy (HAADF-STEM). Images were collected at the Pacific Northwest National Laboratory using a probe aberration corrected FEI Titan 80-300 STEM. An FEI Helios 600 Ga^+ focused ion beam was used to prepare electron transparent cross sectional lamellas of the samples. A procedure similar to the Wedge Prep Method was used with final thinning and polishing performed using 2 keV ions.[34]

To measure electrical properties, films were deposited onto masked quartz substrates to create a diagonal cross geometry optimal for use of the standard van der Pauw technique.[35–37] Resistivity and Hall coefficient measurements were collected in a closed-cycle He cryostat between 20 and 295 K using a custom-made Hall measurement system. Hall coefficients were determined by averaging the Hall voltage vs magnetic field slopes between 4 sets of contacts. The maximum magnetic field strength was 1.6 T and a constant current less than 0.0001 A was sourced. Resistivity measurements were gathered using the van der

Pauw method sourcing a current between 0 and 0.001 A. Room temperature Seebeck coefficients were measured using a home-built measurement system. One half of the sample was cooled slightly (the initial temperature difference was less than 2 °C, and V/ ΔT curves were collected as the temperature equilibrated across the sample. Thermocouples were used to measure each temperature and the individual metal junctions were used to measure voltages across the films. The measured slopes were corrected for the Seebeck coefficients of the copper and the constantan measurement junctions and the two corrected values agreed to within 3 μV K^{-1}.

9.3. RESULTS AND DISCUSSION

9.3.1. Synthesis

A series of designed precursors were deposited by physical vapor deposition with the objective of preparing $[(SnSe)_{1+\delta}]_m[TiSe_2]_n$ ($1 \leq m, n \leq 8$) heterostructures. Precursors were formed by systematically depositing Sn|Se layers with a 1:1 ratio to form SnSe bilayers and Ti|Se layers with a 1:2 ratio to form $TiSe_2$ trilayers. The thickness of the deposited Ti|Se and Sn|Se precursor layers was representative of the thickness expected for crystallized layers of the $TiSe_2$ trilayer and SnSe bilayer, respectively. The number of Sn|Se and Ti|Se precursor layers in the repeat unit ranged from 1 – 8, but always maintain the same ratio between the two constituents. The repeating unit sequence for each isomer was deposited as many times as necessary to make ~50 nm films. The amount of material required in each constituent layer was determined by an iterative calibration process using X-ray fluorescence (XRF), X-ray reflectivity (XRR), and X-ray diffraction (XRD).[33] Formation of the targeted compounds was monitored and confirmed by the same x-ray techniques listed above. An annealing study was conducted on the *m, n* = 3 sample, to determine the optimal annealing conditions for the system. Ideally, this allows the elemental layers to diffuse sufficiently to form the

desired product without disproportionating to form the thermodynamic product. Based on the XRR and XRD scans shown in Figure F.1, the ideal annealing temperature was determined to be 350 °C for 30 m in an N_2 environment, as evidenced by the narrowest and most intense reflections observed at this temperature.

9.3.2. Structure

Figure 9.1 shows the annealed XRR scans for the $m = n$, $[(SnSe)_{1+\delta}]_m[TiSe_2]_n$, heterostructures. In addition to the Bragg maxima corresponding to *00l* reflections of the layered structure, Kiessig fringes, occurring at lower angles correspond to interference between the top and bottom of the film, and Laue oscillations, occurring at higher angles result from the finite number of unit cells in the film, were observed in the XRR spectra. For all of the samples, the number of Kiessig fringes is equal to the number of Laue oscillations indicating that the entire film consists of the targeted heterostructure sequence. The number of deposited and crystallized repeat units are shown in Table 9.1. Samples with the largest number of constituent layers in their repeating unit do not lose any layers upon annealing, while samples with smaller repeating units lose 1 or 2 layers upon annealing. The loss of a layer is likely the result of not having enough material in each as-deposited layer to form the targeted heterostructure. If this is the case, it is much easier for thinner repeating units to rearrange to form fewer repeats with the correct amount of material per layer relative to thicker repeating units, which must move further and disperse more material to achieve the same outcome. As expected, the 2θ values of the first order Bragg peaks decrease as the number of SnSe and $TiSe_2$ layers increase, corresponding to a doubling of *c*-lattice parameter with each increase in *m* and *n.*

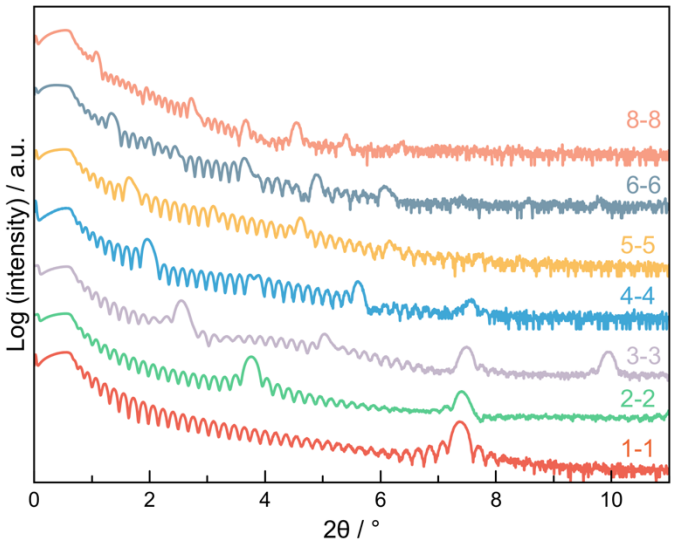

Figure 9.1. X-ray reflectivity patterns of the series of layered compounds, $[(SnSe)_{1+\delta}]_m[TiSe_2]_n$, $m = n$, after annealing at 350°C for 30 minutes in a N_2 environment.

Table 9.1. Comparison of Deposited vs. Crystallized Repeating Units (RU's) for the $[(SnSe)_{1+\delta}]_m[TiSe_2]_n$ series

m,n	RU's deposited	RU's crystallized
1	42	39
2	21	20
3	14	13
4	11	11
5	9	9
6	8	8
8	8	8

XRF data was collected for all $[(SnSe)_{1+\delta}]_m[TiSe_2]_n$ heterostructures to determine the amount of material present in each compound. To determine the number of atoms / Å^2 of each element in the film, the raw XRF intensity was integrated, background corrected, and converted using a previously determined calibration curve relating XRF signal to atomic areal density of each element.[33] The total atoms / Å^2 for each element was normalized to the total number of crystallized SnSe and $TiSe_2$ layers in each heterostructure. This value was obtained from the product of the number of layers in each repeat unit and the number of

crystallized repeat units, and is used to determine how close the amount of material in each sample was relative to the targeted values. Figure 9.2 shows both the targeted atoms / Å^2 for each element and the measured values corresponding to each heterostructure. For these samples, there is good agreement between the amount of measured material and the amount targeted. All of the samples have approximately the targeted amount of Sn and Ti atoms / Å^2. There is a larger variation in the amount of Se atoms / Å^2 in each sample, but it is usually in excess, so the samples still had enough material to form their targeted structure. Additional annealing at low temperatures would result in the removal of the excess Se without disturbing the nanoarchitecture of the material. This good agreement with the targeted values upon normalization to the number of repeating units supports the proposed rearrangement for the lower *m, n* samples to have fewer repeating units than deposited. Samples that did not have enough initial material deposited to form the targeted number of repeating units moved material to lose layers during annealing, resulting in fewer repeating units with the correct atoms / Å^2, as was observed in the XRR patterns.

To further characterize the nanoarchitecture of each film, specular diffraction patterns were collected for all of the $[(SnSe)_{1+\delta}]_m[TiSe_2]_n$ heterostructures and are shown in Figure 9.3. As the values of *m* and *n* increase, the position of the first Bragg reflection shifts to lower angles and the number of reflections observed within the same angular range increases, as expected for a heterostructure with a larger repeating unit cell size. All observed Bragg reflections in the specular diffraction pattern can be index to 00*l* indices that match values expected for the series of targeted heterostructure, indicating that the samples are crystallographically aligned with the *c*-axis lattice parameter perpendicular to the substrate. Based on Le Bail fits of the specular diffraction patterns, the *c*-axis lattice parameters were calculated for

each of the $[(SnSe)_{1+\delta}]_m[TiSe_2]_n$ heterostructures and are shown in Table 9.2. Because the thickness increases systematically with the number of SnSe and $TiSe_2$ layers in each repeating unit, the *c*-axis lattice parameter was plotted as a function of the number of constituent layers in the repeating unit to determine the combined thickness of a single SnSe and $TiSe_2$ layer. A linear regression of *m, n* vs. the calculated *c*-axis lattice parameters, shown in Figure 9.3b, gives a slope of 11.825(4) Å. This agrees well with, 12.05 Å, the value previously reported for the *c*- axis lattice parameter of the $[(SnSe)_{1.2}]_1[TiSe_2]_1$ heterostructure.[24,25,38] The small discrepancy has been previously noted in $([PbSe]_{1+\delta})_m(TiSe_2)_n$ nanolaminates and was attributed to thickening of existing structures as opposed to forming additional rock salt-dichalcogenide interfaces.[39] The regular increase in layer thicknesses and sharp diffraction peaks indicate the crystallized heterostructures contain the targeted nanoarchitecture, but does not inform on the structure of each constituent.

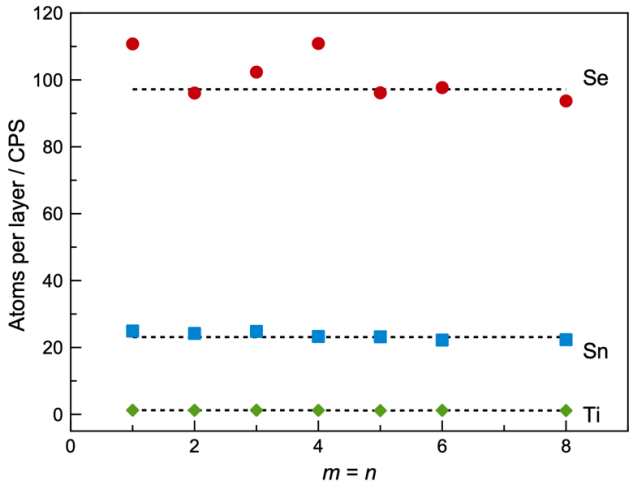

Figure 9.2. XRF data was collected from the annealed heterostructures and is plotted in atoms / Å^2, normalized to the total number of crystallized SnSe and $TiSe_2$ layers that make up each nanoarchitecture. The integrated and background corrected values normalized for the number of crystallized repeat units for each element are shown with a symbol (red circle – Se, blue square – Sn, green triangle – Ti) and the targeted value for each element is shown as a dotted line.

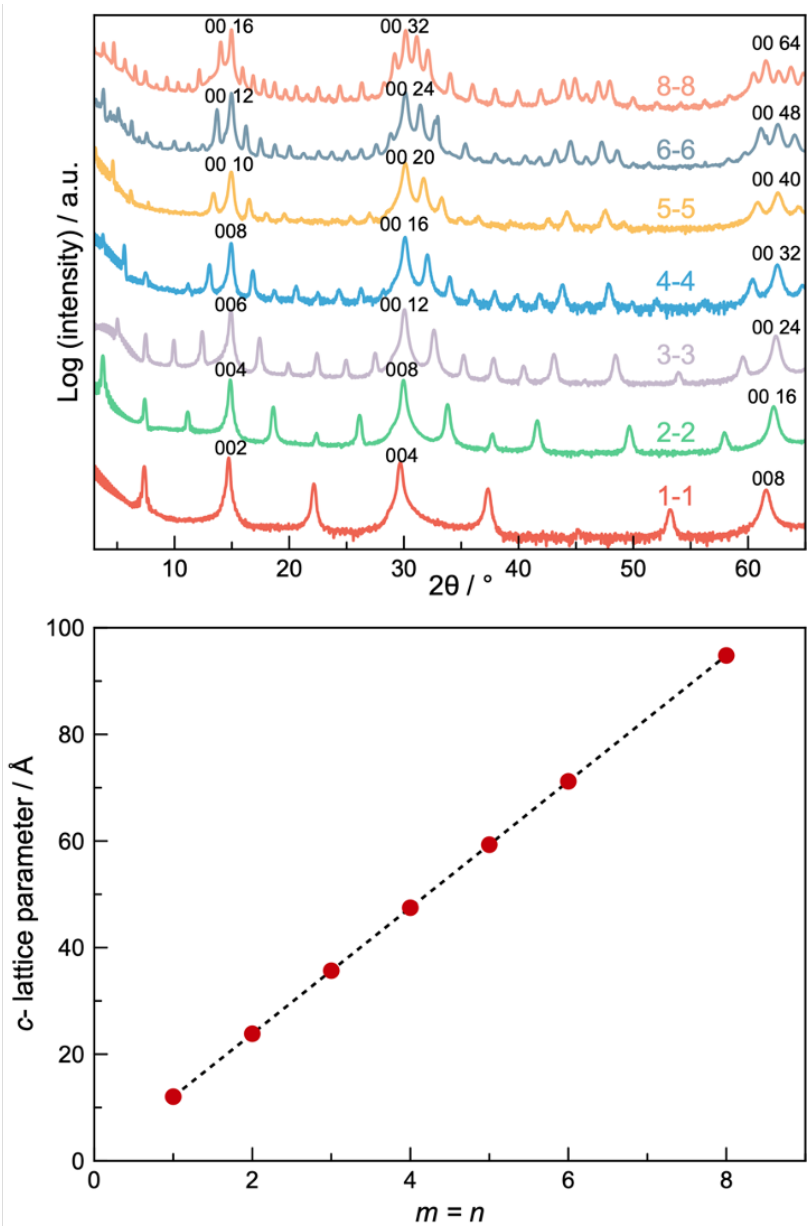

Figure 9.3. Specular X-ray diffraction patterns of annealed $[(SnSe)_{1+\delta}]_m[TiSe_2]_n$ heterostructures (a.) and a linear regression of the *c*-lattice parameter vs. the number of SnSe and $TiSe_2$ layers in each repeating unit (b.).

Grazing incidence in-plane diffraction patterns were collected from the $[(SnSe)_{1+\delta}]_m[TiSe_2]_n$ heterostructures to characterize the basal plane structure of the two constituents that comprise the materials, shown in Figure 9.4. All reflections can be indexed to either a rectangular or hexagonal unit cell, except those marked with an asterisk, which

indicates an impurity phase with lattice parameters matching those expected for $SnSe_2$. This impurity accounts for the excess Se observed in the calculated atoms / Å^2 and can be eliminated by annealing the sample for longer times at a lower temperature after annealing at the optimal temperature of 350 °C. For all heterostructures, the hexagonal unit cell has an *a*-axis lattice parameter that matches what is expected for $TiSe_2$.[16,24,25,40–44] The rectangular unit cell matches what has previously been published for SnSe, but the size of the unit cell depends on the number of SnSe layers contained in the repeating unit.[24,25,45–49] The change in the SnSe basal plane structure is a result of the interplay between bulk and surface free energy.[24,25] The in-plane lattice parameters, shown in Table 9.2, were determined from full pattern Le Bail fits. SnSe in the $[(SnSe)_{1.2}]_1[TiSe_2]_1$ heterostructure has a distinct tetragonal basal plane, indicated by the split peaks in the diffraction pattern.[24,25] This pattern must be indexed to a unit cell that is larger than bulk SnSe, with *a*- and *b*- lattice parameters of 6.094 and 5.974 Å, respectively. This distortion is distinct to heterostructures containing $TiSe_2$ and SnSe layers, as other SnSe containing systems, including ($[(SnSe)_{1+\delta}]_m[MSe_2]_n$ where M = V, Mo, Nb) typically converge to $a = b$ as m approaches 1.[24,25,48–51] The in-plane diffraction patterns for the heterostructures with $m, n \geq 2$ are distinctly different from that observed for the $[(SnSe)_{1+\delta}]_1[TiSe_2]_1$ compound. These patterns can still be fitted to a rectangular basal plane structure, but are indexed to a smaller unit cell, as can be observed in Figure 9.4 and the lattice parameters shown in Table 9.2. This phenomenon is discussed at length elsewhere,[24,25] but is indicated by slight shifts in SnSe reflections, particularly at 96.6° and 101.5°, and changes to the splitting and asymmetry of the reflections. This change in lattice parameters is best explained by a face-centered to body-centered symmetry shift (as observed in the schematic shown in Figure 9.4a) and a corresponding ~ $\frac{1}{\sqrt{2}}$ ratio between lattice parameters

which also fits the expected systematic absences observed in the indexing of Figure 9.4.

Table 9.2. Heterostructure *c*-axis lattice parameter and in-plane lattice parameters for SnSe and $TiSe_2$ of $[(SnSe)_{1+\delta}]_m[TiSe_2]_n$ heterostructures determined from Le Bail fits.

m, *n*	*c* (Å)	*a* $TiSe_2$ (Å)	*a* SnSe (Å)	*b* SnSe (Å)
1	12.04(1)	3.5589(5)	6.0966(9)	5.9795(8)
2	23.84(1)	3.5667(3)	4.275(1)	4.272(1)
3	35.67(1)	3.5702(3)	4.2960(7)	4.2742(7)
4	47.48(1)	3.5654(2)	4.3114(6)	4.2465(5)
5	59.30(3)	3.5684(2)	4.3173(5)	4.2440(4)
6	71.18(2)	3.5666(1)	4.3265(3)	4.2372(2)
8	94.80(1)	3.5674(1)	4.3382(3)	4.2301(2)

While the $[(SnSe)_{1+\delta}]_m[TiSe_2]_n$ heterostructures with $m, n \geq 2$ are all indexed to the same unit cell, there are distortions within the lattice parameters that occur as *m* and *n* increase. Figure 9.4b shows the increase in the *a*-axis and decrease in the *b*-axis lattice parameters with increasing *m* and *n* values for all heterostructures with $m, n \geq 2$. For heterostructures where $2 \leq m, n \leq 4$, the unit cell approaches square, and splitting of Bragg reflections into two distinct *hk*0 peaks is no longer observed. However, these reflections are broadened, indicating that the unit cell is still rectangular. In heterostructures where $5 \leq m, n \leq 8$, the smaller redefined unit cell is maintained, but splitting of the SnSe peaks is observed again, becoming more rectangular with increasing *m, n*. As expected, the number of SnSe layers increases, the in-plane lattice parameters approach those reported for bulk SnSe, $a = 4.445(1)$ and $b = 4.153(1)$.[45] The convergence to agreement with bulk parameters with increasing *m* suggests that bulk SnSe's orthorhombic unit cell is more energetically favorable relative to the strained structure observed for the $m, n = 1$ heterostructure.[24,25,45–47] This is accompanied by a

corresponding decrease in lattice strain caused by fewer interactions at SnSe|$TiSe_2$ interfaces.

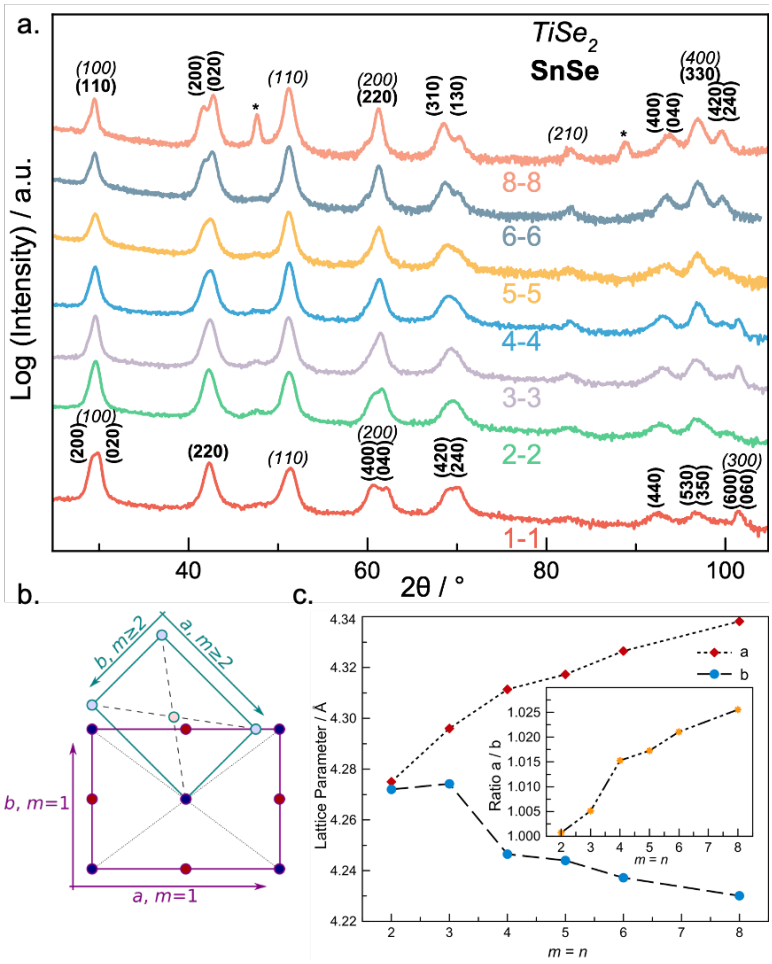

Figure 9.4. Specular X-ray diffraction patterns of annealed $[(SnSe)_{1+\delta}]_m[TiSe_2]_n$ heterostructures (a.) and a linear regression of the *c*-lattice parameter vs. the number of SnSe and $TiSe_2$ layers in each repeating unit (b.).

HAADF-STEM images of the *m, n* = 1, 2, and 3 heterostructures provide a real-space picture of the material's structure and are shown in Figure 9.5 A-C, D-H, and E, respectively. Initial inspection shows regular layering with sharp interfaces between rock salt and dichalcogenide layers. The global layering reflects the structure expected from each precursor with periodic layering defects due to slight precursor non-stoichiometry (for example in the lower-right of the *m, n* = 3 image,

Figure 9.5e). Zone axes of the constituent lattices manifest as bright distinct points in the image, with the brighter layers corresponding to the heavier Sn-containing constituent. Within each structure, multiple zone axis orientations are visible, indicating some degree of interlayer rotational disorder.

Interestingly, the $m = n = 1$ structure exhibits far less misregistration, appearing nearly epitaxial for several adjacent layers. In the representative HAADF-STEM images collected from the $[(SnSe)_{1.2}]_1[TiSe_2]_1$ heterostructure, two primary regions demonstrate templating between the constituents, shown in panes B and C of Figure 9.5. These have corresponding labels to the right of the figure that indicate the constituent and identity of the observed zone axis. Octahedrally coordinated $TiSe_2$ is a dumbbell-like structure when the (110) and (1-20) planes are visible. On the other hand, this structure appears as vertical bars when looking across the (100) and (1-10) planes. SnSe is visible as either indistinguishable 'smears' due to being off-axis or distinct points corresponding to the (100) plane. The off-axis SnSe is regularly seen adjacent to the $TiSe_2$ (100)/(1-10) planes whereas the (100) SnSe plane is seen adjacent to the $TiSe_2$ (110)/(1-20) planes. An interfacial region where the layers cleanly change from one sequence to the next is also visible.

This layering can be understood by considering the templating mechanism between $TiSe_2$ and SnSe.[24,25] The lattice parameters of SnSe and $TiSe_2$ for $m, n = 1$ (Table 9.2) show a $\sqrt{3}$ ratio between a-lattice parameters, which corresponds exactly with the expected ratio for the formation of a commensurate interface between tetragonal and hexagonal structures along the <100> and <1 -1 0> directions, respectively. This also agrees with the STEM image seen in Figure 9.5C. Considering the distortion and alignment of the SnSe lattice to accommodate this orientation, the region in Figure 9.5B is also

understood by considering the $TiSe_2$ <100> axis, which appears as off zone-axis in SnSe. The $TiSe_2$ interface between the two may occur both looking along the $TiSe_2$ (1-10) plane or $TiSe_2$ (100) plane, which would result in SnSe on or off zone axis as observed in the lower and upper SnSe layers, respectively. These distortions are likely driven by interface energetics and seem to be unique to 'soft' SnSe layers paired with $TiSe_2$, which has a larger *a*-lattice parameter than other dichalcogenides.[25]

In the *m, n* = 2 heterostructure, several structural details can be seen within the SnSe layers. Looking down the <110> axis of SnSe in Figure 9.5F, the typical α-SnSe structure is observed, highlighted by the stacked triangle pointing in the same direction. On the other hand, Figure 9.5h shows another region of the film where β-SnSe is seen looking down the same axis, as highlighted by the stacked triangles pointing in the opposite direction. Figure 9.5g highlights a slip plane occurring along the <100> axis in which one bilayer of SnSe is offset from the bilayer below it so the atoms lie in between each other. This misalignment is likely a result of the SnSe layers trying to align with $TiSe_2$ layers on either side of it. The $TiSe_2$ layers above and below the SnSe highlighted in Figure 9.5g, show both dumbbell and vertical bar structures, which correspond to the (110) and (1-10) planes, both of which could be visible when forming the commensurate interface with SnSe. The various defects and structural irregularities observed in the *m*, *n* = 2 structure are also observed in the *m*, *n* = 3 structure and hint at the complex environment the compounds nucleate in. Unlike the *m*, *n* = 1 compound, the introduction of SnSe and $TiSe_2$ layers that lack an adjacent SnSe|$TiSe_2$ interface allows for unique behavior due to a complication of the free energy landscape and balancing of interface and volume terms in approximately equal amounts. These unique stacking structures indicate the occurrence of a strong interaction between the

two constituents, which likely influences the observed transport properties for these materials.

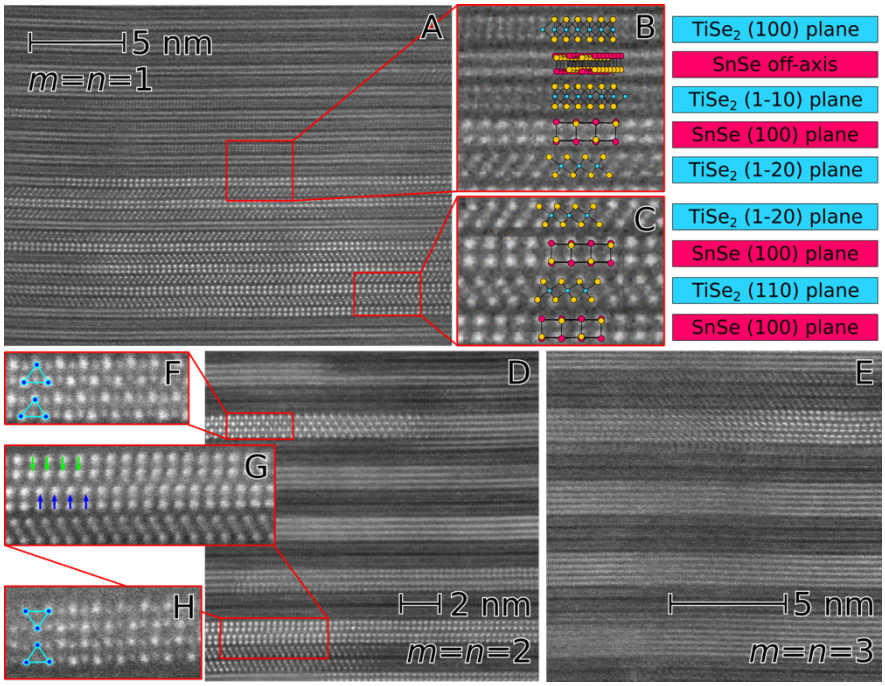

Figure 9.5. HAADF-STEM images of $[(SnSe)_{1+\delta}]_m[TiSe_2]_n$,($m$ = n = 1, 2, 3) nanolaminates showing templated interfaces for m=n=1 and several stabilized structures for m=n=2.

9.3.3. Transport Properties

Seebeck coefficient, Hall coefficient, and resistivity measurements were collected for the $[(SnSe)_{1+\delta}]_m[TiSe_2]_n$ heterostructures to investigate the influence of nanoarchitecture on the material's electrical transport properties including charge donation between layers and majority carrier type. The room temperature values for these measurements are reported in Table 9.3. All of the compounds have nominally the same stoichiometry for each repeating unit, but increased size with increasing m and n value, so if transport was dominated by the ratio of each constituent, the observed behaviors would not change across the series, and should be similar to that observed for the previously reported $[(SnSe)_{1+\delta}]_1[TiSe_2]_1$ heterostructure.[24,38] If there are trends in the observed

behavior as a function of *m* and *n*, then both the stoichiometry and the repeating unit nanoarchitecture are important to consider when describing the transport properties of a heterostructure.

Room temperature Seebeck coefficients were negative for all measured $[(SnSe)_{1+\delta}]_m[TiSe_2]_n$ heterostructures, indicating electrons dominate transport at 300 K. Prior reports of the $[(SnSe)_{1+\delta}]_1[TiSe_2]_n$ heterostructure compounds showed that electrons from the $TiSe_2$ layer were the dominant contribution to the Seebeck coefficient. However, in this work there is large variation in the measured value and no apparent systematic trend as a function of the number of SnSe and $TiSe_2$ layers within the repeating unit. The lack of a systematic trend suggests the carriers measured by the Seebeck coefficient are a result of the sample stoichiometry and not solely the repeat unit thickness. The large variation between measured Seebeck coefficients is likely the result of defects in each heterostructure.

Unlike the room temperature Seebeck coefficient, which is negative for all heterostructures and does not have a systematic trend with respect to *m* and *n*, the room temperature Hall coefficient generally becomes more positive and switches from negative to positive as a function of the *m* and *n* value. The $[(SnSe)_{1+\delta}]_1[TiSe_2]_1$ heterostructures is the only compound with a negative Hall coefficient at room temperature. This behavior is consistent with what was previously observed for the $[(SnSe)_{1+\delta}]_1[TiSe_2]_n$ family of compounds as well as previously published data on the $[(SnSe)_{1+\delta}]_1[TiSe_2]_1$ heterostructure.[24,38] $[(SnSe)_{1+\delta}]_m[TiSe_2]_n$ heterostructures with $m, n \geq 2$ have positive Hall coefficients at room temperature, even though the samples have the same stoichiometry as the $[(SnSe)_{1+\delta}]_1[TiSe_2]_1$ compound. The positive sign indicates that holes are also active at room temperature and are contributing the transport. This data is similar to that reported for the $[(SnSe)_{1+\delta}]_m[TiSe_2]_1$ family of compounds.[24] Assuming a single band model, the increase in the Hall

coefficient would indicate a decrease in the carrier concentration as a function of the number of layers in the repeating unit. Though this is not likely a valid assumption due to the negative Seebeck coefficient, it is what was previously observed for other $[(SnSe)_{1+\delta}]_m[TiSe_2]_n$ heterostructures where $m \neq n$ and provides a starting point for analyzing the intricate behaviors demonstrated by these heterostructure compounds.[24]

Similar to the measured Hall coefficients for the $[(SnSe)_{1+\delta}]_m[TiSe_2]_n$ family of compounds, there is a general trend in the measured resistivity at room temperature. As the number of SnSe and $TiSe_2$ layers in the repeating unit increases, so does the measured room temperature resistivity. This tracks with the general decrease in carriers with increased $m = n$ values. Similar behavior was observed for the $[(SnSe)_{1+\delta}]_1[TiSe_2]_n$ family of compounds where the resistivity increased with a more $TiSe_2$ layers in the repeating unit. The opposite behavior was observed for the $[(SnSe)_{1+\delta}]_m[TiSe_2]_1$ family of compounds where, as the number of SnSe layers in the repeating unit increased, there was a decrease in the resistivity.[24] A possible explanation for this behavior, which will be explored more later, is there is more "bulk" SnSe and $TiSe_2$ in these heterostructures which behave not as a novel combined material, but more as a composite and the amount of charge donated scales with m and n until a certain limit is reached.

Table 9.3. Room temperature electrical transport properties

m, *n*	S (μV K^{-1})	R_H (cm^3 C^{-1})	ρ (μΩ/m)
1	-75	-0.0028	12.6
2	-52	0.0018	17.9
3	-75	0.0126	24.5
4	-75	0.0035	39.4
5	-92	0.0045	56.8
6	-40	0.0411	40.3
8	-40	0.0453	57.0

Temperature dependent Hall coefficient data was collected for the $[(SnSe)_{1+\delta}]_m[TiSe_2]_n$ heterostructure compounds to probe the material's behavior as a function of repeating unit thickness and temperature and is shown in Figure 9.6. The observed behavior can be split into three groups, heterostructures that have a positive Hall coefficient at all temperatures, negative Hall coefficients at all temperatures, and Hall coefficients that switch sign as a function of temperature. The $[(SnSe)_{1+\delta}]_1[TiSe_2]_1$ compound is the only heterostructure that is negative over the entire temperature regime. As the temperature decreases the magnitude of the negative Hall coefficient increases, indicating that electrons dominate transport behavior of this compound. Assuming a single band model, this indicates that there are fewer mobile carriers as temperature is decreased. This is similar to behavior reported previously for the $[(SnSe)_{1+\delta}]_1[TiSe_2]_n$ heterostructure compounds. Heterostructures which display as change in Hall coefficient sign as a function of temperature include the m, n = 2, 4, and 5. These compounds appear to be dominated at lower temperatures by electrons. Between 200 and 250 K, the sign of the Hall coefficient switches from negative to positive and continues to become more positive with increasing temperature. The exact temperature of the switch is nanoarchitecture and defect dependent. It is apparent that both holes and electrons are contributing to the transport properties of these materials and become active at various temperatures resulting in changes in observed properties. This is similar to the behavior that was previously reported for the $[(SnSe)_{1+\delta}]_2[TiSe_2]_1$ heterostructure compound.[24] The heterostructures that have a positive Hall coefficient over the entire temperature regime include the m = n = 3, 6, and 8. While the $[(SnSe)_{1+\delta}]_3[TiSe_2]_3$ is positive over the entire temperature regime, the shape of its curve more closely resembles the behavior of the compounds where the Hall coefficient sign changes as a function of temperature. It is likely that this sample is more

closely related to the *m*, *n* = 2, 4, and 5 compounds, but is dominated by holes over the entire temperature regime as a result of defects. The *m*, *n* = 6 and 8 compounds have a positive Hall coefficient positive over the entire temperature regime and increase in magnitude as the temperature decreases. Assuming a single band model, though not entirely accurate, provides a rough estimate that suggests the number of active carriers decreases with decreasing temperature.

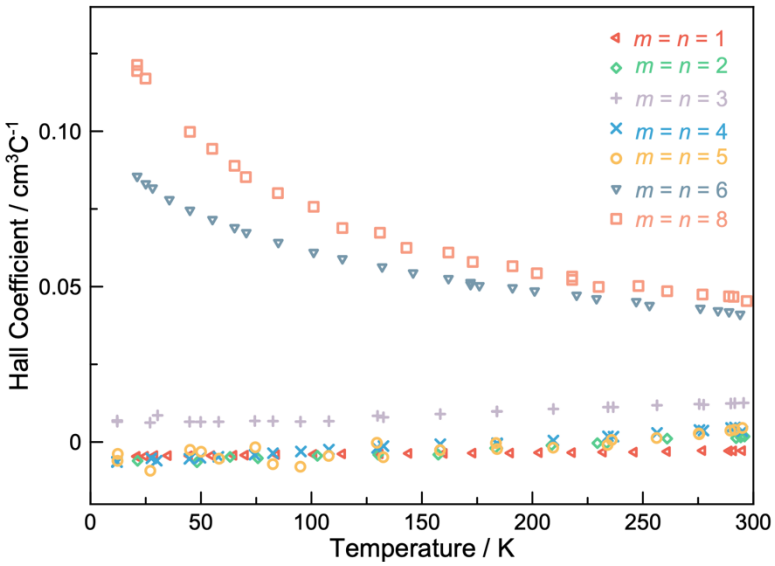

Figure 9.6. Temperature dependent Hall coefficient measurements for $[(SnSe)_{1+\delta}]_m[TiSe_2]_n$ heterostructures with *m*, *n* = 1 – 8.

Temperature dependent resistivity data was collected for all $[(SnSe)_{1+\delta}]_m[TiSe_2]_n$ heterostructure compounds down to ~ 22 K to further investigate the unique transport behavior and is shown in figure 9.7. The general trend observed in the room temperature data, that as *m*, *n* increases so does the resistivity, is maintained over the entire temperature regime. The $[(SnSe)_{1+\delta}]_1[TiSe_2]_1$ compound's resistivity initially decreases as temperature is decrease until ~ 100 K at which point the resistivity starts to increase. For all other $[(SnSe)_{1+\delta}]_m[TiSe_2]_n$ heterostructures, there is an increase in resistivity as temperature is decreased over the entire temperature regime. At lower temperatures, the

upturn in resistivity starts to occur at a faster rate for all of the compounds and it aligns with the start of the increase in resistivity for the $[(SnSe)_{1+\delta}]_1[TiSe_2]_1$ heterostructure. The temperature at which the upturn occurs is dependent on the number of SnSe and $TiSe_2$ layers present in the repeating unit, larger *m, n* values see the upturn in resistivity occurring at higher temperatures. Most increases in resistivity with decreasing temperature are attributed to semiconducting behavior, which should fit to an exponential. The data presented here cannot be fit to an exponential and instead follows a $T^{-1/4}$ behavior that is related to a variable range hopping mechanism.

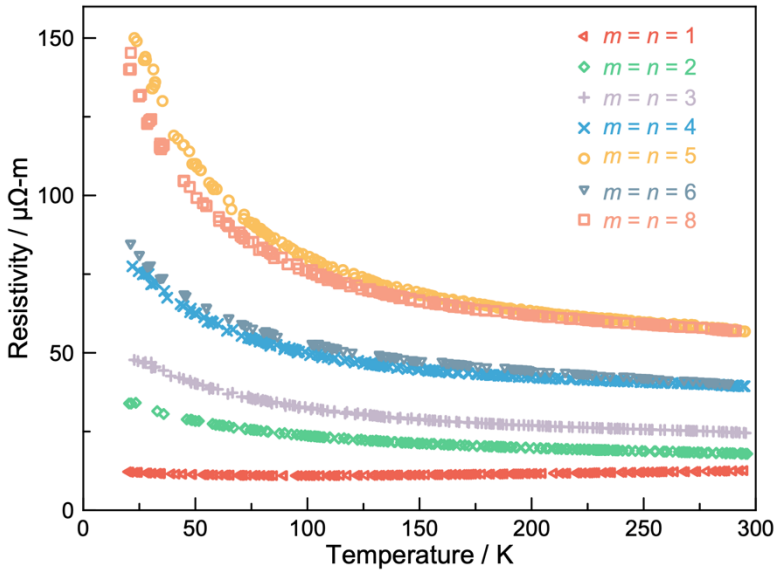

Figure 9.7. Temperature dependent resistivity measurements of $[(SnSe)_{1+\delta}]_m[TiSe_2]_n$ heterostructures with *m, n* = 1 – 8.

While the last couple of paragraphs focused on presenting the measured data, here the data will be discussed together in an attempt to explain the observed complex behavior. The change in slope observed in the temperature-dependent Hall coefficient data occurs at approximately the same temperature as the upturn in resistivity. It was previously reported in the $[(SnSe)_{1+\delta}]_1[TiSe_2]_n$ heterostructure compounds that this was a result of variable range hopping.

It is known that the SnSe layer donates charge to the $TiSe_2$ layer at the interface between the two compounds which results in a conducting block composed of the layers involved in charge donation. There is some extension beyond the interfacial layers, but the majority of layers without an interface retain their bulk-like behaviors. As the temperature decreases, these carriers (electrons) are less mobile, resulting in the observed Hall coefficient and resistivity data.

While all samples contain the novel conducting layer composed of the SnSe and $TiSe_2$ interfacial layers, the extent of its contribution to the observed transport properties is impacted by the number of bulk behaving SnSe and $TiSe_2$ layers that are present in the sample. It was previously reported the conducting interfacial block is dominated by electrons, while the $TiSe_2$ layer's transport is known to have both holes and electrons, and the SnSe layer is dominated by holes. The ratio of the conducting interfacial block to the individual constituents lacking an interface strongly influences the observed transport behavior. The $[(SnSe)_{1+\delta}]_1[TiSe_2]_1$ compound is composed solely of interfacial SnSe and $TiSe_2$ layers, which is why is it completely dominated by electrons at all temperatures and demonstrates more conductive behavior than the other $[(SnSe)_{1+\delta}]_m[TiSe_2]_n$ heterostructure compounds. As the number of SnSe and $TiSe_2$ layers in the compound increases there is more charge donated, but also more contribution from the holes in the observed transport properties. At low temperatures for the m, n = 2, 4, and 5 sample, electrons from the interfacial conducting block dominate the transport at low temperatures, but as temperature is increased, holes in the bulk like material are activated and dominate the transport behavior. In the m, n = 3 sample there are likely enough defects that result in holes even at low temperatures which dominates the hall coefficient data at all temperatures. For the m, n = 6 and 8 samples, the blocks of bulk-like

material are thick enough to provide sufficient quantities of mobile holes at low temperatures, such that holes become the dominant carrier.

The sign discrepancy that occurs between the room temperature Hall and Seebeck coefficients is a result of the mobility differences between the two carrier types. It was previously reported that the holes observed in these materials are much more mobile than the electrons. While both the Seebeck and Hall coefficients are dependent on the mobility and carrier concentrations at high temperatures, the mobility has a much larger impact on the Hall coefficient at high temperatures. Since both carriers are present at room temperature, the more mobile holes dominate the Hall coefficient, while the Seebeck coefficient in dominated by the higher concentration of less mobile electrons.

9.3.4. Temperature Dependent Diffraction

It is apparent from the discussion of the transport data that the $[(SnSe)_{1+\delta}]_m[TiSe_2]_n$ heterostructures are very complex and there are a lot of factors contributing to their unique temperature dependent behavior. To study the effect of temperature on the compounds structure, temperature dependent in-plane diffraction was collected on the $[(SnSe)_{1+\delta}]_4[TiSe_2]_4$ heterostructure compound using the Advanced Photon Source at Argonne National Laboratory. Figure 9.8 visually illustrates the calculated lattice parameters at temperatures ranging from 22 to 300K and a tabular form is provided in Table F.1. There is no change in the lattice parameters for the $TiSe_2$ constituent as a function of temperature, indicating there is no temperature dependent distortion. This is consistent with previously published temperature dependent in-plane lattice parameters for a $[(SnSe)_{1+\delta}]_1[TiSe_2]_8$ which do not change as a function of temperature. On the other hand, the SnSe constituent distorts to a more rectangular unit cell as the temperature is decreased. As the temperature is lowered the in-plane lattice parameters go from being more square-like to approaching the rectangular structure of bulk

SnSe.[45,47,52] This bulk-like structure resembles what is observed at room temperature for the larger $m = n$ compounds. As the sample is heated, there is more energy put into the sample which facilitates the distortion to a square-like structure. This temperature dependent distortion appears to be a function of the number of SnSe layers within the repeat unit, as the $[(SnSe)_{1+\delta}]_1[TiSe_2]_8$ which only has a single SnSe layer in the repeating unit did not have a change in unit cell as a function of temperature. This complex structure change that is both temperature dependent and a function of the number of SnSe layers in the repeating unit plays a role in the complex transport properties and layer interactions that are observed within these compounds.

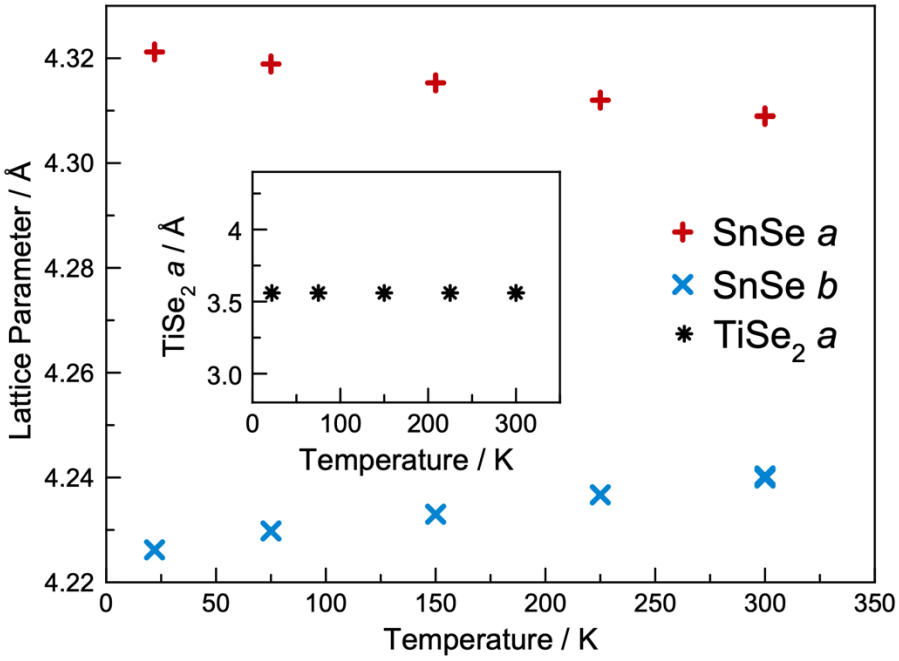

Figure 9.8. Temperature-dependence of *a*- and *b*-axis lattice parameters of an $[(SnSe)_{1+\delta}]_m[TiSe_2]_n$, m, n = 4 heterostructure.

9.4. CONCLUSIONS

Series of compounds with systematic changes in nanoarchitecture provide a platform for investigating size effects and layer interactions in thin film heterostructures. Here a series of $[(SnSe)_{1+\delta}]_m[TiSe_2]_n$

heterostructures were prepared where the ratio of SnSe to $TiSe_2$ in the repeating unit was held constant, but the size of the repeating unit was systematically increased. As the repeating unit size increased, the structure of the SnSe layers transformed from a single layer of SnSe distorting to match the in-plane lattice of $TiSe_2$ to thicker blocks of SnSe with in-plane lattice parameters that approach those of bulk SnSe. This complex structural behavior as a function of nanoarchitecture is mirrored in the transport properties. When there is only a single layer of each constituent in the repeating unit, the charge donation from the SnSe to the $TiSe_2$ creates a strong interaction between the layers, causing them not to act as a composite, but instead as a novel conductive material 'block'. This conductive block persists at the interface when more SnSe and $TiSe_2$ layers are added to the structure, but the non-interfacial SnSe and $TiSe_2$ maintain their independent properties and also significantly contribute to the observed transport behavior. The transport behavior is influenced by both electrons from non-interfacial $TiSe_2$ layers and the conducting interfacial block as well as holes from the non-interfacial $TiSe_2$ and SnSe layers. The degree to which holes, electrons, or both contribute to transport follows similar trends to SnSe's structural distortion. However, further investigation of the materials is warranted to quantitatively understand the observed transport properties. Overall, the complex behavior observed in the $[(SnSe)_{1+\delta}]_m[TiSe_2]_n$ heterostructure series demonstrates the influence of size effects in thin film materials and establishes an avenue for manipulating and tuning desired electronic properties.

9.5. BRIDGE

In this chapter, the influence of size effects on heterostructure properties were investigated in the $[(SnSe)_{1+\delta}]_m[TiSe_2]_n$ heterostructure compounds. It was found that size effects play a large role in these materials as they all had the same ratio of SnSe to $TiSe_2$ but have vastly

different transport properties as a function of nanoarchitecture. Charge donation between the interfacial SnSe and $TiSe_2$ material created a novel conductive material that dominates the properties at low temperatures. As the number of SnSe and $TiSe_2$ layers that don't touch an interface increases, both holes and electrons become important and negate each other. It is observed that this is a complex system that cannot be described by a simple model as there are too many changing variables. In the next chapter the $[(SnSe)_{1+\delta}]_m[TiSe_2]_2$ series of compounds is investigated to further explore the charge donation in these complex materials.

CHAPTER X

ELECTRONIC STURCTURE OF DESIGNED $[(SNSE)_{1+\delta}]_M[TISE_2]_2$ HETEROSTRUCTURE THIN FILMS WITH TUNABLE LAYERING SEQUENCE

10.0. Authorship Statement

This chapter was formatted from a manuscript with the same name, that was published in the Journal of Materials Research (DOI: 10.1557/jmr.2019.128.) on March 21, 2019, and was co-authored by myself, Fabian Göhler, Niels Rösch, Susanne Wolff, Jacob T. Logan, Robert Fischer, Florian Speck, David C. Johnson and Thomas Seyller. Fabian Göhler is the primary author on this paper and he, Niels Rösch, Susanne Wolff, Florian Speck, and Thomas Seyller prepared the samples for XPS and collected the data as well as did the XPS data analysis. Jacob T. Logan assisted me in the collection of the diffraction data. Robert Fischer collected the HAADF-STEM images. David Johnson is my advisor and consulted in the preparation of this publication. I was a part of the experimental design and the conception of the idea. I prepared the films that were studied, characterized their structure and composition, and contributed to the writing of the manuscript.

10.1. Introduction

The stacking of two-dimensional layers into heterostructures with emerging properties is currently at the forefront of materials science research [1, 2, 3, 4, 5]. Understanding the interactions between layers is of paramount importance, especially when considering the effects of different stacking arrangements. For example, single layers of graphene exhibit much improved carrier mobility when they are placed on [6] or encapsulated between [7] hexagonal boron nitride instead of resting on a silicon oxide substrate, and the super- conducting critical temperature of the $NbSe_2$ layers in $[(SnSe)_{1+\delta}]_m(NbSe_2)_1$ is found to decrease with increasing SnSe content due to charge transfer between layers [8].

Changing the composition and stacking sequence of layers in heterostructures consisting of MoS_2 and WS_2 allows for the fabrication of devices with tunable tunnel resistance or band-engineered tunnel diodes [9]. The misfit layer chalcogenides, consisting of alternating layers of a metal chalcogenide and a transition metal dichalcogenide (TMDC), are a promising class of materials for thermoelectric applications, but the control over composition and layering sequence is limited to a few thermodynamically stable compounds accessible via high-temperature synthesis approaches [10, 11, 12].

Preparing samples with the desired stacking arrangements is a great challenge in the experimental study of two-dimensional materials and heterostructures. High-quality samples and devices can be prepared by manual mechanical stacking of exfoliated layers [13]. To pave the way toward wafer scale production, different scalable manufacturing techniques, such as sequential chemical vapor deposition (CVD), direct growth of TMDC heterostructures by vapor–solid reactions, and van der Waals epitaxy, have been under consideration [14], but different growth conditions for each layer limit the complexity that may be achieved [15].

A developing approach to heterostructures that enables wafer scale samples is the self-assembly of designed precursors consisting of a repeating sequence of deposited elemental layers. By precisely controlling constituents and layering sequences of the precursors, a virtually unlimited number of heterostructures can be realized experimentally [16, 17]. While this self-assembly approach can produce specific stacking sequences, the rotational orientation of the layers cannot be controlled, resulting in a random rotational alignment of the layers with respect to each other [18].

Here, we explore the electronic properties of $[(SnSe)_{1+\delta}]_m(TiSe_2)_n$ heterostructures, consisting of m bilayers of SnSe and n layers of $TiSe_2$ in the supercell. Prior research on the $(MS)_{1+\delta}(TiS_2)_2$ misfit layer compounds

showed that the intergrowths containing M = Sn are of special interest for thermoelectric applications [19], and high Seebeck coefficients sensitive to the layering sequence have been observed in similar selenide compounds grown via self-assembly of designed precursors [20, 21]. In contrast to the rotational disorder usually present in samples prepared by this synthesis approach, samples with m = n = 1 showed relatively large regions with long-range order [22]. A series of samples with m = 1, ..., 4 and n = 1 showed unusual transport behavior [23], emphasizing the importance of furthering the understanding of the electronic interactions in this kind of system. Finding proof for the presence of a potential charge transfer into $TiSe_2$ is of special interest, since the controlled doping of $TiSe_2$ can be used to finely tune electronic transitions such as charge density waves or superconductivity [24, 25]. X-ray photoelectron spectroscopy (XPS) has proven to be an effective method to investigate the electronic structure of these systems, as evidence for electron transfer from the metal selenide layer (M = Pb or Sn) into the transition metal dichalcogenide layer was found for $(MSe)_{1+\delta}(NbSe_2)_2$ [26]. In this work, photoelectron spectroscopy was used on a series of $[(SnSe)_{1+\delta}]_m[TiSe_2]_2$ compounds with m = 1, 2, 3, and 7, as well as binary samples of the constituents $TiSe_2$ and SnSe.

10.2. Results and Discussion

10.2.1. Synthesis and Structure

Binary SnSe and $TiSe_2$ and a series of $[(SnSe)_{1+\delta}]_m[TiSe_2]_2$ heterostructures with m = 1, 2, 3, and 7 and were prepared from designed amorphous precursors by physical vapor deposition. A repeating sequence of elemental Ti, Sn, and Se layers was deposited in an order that mimicked the architecture of the desired product [20, 23, 27]. For example, to make the m = 2 compound, the repeating sequence Ti|Se|Ti|Se|Sn|Se|Sn|Se was deposited. For the Sn|Se and Ti|Se bilayers, a 1:1 ratio of Sn to Se and a 1:2 ratio of Ti to Se, respectively,

were targeted with a layer thickness similar to that of the desired product. The sequence of bilayers was repeated until a sample of about 50 nm in total film thickness was reached. The amount of material required to obtain the correct ratio in the Sn|Se layers and Ti|Se layers with the right layer thickness was determined using X-ray fluorescence (XRF) in combination with various X-ray diffraction (XRD) techniques [28].

The layered precursors were converted into the desired crystalline products by annealing on a hot plate in an N_2 atmosphere with,1 ppm of oxygen present. The optimal annealing conditions for SnSe and $TiSe_2$ were estimated from prior studies. An annealing study completed on $TiSe_2$ previously reports the ideal annealing temperature to be 350 °C for 30 min when annealed in an N_2 atmosphere with less than 0.5 ppm of oxygen present [29]. In a recent study, SnSe films were crystallized at 350 °C for 30 min in an N_2 atmosphere [30].

An annealing study of the m = 3 precursor was conducted to determine the best annealing temperature to crystallize the targeted $[(SnSe)_{1+\delta}]_m[TiSe_2]_2$ compounds. Figure 10.1. contains the X-ray reflectivity (XRR), specular XRD, and in-plane XRD data collected on the m = 3 precursor as it was annealed at the indicated temperatures for 30 min. The as deposited XRR pattern contains both Kiessig fringes and the first three Bragg reflections resulting from the repeating sequence of elemental layers. The Kiessig fringes result from interference between the front and back of the film and depend on the smoothness of these interfaces. As the sample is annealed at increasing temperatures, the fringes extend out to higher angles indicating smoother interfaces. Above 450 °C, the Kiessig fringes decrease in intensity. By 500 °C, the Kiessig fringes are gone, indicating that the film has become significantly rougher. The diffraction maxima in the XRR scans result from the artificial layering of the designed precursor from the sequence of

deposited elemental layers. As the sample is annealed to higher temperatures, these reflections shift to higher angles, indicating that the repeat unit thickness is getting smaller. The reflections become commensurate with the 00l reflections present at higher angles as the artificial layering evolves into the product. Above 450 °C, the Bragg reflections decrease in intensity. After the 500 °C annealing, some of the Bragg reflections are no longer visible, indicating that the metastable product is decomposing.

The reflections in the as-deposited specular diffraction pattern can all be indexed as 00l reflections. As the sample is annealed at increasing temperatures, additional reflections grow in and the reflections systematically shift to higher angles, indicating that the *c*-axis lattice parameter is decreasing. The diffraction pattern after annealing at 350 °C contains the most reflections. After annealing at this temperature, the reflections all have similar line widths and can be indexed as 00l reflections of $[(SnSe)_{1+\delta}]_m[TiSe_2]_2$. The reflections broaden and are reduced in intensity when annealed at 400 °C or higher, indicating that the desired product is decomposing. The in-plane diffraction pattern of the as deposited sample contains reflections that can be indexed as those from a rectangular and a hexagonal unit cell. The *a*-axis lattice parameter of the hexagonal unit cell matches that expected for $TiSe_2$. The rectangular lattice parameters are slightly larger than expected for SnSe. On annealing, the lattice parameters of the rectangular unit cell decrease, and weak reflections consistent with the formation of $SnSe_2$ appear after annealing at 200 °C. The $SnSe_2$ reflections are no longer present after annealing at 350 °C, and the in-plane lattice parameters are consistent with those expected for SnSe and $TiSe_2$. After annealing at 500 °C, the intensity of the in-plane reflections are all decreased in intensity, which is consistent either with decomposition or a decrease in preferred alignment of the crystallites. We concluded that the optimal

annealing temperature is 350 °C, as shown in blue in all three of the data sets in Figure 10.1.

High-angle annular dark-field scanning transmission electron microscopy (HAADF-STEM) images were collected on a representative sample to provide real space images as well as a local structure picture of the material. Figure 10.2(a). shows the entire cross-section of the film, from surface to substrate, demonstrating the formation of the desired compound throughout the film. There are clearly 3 bright SnSe layers separated by 2 darker $TiSe_2$ layers in the repeat structure. While a few layering defects can be observed, the film is dominated by the $[(SnSe)_{1+\delta}]_3[TiSe2]_2$ structure. Figures 10.2(b). and 10.2(c). show higher resolution images that clearly resolve the atomic structure. Figure 10.2(b). shows regions with defect-free continuous layering of the $[(SnSe)_{1+\delta}]_3[TiSe_2]_2$ heterostructure, while Figure 10.2(c). shows regions with defects in the layering structure that are likely a result of crystallites started from two nucleation sites growing together. Different zone axis can be observed in the various layers due to the sample's rotational disorder which is a consequence of the designed precursor preparation technique. In the bottom of Figure 10.2(b), the (100) zone axis of $TiSe_2$ can be observed and in the upper left corner of Figure 10.2(c), the (100) zone axis of SnSe can be observed.

Figure 10.3. contains specular and in-plane diffraction scans of the four heterostructure samples studied by XPS. All of the reflections in the specular diffraction pattern can be indexed as 00l reflections consistent with an increasing *c*-axis lattice parameter as m is increased [23]. The *c*-axis unit cell parameter increases as the number of SnSe bilayers in the repeating unit, *m*, is increased. This decreases the spacing between Bragg reflections and the first Bragg reflection moves to smaller angles. The in-plane diffraction patterns have reflections that can all be indexed as hk0 reflections from SnSe or $TiSe_2$, except for the binary SnSe sample,

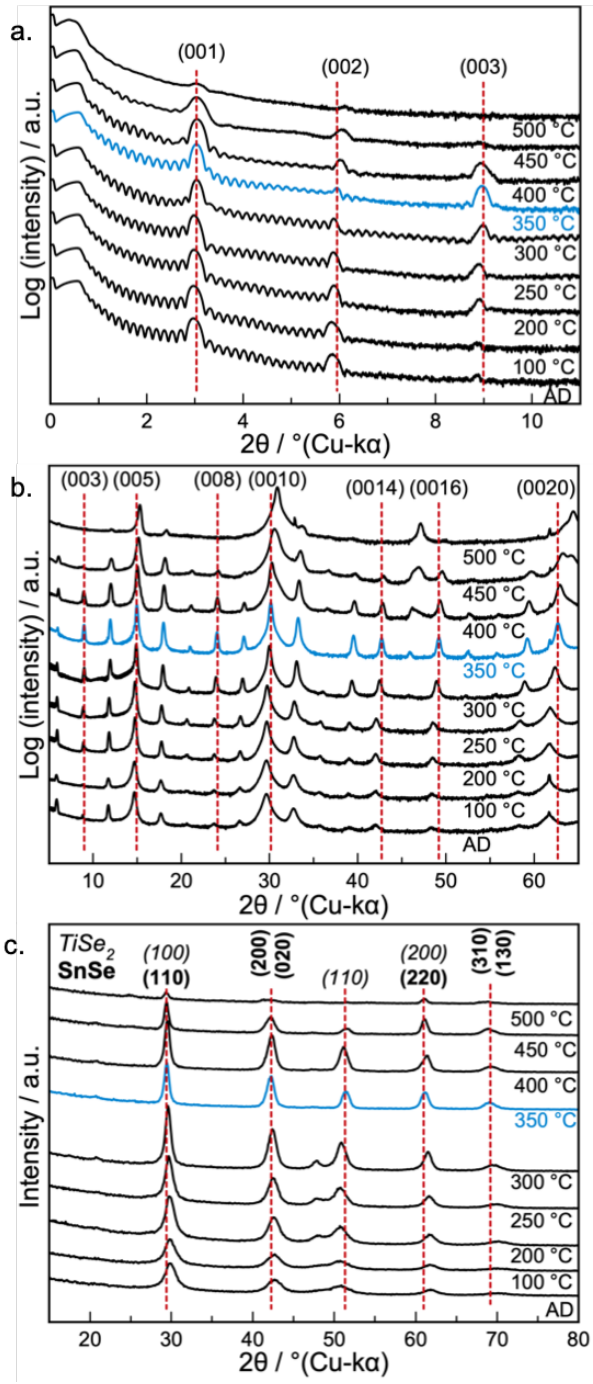

Figure 10.1. XRR (a), Specular XRD (b), and in-plane XRD (c) of the representative $[(SnSe)_{1+\delta}]_m[TiSe_2]_2$ sample with m = 3 as deposited (AD) and annealed at various temperatures. The diffraction pattern of the sample annealed at 350 °C and studied by HAADF-STEM and XPS is highlighted. Dashed lines indicate the position of the Bragg reflections expected for a well crystalized sample.

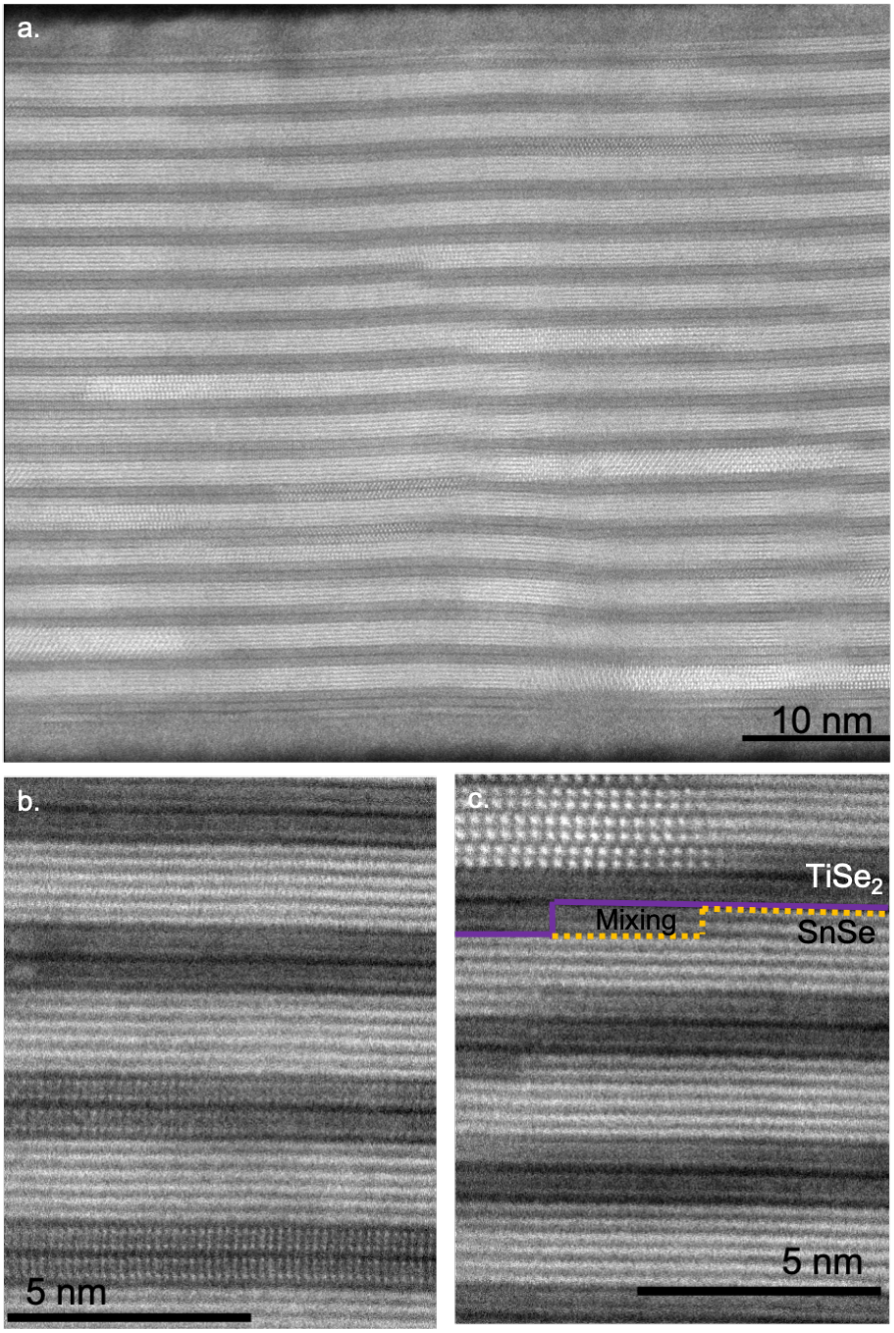

Figure 10.2. Representative HAADF-STEM images of a $[(SnSe)_{1+\delta}]_3[TiSe_2]_2$ sample showing the entire thickness of the film (a), a region with a pristine (3, 2) layering structure (b), and a region where layering defects occur (c). A step fault is marked with a solid purple line demonstrating the bottom border of the $TiSe_2$ layer and a dashed yellow line demonstrating the top of the SnSe layer. There is a layer of mixing between the two layers that is outlined by the two borders of the SnSe and $TiSe_2$ layer, respectively.

which has weak reflections from $SnSe_2$. With increasing value of m in the repeating unit, the reflections from the SnSe constituent grow in intensity and as a result the reflections from $TiSe_2$, become less pronounced. Both diffraction experiments indicate that the samples are crystallographically aligned with the substrate perpendicular to the *c*-axis.

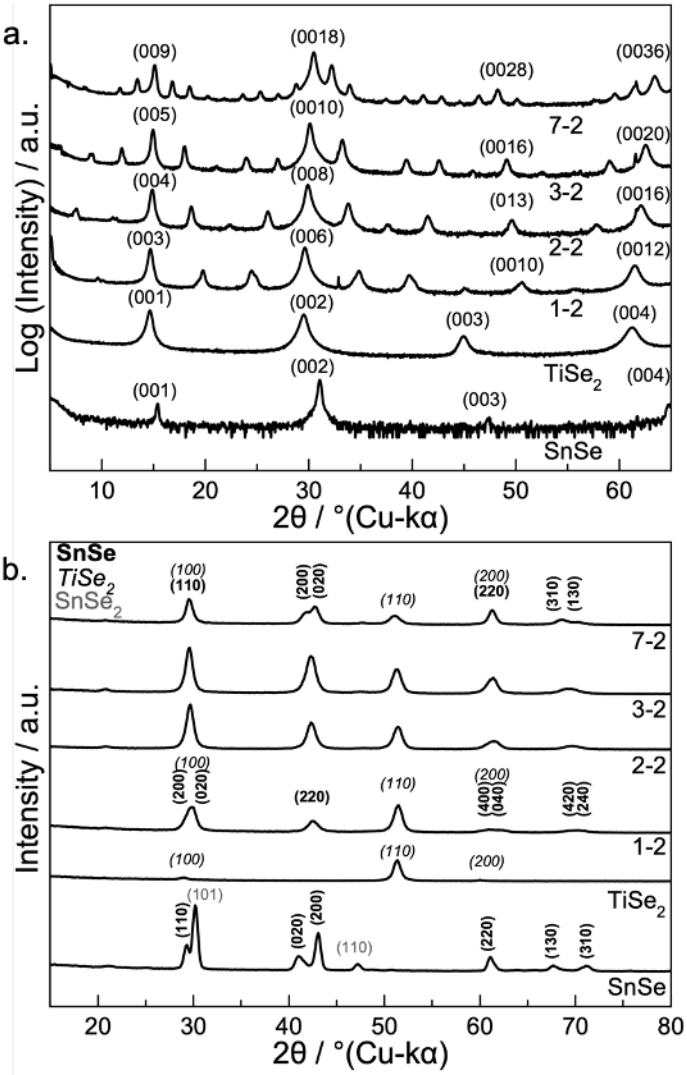

Figure 10.3. Specular (a) and in-plane (b) XRD patterns of the SnSe, $TiSe_2$, and $[(SnSe)_{1+\delta}]_m[TiSe_2]_2$ heterostructures with m = 1, 2, 3, and 7.

10.2.2. Characterization of Electronic Structure via XPS

Prior to investigating the heterostructures containing both SnSe and $TiSe_2$ layers, XPS measurements were conducted on respective binary samples. The spectra of the binary com- pounds SnSe and $TiSe_2$ can be found in the bottom and top rows of Figures 10.4(a).–10.4(d), respectively. As discussed in a previous report [26], binary SnSe is a small band gap semiconductor and, thus, gives symmetric photoelectron peaks. The binding energy of the Sn3$d_{5/2}$ and Se3$d_{5/2}$ core-level peaks is 485.87 eV and 53.77 eV, respectively. In the valence band, one can identify the Se4s state at 13.6 eV and the Sn5s state at 7.6 eV. The energy ranges from 0–5 eV is composed mainly of Sn-*p* and Se-*p* states [31].

$TiSe_2$ on the other hand is heavily debated as being either a semi-metal or very small band gap semiconductor [32]. For a metallic compound, one would expect to observe asymmetric peak shapes in photoemission spectra [33]. Indeed, an asymmetric peak shape, which can be fitted using a line shape as derived by Mahan [34], is observed for the Ti2*p* and Se3*d* core levels. A binding energy of the Ti2$p_{3/2}$ core level at 455.55 eV can be derived, in excellent agreement with literature reports [35], and the Se3$d_{5/2}$ core level is found at 53.20 eV. In the valence band spectrum, we can observe a broad band constituted of Se-*p* and Ti-*d* states, with some prominent features which we find at the same energies as reported by Shkvarin et al. [35]. In our spectrum, the Se4*s* state is located at a binding energy of 13.3 eV, which is about 0.3 eV less than in their work [35]. Right at the Fermi energy (EB 5 0), we can observe a small but not vanishing density of states, consistent with a semi-metal.

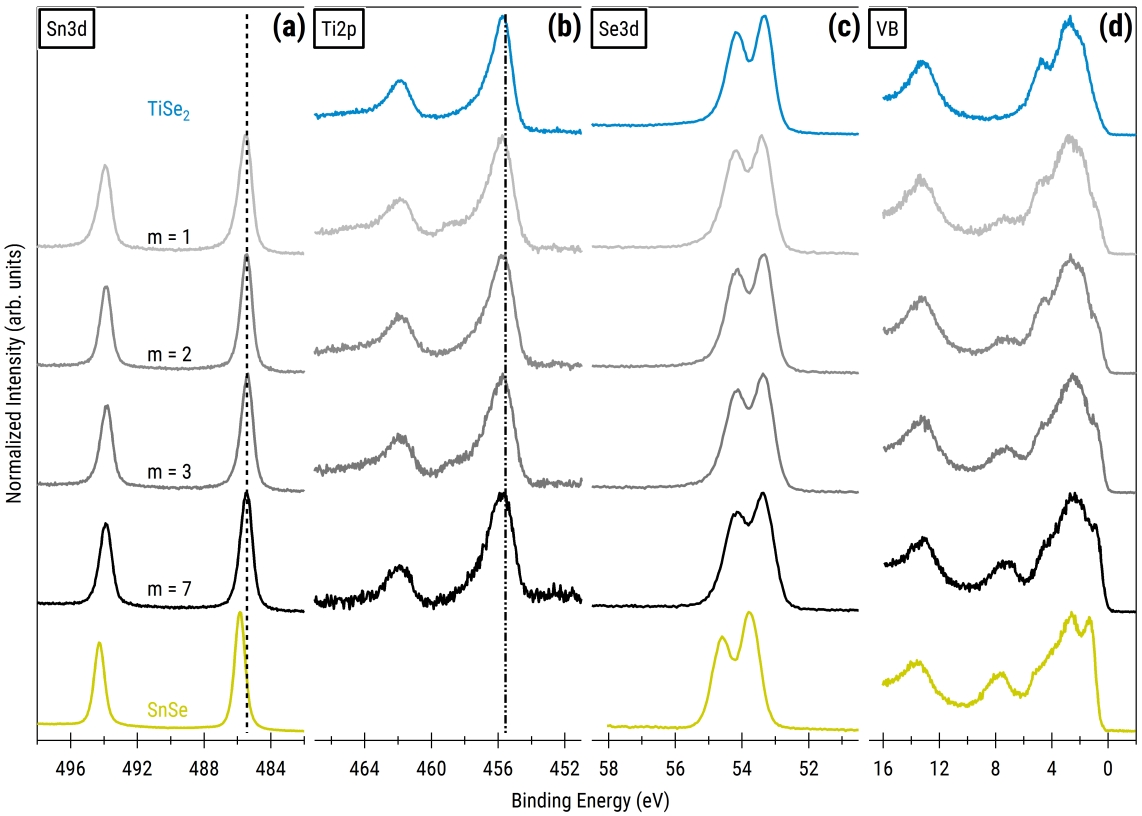

Figure 10.4. Normalized XPS Sn3*d* (a), Ti2*p* (b), and Se3d (c) core-level spectra as well as valence band (d) spectra of binary SnSe (bottom row), binary $TiSe_2$ (top row), and $[(SnSe)_{1+\delta}]_m[TiSe_2]_2$ heterostructures with m = 1, 2, 3, and 7. Dashed lines are added as a guide to the eye, indicating the position of the Sn3*d* and Ti2*p* core levels in the heterostructure.

We now turn our attention to the $[(SnSe)_{1+\delta}]_m[TiSe_2]_2$ heterostructures. After cleaving the samples and transferring them to UHV, XPS survey scans were carried out over a large energy range to assess the quality of the cleaved surface. As expected, the samples were largely free of oxygen compared to uncleaved samples. Only a few samples appeared to have small traces of oxygen left on the surface, which also showed up as a small TiO_x shoulder accompanying the Ti2*p* core level at around 459 eV. From the intensity of the core-level signals, the ratios of the elements present in the samples could be estimated. As expected, an increase in the Sn/Ti ratio with increasing SnSe layer

thickness m can be observed. Additionally, measurements were not only carried out in normal emission geometry but also at a 60° angle between surface normal and analyzer. In the 60°-geometry, surface sensitivity is enhanced because electrons from a certain depth have to travel a longer path through the sample to reach the surface. By comparing the intensity ratios in normal emission and under 60°, we find a decrease in Sn content and an increase in Ti in the more surface sensitive geometry, suggesting that a $TiSe_2$ layer appears to be on the top after the cleave. As mentioned earlier, both halves of the cleaved sample could be investigated. Though some samples showed barely any signal from the grown thin films, suggesting a cleave at the substrate, in the instances where there was still enough film left to be investigated, this behavior of the Sn/Ti ratio could be reproduced. Cleaving the samples again for a second time gave the same qualitative results. This is consistent with a cleave of the crystals occurring primarily at the van der Waals gap between the two $TiSe_2$ layers. For one sample, the cleaved surface was exposed to air for a couple of days after the experiment and then measured again. The spectra showed a much higher degree of oxidation for Ti compared to Sn, which further supports the claim that the samples are cleaved between the $TiSe_2$ layers, leaving them more exposed to ambient oxygen.

The main focus of this work was to investigate the electronic interactions between the layers as a function of SnSe layer thickness m. Figure 10.4(a). shows the normalized Sn3*d* core-level spectra for binary SnSe and the $[(SnSe)_{1+\delta}]_m[TiSe_2]_2$ heterostructures. The binding energy of the Sn3$d_{5/2}$ peak is shifted by an average of 0.44 eV to lower binding energies in the heterostructures compared to binary SnSe. The binding energy is the same within error for all samples and m values. In the previously investigated $[(SnSe)_{1+\delta}]_1[NbSe_2]_2$ system, a pronounced asymmetry and even larger shift of the Sn3d core level was observed [26].

This was explained by the SnSe layers obtaining a metallic character due to electron transfer into the $NbSe_2$ layers. In the $[(SnSe)_{1+\delta}]_m[TiSe_2]_2$ samples presented herein, this asymmetry is very small for m = 1 and completely absent for m = 2. The Ti2*p* core-level spectra are shown in Figure 10.4(b). For all samples, the core-level binding energy and peak shape are the same as in the binary compound. Both the Sn3*d* and Ti2*p* core levels show an increased Gaussian peak width in the heterostructures in comparison to the binary compounds, which we attribute to a higher degree of structural distortions and disorder which are present in these samples. While no dependence of the Gaussian width on the number of SnSe layers was observed for the Sn3*d* core level, the Gaussian width of the Ti2*p* core increases slightly with increasing *m*.

Analyzing the contributions of the two types of layers is more challenging for the Se3*d* core-level and valence band spectra, as both constituents contribute to the measured signal. For the Se3*d*, the data were fitted using a weighted superposition of a SnSe and a $TiSe_2$ component. The relative intensity of these two components was estimated from the elemental Sn/ Ti ratio as determined from survey scans for each sample and was held constant during the fit routine. The peak shape of each component was constrained to the results obtained on the binary compounds. Only a shift in binding energy and a Gaussian broadening of the individual spectra was allowed. An example is shown for the compound with m = 2 in Figure 10.5 (a). A Shirley background is used to account for the increase in background intensity of inelastically scattered electrons at lower kinetic energies (higher binding energies) [36]. The measured spectra are very well reproduced by shifting the SnSe component by about 0.5 eV to lower binding energies from its position in the binary to 53.28 eV, while shifting the $TiSe_2$ component about 0.3 eV to higher binding energies. This procedure was carried out for all measured samples. Within accuracy of the method (approximately 60.10

eV), all samples exhibit the same shifts of the SnSe and $TiSe_2$ components as the sample shown in Figure 10.5(a).

Taking a closer look at the valence band spectra in Figure 10.4(d), it can be seen how the characteristic features of the SnSe valence band are getting more pronounced with increasing m. This is especially true for the Sn5*s* state and the distinct peak below the Fermi energy, which are found at 7.6 eV and 1.3 eV in binary SnSe, respectively. They do, however, appear shifted about 0.4–0.5 eV toward lower binding energies in the heterostructures. In the same manner, the pronounced peak which can be found at 4.85 eV in binary $TiSe_2$ decreases in intensity with increased SnSe layer thickness.

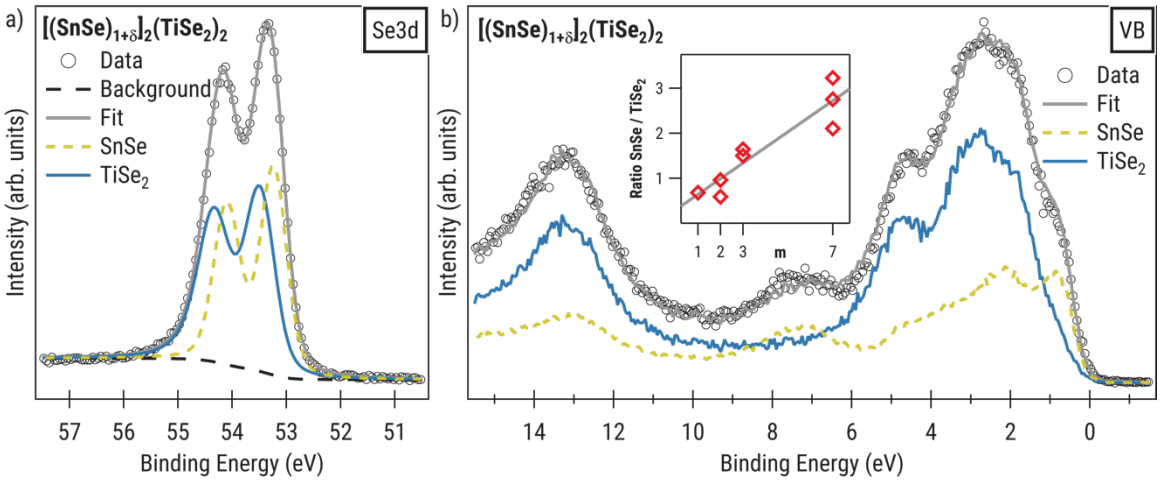

Figure 10.5. Fit of the Se3*d* (a) and valence band (b) spectra using superpositions of the SnSe and TiSe2 components, shown exemplarily for $[(SnSe)_{1+\delta}]_2[TiSe_2]_2$. For the Se3*d* fit, the ratio of the two components was constrained using composition data. The inset in (b) shows the ratio of $SnSe/TiSe_2$ needed to adequately fit the data, showing a linear increase with *m*.

A similar approach as for the Se3*d* core level was used to model the valence band spectra of the heterostructures, as is shown again for $m = 2$ in Figure 10.5(b). Unlike the Se3*d* core level, the different states of the SnSe and $TiSe_2$ valence band are expected to show different photoionization cross-sections. As a consequence, the information on

elemental ratios from the survey scans could not be used to constrain the fit. To fit the measured spectrum of the $[(SnSe)_{1+\delta}]_m[TiSe_2]_2$ heterostructure (data points), a weighted superposition of the measured valence band spectra of the binary samples was carried out. The spectra of the two components were free to shift during the fit routine. The quality of the fits was assessed by how well distinct features of the dataset could be reproduced, especially the Sn5*s* state and the characteristic states between 5 eV and the Fermi energy. As can be seen from the example shown in Figure 10.5(b), with this method, it is possible to reproduce the experimental data fairly well. Consistent with the observations in the Se3d core level, in the valence band, a shift of the SnSe component by 0.4–0.5 eV to lower binding energies was found, while the $TiSe_2$ compo- nent appears shifted 0.10–0.22 eV toward higher binding energies. However, it should be noted that this simple approach has its limitations, as it is not possible to account for possible changes in band filling or band dispersion compared to the binary compounds. The inset in Figure 10.5(b). shows how the ratio of SnSe to $TiSe_2$, needed to adequately reproduce the spectrum of the heterostructure, changes with increasing *m*, where each data point corresponds to a fitted measurement. Even though the data points show some variation, a clear linear trend can be observed, as should be expected for a linearly increasing SnSe layer thickness.

10.2.3. Discussion of XPS Results

Figure 10.6. summarizes the experimental binding energies as well as the position of the valence band maximum for binary SnSe and $TiSe_2$. Since no dependence of the binding energy on the SnSe layer thickness m was observed for the $[(SnSe)_{1+\delta}]_m[TiSe_2]$ heterostructures within the accuracy of our method, average values are given for Sn3*d*, Ti2*p*, and the respective Se3*d* core levels. The SnSe component of the heterostructure shows a rigid band shift of the core levels and the valence band. The

energy shifts are about 0.4–0.5 eV toward lower binding energies for all core levels. This energy shift can be explained by a transfer of charge from the SnSe into the TiSe*2*, similar to that proposed by Merrill et al. [20]: As a binary compound, SnSe is a semiconductor, so the Fermi energy is in the band gap and the topmost energy states (mainly the Se4*p* [31]) are completely filled. When SnSe is interleaved with $TiSe_2$, it donates electrons into the $TiSe_2$ layers, which leads to a shift of E_F to the top of the Se4*p* band, as can be seen in the schematic band structure shown in Figure 10.7. Since binding energies in XPS are measured relative to EF, this electron donation leads to a reduction in the binding energies in SnSe. It is, however, somewhat puzzling that this observed shift is independent of the thickness m of the SnSe layer stack in the heterostructure. With increased thickness, one would expect that the donation efficiency of the innermost SnSe layers is smaller than for the layers at the interface with $TiSe_2$, leading to differently charged layers and, thus, different binding energies for the nonequivalent layers. This is, however, not observed experimentally, but it could be that any difference between the layers is too small to be resolvable in XPS. A similar observation can be made for the case of multilayer graphene grown epitaxially on silicon carbide, where each graphene layer is at a different doping level due to doping from the substrate, but the individual layers cannot be distinguished in the core- level spectra [37, 38, 39]. Given that the information depth in XPS is limited and most of the signal stems from the first 2–3 layers of the surface, the contributions of the innermost SnSe layers are expected to be small for the sample with larger *m*.

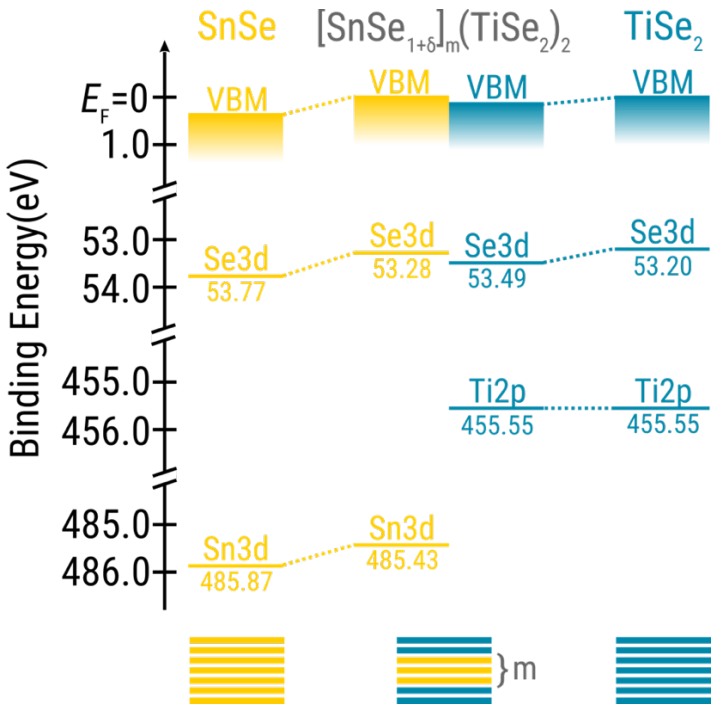

Figure 10.6. Energy diagram of the experimental binding energies of core levels and valence band maximum (VBM) in SnSe (left), $[(SnSe)_{1+\delta}]_m[TiSe_2]_2$ (middle), and $TiSe_2$ (right). The Sn3*d*, Se3*d*, and VBM show an energy shift in the heterostructure compared to the binary compound.

Using the experimental shift ΔE of the valence band in SnSe, it is possible to estimate the amount of charge transferred into $TiSe_2$ for small m values. Considering that there are m layers of SnSe and two layers of $TiSe_2$ in $[(SnSe)_{1+\delta}]_m[TiSe_2]_2$, there are $1/2 \cdot m \cdot (1+\delta)$ SnSe unit cells for each $TiSe_2$ unit cell. The number of electrons transferred on each Ti atom n can then be calculated as follows:

$$n = \frac{1}{4} \cdot m \cdot (1+\delta) \cdot \int_0^{\Delta E} DOS(E)dE. \qquad \text{(Equation 10.1)}$$

The density of states (DOS) in Equation 10.1 was taken from calculations for bulk SnSe by Makistinian et al. [31]. Please note that an additional factor of $1/2$ had to be added in Equation 10.1 because the SnSe unit cell of the $[(SnSe)_{1+\delta}]_m[TiSe_2]_2$ samples only contains one bilayer of SnSe, in contrast to the two bilayers per unit cell for the bulk SnSe used in the calculations. With this approach, the number of

accepted electrons per Ti atom can be estimated to be about 0.12 for m = 1 and 0.24 for m = 2. These values compare very well to the charge carrier density of 0.3 electrons per Ti atom, which Merrill et al. [20] determined from transport data for the similar $(SnSe)_{1.2}TiSe_2$ compound with $m = n = 1$, if we assume that transport is only carried by the donated electrons from the SnSe. In the case of m = 1 for the $[(SnSe)_{1+\delta}]_m[TiSe_2]_2$ samples discussed here, the donated charge has to be distributed over twice the number of $TiSe_2$ layers compared to the compound investigated by Merrill et al., while for m = 2, the ratio of SnSe to $TiSe_2$ layers is the same as in their samples.

Interpretation of the results obtained on the charge accepting $TiSe_2$ layers goes beyond a simple rigid band shift. For the valence band, a small shift of 0.10–0.22 eV toward higher binding energies is observed. The Se3*d* core level is also shifted toward higher binding energies, but the shift is slightly larger at around 0.3 eV. In the binary compound, band structure calculations by Shkvarin et al. [35] suggest that the density of states at E_F is small, but there are empty Ti3*d* states with a high density of states right above the Fermi energy. It is, therefore, reasonable to assume that the Fermi energy is shifted significantly into the Ti3*d* band when accepting the electrons from SnSe, as shown in Figure 10.7. This leads to an increase in binding energy, as is observed for the valence band and the Se3*d* core level. A similar observation of the filling of the Ti3*d* band in such a heterostructure due to electron transfer was made by Brandt et al. in an angle-resolved photoemission spectroscopy (ARPES) study on the ordered misfit layer compound $(PbS)_{1.18}(TiS_2)_n$ with n = 1 and 2 [40], where the constituents PbS and TiS_2 have similar electronic structures as SnSe and $TiSe_2$, respectively [35, 41]. The same mechanism of charge transfer is also discussed for the misfit layer compound $(PbSe)_{1.16}(TiSe_2)_2$ [42] and its rotationally disordered polymorph [43].

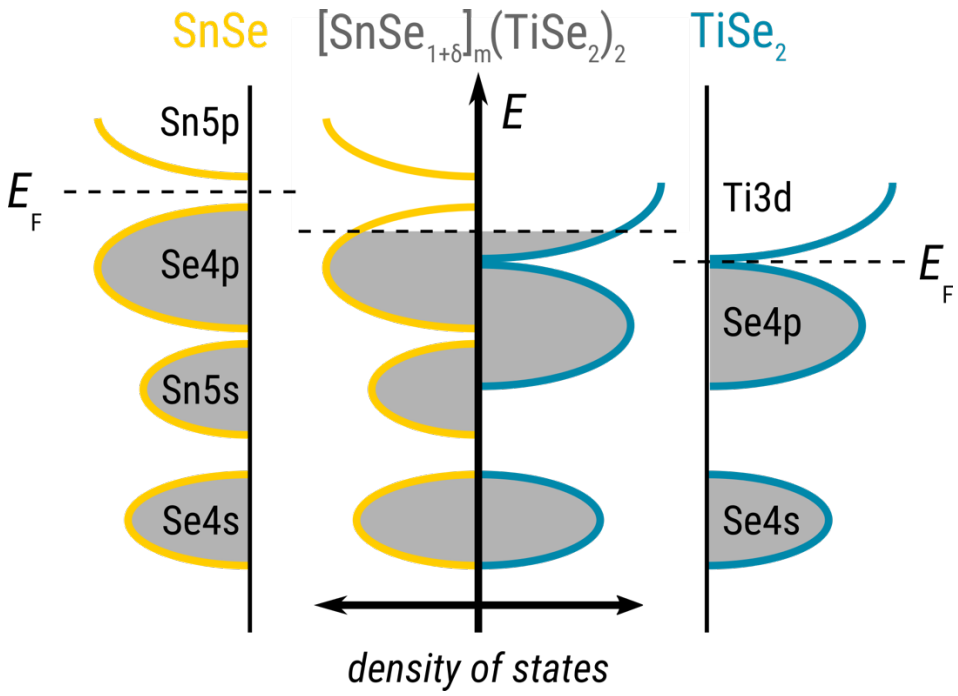

Figure 10.7. Energy diagram of the experimental binding energies of core levels and valence band maximum (VBM) in SnSe (left), $[(SnSe)_{1+\delta}]_m[TiSe_2]_2$ (middle), and $TiSe_2$ (right). The Sn3*d*, Se3*d*, and VBM show an energy shift in the heterostructure compared to the binary compound.

The 2*p* core level of titanium appears at the same binding energy in the heterostructures and the binary compound and shows only a slight increase in Gaussian peak width with increasing *m*. This seems to contradict the observations on the Se3*d* core level and valence band. Similar effects have been observed for example in intercalated graphene, where the rigid core-level shift is counteracted at higher doping levels and, therefore, different than the shift of the Fermi energy [44].

To further substantiate the interpretation of the XPS results, the valence bands of $TiSe_2$ and a representative $[(SnSe)_{1+\delta}]_m[TiSe_2]_2$ sample with $m = 3$ were measured with UPS using He-II excitation to achieve a better resolution and intensity of the spectra. The results of these measurements are shown for polar angles between 0° and 30° in Figure 10.8. By increasing the polar angle between the sample's surface normal

and the analyzer, electrons with a parallel component of the wave vector further away from the Γ-point of the Brillouin zone can be detected. Similar as in the work by Brandt et al. [40], in binary $TiSe_2$, the Ti3*d* band at the Fermi energy can be seen as a weak signal at larger polar angles, which shows that this state is partially filled at room temperature. Upon adding electron-donating SnSe layers in $[(SnSe)_{1+\delta}]_3[TiSe_2]_2$, the overall appearance of the spectrum changes due to contributions from SnSe. Even though the effect is smaller than that observed by Brand et al., the intensity of the Ti3*d* band is increased by a factor of approximately 2–3, which can be explained by a higher electron population in this state in the heterostructure in comparison to the binary sample. This is consistent with the donation of electrons by SnSe and, thus, confirms the conclusions drawn from XPS. The XPS and UPS valence band spectra show a nonzero density of states at the Fermi energy for the investigated $[(SnSe)_{1+\delta}]_m[TiSe_2]_2$ heterostructures. We, therefore, expect the samples to show metallic behavior at room temperature, consistent with a prior report on the electrical properties of $[(SnSe)_{1+\delta}]_mTiSe_2$ compounds [23]. The $[(SnSe)_{1+\delta}]_2[TiSe_2]_2$ sample investigated here has the same stoichiometry as the $(SnSe)_{1+\delta}TiSe_2$ compound, but with a different interface density. We expect that these two com- pounds will have similar electrical properties.

While all the data are consistent with a charge transfer of electrons from SnSe into $TiSe_2$ occurring in $[(SnSe)_{1+\delta}]_m[TiSe_2]_2$, it is still unclear why no significant differences between samples with different m can be observed. Using our simple rigid band model for SnSe and concluding that each layer donates roughly the same amount of electrons, a change of the core-level binding energies or valence band of the $TiSe_2$ layers with increasing *m* would be expected, since the number of charge accepting layers stays the same. This is, however, not observed as even though the total amount of charge distributed along the $TiSe_2$ layers appears to

increase 7-fold from m = 1 to 7, no significant difference in the experimental electronic structure can be observed within the resolution of the XPS instrument. Further research on other stacking arrangements in this family of heterostructures is necessary to fully comprehend the interplay between layers.

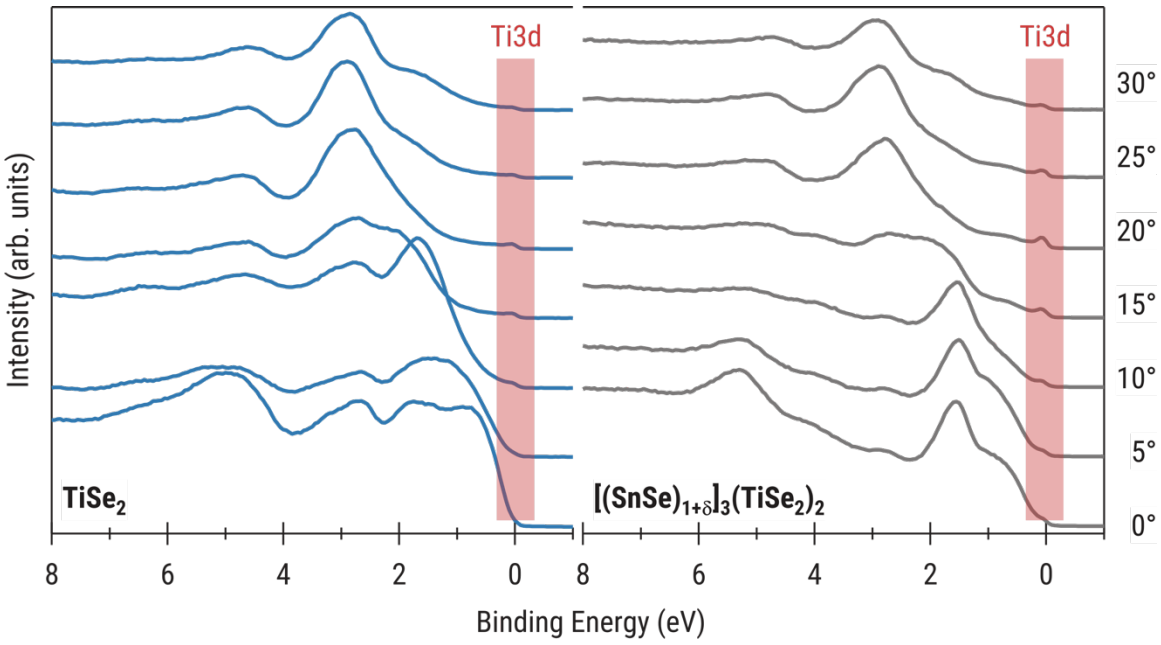

Figure 10.8. Valence bands of TiSe2 and $[(SnSe)_{1+\delta}]_3[TiSe_2]_2$ measured with UPS at different polar angles between sample surface and analyzer. Especially for larger angles, the Ti3*d* state at EF can be observed. In the heterostructure, the intensity of this Ti3*d* peak is increased, confirming a higher electron population in this state.

10.3. Conclusion

A series of $[(SnSe)_{1+\delta}]_m[TiSe_2]_2$ heterostructures with increasing thickness of the SnSe stack m = 1, 2, 3, and 7 was grown by self-assembly from designed amorphous precursors. The optimum crystallization temperature was determined via an annealing study to be 350 °C. Structural investigations using XRR, XRD, and HAADF-STEM showed that the films grow in crystalline layers parallel to the substrate but show rotational disorder between layers, as is common for products

from this synthesis. Their electronic structure was investigated by applying XPS to samples cleaved at the van der Waals gap between the $TiSe_2$ layers and comparing them to the results obtained on binary $TiSe_2$ and SnSe samples grown in the same manner. Contrary to expectations, no significant differences in the electronic structures could be observed between samples with different m. The measured spectra of the heterostructures can be modeled by a weighted superposition of the spectra of the constituent layers. The SnSe component shows a rigid band shift toward lower binding energies, consistent with a transfer of electrons into the $TiSe_2$ layers. By accepting charges from SnSe, the Ti3*d* band of $TiSe_2$ is filled, which is also confirmed by UPS, leading to a shift of the observed valence band and Se3*d* core-level positions toward higher binding energies. To further understand the nature of the interactions in this system, a follow up study on a series of $[(SnSe)_{1+\delta}]_1(TiSe_2)_n$ hetero-structures with increasing thickness n of the $TiSe_2$ layer stack is planned for the immediate future.

10.4. Materials and Methods

10.4.1. Synthesis

Layered amorphous precursors for the preparation of $[(SnSe)_{1+\delta}]_m[TiSe_2]_2$ heterostructures (m = 1, 2, 3, and 7) and binary $TiSe_2$ and SnSe films were deposited in a high-vacuum chamber by physical vapor deposition. All materials were evaporated from elemental sources onto silicon wafer substrates with a native SiO2 layer. Sn and Ti were deposited using electron beam guns, and Se was deposited using a Knudsen effusion cell. Pneumatic shutters and a house written LabView code were used to control the deposition [45]. Quartz crystal microbalances were used to monitor the rate of deposition and the relative amount of material deposited. The amount of material required to crystallize a single bilayer of $TiSe_2$ or SnSe was calibrated using an iterative process, including XRD, XRR, and XRF measurements [28]. The

amorphous precursors were annealed ex situ in a nitrogen atmosphere glove box to facilitate the crystallization of the targeted binary compound or heterostructure. An annealing study was conducted for the hetero-structures to determine the correct conditions for crystallization, which included annealing a sample at multiple temperature steps for 30 min.

10.4.2. Diffraction

XRR, specular XRD, and in-plane XRD were collected to characterize the structure of the samples analyzed in this study as well as to investigate the evolution of their crystallization. All XRD data were collected in house using Cu ka as the source of radiation. XRR and specular XRD were collected on a Bruker D8 Discover diffractometer outfitted with a Göbel mirror. In-plane diffraction was collected on a Rigaku SmartLab using the in-plane general medium resolution and parallel beam optics alignment. A nickel filter was used on both instruments to eliminate any signal from Cu Kb. XRF, used to determine the amount of material needed in each layer, was collected on a Rigaku ZSX Primus II wavelength dispersive XRF spectrometer with a rhodium X-ray source and analyzed using the method described previously by Hamann et al. [28].

10.4.3. HAADF-STEM

HAADF-STEM images were collected for $[(SnSe)_{1+\delta}]_m[TiSe_2]_2$ to provide a real space depiction of the crystallized structure. Ultrathin cross-sections were prepared using an FEI Helios NanoLab 600i FIB-SEM (FEI Company, Hillsboro, OR). As the lamellae approached electron transparency, low-energy 2 kV milling was used to avoid damaging the crystallinity of the sample. The prepared samples were imaged in HAADF-STEM mode at 300 kV using Lawrence Berkeley National Lab's (LBNL) TEAM 0.5 microscope (Berkeley, CA). The camera length was 105 mm.

10.4.4. Photoelectron Spectroscopy

XPS measurements were carried out in ultrahigh vacuum (UHV) at a pressure below 3 x 10^{-10} mbar using Al Kα radiation from a SPECS XR50M X-ray source equipped with a SPECS FOCUS 500 crystal monochromator for excitation and a SPECS Phoibos 150 MCD-9 hemispherical analyzer (SPECS Surface Nano Analysis GmbH, Berlin, Germany) for detection of the photoelectrons. Prior to experiments, the crystals were cleaved to remove surface oxides and contaminants. This was achieved by mounting the samples between two steel plates using epoxy adhesives and breaking off the top plate in the load lock chamber of the UHV system under flow of dry N_2, as demonstrated previously [26]. Insulating EPO-TEK H72 epoxy was used on the sample plane and silver-filled, conductive EPO-TEK H22 (Epoxy Technology, Inc., Billerica, MA) was used at the edges of the sample. This was done to get a good electrical contact, while at the same time preventing contributions from the silver particles of the H22 to the spectra. After cleaving, each half of the cleaved crystal could be investigated. Attaching another steel plate to the cleaved plane after the experiment allowed for a second cleave of the same sample. Estimating an inelastic mean free path λ of 22 Å for electrons with a kinetic energy of about 1000 eV (correspond- ing to Sn3d and Ti2p states), and an information depth of about 3k, most of the measured signal stems from the first 10–12 layers at the surface, covering 2–3 unit cells for the compounds with $m \leq 3$. Selected samples were cleaved in the same way and used for UPS, using monochromatic He-II radiation from a SPECS UVS 300 UV source and SPECS TMM 304 monochromator in combination with a SPECS Phoibos 150 hemispherical analyzer (SPECS Surface Nano Analysis GmbH, Berlin, Germany) equipped with a 2D-CCD detector and operated in wide-angle mode.

10.5. BRIDGE

Chapter 10 investigated the charge donation between layers and the band structure as a function of nanoarchitecture in a series of $[(SnSe)_{1+\delta}]_m[TiSe_2]_2$ heterostructure compounds where m = 1, 2, 3, and 7 via XPS. The results indicated that while there is a structural modification that occurs as the number of SnSe layers in a repeating unit is increased, there is no significant change in charge donation and band structure as a function of the number of SnSe layers. This is interesting when considering the unique transport data that has previously been reported for varies series of $[(SnSe)_{1+\delta}]_m[TiSe_2]_n$ heterostructure compounds. Chapter 11 will focus on how synthesis conditions and understanding the formation of materials can lead to designer materials as well as further evidence for manipulation of material properties via heterostructure nanoarchitecture.

CHAPTER XI

BURIED INTERFACES IN $[(PBSE)_{1+\delta}]_4[TISE_2]_4$ ISOMER HETEROSTRUCTURES.

11.0. AUTHORSHIP STATEMENT

At this time, this work is unpublished and coauthored with Aaron Miller, Sage Bauers, Jeffrey Ditto, Daniel Moore, and David Johnson. I assisted with transport data analysis, XRF data collection, and manuscript preparation. Aaron Miller assisted with the XRR analysis of the isomer heterostructures as well as the manuscript preparation. Sage Bauers prepared and characterized the samples as well as contributed to manuscript preparation. Jeffrey Ditto assisted with sample preparation for and collection of scanning tunneling electron microscopy data. Daniel Moore assisted with sample preparation and characterization. David Johnson is my advisor who assisted in the experimental design, analysis of data, and writing of the manuscript.

11.1. INTRODUCTION

Molecular chemists have developed synthetic methods to prepare kinetically stable compounds with designed structures. This permits them to prepare multiple compounds containing the same number and type of elements that are connected in various ways.[1–3] The local arrangement of atoms in a compound determines the physical, electronic and biological properties it exhibits.[4–11] For example, the five different structural isomers of hexane (hexane, 2-methylpentane, 3-methylpentane, 2,2-dimethylbutane, and 2,3-dimethylbutane) all have different melting and boiling points as a consequence of their varying local arrangements.[12–15] The ability to predict metastable stable compounds via simple bonding rules (ie. each carbon must have 4 bonds, oxygen 2, and hydrogen 1) combined with an understanding of how to control the kinetics by manipulating reaction conditions (solvents,

protecting groups, catalysts) enables molecular chemists to propose and test structure-property relationships towards optimizing desired properties. [2,16–18]

It is more challenging to prepare structural isomers of inorganic compounds with extended structures, which are known as polymorphs.[19] Some well-known examples of polymorphs are vaterite, calcite and aragonite. These compounds are different structural forms of calcium carbonate which exhibit different properties and free energies of formation.[20–23] Typically, polymorphs are prepared by changing the reaction conditions (temperature, pressure, composition of the reacting system, etc.) so that the desired product is the most thermodynamically stable product in that reacting system. The structure of the product cannot be predicted from simple bonding rules or reaction conditions but is instead determined experimentally. For compounds only stable at high temperature or pressures, quenching the system to room temperature and pressure often traps the now metastable polymorph. The lack of knowledge of how to control reaction kinetics to obtain targeted inorganic, extended, targeted structures severely limits the number of polymorphs that can be prepared.[24–27] The holy grail in the synthesis of compounds with extended structures is *a design and mechanism-based approach to the synthesis of metastable compounds with targeted structure.*[28]

Presented here is the synthesis and characterization of six different structural isomers of the compound $[(PbSe)_{1+\delta}]_4[TiSe_2]_4$, which have the same composition and unit cell sizes, but the sequence of PbSe bilayers and $TiSe_2$ trilayers vary between isomers. The different isomers were prepared from precursors with sequences of elemental layer designed to mimic the nanoarchitecture of the targeted isomer. While the amount of lead in the deposited precursors was insufficient to make the desired number of repeating units, the difference in the sequences of deposited

layers still directed the self-assembly of the desired isomers. X-ray diffraction and HAADF-STEM data supports the formation of the desired isomer nanoarchitectures with a decreased number of unit cells and impurity phases present on the top and bottom of the sample. As-deposited structural characterization indicated that $TiSe_2$ and PbSe crystalized during the deposition and were organized in stacking sequences consistent with the targeted isomer. Unexpectedly, Ti_2Se also crystalized during deposition at the interface with the substrate. The HAADF-STEM images suggest that the sample crystalizes from the bottom to the top, with the concentration gradients created at the growth front driving diffusion of Pb and Ti to the growing isomers. The measured electrical transport properties systematically vary with changes in the nanoarchitecture, with lower resistivity and higher carrier concentrations found in compounds with a higher density of PbSe|$TiSe_2$ interfaces within the isomer's unit cell. This is likely the result of charge transfer between materials being dependent on interface interactions. This work indicates that the self-assembly process begins during the deposition itself, driven by the heat of formation of the constituent layers. The nanoarchitecture of the precursor is sufficient to direct the formation of the targeted structure isomers, even if the composition of the precursor deviates significantly from that of the product, suggesting that the compounds are significant local energy minima in the free energy landscape.

11.2. Materials and Methods

The $[(PbSe)_{1+\delta}]_4[TiSe_2]_4$ heterostructure isomer precursors were prepared from physical vapor deposition of elemental layers onto silicon and fused silica substrates. Elemental Pb and Ti were evaporated from electron beam guns operating at 6 kV. Elemental Se was deposited from a Knudsen effusion cell. All elements were purchased from Alfa Aesar and were greater than 99.95% purity. Shutters above each evaporating

source were programmed to sequentially open for the period of time required to deposit the appropriate thickness of each element to form either bilayers of PbSe or trilayers of $TiSe_2$. The thickness of the elemental layers deposited was monitored by quartz crystal microbalances. PbSe bilayers were deposited with a Pb|Se shutter sequence and $TiSe_2$ trilayers with a Ti|Se shutter sequence. The sequence of Pb|Se and Ti|Se layers was controlled such that the nanoarchitecture of the precursor resembled the structure of the targeted isomer.[29] The sequence of Pb|Se and Ti|Se layers for each isomer was repeated 11 times to build a film that was approximately 550 nm thick. The elemental precursors were annealed at 350 °C for 30 minutes in an N_2 atmosphere to promote self-assembly into a crystalline heterostructure.[30–35]

Amount of material per unit area was determined for each heterostructure using wavelength dispersed x-ray fluorescence (XRF) data. The data was analyzed using a previous published method in which the raw intensity of each sample is determined by integrating under the signal curve and subtracting the background signal.[36] Calibration curves for each element were used to relate the measured signal to the number of atoms per unit area in each film.

Locked-coupled θ-2θ and grazing-incidence in-plane x-ray diffraction (XRD) data were both collected using laboratory Cu-Kα radiation with parallel beam optics on a Bruker D8 Discover and Rigaku Smartlab, respectively. Grazing-incidence scans were carried out with an incident angle of 1.0° and the detector 4.0° above the sample plane. Ab-initio reflectivity patterns from the idealized targeted structures were generated with the Bede REFS modeling software assuming bulk densities.

High angle annular dark-field scanning transmission electron microscopy (HAADF-STEM) images were collected using a probe

aberration corrected FEI Titan 80-300 (300kV, 120 mm camera length, C_s<1 um). Energy dispersive X-ray spectroscopy (EDS) data were acquired with a 2.3 ms dwell time per pixel and summed over several drift-corrected frames. Cross-sectional lamellae for STEM imaging were made using an FEI Helios 600 Nanolab dual-beam FIB.[37]

Electrical measurements were carried out on a house-built closed-cycle He cryostat using a 1.5 T magnet. Van der Pauw resistivities and Hall resistivities both were collected on cross-pattern films through Cu wires and In contacts. Reported values were calculated using thicknesses from reflectivity measurements of the annealed films. Seebeck coefficients were also measured using a house-built system. One edge of the film was cooled slightly and both S and ΔT were measured between two type-T thermocouples.

11.3. Results and Discussion

11.3.1. Structure

X-ray reflectivity (XRR) and diffraction data indicate that the as-deposited precursors have a more complex structure than elemental layers in a specific pattern. Figure 11.1 contains a representative XRR pattern of an as deposited $[(PbSe)_{1+\delta}]_4(TiSe_2)_4$ isomer precursor (the 2**1**1**2**1**1** isomer is shown**)**. The pattern contains Kiessig fringes consistent with the 11 layers deposited, the first several Bragg reflections from the element layering, and Laue oscillations between the Bragg maxima. A film composed of 11 repeat units of a $[(PbSe)_{1+\delta}]_4(TiSe_2)_4$ isomer is expected to have a total film thickness of ~535 Å, slightly lower than the observed film thickness for the as-deposited isomers which range from 544 Å – 557 Å. The thickness of the elemental layering determined from the position of the first order Bragg reflection is slightly higher than the targeted value expected for a $[(PbSe)_{1+\delta}]_4(TiSe_2)_4$ repeat unit, 48.68 Å, in all of the samples (ranging from 49.19 Å to 50.81 Å). However, the observed Laue oscillations indicate that there are only 10

layers present in the repeating elemental modulation, requiring that one of the as-deposited layers differs from what was intended. Representative XRD patterns, Figure 11.1, G.1, and G.2, for as-deposited $[(PbSe)_{1+\delta}]_4(TiSe_2)_4$ isomer precursors indicate that PbSe and $TiSe_2$ have nucleated during deposition and that there are already coherent blocks of the $[(PbSe)_{1+\delta}]_m(TiSe_2)_n$ isomer heterostructure before annealing. Surprisingly, we also see reflections consistent with the formation of crystallographically aligned Ti_2Se impurity phase which has a c-axis lattice parameter of 15.6 Å. XRR, XRD, and HAADF-STEM images (to be discussed in subsequent paragraphs) all show that annealing the precursors at 350 °C for 30 minutes in an N_2 atmosphere provides enough energy for the self-assembly of the elemental precursors into the desired $[(PbSe)_{1+\delta}]_4[TiSe_2]_4$ isomer structure, although only 8-9 layers of the intended isomers form and the presence of the Ti_2Se impurity phase remains.

The annealed heterostructures were analyzed by XRF to quantify the amount of material present in each film and the results are summarized in Table 11.1. While the targeted isomer structures all had the same number of total atoms/Å^2 for each element, (see Table 11.2), there is a large variation in the actual amount of material measured in the films after deposition, reflecting the challenges of reproducibly depositing monolayer amounts of various elements. Pb is the limiting element in all of the films, and there is not enough Pb, Ti, or Se in any of the films to form 11-unit cells of any of the targeted isomers (see Table 11.2). The lack of sufficient Pb, Ti, and Se in the precursors explains why fewer unit cells formed compared to what was targeted. To form the intended isomers required diffusion within and between deposited layers to provide Pb to the nucleation sites. This results in less than 11 repeating units forming. Surprisingly, the deposited nanoarchitecture and initial layer growth in the precursors was sufficient to direct the

formation of the targeted isomers despite atoms diffusing between deposited layers and fewer than targeted layers forming.

XRR patterns of the annealed films provide insight to the complex structure of the products that formed during annealing. Information contained in the XRR patterns is detailed in Figure 11.2, using the 3**2**1**2** isomer pattern as a representative example. The 3**2**1**2** isomer has a layer sequence of aaa**bb**a**bb**, where the thicknesses of the PbSe component in the unit cell (a) has a normal typeface and the $TiSe_2$ (b) is bold in the 3**2**1**2** abbreviation. Bragg maxima from the self-assembled product are observed in the XRR pattern and the position of these maxima yield a *c*-axis lattice parameter of 48.60(1) Å, which is consistent with the expected unit cell of a $[(PbSe)_{1+\delta}]_4[TiSe_2]_4$ isomer composed of 4 layers of $TiSe_2$ and 4 layers of PbSe. The XRR pattern also has smaller maxima, which come from two different effects. Near the critical angle, these smaller maxima are called Kiessig fringes, and they are a consequence of the interference of x-rays reflecting from the top and the bottom of the film. At higher angles, the smaller maxima between the Bragg reflections, called Laue oscillations, result from incomplete destructive interference from the finite number of unit cells in the film. The number of Laue oscillations between consecutive Bragg reflections depend on the number of unit cells contributing to the interference effect. The top left panel of Figure 11.2 shows that a film thickness of 491.4 Å results in Kiessig fringes that match those observed for the 3**2**1**2** isomer. A film that is composed of 9-unit cells contributing to the total thickness does not match the experimental low angle data between the critical angle and the first Bragg reflection. The top right panel of Figure 11.2 compares simulations of the Laue fringes for a heterostructure with the targeted 11- unit cells and a heterostructure with 9-unit cells contributing to the interference effect with the experimental data for the 3**2**1**2** isomer.

Simulations for a film composed of 9 repeating unit cells matches the observed experimental data.

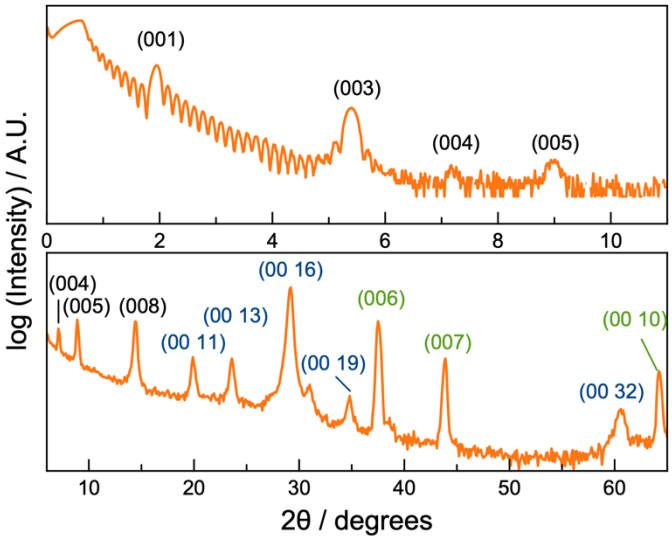

Figure 11.1. As-deposited XRR and XRD for a 2**1**1**2**1**1** isomer providing representative behavior observed in all of the $[(PbSe)_{1+\delta}]_4(TiSe_2)_4$ isomer heterostructures. 00*l* reflections, corresponding to the artificial layering, the crystalized $[(PbSe)_{1+\delta}]_4(TiSe_2)_4$ isomer heterostructure, and the impurity Ti_2S phase, are indexed in black, blue, and green, respectively. Additional as-deposited XRR patterns can be found in the supporting information Figure G.1.

Table 11.1. Total Atoms / Å^2 in each of the annealed $[(PbSe)_{1+\delta}]_4[TiSe_2]_4$ isomer films. The error in the conversion factor between XRF intensity and number of atoms per unit area is 2-3%.

Isomer	Atoms / Å^2		
	Pb	Ti	Se
2**2**1**1**1**1**	3.61(1)	3.65(1)	9.82(2)
2**1**1**2**1**1**	3.64(1)	3.74(1)	10.28(2)
3**3**1**1**	3.71(1)	3.61(1)	9.78(2)
3**2**1**2**	3.65(1)	3.59(1)	10.02(2)
2**3**2**1**	3.60 (1)	3.87(1)	10.33(2)
4**4**	3.38 (1)	4.02(1)	10.47(2)

Table 11.2. Calculated number of atoms / Å^2 for each element for the $[(PbSe)_{1+\delta}]_4(TiSe_2)_4$ isomers for different film thicknesses.

Number of $[(PbSe)_{1+\delta}]_4[TiSe_2]_4$ Repeating Units	Atoms / Å^2 Pb	Ti	Se
8	3.39	2.91	9.19
9	3.82	3.28	10.34
10	4.24	3.64	11.49
11	4.37	4.00	12.64

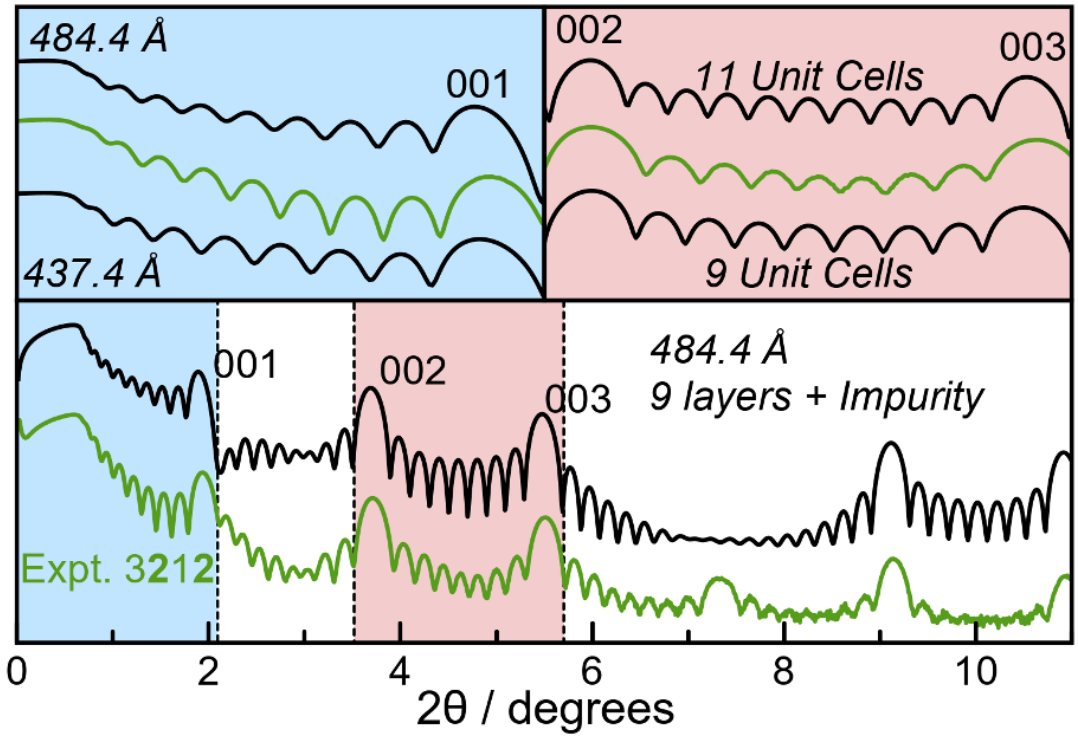

Figure 11.2. Experimental and simulated XRR patterns for the 3**2**1**2** structural isomer. The upper left panel focuses on the Kiessig fringes, indicating that the total film thickness is 491.4 Å. The upper right panel emphasizes the Laue oscillations, showing that 9-unit cells are present, not the 11 expected from the deposition sequence. The bottom panel compares the simulated and experimental patterns based on the complete model described in the text.

Since Kiessig fringes are extremely sensitive to the quality of interfaces (roughness) while the Laue oscillations are sensitive to the number of unit cells interfering in the sample and the extent of their disorder, the experimental low angle patterns reflect the changing contributions of both diffraction effects throughout the presented angular range. The discrepancy between the total film thickness and the number of repeating units indicates there is extra material present in the films. This extra material can exist either above and/or below the 9-unit cells of the 3**2**1**2** isomer. The relative thickness of the top and bottom impurity layers influences the rate of decay of the intensity above the critical angle. The roughness of the layer on top of the 3**2**1**2** block determines the angular dependence of the relative contributions of the Kiessig and Laue interference effects. The bottom panel in Figure 11.2 shows a simulated pattern containing 9-unit cells of the 3**2**1**2** isomer with 47 Å of extra thickness divided between a 35 Å layer underneath and a 12 Å on top with the top thickness having a roughness of 5Å. The positions of the maxima line are consistent between the simulated and experimental patterns. The magnitude of the Laue oscillations is larger in the simulated pattern because the 3**2**1**2** block was modeled as an ideal film. The intensity of the Laue oscillations can be suppressed and the intensity of the 4th order Bragg reflection can be increased by adding roughness to one or more of the unit cells. The 35 Å layer underneath the 3**2**1**2** isomer block is likely the Ti_2Se impurity phase observed in the as-deposited XRD and is likely responsible for the as-deposited XRR patterns containing Laue fringes for only 10 layers.

Similar models were created for all of the targeted $[(PbSe)_{1+\delta}]_4[TiSe_2]_4$ heterostructure isomers, varying the stacking sequence of the 8 layer blocks. Assuming atomically sharp interfaces between the constituent structures and a constant electron density within each constituent results in a square-wave function for the electron

density as shown in Figure 11.3. This simple model assumed the *c*-lattice parameters for the heterostructures were equal and the interfaces between the 8 constituent unit cells occurred at intervals of $\frac{1}{8}$ of the unit cell. The 2**2**1111 and 211**2**1 compounds have 5 interfaces, the 3**3**11, 3**2**1**2**, and 2**3**21 compounds have 3 interfaces, and the 4**4** profile has 1 interface within the unit cell. The Fourier transform of the electron density of each $[(PbSe)_{1+\delta}]_4[TiSe_2]_4$ heterostructure isomer is different due to the distinctive placement of the 8 constituent layers within the unit cell. Consequently, the pattern of intensities of the 00l reflections in the specular diffraction will be unique for each structural isomer.

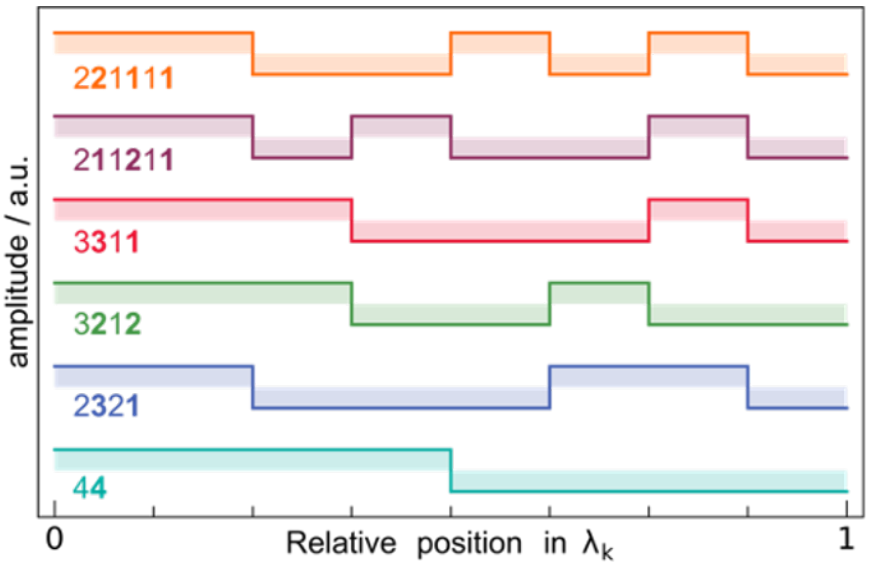

Figure 11.3. Schematic representation of the variation of electron density through a unit cell for each of the $[(PbSe)_{1+\delta}]_4[TiSe_2]_4$ isomers.

Experimental XRR patterns for each of the $[(PbSe)_{1+\delta}]_4[TiSe_2]_4$ isomers are shown in Figure 11.4 along with simulated patterns using both the electron density profiles determined from Figure 11.3 and the parameters gathered using the method described for the 3**2**1**2** isomer. Bragg reflections observed in the XRR patterns occur at nominally the same 2θ angle, for all of the $[(PbSe)_{1+\delta}]_4[TiSe_2]_4$ isomers, indicating the repeating unit is similar. Relative patterns of the of the Bragg reflection

intensities correlates well between the models and experimental data. Small intensities experimentally observed when the models predict zero intensity result from approximations made for the models shown in Figure 11.3. For the model it was assumed the interfaces were located at exactly 1/8th intervals of the unit cell, but experimentally the Se-Ti-Se trilayer and a Pb-Se bilayer thicknesses are not equal. Another assumption used to make the model is that the layers are perfectly smooth, when in reality there is some observed roughness. The positions of the Laue oscillations in the models were adjusted by varying the number of unit cells of each isomer to match the experimental data. Kiessig fringes observed in the models were made to match the experimental data by varying the total thickness of the samples via adding more excess material on the top or bottom of the film, using the STEM images of each isomer as a guide to approximate how much extra material was present. The patterns are somewhat insensitive to the exact ratio of thickness of the top/bottom impurity layers, so the decay of the intensity from the critical angle to the first Bragg maxima was adjusted by varying the exact thicknesses of the top and bottom impurity layers. The roughness of the layer on top of the isomer block was adjusted to match the observed change from Kiessig fringes to Laue oscillations, which differs slightly based on impurity thicknesses and number of unit cells. All of the parameters from the models are summarized in Table 11.3. All of the $[(PbSe)_{1+\delta}]_4[TiSe_2]_4$ isomers have fewer unit cells in the isomer blocks than the targeted number. The total thicknesses of the isomers are all less than what was measured for the as-deposited samples as a result of Se loss during annealing in an open system. It was determined that all $[(PbSe)_{1+\delta}]_4[TiSe_2]_4$ isomers have impurity layers above and below the block of repeating units.

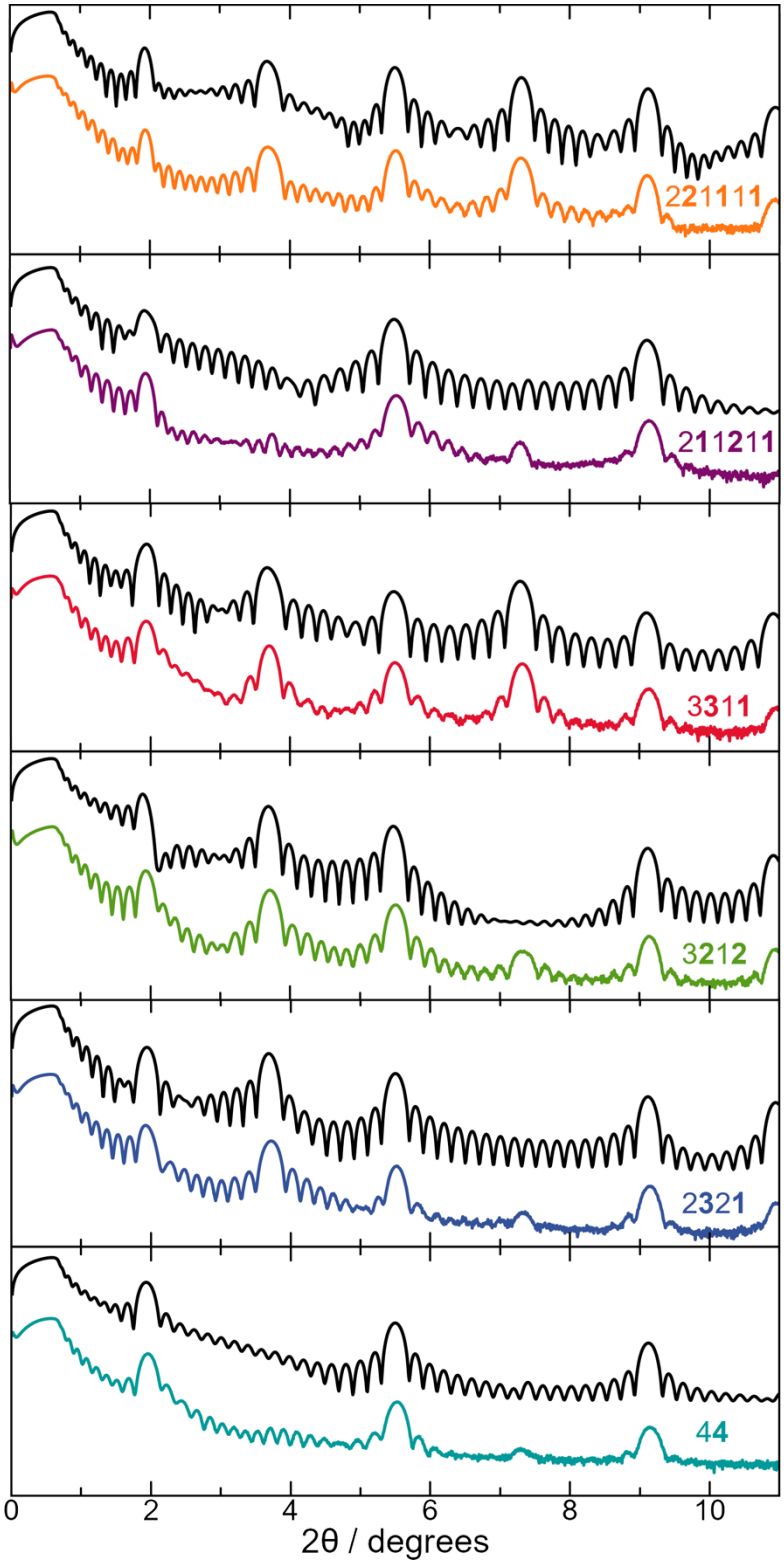

Figure 11.4. X-ray reflectivity patterns (in color) shown against simulated patterns created using models of the targeted isomers (in black) described in Figure 11.3.

Table 11.3. Parameters extracted from the XRR patterns as described in the text. Not shown in the table are parameters that do not vary the calculated patterns significantly. These parameters (the bottom impurity roughness (5Å), and the roughness of the Si substrate (5Å)) were held constant in all of the models.

Sample	Number of unit cells in isomer block	Total Thickness (Å)	Thickness of Isomer Block	Bottom Impurity Thickness (Å) (+/- 5)	Top Impurity Thickness (Å) (+/- 5)	Bottom Impurity Roughness (Å)
2**2**1**1**1**1**	9	514	438	40	36	1.0
2**1**1**2**1**1**	8	498	389	48	34	5.0
3**3**1**1**	8	482	389	60	40	5.0
3**2**1**2**	9	484	437	35	12	5.0
2**3**2**1**	9	481	437	14	30	8.0
4**4**	9	491	437	27	27	5.0

Specular and in-plane XRD patterns of the crystalized isomer heterostructures are shown in Figure 11.5. Lattice parameters were determined for each of the $[(PbSe)_{1+\delta}]_4[TiSe_2]_4$ isomers and are summarized in Table 11.4. All but three of the maxima in the specular x-ray diffraction patterns can be indexed as 00*l* reflections corresponding to the nanoarchitecture of the targeted isomers. The *c*-axis lattice parameters, determined from the position of the 00*l* reflections, are similar for all of the isomers and are consistent with a repeating unit composed of four layers of PbSe and four layers of $TiSe_2$. The three reflections not belonging to the isomer's unit cell can be indexed as 00*l* reflections from Ti_2Se. The lattice parameter obtained, 14.52(5) Å, matches that expected for Ti_2Se.[38] This is consistent with the excess Ti observed in the number of atoms/ Å^2 determined from the XRF data for the annealed compounds and the impurity phase observed in the

representative as-deposited diffraction. All of the reflections in the in-plane diffraction scan can be indexed as *hk*0 reflections from either a hexagonal or square unit cell, whose lattice parameters correspond to either the $TiSe_2$ or the PbSe constituent, respectively Table 11.4). Relative intensities of the reflections from each constituent are constant between isomers, indicating that there are similar relative amounts of PbSe and $TiSe_2$ in each of the heterostructures. Both the PbSe and $TiSe_2$ in-plane lattice parameters remain constant as the isomer nanoarchitecture is varied indicating there is no structural change as a function of layer sequence. There are no observed reflections corresponding to the Ti_2Se impurity phase in the in-plane diffraction. The (110) and (310) reflections observed in the square unit cell indicate that PbSe does not have the bulk rock salt structure, because these reflections are forbidden in the *Fm*-3*m* rock-salt space group. This indicates that the PbSe structure has distorted with either Pb or Se no longer on special position sites, which is not unexpected for these ultrathin layers.

HAADF-STEM images, collected for each of the $[(PbSe)_{1+\delta}]_4(TiSe_2)_4$ isomers, provide local information about defects and overall sample structure. Figure 11.6 shows a full film image of the 4**4** $[(PbSe)_{1+\delta}]_4(TiSe_2)_4$ isomer. Rock-salt layers containing Pb show up as bright regions due to the higher average atomic number relative to $TiSe_2$ layers, which are darker. STEM-EDS data for the 2**3**2**1** isomer, shown in the SI Figure G.3, confirms this assignment. Distinct bright atomic columns of atoms can be seen in regions where the electron beam aligns with a crystallite's zone axis. Different layers and regions within the same layer have different orientations indicating both rotational disorder and some stacking defects. The majority of the film consists of 9-unit cells of the isomer, which is consistent with the XRR data discussed previously. At the top and bottom of the film there is material that is not consistent with the repeating blocks of the of the isomer. In the layer closest to the

substrate there are regions where Ti_2Se grains can be found in addition to smaller regions of $TiSe_2$ and $(PbSe)_1(TiSe_2)_1$. These observations are consistent with the analysis of the XRF, XRR and XRD data discussed previously.

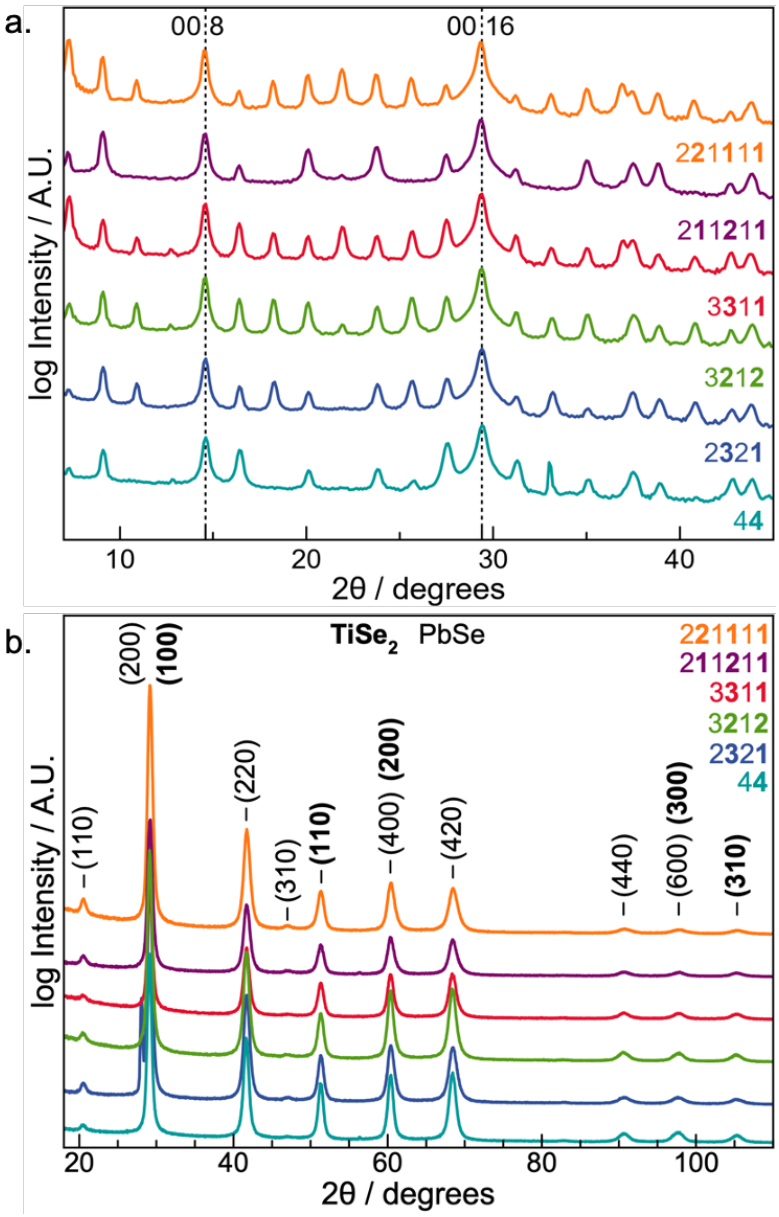

Figure 11.5. Specular (a.) and in-plane (b.) XRD patterns of the $[(PbSe)_{1+\delta}]_4[TiSe_2]_4$ structural isomers. The indices of the observed reflections are shown above each reflection in the in-plane pattern and representative indices are indicated in the specular pattern.

Table 11.4. Lattice parameters for the $[(PbSe)_{1+\delta}]_4[TiSe_2]_4$ structural isomers determined from the annealed diffraction patterns.

Sample	*c*-axis lattice parameter (Å)	PbSe *a*-axis lattice parameter (Å)	$TiSe_2$ *a*-axis lattice parameter (Å)	Impurity Phase
2**2**1**1**1**1**	48.66(1)	6.121(1)	3.560(1)	14.41(4)
2**1**1**2**1**1**	48.64(1)	6.132(1)	3.566(1)	14.54(1)
3**3**1**1**	48.62(1)	6.131(1)	3.561(1)	14.53(3)
3**2**1**2**	48.60(1)	6.134(1)	3.563(1)	14.55(2)
2**3**2**1**	48.56(1)	6.128(2)	3.561(2)	14.54(1)
4**4**	48.52(2)	6.132(1)	3.560(1)	14.55(1)

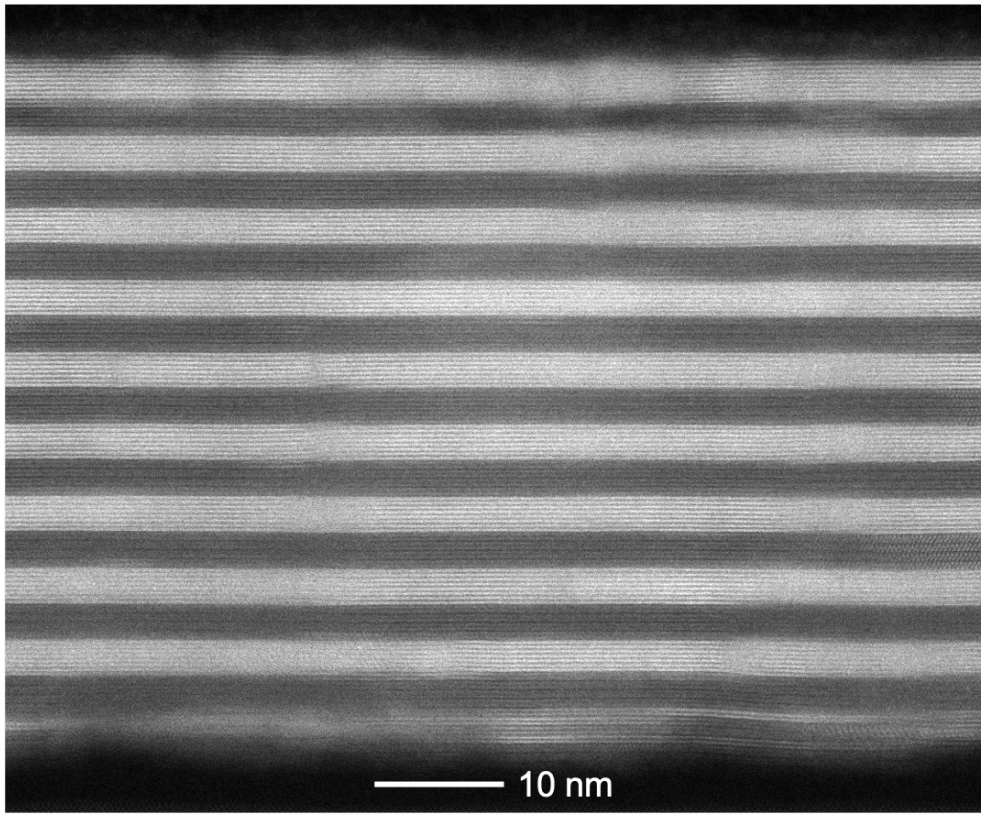

Figure 11.6. HAADF-STEM image of the 4**4** $[(PbSe)_{1+\delta}]_4[TiSe_2]_4$ structural isomer showing the entire film from substrate to surface.

Figure 11.7 shows HAADF-STEM images of all $[(PbSe)_{1+\delta}]_4[TiSe_2]_4$ structural isomers. These images demonstrate that the films consist of different sequences of PbSe and $TiSe_2$ layers with sharp planar interfaces between them. There is extensive rotational disorder occurring between

the different constituent layers in each block, evident by zone axis orientations appearing in only some of the layers. The different layering schemes for each of the 6 isomers can be clearly identified and is further supported by the EDS profile shown in G.3. As observed in the specular XRD patterns, the thickness of the repeating layer schemes is the same for all six isomers. The majority of the samples are composed of a central block of the targeted isomer and the number of unit cells in the blocks agrees with that determined from the Laue fringes in the XRR patterns. While there are stacking defects in all of the isomer domains, it is quite surprising that the imperfect 11 repeating sequences deposited in the precursors contains sufficient information to direct the self-assembly of 8-9 unit cells into the targeted isomer stacking sequences.

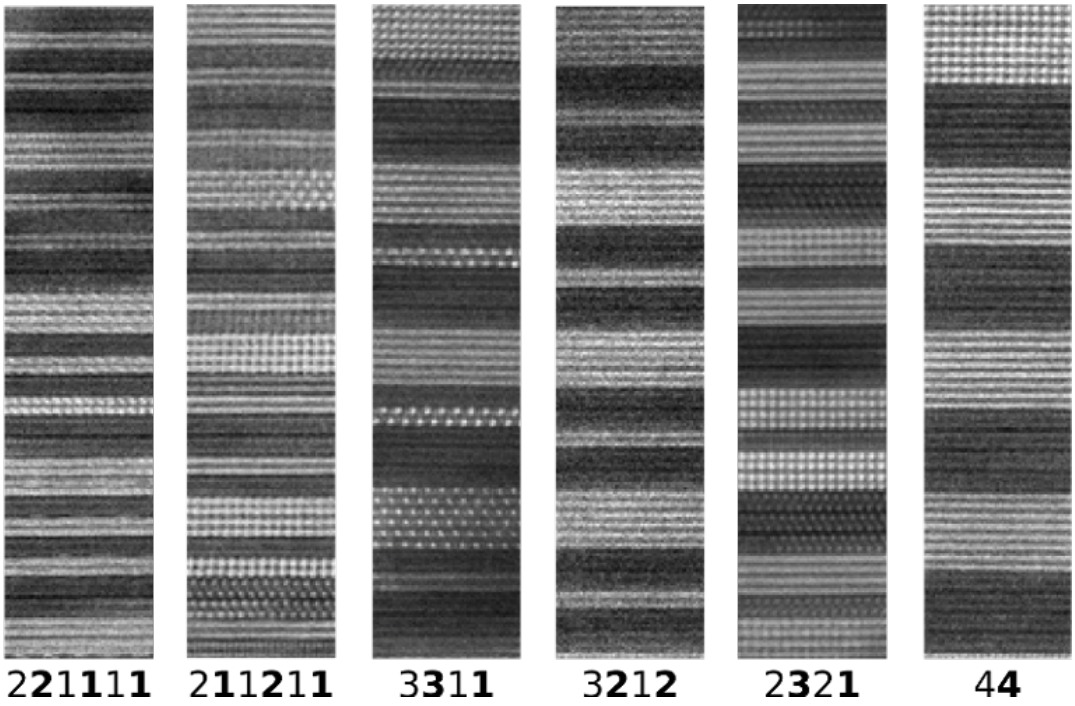

Figure 11.7. HAADF-STEM images of each isomer heterostructure highlighting the formation of the targeted nanoarchitecture, sharp interfaces between constituents, and rotational misregistration between layers.

11.3.2. Formation Discussion

The structural data presented above provides insight to the isomers' growth from the deposited precursor. It suggests that Ti_2Se forms at the substrate surface when Se is deposited onto the initial Ti layer. We tested this in a separate experiment, showing Ti_2Se forms when depositing Se on Ti in a Ti-Se precursor, even when the Ti to Se ratio is one to two. Forming Ti_2Se as the initial layer results in an excess Se concentration since the amount of Ti and Se deposited was intended to form a $TiSe_2$ layer in the isomer samples. When Pb intended to form PbSe in the first repeat unit is deposited, it reacts with the excess Se from the first Ti|Se layer to form a PbSe layer. When the next layer of Ti is deposited (intended for the second repeat unit), it is deposited on a Se rich layer which allows the formation of $TiSe_2$ to occur. The $TiSe_2$ grows out horizontally from its nucleation site. Since the repeating sequence is low on Ti, the formation of the growth stops when the Ti at the growth front has been depleted, leaving some amorphous material in the layer. Similar behavior occurs for the next Pb|Se layer, but the $TiSe_2$ basal plane surface results in the formation of crystallographically aligned PbSe at the interface. Since the repeating sequence is also low on Pb, the formation of the growth stops when the Pb at the growth front has been depleted, leaving some amorphous material in the layer. This process continues, on average, for about 4-unit cells, which corresponds to a crystallite size of ~200 Å perpendicular to the substrate. Subsequent deposited layers are more disordered.

A schematic illustrating the as deposited structure and how it evolves is shown in Figure 11.8. To simplify the image a $([PbSe]_{1+\delta})_1(TiSe_2)_1$ repeating unit structure was used in place of the more complex $([PbSe]_{1+\delta})_4(TiSe_2)_4$ isomer structure. When the temperature is increased during annealing, the concentration gradients drives diffusion of Pb and Ti to the growth front. In addition to growth parallel to the

substrate, additional layers crystalize perpendicular to the substrate facilitating further growth of the isomer heterostructure. Around the crystallized structure is a region that is metal poor / Se rich as a result of the nucleation site stealing metal from the surrounding area to form the structure. The requirement to steal material from the surrounding area is the result of the wrong atoms/ $Å^2$ being deposited per layer in the precursor. Since all of the samples were most deficient in Pb, it is the species that will be depleted first, leaving a Ti|Se top layer which reacts with oxygen during annealing to form an amorphous oxide. The thickness of the isomer layer therefore ends up being two- or three-unit cells less than the 11 that were targeted, consistent with the number of Laue oscillations seen in the XRR scans and the HAADF-STEM images. The ability to prepare the metastable isomers without being precisely on composition is an advantage in the quest to find new material phases, since it is challenging to precisely control the absolute amount of an element at the monolayer level. These metastable compounds have a broad enough energy minimum in the free energy landscape that the system still forms the targeted isomer even if the composition deviates from the target, as long as the nanoarchitecture resembles the targeted compound.

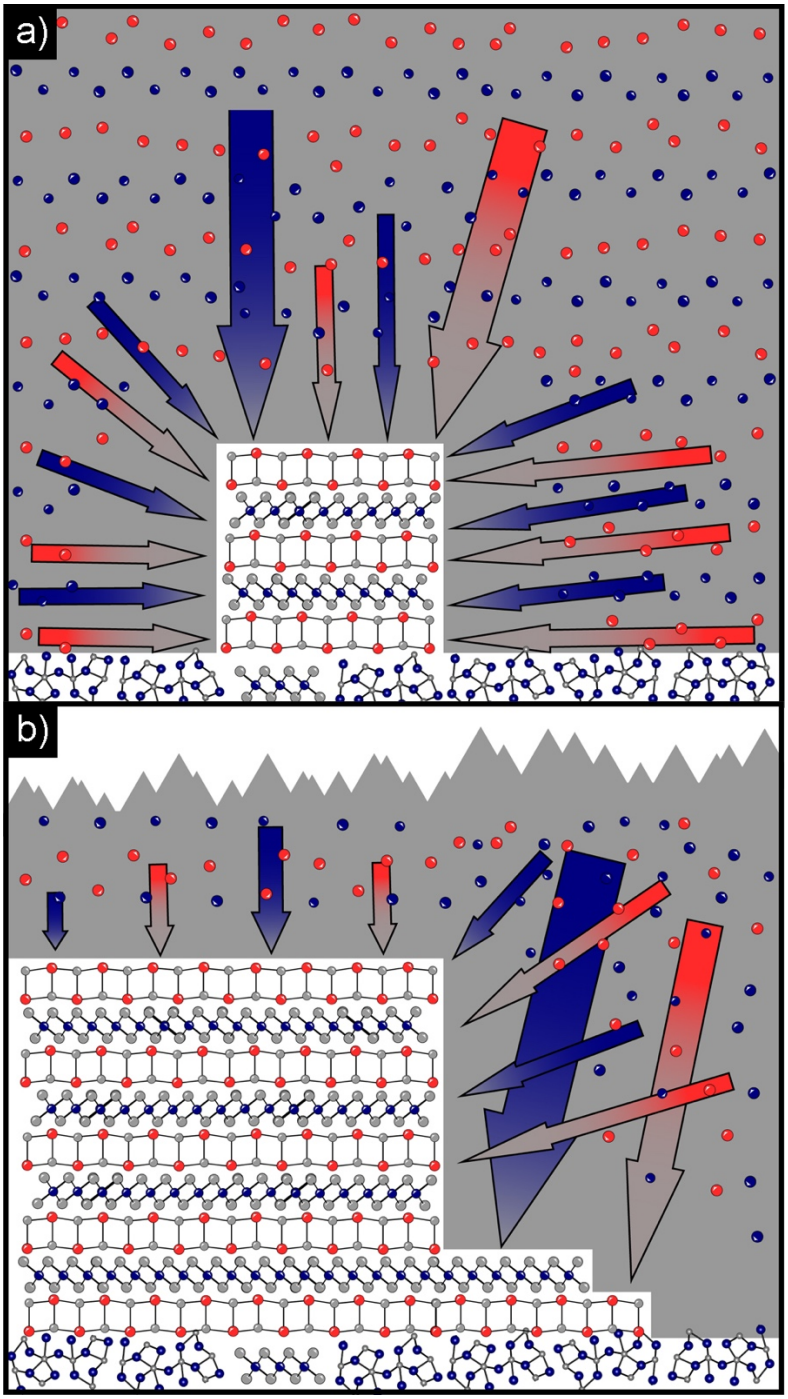

Figure 11.8. Atomistic picture demonstrating the initial crystallization occurring in the material (a.) and a snapshot showing the movement of atoms and further growth of the crystals upon annealing (b.) The arrows demonstrate the concentration gradient of the metals and point to where the metals are diffusing. Upon deposition a layer of Ti_2Se forms and persists even after annealing.

11.3.3. Electrical Transport Properties

Temperature-dependent resistivity of the 6 $[(PbSe)_{1+\delta}]_4[TiSe_2]_4$ isomers are shown in Figure 11.9. The isomer with the smallest number of interfaces per unit cell, the 4**4** isomer, has the highest resistivity while the 2**2**1**1**1**1** isomer, which has the most interfaces, has the lowest resistivity at all temperatures. The magnitude of the resistivity and the slow decrease in resistivity as temperature is decreased from room temperature suggest that these samples are metallic. At low temperatures, however, all the samples have an increase in resistivity similar to those observed in $[(PbSe)_{1+\delta}]_m[TiSe_2]_n$ compounds previously reported.[30,32,35,39] The similarity of the normalized resistivity versus temperature plots, Figure 11.9b, suggest that the same phenomena are occurring in all of the isomers. Minima in the resistivity for the isomers are between 50 K and 100 K, with the 4**4** isomer having the highest temperature minima and the 2**2**1**1**1**1** isomer the lowest.

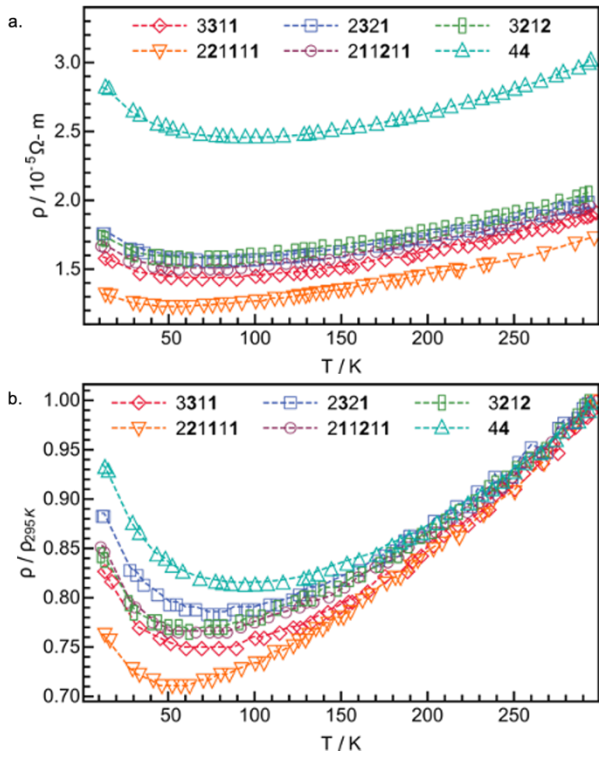

Figure 11.9. Temperature dependent resistivity of 6 $[(PbSe)_{1+\delta}]_4(TiSe_2)_4$ isomer heterostructures, both measured (a.) and normalized (b.) values.

Hall coefficients were measured as a function of temperature to provide more information about the increase in resistivity at low temperatures. The Hall coefficients were negative for all isomers over the entire temperature regime, indicating that electrons dominate the electrical transport. Carrier concentrations were calculated from the Hall data, assuming a single band model and are plotted as a function of temperature in Figure 11.10a. The carrier concentrations slowly decrease as temperature is decreased in all of the samples. The decrease in carrier concentration has a very weak temperature dependence, suggesting that an activated process is not the source of the increasing carrier concentration with increasing temperature. Isomers with the same number of interfaces in the unit cell have similar carrier concentrations, with the 4**4**-structure having the lowest and the 2**2**1**1**1**1** and the 2**1**1**2**1**1** isomers the highest. Carrier mobility, calculated from the resistivity and Hall data, are shown in Figure 11.10b. The mobility values and their temperature dependences are similar for all of the isomers, with mobility increasing with decreasing temperature before becoming constant below 50K. At low temperatures, higher mobilities correlate with increasing buried interface density. This is somewhat surprising as more interfacial scattering from the layers, which should be relatively temperature independent unlike other mechanisms (e.g. electron-electron or electron-phonon scattering), would be expected for structures with high interface density. The minima in the resistivity appears to be a consequence of the interplay between the decreasing carrier concentration and increasing mobility as temperature is decreased. As the temperature decreases the mobility increases at a faster rate than the carrier concentration decreases, resulting in observed resistivity decrease. At low temperatures, the decreasing carrier concentration, and plateau of the mobility results in the resistivity increase.

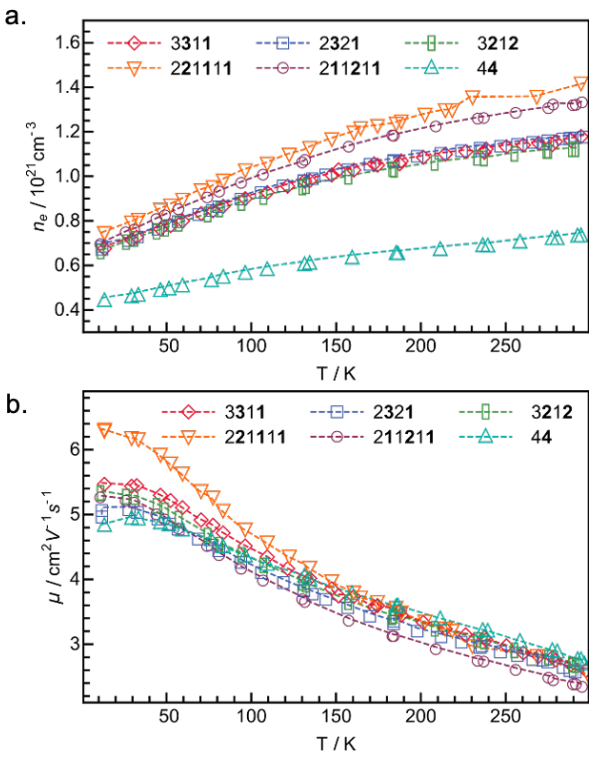

Figure 11.10. Temperature dependent carrier concentration (a.) and mobility (b.) of 6 $[(PbSe)_{1+\delta}]_4(TiSe_2)_4$ isomer heterostructures. Values are calculated assuming a single n-type band.

The room temperature Seebeck coefficient was collected for each isomer compound and the values are shown in Figure 11.11. Several $([PbSe]_{1+\delta})_4(TiSe_2)_4$ isomers were measured to explore how much the room temperature transport measurements varied between samples. There was a 5% variation of the Seebeck coefficient between the 4 samples measured. The negative Seebeck coefficients obtained for all of the isomers agree with the Hall measurements, indicating that electrons are the majority carrier type. The magnitude of the Seebeck coefficients systematically decrease as the interface density decreases in the $([PbSe]_{1+\delta})_4(TiSe_2)_4$ isomers. This and the Hall data suggest that band alignments in $[(PbSe)_{1+\delta}]_4[TiSe_2]_4$ isomers result in charge transfer from PbSe into $TiSe_2$. The PbSe-$TiSe_2$ bilayers should be thought of as a conducting entity due to charge transfer between the constituents. The

more PbSe-$TiSe_2$ interfaces, the higher the carrier concentration as charge transfer occurs at each interface as shown schematically in Figure 11.12. The unusual decrease in the carrier concentration with temperature may be a consequence of the two structures changing independently with temperature, resulting in a change in the amount of charge transfer between the two constituents as a function temperature.

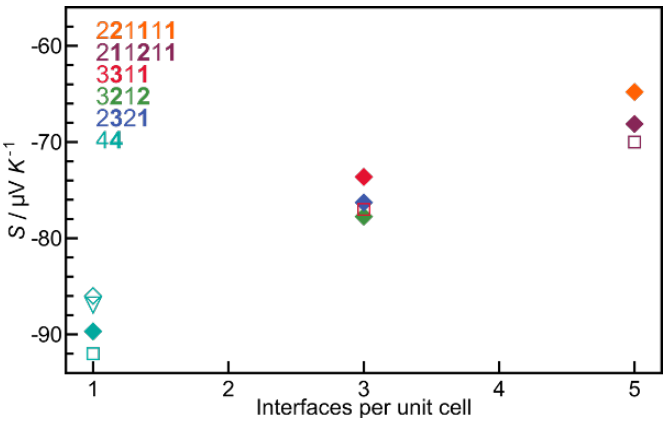

Figure 11.11. Room-temperature Seebeck coefficients for each of the $[(PbSe)_{1+\delta}]_4(TiSe_2)_4$ isomer heterostructures. Colors correspond to nanoarchitecture and symbols correspond to precursor parameters.

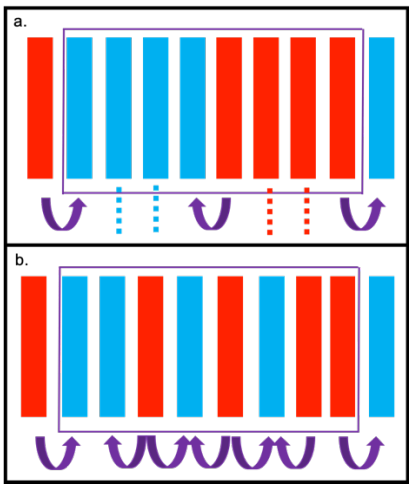

Figure 11.12. Schematic demonstrating charge donation occurring in isomers containing different numbers of buried interfaces, the 4**4** (a.) and the 2**2**1**1**1**1** (b.). The SnSe layers are shown in red, the $TiSe_2$ is shown in blue, and purple arrows depict the charge donation from the SnSe to the $TiSe_2$ layers. The purple boxes indicter a single isomer repeating unit.

11.4. Conclusion

This work investigated the synthesis, formation, structure, and transport properties of $[(PbSe)_{1+\delta}]_4(TiSe_2)_4$ isomers. While the correct amount of material deposited was not enough to form 11 repeat units of a $[(PbSe)_{1+\delta}]_4(TiSe_2)_4$ isomers, the intended nanoarchitectures still formed albeit with fewer unit cells than targeted. During deposition, an impurity Ti_2Se phase formed at the substrate interface and there was initial crystallization of both $TiSe_2$ and PbSe in sequences that match the structure of the targeted isomers. Both the initial layering scheme and the heat of formation of the targeted isomers drives the formation of the resulting material. XRR, XRR, and HAADF-STEM confirm the formation of approximately 8 or 9 repeating units with the correct nanoarchitecture, with thin impurity phases present on the top and bottom. Transport data collected for the isomers indicates that the resistivity and carrier concentration depend on the number of interfaces in the unit cell of the isomers. This suggests that that charge transfer between the constituent layers is the source of the electrons. The mobility and carrier concentration vary inversely with temperature, resulting in a minima in the resistivity between 50 and 100K. The ability to prepare metastable isomers provides a new handle for tuning properties in thin film materials and the tolerance of the self-assembly process to deviations from stoichiometry facilitates the discovery of new compounds using this synthesis approach.

11.5. Bridge

In chapter 11 the Modulated Elemental Reactants method was used to successfully prepare a series of $[(PbSe)_{1+\delta}]_4[TiSe_2]_4$ isomer heterostructures which had nominally the same amount of materials per unit area and repeat unit thickness, but varying repeat unit nanoarchitectures. The results demonstrated that the precursor architecture drives the formation of the subsequent compound even

when the amount of material deposited varies from the target. It was also found that the number of interfaces within a repeating unit has an influence on the observed transport properties. Preparing heterostructure isomers is one method to modify and tune solid state materials properties. The next two chapters will use the Modulated Elemental Reactants method to prepare Mn-containing compounds to study the structure and properties of the materials that formed.

CHAPTER XII

THE REACTION BETWEEN MN AND SE LAYERS.

12.0. Authorship Statement

The work in this chapter was published in Zeitschrift für anorganische und allgemeine Chemie (DOI:10.1002/zaac.201800378) on November 30, 2018. David C. Johnson is my advisor and consulted in the preparation of this publication. Marissa A. Choffel is the primary author on this work and assisted in sample preparation, diffraction studies, data analysis, and manuscript synthesis. Jordan A. Joke aided in the sample preparation, synthesis conditions, and data collection. Dmitri Leo M. Cordova helped with the determination of lattice parameters. I aided in the project design, sample synthesis, data analysis and manuscript preparation.

12.1. Introduction

In general, the formation of crystalline solids from the elements or via the reaction between compounds is not well understood.[1–3] While there is a consensus that interdiffusion, nucleation, and growth are key parts of the formation process, there is little understanding of how these fundamental reaction steps can be controlled with experimental parameters. This knowledge is crucial for planning a directed synthesis.[4] A promising approach to investigate the formation mechanism of crystalline solids is based on using precursors containing alternating layers of the elements.[5] An advantage of this approach, called modulated elemental reactants [6] or nanoalloying [7] is the ability to form a homogenous, amorphous intermediate.[8] Synthetically accessible metastable compounds need to be more stable than an amorphous intermediate of the same composition.[9] Fortunately, the composition of amorphous intermediates can be systematically controlled to influence

which compounds nucleate first.[10–12] This has enabled the synthesis of a number of metastable compounds.[13]

The Mn-Se system has been the subject of multiple recent investigations using epitaxial growth techniques[14–16] and solution phase synthesis approaches,[14,15,17–21] which were driven by the desire to make discrete magnetic layers, magnetic nanoparticles, or diluted magnetic semiconductors.[22–24] Only two thermodynamically stable compounds are known in the Mn-Se system. Both can be prepared using traditional high temperature reactions of the elements.[25,26] The monoselenide, α-MnSe, has a sodium chloride crystal structure and the diselenide, $MnSe_2$, has a cubic pyrite structure. In both compounds Mn is octahedrally coordinated by Se. In α-MnSe, Se is octahedrally coordinated by Mn. In $MnSe_2$, there are discrete Se_2 dimers, and the Se is tetrahedrally coordinated by one Se atom and three Mn atoms. These structures are closely related. Replacing the Se dimers in the pyrite by Se atoms at the center of mass of the Se dimers results in the rock salt structure. In addition to the two thermodynamically stable compounds, two metastable MnSe polymorphs (β-MnSe and γ-MnSe) have been reported to form as nanocrystals from solutions.[27,28]

The purpose of the present investigation is to study the formation mechanisms of MnSe and $MnSe_2$ from multilayered Mn-Se precursors where the ratio of the elements and the total amount of elements per repeating layer were varied to determine parameters required to form amorphous reaction intermediates and to discover if any metastable compounds nucleate at low reaction temperatures. A number of films with different ratios of Mn and Se were prepared with two bilayer thicknesses. Alternating layers of Mn and Se were deposited to obtain the four target compositions and different bilayer thicknesses. The bilayers were repeated multiple times to increase the sample volume. The evolution of the films as a function of temperature was followed using X-

ray diffraction. The sequence of phase formation changed with both composition and bilayer thickness. MnSe formed from films that were close to a one to one ratio of Se and Mn during the deposition. For compositions containing ~60% Se, an amorphous intermediate formed and the first compound crystalized depended on bilayer thickness. MnSe formed first in the film with thin bilayers while a mixture of $MnSe_2$ and MnSe formed in the film with thicker bilayers. Both the thin and thicker bilayer films with a 1:2 ratio of Mn to Se were amorphous as deposited and the first crystalline compound formed was $MnSe_2$ from both precursors. Both of the films with initial compositions of ~80% Se formed a new metastable compound whose diffraction pattern was consistent with a monoclinic unit cell. These results show that amorphous intermediates can be formed from precursors with thin bilayer thicknesses and that both the composition and the bilayer thickness influence which compound nucleates first.

12.2. Results and Discussion

A number of precursor films were prepared with systematic changes in composition and layer thickness to probe how the reaction mechanism varies as a function of these experimental parameters. One set of precursors was prepared where the bilayer Mn|Se thicknesses were on the order of that require to form a single unit cell of MnSe or $MnSe_2$. Four films (A1-D1) were made with compositions shown in Figure 12.1. A second set of four precursors (A2-D2) was prepared with bilayer thicknesses approximately twice that of the precursors A1-D1 with similar compositions (see Figure 12.1). X-ray reflectivity scans of the as deposited samples contained only a few Kiessig fringes. While there were enough Kiessig fringes to determine the film thickness, the termination of fringes at 2.5 to 6.5 degrees indicates a surface roughness of ~ 20 Å calculated using the approach of Parratt.[29]

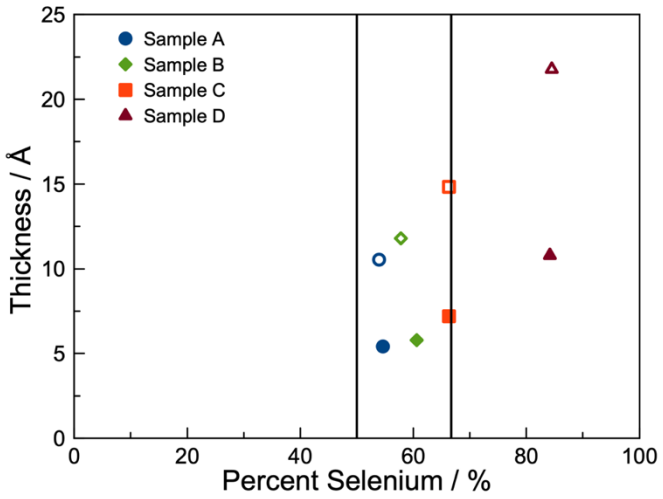

Figure 12.1. Summary of the composition and thickness of the prepared precursors.

The grazing incidence diffraction patterns of the as deposited precursors are shown in Figure 12.2. The diffraction patterns of the two samples with a starting composition of ~ 54 % selenium, A1 and A2, indicated that both crystalized α-MnSe during the deposition. Distinct reflections at 32.9 and 47.2 degrees from the (200) and (220) reflections and a weak reflection at 58.7 degrees from the (222) reflection are apparent in the scans. The vertical dashed lines in Figure 12.2 indicate the locations of these reflections for α-MnSe. In addition to the α-MnSe reflections, there is a broad maximum centered at ~55 degrees with a sharp maximum at 54 degrees that are assigned to a surface component, as these features are not apparent in specular diffraction scans. We suspect that this feature is due to a surface oxide from the magnitude of the intensity of the oxygen signal in the X-ray fluorescence (XRF) data. This surface component is present in all of the as deposited samples. The rest of the samples, all more Se rich than A1 and A2, have much broader and weaker maxima in the as deposited scans, suggesting that they may be amorphous as deposited. The broad maximum at ~32 degrees shifts to a lower angle as the samples become more Se rich. Even for the B

samples this maximum is at an angle lower than that expected for the (200) reflection of α-MnSe.

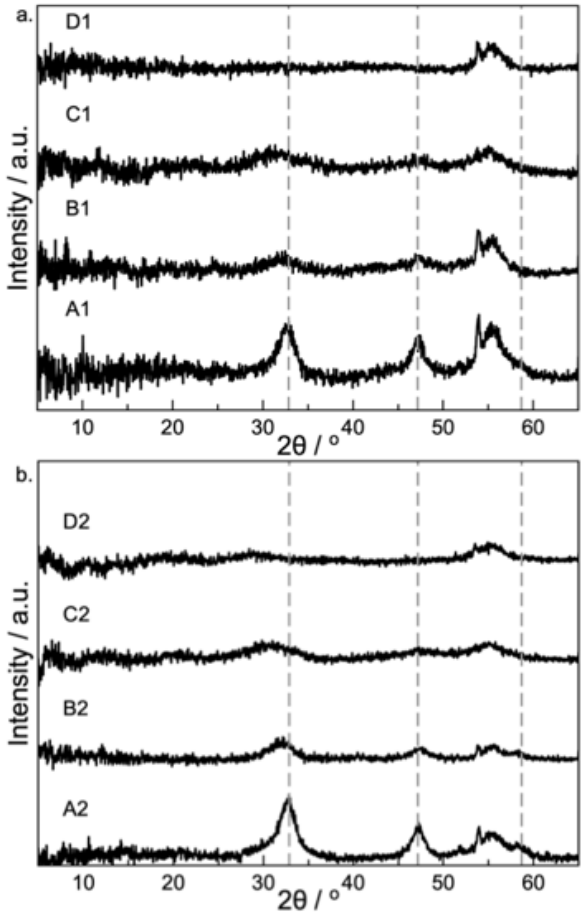

Figure 12.2. Grazing incidence diffraction scans of the eight precursors before any annealing (a. films A1-D1 and b. films A2-D2). The dashed vertical lines at 32.9, 47.2, and 58.7° mark the locations of the (200), (220), and (222) reflections of the α-MnSe.

All of the samples were annealed at sequentially higher temperatures to follow the evolution of the films. Diffraction patterns and XRF data were obtained after each annealing temperature. The XRF data for samples A1 and A2 showed that the initial films were 54% Se and 46% Mn. The Se content of the films decreased due to sublimation of Se between 100 and 250°C. The composition of the films remained approximately constant between 250 and 400°C, slightly Mn rich relative to the stoichiometry of MnSe. This difference is presumably due to the

presence of a Mn oxide on the surface of the samples. Both samples showed increasing oxygen content and decreased Se content after annealing at 450°C. Figure 12.3 contains the diffraction patterns collected during the annealing study for samples A1 and A2. For both the A1 and A2 sample, the reflections of MnSe in the as deposited films sharpen and increase in intensity as the annealing temperature is increased. In sample A2, the weak (111) reflection of MnSe becomes visible after annealing at 300°C, reflecting the increasing crystallinity of the samples. There is a decrease in the intensity of the Bragg reflections at 450°C, which is correlated with an increase in the oxygen fluorescence signal and decrease in Se fluorescence as measured by XRF. This annealing data confirms that the as deposited films of both thicknesses formed MnSe on deposit, even though the films contained extra Se. The lattice parameter of the MnSe in both samples (5.44(1) Å) is independent of annealing temperature and in agreement with the 5.45 Å cubic unit cell reported in the literature.[30] This data suggests that it will be difficult to obtain amorphous films with compositions near a 1 to 1 ratio of Mn to Se using modulated precursors.

Samples B1 and B2, which were approximately 60% Se and 40% Mn as deposited, evolved differently due to their different bilayer thicknesses. Figure 12.4 contains the grazing incidence diffraction scans collected from these samples after each annealing temperature. In sample B1, which is slightly more Se rich than sample B2, the broad diffraction maxima present in the as deposited film change, becoming consistent with the formation of MnSe after annealing at 150° C. Sample B2, which has thicker bilayers and is slightly more Mn rich than sample B1, forms a mixture of $MnSe_2$ and MnSe during this annealing step. This may be a consequence of a non-uniform composition in sample B2 due to the thicker bilayers. The $MnSe_2$ lattice parameters determined from the diffraction scans for sample B2 are smaller (6.40(1) Å) than the literature

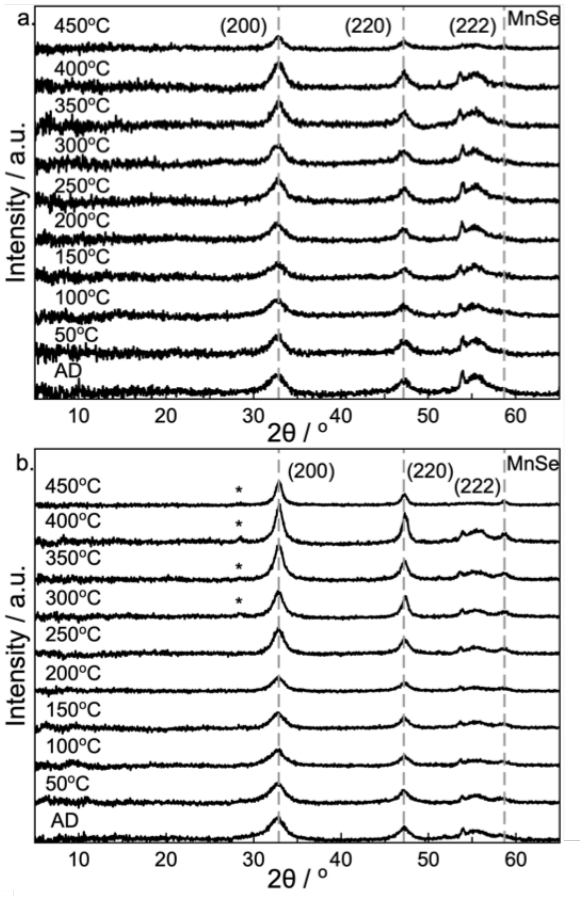

Figure 12.3. Grazing incidence diffraction scans collected for samples A1(a) and A2(b) as a function of annealing temperature. The (111) reflection of α-MnSe has been marked by an asterisk.

value of c = 6.417 Å.[26] During the higher temperature anneals, sample B1 behaves similarly to sample A1. The rate of Se loss decreases during the 250 and 400°C anneals, with its composition becoming Mn rich relative to MnSe, presumably due to a surface oxide. The MnSe reflections become sharper and more intense as annealing temperature is increased. During the 200 and 250°C annealing of sample B2, the reflections of $MnSe_2$ sharpen and grow in intensity. There is Se loss during the 300°C annealing of sample B2, and the diffraction pattern after this anneal shows a significant increase in the intensity of MnSe reflections. Only reflections for MnSe are visible in the diffraction patterns obtained after the 350°C anneal. The sample after annealing at

400°C has a composition of 52% Mn and 48% Se, with the excess Mn again due to the existence of a surface oxide.

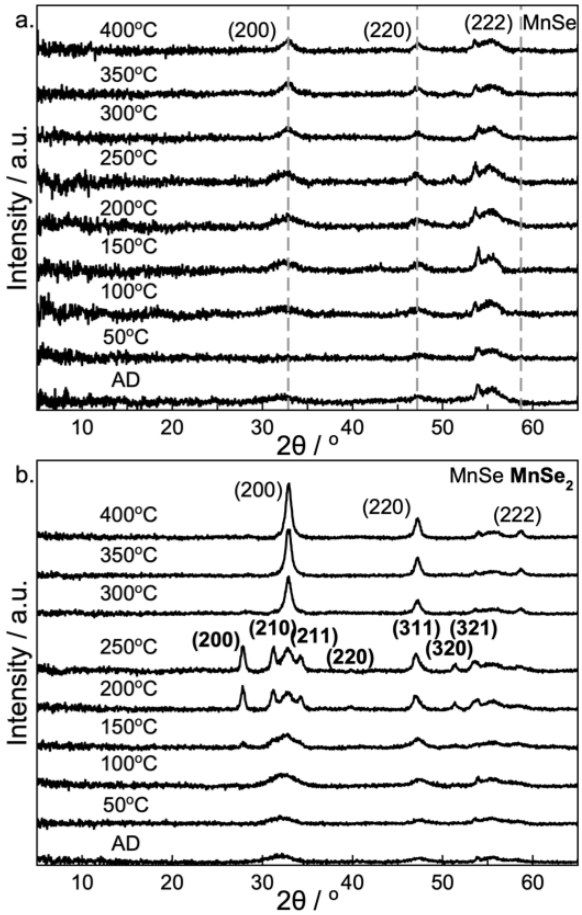

Figure 12.4. Grazing incidence diffraction scans of samples B1 (a) and B2 (b) as a function of annealing temperature.

Precursors C1 and C2 behaved similarly as a function of annealing temperature. They were both amorphous and had compositions close to stoichiometry of $MnSe_2$ as deposited. As shown in Figure 12.5, both samples formed $MnSe_2$ after annealing at 150°C. The $MnSe_2$ lattice parameter 6.41(1) Å, determined from the diffraction patterns of both samples, matches the literature value of 6.417 Å.[26] To decrease the loss of Se from sublimation, sample C2 was covered with a silicon wafer while C1 was not. As a consequence, sample C1 loses Se at a much faster rate as a function of annealing temperature than sample C2 and reflections

for MnSe are visible at a much lower annealing temperature. The ratio of Mn to Se in sample C2 remained near a 1 to 2 ratio until 350°C. After annealing at 400°C, the ratio of Mn to Se changed, becoming 1 to 1.1. After this annealing temperature MnSe was the dominant compound in the diffraction pattern.

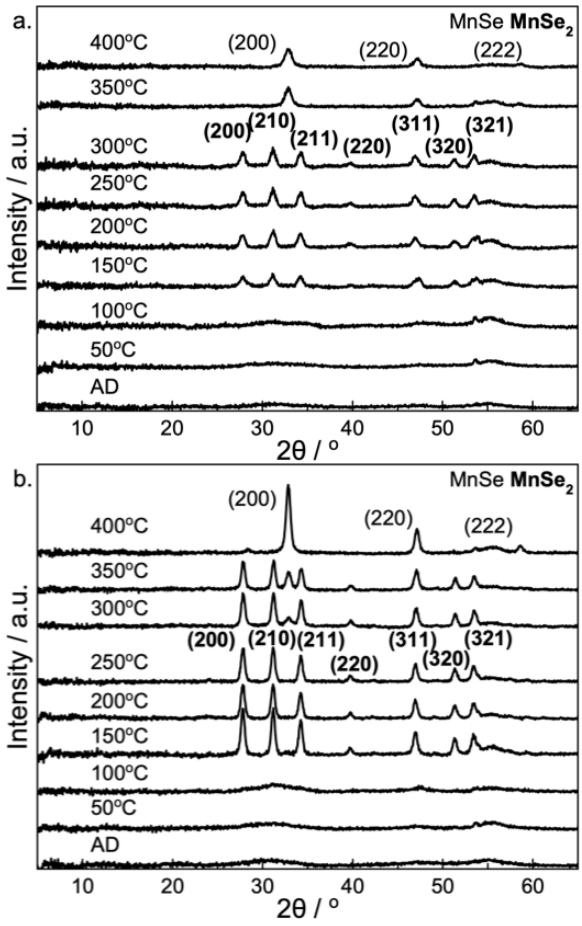

Figure 12.5. Grazing incidence diffraction scans collected from samples C1 (a) and C2 (b) as a function of annealing temperature.

Precursors D1 and D2 surprised us, forming a compound not found on the equilibrium phase diagram during the annealing study. The as deposited precursors were both greater than 80% selenium and the equilibrium phase diagram indicates they should evolve to form a mixture of $MnSe_2$ and Se. Both samples were amorphous as deposited and did not change during the 50 and 100°C annealing as shown in

Figure 12.6. Both samples form a previously unreported compound on annealing at 150°C, and all the reflections in both samples can be indexed to a small monoclinic unit cell with lattice parameters a = 4.942(2) Å, b = 4.32(3) Å, c = 3.779(1) Å, and β = 90.13(3)°. The relative intensities of the reflections, however, are different in the two scans, suggesting that there may be different amounts of preferred orientation or there may be different relative occupancies of crystallographic sites in the two samples. The composition of the D1 sample is close to a 1 to 2 ratio of Mn to Se as a result of significant Se loss during annealing at 150°C. This suggests that the composition of the new compound is likely to be near a 1 to 2 ratio of Mn to Se. The composition of the D2 sample did not change significantly on annealing at 150°C, perhaps as a consequence of it being much thicker than sample D1. After annealing at 200°C, the diffraction pattern of sample D2 has small reflections consistent with the formation of $MnSe_2$ and the reflections for the new compound have sharpened. After annealing at 200°C, the diffraction pattern of sample D1 is very different, without any sharp reflections. The XRF data indicates that sample D1 lost a significant amount of Se at this annealing temperature, with a final composition close to 1 to 1 between Mn and Se. At 250°C, the diffraction pattern for sample D2 contains reflections consistent with a film of $MnSe_2$ and the composition from the XRF data is consistent with this. At higher annealing temperatures, sample D2 behaves similar to sample C2, losing Se and forming MnSe.

There are several differences between the samples with thinner bilayers (A1-D1) and those with thicker bilayers (A2-D2). The samples with thinner bilayers all lose Se at a faster rate than the samples with thicker bilayers. Since samples A1-D1 are all much thinner in total thickness than A2-D2, this suggests that Se loss is limited by diffusion of Se to the surface. The samples with thinner bilayers also end up being more Mn rich (and Se poor) relative to the samples with thicker bilayers.

We believe that this is due to the Mn containing oxide forming on surface of the samples. Since the samples with thinner bilayers are also thinner in total thickness, this oxide consumes a larger fraction of the total Mn in the film.

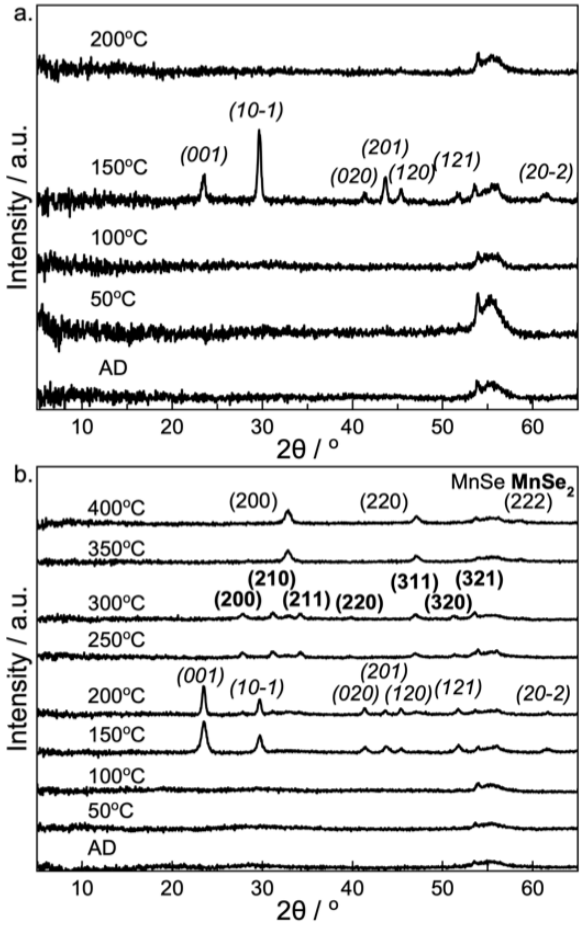

Figure 12.6. Grazing incidence diffraction scans of samples D1 (a) and D2 (b) as a function of annealing temperature.

Previous investigations using modulated elemental reactants indicated that there is a critical bilayer thickness, with precursors layered below the critical thickness forming amorphous intermediates and those layered above the critical thickness nucleating binary compounds at the interface between elemental layers.[31] The results of the annealing studies as a function of composition and bilayer thickness of the Mn-Se samples suggest that the critical bilayer thickness in this

system is a function of composition. Both the thicker and the thinner samples closest in composition to the stoichiometry of MnSe (A1 and A2) formed MnSe during the deposition. The samples with ~ 60% Se, B1 and B2, were x-ray amorphous but evolved differently. We suspect that at this composition sample B1 was below the critical thickness while sample B2 was above the critical thickness. All of the samples with a lower Mn to Se ratio formed amorphous intermediates. The thicker and thinner bilayer samples (C1 and C2, D1 and D2) nucleated the same first compound.

12.3. Conclusion

This study showed that it is possible to form amorphous Mn-Se intermediates from modulated elemental reactants if they are more than 60% Se. The critical bilayer thickness at this composition is on the order of 1 nm. Films that were more Mn rich formed MnSe during deposition. Films that were more Se rich formed amorphous intermediates and no difference in the evolution of the films were observed for bilayer thicknesses less than ~ 2 nm. In the most Se rich films investigated, a new metastable compound was discovered. The diffraction pattern can be indexed to a monoclinic unit cell with lattice parameters of a = 4.942(2) Å, b = 4.32(3) Å, c = 3.779(1) Å, and β = 90.13(3)°.

12.4. Materials and Methods

The precursors were synthesized using a vacuum depositions chamber operating at pressures below 5×10^{-7} Torr. Manganese was deposited using an electron beam gun and selenium was deposited using a Knudson effusion cell. All films were deposited on silicon wafers with a native oxide layer. Deposition was controlled using quartz crystal microbalances (QCM) to monitor the rate of deposition and the amount of material deposited in each layer. Different amounts of manganese and selenium were deposited for each precursor in order to target four

different compositions. For each of the compositions investigated, precursors with two different bilayer thicknesses were prepared. Twenty-four bilayers were deposited in each precursor.

The samples were annealed at each temperature for 30 minutes on a hot plate in a nitrogen atmosphere with an oxygen pressure of less than 1 ppm. The initial annealing temperature was 50°C and the annealing temperatures were increased in steps of 50°C. X-ray reflectivity, X-ray fluorescence and grazing incidence x-ray diffraction scans were collected after each annealing step. X-ray reflectivity was collected using a Burker D8 Discover diffractometer using Cu-Kα radiation. Grazing incidence x-ray diffraction (XRD) scans were collected on a Rigaku SmartLab with a Cu source. X-ray fluorescence data was collected on a Rigaku ZSX Primus-II with a rhodium X-ray tube.

Calibration samples containing Mn and Se were annealed in a selenium atmosphere, forcing the formation of pure $MnSe_2$ films as confirmed by diffraction scans. The X-ray fluorescence intensity of both Mn and Se were measured. Since the proportionality factor between Se intensity and the number of Se atoms per unit area was known from an earlier study,[32] we could calculate the number of Se atoms per unit area in each sample. The number of manganese atoms/ unit area in each sample was calculated from this using the stoichiometric ratio between manganese and selenium. The linear relationship between XRF intensity and atoms per unit area for both Mn and Se were used to determine the composition of the films in this study.

12.5. BRIDGE

Chapter 12 explored the interaction between Mn and Se when deposited as thin layers of material via the Modulated Elemental Reactants Method. By varying the amount of material deposited in each layer, the formation mechanism and compound that formed was

influenced. This demonstrated the role that precursor composition and layer thickness have on the compound that crystalizes. This understanding provides the foundation for the use of Mn in various other heterostructure building blocks. Chapter 13 will focus on novel heterostructures with Mn containing layers, including the synthesis, structure, and determination of which materials would be kinetically stable.

CHAPTER XIII

EMERGENT STRUCTURES AND PROPERTIES IN INTERFACE STABILIZED 2D-LAYERS

13.0. AUTHORSHIP STATEMENT

This chapter is an unpublished manuscript that is coauthored with to Sven Rudin, Tomoya Asaba, Filip Ronning, Dmitri Cordova, Ping Lu, and David Johnson. I developed the project, prepared and characterized samples, and wrote and edited the manuscript. Sven Rudin completed the computational work included in this manuscript and assisted with the writing and editing. Tomoya Asaba and Filip Ronning collected and analyzed the transport and magnetic measurement data. Dmitri Cordova assisted with the sample preparation and characterization. Ping Lu collected the HAADF-STEM images presented in this paper. David Johnson is my advisor who assisted in the experimental design, analysis of data, and writing of the manuscript.

13.1. INTRODUCTION

Van der Waals heterostructures are materials containing sequences of different 2D layers such that the chemical composition and/or structure changes with position.[1] The excitement in this area results from the promise of heterostructures having emergent novel properties of scientific and technological significance.[2–8] Since each constituent combines a number of chemical elements in a specific structure, there are endless conceivable combinations of elements and layers. The immense quantity of such combinations presents both a promise and a problem: the promise of preparing many novel heterostructures with exciting properties and the problem of exploring the vast number of conceivable possibilities. The exploration of this space to find unprecedented structures and properties has become one of material science's contemporary grand challenges.[9–11]

Recent successes in meeting this challenge focus on exploring properties of heterostructures that combine constituents drawn from naturally layered compounds.[12–17] This focus on thermodynamically stable individual constituents severely stunts the combinatorial choices. It omits fragments of 3D structures and kinetically stabilized combinations of chemical elements emerging in new and unique bonding environments.[18–25] These artificial structures promise new properties resulting from unique bonding arrangements, but the systematic discovery of these unknown structures poses a problem for existing procedures. Attempting the synthesis of every conceivable chemical combination in every possible structural configuration proves too costly in both time (due to numerous unknown reaction pathways) and materials, while computational search algorithms are challenged by the many structural unknowns.

We suggest that the solution resides in a collaborative search and synthesis approach, utilizing techniques which complement one another. Our computational search consists of many independent structural optimizations within density functional theory (DFT) calculations and focuses on kinetic stability. These calculations explore intermediate configurations as a designed precursor evolves to a specific heterostructure. The intermediate configurations are composed of an island of individual constituents with various stoichiometries and crystal structures between layers of a different constituent (details in the SI).[26,27] The synthesis relies on the modulated elemental reactant (MER) method, which can prepare metastable compounds via near diffusionless transformations of designed precursors.[28–31] The precursors consist of sequences of elemental layers that mimic the proposed composition and layer sequence of the targeted heterostructures deposited on a nominally room temperature silicon wafer.

13.2. Materials and Methods

13.2.1. Density Functional Theory

The density functional theory (DFT) calculations employ the PAW method in the generalized gradient approximation (GGA) of Perdew, Burke, and Ernzerhof (PBE) implemented in the electronic structure code VASP.[32–35] Evaluation of the electronic structure involves first - order Methfessel - Paxton smearing with σ = 200 meV and a convergence criteria of 10 - 5 eV; optimization of the structures uses a convergence criteria of 10 - 4 eV.[36] The van der Waals interactions are treated using the method of Tkatchenko - Scheffler.[37] The calculations serving to optimize island structures employ a single k-point; the calculation optimizing the complete (PbSe-MnSe-PbSe)15 - (VSe_2)25 unit cell employs a 3 x 3x 3 k-point mesh.The structures are relaxed via the conjugate gradient method with no imposed constraints.

The 35 initial island structures are truncated slices of simple lattices (simple cubic, body-centered cubic, face-centered cubic, hexagonal close-packed) taken along high-symmetry directions with the lattice sites (numbering between 20 and 70) replaced by atoms of the two or three types to create symmetric patterns. These islands are sandwiched between either 36 or 49 VSe_2 primitive cells in the continuous VSe_2 layer, or 64 PbSe primitive rock salt cells in the continuous PbSe layer.

13.2.2. Materials

(100) Silicon with a native oxide layer was used as a substrate for deposition. Lead rods (99.98%), Selenium pellets (99.999%), and Vanadium slugs (99.8%) were purchased from Alfa Aesar. Manganese rods (99.9%) were purchased from American Elements. Elements were outgassed within the deposition chamber prior to sample preparation to remove any impurities and oxide coatings.

13.2.3. Heterostructure Synthesis via Modulated Elemental Reactants

Heterostructures made as a way to experimentally test the island predictions were prepared in a high vacuum deposition chamber using the modulated elemental reactants synthesis approach via physical vapor deposition. Pressure was kept below 10^{-7} Torr during the deposition of all samples. Selenium was deposited using a Knudson effusion cell while all other metals were deposited with electron beam guns. The nanoarchitecture was controlled using pneumatic shutters directed by a custom written deposition software for an Inficon IC-6 deposition controller.[38] The deposited precursors had nanoarchitectures that mimicked that of the desired heterostructure. Precursors were annealed on a hot plate in a nitrogen atmosphere with >10 ppm oxygen to facilitate heterostructure crystallization.

13.2.4. Compositional and Structural Characterization

The number of atoms per unit area was measured for each sample using a Rigaku ZSX Primus II with a rhodium tube. Raw counts were collected, integrated, and interpreted using a previously developed method.[39] X-ray diffraction was collected using a Cu-Kα source. Specular X-ray diffraction and X-ray reflectivity were collected with a Bruker D8 discover and in-plane X-ray diffraction was collected using a Rigaku Smartlab. High-angle annular dark-field scanning electron microscopy images were collected using a FEI titan G2 80-200 STEM with a Cs probe collector. ChemiSTEM technology was used to collected STEM-EDS data and details about the procedure can be found elsewhere.[40] An FEI Helios 600 Ga+ FIB was used to prepare cross sections for HAADF-STEM analysis and STEM-EDS mapping.

13.2.5. Transport Measurements

A standard Hall-bar configuration was used for transport measurements in a Quantum Design PPMS. A Lake Shore LS372 AC resistance bridge was used to measure the sample resistivity. The typical measurement frequency is ~13 Hz.

13.3. Results and Discussion

Both the computational and the synthesis procedures rely on local explorations of the vast volume of conceivable possibilities. Individual search and synthesis procedures start from an initial configuration and, if a kinetically stable structure exists near this precursor, then the procedures find that structure. The precursor is optimized or annealed, respectively, until the procedure reaches convergence in the total energy (with respect to optimization steps) or a heterostructure self assembles as annealing temperature is increased. Both procedures depend on their control over the extent of the exploration. The synthesis accomplishes the local exploration by controlling the extent of atomic diffusion via annealing temperature and time. A successful synthesis depends on finding an annealing temperature high enough to attain the kinetically stabilized heterostructure, but not so high that the structure disproportionates into thermodynamically stable compounds. The computation accomplishes the local exploration by replacing one constituent of the heterostructure with a fragment surrounded by vacuum. This "island approximation" has been shown to successfully describe known incommensurate heterostructures.[26,41] Figure 13.1 shows the two general outcomes of the optimization step: the atoms in the island move either toward a recognizable, periodic pattern or toward an arrangement without forming such a pattern. The control of the optimization depends on finding an island size small enough to give a wide extent of the exploration, but not too small to support a periodic pattern. The optimization aims solely to test one property of the potential heterostructure: kinetic stability. Optimized heterostructures with islands in a recognizable, periodic pattern become candidates for synthesis.

Figure 13.2 shows one of two critical advantages of representing one constituent layer as an island surrounded by vacuum between

continuous slabs of the other constituent (as opposed to a complete layer under the same conditions). First, the atoms in the island can move and rearrange more easily on the edges of the island, potentially with substantial changes to the bonding. For the precursor in Figure 13.2a, the optimization changes the Se atoms' initial bonding with four Mn to a bonding with three Mn (Figure 13.2b). Second, the continuous layer of the second constituent fully determines the planar dimensions of the unit cell. This circumvents the need to construct a unit cell commensurate with the potential constituent layer, which *a priori* has unknown dimensions and orientation and may be incommensurate with the second constituent's dimensions. Finally, though not a critical advantage, the smaller number of atoms accelerates the calculation.

The advantage of the collaborative aspect ensues from complementary strengths. The computational search excels at finding promising short-range, in-plane patterns which mimic the nucleation of a constituent; the synthesis method excels at discovering structural homologs with specific stacking sequences and increased constituent layer thicknesses. Conceptualizing both as algorithms, the computational search has a smaller prefactor and is perfectly parallel, while the synthesis method scales better with the number of atoms. The smaller prefactor eases the computational switch from one combination of chemical elements to another, and the independent optimization of precursors makes the number of simultaneous optimizations limited only by computational resources. The synthesis method, upon overcoming the prefactor (i.e., determining the growth conditions), can rapidly explore heterostructures with thicker constituent layers and more intricate heterogeneity along the stacking direction.

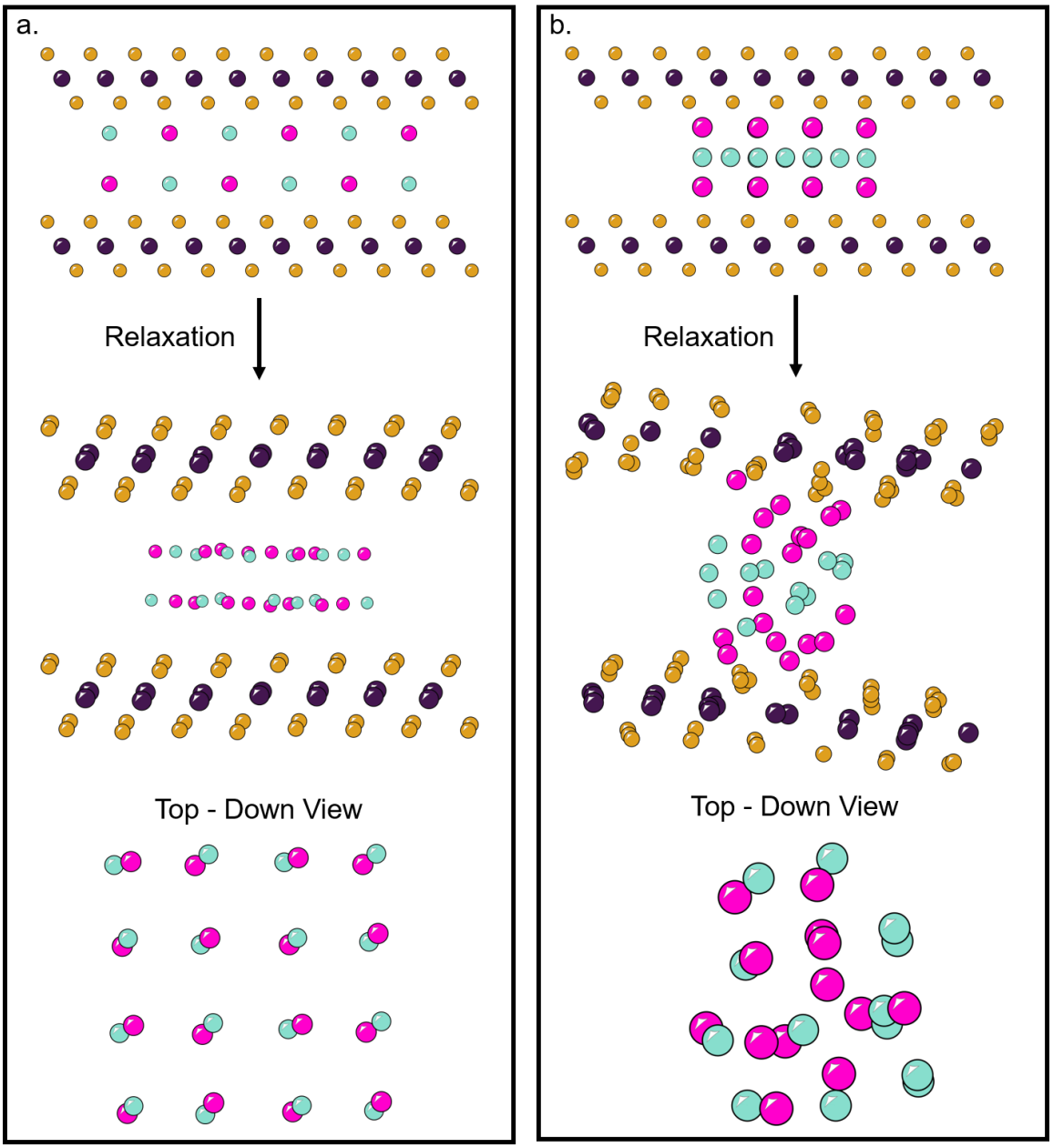

Figure 13.1. A schematic of the theoretical approach used to examine the kinetic stability of constituent compound candidates. A candidate model structure of an AB compound with a rock salt structure that remains intact when relaxed (a.). Also included is the top-down view of the promising system after relaxation, which emphasizes the recognizable structure as well as the systematic distortions from the initial model. A candidate model structure of an AB_2 compound which forms a fragment without long-range ordering when allowed to relax and its top down view (b.).

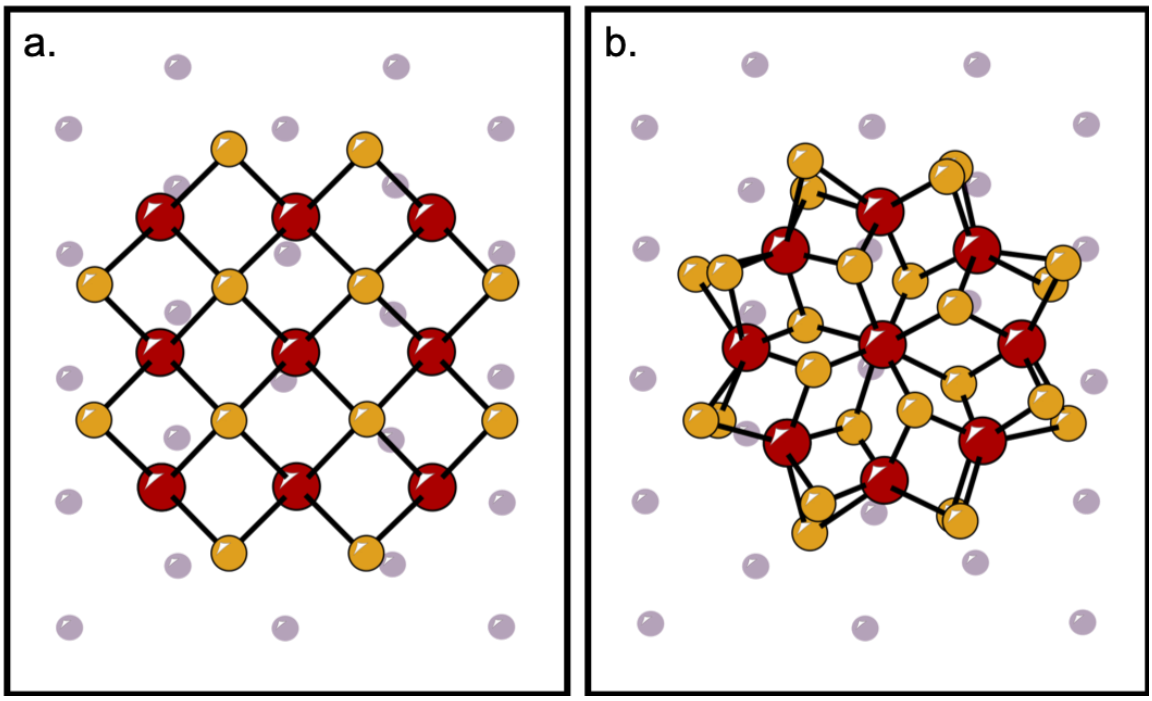

Figure 13.2. Example of an island structure before (a) and after (b) optimization. Sandwiched between a complete VSe_2 layer (only V shown in purple), the structure of nine Mn (red) and 24 Se (yellow) dramatically changes its bonding structure, enabled by the island structure.

We investigated the Mn-Pb-Se-V quaternary space, shown as a tetrahedron in Figure 13.3, to search for potential 2D magnetic layers. This system was chosen for several reasons. First, there are no known ternary or quaternary compounds in this phase space. Second, there are several metastable $[(PbSe)_{1+\delta}]_m[VSe_2]_n$ intergrowths reported in the recent literature,[42,43] providing a test of our theoretical search approach. Third, there are several known binary compounds (PbSe, MnSe, $MnSe_2$, VSe, VSe_2, V_2Se_9, V_5Se_8, V_3Se_4, V_5Se_4, VMn, and VMn_4), shown as grey or black dots on the edges of the quaternary space, which could be potential constituents in heterostructures. We focused on the VSe_2-MnSe-PbSe slice of the quaternary phase space, which is shown in Figure 13.3. VSe_2 is a layered compound containing octahedrally coordinated V between Se layers and is isostructural with CdI_2 (1T-VSe_2). Both MnSe and PbSe are isostructural with NaCl.

Our computational search included both known and novel kinetically stabilized heterostructures and the results of both the computational and experimental exploration are discussed in detail below. The agreement between search and synthesis is not perfect. Not all computationally predicted materials are successfully synthesized using MER. A theoretically stable heterostructure can only be synthesized if the necessary annealing conditions (temperature, time, partial pressure of Se, …) exists to convert the MER precursor to the targeted heterostructure without disproportionating to the thermodynamically stable mixture of binary compounds. However, all successfully synthesized materials are computationally stable as the structures are relaxed. Meanwhile, experimental observations help prioritize the available phase space for computational exploration (e.g. distorted PbSe bilayer found experimentally suggested that ordered alloys, $Pb_{(1-x)}Mn_xSe$, might be stable between VSe_2 layers.). Consequently, the combination of theory and experiment enables a faster convergence to new heterostructures than either approach in isolation.

Results for PbSe-VSe_2. The known metastable $(PbSe)_{1.1}VSe_2$ heterostructure emerges in both computational search and synthesis. Computationally, an island of rock-salt structured PbSe was allowed to relax between continuous slabs of (001) trilayer slices of CdI_2-type structured VSe_2. The relaxed heterostructure approximates a fragment of a (001) bilayer slice of NaCl-type PbSe between VSe_2 layers. Other PbSe islands of different thicknesses and crystallographic orientations between VSe_2 layers also optimize into recognizable, periodic patterns of NaCl-type PbSe including fragments of (001) monolayer, (011) bilayer, and (111) trilayers. MER precursors with a Pb|Se|V|Se layer sequence containing the correct number of atoms to form a rock salt structured PbSe bilayer and a VSe_2 trilayer self-assemble into $(PbSe)_{1.1}VSe_2$ as a result of low temperature annealing. The PbSe layer has a (001)

orientation. Given the necessary number of atoms, it is not possible to form a monolayer or a trilayer of PbSe. When the $(PbSe)_{1.1}VSe_2$ heterostructure was annealed above 400°C, it decomposed into a mix of

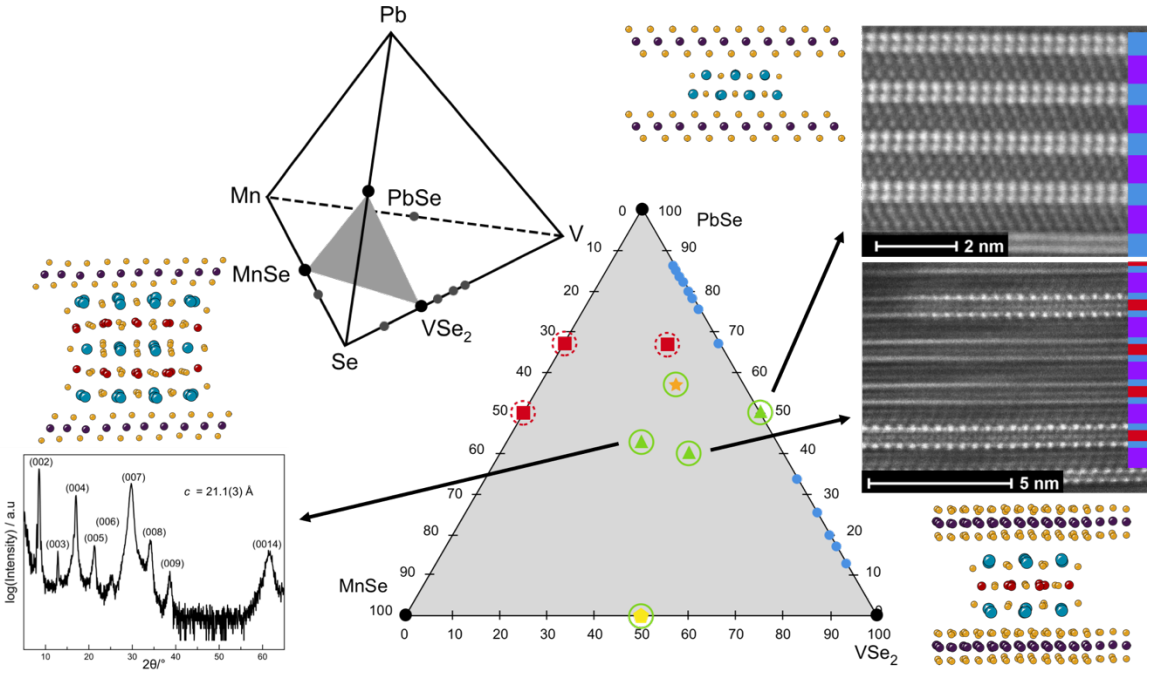

Figure 13.3. The grey plane in the quaternary phase diagram was explored for synthesizable heterostructures. There are no known ternary or higher order compounds in this phase diagram. The circles indicate systems that were computationally explored as described in the text. Systems that relaxed to ill-formed fragments that lack a recognizable pattern have red circles and systems that formed fragments with recognizable periodic structures have green circles. The results of synthetic attempts are shown as filled symbols. Red indicates that the nanoarchitecture of the MER precursor is destroyed during annealing. Green symbols indicate that the targeted heterostructure formed. Orange indicates that a heterostructure formed with a structure close to that of the computational search. Yellow indicates that the nanoarchitecture is enhanced on annealing, but the processing conditions have yet to be optimized. Representative HAADF-STEM images and their respective structure schematics are shown for the $(PbSe)_{1.1}VSe_2$ and $(Pb_2MnSe_3)_{0.6}VSe_2$ heterostructures. A diffraction pattern and structure schematic are included for synthetic attempts at the $(Pb_3Mn_2Se_5)_{1+\delta}VSe_2$ heterostructure.

PbSe and VSe_2 as expected from the equilibrium phase diagram. A representative HAADF-STEM cross-section image of the $(PbSe)_{1.1}VSe_2$ heterostructure is shown in the top right corner of Figure 13.3 along with an image of the relaxed island structure from the calculations to its left.

Results for MnSe-VSe_2. Two MnSe-VSe_2 heterostructures emerged from the computational search with the MnSe island exhibiting a recognizable, periodic pattern. One approximates a fragment of a (001) trilayer slice of iron stannide-type structured MnSe, the other a (001) trilayer slice of CdI_2-type structured MnSe. The latter can also be viewed as a (111) trilayer slice of NaCl-type structured MnSe. NaCl-type structured MnSe as a (001) slice does not appear well-ordered after relaxation. Annealing MER precursors with Mn|Se|V|Se layer sequences at low temperatures (T < 250°C) results in an increase in the intensity of Bragg reflections consistent with the formation of the targeted MnSe-VSe_2 heterostructures. The rate of the increase in intensity decreases to zero at long annealing times. Despite the initial intensity increase, annealing above 250°C resulted in disproportionation to the binary compounds, before the heterostructure could fully crystalize.

Results for PbSe-MnSe. The computational search layering (001) bilayer NaCl-type structured PbSe with MnSe islands finds multiple kinetically stable heterostructures. All of these systems involve NaCl-type structured MnSe islands, which differ in orientation ((001), (011), and (111)) and thickness (mono-, bi-, and trilayer). All MER precursors with Pb|Se|Mn|Se layer sequences disproportionated immediately on annealing, even at low temperatures (T ~ 100°C).

Results for PbSe-MnSe-VSe_2. The above results for ternary systems show that computationally both PbSe and MnSe favor similar NaCl-type structures between VSe_2 layers. Synthesis attempts targeting MnSe-VSe_2 heterostructures do not succeed. These results strike a stark contrast, but the underlying competition between stabilities can be a subtle

balance. The subtle balance can be tipped with small changes, achieved here by going to quaternary systems: a precursor with a V|Se|Pb|Se|Mn|Se|Pb|Se sequence annealed at low temperatures self-assembles into a kinetically stabilized heterostructure. Figure 13.3 shows a representative HAADF-STEM image depicting a NaCl-type structured PbSe-MnSe-PbSe trilayer alternating with a CdI_2-type structured VSe_2 layer. Annealing the sample above 250 °C resulted in decomposition of the $(Pb_2MnSe_3)_{0.6}VSe_2$ heterostructure. The sample rearranges into a mixture of MnSe and a $[PbSe]_{1.1}VSe_2$ heterostructure. Computationally, a NaCl-type structured PbSe-MnSe-PbSe trilayer island alternating with a complete CdI_2-type structured VSe_2 layer relaxes to the $(Pb_2MnSe_3)_{0.6}VSe_2$ heterostructure (Figure 13.3). Similarly, a heterostructure that extends the trilayer to a PbSe-MnSe-PbSe-MnSe-PbSe pentalayer island retains its structure upon optimization. Annealing a MER precursor with this stacking sequence results in diffraction patterns consistent with the formation of the structure, as shown in Figure 13.3. We speculate that the thickness of the interior PbSe layer can be increased. NaCl-type structured PbSe-*T*Se-PbSe trilayer islands alternating with a complete CdI_2-type structured VSe_2 also are computationally stable when relaxed for *T* = Co, Cr, Fe, Ni, and Zn. This suggests that an entire family of prospective new materials, isostructural $(Pb_2TSe_3)_{1+\delta}VSe_2$ heterostructures, can be prepared. Reports suggest, it may also be possible to change the identity of the dichalcogenide layer from V to other transition metals.[44–46]

The structure of the synthesized $(Pb_2MnSe_3)_{0.6}VSe_2$ heterostructure is determined computationally and experimentally using a combination of techniques. Calculation of the structure of $(Pb_2MnSe_3)_{0.6}VSe_2$ was conducted with a unit cell containing a complete layer of VSe_2 (25 unit cells) and a complete layer of Pb_2MnSe_3 (15 unit cells). The orientation between the two layers differs from that of the optimized island

structure, where the Pb-Pb bonds are parallel to V-V bonds. In the complete cell the layers are rotated by 15°, which is necessary to construct a computationally tractable unit cell. Experimentally, x-ray fluorescence data collected on the annealed sample are consistent with the chemical formula $(Pb_2MnSe_3)_{0.6}VSe_2$. Specular diffraction data, shown in Figure 13.4a, contain reflections that can all be indexed as 00*l* reflections. Rocking curve scans of the 00*l* reflections indicate that the $(Pb_2MnSe_3)_{0.6}VSe_2$ compound is crystallographically aligned with the *c*-axis perpendicular to the substrate. The *c*-axis lattice parameter after annealing at 250 °C (14.96 Å) is consistent with that expected for the targeted $(Pb_2MnSe_3)_{0.6}VSe_2$ compound based on the expected constituent layers and close to the *c*-axis lattice parameter for the relaxed structure after the DFT structural optimization (14.70 Å). In-plane diffraction data collected after annealing at 250 °C, (Figure 15.4b) contains intensity maxima that can be indexed as *hk*0 reflections coming from independent hexagonal and square lattices. The lattice parameter of the hexagonal phase (3.44 Å, computationally 3.46 Å) is close to that found for VSe_2 monolayers in $[(PbSe)_{1+\delta}]_mVSe_2$ compounds.[43] The lattice parameter of the square phase (5.99 Å, computationally 5.89 Å) is close to that found for rock salt structured PbSe bilayers in $(PbSe)_{1.1}VSe_2$.[42,43]

An atomic-scale EDS-STEM map of a representative area (Figure 13.4c) shows that there is a VSe_2 layer on either side of a Pb_2MnSe_3 layer, while the Pb_2MnSe_3 layer contains a MnSe middle layer with PbSe on either side. The average changes in the EDS intensities for Mn, Pb, Se, and V through a single unit cell are shown in Figure 13.4d along with a schematic of the proposed structure in Figure 13.4e. The bottom HAADF-STEM image of a representative area of $(Pb_2MnSe_3)_{0.6}VSe_2$ in Figure 13.3 shows precise stacking of Pb_2MnSe_3 and VSe_2 layers. Zone axis orientations are consistent with the Pb_2MnSe_3 having a distorted rock salt structure. The top and bottom PbSe layers are puckered, with

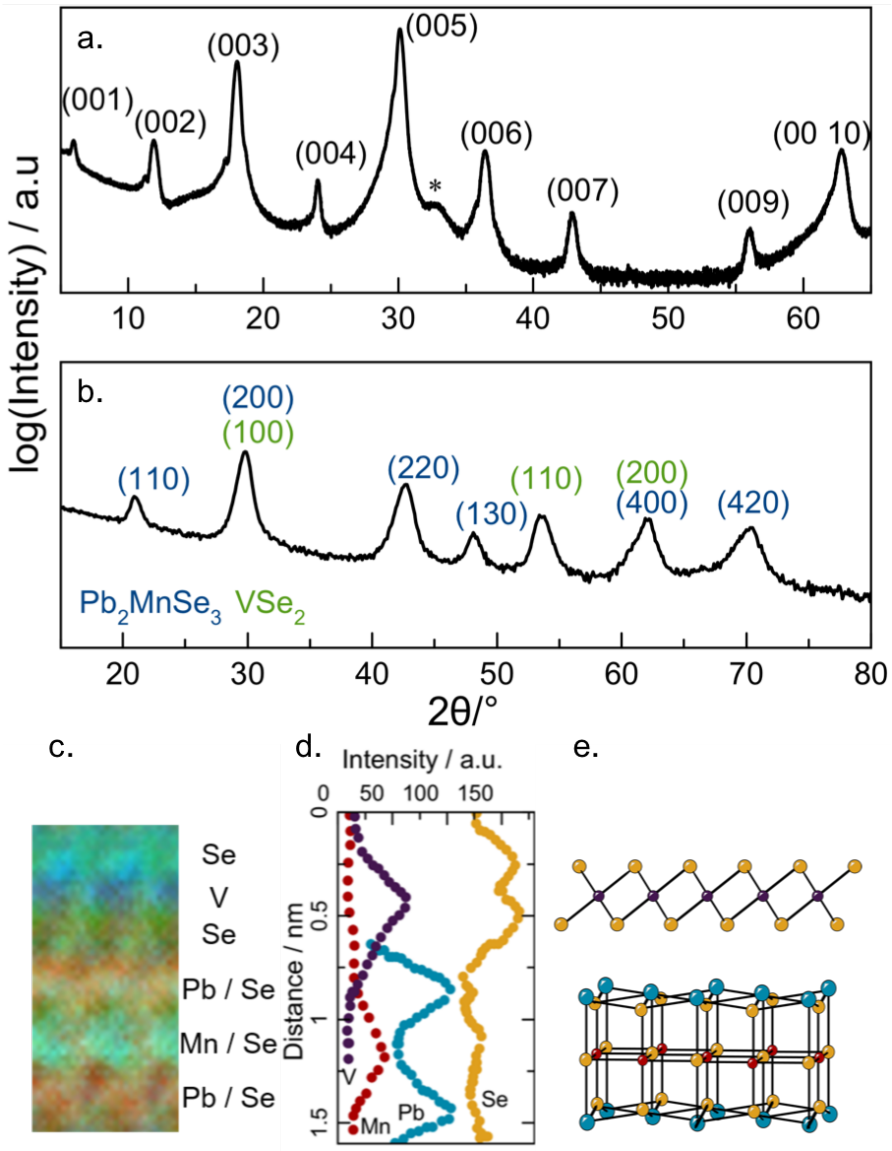

Figure 13.4. Structural characterization of the $(Pb_2MnSe_3)_{0.6}VSe_2$ heterostructure. The specular diffraction pattern contains only reflections that can be indexed to the same *d*-spacing (a.). Reflections in the in-plane diffraction pattern can be indexed to either hk0 reflections for a hexagonal or cubic unit cell which correspond to either VSe_2 or Pb_2MnSe_3, respectively(b.). EDS map (c.) and intensity profile (d.) of the STEM-EDS map clearly show V between planes of Se alternating with a Mn/Se plane between Pb/Se planes. This structure is shown as a schematic with Se atoms shown in yellow, V atoms in purple, Mn atoms in red and Pb atoms in blue (e.).

the Se atoms displaced towards the MnSe layer and the Pb atoms pushed out from the central plane (computationally by 0.67 Å, on average). This results in the Mn cations having four long bonds to Se within the Mn-Se plane and two shorter Mn-Se bond distances with the Se atoms in the Pb-Se plane. The smaller size of the Mn atom relative to Pb enables the central Mn-Se layer to stabilize the puckering of the outer PbSe layer[44].

The calculations of the properties of $(Pb_2MnSe_3)_{0.6}VSe_2$, conducted with the same relaxed supercell used to calculate the structure, suggest that it should be a ferromagnetic metal. The electronic density of states at the Fermi level is contributed mainly by the V atoms and the magnetic moment is primarily from the Mn atoms. The measured electrical transport properties of $(PbSe)_{1.1}VSe_2$ and $(Pb_2MnSe_3)_{0.6}VSe_2$ are shown in Figure 13.5. The upturn in resistivity in the $(PbSe)_{1.1}VSe_2$ data has previously been attributed to the onset of a charge density wave (CDW) in the VSe_2 monolayers, which is distinctly different than that found in bulk VSe_2.[42,43,47] The Hall coefficient is positive in $(PbSe)_{1.1}VSe_2$, suggesting that holes are the majority carrier and the magnitude of the Hall coefficient increases sharply below the CDW onset temperature.[42,43] This contrasts with what is found for bulk VSe_2, which has a negative Hall coefficient and only a small change in slope as temperature is varied through the CDW transition.[47] The resistivity of $(Pb_2MnSe_3)_{0.6}VSe_2$ is higher than that measured for $(PbSe)_{1.1}VSe_2$ at room temperature, as the VSe_2 is a smaller percentage of the total thickness. The samples have similar temperature dependencies over the range they were measured. The resistivity increases rapidly as temperature is decreased below 100K, suggesting that $(Pb_2MnSe_3)_{0.6}VSe_2$ also has a CDW, though this is not seen in the relaxed unit cell from the DFT calculations. The onset temperatures of the transition are very similar between the two compounds, though it appears to be a little less pronounced in the $(Pb_2MnSe_3)_{0.6}VSe_2$. This is consistent with prior reports of the onset

temperature not changing as the thickness of PbSe is varied in $[(PbSe)_{1+\delta}]_mVSe_2$ heterostructures.[43] There is a kink in the resistivity curve at around ~30 K, however, which is not present in any of the $[(PbSe)_{1+\delta}]_mVSe_2$ compounds. The $(Pb_2MnSe_3)_{0.6}VSe_2$ Hall coefficient is positive and increases as temperature is decreased below the CDW temperature of ~100K. This data suggests that Mn is divalent in the Pb_2MnSe_3 layer and that the extent of charge transfer and bonding between the Pb_2MnSe_3 layer and VSe_2 is similar to that found for the PbSe layer. Bader analysis of the total spin density in the DFT calculations attributes around 4 μ_B to each Mn atom.[48] Mn^{2+} has 5 electrons in the 3d orbitals and in a high spin D_{4h} local environment a magnetic moment of 5.9 μ_B is expected for Mn^{2+}.[49] The smaller magnetic moment may be a consequence of charge transfer from the Pb_2MnSe_3 layer to VSe_2. Evidence for a ferromagnetic ordering of the Mn orbital moments is found in the anomalous Hall effect observed in the field dependence of the Hall coefficient at low fields (figure 13.5c). The Hall coefficient becomes non-linear below about ~ 30 K, which is the same temperature where we observe a kink in the resistivity curve. This anomalous Hall effect suggests that the sample is ferromagnetically ordered.[50] Further evidence for ferromagnetic behavior is observed in the hysteresis of the Hall resistivity verses field measurement shown in Fig H.1.

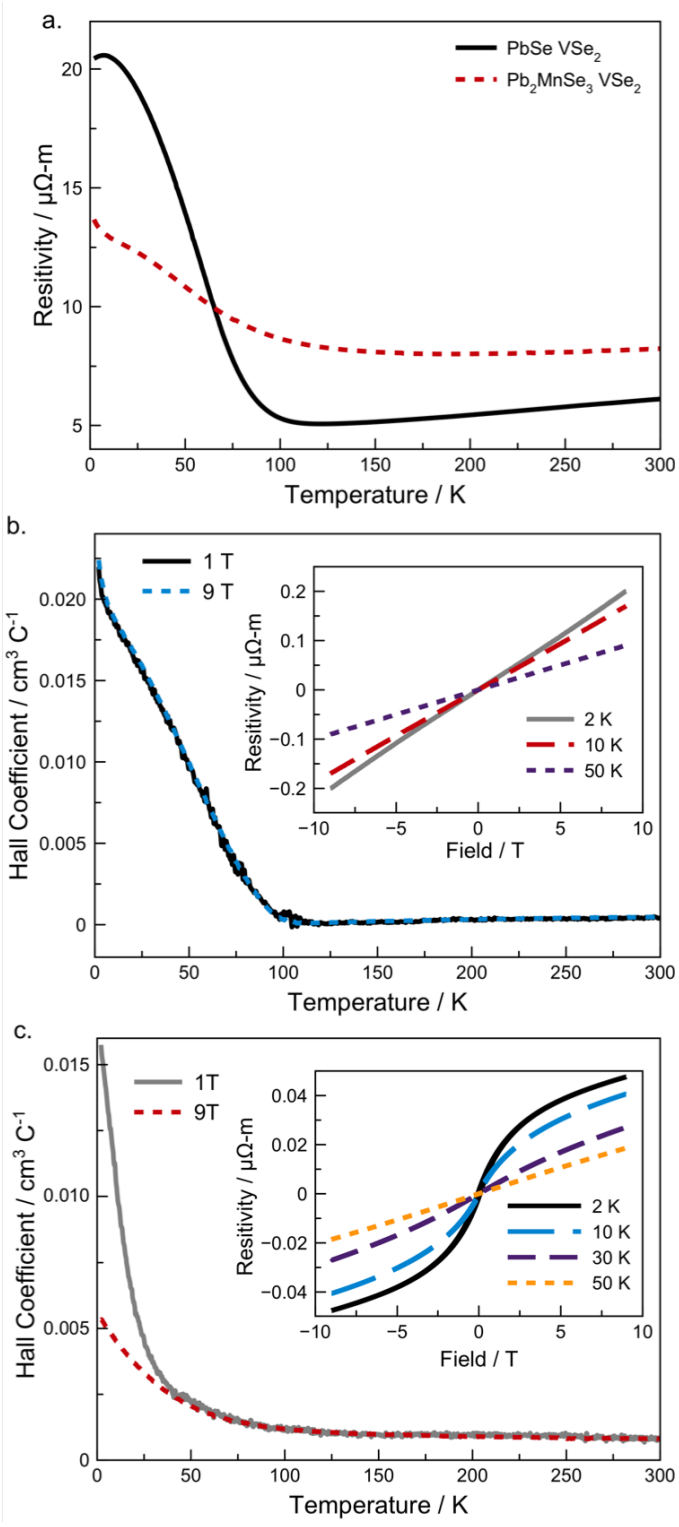
a.
PbSe VSe2
Pb2MnSe3 VSe2
Resitivity / μΩ-m
Temperature / K
b.
1 T
9 T
Hall Coefficient / cm3 C-1
Resitivity / μΩ-m
2 K
10 K
50 K
Field / T
Temperature / K
c.
1T
9T
Hall Coefficient / cm3 C-1
Resitivity / μΩ-m
2 K
10 K
30 K
50 K
Field / T
Temperature / K

Figure 13.5. Resistivity and hall coefficient plots of $(Pb_2MnSe_3)_{0.6}VSe_2$ and $(PbSe)_{1.1}VSe_2$ heterostructures. Both heterostructures have an upturn in the temperature dependent resistivity (a.) at ~100 K, consistent with the VSe_2 charge density wave, though the $(Pb_2MnSe_3)_{0.6}VSe_2$ turn on appears to be smeared out. The $(PbSe)_{1.1}VSe_2$ Hall coefficient as a function of temperature (b.) has a similar upturn at about 100 K at different fields and linear resistivity measurements as a function of field supporting that there is not a magnetic moment (inset). The $(Pb_2MnSe_3)_{0.6}VSe_2$ temperature dependent Hall coefficient (c.) has a slight kink at 100 K, but also has a field dependent upturn that occurs around 50 K. The inset shows field dependent resistivity that goes from linearly to sigmoidal as temperature is decreased. The transition from linear to sigmoidal appears to occur between 30 K and 10 K. This switch as well as the hysteresis observed in Fig. H.1 indicates a magnetic moment is occurring.

13.4. CONCLUSIONS

Accelerating discovery of new materials with unusual properties is one of the grand challenges in materials science and advances the field toward designing new materials with desired functionality. This work demonstrates a collaborative search and synthesis approach that leverages, complementary strengths to solve the problem of finding such materials among the myriad of possible heterostructures. The synthesis relies on the MER procedure to locally find kinetically stable heterostructures similar to the designed precursors, while the search relies on DFT optimization of precursor structures devised in the island approximation to gain a critical advantage in confronting the unknown reaction kinetics and potential structures. This approach led to layered heterostructures in the previously compound-free quaternary phase diagram of Mn-Pb-Se-V, and the calculations show that isostructural compounds containing Cr, Fe, Co, Ni, and Zn in place of Mn may be synthesizable. The unusual coordination environments found at the surface of constituents and unique combinations of elements in each constituent provides opportunities to obtain properties that cannot be

found in stable bulk structures. The collaborative approach explored here demonstrates great potential in accelerating the discovery of these kinetically stable materials.

13.5. BRIDGE

This chapter focused on the synergistic relationship between computation and experiment in the search for finding novel thin film materials with emergent properties for use in heterostructures. A series of compounds were predicted to be metastable using a computational DFT islands methods that resembles the experimental MER synthesis method. A novel Mn-Pb-Se-V containing heterostructure with the formula $(Pb_2MnSe_3)_{0.6}VSe_2$, was computationally predicted to be stable and was successfully prepared experimentally. This material is composed of a 3-layer Pb-Mn-Se building blocks layered with VSe2 and exhibits ferromagnetic properties. The ability to successfully link computation and experiment to drive forward the discovery of new materials will help to accelerate the field of heterostructures with emergent properties. The final chapter will provide a summary of the work conducted in this dissertation as well as an outlook on future work, especially focusing on the projects driven forward by computational prediction.

CHAPTER XIV

CONCLUSIONS, SUMMARY, AND FUTURE OUTLOOK

The emergent properties discovered in thin film materials and the desire to implement them into technological devices has made them a major topic of interest. In order to harness these properties and successfully use them in devices, it is necessary to understand how they form, how deposition influences their properties, and the role that heterostructure architecture has on these materials. The Modulated Elemental Reactants (MER) synthesis method allows for the synthesis and systematic study of single-phase materials and heterostructures, including novel materials and families of compounds with systematic changes in structure. The materials are accessed by preparing designed precursors composed of elemental layers whose structures mimic that of the desired product and annealing them at low temperatures, subsequently trapping the materials in the local minima as opposed to the global minimum in the energy landscape. This work discussed a wide variety of compounds prepared by the MER method, all of which were investigated to inform on how material nanoarchitecture and composition influence the observed materials properties.

X-ray fluorescence is a powerful tool with monolayer sensitivity and the ability to determine the absolute amount of a material in a compound. Here it was shown that by using a unique data treatment, including signal integration and background subtraction, the measured intensity can be directly related to the atoms / unit area of an element within a thin film compound. Eliminating the need to rely on relative amounts, the ability to measure the absolute amount of material in a sample facilitates the ability to consistently prepare thin films with a precise number of layers as well as efficiently target novel materials and homologous series of heterostructure compounds. This measurement

technique was utilized throughout the entirety of this body of work and was essential to investigating the evolution of a precursor to a crystalized thin film and unraveling the influence on composition related defects on the observed transport properties.

The heterostructures presented in this work are composed of two constituents layered specifically to investigate questions about charge donation and layer interactions in thin film materials. To understand how the properties are modified when put in a heterostructure, the structures and properties of the individual constituent, composing the $[(SnSe)_{1+\delta}]_m[TiSe_2]_n$ heterostructure compounds, SnSe and $TiSe_2$ were investigated independently. When deposited via the MER synthesis method, SnSe is a preferentially aligned compound with lattice parameters similar to what is observed in the bulk compound. Post-annealing treatment of the preferentially aligned SnSe readily converts it to $SnSe_2$, providing an additionally method for preparing unique heterostructures. $TiSe_2$ prepared by MER forms over a wide compositional range and crystalizes on deposition. Even when the incorrect amount of material is deposited to form $TiSe_2$, the compound will rearrange on deposition and push all the excess material out of the structure to form as much on-composition $TiSe_2$ as possible. It was also found that this process is aided by the presence of excess Se. Understanding how the synthesis conditions impact the formation of the compound, methods for post-synthetic modification of these materials, and understanding the independent constituents provides insight useful for future heterostructure synthesis.

The nature of the MER method allows for the independent constituents to be combined into nearly infinite series of homologous heterostructures by modifying the layering scheme or thickness of each constituent layer in the designed elemental precursor. Analyzing a homologous series builds a picture of how the two constituent materials

interact as well as how the nanoarchitecture can be modified to tune the observed transport properties. For example, when a single layer of SnSe and $TiSe_2$ are combined to create the repeating unit cell, there is a distortion that occurs in the SnSe in-plane structure. The distortion is a result of interaction between the two constituent layers. By distorting, there is an accidental lattice match that occurs between the SnSe and $TiSe_2$ layers, creating a misfit layer compound with regions of rotational disorder. When the number of $TiSe_2$ layers in the repeating unit cell is increased, the distortion in the in-plane unit cell persists, but the in-plane long range order disappears. As the number of SnSe layers in the repeating unit cell is increased, the area of the basal plane changes, going through an almost square distortion, before taking on a structure that approaches that reported for bulk SnSe. Temperature dependent studies of the in-plane structure indicate that as the temperature is decreased, the in-plane lattice parameters also approach that of the bulk, further demonstrating the complex structural behavior observed in these family of heterostructure compounds.

The strong interaction between the SnSe and $TiSe_2$ constituent layers, which influences the constituent structure, also dictates the electrical transport properties. The $[(SnSe)_{1+\delta}]_1[TiSe_2]_1$ heterostructure has the strongest observed interaction between layers as there are no layers without an adjacent SnSe|$TiSe_2$ interface present in the compound. This results in the material displaying metallic transport behavior that is not representative of either individual constituent, but instead a novel material composed of single layers of SnSe and $TiSe_2$. This behavior is not observed for any compounds with increased numbers of SnSe, $TiSe_2$, or both in the repeating unit. Electrical transport data indicates that all of the materials are dominated by variable range hopping at low temperatures which is a result of the charge donation from SnSe to $TiSe_2$ at the interface. In the

$[(SnSe)_{1+\delta}]_1[TiSe_2]_1$ film, this behavior dominates over the entire temperature regime. As the number of layers in the repeating unit, regardless or the nanoarchitecture, increases, the behavior becomes more complex. When the number of $TiSe_2$ layers in the repeating unit is increased and the number of SnSe layers is held constant, at high temperature, the $TiSe_2$ constituent dominates and the carriers are dominated by both active electrons and mobile holes. When the number of SnSe layers is increased, regardless of the number of $TiSe_2$ layers in the compound, holes become increasingly important and dominate the transport at all temperatures, while electron are still present. This observed transport behavior demonstrates the complex electronic behavior occurring in these materials. Further studies systematically changing the nanoarchitecture and observing both the electronic transport properties and the band structure via XPS could be done to further elucidate the origin of the observed properties.

While XRF has the capability of detecting a monolayer of material and MER allows the synthesis of complex heterostructures via designed precursors, it is still difficult to reproducibly deposit monolayer amounts of material. Even with layered elemental precursors that did not contain the correct amount of material to prepare a targeted series of $[(PbSe)_{1+\delta}]_4[TiSe_2]_4$ isomer heterostructures, the desired compounds still formed the majority of the sample, albeit with fewer repeating units than targeted. This is a result of the initial crystallization and the designed precursor nanoarchitecture directing the formation of the heterostructure. It was found that when Se is deposited on the first Ti layer, Ti_2Se nucleates, leaving excess Se to react with the Pb deposited on it. This initial crystallization set the tone for the subsequent nucleation and crystallization in the material. In this case, Ti_2Se persists even after annealing as an impurity phase and impurity TiO_2 is found on the surface. The ability to form the isomers even when an incorrect amount

of material is deposited demonstrates the wide local energy minima these materials exist in and the materials resilience to compositional defects. Electrical transport analysis of these materials demonstrated that the number of buried interfaces in the compound influenced the carrier concentration and resistivity of the compound. This is likely the result of charge donation from PbSe to $TiSe_2$ occurring at the interfaces between the two constituents. The obtained understanding of the heterostructures formation mechanism and the influence of interfaces on observed properties is useful information for the synthesis of novel heterostructure building blocks.

Single phase and heterostructure compounds containing MnSe were successful prepared and characterized. A series of Mn|Se precursors with varying compositions and elemental layer thicknesses were investigated to understand how Mn containing compounds form via the MER synthesis method. Not only did this work facilitate the preparation of novel Mn containing heterostructure building blocks, but it also discovered a new Mn|Se phase. The Mn containing heterostructures that were prepared were computationally predicted to be kinetically stable via a DFT "islands" analysis method. A predicted $(Pb_2MnSe_3)_{0.6}VSe_2$ heterostructure was successfully synthesized and its structure and properties were characterized. This material is composed of alternating layers of VSe_2 and a three-layer building block with PbSe surrounding a monolayer of MnSe. The building block is stabilized due to the smaller Mn cations facilitating puckering of the outer PbSe layer which contains the large Pb atoms. Only compounds with MnSe in the layer second from the outside were successfully prepared due to this puckering facilitation. The novel $(Pb_2MnSe_3)_{0.6}VSe_2$ was also found to be a ferromagnetic compound, which was supported by further computational evaluation. This novel three-layer building block and observed ferromagnetic behavior provides precedent for the ability to

prepare more complex heterostructures as well as an avenue to prepare and manipulate magnetic behavior in thin film materials.

The ability to predicted possible metastable materials opens the doors to efficiently prepare novel materials with targeted properties. The ability to use MER to prepare homologous series of compounds allows the observed properties to be manipulated to vary the result. This interplay between theory and experiment is a viable method for efficiently preparing designer materials with targeted properties. Based on the success of the predicted and prepared $(Pb_2MnSe_3)_{0.6}VSe_2$ compound, a PbSe -MnSe-PbSe-MnSe-PbSe building block was successfully layered with VSe_2 to prepare a novel heterostructure. In the future, this material's transport properties should be characterized, and a homologous series of compounds with an increasing number of PbSe layers between the MnSe layers should be synthesized and characterized to try to manipulate ferromagnetic behavior. Another viable method for manipulation of magnetic behavior in these types of compounds involves preparation of other 3-layer building block compounds similar to the Pb_2MnSe_3 constituent but with other cation species. Compounds of this type were predicted to be metastable via the DFT "islands" method and they should be fully investigated to prepare potentially novel materials with interesting properties. Overall, layering these 3-layer building blocks with other TMD's in heterostructures should provide a facile method of manipulating novel observed properties.

Overall, MER synthesis has facilitated the preparation of novel thin film materials and investigation of layer interactions in heterostructure materials. The ability to precisely place material allows for a wide variety of materials to be studied and allow for systematic studies of properties as a function of nanoarchitecture. The ability to systematically study changes in material properties based on layer interactions is the first

step towards obtaining the ultimate goal of materials science – preparing materials with targeted properties for use in specific devices.

Appendix A

SUPPORTING INFORMATION FOR CHAPTER II

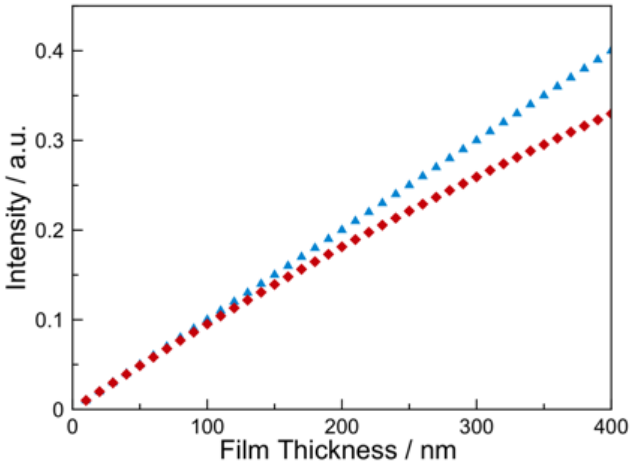

Figure A.1. Graph of intensity (arbitrary units) versus film thickness (nm) according to Equation 2.1 (red diamonds) and Equation 2.2 (blue triangles). The error in intensity of assuming film thickness is small is less than 5% for thicknesses below 100 nm. For this plot, the mass absorption coefficient $\mu_T(\lambda_i)$ of the wavelength of interest and film density ρ were chosen to be 1000 cm^2/g and 7 g/cm^3, respectively. The values of each were chosen to be representative of typical films with a Lα emission lines.

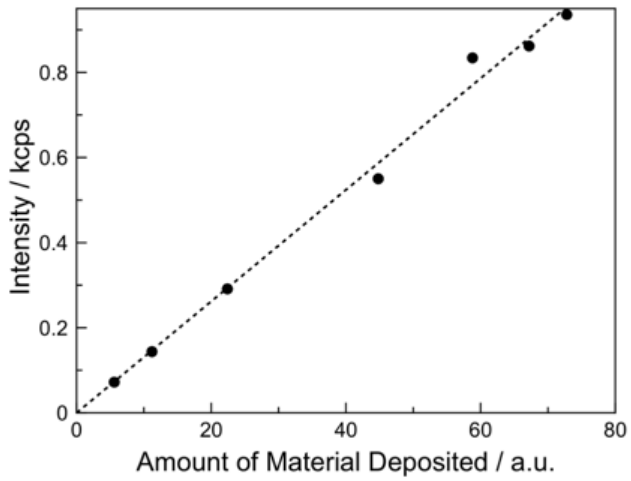

Figure A.2. XRF intensity as a function of the amount of molybdenum deposited from an electron beam gun. Mo was deposited using a different physical vapor deposition system and a different XRF diaphragm was used to define an area during the XRF experiments, so there is a different metric for the arbitrary units of the amount of material deposited and in the XRF intensity in Figure A.2 versus the films shown in Figure 2.1.

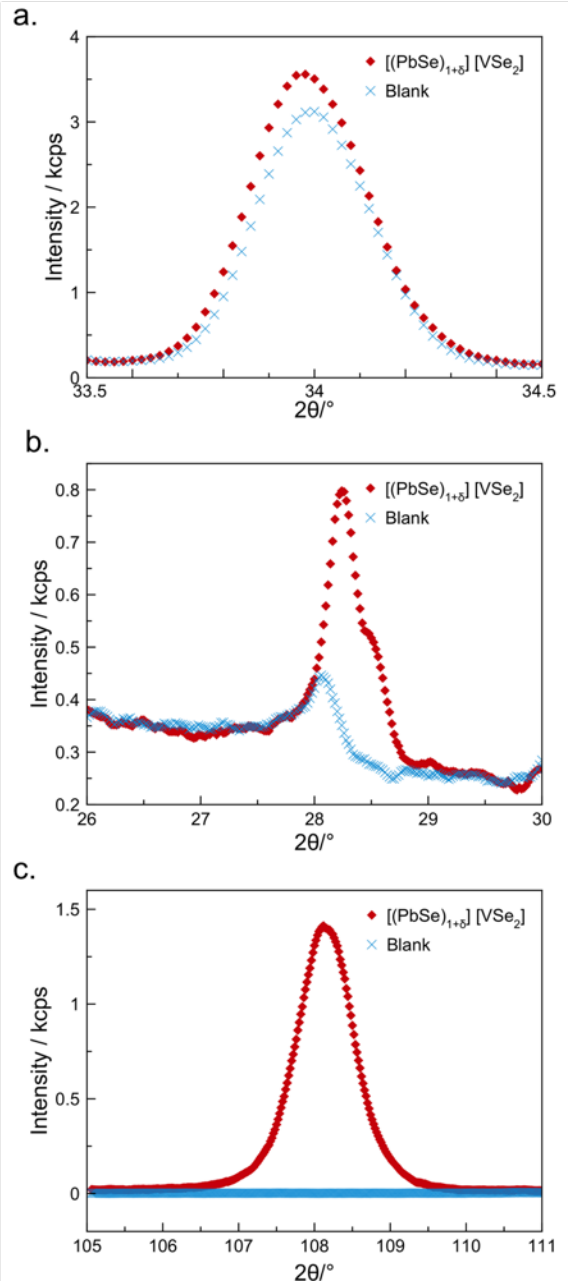

Figure A.3. X-ray emission lines for the (a) Lα, (b) $L\beta_1$, and (c) Mα of Pb were tested to determine the best parameters for measuring the amount of Pb in each sample. The Mα line was chosen as it showed the largest difference in intensity between the sample containing Pb and the blank substrate.

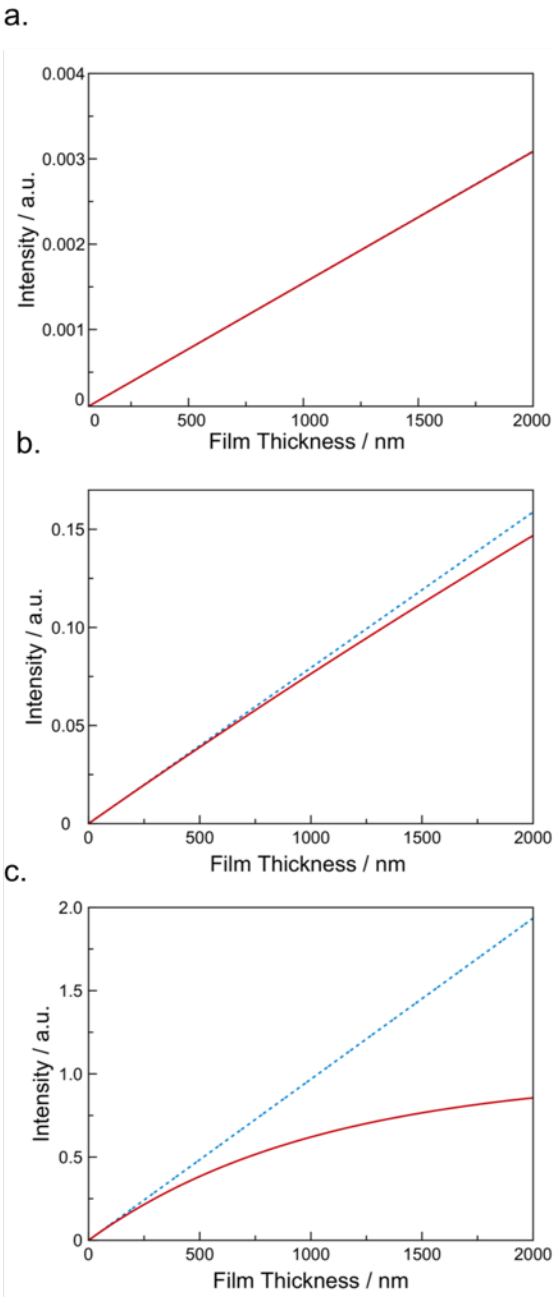

Figure A.4. Calculated X-ray emission intensities for the (a) Kα, (b) Lα, and (c) Mα lines of Bi in a film of Bi_2Se_3. The values inserted into Equations 2.1 and 2.2 are: ρ = 7.71 g/cm^3, μ(Mα) = 1300 cm^2/g, μ(Lα) = 100 cm^2/g, and μ(Kα) = 2.0 cm^2/g. The total mass attenuation coefficient μ is calculated form the weighted average of the individual attenuation coefficients of each element present in the film. Equation 2.2 yields the blue dashed line and the values from Equation 2.1 are given by the red continuous line.

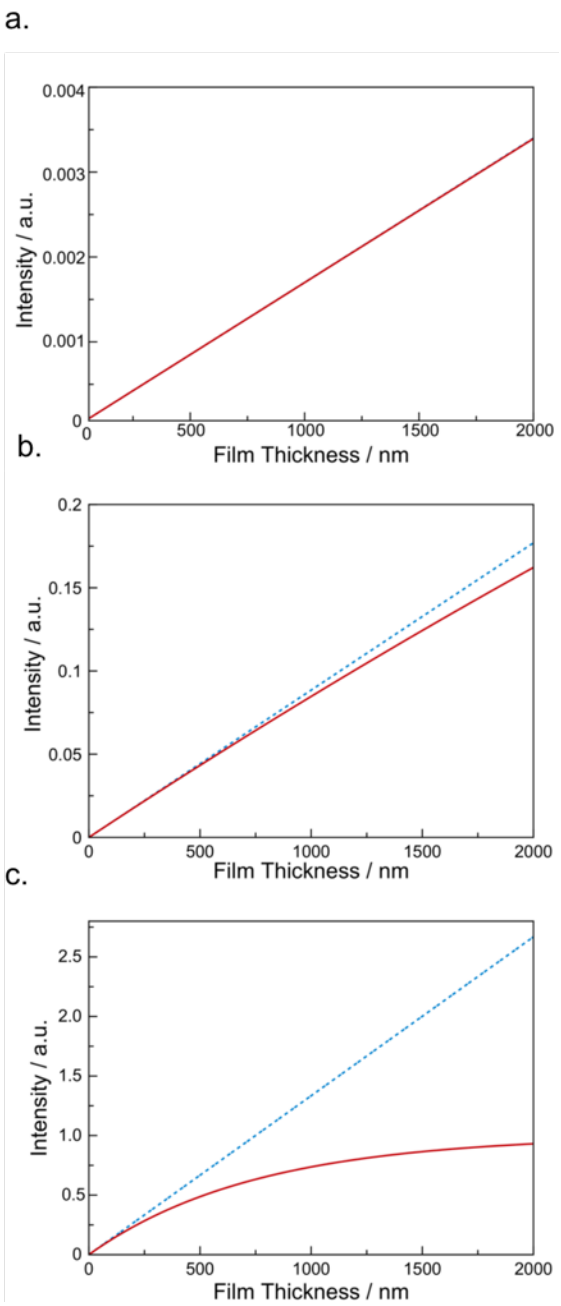

Figure A.5. Calculated X-ray emission intensities for the (a) Kα, (b) Lα, and (c) Mα lines of Pb in a film of PbSe. The values inserted into Equations 2.1 and 2.2 are: ρ = 8.29 g/cm^3, μ(Mα) = 1600 cm^2/g, μ(Lα) = 100 cm^2/g, and μ(Kα) = 2.0 cm^2/g. The total mass attenuation coefficient μ is calculated form the weighted average of the individual attenuation coefficients of each element present in the film. Equation 2.2 yields the blue dashed line and the values from Equation 2.1 are given by the red continuous line.

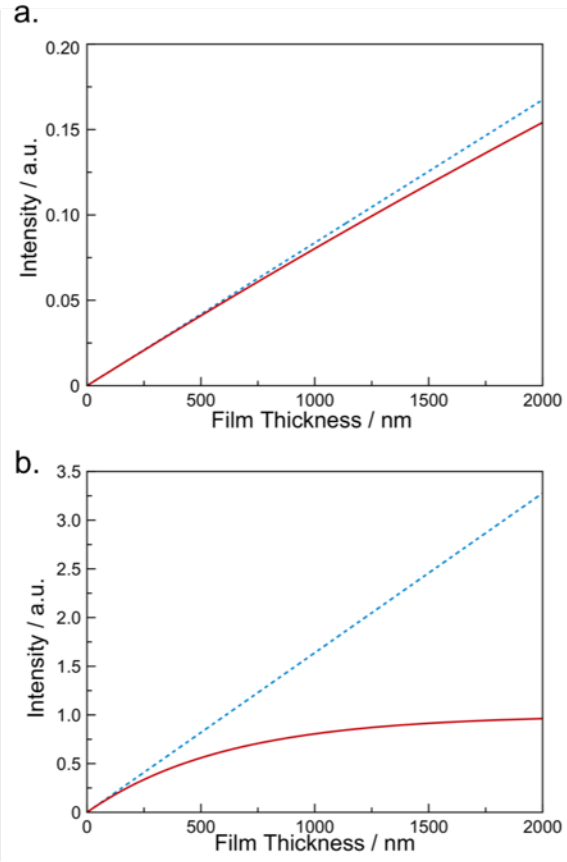

Figure A.6. Calculated X-ray emission intensities for the (a) Kα and (b) Lα lines of Se in a film of PbSe. The values inserted into Equations 2.1 and 2.2 are: ρ = 8.29 g/cm^3, μ(Lα) = 2000 cm^2/g, and μ(Kα) = 100 cm^2/g. The total mass attenuation coefficient μ is calculated form the weighted average of the individual attenuation coefficients of each element present in the film. Equation 2.2 yields the blue dashed line and the values from Equation 2.1 are given by the red continuous line.

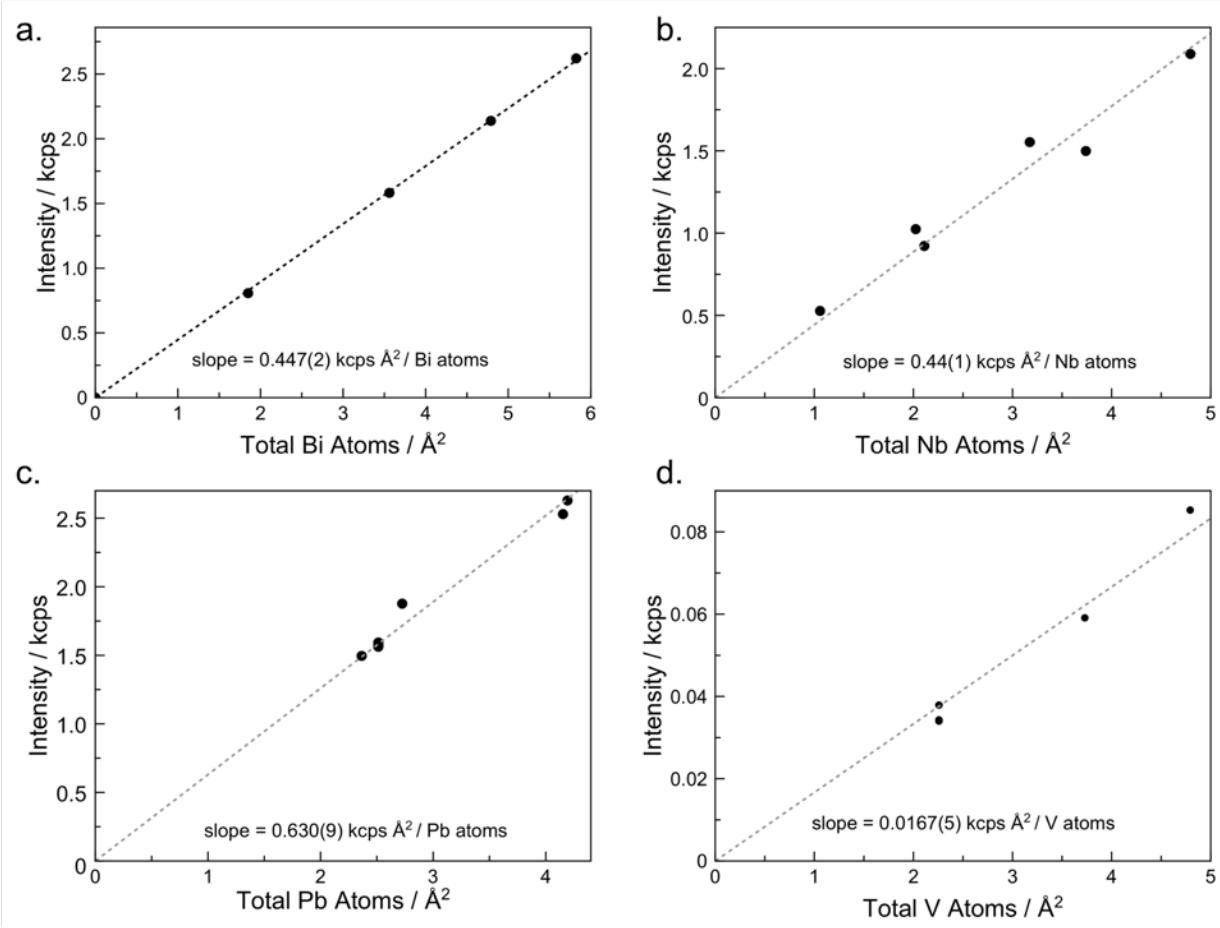

Figure A.7. A graph of intensity versus atoms per Å^2 for the elements (a) Bi, (b) Nb, (c) Pb, and (d) V found in a variety of samples, each consisting of a different element matrix. This shows the versatility of using XRF to probe various elements in a variety of samples.

Appendix B

SUPPORTING INFORMATION FOR CHAPTER IV

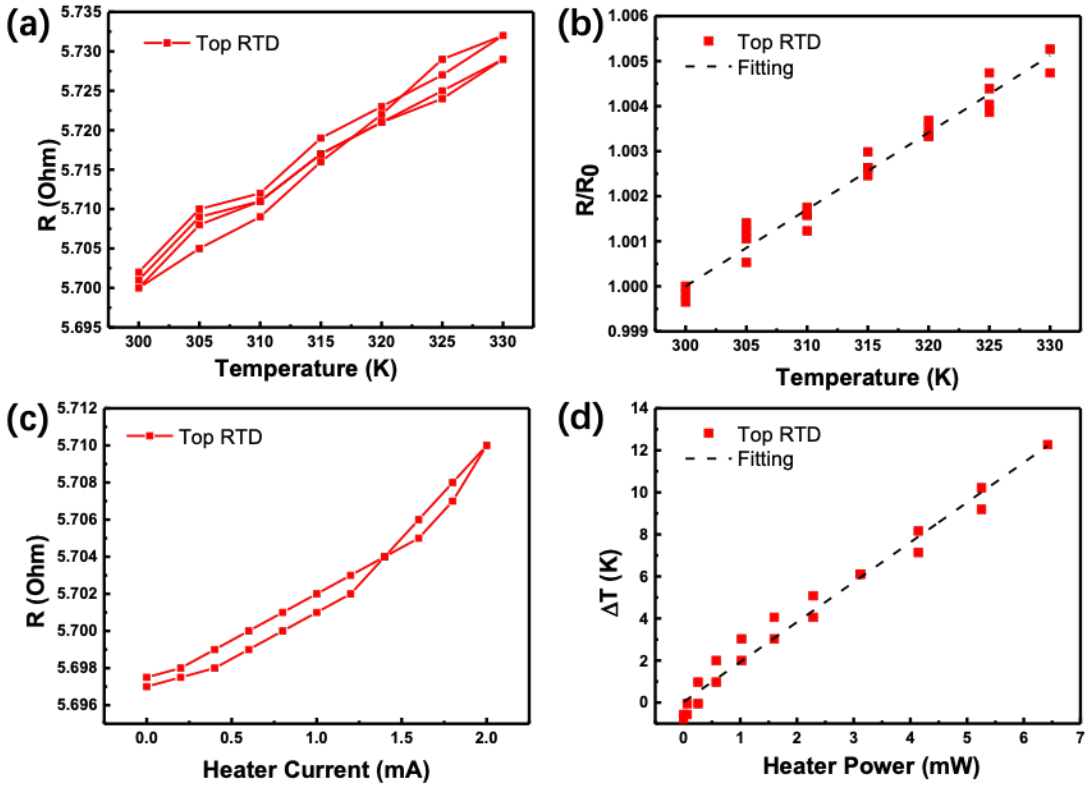

Figure B.1. Temperature calibration of the top resistive temperature detector (RTD) of 50nm SnSe film without Se-vapor annealing. (a) The resistance of the RTD measured at different temperatures. (b) Normalized resistance (R/R_0, where R_0 is the resistance at 300K) plotted as a function of T. (c) The resistance change of the RTD under various heating currents. (d) Temperature change of the metal RTD plotted as a function of heating power.

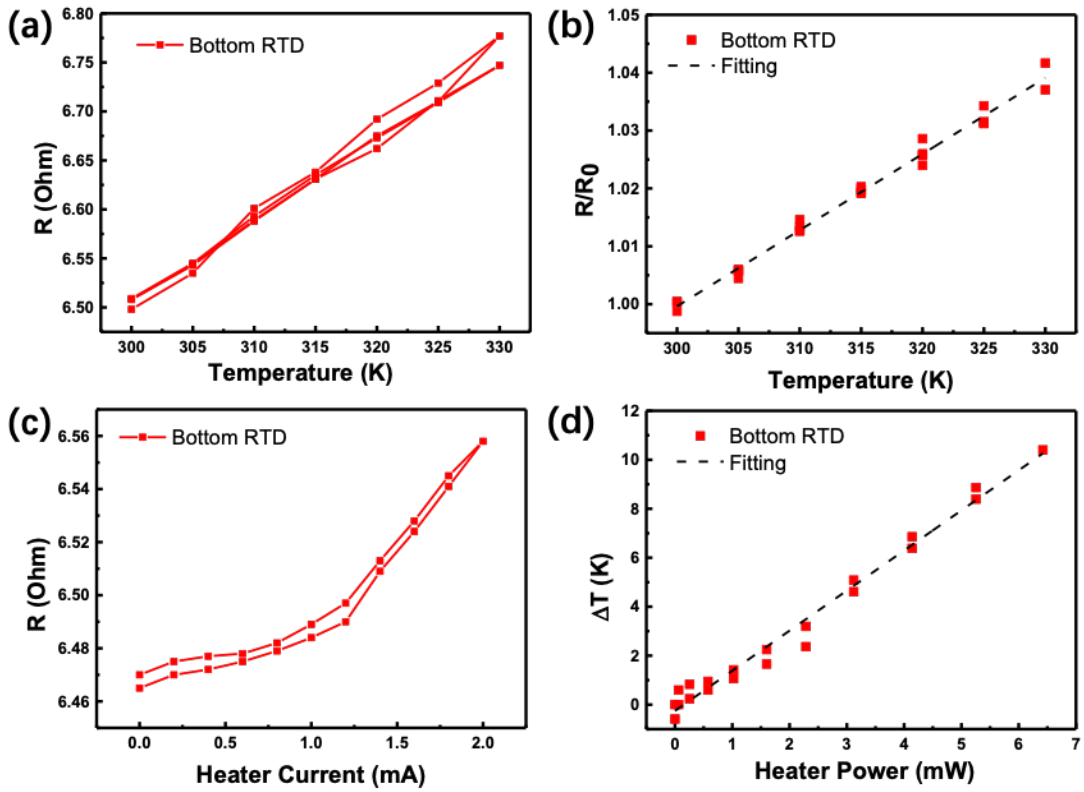

Figure B.2. Temperature calibration of the bottom RTD of 50nm SnSe film without Se-vapor annealing. (a) The resistance of the RTD measured at different temperatures. (b) Normalized resistance (R/R_0, where R_0 is the resistance at 300K) plotted as a function of T. (c) The resistance change of the RTD under various heating currents. (d) Temperature change of the metal RTD plotted as a function of heating power.

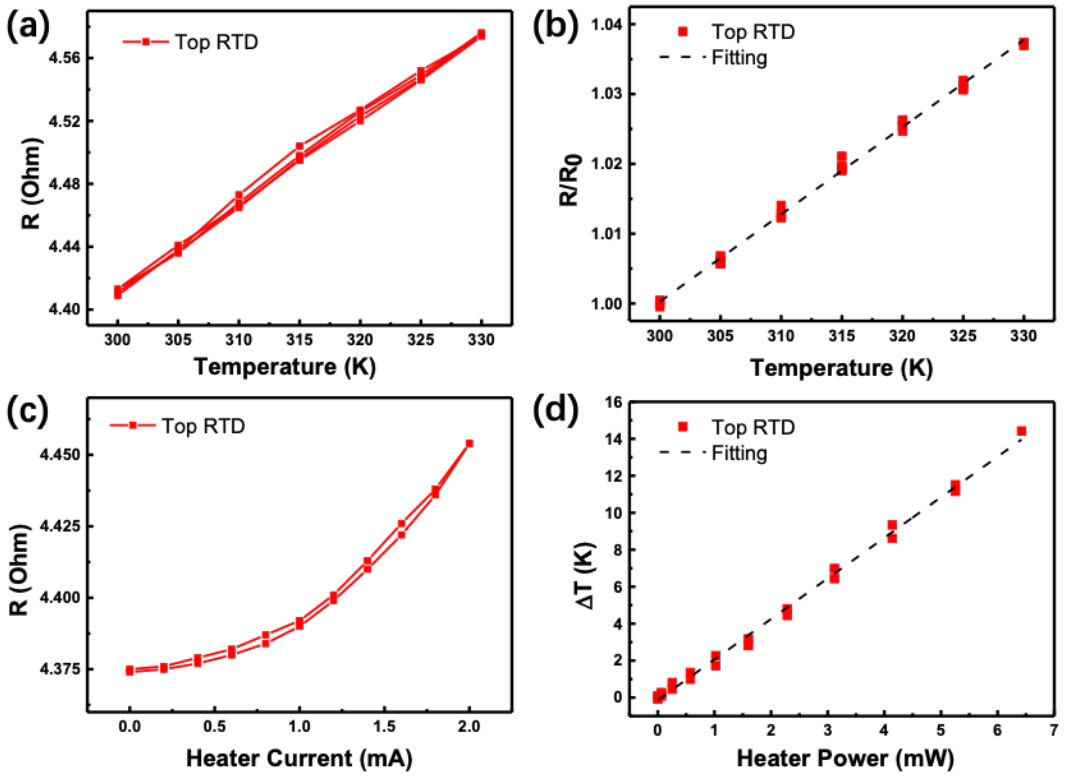

Figure B.3. Temperature calibration of the top RTD of 50nm $SnSe_2$ film after Se-vapor annealing. (a) The resistance of the RTD measured at different temperatures. (b) Normalized resistance (R/R_0, where R_0 is the resistance at 300K) plotted as a function of T. (c) The resistance change of the RTD under various heating currents. (d) Temperature change of the metal RTD plotted as a function of heating power.

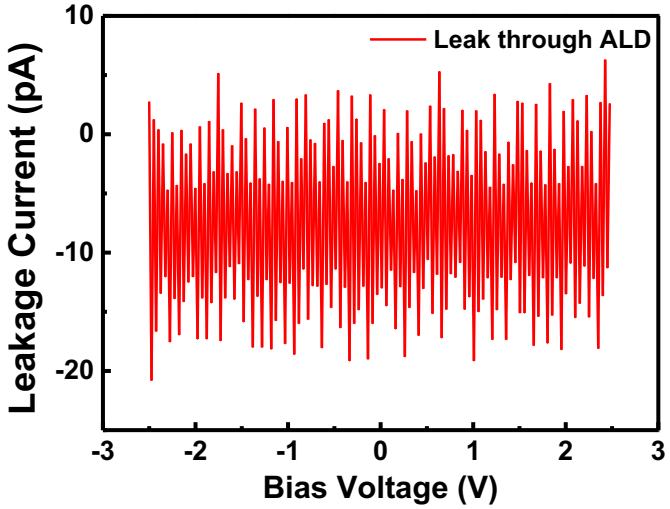

Figure B.4. Leakage current measurement through the atomic layer deposition layer.

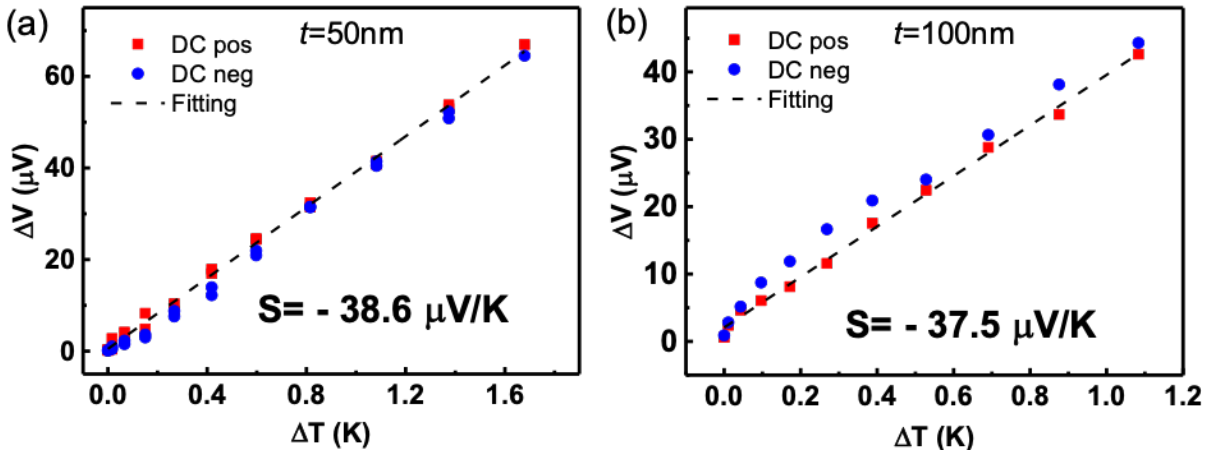

Figure B.5. Cross-plane Seebeck coefficient of a (a) 50nm-thick and (b)100nm-thick SnSe film (without Se annealing).

The cross-plane electrical resistances of the 50nm and 100nm samples were 116Ω and 197Ω, respectively. The thermal resistance of the 50nm and 100nm samples were 261 K/W and 455 K/W, respectively. Based on these values, we can estimate that the electrical contact resistance is 35Ω, the intrinsic cross-plane resistivity of $SnSe_2$ is 1.89 Ω-m, the thermal contact resistance is 67 K/W, and the intrinsic cross-plane thermal conductivity of $SnSe_2$ is 0.89 W/m·K. Using these value, we

estimate that the intrinsic figure of merit for the film in Figure 5 of main manuscript to be approximately $ZT \approx 7.1 \times 10^{-5}$ after removing the effects of contact resistance.

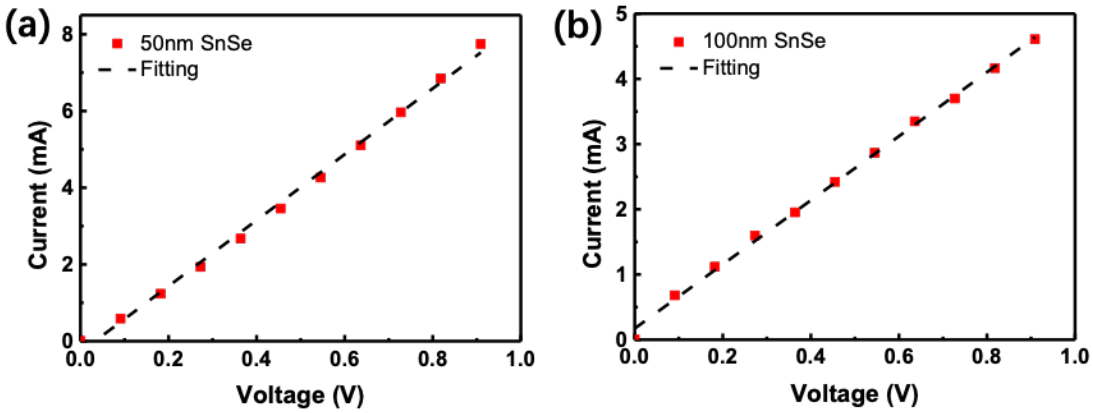

Figure B.6. Cross-plane electrical resistances of (a) 50nm-thick and (b)100nm-thick SnSe film (without Se annealing), respectively.

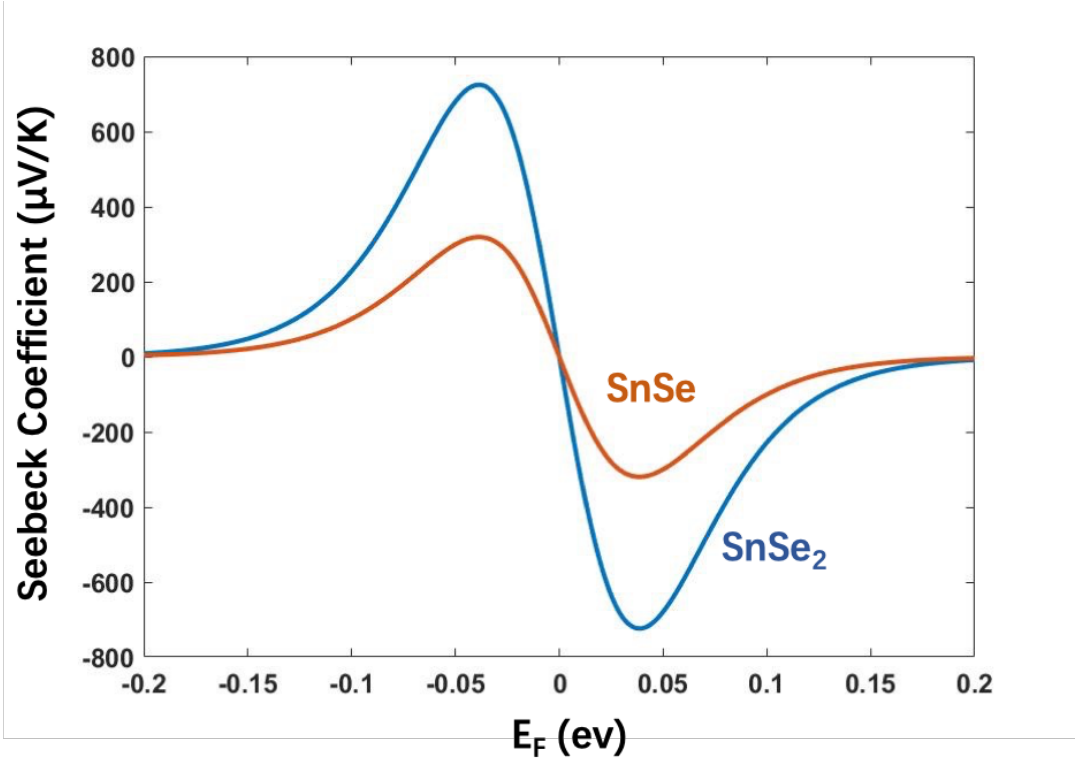

Figure B.7. Seebeck coefficient as a function of Fermi energy for SnSe and $SnSe_2$, respectively.

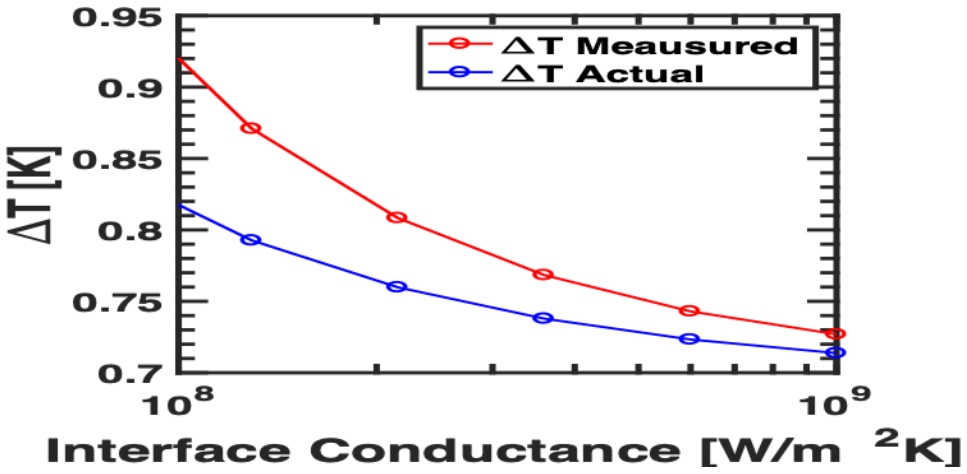

Figure B.8. Calculated range of errors that correspond to the expected range of interface conductance values found in the literature.

The in-plane resistivities of samples annealed in nitrogen and Se were 38.64 mΩ-m and 23.33 mΩ-m, respectively. Here, we observe a 40% reduction in the resistivity due to the mitigation of Se vacancies. This is compared to the 6.6-fold increase in the cross-plane resistance observed after Se annealing. The in-plane Seebeck coefficients of samples annealed in nitrogen and Se were 592mV/K and -342mV/K, respectively. Here, we observe a dramatic change in sign of the thermopower due to the mitigation of Se vacancies. This is compared to the 16-fold increase in the cross-plane thermopower observed after Se annealing. Here, the large discrepancy between in-plane and cross-plane transport behavior further demonstrates the highly anisotropic nature of these rotationally-disordered layered materials. In these anisotropic layered materials, in-plane transport is dominated by the more conducting layer, while the cross-plane transport is dominated by the more insulating layer.

Appendix C

SUPPORTING INFORMATION FOR CHAPTER V

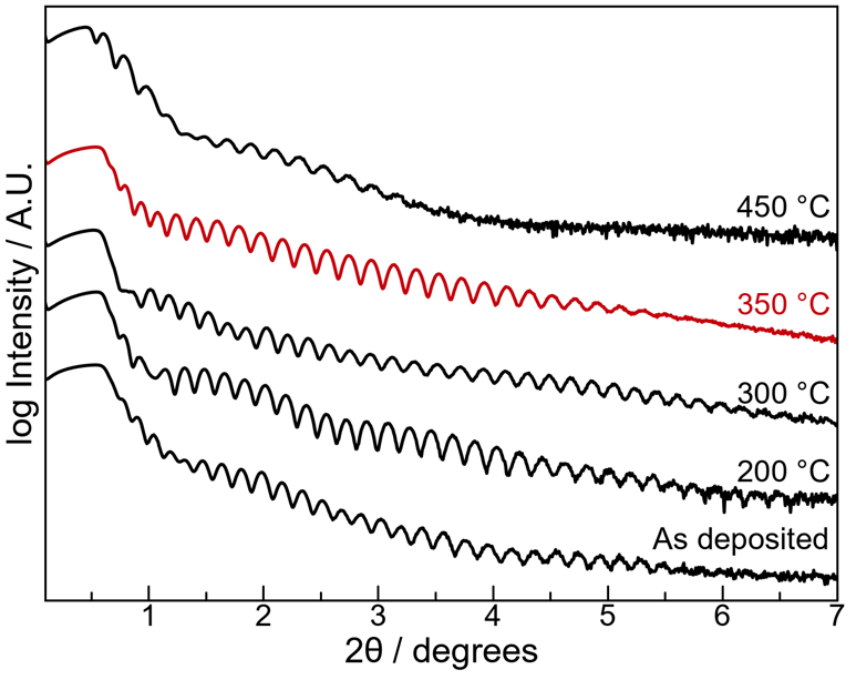

Figure C.1. XRR of Ti|Se annealing study showing evolution of film thickness and roughness as energy is applied to the system.

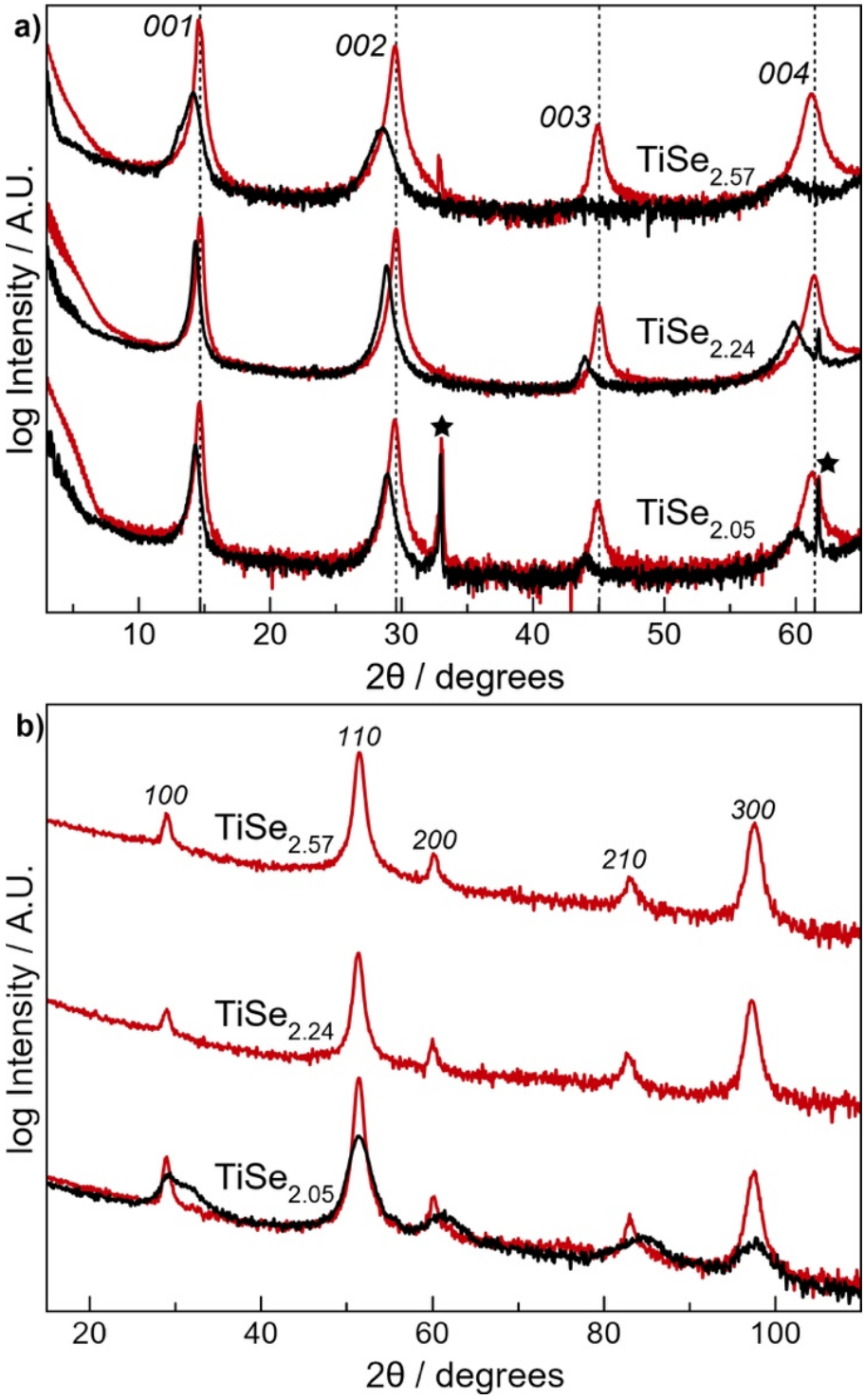

Figure C.2. Specular (a.) and in-plane (b.) XRD patterns for additional Ti|Se precursors annealed at 350°C showing the influence of precursor composition on structure.

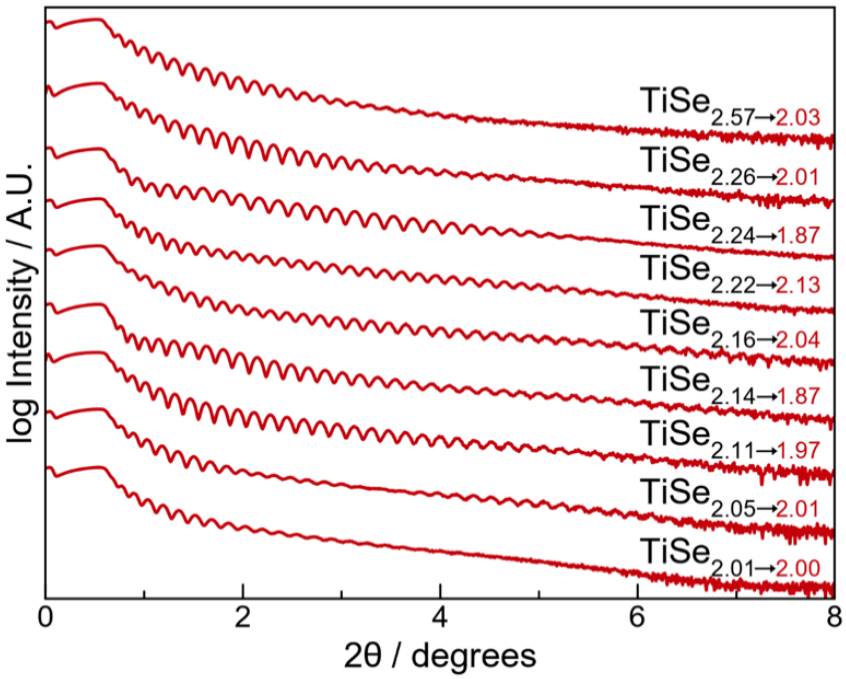

Figure C.3. XRR patterns for various Ti|Se precursors annealed at 350 °C showing the variation in roughness and loss of layers as a function of stoichiometry.

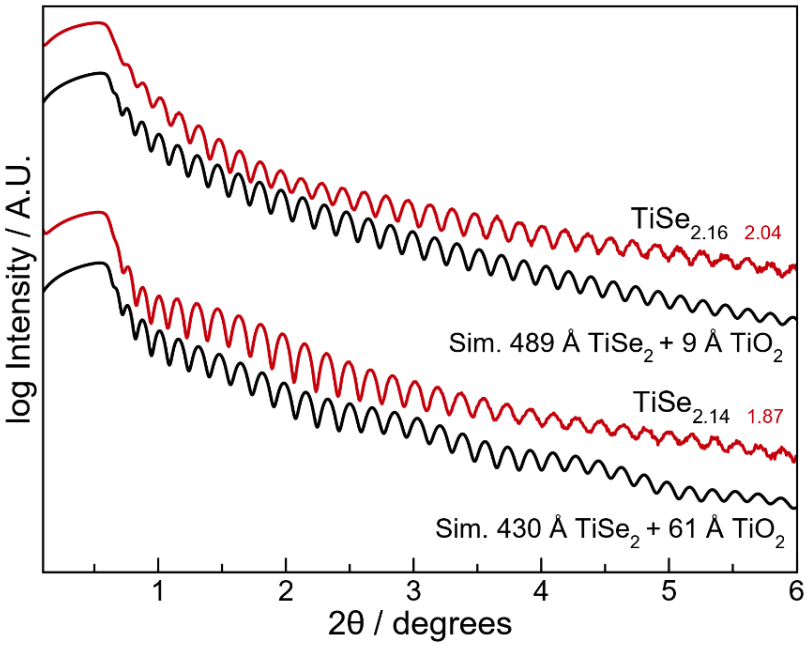

Figure C.4. Experimental (red) and simulated (black) XRR patterns demonstrating effect of oxide growth. Based on the amount of excess material in each film, the annealed films developed either a thin (~9 Å) or thick (~60 Å) oxide layer.

Appendix D

SUPPORTING INFORMATION FOR CHAPTER VII

In-plane Diffraction Pattern Fits

Le Bail fits[1] on in-plane x-ray diffraction patterns of $[(SnSe)_{1+\delta}]_mTiSe_2$ were performed using the FullProf suite.[2,3] The background was fit using a linear interpolation between points. The SnSe phase was modeled using an orthorhombic crystal system and the $TiSe_2$ phase was modeled using a hexagonal crystal system. The peak shapes were fitted using pseudo-Voigt functions. The lattice parameters, line width parameters, and pseudo-Voigt weighting term were refined until convergence was reached. The (110) reflection of $SnSe_2$ in the $m \geq 2$ compounds were included in the background.

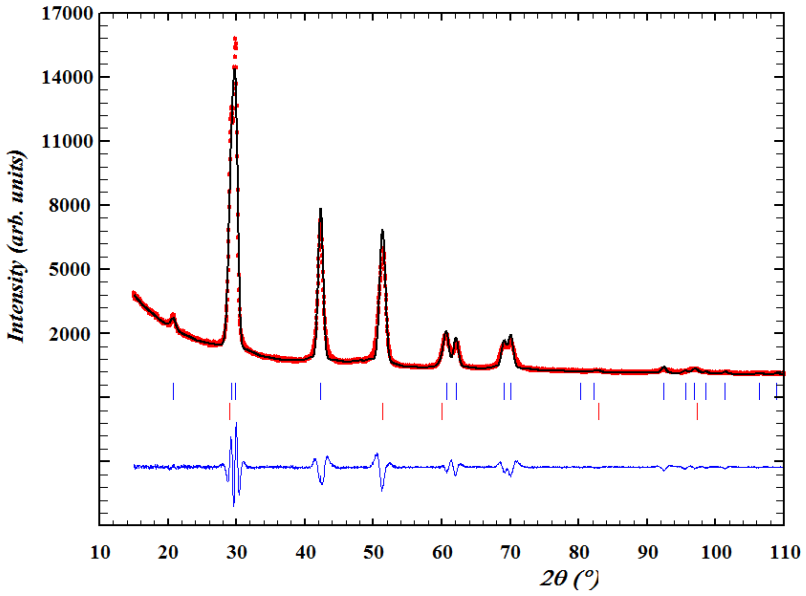

Figure D.1. Le Bail fit of the in-plane diffraction pattern for $m = 1$. Blue tick marks indicate the position of SnSe reflections and red tick marks indicate the position of $TiSe_2$ reflections.

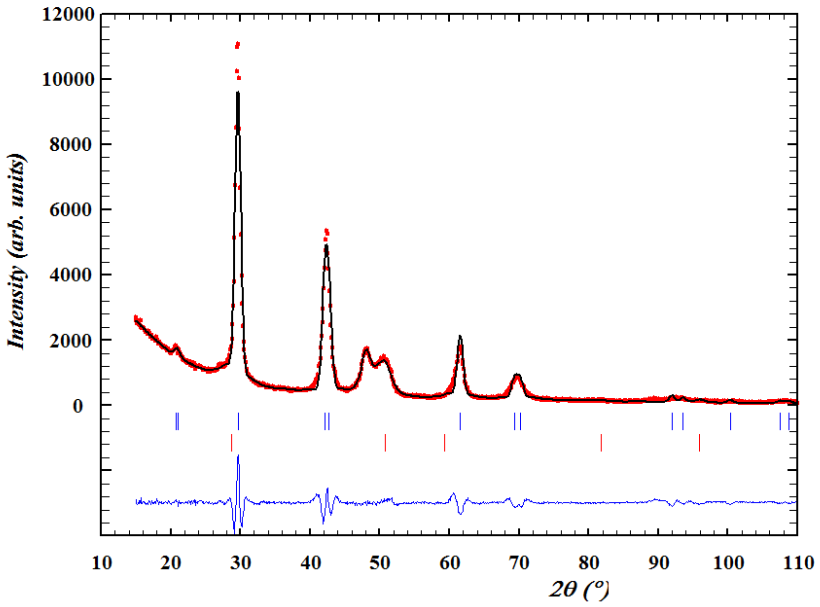

Figure D.2. Le Bail fit of the in-plane diffraction pattern for m = 2. Blue tick marks indicate the position of SnSe reflections and red tick marks indicate the position of $TiSe_2$ reflections. The reflection at approximately 47° is the (110) reflection of $SnSe_2$

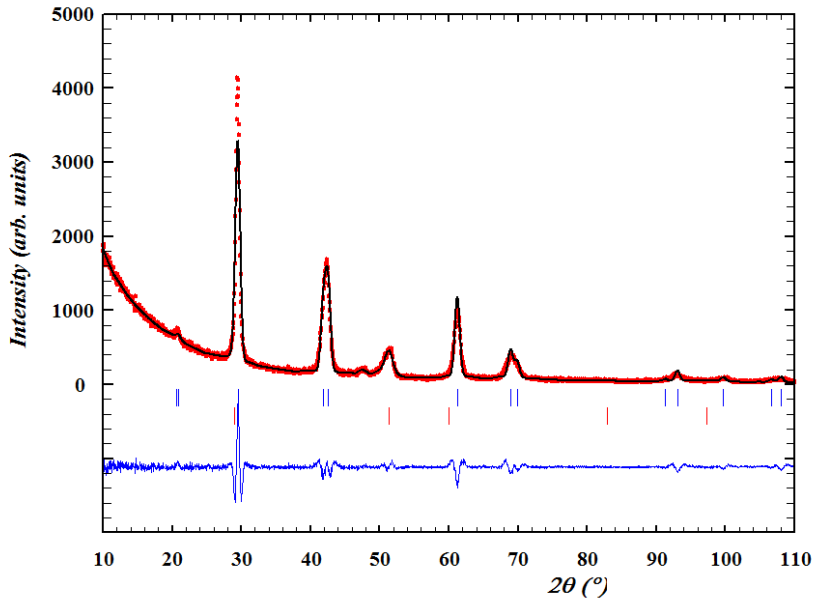

Figure D.3. Le Bail fit of the in-plane diffraction pattern for m = 3. Blue tick marks indicate the position of SnSe reflections and red tick marks indicate the position of $TiSe_2$ reflections. The reflection at approximately 47° is the (110) reflection of $SnSe_2$.

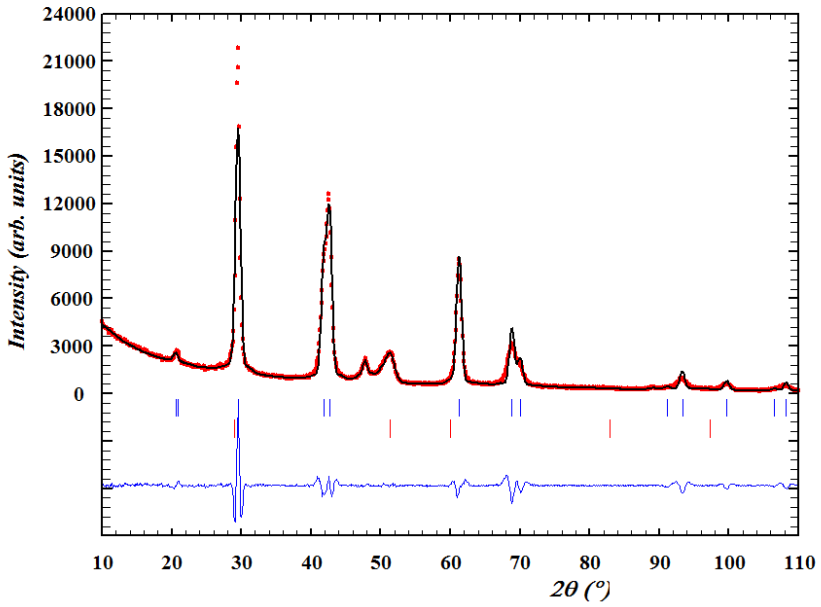

Figure D.4. Le Bail fit of the in-plane diffraction pattern for m = 4. Blue tick marks indicate the position of SnSe reflections and red tick marks indicate the position of $TiSe_2$ reflections. The reflection at approximately 47° is the (110) reflection of $SnSe_2$.

HAADF-STEM Image

Cross sectional HAADF-STEM image of $(SnSe)_{1.2}TiSe_2$ displaying both the top and bottom interface of the film. $SnSe_2$ is visible on the top of the film as a result of excess Sn and Se migrating to the surface.

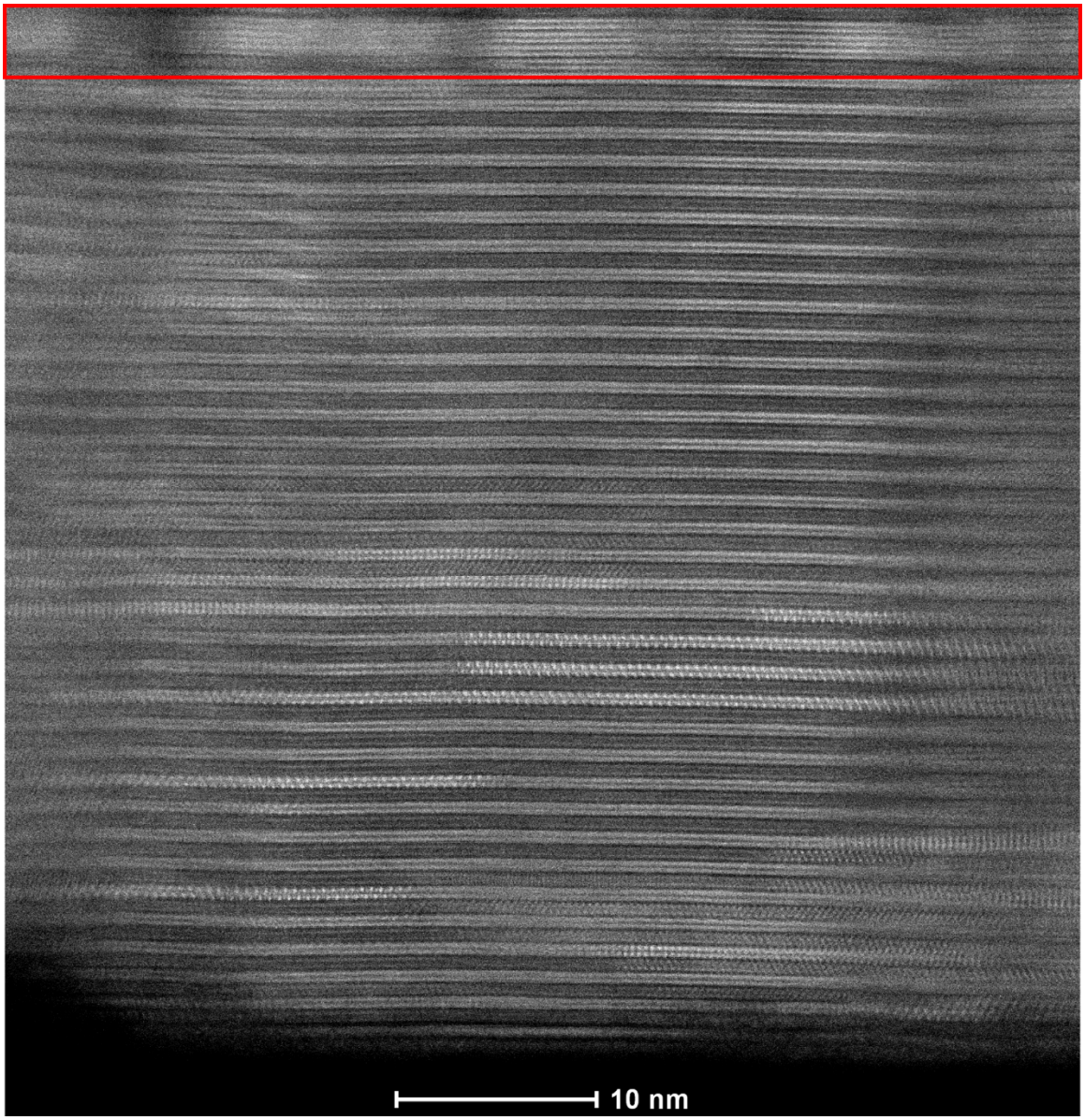

Figure D.5. HAADF-STEM of $(SnSe)_{1.2}TiSe_2$ showing $SnSe_2$ on the surface, outlined in red.

Density Functional Theory on Defects in SnSe

To explain the different structural distortions that are seen in the HAADF-STEM images (Figure 5 of the main text), structural relaxation calculations were performed on distorted TlI structures shown in Figure D6. The type I distortion is a shift of the top bilayer by the vector $\left(\frac{a}{2}, 0, 0\right)$, and type II describes a shift of the top bilayer along $\left(\frac{a}{2}, \frac{b}{2}, 0\right)$. As Table D1 shows, the in-plane lattice parameters of the distorted types deviate by less than 0.005 Å from the undistorted type, so it would be impossible to resolve these differences using the x-ray diffraction employed in this study.

The energy differences between the distorted and undistorted TlI structures are very small with less than 4 meV per formula unit, so there is little energy loss from adopting the distorted structure instead of the undistorted structure. The energy of type II is practically the same as the energy of the undistorted TlI structure. Comparing those two structures, one can see that along each axis, one-unit cell of the undistorted TlI structure (top two bilayers along *a* and bottom two bilayers along *b*) is visible along with an extra layer that is shifted by half a unit cell. This results in an equal number of Sn-Sn, Sn-Se, and Se-Se stackings in each structure, which explains why the energies are equal. The overall similar energies indicate that the structure observed in the HAADF-STEM images is a result of nucleation and growth kinetics rather than thermodynamic stability.

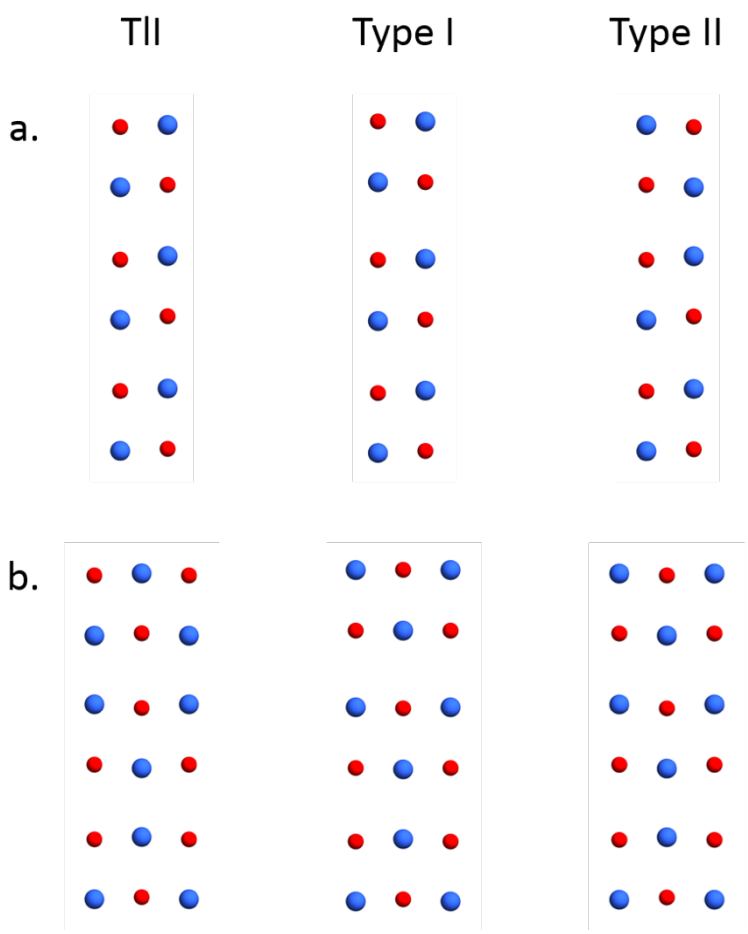

Figure D.6. Relaxed structures of an (010) slab of SnSe with three bilayers in the TlI structure and its distorted relatives (see text) as viewed along (a) the [100] axis and (b) the [010] axis. Sn atoms are blue and Se atoms are red.

Table D.1. In-plane lattice parameters a and b of the structures shown in Figure D6, and the energy differences per formula unit between these structures and the undistorted slab in the TlI structure ΔE_{TlI}. The energy difference per formula unit to a (001) slab of three bilayers in the GeS structure ΔE_{GeS} is added for comparison.

Structure	a (Å)	b (Å)	ΔE_{TlI}/f.u. (meV)	ΔE_{GeS}/f.u. (meV)
TlI	4.301	4.309	0	15
Type I	4.301	4.313	3.7	19
Type II	4.304	4.305	0.2	15

Appendix E

SUPPORTING INFORMATION FOR CHAPTER VIII

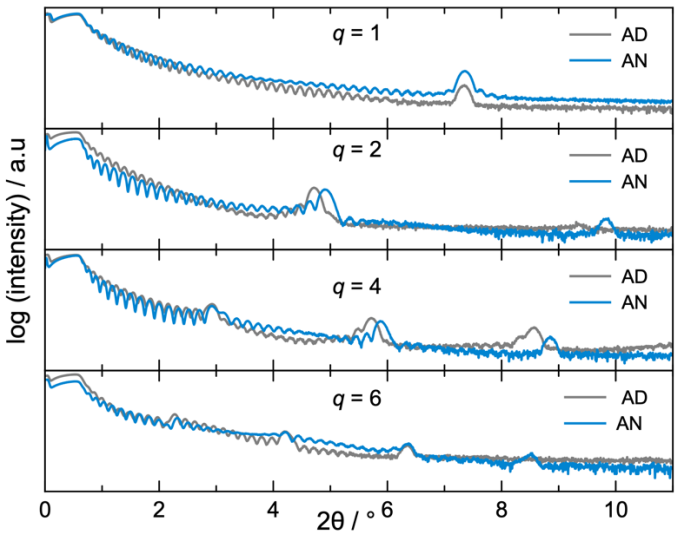

Figure E.1. X-ray reflectivity patterns of representative, as-deposited (AD) heterostructure precursors and their annealed (AN) counterparts. This data demonstrates the changes in the entire film that occur when the samples undergo heating at 350 °C for 30 minutes in an inert atmosphere.

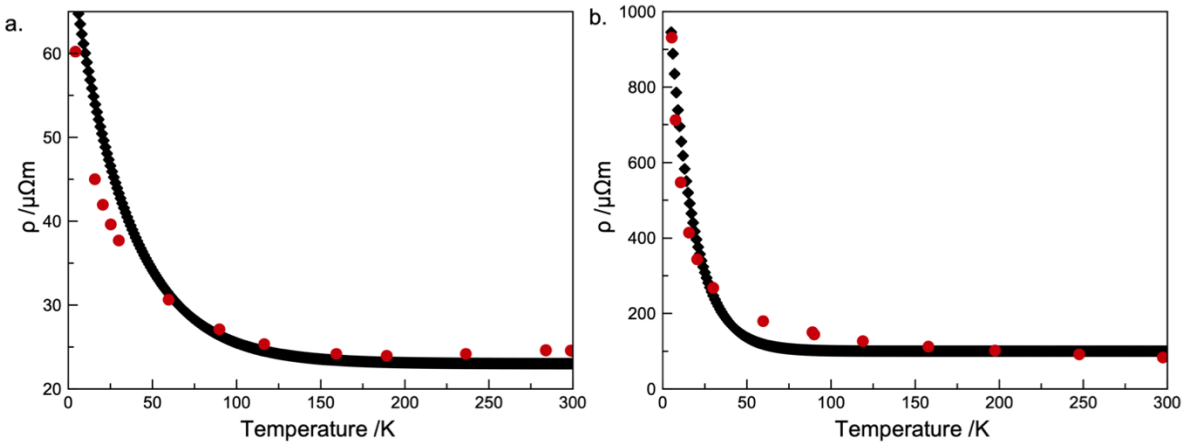

Figure E.2. Temperature dependent resistivity curves of the $[(SnSe)_{1+\delta}][TiSe_2]_3$ layered heterostructures (a) and the $[(SnSe)_{1+\delta}][TiSe_2]_{11}$ layered heterostructure (b.) plotted with the exponential equations $y = 50\ e^{(-0.03)} + 23$ and $y = 1200\ e^{(-0.07)} + 100$, respectively. This data emphasizes the deviation at low temperatures from exponential behavior and the constant offset that is required.

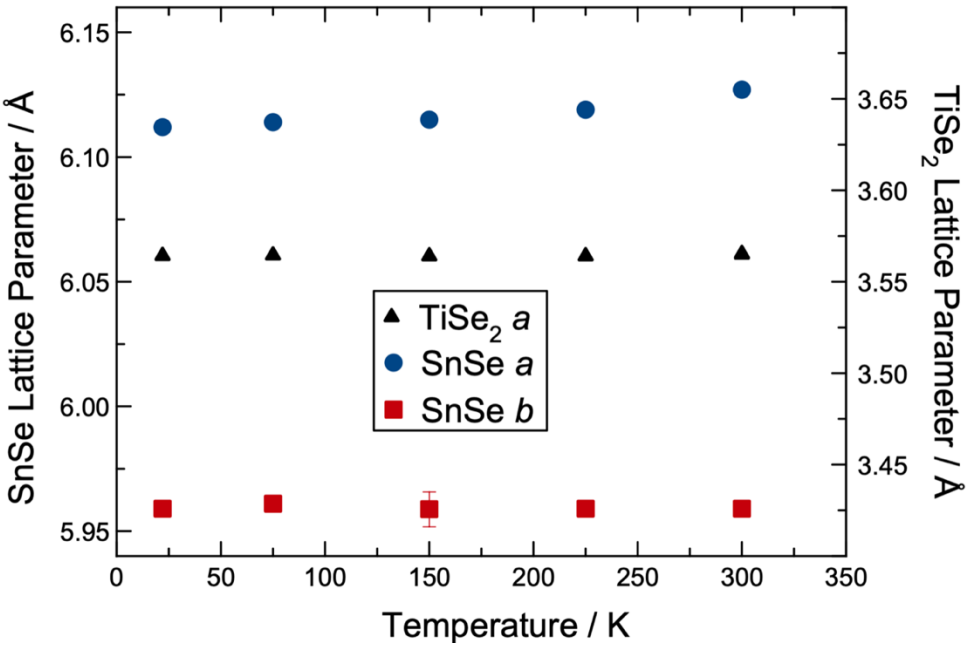

Figure E.3. In-plane lattice parameters determined from in-plane grazing incidence diffraction collected at various temperatures for a $[(SnSe)_{1+\delta}][TiSe_2]_8$ heterostructure. There is no significant change in the basal plane structure of either constituent upon cooling. This indicates that the unique transport behavior is not the result of a structure change. This data was collected at the advanced photon source using beamline 33 BM.

Table E.1. Calculated electronic band gaps of the explored alternative crystal polymorphs are presented. These electronic band gaps were obtained using the procedure outlined in the Materials and Methods section. The computational models were prepared from the computationally ready structures from Materials Project.

Space Group	**Band Gap (eV)**
$Fm\bar{3}m$	1.5484
Cmcm	1.4276

Appendix F

SUPPORTING INFORMATION FOR CHAPTER IX

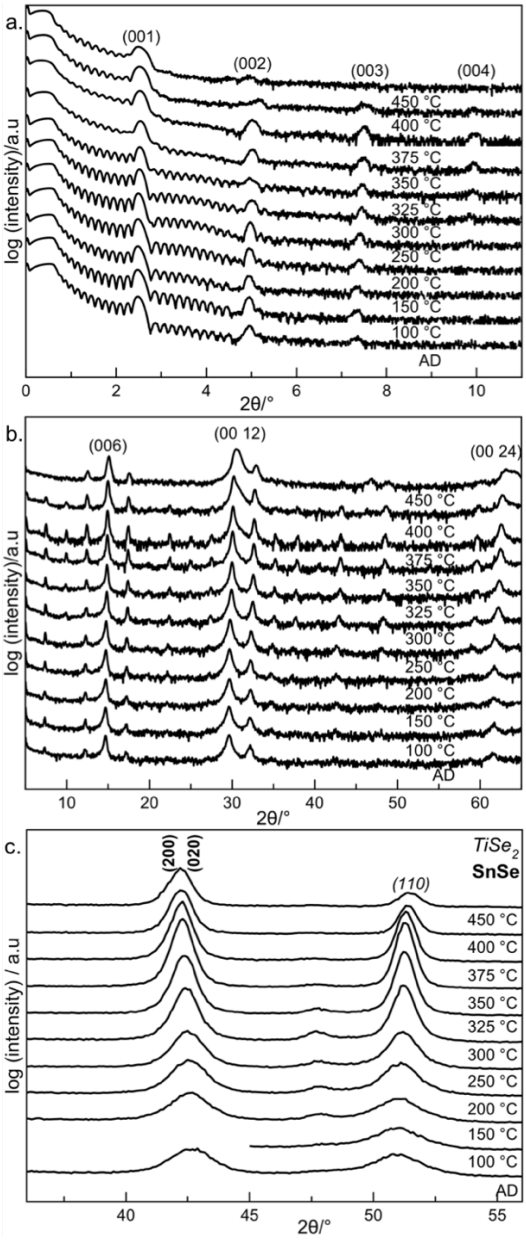

Figure F.1. Annealing study for *m, n* = 3 sample to study the formation and subsequent decomposition of the superlattice structure as seen with XRR (a.) specular XRD (b.) and in-plane XRD (c.) From this data, 350 °C was determined to be the optimal annealing temperature for the system and was subsequently used to crystallize the remaining samples.

Prior to synthesizing the whole series of layered compounds, an annealing study was conducted on the *m, n = 3* sample to determine the optimal annealing conditions for the system. A single piece of the sample was annealed subsequently at each temperature for 30 minutes before being analyzed by the various X-ray techniques. Figure F.1 provides XRR, specular *(00l)* XRD, and in-plane *(hk0)* XRD patterns of the $[(SnSe)_{1+\delta}]_3[TiSe_2]_3$ sample as a function of annealing temperature to demonstrate the evolution of the film. Using Bragg reflection intensities and widths as an indicator of film quality, the study determined the optimum annealing conditions to be 350˚C for 30 minutes in an N_2 atmosphere. Below this temperature, there is not enough thermal energy provided for the atomic constituents to diffuse across the designed layering to reach the targeted meta-stable product. With increasing temperature up to 350 ˚C the reflections become narrower, more intense, and the films become less rough. At 350 ˚C the reflections in all diffraction scans have the narrowest full width at half max and the greatest intensity. Above this temperature, the reflections decrease in intensity, become broader, and some even disappear. There is also an increase in roughness observed by loss of Kiessig fringes as well as the disappearance of some low angle diffraction reflections. The degradation of the film that occurs beyond 350 ˚C is a result of sufficient thermal energy to the elemental precursor providing access to a more stable kinetic or thermodynamic product via longer range diffusion and reorganization of the material. The optimal annealing condition of 350 ˚C was used to crystalize the rest of the $[(SnSe)_{1+\delta}]_m[TiSe_2]_n$ heterostructures from their designed precursors.

Table F.1 Temperature Dependence in Lattice Parameters for the $[(SnSe)_{1+\delta}]_m[TiSe_2]_n$, m, n = 4 heterostructure.

Temperature (K)	a SnSe (Å)	b SnSe (Å)	a $TiSe_2$ (Å)
300	4.3090(2)	4.2399(1)	3.56375(6)
22	4.3212(2)	4.2262(1)	3.56194(7)
75	4.3189(2)	4.2298(1)	3.56218(6)
150	4.3153(2)	4.2330(1)	3.56238(6)
225	4.3120(2)	4.2367(1)	3.56301(6)
300	4.3089(2)	4.2403(1)	3.56414(6)

Appendix G

SUPPORTING INFORMATION FOR CHAPTER XI

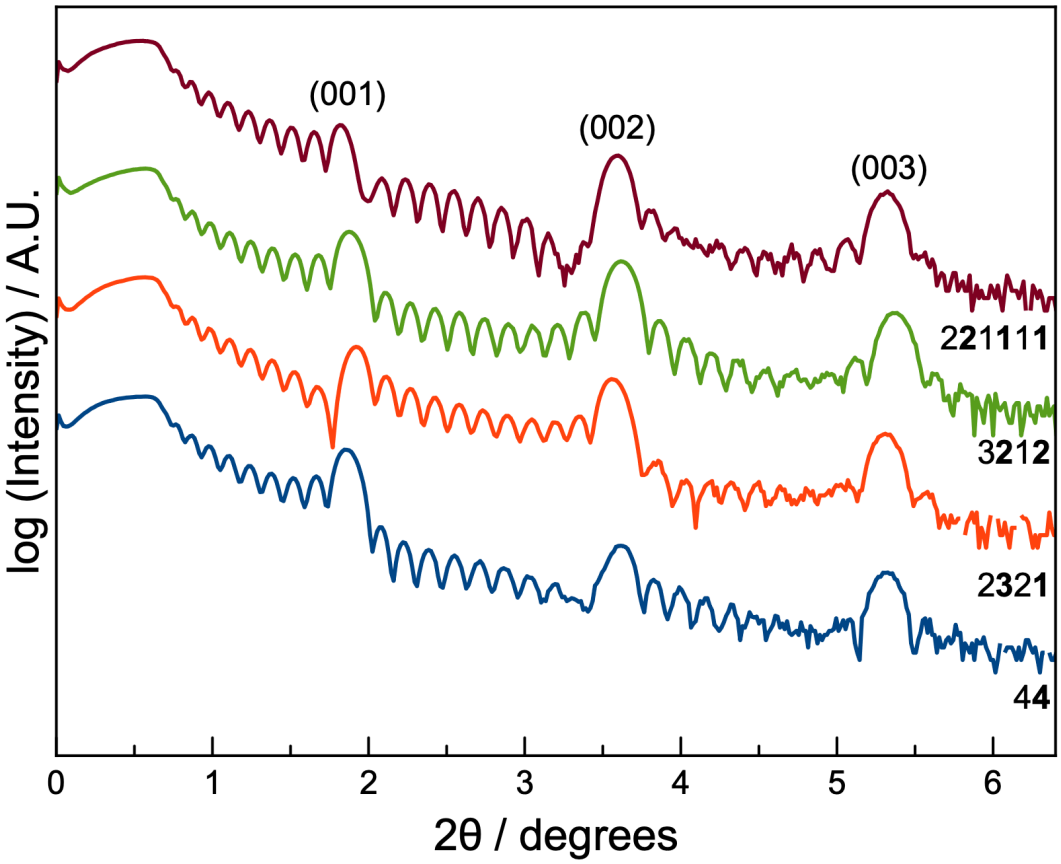

Figure G.1. Representative as-deposited XRR patterns demonstrating the initial layering and rearrangement occurring in the sample before annealing occurs.

Table G1. Total Film thickness and repeat layer thickness for representative $[(PbSe)_{1+\delta}]_4[TiSe_2]_4$ isomer heterostructures. AD total thickness obtained from BedeREFS by assuming an 11-layer isomer block with no impurities and varying the *c*-lattice parameter of the isomer block until the simulated Kiessig fringes between θ_c and the 001 reflection maxima matched those of the experimental XRR pattern. The simulated electron density was scaled by a factor of 0.9 – 0.95 to get a precise match for the experimental θ_c. The as-deposited repeat unit thickness was calculated using a modified version of Bragg's Law, which corrected for refraction, and the first two Bragg reflections observed in the low angle diffraction patterns.

Isomer	As-Deposited Total Film Thickness (Å)	As-Deposited Repeat Thickness (Å)
2**2**1**1**1**1**	557	49.34
2**1**1**2**1**1**	545	49.05
3**3**1**1**	--	--
3**2**1**2**	546	49.34
2**3**2**1**	544	50.81
4**4**	553	49.19

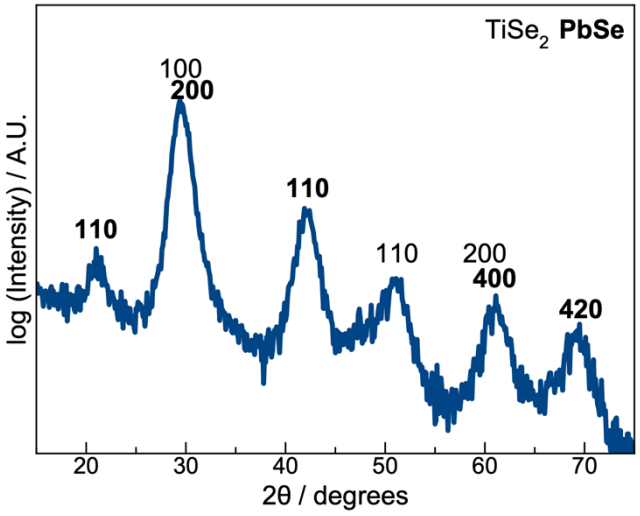

Figure G.2. Representative grazing incidence in-plane diffraction of an as-deposited $[(PbSe)_{1+\delta}]_1[TiSe_2]_1$ heterostructure demonstrating the initial nucleation of both PbSe and TiSe2 crystallites before annealing.

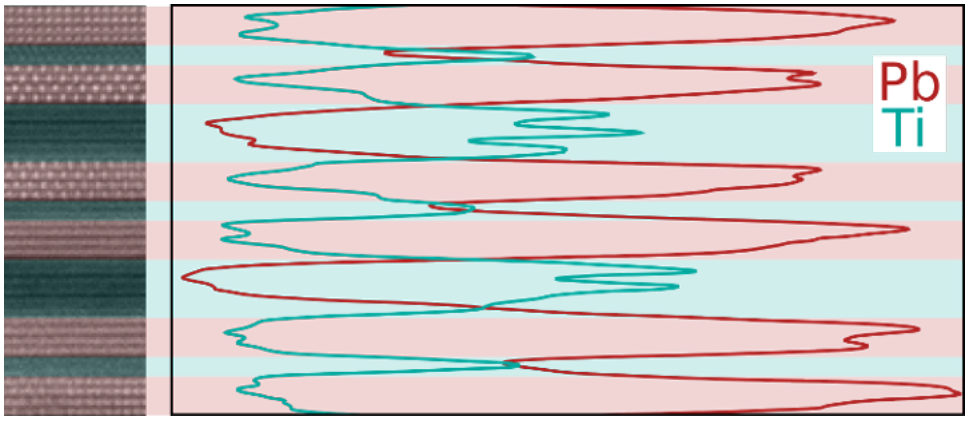

Figure G.3. STEM-EDS showing the relative intensity of characteristic X-ray signals from Pb and Ti when moving down the *k*=2**3**2**1** structure.

Appendix H

SUPPORTING INFORMATION FOR CHAPTER XIII

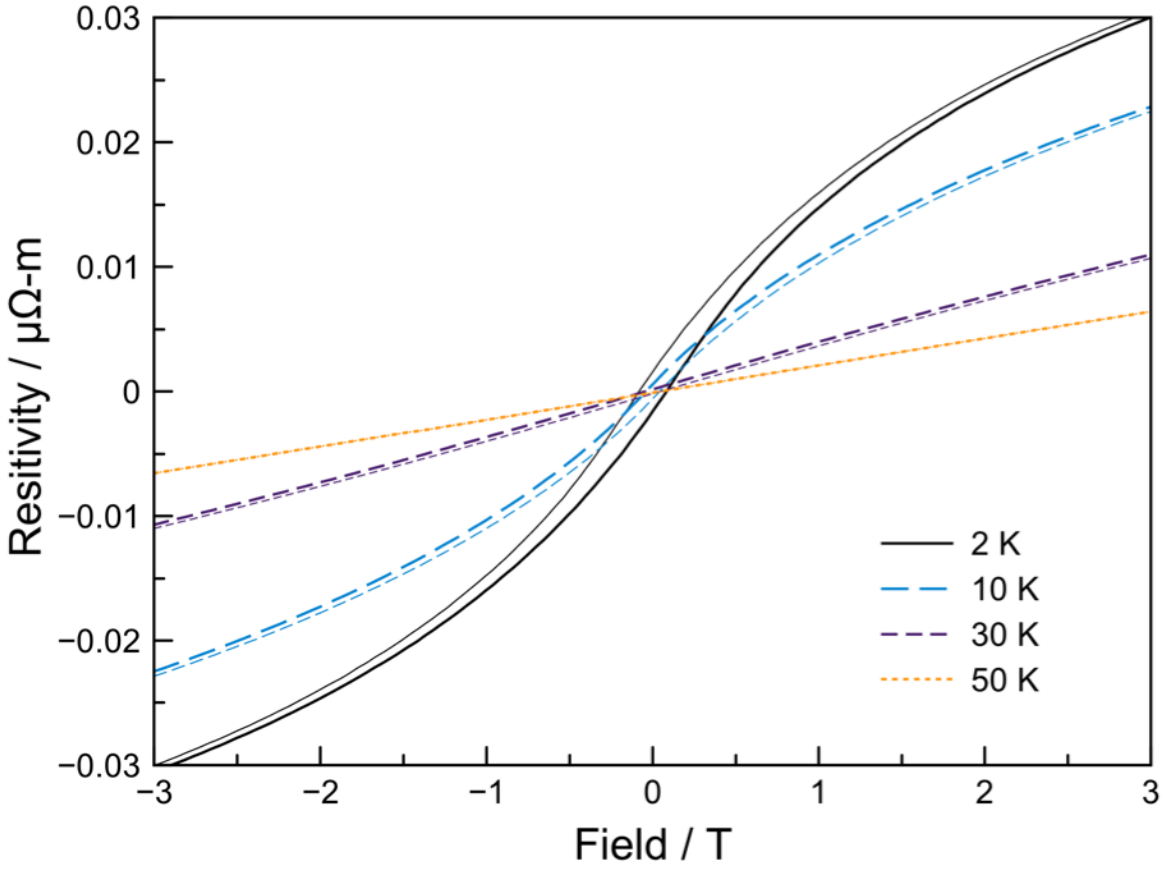

Figure H.1. Field dependent resistivity measured at various temperatures emphasizing the hysteresis. Hysteresis appears at 30 K and continues are lower temperatures which is in the region where the non-linearity occurs in the magnetoresistance measurements. This is also where the low temperature discontinuity in the temperature dependent resistivity occurs. The hysteresis supports that ferromagnetic ordering is occurring in the samples as a result of the Mn constituent and is not the result of multi-band physics.

REFERENCES CITED

Chapter I

(1) Frindt, R. F. Single Crystals of MoS_2 Several Molecular Layers Thick. *J. Appl. Phys.* **1966**, *37*, 1928–1929.

(2) Consadori, F.; Frindt, R. F. Crystal Size Effects on the Exciton Absorption Spectrum of WSe_2. *Phys. Rev. B* **1970**, *2*, 4893–4896.

(3) Gavaler, J. R.; Janocko, M. A.; Hulm, J. K.; Jones, C. K. Superconducting Properties as a Function of Thickness in NbN Films. *Physica* **1971**, *55*, 585–591.

(4) Frindt, R. F. Superconductivity in Ultrathin $NbSe_2$ Layers. *Phys. Rev. Lett.* **1972**, *28*, 299–301.

(5) Cho, A. Y.; Arthur, J. R. Molecular Beam Epitaxy. *Prog. Solid State Chem.* **1975**, *10*, 157–191.

(6) Veuhoff, E. *Handbook of Compound Semiconductors: Growth, Processing, Characterization and Devices*; Holloway, P. H., McGuire, G. E., Eds.; Noyes Publications: Park Ridge, NJ, 1995.

(7) von Klitzing, K. The Quantized Hall Effect. *Rev. Mod. Phys.* **1986**, *58*, 519–531.

(8) Thornton, T. J.; Pepper, M.; Ahmed, H.; Andrews, D.; Davies, G. J. One-Dimensional Conduction in the 2D Electron Gas of a GaAs-AlGaAs Heterojunction. *Phys. Rev. Lett.* **1986**, *56*, 1198–1201.

(9) Dingle, R.; Störmer, H. L.; Gossard, A. C.; Wiegmann, W. Electron Mobilities in Modulation-doped Semiconductor Heterojunction Superlattices. *Appl. Phys. Lett.* **1978**, *33*, 665–667.

(10) Wierer, J. J.; David, A.; Megens, M. M. III-Nitride Photonic-Crystal Light-Emitting Diodes with High Extraction Efficiency. *Nat. Photonics* **2009**, *3*, 163–169.

(11) Faist, J.; Capasso, F.; Sirtori, C. Quantum Cascade Laser. *Science.* **1994**, *264*, 1–4.

(12) Koma, A.; Sunouchi, K.; Miyajima, T. Fabrication and Characterization of Heterostructures with Subnanometer Thickness. *Microelectron. Eng.* **1984**, *2*, 129–136.

(13) Koma, A. Van Der Waals Epitaxy—a New Epitaxial Growth Method for a Highly Lattice-Mismatched System. *Thin Solid Films* **1992**, *216*, 72–76.

(14) Koma, A.; Yoshimura, K. Ultrasharp Interfaces Grown with Van Der Waals Epitaxy. *Surf. Sci.* **1986**, *174*, 556–560.

(15) Wiegers, G. A. Misfit Layer Compounds: Structures and Physical Properties. *Prog. SolidSt. Chem* **1996**, *24*, 1–139.

(16) Wulff, J.; Meetsma, A.; Van Smaalen, S.; Haange, R. J.; De Boer, J. L.; Wiegers, G. A. Structure, Electrical Transport, and Magnetic Properties of the Misfit Layer Compound $(PbS)_{1.13}TaS_2$. *J. Solid State Chem.* **1990**, *84*, 118–129.

(17) Novoselov, K. S.; Geim, A. K.; Morozov, S. V; Jiang, D.; Zhang, Y.; Dubonos, S. V; Grigorieva, I. V; Firsov, A. A.; Novoselov, K. S. Electric Field Effect in Atomically Thin Carbon Films. *Science.* **2007**, *306*, 183–191.

(18) Novoselov, K. S. Nobel Lecture: Graphene: Materials in the Flatland. *Rev. Mod. Phys.* **2011**, *83*, 837–849.

(19) Geim, A. K. Nobel Lecture: Random Walk to Graphene. *Rev. Mod. Phys.* **2011**, *83*, 851–862.

(20) Novoselov, K. S.; Jiang, D.; Schedin, F.; Booth, T. J.; Khotkevich, V. V; Morozov, S. V; Geim, A. K. Two-Dimensional Atomic Crystals. *Proc. Natl. Acad. Sci. U. S. A.* **2005**, *102*, 10451–10453.

(21) Abergel, D. S. L.; Russell, A.; Fal'ko, V. I. Visibility of Graphene Flakes on a Dielectric Substrate. *Appl. Phys. Lett.* **2007**, *91*, 063125.

(22) Blake, P.; Hill, E. W.; Castro Neto, A. H.; Novoselov, K. S.; Jiang, D.; Yang, R.; Booth, T. J.; Geim, A. K. Making Graphene Visible. *Appl. Phys. Lett.* **2007**, *91*, 063124.

(23) Geim, A. K.; Grigorieva, I. V. Van Der Waals Heterostructures. *Nature* **2013**, *499*, 419–425.

(24) Lee, G.-H.; Yu, Y.-J.; Lee, C.; Dean, C.; Shepard, K. L.; Kim, P.; Hone, J. Electron Tunneling through Atomically Flat and Ultrathin Hexagonal Boron Nitride. *Appl. Phys. Lett.* **2011**, *99*, 243114.

(25) Britnell, L.; Gorbachev, R. V.; Jalil, R.; Belle, B. D.; Schedin, F.; Katsnelson, M. I.; Eaves, L.; Morozov, S. V.; Mayorov, A. S.; Peres, N. M. R.; et al. Electron Tunneling through Ultrathin Boron Nitride Crystalline Barriers. *Nano Lett.* **2012**, *12*, 1707–1710.

(26) Splendiani, A.; Sun, L.; Zhang, Y.; Li, T.; Kim, J.; Chim, C.-Y.; Galli, G.; Wang, F. Emerging Photoluminescence in Monolayer MoS_2. *Nano Lett.* **2010**, *10*, 1271–1275.

(27) Mak, K. F.; Lee, C.; Hone, J.; Shan, J.; Heinz, T. F. Atomically Thin MoS_2: A New Direct-Gap Semiconductor. *Phys. Rev. Lett.* **2010**, *105*.

(28) Zeng, H.; Dai, J.; Yao, W.; Xiao, D.; Cui, X. Valley Polarization in MoS2 Monolayers by Optical Pumping. *Nat. Nanotechnol.* **2012**, *7*, 490–493.

(29) Mak, K. F.; He, K.; Shan, J.; Heinz, T. F. Control of Valley Polarization in Monolayer MoS_2 by Optical Helicity. *Nat. Nanotechnol.* **2012**, *7*, 494–498.

(30) Fang, H.; Chuang, S.; Chang, T. C.; Takei, K.; Takahashi, T.; Javey, A. High-Performance Single Layered WSe_2 p-FETs with Chemically Doped Contacts. *Nano Lett.* **2012**, *12*, 3788–3792.

(31) Zhao, W.; Ghorannevis, Z.; Chu, L.; Toh, M.; Kloc, C.; Tan, P. H.; Eda, G. Evolution of Electronic Structure in Atomically Thin Sheets of WS_2 and WSe_2. *ACS Nano* **2013**, *7*, 791–797.

(32) Tonndorf, P.; Schmidt, R.; Böttger, P.; Zhang, X.; Börner, J.; Liebig, A.; Albrecht, M.; Kloc, C.; Gordan, O.; Zahn, D. R. T.; et al. Photoluminescence Emission and Raman Response of Monolayer MoS_2, MoSe, and WSe_2. *Opt. Express* **2013**, *21*, 4908.

(33) Nair, R. R.; Ren, W.; Jalil, R.; Riaz, I.; Kravets, V. G.; Britnell, L.; Blake, P.; Schedin, F.; Mayorov, A. S.; Yuan, S.; et al. Fluorographene: A Two-Dimensional Counterpart of Teflon. *Small* **2010**, *6*, 2877–2884.

(34) Bianco, E.; Butler, S.; Jiang, S.; Restrepo, O. D.; Windl, W.; Goldberger, J. E. Stability and Exfoliation of Germanane: A Germanium Graphane Analogue. *ACS Nano* **2013**, *7*, 4414–4421.

(35) Dávila, M. E.; Le Lay, G. Few Layer Epitaxial Germanene: A Novel Two-Dimensional Dirac Material. *Sci. Rep.* **2016**, *6*, 20714.

(36) Acun, A.; Zhang, L.; Bampoulis, P.; Farmanbar, M.; van Houselt, A.; Rudenko, A. N.; Lingenfelder, M.; Brocks, G.; Poelsema, B.; Katsnelson, M. I.; et al. Germanene: The Germanium Analogue of Graphene. *J. Phys. Condens. Matter* **2015**, *27*, 443002.

(37) Zhao, J.; Liu, H.; Yu, Z.; Quhe, R.; Zhou, S.; Wang, Y.; Liu, C. C.; Zhong, H.; Han, N.; Lu, J.; et al. Rise of Silicene: A Competitive 2D Material. *Prog. Mater. Sci.* **2016**, *83*, 24–151.

(38) Liu, H.; Neal, A. T.; Zhu, Z.; Luo, Z.; Xu, X.; Tománek, D.; Ye, P. D. Phosphorene: An Unexplored 2D Semiconductor with a High Hole Mobility. *ACS Nano* **2014**, *8*, 4033–4041.

(39) Li, L.; Yu, Y.; Ye, G. J.; Ge, Q.; Ou, X.; Wu, H.; Feng, D.; Chen, X. H.; Zhang, Y. Black Phosphorus Field-Effect Transistors. *Nat. Nanotechnol.* **2014**, *9*, 372–377.

(40) Novoselov, K. S.; Mishchenko, A.; Carvalho, A.; Neto, A. H. C.; Road, O. 2D Materials and van Der Waals Heterostructures. *Science.* **2016**, *353*, aac9439.

(41) Liu, Y.; Weiss, N. O.; Duan, X.; Cheng, H.-C.; Huang, Y.; Duan, X. Van Der Waals Heterostructures and Devices. *Nat. Rev. Mater.* **2016**, *1*, 16042.

(42) Ulstrup, S.; Čabo, A. G.; Miwa, J. A.; Riley, J. M.; Grønborg, S. S.; Johannsen, J. C.; Cacho, C.; Alexander, O.; Chapman, R. T.; Springate, E.; et al. Ultrafast Band Structure Control of a Two-Dimensional Heterostructure. *ACS Nano* **2016**, *10*, 6315–6322.

(43) Ugeda, M. M.; Bradley, A. J.; Shi, S. F.; da Jornada, F. H.; Zhang, Y.; Qiu, D. Y.; Ruan, W.; Mo, S. K.; Hussain, Z.; Shen, Z. X.; et al. Giant Bandgap Renormalization and Excitonic Effects in a Monolayer Transition Metal Dichalcogenide Semiconductor. *Nat. Mater.* **2014**, *13*, 1091–1095.

(44) Ding, H.; Lv, Y.F.; Zhao, K.; Wang, W.-L.; Wang, L.; Song, C.-L.; Chen, X.; Ma, X.C.; Xue, Q.K. High-Temperature Superconductivity in Single-Unit-Cell FeSe Films on Anatase TiO_2 (001). *Phys. Rev. Lett.* **2016**, *117*, 067001.

(45) Zhang, L.; Bampoulis, P.; Rudenko, A. N.; Yao, Q.; van Houselt, A.; Poelsema, B.; Katsnelson, M. I.; Zandvliet, H. J. W. Structural and Electronic Properties of Germanene on MoS_2. *Phys. Rev. Lett.* **2016**, *116*, 256804.

(46) Amlaki, T.; Bokdam, M.; Kelly, P. J. Z_2 Invariance of Germanene on MoS_2 from First Principles. *Phys. Rev. Lett.* **2016**, *116*, 256805.

(47) Zhang, J.; Xie, W.; Zhao, J.; Zhang, S. Band Alignment of Two-Dimensional Lateral Heterostructures. *2D Mater.* **2016**, *4*, 015038.

(48) Kaplan, D.; Gong, Y.; Mills, K.; Swaminathan, V.; Ajayan, P. M.; Shirodkar, S.; Kaxiras, E. Excitation Intensity Dependence of Photoluminescence from Monolayers of MoS_2 and WS_2 /MoS_2 Heterostructures. *2D Mater.* **2016**, *3* , 015005.

(49) Sun, Q.; Dai, Y.; Ma, Y.; Yin, N.; Wei, W.; Yu, L.; Huang, B. Design of Lateral Heterostructure from Arsenene and Antimonene. *2D Mater.* **2016**, *3*, 035017.

(50) Steinhoff, A.; Rösner, M.; Jahnke, F.; Wehling, T. O.; Gies, C. Influence of Excited Carriers on the Optical and Electronic Properties of MoS_2. *Nano Lett.* **2014**, *14*, 3743–3748.

(51) Chernikov, A.; Ruppert, C.; Hill, H. M.; Rigosi, A. F.; Heinz, T. F. Population Inversion and Giant Bandgap Renormalization in Atomically Thin WS_2 Layers. *Nat. Photonics* **2015**, *9*, 466–470.

(52) Chernikov, A.; van der Zande, A. M.; Hill, H. M.; Rigosi, A. F.; Velauthapillai, A.; Hone, J.; Heinz, T. F. Electrical Tuning of Exciton Binding Energies in Monolayer WS_2. *Phys. Rev. Lett.* **2015**, *115*, 126802.

(53) Pogna, E. A. A.; Marsili, M.; De Fazio, D.; Dal Conte, S.; Manzoni, C.; Sangalli, D.; Yoon, D.; Lombardo, A.; Ferrari, A. C.; Marini, A.; et al. Photo-Induced Bandgap Renormalization Governs the Ultrafast Response of Single-Layer MoS_2. *ACS Nano* **2016**, *10*, 1182–1188.

(54) Grubišić Čabo, A.; Miwa, J. A.; Grønborg, S. S.; Riley, J. M.; Johannsen, J. C.; Cacho, C.; Alexander, O.; Chapman, R. T.; Springate, E.; Grioni, M.; et al. Observation of Ultrafast Free Carrier Dynamics in Single Layer MoS_2. *Nano Lett.* **2015**, *15*, 5883–5887.

(55) Bruix, A.; Miwa, J. A.; Hauptmann, N.; Wegner, D.; Ulstrup, S.; Grønborg, S. S.; Sanders, C. E.; Dendzik, M.; Grubišić Čabo, A.; Bianchi, M.; et al. Single-Layer MoS_2 on Au(111): Band Gap Renormalization and Substrate Interaction. *Phys. Rev. B* **2016**, *93*, 165422.

(56) Zhou, X.; Shi, J.; Qi, Y.; Liu, M.; Ma, D.; Zhang, Y.; Ji, Q.; Zhang, Z.; Li, C.; Liu, Z.; et al. Periodic Modulation of the Doping Level in Striped MoS_2 Superstructures. *ACS Nano* **2016**, *10*, 3461–3468.

(57) Zhang, C.; KC, S.; Nie, Y.; Liang, C.; Vandenberghe, W. G.; Longo, R. C.; Zheng, Y.; Kong, F.; Hong, S.; Wallace, R. M.; et al. Charge Mediated Reversible Metal–Insulator Transition in Monolayer $MoTe_2$ and $W_xMo_{1-x}Te_2$ Alloy. *ACS Nano* **2016**, *10*, 7370–7375.

(58) Millen, J.; Xuereb, A. The Rise of the Quantum Machines. *Phys. World* **2016**, *29* , 23–26.

(59) Castro Neto, A. H.; Guinea, F.; Peres, N. M. R.; Novoselov, K. S.; Geim, A. K. The Electronic Properties of Graphene. *Rev. Mod. Phys.* **2009**, *81*, 109–162.

(60) Komsa, H. P.; Krasheninnikov, A. V. Electronic Structures and Optical Properties of Realistic Transition Metal Dichalcogenide Heterostructures from First Principles. *Phys. Rev. B* **2013**, *88*, 085318.

(61) Partoens, B.; Peeters, F. M. From Graphene to Graphite: Electronic Structure around the K Point. *Phys. Rev. B* **2006**, *74*, 075404.

(62) Zhang, L.; Zunger, A. Evolution of Electronic Structure as a Function of Layer Thickness in Group-VIB Transition Metal Dichalcogenides: Emergence of Localization Prototypes. *Nano Lett.* **2015**, *15*, 949–957.

(63) Smeller, M. M.; Heideman, C. L.; Lin, Q.; Beekman, M.; Anderson, M. D.; Zschack, P.; Anderson, I. M.; Johnson, D. C. Structure of Turbostratically Disordered Misfit Layer Compounds $[(PbSe)_{0.99}]_1[WSe_2]_1$, $[(PbSe)_{1.00}]_1[MoSe_2]_1$, and $[(SnSe)_{1.03}]_1$. *Zeitschrift für Anorg. und Allg. Chemie* **2012**, *638*, 2632–2639.

(64) Ruban, A. V.; Skriver, H. L.; Nørskov, J. K. Surface Segregation Energies in Transition-Metal Alloys. *Phys. Rev. B* **1999**, *59*, 15990–16000.

(65) Mrårtensson, N.; Saalfeld, H. B.; Kuhlenbeck, H.; Neumann, M. Structural Dependence of the 5 *d* -Metal Surface Energies as Deduced from Surface Core-Level Shift Measurements. *Phys. Rev. B* **1989**, *39*, 8181–8186.

(66) Merrill, D. R.; Sutherland, D. R.; Ditto, J.; Bauers, S. R.; Falmbigl, M.; Medlin, D. L.; Johnson, D. C. Kinetically Controlled Site-Specific Substitutions in Higher-Order Heterostructures. *Chem. Mater.* **2015**, *27*, 4066–4072.

(67) Cahay, M.; Electrochemical Society (United States). Dielectric Science and Technology Division. *Quantum Confinement VI: Nanostructured Materials and Devices : Proceedings of the International Symposium*; Electrochemical Society, 2001.

(68) Hicks, L. D.; Dresselhaus, M. S. Effect of Quantum-Well Structures on the Thermoelectric Figure of Merit. *Phys. Rev. B* **1993**, *47*, 12727–12731.

(69) Martin Eisberg, R.; Resnick, R. *Quantum Physics of Atoms, Molecules, Solids, Nuclei, and Particles, 2nd Ed.*; John Wiley and Sons, Inc, 1974.

(70) Zhang, Y.; Chang, T.-R.; Zhou, B.; Cui, Y.-T.; Yan, H.; Liu, Z.; Schmitt, F.; Lee, J.; Moore, R.; Chen, Y.; et al. Direct Observation of the Transition from Indirect to Direct Bandgap in Atomically Thin Epitaxial $MoSe_2$. *Nat. Nanotechnol.* **2013**, *9*, 111–115.

(71) Jin, W.; Yeh, P.-C.; Zaki, N.; Zhang, D.; Sadowski, J. T.; Al-Mahboob, A.; van der Zande, A. M.; Chenet, D. A.; Dadap, J. I.; Herman, I. P.; et al. Direct Measurement of the Thickness-Dependent Electronic Band Structure of MoS_2 Using Angle-Resolved Photoemission Spectroscopy. *Phys. Rev. Lett.* **2013**, *111*, 106801.

(72) Xiao, D.; Liu, G.-B.; Feng, W.; Xu, X.; Yao, W. Coupled Spin and Valley Physics in Monolayers of MoS_2 and Other Group-VI Dichalcogenides. *Phys. Rev. Lett.* **2012**, *108*, 196802.

(73) Cao, T.; Wang, G.; Han, W.; Ye, H.; Zhu, C.; Shi, J.; Niu, Q.; Tan, P.; Wang, E.; Liu, B.; et al. Valley-Selective Circular Dichroism of Monolayer Molybdenum Disulphide. *Nat. Commun.* **2012**, *3*, 887.

(74) Wang, Q. H.; Kalantar-Zadeh, K.; Kis, A.; Coleman, J. N.; Strano, M. S. Electronics and Optoelectronics of Two-Dimensional Transition Metal Dichalcogenides. *Nat. Nanotechnol.* **2012**, *7*, 699–712.

(75) Xu, X.; Yao, W.; Xiao, D.; Heinz, T. F. Spin and Pseudospins in Layered Transition Metal Dichalcogenides. *Nat. Phys.* **2014**, *10*, 343–350.

(76) Yu, H.; Liu, G.-B.; Gong, P.; Xu, X.; Yao, W. Dirac Cones and Dirac Saddle Points of Bright Excitons in Monolayer Transition Metal Dichalcogenides. *Nat. Commun.* **2014**, *5*, 3876.

(77) Li, Y.; Ludwig, J.; Low, T.; Chernikov, A.; Cui, X.; Arefe, G.; Kim, Y. D.; van der Zande, A. M.; Rigosi, A.; Hill, H. M.; et al. Valley Splitting and Polarization by the Zeeman Effect in Monolayer $MoSe_2$. *Phys. Rev. Lett.* **2014**, *113*, 266804.

(78) MacNeill, D.; Heikes, C.; Mak, K. F.; Anderson, Z.; Kormányos, A.; Zólyomi, V.; Park, J.; Ralph, D. C. Breaking of Valley Degeneracy by Magnetic Field in Monolayer $MoSe_2$. *Phys. Rev. Lett.* **2015**, *114*, 037401.

(79) Srivastava, A.; Sidler, M.; Allain, A. V.; Lembke, D. S.; Kis, A.; Imamoğlu, A. Valley Zeeman Effect in Elementary Optical Excitations of Monolayer WSe_2. *Nat. Phys.* **2015**, *11*, 141–147.

(80) Aivazian, G.; Gong, Z.; Jones, A. M.; Chu, R.L.; Yan, J.; Mandrus, D. G.; Zhang, C.; Cobden, D.; Yao, W.; Xu, X. Magnetic Control of Valley Pseudospin in Monolayer WSe_2. *Nat. Phys.* **2015**, *11*, 148–152.

(81) Xia, F.; Wang, H.; Xiao, D.; Dubey, M.; Ramasubramaniam, A. Two-Dimensional Material Nanophotonics. *Nat. Photonics* **2014**, *8*, 899–907.

(82) Liu, X.; Galfsky, T.; Sun, Z.; Xia, F.; Lin, E.; Lee, Y.H.; Kéna-Cohen, S.; Menon, V. M. Strong Light–Matter Coupling in Two-Dimensional Atomic Crystals. *Nat. Photonics* **2014**, *9*, 30–34.

(83) Wang, K.; Huang, B.; Tian, M.; Ceballos, F.; Lin, M.-W.; Mahjouri-Samani, M.; Boulesbaa, A.; Puretzky, A. A.; Rouleau, C. M.; Yoon, M.; et al. Interlayer Coupling in Twisted WSe_2 /WS_2 Bilayer Heterostructures Revealed by Optical Spectroscopy. *ACS Nano* **2016**, *10*, 6612–6622.

(84) Lopes dos Santos, J. M. B.; Peres, N. M. R.; Castro Neto, A. H. Graphene Bilayer with a Twist: Electronic Structure. *Phys. Rev. Lett.* **2007**, *99*, 256802.

(85) Trambly de Laissardière, G.; Mayou, D.; Magaud, L. Localization of Dirac Electrons in Rotated Graphene Bilayers. *Nano Lett.* **2010**, *10*, 804–808.

(86) Park, C.-H.; Yang, L.; Son, Y.-W.; Cohen, M. L.; Louie, S. G. Anisotropic Behaviours of Massless Dirac Fermions in Graphene under Periodic Potentials. *Nat. Phys.* **2008**, *4*, 213–217.

(87) Barbier, M.; Vasilopoulos, P.; Peeters, F. M.; Pereira, J. M. Bilayer Graphene with Single and Multiple Electrostatic Barriers: Band Structure and Transmission. *Phys. Rev. B* **2009**, *79*, 155402.

(88) Hass, J.; Varchon, F.; Millán-Otoya, J. E.; Sprinkle, M.; Sharma, N.; de Heer, W. A.; Berger, C.; First, P. N.; Magaud, L.; Conrad, E. H. Why Multilayer Graphene on 4*H*−SiC (000-1) Behaves Like a Single Sheet of Graphene. *Phys. Rev. Lett.* **2008**, *100*, 125504.

(89) Shallcross, S.; Sharma, S.; Pankratov, O. A. Quantum Interference at the Twist Boundary in Graphene. *Phys. Rev. Lett.* **2008**, *101*, 056803.

(90) Latil, S.; Meunier, V.; Henrard, L. Massless Fermions in Multilayer Graphitic Systems with Misoriented Layers: *Ab Initio* Calculations and Experimental Fingerprints. *Phys. Rev. B* **2007**, *76*, 201402.

(91) Varchon, F.; Mallet, P.; Veuillen, J.-Y.; Magaud, L. Ripples in Epitaxial Graphene on the Si-Terminated SiC(0001) Surface. *Phys. Rev. B* **2008**, *77*, 235412.

(92) Tu, Q.; Lange, B.; Parlak, Z.; Lopes, J. M. J.; Blum, V.; Zauscher, S. Quantitative Subsurface Atomic Structure Fingerprint for 2D Materials and Heterostructures by First-Principles-Calibrated Contact-Resonance Atomic Force Microscopy. *ACS Nano* **2016**, *10*, 6491–6500.

(93) Tan, Y.; Chen, F. W.; Ghosh, A. W. First Principles Study and Empirical Parametrization of Twisted Bilayer MoS_2 Based on Band-Unfolding. *Appl. Phys. Lett.* **2016**, *109*, 101601.

(94) Lee, C.-H.; Lee, G.-H.; van der Zande, A. M.; Chen, W.; Li, Y.; Han, M.; Cui, X.; Arefe, G.; Nuckolls, C.; Heinz, T. F.; et al. Atomically Thin p–n Junctions with van Der Waals Heterointerfaces. *Nat. Nanotechnol.* **2014**, *9*, 676–681.

(95) Gong, Y.; Lin, J.; Wang, X.; Shi, G.; Lei, S.; Lin, Z.; Zou, X.; Ye, G.; Vajtai, R.; Yakobson, B. I.; et al. Vertical and In-Plane Heterostructures from WS_2/MoS_2 Monolayers. *Nat. Mater.* **2014**, *13*, 1135–1142.

(96) Jiang, T.; Liu, H.; Huang, D.; Zhang, S.; Li, Y.; Gong, X.; Shen, Y.-R.; Liu, W.-T.; Wu, S. Valley and Band Structure Engineering of Folded MoS_2 Bilayers. *Nat. Nanotechnol.* **2014**, *9* (10), 825–829.

(97) Terrones, H.; Lopez-Urias, F.; Terrones, M. Novel Hetero-Layered Materials with Tunable Direct Band Gaps by Sandwiching Different Metal Disulfides and Diselenides. *Sci Rep* **2013**, *3*, 1549.

(98) He, J.; Hummer, K.; Franchini, C. Stacking Effects on the Electronic and Optical Properties of Bilayer Transition Metal Dichalcogenides MoS_2, $MoSe_2$, WS_2, and WSe_2. *Phys. Rev. B* **2014**, *89*, 075409.

(99) Heo, H.; Sung, J. H.; Cha, S.; Jang, B.G.; Kim, J.Y.; Jin, G.; Lee, D.; Ahn, J.-H.; Lee, M.-J.; Shim, J. H.; et al. Interlayer Orientation-Dependent Light Absorption and Emission in Monolayer Semiconductor Stacks. *Nat. Commun.* **2015**, *6*, 7372.

(100) Huang, S.; Ling, X.; Liang, L.; Kong, J.; Terrones, H.; Meunier, V.; Dresselhaus, M. S. Probing the Interlayer Coupling of Twisted Bilayer MoS_2 Using Photoluminescence Spectroscopy. *Nano Lett.* **2014**, *14*, 5500–5508.

(101) Kang, J.; Li, J.; Li, S.S.; Xia, J.B.; Wang, L.-W. Electronic Structural Moiré Pattern Effects on MoS_2 /$MoSe_2$ 2D Heterostructures. *Nano Lett.* **2013**, *13* (11), 5485–5490.

(102) Radisavljevic, B.; Radenovic, A.; Brivio, J.; Giacometti, V.; Kis, A. Single-Layer MoS_2 Transistors. *Nat. Nanotechnol.* **2011**, *6* (3), 147–150.

(103) Gong, C.; Zhang, H.; Wang, W.; Colombo, L.; Wallace, R. M.; Cho, K. Band Alignment of Two-Dimensional Transition Metal Dichalcogenides: Application in Tunnel Field Effect Transistors. *Appl. Phys. Lett.* **2013**, *103* (5), 053513.

(104) Huang, J.K.; Pu, J.; Hsu, C.L.; Chiu, M.-H.; Juang, Z.Y.; Chang, Y.H.; Chang, W.H.; Iwasa, Y.; Takenobu, T.; Li, L.J. Large-Area Synthesis of Highly Crystalline WSe_2 Monolayers and Device Applications. *ACS Nano* **2014**, *8* (1), 923–930.

(105) Kappera, R.; Voiry, D.; Yalcin, S. E.; Branch, B.; Gupta, G.; Mohite, A. D.; Chhowalla, M. Phase-Engineered Low-Resistance Contacts for Ultrathin MoS2 Transistors. *Nat. Mater.* **2014**, *13* (12), 1128–1134.

(106) Lee, Y. H.; Zhang, X. Q.; Zhang, W.; Chang, M. T.; Lin, C. Te; Chang, K. Di; Yu, Y. C.; Wang, J. T. W.; Chang, C. S.; Li, L. J.; et al. Synthesis of Large-Area MoS_2 Atomic Layers with Chemical Vapor Deposition. *Adv. Mater.* **2012**, *24*, 2320–2325.

(107) Lu, X.; Utama, M. I. B.; Lin, J.; Gong, X.; Zhang, J.; Zhao, Y.; Pantelides, S. T.; Wang, J.; Dong, Z.; Liu, Z.; et al. Large-Area Synthesis of Monolayer and Few-Layer $MoSe_2$ Films on SiO_2 Substrates. *Nano Lett.* **2014**, *14* (5), 2419–2425.

(108) Oura, K.; Lifshits, V. G.; Saranin, A. A.; Zotov, A. V.; Katayama, M. *Surface Science: An Introduction*; Springer-Verlag: Berlin, 2003.

(109) Lee, J.-U.; Kim, K.; Han, S.; Ryu, G. H.; Lee, Z.; Cheong, H. Raman Signatures of Polytypism in Molybdenum Disulfide. *ACS Nano* **2016**, *10* (2), 1948–1953.

(110) Zhang, X.; Qiao, X.-F.; Shi, W.; Wu, J.-B.; Jiang, D.-S.; Tan, P.-H. Phonon and Raman Scattering of Two-Dimensional Transition Metal Dichalcogenides from Monolayer, Multilayer to Bulk Material. *Chem. Soc. Rev.* **2015**, *44*, 2757–2785.

(111) Mitchson, G.; Ditto, J.; Woods, K. N.; Westover, R.; Page, C. J.; Johnson, D. C. Application of HAADF STEM Image Analysis to Structure Determination in Rotationally Disordered and Amorphous Multilayered Films. *Semicond. Sci. Technol.* **2016**, *31*, 084003.

(112) Anderson, M. D.; Heideman, C. L.; Lin, Q.; Smeller, M.; Kokenyesi, R.; Herzing, A. A.; Anderson, I. M.; Keszler, D. A.; Zschack, P.; Johnson, D. C. Size-Dependent Structural Distortions in One-Dimensional Nanostructures. *Angew. Chemie Int. Ed.* **2013**, *52*, 1982–1985.

(113) Atkins, R.; Wilson, J.; Zschack, P.; Grosse, C.; Neumann, W.; Johnson, D. C. Synthesis of $[(SnSe)_{1.15}]_m(TaSe_2)_n$ Ferecrystals: Structurally Tunable Metallic Compounds. *Chem. Mater.* **2012**, *24*, 4594–4599.

(114) Beekman, M.; Cogburn, G.; Heideman, C.; Rouvimov, S.; Zschack, P.; Neumann, W.; Johnson, D. C. New Layered Intergrowths in the Sn-Mo-Se System. *J. Electron. Mater.* **2012**, *41*, 1476–1480.

(115) Falmbigl, M.; Alemayehu, M. B.; Merrill, D. R.; Beekman, M.; Johnson, D. C. In-Plane Structure of Ferecrystalline Compounds. *Cryst. Res. Technol.* **2015**, *50*, 464–472.

(116) Beekman, M.; Disch, S.; Rouvimov, S.; Kasinathan, D.; Koepernik, K.; Rosner, H.; Zschack, P.; Neumann, W. S.; Johnson, D. C. Controlling Size-Induced Phase Transformations Using Chemically Designed Nanolaminates. *Angew. Chemie - Int. Ed.* **2013**, *52*, 13211–13214.

(117) Merrill, D. R.; Moore, D. B.; Coffey, M. N.; Jansons, A. W.; Falmbigl, M.; Johnson, D. C. Synthesis and Characterization of Turbostratically Disordered $(BiSe)_{1.15}TiSe_2$. *Semicond. Sci. Technol.* **2014**, *29*, 064004.

(118) Mitchson, G.; Falmbigl, M.; Ditto, J.; Johnson, D. C. Antiphase Boundaries in the Turbostratically Disordered Misfit Compound $(BiSe)_{1+\delta}NbSe_2$. *Inorg. Chem.* **2015**, *54* (21), 10309–10315.

(119) Sun, Y.; Thompson, S. E.; Nishida, T. Physics of Strain Effects in Semiconductors and Metal-Oxide-Semiconductor Field-Effect Transistors. *J. Appl. Phys.* **2007**, *101* (10), 104503.

(120) Smith, C. S. Piezoresistance Effect in Germanium and Silicon. *Phys. Rev.* **1954**, *94* (1), 42–49.

(121) CAPASSO, F. Band-Gap Engineering: From Physics and Materials to New Semiconductor Devices. *Science.* **1987**, *235* (4785).

(122) Smith, A. M.; Nie, S. Semiconductor Nanocrystals: Structure, Properties, and Band Gap Engineering. *Acc. Chem. Res.* **2010**, *43* (2), 190–200.

(123) Si, C.; Sun, Z.; Liu, F. Strain Engineering of Graphene: A Review. *Nanoscale* **2016**, *8* (6), 3207–3217.

(124) Ohuchi, F. S.; Parkinson, B. A.; Ueno, K.; Koma, A. Van Der Waals Epitaxial Growth and Characterization of $MoSe_2$ Thin Films on SnS_2. *J. Appl. Phys.* **1990**, *68* (5), 2168–2175.

(125) Shi, Y.; Zhou, W.; Lu, A.Y.; Fang, W.; Lee, Y.H.; Hsu, A. L.; Kim, S. M.; Kim, K. K.; Yang, H. Y.; Li, L.J.; et al. Van Der Waals Epitaxy of MoS_2 Layers Using Graphene As Growth Templates. *Nano Lett.* **2012**, *12* (6), 2784–2791.

(126) Roldán, R.; Castellanos-Gomez, A.; Cappelluti, E.; Guinea, F. Strain Engineering in Semiconducting Two-Dimensional Crystals. *J. Phys. Condens. Matter* **2015**, *27* (31), 313201.

(127) Huang, M.; Yan, H.; Chen, C.; Song, D.; Heinz, T. F.; Hone, J. Phonon Softening and Crystallographic Orientation of Strained Graphene Studied by Raman Spectroscopy. *Proc. Natl. Acad. Sci. U. S. A.* **2009**, *106* (18), 7304–7308.

(128) Conley, H. J.; Wang, B.; Ziegler, J. I.; Haglund, R. F.; Pantelides, S. T.; Bolotin, K. I. Bandgap Engineering of Strained Monolayer and Bilayer MoS_2. *Nano Lett.* **2013**, *13* (8), 3626–3630.

(129) Sun, Y.; Liu, K.; Hong, X.; Chen, M.; Kim, J.; Shi, S.; Wu, J.; Zettl, A.; Wang, F. Probing Local Strain at MX_2 –Metal Boundaries with Surface Plasmon-Enhanced Raman Scattering. *Nano Lett.* **2014**, *14* (9), 5329–5334.

(130) Ambrosetti, A.; Ferri, N.; DiStasio, R. A.; Tkatchenko, A. Wavelike Charge Density Fluctuations and van Der Waals Interactions at the Nanoscale. *Science.* **2016**, *351* (6278).

(131) Xi, X.; Berger, H.; Forró, L.; Shan, J.; Mak, K. F. Gate Tuning of Electronic Phase Transitions in Two-Dimensional $NbSe_2$. *Phys. Rev. Lett.* **2016**, *117* (10), 106801.

(132) Song, C.L.; Zhang, H.-M.; Zhong, Y.; Hu, X.P.; Ji, S.H.; Wang, L.; He, K.; Ma, X.C.; Xue, Q.K. Observation of Double-Dome Superconductivity in Potassium-Doped FeSe Thin Films. *Phys. Rev. Lett.* **2016**, *116* (15), 157001.

(133) Feng, Z.; Chen, B.; Qian, S.; Xu, L.; Feng, L.; Yu, Y.; Zhang, R.; Chen, J.; Li, Q.; Li, Q.; et al. Chemical Sensing by Band Modulation of a Black Phosphorus/Molybdenum Diselenide van Der Waals Hetero-Structure. *2D Mater.* **2016**, *3* (3), 035021.

(134) Oakes, L.; Carter, R.; Hanken, T.; Cohn, A. P.; Share, K.; Schmidt, B.; Pint, C. L.; Liu, J. H.; Liu, X. W.; Gong, Y. J.; et al. Interface Strain in Vertically Stacked Two-Dimensional Heterostructured Carbon-MoS_2 Nanosheets Controls Electrochemical Reactivity. *Nat. Commun.* **2016**, *7*, 11796.

(135) Amin, B.; Singh, N.; Schwingenschlögl, U. Heterostructures of Transition Metal Dichalcogenides. *Phys. Rev. B* **2015**, *92* (7), 075439.

(136) Park, Y. H.; Kim, M. H.; Kim, S. Bin; Jung, H. J.; Chae, K.; Ahn, Y. H.; Park, J. Y.; Rotermund, F.; Lee, S. W. Enhanced Nucleation of High-k Dielectrics on Graphene by Atomic Layer Deposition. *Chem. Mater.* **2016**, *28* (20), 7268–7275.

(137) Wallbank, J. R.; Ghazaryan, D.; Misra, A.; Cao, Y.; Tu, J. S.; Piot, B. A.; Potemski, M.; Pezzini, S.; Wiedmann, S.; Zeitler, U.; et al. Tuning the Valley and Chiral Quantum State of Dirac Electrons in van Der Waals Heterostructures. *Science.* **2016**, *353* (6299).

(138) Byun, S.; Kim, J. H.; Song, S. H.; Lee, M.; Park, J.J.; Lee, G.; Hong, S. H.; Lee, D. Ordered, Scalable Heterostructure Comprising Boron Nitride and Graphene for High-Performance Flexible Supercapacitors. *Chem. Mater.* **2016**, *28* (21), 7750–7756.

(139) Zhang, J.; Xie, W.; Xu, X.; Zhang, S.; Zhao, J. Structural and Electronic Properties of Interfaces in Graphene and Hexagonal Boron Nitride Lateral Heterostructures. *Chem. Mater.* **2016**, *28* (14), 5022–5028.

(140) Politano, A.; Slotman, G. J.; Roldán, R.; Chiarello, G.; Campi, D.; Katsnelson, M. I.; Yuan, S. Effect of Moiré Superlattice Reconstruction in the Electronic Excitation Spectrum of Graphene-Metal Heterostructures. *2D Mater.* **2017**, *4* (2), 021001.

(141) Sadeghi, H.; Sangtarash, S.; Lambert, C. J. Cross-Plane Enhanced Thermoelectricity and Phonon Suppression in Graphene/MoS_2 van Der Waals Heterostructures. *2D Mater.* **2016**, *4* (1), 015012.

(142) Liu, C.-H.; Clark, G.; Fryett, T.; Wu, S.; Zheng, J.; Hatami, F.; Xu, X.; Majumdar, A. Nanocavity Integrated van Der Waals Heterostructure Light-Emitting Tunneling Diode. *Nano Lett.* **2017**, *17* (1), 200–205.

(143) Vu, Q. A.; Lee, J. H.; Nguyen, V. L.; Shin, Y. S.; Lim, S. C.; Lee, K.; Heo, J.; Park, S.; Kim, K.; Lee, Y. H.; et al. Tuning Carrier Tunneling in van Der Waals Heterostructures for Ultrahigh Detectivity. *Nano Lett.* **2017**, *17* (1), 453–459.

(144) Heo, J.; Jeong, H.; Cho, Y.; Lee, J.; Lee, K.; Nam, S.; Lee, E.-K.; Lee, S.; Lee, H.; Hwang, S.; et al. Reconfigurable van Der Waals Heterostructured Devices with Metal–Insulator Transition. *Nano Lett.* **2016**, *16* (11), 6746–6754.

(145) Long, M.; Liu, E.; Wang, P.; Gao, A.; Xia, H.; Luo, W.; Wang, B.; Zeng, J.; Fu, Y.; Xu, K.; et al. Broadband Photovoltaic Detectors Based on an Atomically Thin Heterostructure. *Nano Lett.* **2016**, *16* (4), 2254–2259.

(146) Giusca, C. E.; Rungger, I.; Panchal, V.; Melios, C.; Lin, Z.; Lin, Y.-C.; Kahn, E.; Elías, A. L.; Robinson, J. A.; Terrones, M.; et al. Excitonic Effects in Tungsten Disulfide Monolayers on Two-Layer Graphene. *ACS Nano* **2016**, *10* (8), 7840–7846.

(147) Wang, F.; Yin, L.; Wang, Z.; Xu, K.; Wang, F.; Shifa, T. A.; Huang, Y.; Wen, Y.; Jiang, C.; He, J. Strong Electrically Tunable $MoTe_2$ /Graphene van Der Waals Heterostructures for High-Performance Electronic and Optoelectronic Devices. *Appl. Phys. Lett.* **2016**, *109* (19), 193111.

(148) Gao, Y.; Liu, Q.; Xu, B. Lattice Mismatch Dominant Yet Mechanically Tunable Thermal Conductivity in Bilayer Heterostructures. *ACS Nano* **2016**, *10* (5), 5431–5439.

(149) Vu, Q. A.; Shin, Y. S.; Kim, Y. R.; Nguyen, V. L.; Kang, W. T.; Kim, H.; Luong, D. H.; Lee, I. M.; Lee, K.; Ko, D.-S.; et al. Two-Terminal Floating-Gate Memory with van Der Waals Heterostructures for Ultrahigh on/off Ratio. *Nat. Commun.* **2016**, *7*, 12725.

(150) Leenaerts, O.; Vercauteren, S.; Schoeters, B.; Partoens, B. System-Size Dependent Band Alignment in Lateral Two-Dimensional Heterostructures. *2D Mater.* **2016**, *3* (2), 025012.

(151) Wei, P.; Lee, S.; Lemaitre, F.; Pinel, L.; Cutaia, D.; Cha, W.; Katmis, F.; Zhu, Y.; Heiman, D.; Hone, J.; et al. Strong Interfacial Exchange Field in the Graphene/EuS Heterostructure. *Nat. Mater.* **2016**, *15* (7), 711–716.

(152) Mohanty, D.; Xie, W.; Wang, Y.; Lu, Z.; Shi, J.; Zhang, S.; Wang, G.-C.; Lu, T.-M.; Bhat, I. B. Van Der Waals Epitaxy of CdTe Thin Film on Graphene. *Appl. Phys. Lett.* **2016**, *109* (14), 143109.

(153) Kelly, A. G.; Finn, D.; Harvey, A.; Hallam, T.; Coleman, J. N. All-Printed Capacitors from Graphene-BN-Graphene Nanosheet Heterostructures. *Appl. Phys. Lett.* **2016**, *109* (2), 023107.

(154) Youn, D. H.; Stauffer, S. K.; Xiao, P.; Park, H.; Nam, Y.; Dolocan, A.; Henkelman, G.; Heller, A.; Mullins, C. B. Simple Synthesis of Nanocrystalline Tin Sulfide/N-Doped Reduced Graphene Oxide Composites as Lithium Ion Battery Anodes. *ACS Nano* **2016**, *10* (12), 10778–10788.

(155) Pizzocchero, F.; Gammelgaard, L.; Jessen, B. S.; Caridad, J. M.; Wang, L.; Hone, J.; Bøggild, P.; Booth, T. J. The Hot Pick-up Technique for Batch Assembly of van Der Waals Heterostructures. *Nat. Commun.* **2016**, *7*, 11894.

(156) Henck, H.; Pierucci, D.; Chaste, J.; Naylor, C. H.; Avila, J.; Balan, A.; Silly, M. G.; Asensio, M. C.; Sirotti, F.; Johnson, A. T. C.; et al. Electrolytic Phototransistor Based on Graphene-MoS_2 van Der Waals p-n Heterojunction with Tunable Photoresponse. *Appl. Phys. Lett.* **2016**, *109* (11), 113103.

(157) Clark, G.; Schaibley, J. R.; Ross, J.; Taniguchi, T.; Watanabe, K.; Hendrickson, J. R.; Mou, S.; Yao, W.; Xu, X. Single Defect Light-Emitting Diode in a van Der Waals Heterostructure. *Nano Lett.* **2016**, *16* (6), 3944–3948.

(158) Jobst, J.; van der Torren, A. J. H.; Krasovskii, E. E.; Balgley, J.; Dean, C. R.; Tromp, R. M.; van der Molen, S. J.; Cuk, T.; Tanaka, S.; Matsunami, M.; et al. Quantifying Electronic Band Interactions in van Der Waals Materials Using Angle-Resolved Reflected-Electron Spectroscopy. *Nat. Commun.* **2016**, *7*, 13621.

(159) Chen, H.; Wen, X.; Zhang, J.; Wu, T.; Gong, Y.; Zhang, X.; Yuan, J.; Yi, C.; Lou, J.; Ajayan, P. M.; et al. Ultrafast Formation of Interlayer Hot Excitons in Atomically Thin MoS_2/WS_2 Heterostructures. *Nat. Commun.* **2016**, *7*, 12512.

(160) Yu, W. J.; Vu, Q. A.; Oh, H.; Nam, H. G.; Zhou, H.; Cha, S.; Kim, J.-Y.; Carvalho, A.; Jeong, M.; Choi, H.; et al. Unusually Efficient Photocurrent Extraction in Monolayer van Der Waals Heterostructure by Tunnelling through Discretized Barriers. *Nat. Commun.* **2016**, *7*, 13278.

(161) Schaibley, J. R.; Rivera, P.; Yu, H.; Seyler, K. L.; Yan, J.; Mandrus, D. G.; Taniguchi, T.; Watanabe, K.; Yao, W.; Xu, X.; et al. Directional Interlayer Spin-Valley Transfer in Two-Dimensional Heterostructures. *Nat. Commun.* **2016**, *7*, 13747.

(162) Zhang, Q.; Chen, Y.; Zhang, C.; Pan, C.-R.; Chou, M.-Y.; Zeng, C.; Shih, C.-K.; Wang, Q. H.; Kalantar-Zadeh, K.; Kis, A.; et al. Bandgap Renormalization and Work Function Tuning in $MoSe_2$/HBN/Ru(0001) Heterostructures. *Nat. Commun.* **2016**, *7*, 13843.

(163) Li, M. Y.; Chen, C. H.; Shi, Y.; Li, L. J. Heterostructures Based on Two-Dimensional Layered Materials and Their Potential Applications. *Mater. Today* **2016**, *19*, 322–335.

(164) He, X.; Li, H.; Zhu, Z.; Dai, Z.; Yang, Y.; Yang, P.; Zhang, Q.; Li, P.; Schwingenschlogl, U.; Zhang, X. Strain Engineering in Monolayer WS_2, MoS_2 , and the WS_2 /MoS_2 Heterostructure. *Appl. Phys. Lett.* **2016**, *109* (17), 173105.

(165) Xi, X.; Zhao, L.; Wang, Z.; Berger, H.; Forró, L.; Shan, J.; Mak, K. F. Strongly Enhanced Charge-Density-Wave Order in Monolayer NbSe2. *Nat. Nanotechnol.* **2015**, *10* (9), 765–769.

(166) Eichfeld, S. M.; Colon, V. O.; Nie, Y.; Cho, K.; Robinson, J. A. Controlling Nucleation of Monolayer WSe_2 during Metal-Organic Chemical Vapor Deposition Growth. *2D Mater.* **2016**, *3* (2), 025015.

(167) Fu, W.; Chen, Y.; Lin, J.; Wang, X.; Zeng, Q.; Zhou, J.; Zheng, L.; Wang, H.; He, Y.; He, H.; et al. Controlled Synthesis of Atomically Thin 1T-TaS_2 for Tunable Charge Density Wave Phase Transitions. *Chem. Mater.* **2016**, *28*, 7613–7618.

(168) Samassekou, H.; Alkabsh, A.; Wasala, M.; Eaton, M.; Walber, A.; Walker, A.; Pitkänen, O.; Kordas, K.; Talapatra, S.; Jayasekera, T.; et al. Viable Route towards Large-Area 2D MoS_2 Using Magnetron Sputtering. *2D Mater.* **2017**, *4*, 021002.

(169) Tu, Z.; Li, G.; Ni, X.; Meng, L.; Bai, S.; Chen, X.; Lou, J.; Qin, Y. Synthesis of Large Monolayer Single Crystal MoS_2 Nanosheets with Uniform Size through a Double-Tube Technology. *Appl. Phys. Lett.* **2016**, *109* (22), 223101.

(170) Bogaert, K.; Liu, S.; Chesin, J.; Titow, D.; Gradečak, S.; Garaj, S. Diffusion-Mediated Synthesis of MoS_2 /WS_2 Lateral Heterostructures. *Nano Lett.* **2016**, *16* (8), 5129–5134.

(171) Samad, L.; Bladow, S. M.; Ding, Q.; Zhuo, J.; Jacobberger, R. M.; Arnold, M. S.; Jin, S. Layer-Controlled Chemical Vapor Deposition Growth of MoS_2 Vertical Heterostructures via van Der Waals Epitaxy. *ACS Nano* **2016**, *10*, 7039–7046.

(172) Vilá, R. A.; Momeni, K.; Wang, Q.; Bersch, B. M.; Lu, N.; Kim, M. J.; Chen, L. Q.; Robinson, J. A. Bottom-up Synthesis of Vertically Oriented Two-Dimensional Materials. *2D Mater.* **2016**, *3* (4), 041003.

(173) Zheng, B.; Chen, Y.; Wang, Z.; Qi, F.; Huang, Z.; Hao, X.; Li, P.; Zhang, W.; Li, Y. Vertically Oriented Few-Layered HfS_2 Nanosheets: Growth Mechanism and Optical Properties. *2D Mater.* **2016**, *3* (3), 035024.

(174) Li, C.I.; Lin, J.C.; Liu, H.J.; Chu, M.W.; Chen, H.W.; Ma, C.H.; Tsai, C.Y.; Huang, H.W.; Lin, H.J.; Liu, H.L.; et al. Van Der Waal Epitaxy of Flexible and Transparent VO_2 Film on Muscovite. *Chem. Mater.* **2016**, *28* (11), 3914–3919.

(175) Dau, M. T.; Vergnaud, C.; Marty, A.; Rortais, F.; Beigné, C.; Boukari, H.; Bellet-Amalric, E.; Guigoz, V.; Renault, O.; Alvarez, C.; et al. Millimeter-Scale Layered $MoSe_2$ Grown on Sapphire and Evidence for Negative Magnetoresistance. *Appl. Phys. Lett.* **2017**, *110* (1), 011909.

(176) Park, Y. W.; Jerng, S.-K.; Jeon, J. H.; Roy, S. B.; Akbar, K.; Kim, J.; Sim, Y.; Seong, M.-J.; Kim, J. H.; Lee, Z.; et al. Molecular Beam Epitaxy of Large-Area $SnSe_2$ with Monolayer Thickness Fluctuation. *2D Mater.* **2016**, *4* (1), 014006.

(177) Ji, J.; Song, X.; Liu, J.; Yan, Z.; Huo, C.; Zhang, S.; Su, M.; Liao, L.; Wang, W.; Ni, Z.; et al. Two-Dimensional Antimonene Single Crystals Grown by van Der Waals Epitaxy. *Nat. Commun.* **2016**, *7*, 13352.

(178) Aminalragia-Giamini, S.; Marquez-Velasco, J.; Tsipas, P.; Tsoutsou, D.; Renaud, G.; Dimoulas, A. Molecular Beam Epitaxy of Thin $HfTe_2$ Semimetal Films. *2D Mater.* **2016**, *4* (1), 015001.

(179) Middey, S.; Meyers, D.; Doennig, D.; Kareev, M.; Liu, X.; Cao, Y.; Yang, Z.; Shi, J.; Gu, L.; Ryan, P. J.; et al. Mott Electrons in an Artificial Graphenelike Crystal of Rare-Earth Nickelate. *Phys. Rev. Lett.* **2016**, *116* (5), 056801.

(180) Atosuo, E.; Ma¨ Ntyma¨ Ki, M.; Mizohata, K.; Heikkila¨, M. J.; Ra¨ Isa¨ Nen, J.; Ritala, M.; Leskela¨, M. Preparation of Lithium Containing Oxides by the Solid State Reaction of Atomic Layer Deposited Thin Films. *Chem. Mater.* **2017**, *29*, 998–1005.

(181) Park, K.; Kim, Y.; Song, J.-G.; Jin Kim, S.; Wan Lee, C.; Hee Ryu, G.; Lee, Z.; Park, J.; Kim, H. Uniform, Large-Area Self-Limiting Layer Synthesis of Tungsten Diselenide. *2D Mater.* **2016**, *3* (1), 014004.

(182) Nanayakkara, C. E.; Vega, A.; Liu, G.; Dezelah, C. L.; Kanjolia, R. K.; Chabal, Y. J. Role of Initial Precursor Chemisorption on Incubation Delay for Molybdenum Oxide Atomic Layer Deposition. *Chem. Mater.* **2016**, *28* (23), 8591–8597.

(183) Wu, C.-R.; Chang, X.-R.; Chu, T.-W.; Chen, H.-A.; Wu, C.-H.; Lin, S.-Y. Establishment of 2D Crystal Heterostructures by Sulfurization of Sequential Transition Metal Depositions: Preparation, Characterization, and Selective Growth. *Nano Lett.* **2016**, *16* (11), 7093–7097.

(184) Xia, C.; Li, P.; Li, J.; Jiang, Q.; Zhang, X.; Alshareef, H. N. General Top-Down Ion Exchange Process for the Growth of Epitaxial Chalcogenide Thin Films and Devices. *Chem. Mater.* **2017**, *29* (2), 690–698.

(185) Jawaid, A.; Che, J.; Drummy, L. F.; Bultman, J.; Waite, A.; Hsiao, M.-S.; Vaia, R. A. Redox Exfoliation of Layered Transition Metal Dichalcogenides. *ACS Nano* **2017**, *11* (1), 635–646.

(186) Sun, D.; Schaak, R. E. Solution-Mediated Growth of Two-Dimensional SnSe@GeSe Nanosheet Heterostructures. *Chem. Mater.* **2017**, *29* (2), 817–822.

(187) Cheng, Z.; Wang, F.; Shifa, T. A.; Liu, K.; Huang, Y.; Liu, Q.; Jiang, C.; He, J. Carbon Dots Decorated Vertical SnS_2 Nanosheets for Efficient Photocatalytic Oxygen Evolution. *Appl. Phys. Lett.* **2016**, *109* (5), 053905.

(188) Manna, K.; Huang, H.-N.; Li, W.-T.; Ho, Y.-H.; Chiang, W.-H. Toward Understanding the Efficient Exfoliation of Layered Materials by Water-Assisted Cosolvent Liquid-Phase Exfoliation. *Chem. Mater.* **2016**, *28* (21), 7586–7593.

(189) Chao, D.; Liang, P.; Chen, Z.; Bai, L.; Shen, H.; Liu, X.; Xia, X.; Zhao, Y.; Savilov, S. V.; Lin, J.; et al. Pseudocapacitive Na-Ion Storage Boosts High Rate and Areal Capacity of Self-Branched 2D Layered Metal Chalcogenide Nanoarrays. *ACS Nano* **2016**, *10* (11), 10211–10219.

(190) Leng, K.; Chen, Z.; Zhao, X.; Tang, W.; Tian, B.; Nai, C. T.; Zhou, W.; Loh, K. P. Phase Restructuring in Transition Metal Dichalcogenides for Highly Stable Energy Storage. *ACS Nano* **2016**, *10* (10), 9208–9215.

(191) Jawaid, A.; Nepal, D.; Park, K.; Jespersen, M.; Qualley, A.; Mirau, P.; Drummy, L. F.; Vaia, R. A. Mechanism for Liquid Phase Exfoliation of MoS_2. *Chem. Mater.* **2016**, *28* (1), 337–348.

(192) Coleman, J. N.; Lotya, M.; O'Neill, A.; Bergin, S. D.; King, P. J.; Khan, U.; Young, K.; Gaucher, A.; De, S.; Smith, R. J.; et al. Two-Dimensional Nanosheets Produced by Liquid Exfoliation of Layered Materials. *Science.* **2011**, *331* (6017).

(193) Nicolosi, V.; Chhowalla, M.; Kanatzidis, M. G.; Strano, M. S.; Coleman, J. N. Liquid Exfoliation of Layered Materials. *Science.* **2013**, *340* (6139).

(194) Stöter, M.; Rosenfeldt, S.; Breu, J. Tunable Exfoliation of Synthetic Clays. *Annu. Rev. Mater. Res.* **2015**, *45* (1), 129–151.

(195) Choudalakis, G. a.; Kalo, H.; Breu, J.; Gotsis, A. D. CO_2 Gas Barrier Properties in Polymer Nanocomposite Coatings Containing Li-Hectorite Clays. *J. Appl. Polym. Sci.* **2014**, *131* (18).

(196) Madauß, L.; Ochedowski, O.; Lebius, H.; Ban-d'Etat, B.; Naylor, C. H.; Johnson, A. T. C.; Kotakoski, J.; Schleberger, M. Defect Engineering of Single- and Few-Layer MoS_2 by Swift Heavy Ion Irradiation. *2D Mater.* **2016**, *4* (1), 015034.

(197) Alemayehu, M. B.; Falmbigl, M.; Ta, K.; Ditto, J.; Medlin, D. L.; Johnson, D. C. Designed Synthesis of van Der Waals Heterostructures: The Power of Kinetic Control. *Angew. Chemie Int. Ed.* **2015**, *54*, 15468–15472.

(198) Wood, S. R.; Merrill, D. R.; Mitchson, G.; Lygo, A. C.; Bauers, S. R.; Hamann, D. M.; Sutherland, D. R.; Ditto, J.; Johnson, D. C. Modulation Doping in Metastable Heterostructures via Kinetically Controlled Substitution. *Chem. Mater.* **2017**, *29*, 773–779.

(199) Mitchson, G.; Hadland, E.; Göhler, F.; Wanke, M.; Esters, M.; Ditto, J.; Bigwood, E.; Ta, K.; Hennig, R. G.; Seyller, T.; et al. Structural Changes in 2D BiSe Bilayers as n Increases in $(BiSe)_{1+\delta}(NbSe_2)_n$ (n = 1–4) Heterostructures. *ACS Nano* **2016**, *10*, 9489–9499.

(200) Westover, R. D.; Ditto, J.; Falmbigl, M.; Hay, Z. L.; Johnson, D. C. Synthesis and Characterization of Quaternary Monolayer Thick $MoSe_2$/SnSe/$NbSe_2$/SnSe Heterojunction Superlattices. *Chem. Mater.* **2015**, *27*, 6411–6417.

(201) Bauers, S.; Ditto, J.; Moore, D. B.; Johnson, D. C. Structure-Property Relationships in Non-Epitaxial Chalcogenide Heterostructures: The Role of Interface Density on Charge Exchange. *Nanoscale* **2016**, *8*, 14665–14672.

(202) Shang, S.-L.; Lindwall, G.; Wang, Y.; Redwing, J. M.; Anderson, T.; Liu, Z.K. Lateral Versus Vertical Growth of Two-Dimensional Layered Transition-Metal Dichalcogenides: Thermodynamic Insight into MoS_2. *Nano Lett.* **2016**, *16*, 5742–5750.

(203) Nie, Y.; Liang, C.; Zhang, K.; Zhao, R.; Eichfeld, S. M.; Cha, P.-R.; Colombo, L.; Robinson, J. A.; Wallace, R. M.; Cho, K. First Principles Kinetic Monte Carlo Study on the Growth Patterns of WSe_2 Monolayer. *2D Mater.* **2016**, *3* (2), 025029.

(204) Esters, M.; Johnson, D. C. Targeted Synthesis of Metastable Compounds and Intergrowths: The Modulated Elemental Reactants Method. In *Crystal Growth: Concepts, Mechanisms, and Applications*; Li, J., Li, J., Chi, Y., Eds.; Nova Science Publishers: New York, 2017; 35–118.

(205) Schön, J. C.; Jansen, M. First Step Towards Planning of Syntheses in Solid-State Chemistry: Determination of Promising Structure Candidates by Global Optimization. *Angew. Chemie Int. Ed. English* **1996**, *35* (12), 1286–1304.

(206) Chason, E.; Mayer, T. M. Thin Film and Surface Characterization by Specular X-Ray Reflectivity. *Crit. Rev. Solid State Mater. Sci.* **1997**, *22* (1), 1–67.

(207) Macke, S.; Radi, A.; Hamann-Borrero, J. E.; Verna, A.; Bluschke, M.; Brück, S.; Goering, E.; Sutarto, R.; He, F.; Cristiani, G.; et al. Element Specific Monolayer Depth Profiling. *Adv. Mater.* **2014**, *26* (38), 6554–6559.

(208) Zhou, Z.; Palatinus, L.; Sun, J.; Kopeček, J.; Palatinus, L.; Djelal, N.; Roussel, P.; Tendeloo, G. Van; Antipov, E. V.; Kato, K.; et al. Structure Determination of Modulated Structures by Powder X-Ray Diffraction and Electron Diffraction. *Inorg. Chem. Front.* **2016**, *3* (11), 1351–1362.

(209) Moore, D. B.; Beekman, M.; Disch, S.; Zschack, P.; Häusler, I.; Neumann, W.; Johnson, D. C. Synthesis, Structure, and Properties of Turbostratically Disordered $(PbSe)_{1.18}(TiSe_2)_2$. *Chem. Mater.* **2013**, *25*, 2404–2409.

(210) Atkins, R.; Disch, S.; Jones, Z.; Haeusler, I.; Grosse, C.; Fischer, S. F.; Neumann, W.; Zschack, P.; Johnson, D. C. Synthesis, Structure and Electrical Properties of a New Tin Vanadium Selenide. *J. Solid State Chem.* **2013**, *202*, 128–133.

(211) Oviedo, J. P.; KC, S.; Lu, N.; Wang, J.; Cho, K.; Wallace, R. M.; Kim, M. J. *In Situ* TEM Characterization of Shear-Stress-Induced Interlayer Sliding in the Cross Section View of Molybdenum Disulfide. *ACS Nano* **2015**, *9* (2), 1543–1551.

(212) Gunning, N. S.; Feser, J.; Beekman, M.; Cahill, D. G.; Johnson, D. C. Synthesis and Thermal Properties of Solid-State Structural Isomers: Ordered Intergrowths of SnSe and $MoSe_2$. *J. Am. Chem. Soc.* **2015**, *137*, 8803–8809.

(213) Zhang, K.; Feng, S.; Wang, J.; Azcatl, A.; Lu, N.; Addou, R.; Wang, N.; Zhou, C.; Lerach, J.; Bojan, V.; et al. Manganese Doping of Monolayer MoS_2 : The Substrate Is Critical. *Nano Lett.* **2015**, *15* (10), 6586–6591.

(214) Merrill, D. R.; Sutherland, D. R.; Ditto, J. J.; Moore, D. B.; Falmbigl, M.; Medlin, D. L.; Johnson, D. C. The Synthesis of $[(PbSe)_{1+\delta}]_m(TiSe_2)_n[(SnSe_2)_{1+\gamma}]_m(TiSe_2)_n$ Heterostructures with Designed Nanoarchitectures by Self Assembly of Amorphous Precursors. *Nanoscale* **2016**, *8*.

(215) Fei, L.; Lei, S.; Zhang, W.-B.; Lu, W.; Lin, Z.; Lam, C. H.; Chai, Y.; Wang, Y.; Guo, Y.; Qiu, H.; et al. Direct TEM Observations of Growth Mechanisms of Two-Dimensional MoS_2 Flakes. *Nat. Commun.* **2016**, *7*, 12206.

(216) Li, F.; Zhang, Q.; Tang, C.; Liu, C.; Shi, J.; Nie, C.; Zhou, G.; Li, Z.; Zhang, W.; Song, C.-L.; et al. Atomically Resolved FeSe/SrTiO 3 (001) Interface Structure by Scanning Transmission Electron Microscopy. *2D Mater.* **2016**, *3* (2), 024002.

(217) Liu, H. J.; Jiao, L.; Xie, L.; Yang, F.; Chen, J. L.; Ho, W. K.; Gao, C. L.; Jia, J. F.; Cui, X. D.; Xie, M. H. Molecular-Beam Epitaxy of Monolayer and Bilayer WSe_2 : A Scanning Tunneling Microscopy/Spectroscopy Study and Deduction of Exciton Binding Energy. *2D Mater.* **2015**, *2* (3), 034004.

(218) Liu, H.; Jiao, L.; Yang, F.; Cai, Y.; Wu, X.; Ho, W.; Gao, C.; Jia, J.; Wang, N.; Fan, H.; et al. Dense Network of One-Dimensional Midgap Metallic Modes in Monolayer $MoSe_2$ and Their Spatial Undulations. *Phys. Rev. Lett.* **2014**, *113* (6), 066105.

(219) Park, J. H.; Vishwanath, S.; Liu, X.; Zhou, H.; Eichfeld, S. M.; Fullerton-Shirey, S. K.; Robinson, J. A.; Feenstra, R. M.; Furdyna, J.; Jena, D.; et al. Scanning Tunneling Microscopy and Spectroscopy of Air Exposure Effects on Molecular Beam Epitaxy Grown WSe_2 Monolayers and Bilayers. *ACS Nano* **2016**, *10* (4), 4258–4267.

(220) Hill, H. M.; Rigosi, A. F.; Rim, K. T.; Flynn, G. W.; Heinz, T. F. Band Alignment in MoS_2 /WS_2 Transition Metal Dichalcogenide Heterostructures Probed by Scanning Tunneling Microscopy and Spectroscopy. *Nano Lett.* **2016**, *16* (8), 4831–4837.

(221) Jespersen, M. L.; Inman, C. E.; Kearns, G. J.; Foster, E. W.; Hutchison, J. E. Alkanephosphonates on Hafnium-Modified Gold: A New Class of Self-Assembled Organic Monolayers. *J. Am. Chem. Soc.* **2007**, *129* (10), 2803–2807.

(222) Ren, X.; Singh, A. K.; Fang, L.; Kanatzidis, M. G.; Tavazza, F.; Davydov, A. V.; Lauhon, L. J. Atom Probe Tomography Analysis of Ag Doping in 2D Layered Material $(PbSe)_5(Bi_2Se_3)_3$. *Nano Lett.* **2016**, *16*, 6064–6069.

(223) O'Brien, M.; McEvoy, N.; Motta, C.; Zheng, J.-Y.; Berner, N. C.; Kotakoski, J.; Elibol, K.; Pennycook, T. J.; Meyer, J. C.; Yim, C.; et al. Raman Characterization of Platinum Diselenide Thin Films. *2D Mater.* **2016**, *3* (2), 021004.

(224) Grzeszczyk, M.; Gołasa, K.; Zinkiewicz, M.; Nogajewski, K.; Molas, M. R.; Potemski, M.; Wysmołek, A.; Babiński, A. Raman Scattering of Few-Layers $MoTe_2$. *2D Mater.* **2016**, *3* (2), 025010.

(225) Shi, W.; Lin, M.-L.; Tan, Q.-H.; Qiao, X.-F.; Zhang, J.; Tan, P.-H. Raman and Photoluminescence Spectra of Two-Dimensional Nanocrystallites of Monolayer WS_2 and WSe_2. *2D Mater.* **2016**, *3* (2), 025016.

(226) Wang, X.; Du, K.; Fredrik Liu, Y. Y.; Hu, P.; Zhang, J.; Zhang, Q.; Owen, M. H. S.; Lu, X.; Gan, C. K.; Sengupta, P.; et al. Raman Spectroscopy of Atomically Thin Two-Dimensional Magnetic Iron Phosphorus Trisulfide ($FePS_3$) Crystals. *2D Mater.* **2016**, *3* (3), 031009.

(227) Kim, J.-S.; Moran, S. T.; Nayak, A. P.; Pedahzur, S.; Ruiz, I.; Ponce, G.; Rodriguez, D.; Henny, J.; Liu, J.; Lin, J.-F.; et al. High Pressure Raman Study of Layered $Mo_{0.5}W_{0.5}S_2$ Ternary Compound. *2D Mater.* **2016**, *3*, 025003.

(228) Kim, K.; Lee, J.-U.; Nam, D.; Cheong, H. Davydov Splitting and Excitonic Resonance Effects in Raman Spectra of Few-Layer $MoSe_2$. *ACS Nano* **2016**, *10* (8), 8113–8120.

(229) Saito, R.; Tatsumi, Y.; Huang, S.; Ling, X.; Dresselhaus, M. S. Raman Spectroscopy of Transition Metal Dichalcogenides. *J. Phys. Condens. Matter* **2016**, *28* (35), 353002.

(230) Terrones, H.; Corro, E. Del; Feng, S.; Poumirol, J. M.; Rhodes, D.; Smirnov, D.; Pradhan, N. R.; Lin, Z.; Nguyen, M. A. T.; Elías, A. L.; et al. New First Order Raman-Active Modes in Few Layered Transition Metal Dichalcogenides. *Sci. Rep.* **2015**, *4* (1), 4215.

(231) Huang, S.; Liang, L.; Ling, X.; Puretzky, A. A.; Geohegan, D. B.; Sumpter, B. G.; Kong, J.; Meunier, V.; Dresselhaus, M. S. Low-Frequency Interlayer Raman Modes to Probe Interface of Twisted Bilayer MoS_2. *Nano Lett.* **2016**, *16* (2), 1435–1444.

(232) Zhang, X.; Tan, Q.-H.; Wu, J.-B.; Shi, W.; Tan, P.-H.; Xiong, Q.; Quek, S. Y.; Neto, A. H. C.; Krasheninnikov, A. V.; Suenaga, K.; et al. Review on the Raman Spectroscopy of Different Types of Layered Materials. *Nanoscale* **2016**, *8* (12), 6435–6450.

(233) Puretzky, A. A.; Liang, L.; Li, X.; Xiao, K.; Wang, K.; Mahjouri-Samani, M.; Basile, L.; Idrobo, J. C.; Sumpter, B. G.; Meunier, V.; et al. Low-Frequency Raman Fingerprints of Two-Dimensional Metal Dichalcogenide Layer Stacking Configurations. *ACS Nano* **2015**, *9* (6), 6333–6342.

(234) Kurosawa, K.; Saito, S.; Yamaguchi, Y. Neutron Diffraction Study on $MnPS_3$ and $FePS_3$. *J. Phys. Soc. Japan* **1983**, *52* (11), 3919–3926.

(235) Ouvrard, G.; Brec, R.; Rouxel, J. Structural Determination of Some MPS_3 Layered Phases (M = Mn, Fe, Co, Ni and Cd). *Mater. Res. Bull.* **1985**, *20* (10), 1181–1189.

(236) Le Flem, G.; Brec, R.; Ouvard, G.; Louisy, A.; Segransan, P. Magnetic Interactions in the Layer Compounds MPX_3 (M = Mn, Fe, Ni; X = S, Se). *J. Phys. Chem. Solids* **1982**, *43* (5), 455–461.

(237) Brec, R. Review on Structural and Chemical Properties of Transition Metal Phosphorous Trisulfides MPS3. *Solid State Ionics* **1986**, *22* (1), 3–30.

(238) Wildes, A. R.; Roessli, B.; Lebech, B.; Godfrey, K. W. Spin Waves and the Critical Behaviour of the Magnetization In. *J. Phys. Condens. Matter* **1998**, *10* (28), 6417–6428.

(239) Prouzet, E.; Ouvrard, G.; Brec, R. Structure Determination of $ZnPS_3$. *Mater. Res. Bull.* **1986**, *21* (2), 195–200.

(240) Ouvrard, G.; Fréour, R.; Brec, R.; Rouxel, J. A Mixed Valence Compound in the Two Dimensional MPS_3 Family: $V_{0.78}PS_3$ Structure and Physical Properties. *Mater. Res. Bull.* **1985**, *20* (9), 1053–1062.

(241) Ressouche, E.; Loire, M.; Simonet, V.; Ballou, R.; Stunault, A.; Wildes, A. Magnetoelectric $MnPS_3$ as a Candidate for Ferrotoroidicity. *Phys. Rev. B* **2010**, *82* (10), 100408.

(242) Kurita, N.; Nakao, K. Band Structure of Magnetic Layered Semiconductor $NiPS_3$. *J. Phys. Soc. Japan* **1989**, *58* (1), 232–243.

(243) Rule, K. C.; McIntyre, G. J.; Kennedy, S. J.; Hicks, T. J. Single-Crystal and Powder Neutron Diffraction Experiments on $FePS_3$: Search for the Magnetic Structure. *Phys. Rev. B* **2007**, *76* (13), 134402.

(244) Kurita, N.; Nakao, K. Band Structures and Physical Properties of Magnetic Layered Semiconductors MPS_3. *J. Phys. Soc. Japan* **1989**, *58* (2), 610–621.

(245) Gutiérrez, H. R.; Perea-López, N.; Elías, A. L.; Berkdemir, A.; Wang, B.; Lv, R.; López-Urías, F.; Crespi, V. H.; Terrones, H.; Terrones, M. Extraordinary Room-Temperature Photoluminescence in Triangular WS_2 Monolayers. *Nano Lett.* **2013**, *13* (8), 3447–3454.

(246) Huang, Y.; Sutter, E.; Sadowski, J. T.; Cotlet, M.; Monti, O. L. A.; Racke, D. A.; Neupane, M. R.; Wickramaratne, D.; Lake, R. K.; Parkinson, B. A.; et al. Tin Disulfide—An Emerging Layered Metal Dichalcogenide Semiconductor: Materials Properties and Device Characteristics. *ACS Nano* **2014**, *8* (10), 10743–10755.

(247) Schlaf, R.; Pettenkofer, C.; Jaegermann, W. Band Lineup of a $SnS_2/SnSe_2/SnS_2$ Semiconductor Quantum Well Structure Prepared by van Der Waals Epitaxy. *J. Appl. Phys.* **1999**, *85* (9), 6550.

(248) Zhang, C.; Gong, C.; Nie, Y.; Min, K.-A.; Liang, C.; Oh, Y. J.; Zhang, H.; Wang, W.; Hong, S.; Colombo, L.; et al. Systematic Study of Electronic Structure and Band Alignment of Monolayer Transition Metal Dichalcogenides in Van Der Waals Heterostructures. *2D Mater.* **2016**, *4* (1), 015026.

(249) Kang, J.; Tongay, S.; Zhou, J.; Li, J.; Wu, J. Band Offsets and Heterostructures of Two-Dimensional Semiconductors. *Appl. Phys. Lett.* **2013**, *102* (1), 012111.

(250) Li, M.Y.; Shi, Y.; Cheng, C.C.; Lu, L.S.; Lin, Y.C.; Tang, H.L.; Tsai, M.L.; Chu, C.W.; Wei, K.H.; He, J.H.; et al. Epitaxial Growth of a Monolayer WSe_2-MoS_2 Lateral p-n Junction with an Atomically Sharp Interface. *Science.* **2015**, *349* (6247), 524–528.

(251) Zhang, C.; Chen, Y.; Huang, J.-K.; Wu, X.; Li, L.-J.; Yao, W.; Tersoff, J.; Shih, C.-K.; Geim, A. K.; Grigorieva, I. V.; et al. Visualizing Band Offsets and Edge States in Bilayer–Monolayer Transition Metal Dichalcogenides Lateral Heterojunction. *Nat. Commun.* **2016**, *7*, 10349.

(252) Hong, X.; Kim, J.; Shi, S.-F.; Zhang, Y.; Jin, C.; Sun, Y.; Tongay, S.; Wu, J.; Zhang, Y.; Wang, F. Ultrafast Charge Transfer in Atomically Thin MoS_2/WS_2 Heterostructures. *Nat. Nanotechnol.* **2014**, *9* (9), 682–686.

(253) Yu, Y.; Hu, S.; Su, L.; Huang, L.; Liu, Y.; Jin, Z.; Purezky, A. A.; Geohegan, D. B.; Kim, K. W.; Zhang, Y.; et al. Equally Efficient Interlayer Exciton Relaxation and Improved Absorption in Epitaxial and Nonepitaxial MoS_2 /WS_2 Heterostructures. *Nano Lett.* **2015**, *15* (1), 486–491.

(254) Peng, B.; Yu, G.; Liu, X.; Liu, B.; Liang, X.; Bi, L.; Deng, L.; Sum, T. C.; Loh, K. P. Ultrafast Charge Transfer in MoS_2 /WSe_2 p–n Heterojunction. *2D Mater.* **2016**, *3* (2), 025020.

(255) Pan, S.; Ceballos, F.; Bellus, M. Z.; Zereshki, P.; Zhao, H. Ultrafast Charge Transfer between $MoTe_2$ and MoS_2 Monolayers. *2D Mater.* **2016**, *4* (1), 015033.

(256) Rivera, P.; Schaibley, J. R.; Jones, A. M.; Ross, J. S.; Wu, S.; Aivazian, G.; Klement, P.; Seyler, K.; Clark, G.; Ghimire, N. J.; et al. Observation of Long-Lived Interlayer Excitons in Monolayer $MoSe_2$–WSe_2 Heterostructures. *Nat. Commun.* **2015**, *6*, 6242.

(257) Wang, H.; Bang, J.; Sun, Y.; Liang, L.; West, D.; Meunier, V.; Zhang, S.; Kudo, A.; Miseki, Y.; Alferov, Z. I.; et al. The Role of Collective Motion in the Ultrafast Charge Transfer in van Der Waals Heterostructures. *Nat. Commun.* **2016**, *7*, 11504.

(258) Li, L.; Long, R.; Prezhdo, O. V. Charge Separation and Recombination in Two-Dimensional MoS_2/WS_2: Time-Domain Ab Initio Modeling. *Chem. Mater.* **2017**, *29* (6), 2466–2473.

(259) Amin, B.; Kaloni, T. P.; Schreckenbach, G.; Freund, M. S. Materials Properties of Out-of-Plane Heterostructures of MoS_2 - WSe_2 and WS_2 -$MoSe_2$. *Appl. Phys. Lett.* **2016**, *108* (6), 063105.

(260) Cao, L. Two-Dimensional Transition-Metal Dichalcogenide Materials: Toward an Age of Atomic-Scale Photonics. *MRS Bull.* **2015**, *40* (07), 592–599.

(261) Chernikov, A.; Berkelbach, T. C.; Hill, H. M.; Rigosi, A.; Li, Y.; Aslan, O. B.; Reichman, D. R.; Hybertsen, M. S.; Heinz, T. F. Exciton Binding Energy and Nonhydrogenic Rydberg Series in Monolayer WS_2. *Phys. Rev. Lett.* **2014**, *113* (7), 076802.

(262) Rivera, P.; Seyler, K. L.; Yu, H.; Schaibley, J. R.; Yan, J.; Mandrus, D. G.; Yao, W.; Xu, X. Valley-Polarized Exciton Dynamics in a 2D Semiconductor Heterostructure. *Science.* **2016**, *351* (6274).

(263) Lundt, N.; Klembt, S.; Cherotchenko, E.; Betzold, S.; Iff, O.; Nalitov, A. V.; Klaas, M.; Dietrich, C. P.; Kavokin, A. V.; Höfling, S.; et al. Room-Temperature Tamm-Plasmon Exciton-Polaritons with a WSe_2 Monolayer. *Nat. Commun.* **2016**, *7*, 13328.

(264) Ahn, J.; Jeon, P. J.; Raza, S. R. A.; Pezeshki, A.; Min, S.-W.; Hwang, D. K.; Im, S. Transition Metal Dichalcogenide Heterojunction Pn Diode toward Ultimate Photovoltaic Benefits. *2D Mater.* **2016**, *3* (4), 045011.

(265) Xu, Z.-Q.; Zhang, Y.; Wang, Z.; Shen, Y.; Huang, W.; Xia, X.; Yu, W.; Xue, Y.; Sun, L.; Zheng, C.; et al. Atomically Thin Lateral p–n Junction Photodetector with Large Effective Detection Area. *2D Mater.* **2016**, *3* (4), 041001.

(266) Zhou, H.; Yu, F.; Sun, J.; Zhu, H.; Mishra, I. K.; Chen, S.; Ren, Z. Highly Efficient Hydrogen Evolution from Edge-Oriented $WS_{2(1-x)}Se_{2x}$ Particles on Three-Dimensional Porous $NiSe_2$ Foam. *Nano Lett.* **2016**, *16* (12), 7604–7609.

(267) Voiry, D.; Fullon, R.; Yang, J.; de Carvalho Castro e Silva, C.; Kappera, R.; Bozkurt, I.; Kaplan, D.; Lagos, M. J.; Batson, P. E.; Gupta, G.; et al. The Role of Electronic Coupling between Substrate and 2D MoS_2 Nanosheets in Electrocatalytic Production of Hydrogen. *Nat. Mater.* **2016**, *15*, 1003–1009.

(268) Chen, J.; Zhou, W.; Tang, W.; Tian, B.; Zhao, X.; Xu, H.; Liu, Y.; Geng, D.; Tan, S. J. R.; Fu, W.; et al. Lateral Epitaxy of Atomically Sharp WSe_2 /WS_2 Heterojunctions on Silicon Dioxide Substrates. *Chem. Mater.* **2016**, *28* (20), 7194–7197.

(269) Chen, Y.; Dumcenco, D. O.; Zhu, Y.; Zhang, X.; Mao, N.; Feng, Q.; Zhang, M.; Zhang, J.; Tan, P.-H.; Huang, Y.-S.; et al. Composition-Dependent Raman Modes of $Mo_{1-x}W_xS_2$ Monolayer Alloys. *Nanoscale* **2014**, *6*, 2833–2839.

(270) Feng, Q.; Mao, N.; Wu, J.; Xu, H.; Wang, C.; Zhang, J.; Xie, L. Growth of $MoS_{2(1-x)}Se_{2x}$ (x = 0.41–1.00) Monolayer Alloys with Controlled Morphology by Physical Vapor Deposition. *ACS Nano* **2015**, *9* (7), 7450–7455.

(271) Duerloo, K.-A. N.; Reed, E. J. Structural Phase Transitions by Design in Monolayer Alloys. *ACS Nano* **2016**, *10* (1), 289–297.

(272) Kang, J.; Tongay, S.; Li, J.; Wu, J. Monolayer Semiconducting Transition Metal Dichalcogenide Alloys: Stability and Band Bowing. *J. Appl. Phys.* **2013**, *113* (14), 143703.

(273) Tongay, S.; Narang, D. S.; Kang, J.; Fan, W.; Ko, C.; Luce, A. V.; Wang, K. X.; Suh, J.; Patel, K. D.; Pathak, V. M.; et al. Two-Dimensional Semiconductor Alloys: Monolayer $Mo_{1-x}W_xSe_2$. *Appl. Phys. Lett.* **2014**, *104* (1), 012101.

(274) Karande, S. D.; Kaushik, N.; Narang, D. S.; Late, D.; Lodha, S. Thickness Tunable Transport in Alloyed WSSe Field Effect Transistors. *Appl. Phys. Lett.* **2016**, *109* (14), 142101.

(275) Wilson, J. A.; Di Salvo, F. J.; Mahajan, S. Charge-Density Waves and Superlattices in the Metallic Layered Transition Metal Dichalcogenides. *Adv. Phys.* **1975**, *24* (2), 117–201.

(276) Friend, R. H.; Yoffe, A. D. Electronic Properties of Intercalation Complexes of the Transition Metal Dichalcogenides. *Adv. Phys.* **1987**, *36* (1), 1–94.

(277) Wilson, J. A.; Yoffe, A. D. The Transition Metal Dichalcogenides Discussion and Interpretation of the Observed Optical, Electrical and Structural Properties. *Adv. Phys.* **1969**, *18* (73), 193–335.

(278) Cao, Y.; Mishchenko, A.; Yu, G. L.; Khestanova, E.; Rooney, A. P.; Prestat, E.; Kretinin, A. V.; Blake, P.; Shalom, M. B.; Woods, C.; et al. Quality Heterostructures from Two-Dimensional Crystals Unstable in Air by Their Assembly in Inert Atmosphere. *Nano Lett.* **2015**, *15* (8), 4914–4921.

(279) Tsen, A. W.; Hovden, R.; Wang, D.; Kim, Y. D.; Okamoto, J.; Spoth, K. A.; Liu, Y.; Lu, W.; Sun, Y.; Hone, J. C.; et al. Structure and Control of Charge Density Waves in Two-Dimensional 1T-TaS_2. *Proc. Natl. Acad. Sci. U. S. A.* **2015**, *112* (49), 15054–15059.

(280) Tsen, A. W.; Hunt, B.; Kim, Y. D.; Yuan, Z. J.; Jia, S.; Cava, R. J.; Hone, J.; Kim, P.; Dean, C. R.; Pasupathy, A. N. Nature of the Quantum Metal in a Two-Dimensional Crystalline Superconductor. *Nat. Phys.* **2015**, *12* (3), 208–212.

(281) Alemayehu, M. B.; Falmbigl, M.; Ta, K.; Grosse, C.; Westover, R. D.; Bauers, S. R.; Fischer, S. F.; Johnson, D. C. Structural and Electrical Properties of $([SnSe]_{1+\delta})_M(NbSe_2)_1$ Compounds: Single $NbSe_2$ Layers Separated by Increasing Thickness of SnSe. *Chem. Mater.* **2015**, *27*, 867–875.

(282) Alemayehu, M. B.; Ta, K.; Falmbigl, M.; Johnson, D. C. Structure, Stability, and Properties of the Intergrowth Compounds $([SnSe]_{1+\delta})_m(NbSe_2)_n$, Where $m = n = 1–20$. *J. Am. Chem. Soc.* **2015**, *137*, 4831–4839.

(283) Wiegers, G. A.; Meetsma, A.; Haange, R. J.; de Boer, J. L. Structure and Physical Properties of $(SnS)_{1.18}NbS_2$, "$SnNbS_3$", a Compound with Misfit Layer Structure. *Mater. Res. Bull.* **1988**, *23* (11), 1551–1559.

(284) Meerschaut, A.; Rabu, P.; Rouxel, J. Preparation and Characterization of New Mixed Sandwiched Layered Compounds $Ln_{32}Nb_{28}S_{88}$(Ln =La, Ce). *J. Solid State Chem.* **1989**, *78* (1), 35–45.

(285) Onoda, M.; Saeki, M.; Yamamoto, A.; Kato, K.; IUCr. Structure Refinement of the Incommensurate Composite Crystal $Sr_{1.145}TiS_3$ through the Rietveld Analysis Process. *Acta Crystallogr. Sect. B Struct. Sci.* **1993**, *49* (6), 929–936.

(286) Gotoh, Y.; Goto, M.; Kawaguchi, K.; Oosawa, Y.; Onoda, M. Preparation and Characterization of a New Composite-Layered Sulfide, $(PbS)_{1.12}VS_2$, "$PbVS_3$." *Mater. Res. Bull.* **1990**, *25* (3), 307–314.

(287) Auriel, C.; Roesky, R.; Meerschaut, A.; Rouxel, J. Structure Determination and Electrical Properties of a New Misfit Layered Selenide $[(PbSe)_{1.10}NbSe_2]$. *Mater. Res. Bull.* **1993**, *28* (3), 247–254.

(288) Ohno, Y. Electronic Structure of the Misfit-Layer Compounds $PbTiS_3$ and $SnNbS_3$. *Phys. Rev. B* **1991**, *44* (3), 1281–1291.

(289) Kalläne, M.; Rossnagel, K.; Marczynski-Bühlow, M.; Kipp, L.; Starnberg, H. I.; Stoltz, S. E. Stabilization of the Misfit Layer Compound $(PbS)_{1.13}TaS_2$ by Metal Cross Substitution. *Phys. Rev. Lett.* **2008**, *100* (6), 065502.

(290) Wiegers, G. A.; Meerschaut, A. Structures of Misfit Layer Compounds $(MS)_nTS_2$ (M =Sn, Pb, Bi, Rare Earth Metals; T = Nb, Ta, Ti, V, Cr; $1.08<n<1.23$). *J. Alloys Compd.* **1992**, *178* (1–2), 351–368.

(291) Lin, Q.; Heideman, C. L.; Nguyen, N.; Zschack, P.; Chiritescu, C.; Cahill, D. G.; Johnson, D. C. Designed Synthesis of Families of Misfit-Layered Compounds. *Eur. J. Inorg. Chem.* **2008**, *2008*, 2382–2385.

(292) Beekman, M.; Heideman, C. L.; Johnson, D. C. Ferecrystals: Non-Epitaxial Layered Intergrowths. *Semicond. Sci. Technol.* **2014**, *29*, 064012.

(293) Silva-Guillén, J. Á.; Ordejón, P.; Guinea, F.; Canadell, E. Electronic Structure of 2 H -$NbSe_2$ Single-Layers in the CDW State. *2D Mater.* **2016**, *3* (3), 035028.

(294) Li, Y.; Duerloo, K.-A. N.; Wauson, K.; Reed, E. J.; Lencer, D.; Wong, H.-S. P.; Wong, H.-S. P.; Zhou, Y.; Ramanathan, S.; Shu, M. J.; et al. Structural Semiconductor-to-Semimetal Phase Transition in Two-Dimensional Materials Induced by Electrostatic Gating. *Nat. Commun.* **2016**, *7*, 10671.

(295) Wang, H.; Qian, X. Two-Dimensional Multiferroics in Monolayer Group IV Monochalcogenides. *2D Mater.* **2017**, *4* (1), 015042.

(296) Fei, R.; Kang, W.; Yang, L. Ferroelectricity and Phase Transitions in Monolayer Group-IV Monochalcogenides. *Phys. Rev. Lett.* **2016**, *117* (9), 097601.

(297) Soares Jr, A. L.; Dos Santos, E. C.; Morales-García, A.; Heine, T.; De Abreu, H. A.; Duarte, H. A. Two-Dimensional Crystal CuS—Electronic and Structural Properties. *2D Mater.* **2016**, *4* (1), 015041.

(298) Song, K.; Soriano, D.; Robles, R.; Ordejon, P.; Roche, S. How Disorder Affects Topological Surface States in the Limit of Ultrathin Bi_2Se_3 Films. *2D Mater.* **2016**, *3* (4), 045007.

(299) Liu, J.; Wang, H.; Fang, C.; Fu, L.; Qian, X. Van Der Waals Stacking-Induced Topological Phase Transition in Layered Ternary Transition Metal Chalcogenides. *Nano Lett.* **2017**, *17* (1), 467–475.

(300) Liu, F.; You, L.; Seyler, K. L.; Li, X.; Yu, P.; Lin, J.; Wang, X.; Zhou, J.; Wang, H.; He, H.; et al. Room-Temperature Ferroelectricity in CuInP2S6 Ultrathin Flakes. *Nat. Commun.* **2016**, *7*, 12357.

(301) Atkins, R.; Wilson, J.; Zschack, P.; Grosse, C.; Neumann, W.; Johnson, D. C. Synthesis of $[(SnSe)_{1.15}]_m((TaSe_2)_n$ Ferecrystals: Structurally Tunable Metallic Compounds. *Chem. Mater.* **2012**, *24*, 4594–4599.

(302) Atkins, R.; Dolgos, M.; Fiedler, A.; Grosse, C.; Fischer, S. F.; Rudin, S. P.; Johnson, D. C. Synthesis and Systematic Trends in Structure and Electrical Properties of $[(SnSe)_{1.15}]_m(VSe_2)_1$, m = 1, 2, 3, and 4. *Chem. Mater.* **2014**, *26*, 2862–2872.

(303) Zhao, S.; Hotta, T.; Koretsune, T.; Watanabe, K.; Taniguchi, T.; Sugawara, K.; Takahashi, T.; Shinohara, H.; Kitaura, R. Two-Dimensional Metallic NbS 2 : Growth, Optical Identification and Transport Properties. *2D Mater.* **2016**, *3* (2), 025027.

(304) Alemayehu, M. B.; Ta, K.; Falmbigl, M.; Johnson, D. C.; Grosse, C.; Fischer, S. F.; Neumann, W.; Zschack, P.; Johnson, D. C. Charge Transfer vs. Dimensionality: What Affects the Transport Properties of Ferecrystals? *Nanoscale* **2015**, *7* (16), 7378–7385.

(305) Grosse, C.; Alemayehu, M. B.; Falmbigl, M.; Mogilatenko, A.; Chiatti, O.; Johnson, D. C.; Fischer, S. F. Superconducting Ferecrystals: Turbostratically Disordered Atomic-Scale Layered $(PbSe)_{1.14}(NbSe_2)_n$ Thin Films. *Sci. Rep.* **2016**, *6* (1), 33457.

(306) Goli, P.; Khan, J.; Wickramaratne, D.; Lake, R. K.; Balandin, A. A. Charge Density Waves in Exfoliated Films of van Der Waals Materials: Evolution of Raman Spectrum in $TiSe_2$. *Nano Lett.* **2012**, *12* (11), 5941–5945.

(307) Yang, J.; Wang, W.; Liu, Y.; Du, H.; Ning, W.; Zheng, G.; Jin, C.; Han, Y.; Wang, N.; Yang, Z.; et al. Thickness Dependence of the Charge-Density-Wave Transition Temperature in VSe_2. *Appl. Phys. Lett.* **2014**, *105* (6), 063109.

(308) Sugawara, K.; Nakata, Y.; Shimizu, R.; Han, P.; Hitosugi, T.; Sato, T.; Takahashi, T. Unconventional Charge-Density-Wave Transition in Monolayer 1 *T* -$TiSe_2$. *ACS Nano* **2016**, *10* (1), 1341–1345.

(309) He, R.; van Baren, J.; Yan, J.-A.; Xi, X.; Ye, Z.; Ye, G.; Lu, I.-H.; Leong, S. M.; Lui, C. H. Interlayer Breathing and Shear Modes in $NbSe_2$ Atomic Layers. *2D Mater.* **2016**, *3* (3), 031008.

(310) Hajiyev, P.; Cong, C.; Qiu, C.; Yu, T.; Lau, C. N. Contrast and Raman Spectroscopy Study of Single- and Few-Layered Charge Density Wave Material: 2H-$TaSe_2$. *Sci. Rep.* **2013**, *3*, 104101.

(311) Ogawa, N.; Miyano, K. Charge-Density Wave as an Electro-Optical Switch and Memory. *Appl. Phys. Lett.* **2002**, *80* (17), 3225–3227.

(312) Khan, J.; Nolen, C. M.; Teweldebrhan, D.; Wickramaratne, D.; Lake, R. K.; Balandin, A. A. Anomalous Electron Transport in Back-Gated Field-Effect Transistors with $TiTe_2$ Semimetal Thin-Film Channels. *Appl. Phys. Lett.* **2012**, *100* (4), 043109.

(313) Neal, A. T.; Du, Y.; Liu, H.; Ye, P. D. Two-Dimensional $TaSe_2$ Metallic Crystals: Spin–Orbit Scattering Length and Breakdown Current Density. *ACS Nano* **2014**, *8* (9), 9137–9142.

(314) Hollander, M. J.; Liu, Y.; Lu, W.-J.; Li, L.-J.; Sun, Y.-P.; Robinson, J. A.; Datta, S. Electrically Driven Reversible Insulator–Metal Phase Transition in 1T-TaS_2. *Nano Lett.* **2015**, *15* (3), 1861–1866.

(315) Ugeda, M. M.; Bradley, A. J.; Zhang, Y.; Onishi, S.; Chen, Y.; Ruan, W.; Ojeda Aristizabal, C.; Ryu, H.; Edmonds, M. T.; Tsai, H. Z.; et al. Characterization of Collective Ground States in Single-Layer $NbSe_2$. *Nat. Phys.* **2015**, *12* (1), 92–97.

(316) Bayard, M.; Sienko, M. J. Anomalous Electrical and Magnetic Properties of Vanadium Diselenide. *J. Solid State Chem.* **1976**, *19* (4), 325–329.

(317) Xu, K.; Chen, P.; Li, X.; Wu, C.; Guo, Y.; Zhao, J.; Wu, X.; Xie, Y. Ultrathin Nanosheets of Vanadium Diselenide: A Metallic Two-Dimensional Material with Ferromagnetic Charge-Density-Wave Behavior. *Angew. Chemie Int. Ed.* **2013**, *52* (40), 10477–10481.

(318) Falmbigl, M.; Fiedler, A.; Atkins, R. E.; Fischer, S. F.; Johnson, D. C. Suppressing a Charge Density Wave by Changing Dimensionality in the Ferecrystalline Compounds $([SnSe]_{1.15})_1(VSe_2)_n$ with n = 1, 2, 3, 4. *Nano Lett.* **2015**, *15*, 943–948.

(319) Li, L. J.; Zhao, W. J.; Liu, B.; Ren, T. H.; Eda, G.; Loh, K. P. Enhancing Charge-Density-Wave Order in 1T-$TiSe_2$ Nanosheet by Encapsulation with Hexagonal Boron Nitride. *Appl. Phys. Lett.* **2016**, *109* (14), 141902.

(320) Xi, X.; Wang, Z.; Zhao, W.; Park, J.-H.; Law, K. T.; Berger, H.; Forró, L.; Shan, J.; Mak, K. F. Ising Pairing in Superconducting $NbSe_2$ Atomic Layers. *Nat. Phys.* **2015**, *12* (2), 139–143.

(321) Navarro-Moratalla, E.; Island, J. O.; Mañas-Valero, S.; Pinilla-Cienfuegos, E.; Castellanos-Gomez, A.; Quereda, J.; Rubio-Bollinger, G.; Chirolli, L.; Silva-Guillén, J. A.; Agraït, N.; et al. Enhanced Superconductivity in Atomically Thin TaS_2. *Nat. Commun.* **2016**, *7*, 11043.

(322) Saito, Y.; Nakamura, Y.; Bahramy, M. S.; Kohama, Y.; Ye, J.; Kasahara, Y.; Nakagawa, Y.; Onga, M.; Tokunaga, M.; Nojima, T.; et al. Superconductivity Protected by Spin–Valley Locking in Ion-Gated MoS_2. *Nat. Phys.* **2015**, *12* (2), 144–149.

(323) Staley, N. E.; Wu, J.; Eklund, P.; Liu, Y.; Li, L.; Xu, Z. Electric Field Effect on Superconductivity in Atomically Thin Flakes of $NbSe_2$. *Phys. Rev. B* **2009**, *80* (18), 184505.

(324) Alemayehu, M. B.; Falmbigl, M.; Ta, K.; Johnson, D. C. Effect of Local Structure of $NbSe_2$ on the Transport Properties of $[(SnSe)_{1.16}]_1[(NbSe_2)]_n$ Ferecrystals. *Chem. Mater.* **2015**, *27*, 2158–2164.

(325) Alemayehu, M. B.; Mitchson, G.; Ditto, J.; Hanken, B. E.; Asta, M.; Johnson, D. C. Charge Transfer between PbSe and $NbSe_2$ in $[(PbSe)_{1.14}]_m(NbSe_2)_1$ Ferecrystalline Compounds. *Chem. Mater.* **2014**, *26* (5), 1859–1866.

(326) Manna, S.; Kamlapure, A.; Cornils, L.; Hänke, T.; Hedegaard, E. M. J.; Bremholm, M.; Iversen, B. B.; Hofmann, P.; Wiebe, J.; Wiesendanger, R.; et al. Interfacial Superconductivity in a Bi-Collinear Antiferromagnetically Ordered FeTe Monolayer on a Topological Insulator. *Nat. Commun.* **2017**, *8*, 14074.

(327) Hänke, T.; Singh, U. R.; Cornils, L.; Manna, S.; Kamlapure, A.; Bremholm, M.; Hedegaard, E. M. J.; Iversen, B. B.; Hofmann, P.; Hu, J.; et al. Reorientation of the Diagonal Double-Stripe Spin Structure at $Fe_{1+y}Te$ Bulk and Thin-Film Surfaces. *Nat. Commun.* **2017**, *8*, 13939.

(328) Tian, Y. C.; Zhang, W. H.; Li, F. S.; Wu, Y. L.; Wu, Q.; Sun, F.; Zhou, G. Y.; Wang, L.; Ma, X.; Xue, Q.-K.; et al. Ultrafast Dynamics Evidence of High Temperature Superconductivity in Single Unit Cell FeSe on $SrTiO_3$. *Phys. Rev. Lett.* **2016**, *116* (10), 107001.

(329) Zhang, Y.; Lee, J. J.; Moore, R. G.; Li, W.; Yi, M.; Hashimoto, M.; Lu, D. H.; Devereaux, T. P.; Lee, D.-H.; Shen, Z.-X. Superconducting Gap Anisotropy in Monolayer FeSe Thin Film. *Phys. Rev. Lett.* **2016**, *117* (11), 117001.

(330) Lei, B.; Cui, J. H.; Xiang, Z. J.; Shang, C.; Wang, N. Z.; Ye, G. J.; Luo, X. G.; Wu, T.; Sun, Z.; Chen, X. H. Evolution of High-Temperature Superconductivity from a Low- T_c Phase Tuned by Carrier Concentration in FeSe Thin Flakes. *Phys. Rev. Lett.* **2016**, *116* (7), 077002.

(331) Huang, Z. C.; Pu, Y. J.; Xu, H. C.; Xu, D. F.; Song, Q.; Lou, X.; Wen, C. H. P.; Peng, R.; Feng, D. L. Electronic Structure and Superconductivity of Single-Layer FeSe on $Nb:SrTiO_3$ /$LaAlO_3$ with Varied Tensile Strain. *2D Mater.* **2016**, *3* (1), 014005.

(332) Zhao, L.; Liang, A.; Yuan, D.; Hu, Y.; Liu, D.; Huang, J.; He, S.; Shen, B.; Xu, Y.; Liu, X.; et al. Common Electronic Origin of Superconductivity in (Li,Fe)OHFeSe Bulk Superconductor and Single-Layer FeSe/$SrTiO_3$ Films. *Nat. Commun.* **2016**, *7*, 10608.

(333) Wang, Z. F.; Zhang, H.; Liu, D.; Liu, C.; Tang, C.; Song, C.; Zhong, Y.; Peng, J.; Li, F.; Nie, C.; et al. Topological Edge States in a High-Temperature Superconductor FeSe/$SrTiO_3$ (001) Film. *Nat. Mater.* **2016**, *15* (9), 968–973.

(334) Zhu, X.; Guo, Y.; Cheng, H.; Dai, J.; An, X.; Zhao, J.; Tian, K.; Wei, S.; Cheng Zeng, X.; Wu, C.; et al. Signature of Coexistence of Superconductivity and Ferromagnetism in Two-Dimensional NbSe2 Triggered by Surface Molecular Adsorption. *Nat. Commun.* **2016**, *7*, 11210.

(335) Chiritescu, C.; Cahill, D. G.; Nguyen, N.; Johnson, D.; Bodapati, A.; Keblinski, P.; Zschack, P. Ultralow Thermal Conductivity in Disordered, Layered WSe_2 Crystals. *Science.* **2007**, *315* (5810), 351–353.

(336) Chiritescu, C.; Cahill, D. G.; Heideman, C.; Lin, Q.; Mortensen, C.; Nguyen, N. T.; Johnson, D.; Rostek, R.; Böttner, H. Low Thermal Conductivity in Nanoscale Layered Materials Synthesized by the Method of Modulated Elemental Reactants. *J. Appl. Phys.* **2008**, *104* (3), 033533.

(337) Chiritescu, C.; Mortensen, C.; Cahill, D. G.; Johnson, D.; Zschack, P. Lower Limit to the Lattice Thermal Conductivity of Nanostructured Bi_2Te_3-Based Materials. *J. Appl. Phys.* **2009**, *106* (7), 073503.

(338) Nguyen, N. T.; Berseth, P. A.; Lin, Q.; Chiritescu, C.; Cahill, D. G.; Mavrokefalos, A.; Shi, L.; Zschack, P.; Anderson, M. D.; Anderson, I. M.; et al. Synthesis and Properties of Turbostratically Disordered, Ultrathin WSe_2 Films. *Chem. Mater.* **2010**, *22* (9), 2750–2756.

(339) Wan, C.; Wang, Y.; Norimatsu, W.; Kusunoki, M.; Koumoto, K. Nanoscale Stacking Faults Induced Low Thermal Conductivity in Thermoelectric Layered Metal Sulfides. *Appl. Phys. Lett.* **2012**, *100* (10), 101913.

(340) Mavrokefalos, A.; Lin, Q.; Beekman, M.; Seol, J. H.; Lee, Y. J.; Kong, H.; Pettes, M. T.; Johnson, D. C.; Shi, L. In-Plane Thermal and Thermoelectric Properties of Misfit-Layered $[(PbSe)_{0.99}]_x(WSe_2)_x$ Superlattice Thin Films. *Appl. Phys. Lett.* **2010**, *96* (18), 181908.

(341) Ma, J.; Chen, Y.; Han, Z.; Li, W. Strong Anisotropic Thermal Conductivity of Monolayer WTe_2. *2D Mater.* **2016**, *3* (4), 045010.

(342) Bhatt, R.; Basu, R.; Bhattacharya, S.; Singh, A.; Aswal, D. K.; Gupta, S. K.; Okram, G. S.; Ganesan, V.; Venkateshwarlu, D.; Surgers, C.; et al. Low Temperature Thermoelectric Properties of Cu Intercalated TiSe2: A Charge Density Wave Material. *Appl. Phys. A* **2013**, *111* (2), 465–470.

(343) Cho, J.; Losego, M. D.; Zhang, H. G.; Kim, H.; Zuo, J.; Petrov, I.; Cahill, D. G.; Braun, P. V. Electrochemically Tunable Thermal Conductivity of Lithium Cobalt Oxide. *Nat. Commun.* **2014**, *5*, 862–868.

(344) Li, G.; Ding, G.; Gao, G. Thermoelectric Properties of $SnSe_2$ Monolayer. *J. Phys. Condens. Matter* **2017**, *29* (1), 015001.

(345) Ding, G.; Gao, G. Y.; Huang, Z.; Zhang, W.; Yao, K. Thermoelectric Properties of Monolayer MSe_2 (M = Zr, Hf): Low Lattice Thermal Conductivity and a Promising Figure of Merit. *Nanotechnology* **2016**, *27* (37), 375703.

(346) Yin, C.; Hu, Q.; Wang, G.; Huang, T.; Zhou, X.; Zhang, X.; Dou, Y.; Kang, B.; Tang, J.; Liu, N.; et al. Intriguing Substitution of Conducting Layer Triggered Enhancement of Thermoelectric Performance in Misfit-Layered $(SnS)_{1.2}(TiS_2)_2$. *Appl. Phys. Lett.* **2017**, *110* (4), 043507.

(347) Wan, C.; Wang, Y.; Wang, N.; Norimatsu, W.; Kusunoki, M.; Koumoto, K. Intercalation: Building a Natural Superlattice for Better Thermoelectric Performance in Layered Chalcogenides. *J. Electron. Mater.* **2011**, *40* (5), 1271–1280.

(348) Merrill, D.; Moore, D.; Bauers, S.; Falmbigl, M.; Johnson, D. Misfit Layer Compounds and Ferecrystals: Model Systems for Thermoelectric Nanocomposites. *Materials (Basel).* **2015**, *8*, 2000–2029.

(349) Mashhadi, S.; Duong, D. L.; Burghard, M.; Kern, K. Efficient Photothermoelectric Conversion in Lateral Topological Insulator Heterojunctions. *Nano Lett.* **2017**, *17*, 214–219.

(350) Das, P. K.; Di Sante, D.; Vobornik, I.; Fujii, J.; Okuda, T.; Bruyer, E.; Gyenis, A.; Feldman, B. E.; Tao, J.; Ciancio, R.; et al. Layer-Dependent Quantum Cooperation of Electron and Hole States in the Anomalous Semimetal WTe_2. *Nat. Commun.* **2016**, *7*, 10847.

(351) Chang, T.-R.; Xu, S.-Y.; Chang, G.; Lee, C.-C.; Huang, S.-M.; Wang, B.; Bian, G.; Zheng, H.; Sanchez, D. S.; Belopolski, I.; et al. Prediction of an Arc-Tunable Weyl Fermion Metallic State in $Mox W_{1-x}Te_2$. *Nat. Commun.* **2016**, *7*, 10639.

(352) Wang, Z.; Gresch, D.; Soluyanov, A. A.; Xie, W.; Kushwaha, S.; Dai, X.; Troyer, M.; Cava, R. J.; Bernevig, B. A. $MoTe_2$: A Type-II Weyl Topological Metal. *Phys. Rev. Lett.* **2016**, *117* (5), 056805.

(353) Sankar, R.; Narsinga Rao, G.; Muthuselvam, I. P.; Butler, C.; Kumar, N.; Senthil Murugan, G.; Shekhar, C.; Chang, T.-R.; Wen, C.-Y.; Chen, C.-W.; et al. Polymorphic Layered $MoTe_2$ from Semiconductor, Topological Insulator, to Weyl Semimetal. *Chem. Mater.* **2017**, *29* (2), 699–707.

(354) Zeugner, A.; Kaiser, M.; Schmidt, P.; Menshchikova, T. V.; Rusinov, I. P.; Markelov, A. V.; Van den Broek, W.; Chulkov, E. V.; Doert, T.; Ruck, M.; et al. Modular Design with 2D Topological-Insulator Building Blocks: Optimized Synthesis and Crystal Growth, Crystal and Electronic Structures of Bi_xTeI (x = 2, 3). *Chem. Mater.* **2017**, acs.chemmater.6b05038.

(355) Dai, J.; West, D.; Wang, X.; Wang, Y.; Kwok, D.; Cheong, S.-W.; Zhang, S. B.; Wu, W. Toward the Intrinsic Limit of the Topological Insulator Bi_2Se_3. *Phys. Rev. Lett.* **2016**, *117* (10), 106401.

(356) Buchenau, S.; Sergelius, P.; Wiegand, C.; Bäß ler, S.; Zierold, R.; Shin, H. S.; Rübhausen, M.; Gooth, J.; Nielsch, K. Symmetry Breaking of the Surface Mediated Quantum Hall Effect in Bi_2Se_3 Nanoplates Using Fe_3O_4 Substrates. *2D Mater.* **2017**, *4* (1), 015044.

(357) Vajner, C.; Yan, H.; Guo, L.; Mathews, M.; Kuhlman, M.; Benefield, S.; Ulrich, S.; Zolghadr, E.; Kung, P.; Li, L.; et al. Thickness Identification of Epitaxial Bi_2Te_3 via Optical Contrast. *2D Mater.* **2016**, *3* (2), 021010.

(358) Park, J. Y.; Lee, G.-H.; Jo, J.; Cheng, A. K.; Yoon, H.; Watanabe, K.; Taniguchi, T.; Kim, M.; Kim, P.; Yi, G.-C. Molecular Beam Epitaxial Growth and Electronic Transport Properties of High Quality Topological Insulator Bi_2Se_3 Thin Films on Hexagonal Boron Nitride. *2D Mater.* **2016**, *3* (3), 035029.

(359) Tu, N. H.; Tanabe, Y.; Satake, Y.; Huynh, K. K.; Tanigaki, K.; Fu, L.; Kane, C. L.; Mele, E. J.; Chen, Y. L.; Hsieh, D.; et al. In-Plane Topological p-n Junction in the Three-Dimensional Topological Insulator $Bi_{2-x}SbxTe_{3-y}Se_y$. *Nat. Commun.* **2016**, *7*, 13763.

(360) Takane, D.; Souma, S.; Sato, T.; Takahashi, T.; Segawa, K.; Ando, Y. Work Function of Bulk-Insulating Topological Insulator $Bi_{2-x}Sb_xTe_{3-y}Se_Y$. *Appl. Phys. Lett.* **2016**, *109* (9), 091601.

(361) Yan, H.; Vajner, C.; Kuhlman, M.; Guo, L.; Li, L.; Araujo, P. T.; Wang, H.T. Elastic Behavior of Bi_2Se_3 2D Nanosheets Grown by van Der Waals Epitaxy. *Appl. Phys. Lett.* **2016**, *109* (3), 032103.

(362) Whitney, W. S.; Brar, V. W.; Ou, Y.; Shao, Y.; Davoyan, A. R.; Basov, D. N.; He, K.; Xue, Q.-K.; Atwater, H. A. Gate-Variable Mid-Infrared Optical Transitions in a $(Bi_{1-x}Sb_x)_2Te_3$ Topological Insulator. *Nano Lett.* **2017**, *17* (1), 255–260.

(363) Kim, J.; Jhi, S.-H.; Wu, R. Engineering Topological Surface States of Cr-Doped Bi_2Se_3 Films by Spin Reorientation and Electric Field. *Nano Lett.* **2016**, *16* (10), 6656–6660.

(364) Salehi, M.; Shapourian, H.; Koirala, N.; Brahlek, M. J.; Moon, J.; Oh, S. Finite-Size and Composition-Driven Topological Phase Transition in $(Bi_{1-x}In_x)_2Se_3$ Thin Films. *Nano Lett.* **2016**, *16* (9), 5528–5532.

(365) Krieg, J.; Chen, C.; Avila, J.; Zhang, Z.; Sigle, W.; Zhang, H.; Trautmann, C.; Asensio, M. C.; Toimil-Molares, M. E. Exploring the Electronic Structure and Chemical Homogeneity of Individual Bi_2Te_3 Nanowires by Nano-Angle-Resolved Photoemission Spectroscopy. *Nano Lett.* **2016**, *16* (7), 4001–4007.

(366) Huang, W.-K.; Zhang, K.-W.; Yang, C.-L.; Ding, H.; Wan, X.; Li, S.-C.; Evans, J. W.; Han, Y. Tailoring Kinetics on a Topological Insulator Surface by Defect-Induced Strain: Pb Mobility on Bi_2Te_3. *Nano Lett.* **2016**, *16* (7), 4454–4461.

(367) Caputo, M.; Panighel, M.; Lisi, S.; Khalil, L.; Santo, G. Di; Papalazarou, E.; Hruban, A.; Konczykowski, M.; Krusin-Elbaum, L.; Aliev, Z. S.; et al. Manipulating the Topological Interface by Molecular Adsorbates: Adsorption of Co-Phthalocyanine on Bi_2Se_3. *Nano Lett.* **2016**, *16* (6), 3409–3414.

(368) Parra, C.; Rodrigues da Cunha, T. H.; Contryman, A. W.; Kong, D.; Montero-Silva, F.; Rezende Gonçalves, P. H.; Dos Reis, D. D.; Giraldo-Gallo, P.; Segura, R.; Olivares, F.; et al. Phase Separation of Dirac Electrons in Topological Insulators at the Spatial Limit. *Nano Lett.* **2017**, *17* (1), 97–103.

(369) Sánchez-Barriga, J.; Varykhalov, A.; Springholz, G.; Steiner, H.; Kirchschlager, R.; Bauer, G.; Caha, O.; Schierle, E.; Weschke, E.; Ünal, A. A.; et al. Nonmagnetic Band Gap at the Dirac Point of the Magnetic Topological Insulator $(Bi_{1-x}Mn_x)_2Se_3$. *Nat. Commun.* **2016**, *7*, 10559.

(370) He, Q. L.; Kou, X.; Grutter, A. J.; Yin, G.; Pan, L.; Che, X.; Liu, Y.; Nie, T.; Zhang, B.; Disseler, S. M.; et al. Tailoring Exchange Couplings in Magnetic Topological-Insulator/Antiferromagnet Heterostructures. *Nat. Mater.* **2016**, *16* (1), 94–100.

Chapter II

(1) Novoselov, K. S.; Geim, A. K.; Morozov, S. V; Jiang, D.; Zhang, Y.; Dubonos, S. V; Grigorieva, I. V; Firsov, A. A.; Novoselov, K. S. Electric Field Effect in Atomically Thin Carbon Films. *Science.* **2007**, *306*, 183–191.

(2) Novoselov, K. S. Nobel Lecture: Graphene: Materials in the Flatland. *Rev. Mod. Phys.* **2011**, *83*, 837–849.

(3) Grubišić Čabo, A.; Miwa, J. A.; Grønborg, S. S.; Riley, J. M.; Johannsen, J. C.; Cacho, C.; Alexander, O.; Chapman, R. T.; Springate, E.; Grioni, M.; et al. Observation of Ultrafast Free Carrier Dynamics in Single Layer MoS_2. *Nano Lett.* **2015**, *15*, 5883–5887.

(4) Bruix, A.; Miwa, J. A.; Hauptmann, N.; Wegner, D.; Ulstrup, S.; Grønborg, S. S.; Sanders, C. E.; Dendzik, M.; Grubišić Čabo, A.; Bianchi, M.; et al. Single-Layer MoS_2 on Au(111): Band Gap Renormalization and Substrate Interaction. *Phys. Rev. B* **2016**, *93*, 165422.

(5) Geim, A. K. Nobel Lecture: Random Walk to Graphene. *Rev. Mod. Phys.* **2011**, *83*, 851–862.

(6) Hamann, D. M.; Hadland, E. C.; Johnson, D. C. Heterostructures Containing Dichalcogenides-New Materials with Predictable Nanoarchitectures and Novel Emergent Properties. *Semicond. Sci. Technol.* **2017**, *32*, 093004.

(7) Jariwala, D.; Marks, T. J.; Hersam, M. C. Mixed-Dimensional van Der Waals Heterostructures. *Nat. Mater.* **2016**, *16*, 170–181.

(8) Mak, K. F.; Lee, C.; Hone, J.; Shan, J.; Heinz, T. F. Atomically Thin MoS_2: A New Direct-Gap Semiconductor. *Phys. Rev. Lett.* **2010**, *105*.

(9) Zhao, W.; Ghorannevis, Z.; Chu, L.; Toh, M.; Kloc, C.; Tan, P. H.; Eda, G. Evolution of Electronic Structure in Atomically Thin Sheets of WS_2 and WSe_2. *ACS Nano* **2013**, *7*, 791–797.

(10) Komsa, H. P.; Krasheninnikov, A. V. Electronic Structures and Optical Properties of Realistic Transition Metal Dichalcogenide Heterostructures from First Principles. *Phys. Rev. B* **2013**, *88*, 085318.

(11) Ulstrup, S.; Čabo, A. G.; Miwa, J. A.; Riley, J. M.; Grønborg, S. S.; Johannsen, J. C.; Cacho, C.; Alexander, O.; Chapman, R. T.; Springate, E.; et al. Ultrafast Band Structure Control of a Two-Dimensional Heterostructure. *ACS Nano* **2016**, *10*, 6315–6322.

(12) Ugeda, M. M.; Bradley, A. J.; Shi, S. F.; da Jornada, F. H.; Zhang, Y.; Qiu, D. Y.; Ruan, W.; Mo, S. K.; Hussain, Z.; Shen, Z. X.; et al. Giant Bandgap Renormalization and Excitonic Effects in a Monolayer Transition Metal Dichalcogenide Semiconductor. *Nat. Mater.* **2014**, *13*, 1091–1095.

(13) Xie, Y.; Wang, Z.; Zhan, Y.; Zhang, P.; Wu, R.; Jiang, T.; Wu, S.; Wang, H.; Zhao, Y.; Nan, T.; et al. Controllable Growth of Monolayer MoS_2 by Chemical Vapor Deposition via Close MoO_2 Precursor for Electrical and Optical Applications. *Nanotechnology* **2017**, *28*, 084001.

(14) Shaw, J. C.; Zhou, H.; Chen, Y.; Weiss, N. O.; Liu, Y.; Huang, Y.; Duan, X. Chemical Vapor Deposition Growth of Monolayer $MoSe_2$ Nanosheets. *Nano Res.* **2014**, *7*, 511–517.

(15) Schmidt, H.; Wang, S.; Chu, L.; Toh, M.; Kumar, R.; Zhao, W.; Castro Neto, A. H.; Martin, J.; Adam, S.; Özyilmaz, B.; et al. Transport Properties of Monolayer MoS_2 Grown by Chemical Vapor Deposition. *Nano Lett.* **2014**, *14*, 1909–1913.

(16) Shang, S.-L.; Lindwall, G.; Wang, Y.; Redwing, J. M.; Anderson, T.; Liu, Z.-K. Lateral Versus Vertical Growth of Two-Dimensional Layered Transition-Metal Dichalcogenides: Thermodynamic Insight into MoS_2. *Nano Lett.* **2016**, *16*, 5742–5750.

(17) Ling, X.; Lee, Y. H.; Lin, Y.; Fang, W.; Yu, L.; Dresselhaus, M. S.; Kong, J. Role of the Seeding Promoter in MoS_2 Growth by Chemical Vapor Deposition. *Nano Lett.* **2014**, *14*, 464–472.

(18) Tsai, M. L.; Su, S. H.; Chang, J. K.; Tsai, D. S.; Chen, C. H.; Wu, C. I.; Li, L. J.; Chen, L. J.; He, J. H. Monolayer MoS_2 Heterojunction Solar Cells. *ACS Nano* **2014**, *8*, 8317–8322.

(19) Cain, J. D.; Shi, F.; Wu, J.; Dravid, V. P. Growth Mechanism of Transition Metal Dichalcogenide Monolayers: The Role of Self-Seeding Fullerene Nuclei. *ACS Nano* **2016**, *10*, 5440–5445.

(20) Kang, K.; Xie, S.; Huang, L.; Han, Y.; Huang, P. Y.; Mak, K. F.; Kim, C. J.; Muller, D.; Park, J. High-Mobility Three-Atom-Thick Semiconducting Films with Wafer-Scale Homogeneity. *Nature* **2015**, *520*, 656–660.

(21) Ji, Q.; Zhang, Y.; Gao, T.; Zhang, Y.; Ma, D.; Liu, M.; Chen, Y.; Qiao, X.; Tan, P. H.; Kan, M.; et al. Epitaxial Monolayer MoS_2 on Mica with Novel Photoluminescence. *Nano Lett.* **2013**, *13*, 3870–3877.

(22) Lee, Y. H.; Zhang, X. Q.; Zhang, W.; Chang, M. T.; Lin, C. Te; Chang, K. Di; Yu, Y. C.; Wang, J. T. W.; Chang, C. S.; Li, L. J.; et al. Synthesis of Large-Area MoS_2 Atomic Layers with Chemical Vapor Deposition. *Adv. Mater.* **2012**, *24*, 2320–2325.

(23) Najmaei, S.; Liu, Z.; Zhou, W.; Zou, X.; Shi, G.; Lei, S.; Yakobson, B. I.; Idrobo, J. C.; Ajayan, P. M.; Lou, J. Vapour Phase Growth and Grain Boundary Structure of Molybdenum Disulphide Atomic Layers. *Nat. Mater.* **2013**, *12*, 754–759.

(24) Govind Rajan, A.; Warner, J. H.; Blankschtein, D.; Strano, M. S. Generalized Mechanistic Model for the Chemical Vapor Deposition of 2D Transition Metal Dichalcogenide Monolayers. *ACS Nano* **2016**, *10*, 4330–4344.

(25) Wang, S.; Rong, Y.; Fan, Y.; Pacios, M.; Bhaskaran, H.; He, K.; Warner, J. H. Shape Evolution of Monolayer MoS_2 Crystals Grown by Chemical Vapor Deposition. *Chem. Mater.* **2014**, *26*, 6371–6379.

(26) Liu, B.; Fathi, M.; Chen, L.; Abbas, A.; Ma, Y.; Zhou, C. Chemical Vapor Deposition Growth of Monolayer WSe_2 with Tunable Device Characteristics and Growth Mechanism Study. *ACS Nano* **2015**, *9*, 6119–6127.

(27) Dumcenco, D. O.; Kobayashi, H.; Liu, Z.; Huang, Y. S.; Suenaga, K. Visualization and Quantification of Transition Metal Atomic Mixing in $Mo_{1-x}WxS_2$ Single Layers. *Nat. Commun.* **2013**, *4*, 1351.

(28) Matetskiy, A. V.; Kibirev, I. A.; Hirahara, T.; Hasegawa, S.; Zotov, A. V.; Saranin, A. A. Direct Observation of a Gap Opening in Topological Interface States of $MnSe/Bi_2Se_3$ Heterostructure. *Appl. Phys. Lett.* **2015**, *107*, 091604.

(29) Hirahara, T.; Eremeev, S. V.; Shirasawa, T.; Okuyama, Y.; Kubo, T.; Nakanishi, R.; Akiyama, R.; Takayama, A.; Hajiri, T.; Ideta, S.; et al. Large-Gap Magnetic Topological Heterostructure Formed by Subsurface Incorporation of a Ferromagnetic Layer. *Nano Lett.* **2017**, *17*, 3493–3500.

(30) Ohlhausen, J. A.; Zavadil, K. R. Time-of-Flight Secondary Ion Mass Spectrometry Measurements of a Fluorocarbon-Based Self-Assembled Monolayer on Si. *J. Vac. Sci. Technol. A Vacuum, Surfaces, Film.* **2006**, *24*, 1172–1178.

(31) Laguitton, D.; Parrish, W. Simultaneous Determination of Composition and Mass Thickness of Thin Films by Quantitative X-Ray Fluorescence Analysis. *Anal. Chem.* **1977**, *49*, 1152–1156.

(32) Remmel, T.; Werho, D. Development of an Xrf Metrology Method for Composition and Thickness of Barium Strontium Titanate Thin Films. In *Advances*; 2000; Vol. 42, pp 99–108.

(33) De Weijer, P. Van; De Boer, D. K. G. Elemental Analysis of Thin Layers by X-Rays. *Philips J. Res.* **1993**, *4747*, 247–2623.

(34) Sitko, R.; Zawisz, B. Quantification in X-Ray Fluorescence Spectrometry. In *X-Ray Spectroscopy*; 2012.

(35) Vrielink, J. A. M.; Tiggelaar, R. M.; Gardeniers, J. G. E.; Lefferts, L. Applicability of X-Ray Fluorescence Spectroscopy as Method to Determine Thickness and Composition of Stacks of Metal Thin Films: A Comparison with Imaging and Profilometry. *Thin Solid Films* **2012**, *520*, 1740–1744.

(36) Klenk, M.; Schenker, O.; Probst, U.; Bucher, E. X-Ray Fluorescence Measurements of Thin Film Chalcopyrite Solar Cells. *Sol. Energy Mater. Sol. Cells* **1999**, *58*, 299–319.

(37) Esters, M. Deposition Software for the Inficon IC6 Deposition Controller https://github.com/marcoesters/deposition_ic6.

(38) Fister, L.; Li, X.; McConnell, J.; Novet, T.; Johnson, D. C. Deposition System for the Synthesis of Modulated, Ultrathin-film Composites. *J. Vac. Sci. Technol. A Vacuum, Surfaces, Film.* **1993**, *11*, 3014–3019.

(39) Sherman, J. The Theoretical Derivation of Fluorescent X-Ray Intensities from Mixtures. *Spectrochim. Acta* **1955**, *7*, 283–306.

(40) Sauter, F. Über Den Atomaren Photoeffekt Bei Großer Härte Der Anregenden Strahlung. *Ann. d. Phys* **1931**, *9*, 217.

(41) Sauter, F. Über Den Atomaren Photoeffekt in Der K-Schale Nach Der Relativistischen Wellenmechanik Diracs. *Ann. d. Phys* **1931**, *11*, 454.

(42) Alemayehu, M. B.; Mitchson, G.; Ditto, J.; Hanken, B. E.; Asta, M.; Johnson, D. C. Charge Transfer between PbSe and $NbSe_2$ in $[(PbSe)_{1.14}]_m(NbSe_2)_1$ Ferecrystalline Compounds. *Chem. Mater.* **2014**, *26* (5), 1859–1866.

(43) Bronsema, K. D.; De Boer, J. L.; Jellinek, F. On the Structure of Molybdenum Diselenide and Disulfide. *Zeitschrift für Anorg. und Allg. Chemie* **1986**, *540*, 15–17.

Chapter III

(1) Noh, M.; Thiel, J.; Johnson, D. C. Synthesis of Crystalline Superlattices by Controlled Crystallization of Modulated Reactants. *Science.* **1995**, *270* (5239), 1181–1184.

(2) Johnson, D. C. Controlled Synthesis of New Compounds Using Modulated Elemental Reactants. *Curr. Opin. Solid State Mater. Sci.* **1998**, *3*, 159–167.

(3) Stein, A.; Keller, S. W.; Mallouk, T. E. Turning down the Heat: Design and Mechanism in Solid-State Synthesis. *Science* **1993**, *259* (5101), 1558–1564.

(4) Disalvo, F. J. Solid-State Chemistry: A a Rediscovered Chemical Frontier. *Science* **1990**, *247* (4943), 649–655.

(5) Noh, M; Johnson, C.D.; Hornbostel, M.D.; Thiel, J.; Johnson, D. C. Control of Reaction Pathway and the Nanostructure of Final Products through the Design of Modulated Elemental Reactants. *Chem. Mater.* **1996**, *8*, 1625-1635.

(6) Novet, T.; Johnson, D. C. New Synthetic Approach to Extended Solids: Selective Synthesis of Iron Silicides via the Amorphous State. *J. Am. Chem. Soc.* **1991**, *113* (9), 3398–3403.

(7) Fister, L.; Li, X.; McConnell, J.; Novet, T.; Johnson, D. C. Deposition System for the Synthesis of Modulated, Ultrathin-film Composites. *J. Vac. Sci. Technol. A Vacuum, Surfaces, Film.* **1993**, *11*, 3014–3019.

(8) Esters, M. Deposition Software for the Inficon IC6 Deposition Controller https://github.com/marcoesters/deposition_ic6.

(9) Choffel, M. A.; Hamann, D. M.; Joke, J. A.; Cordova, D. L. M.; Johnson, D. C. The Reaction between Mn and Se Layers. *Zeitschrift für Anorg. und Allg. Chemie* **2018**, *644* (24), 1875–1880.

(10) Westover, R. D.; Ditto, J.; Falmbigl, M.; Hay, Z. L.; Johnson, D. C. Synthesis and Characterization of Quaternary Monolayer Thick $MoSe_2$/SnSe/$NbSe_2$/SnSe Heterojunction Superlattices. *Chem. Mater.* **2015**, *27*, 6411–6417.

(11) Wood, S. R.; Merrill, D. R.; Mitchson, G.; Lygo, A. C.; Bauers, S. R.; Hamann, D. M.; Sutherland, D. R.; Ditto, J.; Johnson, D. C. Modulation Doping in Metastable Heterostructures via Kinetically Controlled Substitution. *Chem. Mater.* **2017**, *29*, 773–779.

(12) Lin, Q.; Heideman, C. L.; Nguyen, N.; Zschack, P.; Chiritescu, C.; Cahill, D. G.; Johnson, D. C. Designed Synthesis of Families of Misfit-Layered Compounds. *Eur. J. Inorg. Chem.* **2008**, *2008*, 2382–2385.

(13) Merrill, D. R.; Sutherland, D. R.; Ditto, J. J.; Moore, D. B.; Falmbigl, M.; Medlin, D. L.; Johnson, D. C. The Synthesis of $[(PbSe)_{1+\delta}]_m(TiSe_2)_n[(SnSe_2)_{1+\gamma}]_m(TiSe_2)_n$ Heterostructures with Designed Nanoarchitectures by Self Assembly of Amorphous Precursors. *Nanoscale* **2016**, *8*.

(14) Chiritescu, C.; Cahill, D. G.; Nguyen, N.; Johnson, D.; Bodapati, A.; Keblinski, P.; Zschack, P. Ultralow Thermal Conductivity in Disordered, Layered WSe2 Crystals. *Science.* **2007**, *315* (5810), 351–353.

(15) Atkins, R.; Wilson, J.; Zschack, P.; Grosse, C.; Neumann, W.; Johnson, D. C. Synthesis of $[(SnSe)_{1.15}]_m((TaSe_2)_n$ Ferecrystals: Structurally Tunable Metallic Compounds. *Chem. Mater.* **2012**, *24*, 4594–4599.

(16) Moore, D. B.; Beekman, M.; Disch, S.; Zschack, P.; Häusler, I.; Neumann, W.; Johnson, D. C. Synthesis, Structure, and Properties of Turbostratically Disordered $(PbSe)_{1.18}(TiSe_2)_2$. *Chem. Mater.* **2013**, *25*, 2404–2409.

(17) Merrill, D. R.; Moore, D. B.; Ditto, J.; Sutherland, D. R.; Falmbigl, M.; Winkler, M.; Pernau, H.-F.; Johnson, D. C. The Synthesis, Structure, and Electrical Characterization of $(SnSe)_{1.2}TiSe_2$. *Eur. J. Inorg. Chem.* **2015**, *2015*, 83–91.

(18) Harris, F. R.; Standridge, S.; Feik, C.; Johnson, D. C. Design and Synthesis of$[(Bi_2Te_3)_x(TiTe_2)_y]$ Superlattices. *Angew. Chemie Int. Ed.* **2003**, *42* (43), 5296–5299.

(19) Smeller, M. M.; Heideman, C. L.; Lin, Q.; Beekman, M.; Anderson, M. D.; Zschack, P.; Anderson, I. M.; Johnson, D. C. Structure of Turbostratically Disordered Misfit Layer Compounds $[(PbSe)_{0.99}]_1[WSe_2]_1$, $[(PbSe)_{1.00}]_1[MoSe_2]_1$, and $[(SnSe)_{1.03}]_1$. *Zeitschrift für Anorg. und Allg. Chemie* **2012**, *638*, 2632–2639.

(20) Hornbostel, M. D.; Hyer, E. J.; Edvalson, J. H.; Johnson, D. C. Systematic Study of New Rare Earth Element-Iron-Antimony Skutterudites Synthesized Using Multilayer Precursors. *Inorg. Chem.* **1997**, *36* (19), 4270–4274.

(21) Esters, M.; Alemayehu, M. B.; Jones, Z.; Nguyen, N. T.; Anderson, M. D.; Grosse, C.; Fischer, S. F.; Johnson, D. C. Synthesis of Inorganic Structural Isomers By Diffusion-Constrained Self-Assembly of Designed Precursors: A Novel Type of Isomerism. *Angew. Chemie Int. Ed.* **2015**, *54* (4), 1130–1134.

(22) Hamann, D. M.; Bardgett, D.; Cordova, D. L. M.; Maynard, L. A.; Hadland, E. C.; Lygo, A. C.; Wood, S. R.; Esters, M.; Johnson, D. C. Sub-Monolayer Accuracy in Determining the Number of Atoms per Unit Area in Ultrathin Films Using X-Ray Fluorescence. *Chem. Mater.* **2018**, *30* (18), 6209–6216.

Chapter IV

(1) Shakouri, A., Recent Developments in Semiconductor Thermoelectric Physics and Materials. In *Annual Review of Materials Research, Vol 41*, Clarke, D. R.; Fratzl, P., Eds. Annual Reviews: Palo Alto, **2011**; 41, 399-431.

(2) Cahill, D. G., Extremes of heat conduction-Pushing the boundaries of the thermal conductivity of materials. *MRS Bulletin* **2012,** *37* (9), 855-863.

(3) Gunning, N. S.; Feser, J.; Beekman, M.; Cahill, D. G.; Johnson, D. C., Synthesis and Thermal Properties of Solid-State Structural Isomers: Ordered lntergrowths of SnSe and $MoSe_2$. *Journal of the American Chemical Society* **2015,** *137* (27), 8803-8809.

(4) Mortensen, C.; Beekman, M.; Johnson, D. C., Probing the effects of alloying, grain size, and turbostratic disorder on thermal conductivity. *Science of Advanced Materials* **2011,** *3* (4), 639-645.

(5) Chiritescu, C.; Mortensen, C.; Cahill, D. G.; Johnson, D.; Zschack, P., Lower limit to the lattice thermal conductivity of nanostructured Bi_2Te_3-based materials. *Journal of Applied Physics* **2009,** *106* (7), 073503.

(6) Chiritescu, C.; Cahill, D. G.; Heideman, C.; Lin, Q.; Mortensen, C.; Nguyen, N. T.; Johnson, D.; Rostek, R.; Böttner, H., Low thermal conductivity in nanoscale layered materials synthesized by the method of modulated elemental reactants. *Journal of Applied Physics* **2008,** *104* (3), 033533.

(7) Johnson, D. C. "Controlled synthesis of new compounds using modulated elemental reactants." *Current Opinion in Solid State and Materials Science* **1998,** *3* (2), 159-167.

(8) Wood, S. R.; Merrill, D. R.; Mitchson, G.; Lygo, A. C.; Bauers, S. R.; Hamann, D. M.; Sutherland, D. R.; Ditto, J.; Johnson, D. C. Modulation Doping in Metastable Heterostructures via Kinetically Controlled Substitution. *Chem. Mater.* **2017**, *29* (2), 773–779.

(9) Mitchson, G.; Hadland, E.; Göhler, F.; Wanke, M.; Esters, M.; Ditto, J.; Bigwood, E.; Ta, K.; Hennig, R. G.; Seyller, T.; Johnson, D. C. Structural Changes in 2D BiSe Bilayers as *n* Increases in $(BiSe)_{1+\delta}$ $(NbSe_2)_n$ (n = 1–4) Heterostructures. *ACS Nano* **2016**, *10* (10), 9489–9499.

(10) Bauers, S.; Ditto, J.; Moore, D. B.; Johnson, D. C. Structure-Property Relationships in Non-Epitaxial Chalcogenide Heterostructures: The Role of Interface Density on Charge Exchange. *Nanoscale* **2016**, *8*, 14665–14672.

(11) Hamann, D. M.; Merrill, D. R.; Bauers, S. R.; Mitchson, G.; Ditto, J.; Rudin, S. P.; Johnson, D. C. Long-Range Order in $[(SnSe)_{1.2}]_1[TiSe_2]_1$ Prepared from Designed Precursors. *Inorg. Chem.* **2017**, *56* (6), 3499–3505.

(12) Alemayehu, M. B.; Falmbigl, M.; Ta, K.; Ditto, J.; Medlin, D. L.; Johnson, D. C. Designed Synthesis of van Der Waals Heterostructures: The Power of Kinetic Control. *Angew. Chemie Int. Ed.* **2015**, *54*, 15468–15472.

(13) Gunning, N. S.; Dankwort, T.; Falmbigl, M.; Ross, U.; Mitchson, G.; Hamann, D. M.; Lotnyk, A.; Kienle, L.; Johnson, D. C. Expanding the Concept of van Der Waals Heterostructures to Interwoven 3D Structures. *Chem. Mater.* **2017**, *29* (19), 8292–8298.

(14) Wiegers, G. A. "Misfit layer compounds: structures and physical properties." *Progress in Solid State Chemistry* **1996,** *24* (1-2), 1-139.

(15) Hamann, D. M.; Hadland, E. C.; Johnson, D. C. Heterostructures Containing Dichalcogenides-New Materials with Predictable Nanoarchitectures and Novel Emergent Properties. *Semicond. Sci. Technol.* **2017**, *32*, 93004.

(16) Fister, L.; Li, X.-M.; Mcconnell, J.; Novet, T.; Johnson, D. C. Deposition System for the Synthesis of Modulated, Ultrathin-Film Composites. *J. Vac. Sci. Technol. A Vacuum, Surfaces, Film.* **1993**, *11* (3014).

(17) Lin, Q.; Tepfer, S.; Heideman, C.; Mortensen, C.; Nguyen, N.; Zschack, P.; Beekman, M.; Johnson, D. C. Influence of Selenium Vapor Postannealing on the Electrical Transport Properties of $PbSeWSe_2$ Nanolaminates. *J. Mater. Res.* **2011**, *26* (15), 1866–1871.

Chapter V

(1) Mayer, J. W.; Tu, K. N. ANALYSIS OF THIN-FILM STRUCTURES WITH NUCLEAR BACKSCATTERING AND X-RAY DIFFRACTION. In *J Vac Sci Technol*; American Vacuum SocietyAVS, 1974; 11, 86–93.

(2) Krautle, H.; Nicolet, M.-A.; Mayer, J. W. Kinetics of Silicide Formation by Thin Films of V on Si and SiO_2 Substrates. *J. Appl. Phys.* **1974**, *45*, 3304.

(3) Mayer, J. W.; Poate, J. M.; Tu, K.-N. Thin Films and Solid-Phase Reactions. *Science.* **1975**, *190* (4211), 228–234.

(4) Walser, R. M.; Bené, R. W. First Phase Nucleation in Silicon-Transition-Metal Planar Interfaces. *Appl. Phys. Lett.* **1976**, *28* (10), 624–625.

(5) Cotts, E. J.; Meng, W. J.; Johnson, W. L. Calorimetric Study of Amorphization in Planar, Binary, Multilayer, Thin-Film Diffusion Couples of Ni and Zr. *Phys. Rev. Lett.* **1986**, *57*, 2295.

(6) Clemens, B. M.; Sinclair, R. Metastable Phase Formation in Thin Films and Multilayers. *MRS Bull.* **1990**, *15* (2), 19–28.

(7) Schneider, L. M.; Lippert, S.; Renaud, D.; Kuhnert, J.; Kang, K. N.; Ajayi, O.; Halbich, M. U.; Abdulmunem, O. M.; Lin, X.; Hassoon, K.; et al. Influence of the Substrate Material on the Optical Properties of Tungsten Diselendide Monolayers. *2D Mater.* **2017**, *4*, 025045.

(8) Niu, Y.; Gonzalez-Abad, S.; Frisenda, R.; Marauhn, P.; Drüppel, M.; Gant, P.; Schmidt, R.; Taghavi, N. S.; Barcons, D.; Molina-Mendoza, A. J.; et al. Thickness-Dependent Differential Reflectance Spectra of Monolayer and Few-Layer MoS_2, $MoSe_2$, WS_2 and WSe_2. *Nanomaterials* **2018**, *8* (9).

(9) Hamann, D. M.; Lygo, A. C.; Esters, M.; Merrill, D. R.; Ditto, J.; Sutherland, D. R.; Bauers, S. R.; Johnson, D. C. Structural Changes as a Function of Thickness in $[(SnSe)_{1+\delta}]_m TiSe_2$ Heterostructures. *ACS Nano* **2018**, acsnano.7b07506.

(10) Biswas, R. K.; Khan, P.; Mukherjee, S.; Mukhopadhyay, A. K.; Ghosh, J.; Muraleedharan, K. Study of Short Range Structure of Amorphous Silica from PDF Using Ag Radiation in Laboratory XRD System, RAMAN and NEXAFS. *J. Non. Cryst. Solids* **2018**, *488*, 1–9.

(11) Hamann, D. M.; Merrill, D. R.; Bauers, S. R.; Mitchson, G.; Ditto, J.; Rudin, S. P.; Johnson, D. C. Long-Range Order in $[(SnSe)_{1.2}]_1[TiSe_2]_1$ Prepared from Designed Precursors. *Inorg. Chem.* **2017**, *56* (6), 3499–3505.

(12) Li, L. J.; O'Farrell, E. C. T.; Loh, K. P.; Eda, G.; Özyilmaz, B.; Castro Neto, A. H. Controlling Many-Body States by the Electric-Field Effect in a Two-Dimensional Material. *Nature* **2016**, *529* (7585), 185–189.

(13) Novoselov, K. S.; Geim, A. K.; Morozov, S. V; Jiang, D.; Zhang, Y.; Dubonos, S. V.; Grigorieva, I. V; Firsov, A. A. Electric Field Effect in Atomically Thin Carbon Films. *Science.* **2004**, *5* (1), 1–12.

(14) Wang, X.; Gong, Y.; Shi, G.; Chow, W. L.; Keyshar, K.; Ye, G.; Vajtai, R.; Lou, J.; Liu, Z.; Ringe, E.; et al. Chemical Vapor Deposition Growth of Crystalline Monolayer $MoSe_2$. *ACS Nano* **2014**, *8* (5), 5125–5131.

(15) Lu, X.; Utama, M. I. B.; Lin, J.; Gong, X.; Zhang, J.; Zhao, Y.; Pantelides, S. T.; Wang, J.; Dong, Z.; Liu, Z.; et al. Large-Area Synthesis of Monolayer and Few-Layer $MoSe_2$ Films on SiO2 Substrates. *Nano Lett.* **2014**, *14* (5), 2419–2425.

(16) Tan, L. K.; Liu, B.; Teng, J. H.; Guo, S.; Low, H. Y.; Loh, K. P. Atomic Layer Deposition of a MoS_2 Film. *Nanoscale* **2014**, *6* (18), 10584–10588.

(17) Song, J.-G.; Park, J.; Lee, W.; Choi, T.; Jung, H.; Lee, C. W.; Hwang, S.-H.; Myoung, J. M.; Jung, J.-H.; Kim, S.-H.; et al. Layer-Controlled, Wafer-Scale, and Conformal Synthesis of Tungsten Disulfide Nanosheets Using Atomic Layer Deposition. *ACS Nano* **2013**, *7* (12), 11333–11340.

(18) Jin, Z.; Shin, S.; Kwon, D. H.; Han, S.-J.; Min, Y.-S. Novel Chemical Route for Atomic Layer Deposition of MoS_2 Thin Film on SiO2/Si Substrate. *Nanoscale* **2014**, *6* (23), 14453–14458.

(19) Kang, K.; Xie, S.; Huang, L.; Han, Y.; Huang, P. Y.; Mak, K. F.; Kim, C. J.; Muller, D.; Park, J. High-Mobility Three-Atom-Thick Semiconducting Films with Wafer-Scale Homogeneity. *Nature* **2015**, *520*, 656–660.

(20) Eichfeld, S. M.; Hossain, L.; Lin, Y.-C.; Piasecki, A. F.; Kupp, B.; Birdwell, A. G.; Burke, R. A.; Lu, N.; Peng, X.; Li, J.; et al. Highly Scalable, Atomically Thin WSe_2 Grown via Metal–Organic Chemical Vapor Deposition. *ACS Nano* **2015**, *9* (2), 2080–2087.

(21) Lin, Y.-C.; Ghosh, R. K.; Addou, R.; Lu, N.; Eichfeld, S. M.; Zhu, H.; Li, M.-Y.; Peng, X.; Kim, M. J.; Li, L.J.; et al. Atomically Thin Resonant Tunnel Diodes Built from Synthetic van Der Waals Heterostructures. *Nat. Commun.* **2015**, *6*, 7311.

(22) Park, J.; Choudhary, N.; Smith, J.; Lee, G.; Kim, M.; Choi, W. Thickness Modulated MoS2 Grown by Chemical Vapor Deposition for Transparent and Flexible Electronic Devices. *Appl. Phys. Lett.* **2015**, *106*, 012104.

(23) Zhan, Y.; Liu, Z.; Najmaei, S.; Ajayan, P. M.; Lou, J. Large-Area Vapor-Phase Growth and Characterization of MoS2 Atomic Layers on a SiO_2 Substrate. *Small* **2012**, *8* (7), 966.

(24) Han, G. H.; Kybert, N. J.; Naylor, C. H.; Lee, B. S.; Ping, J.; Park, J. H.; Kang, J.; Lee, S. Y.; Lee, Y. H.; Agarwal, R.; et al. Seeded Growth of Highly Crystalline Molybdenum Disulphide Monolayers at Controlled Locations. *Nat. Commun.* **2015**, *6*, 6128.

(25) Choi, W.; Choudhary, N.; Han, G. H.; Park, J.; Akinwande, D.; Lee, Y. H. Recent Development of Two-Dimensional Transition Metal Dichalcogenides and Their Applications. *Mater. Today* **2017**, *20* (3), 116–130.

(26) Johnson, D. C. Controlled Synthesis of New Compounds Using Modulated Elemental Reactants. *Curr. Opin. Solid State Mater. Sci.* **1998**, *3*, 159–167.

(27) Esters, M.; Johnson, D. C. Targeted Synthesis of Metastable Compounds and Intergrowths: The Modulated Elemental Reactants Method. In *Crystal Growth: Concepts, Mechanisms, and Applications*; Li, J., Li, J., Chi, Y., Eds.; Nova Science Publishers: New York, 2017; pp 35–118.

(28) Atkins, R.; Wilson, J.; Zschack, P.; Grosse, C.; Neumann, W.; Johnson, D. C. Synthesis of $[(SnSe)_{1.15}]_m(TaSe_2)_n$ Ferecrystals: Structurally Tunable Metallic Compounds. *Chem. Mater.* **2012**, *24* (23), 4594–4599.

(29) Merrill, D. R.; Moore, D. B.; Ditto, J.; Sutherland, D. R.; Falmbigl, M.; Winkler, M.; Pernau, H.-F.; Johnson, D. C. The Synthesis, Structure, and Electrical Characterization of $(SnSe)_{1.2}TiSe_2$. *Eur. J. Inorg. Chem.* **2015**, *2015*, 83–91.

(30) Hamann, D. M.; Bardgett, D.; Cordova, D. L. M.; Maynard, L. A.; Hadland, E. C.; Lygo, A. C.; Wood, S. R.; Esters, M.; Johnson, D. C. Sub-Monolayer Accuracy in Determining the Number of Atoms per Unit Area in Ultrathin Films Using X-Ray Fluorescence. *Chem. Mater.* **2018**, *30* (18), 6209–6216.

(31) Bronsema, K. D.; de Boer, J. L.; Jellinik, F. On the Structure of Molybdenum Diselenide and Disulfide. *Zeitschrift fur Anorg. und Allg. Chemie* **1986**, *540*, 15–17.

(32) Sathe, D. J.; Chate, P. A. Hexagonal Nanosized Molybdenum Diselenide Thin Film Deposited at 333 K by Chemical Method. *Solid State Sci.* **2015**, *48*, 19–22.

(33) Huntley, D. R.; Sienko, M. J.; Hiebl, K. Magnetic Properties of Iron-Intercalated Titanium Diselenide. *J. Solid State Chem.* **1984**, *52* (3), 233–243.

Chapter VI

(1) Triscone, J.-M.; Karkut, M. G.; Antognazza, L.; Brunner, O.; Fischer, Ø. Y-Ba-Cu-O/Dy-Ba-Cu-O Superlattices: A First Step towards the Artificial Construction of High-T_c Superconductors. *Phys. Rev. Lett.* **1989**, *63*, 1016–1019.

(2) John, S. Strong Localization of Photons in Certain Disordered Dielectric Superlattices. *Phys. Rev. Lett.* **1987**, *58*, 2486–2489.

(3) Baibich, M. N.; Broto, J. M.; Fert, A.; Van Dau, F. N.; Petroff, F.; Etienne, P.; Creuzet, G.; Friederich, A.; Chazelas, J. Giant Magnetoresistance of (001)Fe/(001)Cr Magnetic Superlattices. *Phys. Rev. Lett.* **1988**, *61*, 2472–2475.

(4) Wierer, J. J.; David, A.; Megens, M. M. III-Nitride Photonic-Crystal Light-Emitting Diodes with High Extraction Efficiency. *Nat. Photonics* **2009**, *3*, 163–169.

(5) Faist, J.; Capasso, F.; Sirtori, C. Quantum Cascade Laser. *Science.* **1994**, *264*, 1–4.

(6) Chiu, M.-H.; Zhang, C.; Shiu, H.-W.; Chuu, C.-P.; Chen, C.-H.; Chang, C.-Y. S.; Chen, C.-H.; Chou, M.-Y.; Shih, C.-K.; Li, L.-J. Determination of Band Alignment in the Single-Layer MoS_2/WSe_2 Heterojunction. *Nat. Commun.* **2015**, *6*, 1–6.

(7) Geim, A. K.; Grigorieva, I. V. Van Der Waals Heterostructures. *Nature* **2013**, *499*, 419–425.

(8) Rudin, S. P.; Johnson, D. C. Density Functional Theory Calculations of the Turbostratically Disordered Compound $[(SnSe)_{1+y}]_m(VSe_2)_n$. *Phys. Rev. B* **2015**, *91*, 144203.

(9) Liu, K.; Jin, C.; Hong, X.; Kim, J.; Zettl, A.; Wang, E.; Wang, F. Van Der Waals-Coupled Electronic States in Incommensurate Double-Walled Carbon Nanotubes. *Nat. Phys.* **2014**, *10*, 737.

(10) Koshino, M. Interlayer Interaction in General Incommensurate Atomic Layers. *New J. Phys.* **2015**, *17*, 015014.

(11) Koshino, M.; Moon, P. Electronic Properties of Incommensurate Atomic Layers. *J. Phys. Soc. Japan* **2015**, *84*, 121001.

(12) Novoselov, K. S.; Mishchenko, A.; Carvalho, A.; Neto, A. H. C.; Road, O. 2D Materials and van Der Waals Heterostructures. *Science.* **2016**, *353*, aac9439.

(13) Gunning, N. S.; Feser, J.; Beekman, M.; Cahill, D. G.; Johnson, D. C. Synthesis and Thermal Properties of Solid-State Structural Isomers: Ordered Intergrowths of SnSe and $MoSe_2$. *J. Am. Chem. Soc.* **2015**, *137*, 8803–8809.

(14) Heideman, C. L.; Tepfer, S.; Lin, Q.; Rostek, R.; Zschack, P.; Anderson, M. D.; Anderson, I. M.; Johnson, D. C. Designed Synthesis, Structure, and Properties of a Family of Ferecrystalline Compounds $[(PbSe)_{1.00}]_m(MoSe_2)_n$. *J. Am. Chem. Soc.* **2013**, *135*, 11055–11062.

(15) Atkins, R.; Dolgos, M.; Fiedler, A.; Grosse, C.; Fischer, S. F.; Rudin, S. P.; Johnson, D. C. Synthesis and Systematic Trends in Structure and Electrical Properties of $[(SnSe)_{1.15}]_m$ $(VSe_2)_1$, m = 1, 2, 3, and 4. *Chem. Mater.* **2014**, *26*, 2862–2872.

(16) Falmbigl, M.; Fiedler, A.; Atkins, R. E.; Fischer, S. F.; Johnson, D. C. Suppressing a Charge Density Wave by Changing Dimensionality in the Ferecrystalline Compounds $([SnSe]_{1.15})_1$ $(VSe_2)_n$ with n = 1, 2, 3, 4. *Nano Lett.* **2015**, *15*, 943–948.

(17) Novoselov, K. S.; Jiang, D.; Schedin, F.; Booth, T. J.; Khotkevich, V. V; Morozov, S. V; Geim, A. K. Two-Dimensional Atomic Crystals. *Proc. Natl. Acad. Sci. U. S. A.* **2005**, *102*, 10451–10453.

(18) Li, X.; Lin, M.-W.; Lin, J.; Huang, B.; Puretzky, A. A.; Ma, C.; Wang, K.; Zhou, W.; Pantelides, S. T.; Chi, M.; et al. Two-Dimensional GaSe/$MoSe_2$ Misfit Bilayer Heterojunctions by van Der Waals Epitaxy. *Sci. Adv.* **2016**, *2*, e1501882.

(19) Koma, A. Van Der Waals Epitaxy—a New Epitaxial Growth Method for a Highly Lattice-Mismatched System. *Thin Solid Films* **1992**, *216*, 72–76.

(20) Beekman, M.; Heideman, C. L.; Johnson, D. C. Ferecrystals: Non-Epitaxial Layered Intergrowths. *Semicond. Sci. Technol.* **2014**, *29*, 064012.

(21) Alemayehu, M. B.; Falmbigl, M.; Ta, K.; Ditto, J.; Medlin, D. L.; Johnson, D. C. Designed Synthesis of van Der Waals Heterostructures: The Power of Kinetic Control. *Angew. Chemie Int. Ed.* **2015**, *54*, 15468–15472.

(22) Alemayehu, M. B.; Falmbigl, M.; Ta, K.; Johnson, D. C. Effect of Local Structure of NbSe2 on the Transport Properties of $[(SnSe)_{1.16}]_1[(NbSe_2)]_n$ Ferecrystals. *Chem. Mater.* **2015**, *27*, 2158–2164.

(23) Atkins, R.; Moore, D. B.; Johnson, D. C. Insights into the Self-Assembly of Ferecrystalline Compounds from Designed Amorphous Precursors. *Chem. Mater.* **2013**, *25*, 1744–1750.

(24) Lin, Q.; Smeller, M.; Heideman, C. L.; Zschack, P.; Koyano, M.; Anderson, M. D.; Kykyneshi, R.; Keszler, D. a.; Anderson, I. M.; Johnson, D. C. Rational Synthesis and Characterization of a New Family of Low Thermal Conductivity Misfit Layer Compounds $[(PbSe)_{0.99}]_m(WSe_2)_n$. *Chem. Mater.* **2010**, *22*, 1002–1009.

(25) Beekman, M.; Disch, S.; Rouvimov, S.; Kasinathan, D.; Koepernik, K.; Rosner, H.; Zschack, P.; Neumann, W. S.; Johnson, D. C. Controlling Size-Induced Phase Transformations Using Chemically Designed Nanolaminates. *Angew. Chemie - Int. Ed.* **2013**, *52*, 13211–13214.

(26) Alemayehu, M. B.; Ta, K.; Falmbigl, M.; Johnson, D. C. Structure, Stability, and Properties of the Intergrowth Compounds $([SnSe]_{1+\delta})_m(NbSe_2)_n$, where $m = n = 1$-20. *J. Am. Chem. Soc.* **2015**, *137*, 4831–4839.

(27) Atkins, R.; Wilson, J.; Zschack, P.; Grosse, C.; Neumann, W.; Johnson, D. C. Synthesis of $[(SnSe)_{1.15}]_m(TaSe_2)_n$ Ferecrystals: Structurally Tunable Metallic Compounds. *Chem. Mater.* **2012**, *24*, 4594–4599.

(28) Westover, R. D.; Ditto, J.; Falmbigl, M.; Hay, Z. L.; Johnson, D. C. Synthesis and Characterization of Quaternary Monolayer Thick $MoSe_2$ /SnSe/$NbSe_2$/SnSe Heterojunction Superlattices. *Chem. Mater.* **2015**, *27*, 6411–6417.

(29) Rouxel, J.; Meerschaut, A.; Wiegers, G. A. Chalcogenide Misfit Layer Compounds. *ELSEVIER J. Alloy. Compd.* **1995**, *229*, 144–157.

(30) Falmbigl, M.; Alemayehu, M. B.; Merrill, D. R.; Beekman, M.; Johnson, D. C. In-Plane Structure of Ferecrystalline Compounds. *Cryst. Res. Technol.* **2015**, *50*, 464–472.

(31) Merrill, D. R.; Sutherland, D. R.; Ditto, J.; Bauers, S. R.; Falmbigl, M.; Medlin, D. L.; Johnson, D. C. Kinetically Controlled Site-Specific Substitutions in Higher-Order Heterostructures. *Chem. Mater.* **2015**, *27*, 4066–4072.

(32) Merrill, D. R.; Moore, D. B.; Ditto, J.; Sutherland, D. R.; Falmbigl, M.; Winkler, M.; Pernau, H.-F.; Johnson, D. C. The Synthesis, Structure, and Electrical Characterization of $(SnSe)_{1.2}$ $TiSe_2$. *Eur. J. Inorg. Chem.* **2015**, *2015*, 83–91.

(33) Schaffer, M.; Schaffer, B.; Ramasse, Q. Sample Preparation for Atomic-Resolution STEM at Low Voltages by FIB. *Ultramicroscopy* **2012**, *114*, 62–71.

(34) Blöchl, P. E. Projector Augmented- Wave Method. *Phys. Rev. B* **1994**, *50*, 17953–17979.

(35) Perdew, J. P.; Burke, K.; Ernzerhof, M. Generalized Gradient Approximation Made Simple. *Phys. Rev. Lett.* **1996**, *77*, 3865–3868.

(36) Kresse, G.; Furthmüller, J. Efficient Iterative Schemes for Ab Initio Total-Energy Calculations Using a Plane-Wave Basis Set. *Phys. Rev. B* **1996**, *54*, 11169–11186.

(37) Kresse, G.; Joubert, D. From Ultrasoft Pseudopotentials to the Projector Augmented-Wave Method. *Phys. Rev. B* **1999**, *59*, 1758–1775.

(38) Methfessel, M.; Paxton, A. T. High-Precision Sampling for Brillouin-Zone Integration in Metals. *Phys. Rev. B* **1989**, *40*, 3616–3621.

(39) Tkatchenko, A.; Scheffler, M. Accurate Molecular Van Der Waals Interactions from Ground-State Electron Density and Free-Atom Reference Data. *Phys. Rev. Lett.* **2009**, *102*, 073005.

(40) Moore, D. B.; Stolt, M. J.; Atkins, R.; Sitts, L.; Jones, Z.; Disch, S.; Matt, B.; Johnson, D. C. Structural and Electrical Properties of $(PbSe)_{1.16}TiSe_2$. *Emerg. Mater. Res.* **2012**, *1*, 292–298.

(41) Merrill, D. R.; Moore, D. B.; Coffey, M. N.; Jansons, A. W.; Falmbigl, M.; Johnson, D. C. Synthesis and Characterization of Turbostratically Disordered $(BiSe)_{1.15}TiSe_2$. *Semicond. Sci. Technol.* **2014**, *29*, 064004.

(42) Greenaway, D. L.; Nitsche, R. Preparation and Optical Properties of IV-VI2 Chalcogenides Having the CdI_2 Structure. *J. Phys. Chem. Solids* **1965**, *26*, 1445–1458.

(43) Pennycook, S. J. Z-Contrast Stem for Materials Science. *Ultramicroscopy* **1989**, *30*, 58–69.

(44) Ren, Y.; Meetsma, A.; Petricek, V.; van Smaalen, S.; Wiegers, G.; IUCr. (3 + 2)-Dimensional Superspace Approach to the Structure of the Incommensurate Intergrowth Compound: $(SbS)_{1.15}TiS_2$. *Acta Crystallogr. Sect. B Struct. Sci.* **1995**, *51*, 275–287.

(45) Song, Y. J.; Kim, M. J.; Jung, W. G.; Kim, B.-J.; Rhyee, J.-S. Superconducting Properties of the Misfit-Layer Compound $(SnSe)_{1.18}(TiSe_2)_2$. *Phys. status solidi* **2016**, *253*, 1517–1522.

Chapter VII

(1) Novoselov, K. S.; Geim, A. K.; Morozov, S. V; Jiang, D.; Zhang, Y.; Dubonos, S. V; Grigorieva, I. V; Firsov, A. A.; Novoselov, K. S. Electric Field Effect in Atomically Thin Carbon Films. *Science.* **2007**, *306*, 183–191.

(2) Novoselov, K. S. Nobel Lecture: Graphene: Materials in the Flatland. *Rev. Mod. Phys.* **2011**, *83*, 837–849.

(3) Geim, A. K. Nobel Lecture: Random Walk to Graphene. *Rev. Mod. Phys.* **2011**, *83*, 851–862.

(4) Hamann, D. M.; Hadland, E. C.; Johnson, D. C. Heterostructures Containing Dichalcogenides-New Materials with Predictable Nanoarchitectures and Novel Emergent Properties. *Semicond. Sci. Technol.* **2017**, *32*, 093004.

(5) Jariwala, D.; Marks, T. J.; Hersam, M. C. Mixed-Dimensional van Der Waals Heterostructures. *Nat. Mater.* **2016**, *16*, 170–181.

(6) Mak, K. F.; Lee, C.; Hone, J.; Shan, J.; Heinz, T. F. Atomically Thin MoS_2: A New Direct-Gap Semiconductor. *Phys. Rev. Lett.* **2010**, *105*.

(7) Zhao, W.; Ghorannevis, Z.; Chu, L.; Toh, M.; Kloc, C.; Tan, P. H.; Eda, G. Evolution of Electronic Structure in Atomically Thin Sheets of WS_2 and WSe_2. *ACS Nano* **2013**, *7*, 791–797.

(8) Komsa, H. P.; Krasheninnikov, A. V. Electronic Structures and Optical Properties of Realistic Transition Metal Dichalcogenide Heterostructures from First Principles. *Phys. Rev. B* **2013**, *88*, 085318.

(9) Ulstrup, S.; Čabo, A. G.; Miwa, J. A.; Riley, J. M.; Grønborg, S. S.; Johannsen, J. C.; Cacho, C.; Alexander, O.; Chapman, R. T.; Springate, E.; et al. Ultrafast Band Structure Control of a Two-Dimensional Heterostructure. *ACS Nano* **2016**, *10*, 6315–6322.

(10) Ugeda, M. M.; Bradley, A. J.; Shi, S. F.; da Jornada, F. H.; Zhang, Y.; Qiu, D. Y.; Ruan, W.; Mo, S. K.; Hussain, Z.; Shen, Z. X.; et al. Giant Bandgap Renormalization and Excitonic Effects in a Monolayer Transition Metal Dichalcogenide Semiconductor. *Nat. Mater.* **2014**, *13*, 1091–1095.

(11) Grubišić Čabo, A.; Miwa, J. A.; Grønborg, S. S.; Riley, J. M.; Johannsen, J. C.; Cacho, C.; Alexander, O.; Chapman, R. T.; Springate, E.; Grioni, M.; et al. Observation of Ultrafast Free Carrier Dynamics in Single Layer MoS_2. *Nano Lett.* **2015**, *15*, 5883–5887.

(12) Bruix, A.; Miwa, J. A.; Hauptmann, N.; Wegner, D.; Ulstrup, S.; Grønborg, S. S.; Sanders, C. E.; Dendzik, M.; Grubišić Čabo, A.; Bianchi, M.; et al. Single-Layer MoS_2 on Au(111): Band Gap Renormalization and Substrate Interaction. *Phys. Rev. B* **2016**, *93*, 165422.

(13) Geim, A. K.; Grigorieva, I. V. Van Der Waals Heterostructures. *Nature* **2013**, *499*, 419–425.

(14) Anderson, M. D.; Heideman, C. L.; Lin, Q.; Smeller, M.; Kokenyesi, R.; Herzing, A. A.; Anderson, I. M.; Keszler, D. A.; Zschack, P.; Johnson, D. C. Size-Dependent Structural Distortions in One-Dimensional Nanostructures. *Angew. Chemie Int. Ed.* **2013**, *52*, 1982–1985.

(15) Smeller, M. M.; Heideman, C. L.; Lin, Q.; Beekman, M.; Anderson, M. D.; Zschack, P.; Anderson, I. M.; Johnson, D. C. Structure of Turbostratically Disordered Misfit Layer Compounds $[(PbSe)_{0.99}]_1[WSe_2]_1$, $[(PbSe)_{1.00}]_1[MoSe_2]_1$, and $[(SnSe)_{1.03}]_1$. *Zeitschrift für Anorg. und Allg. Chemie* **2012**, *638*, 2632–2639.

(16) Feng, W.; Zhou, H.; Chen, F. Impact of Thickness on Crystal Structure and Optical Properties for Thermally Evaporated PbSe Thin Films. *Vacuum* **2015**, *114*, 82–85.

(17) Alemayehu, M. B.; Falmbigl, M.; Ta, K.; Grosse, C.; Westover, R. D.; Bauers, S. R.; Fischer, S. F.; Johnson, D. C. Structural and Electrical Properties of $([SnSe]_{1+??})_m(NbSe_2)_1$ Compounds: Single $NbSe_2$ Layers Separated by Increasing Thickness of SnSe. *Chem. Mater.* **2015**, *27*, 867–875.

(18) Bauers, S. R.; Merrill, D. R.; Moore, D. B.; Johnson, D. C. Carrier Dilution in $TiSe_2$ Based Intergrowth Compounds for Enhanced Thermoelectric Performance. *J. Mater. Chem. C* **2015**, *3*, 10451–10458.

(19) Falmbigl, M.; Fiedler, A.; Atkins, R. E.; Fischer, S. F.; Johnson, D. C. Suppressing a Charge Density Wave by Changing Dimensionality in the Ferecrystalline Compounds $([SnSe]_{1.15})_1$ $(VSe_2)_n$ with n = 1, 2, 3, 4. *Nano Lett.* **2015**, *15*, 943–948.

(20) Helmholz, L. The Crystal Structure of the Low-Temperature Modification of Thallous Iodide. *Z. Krist.* **1936**, *95*, 129–137.

(21) Chattopadhyay, T.; Pannetier, J.; Von Schnering, H. G. Neutron Diffraction Study of the Structural Phase Transition in SnS and SnSe. *J. Phys. Chem. Solids* **1986**, *47* (9), 879–885.

(22) Wiedemeier, H.; von Schnering, H. G. Refinement of the Structures of GeS, GeSe, SnS and SnSe. *Zeitschrift fUr Krist.* **1978**, *148*, 295–303.

(23) Schnering, H. G. von; Wiedemeier, H. The High Temperature Structure of β-SnS and β-SnSe and the B16-to-B33 Type λ-Transition Path. *Zeitschrift für Krist. - Cryst. Mater.* **1981**, *156*, 143–150.

(24) Atkins, R.; Wilson, J.; Zschack, P.; Grosse, C.; Neumann, W.; Johnson, D. C. Synthesis of $[(SnSe)_{1.15}]_m[TaSe_2]_n$ Ferecrystals: Structurally Tunable Metallic Compounds. *Chem. Mater.* **2012**, *24*, 4594–4599.

(25) Beekman, M.; Disch, S.; Rouvimov, S.; Kasinathan, D.; Koepernik, K.; Rosner, H.; Zschack, P.; Neumann, W. S.; Johnson, D. C. Controlling Size-Induced Phase Transformations Using Chemically Designed Nanolaminates. *Angew. Chemie - Int. Ed.* **2013**, *52*, 13211–13214.

(26) Alemayehu, M. B.; Falmbigl, M.; Ta, K.; Johnson, D. C. Effect of Local Structure of NbSe2 on the Transport Properties of $[(SnSe)_{1.16}]_1[(NbSe_2)]$n Ferecrystals. *Chem. Mater.* **2015**, *27*, 2158–2164.

(27) Falmbigl, M.; Alemayehu, M. B.; Merrill, D. R.; Beekman, M.; Johnson, D. C. In-Plane Structure of Ferecrystalline Compounds. *Cryst. Res. Technol.* **2015**, *50*, 464–472.

(28) Hamann, D. M.; Merrill, D. R.; Bauers, S. R.; Mitchson, G.; Ditto, J.; Rudin, S. P.; Johnson, D. C. Long-Range Order in $[(SnSe)_{1.2}]_1[TiSe_2]_1$ Prepared from Designed Precursors. *Inorg. Chem.* **2017**, *56*, 3499–3505.

(29) Johnson, D. C. Controlled Synthesis of New Compounds Using Modulated Elemental Reactants. *Curr. Opin. Solid State Mater. Sci.* **1998**, *3*, 159–167.

(30) Esters, M.; Johnson, D. C. Targeted Synthesis of Metastable Compounds and Intergrowths: The Modulated Elemental Reactants Method. In *Crystal Growth: Concepts, Mechanisms, and Applications*; Li, J., Li, J., Chi, Y., Eds.; Nova Science Publishers: New York, 2017; pp 35–118.

(31) Merrill, D. R.; Moore, D. B.; Ditto, J.; Sutherland, D. R.; Falmbigl, M.; Winkler, M.; Pernau, H.-F.; Johnson, D. C. The Synthesis, Structure, and Electrical Characterization of $(SnSe)_{1.2}TiSe_2$. *Eur. J. Inorg. Chem.* **2015**, *2015*, 83–91.

(32) Beekman, M.; Cogburn, G.; Heideman, C.; Rouvimov, S.; Zschack, P.; Neumann, W.; Johnson, D. C. New Layered Intergrowths in the Sn-Mo-Se System. *J. Electron. Mater.* **2012**, *41*, 1476–1480.

(33) Moore, D. B.; Sitts, L.; Stolt, M. J.; Beekman, M.; Johnson, D. C. Characterization of Nonstoichiometric $Ti_{1+x}Se_2$ Prepared by the Method of Modulated Elemental Reactants. *J. Electron. Mater.* **2013**, *42*, 1647–1651.

(34) Moore, D. B.; Stolt, M. J.; Atkins, R.; Sitts, L.; Jones, Z.; Disch, S.; Matt, B.; Johnson, D. C. Structural and Electrical Properties of $(PbSe)_{1.16}TiSe_2$. *Emerg. Mater. Res.* **2012**, *1*, 292–298.

(35) Moore, D. B.; Beekman, M.; Disch, S.; Zschack, P.; Häusler, I.; Neumann, W.; Johnson, D. C. Synthesis, Structure, and Properties of Turbostratically Disordered $(PbSe)_{1.18}(TiSe_2)_2$. *Chem. Mater.* **2013**, *25*, 2404–2409.

(36) Le Bail, A.; Duroy, H.; Fourquet, J. L. Ab-Initio Structure Determination of $LiSbWO_6$ by X-Ray Powder Diffraction. *Mater. Res. Bull.* **1988**, *23*, 447–452.

(37) Merrill, D. R.; Moore, D. B.; Coffey, M. N.; Jansons, A. W.; Falmbigl, M.; Johnson, D. C. Synthesis and Characterization of Turbostratically Disordered $(BiSe)_{1.15}TiSe_2$. *Semicond. Sci. Technol.* **2014**, *29*, 064004.

(38) Wood, S. R.; Merrill, D. R.; Falmbigl, M.; Moore, D. B.; Ditto, J.; Esters, M.; Johnson, D. C. Tuning Electrical Properties through Control of $TiSe_2$ Thickness in $(BiSe)_{1+\delta}(TiSe_2)_n$ Compounds. *Chem. Mater.* **2015**, *27*, 6067–6076.

(39) Merrill, D. R.; Sutherland, D. R.; Ditto, J.; Bauers, S. R.; Falmbigl, M.; Medlin, D. L.; Johnson, D. C. Kinetically Controlled Site-Specific Substitutions in Higher-Order Heterostructures. *Chem. Mater.* **2015**, *27*, 4066–4072.

(40) Bauers, S. R.; Moore, D. B.; Ditto, J.; Johnson, D. C. Phase Width of Kinetically Stable $([PbSe]_{1+\delta})_1(TiSe_2)_1$ Ferecrystals and the Effect of Precuror Compostion on Electrical Properties. *J. Alloys Compd.* **2015**, *645*, 118–124.

(41) Grosse, C.; Atkins, R.; Kirmse, H.; Mogilatenko, A.; Neumann, W.; Johnson, D. C. Local Structure and Defect Chemistry of $[(SnSe)_{1.15}]_m(TaSe_2)$ Ferecrystals – A New Type of Layered Intergrowth Compound. *J. Alloys Compd.* **2013**, *579*, 507–515.

(42) Falmbigl, M.; Putzky, D.; Ditto, J.; Esters, M.; Bauers, S. R.; Ronning, F.; Johnson, D. C. Influence of Defects on the Charge Density Wave of $([SnSe]_{1+\delta})_1(VSe_2)_1$ Ferecrystals. *ACS Nano* **2015**, *9*, 8440–8448.

(43) Atkins, R.; Moore, D. B.; Johnson, D. C. Insights into the Self-Assembly of Ferecrystalline Compounds from Designed Amorphous Precursors. *Chem. Mater.* **2013**, *25*, 1744–1750.

(44) Fang, W.; Zhang, L.-C.; Qin, G.; Yan, Q.-B.; Zheng, Q.-R.; Su, G. Layer Dependence of Geometric, Electronic and Piezoelectric Properties of SnSe. **2016**, 18.

(45) Mariano, A. N.; Chopra, K. L. Polymorphism in Some IV-VI Compounds Induced by High Pressure and Thin-Film Epitaxial Growth. *Appl. Phys. Lett.* **1967**, *10*, 282–284.

(46) Grimme, S. Semiempirical GGA-Type Density Functional Constructed with a Long-Range Dispersion Correction. *J. Comput. Chem.* **2006**, *27*, 1787–1799.

(47) Alemayehu, M. B.; Ta, K.; Falmbigl, M.; Johnson, D. C. Structure, Stability, and Properties of the Intergrowth Compounds $([SnSe]_{1+\delta})_m(NbSe_2)_n$, where $m = n = 1–20$. *J. Am. Chem. Soc.* **2015**, *137*, 4831–4839.

(48) Imada, M.; Fujimori, A.; Tokura, Y. Metal-Insulator Transitions. *Rev. Mod. Phys.* **1998**, *70*, 1039–1263.

(49) Di Salvo, F. J.; Moncton, D. E.; Waszczak, J. V. Electronic Properties and Superlattice Formation in the Semimetal $TiSe_2$. *Phys. Rev. B* **1976**, *14*, 4321–4328.

(50) Altshuler, B. L.; Khmel'nitzkii, D.; Larkin, A. I.; Lee, P. A. Magnetoresistance and Hall Effect in a Disordered Two-Dimensional Electron Gas. *Phys. Rev. B* **1980**, *22*, 5142–5153.

(51) Wiegers, G. A. Misfit Layer Compounds: Structures and Physical Properties. *Prog. SolidSt. Chem* **1996**, *24*, 1–139.

(52) Bauers, S. R.; Ditto, J.; Moore, D. B.; Johnson, D. C. Structure–Property Relationships in Non-Epitaxial Chalcogenide Heterostructures: The Role of Interface Density on Charge Exchange. *Nanoscale* **2016**, *8*, 14665–14672.

(53) Esters, M. Deposition Software for the Inficon IC6 Deposition Controller https://github.com/marcoesters/deposition_ic6.

(54) Phung, T.; Jensen, J.; Jonshon, D.; Donovan, J.; McBurnett, B. Determination of the Composition of Ultra-Thin Ni-Si Films on Si: Constrained Modeling of Electron Probe Microanalysis and X-ray Reflectivity Data. *X-Ray Spectrom.* **2008**, *37*, 608–614.

(55) Roisnel, T.; Rodríquez-Carvajal, J. WinPLOTR: A Windows Tool for Powder Diffraction Pattern Analysis. *Mater. Sci. Forum* **2001**, *378–381*, 118–123.

(56) Rodríguez-Carvajal, J. Recent Advances in Magnetic Structure Determination by Neutron Powder Diffraction. *Phys. B Condens. Matter* **1993**, *192*, 55–69.

(57) Schaffer, M.; Schaffer, B.; Ramasse, Q. Sample Preparation for Atomic-Resolution STEM at Low Voltages by FIB. *Ultramicroscopy* **2012**, *114*, 62–71.

(58) Kresse, G.; Hafner, J. Ab Initio Molecular-Dynamics Simulation of the Liquid-Metal–Amorphous-Semiconductor Transition in Germanium. *Phys. Rev. B* **1994**, *49*, 14251–14269.

(59) Kresse, G.; Furthmüller, J. Efficient Iterative Schemes for Ab Initio Total-Energy Calculations Using a Plane-Wave Basis Set. *Phys. Rev. B* **1996**, *54*, 11169–11186.

(60) Kresse, G.; Furthmüller, J. Efficiency of Ab-Initio Total Energy Calculations for Metals and Semiconductors Using a Plane-Wave Basis Set. *Comput. Mater. Sci.* **1996**, *6*, 15–50.

(61) Blöchl, P. E. Projector Augmented- Wave Method. *Phys. Rev. B* **1994**, *50*, 17953–17979.

(62) Kresse, G.; Joubert, D. From Ultrasoft Pseudopotentials to the Projector Augmented-Wave Method. *Phys. Rev. B* **1999**, *59*, 1758–1775.

(63) Perdew, J. P.; Burke, K.; Ernzerhof, M. Generalized Gradient Approximation Made Simple. *Phys. Rev. Lett.* **1996**, *77*, 3865–3868.

(64) Monkhorst, H. J.; Pack, J. D. Special Points for Brillouin-Zone Integrations. *Phys. Rev. B* **1976**, *13*, 5188–5192.

Chapter VIII

(1) Ni, Z. H.; Wang, H. M.; Kasim, J.; Fan, H. M.; Yu, T.; Wu, Y. H.; Feng, Y. P.; Shen, Z. X. Graphene Thickness Determination Using Reflection and Contrast Spectroscopy. *Nano Lett.* **2007**, *7* , 2758–2763.

(2) Mak, K. F.; Lee, C.; Hone, J.; Shan, J.; Heinz, T. F. Atomically Thin MoS2: A New Direct-Gap Semiconductor. *Phys. Rev. Lett.* **2010**, *105*.

(3) Tongay, S.; Zhou, J.; Ataca, C.; Lo, K.; Matthews, T. S.; Li, J.; Grossman, J. C.; Wu, J. Thermally Driven Crossover from Indirect toward Direct Bandgap in 2D Semiconductors: $MoSe_2$ versus MoS_2. *Nano Lett.* **2012**, *12* (11), 5576–5580.

(4) Bolotin, K. I.; Ghahari, F.; Shulman, M. D.; Stormer, H. L.; Kim, P. Observation of the Fractional Quantum Hall Effect in Graphene. *Nature* **2009**, *462* (7270), 196–199.

(5) Dean, C. R.; Wang, L.; Maher, P.; Forsythe, C.; Ghahari, F.; Gao, Y.; Katoch, J.; Ishigami, M.; Moon, P.; Koshino, M.; et al. Hofstadter's Butterfly and the Fractal Quantum Hall Effect in Moiré Superlattices. *Nature* **2013**, *497* (7451), 598–602.

(6) Ponomarenko, L. A.; Gorbachev, R. V.; Yu, G. L.; Elias, D. C.; Jalil, R.; Patel, A. A.; Mishchenko, A.; Mayorov, A. S.; Woods, C. R.; Wallbank, J. R.; et al. Cloning of Dirac Fermions in Graphene Superlattices. *Nature* **2013**, *497* (7451), 594–597.

(7) Hunt, B.; Sanchez-Yamagishi, J. D.; Young, A. F.; Yankowitz, M.; LeRoy, B. J.; Watanabe, K.; Taniguchi, T.; Moon, P.; Koshino, M.; Jarillo-Herrero, P.; et al. Massive Dirac Fermions and Hofstadter Butterfly in a van Der Waals Heterostructure. *Science (80-.).* **2013**, *340* (6139), 1427–1430.

(8) Schaibley, J. R.; Yu, H.; Clark, G.; Rivera, P.; Ross, J. S.; Seyler, K. L.; Yao, W.; Xu, X. Valleytronics in 2D Materials. *Nature Reviews Materials*. Nature Publishing Group August 23, 2016, pp 1–15.

(9) Geim, A. K.; Grigorieva, I. V. Van Der Waals Heterostructures. *Nature* **2013**, *499*, 419–425.

(10) Novoselov, K. S.; Mishchenko, A.; Carvalho, A.; Castro Neto, A. H. 2D Materials and van Der Waals Heterostructures. *Science.* **2016**, *353,* 80.

(11) Jariwala, D.; Sangwan, V. K.; Lauhon, L. J.; Marks, T. J.; Hersam, M. C. Emerging Device Applications for Semiconducting Two-Dimensional Transition Metal Dichalcogenides. *ACS Nano*. American Chemical Society February 25, 2014, 1102–1120.

(12) Cui, X.; Lee, G. H.; Kim, Y. D.; Arefe, G.; Huang, P. Y.; Lee, C. H.; Chenet, D. A.; Zhang, X.; Wang, L.; Ye, F.; et al. Multi-Terminal Transport Measurements of MoS_2 Using a van Der Waals Heterostructure Device Platform. *Nat. Nanotechnol.* **2015**, *10*, 534–540.

(13) Grubišić Čabo, A.; Miwa, J. A.; Grønborg, S. S.; Riley, J. M.; Johannsen, J. C.; Cacho, C.; Alexander, O.; Chapman, R. T.; Springate, E.; Grioni, M.; et al. Observation of Ultrafast Free Carrier Dynamics in Single Layer MoS_2. *Nano Lett.* **2015**, *15*, 5883–5887.

(14) Wang, Y. Y.; Ni, Z. H.; Yu, T.; Shen, Z. X.; Wang, H. M.; Wu, Y. H.; Chen, W.; Wee, A. T. S. Raman Studies of Monolayer Graphene: The Substrate Effect. *J. Phys. Chem. C* **2008**, *112*, 10637–10640.

(15) Song, Y. J.; Kim, M. J.; Jung, W. G.; Kim, B.-J.; Rhyee, J.-S. Superconducting Properties of the Misfit-Layer Compound $(SnSe)_{1.18}(TiSe_2)_2$. *Phys. status solidi* **2016**, *253*, 1517–1522.

(16) Wan, C.; Wang, Y.; Wang, N.; Koumoto, K. Low-Thermal-Conductivity $(MS)_{1+x}(TiS_2)_2$ (M = Pb, Bi, Sn) Misfit Layer Compounds for Bulk Thermoelectric Materials. *Materials (Basel).* **2010**, *3*, 2606–2617.

(17) Ryu, Y. K.; Frisenda, R.; Castellanos-Gomez, A. Superlattices Based on van Der Waals 2D Materials. *Chem. Commun.* **2019**, *55*, 11498–11510.

(18) Radovsky, G.; Popovitz-Biro, R.; Stroppa, D. G.; Houben, L.; Tenne, R. Nanotubes from Chalcogenide Misfit Compounds: Sn-S and Nb-Pb-S. *Acc. Chem. Res.* **2014**, *47*, 406–416.

(19) Meerschaut, A. Misfit Layer Compounds Abbreviations CT DOS REELS XAS XPS VdW Charge Transfer Density of States Reflection Electron Energy Loss Spectroscopy X-Ray Absorption Spectroscopy X-Ray Photoelectron Spectroscopy van Der Waals. *Curr. Opin. Solid State Mater. Sci.* **1996**, *1*, 250–260.

(20) Huang, S. H.; Shu, G. J.; Pai, W. W.; Liu, H. L.; Chou, F. C. Tunable Se Vacancy Defects and the Unconventional Charge Density Wave in 1T-$TiSe_{2-\delta}$. *Phys. Rev. B* **2017**, *95*, 45310.

(21) Levy, F. Electrical Resistivity and Hall Effect in $TiSe_2$ Containing Vanadium Impurities. *J. Phys. C Solid State Phys.* **1979**, *12*, 3725–3732.

(22) Levy, F. The Influence of Impurities on the Electrical Properties of $TiSe_2$ Single Crystals. *J. Phys. C Solid State Phys.* **1980**, *13*, 2901–2912.

(23) Hamann, D. M.; Merrill, D. R.; Bauers, S. R.; Mitchson, G.; Ditto, J.; Rudin, S. P.; Johnson, D. C. Long-Range Order in $[(SnSe)_{1.2}]_1[TiSe_2]_1$ Prepared from Designed Precursors. *Inorg. Chem.* **2017**, *56*, 3499–3505.

(24) Hamann, D. M.; Lygo, A. C.; Esters, M.; Merrill, D. R.; Ditto, J.; Sutherland, D. R.; Bauers, S. R.; Johnson, D. C. Structural Changes as a Function of Thickness in $[(SnSe)_{1+\delta}]_m TiSe_2$ Heterostructures. *ACS Nano* **2018**, *12* (2), 1285–1295.

(25) Rasch, J.; Stemmler, T.; Müller, B.; Dudy, L.; Manzke, R. 1T-$TiSe_2$: Semimetal or Semiconductor? *Phys. Rev. Lett.* **2008**, *237602* (December), 2–5.

(26) Di Salvo, F. J.; Moncton, D. E.; Waszczak, J. V. Electronic Properties and Superlattice Formation in the Semimetal $TiSe_2$. *Phys. Rev. B* **1976**, *14*, 4321–4328.

(27) Fang, C. M.; De Groot, R. A.; Haas, C. *Bulk and Surface Electronic Structure of 1T-TiS 2 and 1T-TiSe 2*; 1997.

(28) Zhao, L.-D.; Lo, S.-H.; Zhang, Y.; Sun, H.; Tan, G.; Uher, C.; Wolverton, C.; Dravid, V. P.; Kanatzidis, M. G. Ultralow Thermal Conductivity and High Thermoelectric Figure of Merit in SnSe Crystals. *Nature* **2014**, *508*.

(29) Jin, W.; Vishwanath, S.; Liu, J.; Kong, L.; Lou, R.; Dai, Z.; Sadowski, J. T.; Liu, X.; Lien, H.-H.; Chaney, A.; et al. Electronic Structure of the Metastable Epitaxial Rock-Salt SnSe {111} Topological Crystalline Insulator.

(30) Cui, Z.; Wang, X.; Ding, Y.; Li, M. Exploration Work Function and Optical Properties of Monolayer SnSe Allotropes. *Superlattices Microstruct.* **2018**, *114*, 251–258.

(31) Merrill, D. R.; Moore, D. B.; Ditto, J.; Sutherland, D. R.; Falmbigl, M.; Winkler, M.; Pernau, H.-F.; Johnson, D. C. The Synthesis, Structure, and Electrical Characterization of $(SnSe)_{1.2}TiSe_2$. *Eur. J. Inorg. Chem.* **2015**, *2015*, 83–91.

(32) Atkins, R.; Wilson, J.; Zschack, P.; Grosse, C.; Neumann, W.; Johnson, D. C. Synthesis of $[(SnSe)_{1.15}]_m[TaSe_2]_n$ Ferecrystals: Structurally Tunable Metallic Compounds. *Chem. Mater.* **2012**, *24*, 4594–4599.

(33) Johnson, D. C. Controlled Synthesis of New Compounds Using Modulated Elemental Reactants. *Curr. Opin. Solid State Mater. Sci.* **1998**, *3*, 159–167.

(34) Esters, M. Deposition Software for the Inficon IC6 Deposition Controller https://github.com/marcoesters/deposition_ic6.

(35) Jain, A.; Ong, S. P.; Hautier, G.; Chen, W.; Richards, W. D.; Dacek, S.; Cholia, S.; Gunter, D.; Skinner, D.; Ceder, G.; et al. Commentary: The Materials Project: A Materials Genome Approach to Accelerating Materials Innovation. *APL Mater.* **2013**, *1*, 011002.

(36) Perdew, J. P.; Burke, K.; Ernzerhof, M. Generalized Gradient Approximation Made Simple. *Phys. Rev. Lett.* **1996**, *77*, 3865–3868.

(37) Perdew, J. P.; Ruzsinszky, A.; Csonka, G. I.; Vydrov, O. A.; Scuseria, G. E.; Constantin, L. A.; Zhou, X.; Burke, K. Restoring the Density-Gradient Expansion for Exchange in Solids and Surfaces. *Phys. Rev. Lett.* **2008**, *100*, 136406.

(38) Tkatchenko, A.; Scheffler, M. Accurate Molecular Van Der Waals Interactions from Ground-State Electron Density and Free-Atom Reference Data. *Phys. Rev. Lett.* **2009**, *102*, 073005.

(39) Blöchl, P. E. Projector Augmented- Wave Method. *Phys. Rev. B* **1994**, *50*, 17953–17979.

(40) Kresse, G.; Hafner, J. Ab Initio Molecular-Dynamics Simulation of the Liquid-Metal–Amorphous-Semiconductor Transition in Germanium. *Phys. Rev. B* **1994**, *49*, 14251–14269.

(41) Kresse, G.; Furthmüller, J. Efficient Iterative Schemes for Ab Initio Total-Energy Calculations Using a Plane-Wave Basis Set. *Phys. Rev. B - Condens. Matter Mater. Phys.* **1996**, *54*, 11169–11186.

(42) Kresse, G.; Furthmüller, J. Efficiency of Ab-Initio Total Energy Calculations for Metals and Semiconductors Using a Plane-Wave Basis Set. *Comput. Mater. Sci.* **1996**, *6*, 15–50.

(43) Kresse, G.; Hafner, J. Ab Initio Molecular Dynamics for Liquid Metals. *Phys. Rev. B* **1993**, *47*, 558–561.

(44) Butler, K. T.; Hendon, C. H.; Walsh, A. Electronic Chemical Potentials of Porous Metal-Organic Frameworks. *J. Am. Chem. Soc.* **2014**, *136*, 2703–2706.

(45) GitHub - WMD-group/MacroDensity: Analyse VASP density & potential grids using python https://github.com/WMD-group/MacroDensity (accessed Mar 15, 2020).

(46) Tang, W.; Sanville, E.; Henkelman, G. A Grid-Based Bader Analysis Algorithm without Lattice Bias. *J. Phys. Condens. Matter* **2009**, *21*.

(47) Henkelman, G.; Arnaldsson, A.; Jónsson, H. A Fast and Robust Algorithm for Bader Decomposition of Charge Density. *Comput. Mater. Sci.* **2006**, *36*, 354–360.

(48) Yu, M.; Trinkle, D. R. Accurate and Efficient Algorithm for Bader Charge Integration. *J. Chem. Phys.* **2011**, *134*, 064111.

(49) Zeppenfeld, A. C.; Fiddler, S. L.; Ham, W. K.; Klopfenstein, B. J.; Page, C. J. Variation of Layer Spacing in Self-Assembled Hafnium-1,10-Decanediylbis(Phosphonate) Multilayers As Determined by Ellipsometry and Grazing Angle X-Ray Diffraction. *J. Am. Chem. Soc.* **1994**, *116*, 9158–9165.

(50) Moore, D. B.; Beekman, M.; Zschack, P.; Johnson, D. C. Synthesis of Four New Members of the $(PbSe)_{1.16}(TiSe_2)_n$ (n = 1, 2, 3, and 4) Family of Ferecrystals. In *2011 11th IEEE International Conference on Nanotechnology*; IEEE, 2011; pp 1363–1366.

(51) Bauers, S. R.; Merrill, D. R.; Moore, D. B.; Johnson, D. C. Carrier Dilution in $TiSe_2$ Based Intergrowth Compounds for Enhanced Thermoelectric Performance. *J. Mater. Chem. C* **2015**, *3*, 10451–10458.

(52) Bauers, S.; Ditto, J.; Moore, D. B.; Johnson, D. C. Structure-Property Relationships in Non-Epitaxial Chalcogenide Heterostructures: The Role of Interface Density on Charge Exchange. *Nanoscale* **2016**, *8*, 14665–14672.

(53) Reshak, A. H.; Auluck, S. Electronic and Optical Properties of the 1T Phases of TiS_2, $TiSe_2$, and $TiTe_2$. *Phys. Rev. B* **2003**, *68* (24), 245113.

(54) Wiedemeier, H.; von Schnering, H. G. Refinement of the Structures of GeS, GeSe, SnS and SnSe. *Zeitschrift für Krist.* **1978**, *148* (3–4), 295–303.

(55) Beekman, M.; Cogburn, G.; Heideman, C.; Rouvimov, S.; Zschack, P.; Neumann, W.; Johnson, D. C. New Layered Intergrowths in the Sn-Mo-Se System. *J. Electron. Mater.* **2012**, *41*, 1476–1480.

(56) Alemayehu, M. B.; Falmbigl, M.; Ta, K.; Grosse, C.; Westover, R. D.; Bauers, S. R.; Fischer, S. F.; Johnson, D. C. Structural and Electrical Properties of $([SnSe]_{1+??})_m(NbSe_2)_1$ Compounds: Single NbSe2 Layers Separated by Increasing Thickness of SnSe. *Chem. Mater.* **2015**, *27*, 867–875.

(57) Atkins, R.; Dolgos, M.; Fiedler, A.; Grosse, C.; Fischer, S. F.; Rudin, S. P.; Johnson, D. C. Synthesis and Systematic Trends in Structure and Electrical Properties of $[(SnSe)_{1.15}]_m(VSe_2)_1$, m = 1, 2, 3, and 4. *Chem. Mater.* **2014**, *26*, 2862–2872.

(58) Lygo, A. C.; Hamann, D. M.; Moore, D. B.; Merrill, D. R.; Ditto, J.; Esters, M.; Orlowicz, J.; Wood, S. R.; Johnson, D. C. Kinetically Controlled Formation and Decomposition of Metastable $[(BiSe)_{1+\delta}]_m[TiSe_2]_m$ Compounds. *J. Am. Chem. Soc.* **2018**, *140*, 3385–3393.

(59) Wood, S. R.; Merrill, D. R.; Mitchson, G.; Lygo, A. C.; Bauers, S. R.; Hamann, D. M.; Sutherland, D. R.; Ditto, J.; Johnson, D. C. Modulation Doping in Metastable Heterostructures via Kinetically Controlled Substitution. *Chem. Mater.* **2017**, *29*, 773–779.

(60) Moore, D. B.; Stolt, M. J.; Atkins, R.; Sitts, L.; Jones, Z.; Disch, S.; Beekman, M.; Johnson, D. C. Structural and Electrical Properties of $(PbSe)_{1.16}TiSe_2$. *Emerg. Mater. Res.* **2012**, *1*, 292–298.

(61) Moore, D. B.; Beekman, M.; Disch, S.; Zschack, P.; Häusler, I.; Neumann, W.; Johnson, D. C. Synthesis, Structure, and Properties of Turbostratically Disordered $(PbSe)_{1.18}(TiSe_2)_2$. *Chem. Mater.* **2013**, *25*, 2404–2409.

(62) Wood, S. R.; Merrill, D. R.; Falmbigl, M.; Moore, D. B.; Ditto, J.; Esters, M.; Johnson, D. C. Tuning Electrical Properties through Control of TiSe2 Thickness in $(BiSe)_{1+\delta}(TiSe_2)_n$ Compounds. *Chem. Mater.* **2015**, *27*, 6067–6076.

(63) Merrill, D. R.; Sutherland, D. R.; Ditto, J.; Bauers, S. R.; Falmbigl, M.; Medlin, D. L.; Johnson, D. C. Kinetically Controlled Site-Specific Substitutions in Higher-Order Heterostructures. *Chem. Mater.* **2015**, *27*, 4066–4072.

(64) Falmbigl, M.; Alemayehu, M. B.; Merrill, D. R.; Beekman, M.; Johnson, D. C. In-Plane Structure of Ferecrystalline Compounds. *Cryst. Res. Technol.* **2015**, *50*, 464–472.

(65) Göhler, F.; Hamann, D. M.; Rösch, N.; Wolff, S.; Logan, J. T.; Fischer, R.; Speck, F.; Johnson, D. C.; Seyller, T. Electronic Structure of Designed $[(SnSe)_{1+\delta}]_m[TiSe_2]_2$ Heterostructure Thin Films with Tunable Layering Sequence. *J. Mater. Res.* **2019**, *34*, 1965–1975.

(66) Bauers, S. R.; Johnson, D. C. Designing Thermoelectric Materials Using 2D Layers. In *Handbook of Solid State Chemistry*; Wiley-VCH Verlag GmbH & Co. KGaA, 2017; pp 93–122.

(67) Sheets, W. C.; Mercey, B.; Prellier, W. Effect of Charge Modulation in $(LaVO_3)_m(SrVO_3)_n$ Superlattices on the Insulator-Metal Transition. *Appl. Phys. Lett.* **2007**, *91*.

(68) Miyasaka, S.; Okuda, T.; Tokura, Y. Critical Behavior of Metal-Insulator Transition in $La_{1-X}Sr_xVO_3$. *Phys. Rev. Lett.* **2000**, *85*, 5388–5391.

(69) Zubair Ansari, M.; Khare, N. Thermally Activated Band Conduction and Variable Range Hopping Conduction in Cu_2ZnSnS_4 Thin Films. *J. Appl. Phys.* **2015**, *117*.

(70) Huang, Y. L.; Chiu, S. P.; Zhu, Z. X.; Li, Z. Q.; Lin, J. J. Variable-Range-Hopping Conduction Processes in Oxygen Deficient Polycrystalline ZnO Films. *J. Appl. Phys.* **2010**, 107.

(71) Khan, M. H.; Pal, S. Nature of Electrical Hopping Conduction and Magnetotransport Studies in the Electron Doped Manganite $Ca_{0.85}Gd_{0.15}MnO_3$. *Phys. Lett. A.* **2015**, *379*, 401–406.

(72) Hill, R. M. Variable-range Hopping. *Phys. status solidi.* **1976**, *34*, 601–613.

(73) Edwards, P. P.; Sienko, M. J. The Transition to the Metallic State. *Acc. Chem. Res.* **1982**, *15*, 87–93.

(74) Möbius, A. The Metal-Insulator Transition in Disordered Solids: How Theoretical Prejudices Influence Its Characterization A Critical Review of Analyses of Experimental Data. *Critical Reviews in Solid State and Materials Sciences*. Taylor and Francis Inc. January 2019, pp 1–55.

(75) Wang, Y.; Nakano, M.; Kashiwabara, Y.; Matsuoka, H.; Iwasa, Y. Transport Properties of a Few Nanometer-Thick $TiSe_2$ Films Grown by Molecular-Beam Epitaxy. *Appl. Phys. Lett.* **2018**, *113*, 073101.

(76) Watson, M. D.; Beales, A. M.; King, P. D. C. On the Origin of the Anomalous Peak in the Resistivity of $TiSe_2$. *Phys. Rev. B* **2019**, *99*.

(77) Di Salvo, F. J.; Moncton, D. E.; Waszczak, J. V. Electronic Properties and Superlattice Formation in Semimetal $TiSe_2$. *Phys. Rev. B* **1976**, *14*, 4321.

(78) Kehoe, A. B.; Scanlon, D. O.; Watson, G. W. Nature of the Band Gap of Tl_2O_3. *Phys. Rev. B - Condens. Matter Mater. Phys.* **2011**, *83*, 233202.

(79) Monney, C.; Battaglia, C.; Cercellier, H.; Aebi, P.; Beck, H. Exciton Condensation Driving the Periodic Lattice Distortion of 1T-$TiSe_2$. *Phys. Rev. Lett.* **2011**, *106*, 106404.

(80) Bianco, R.; Calandra, M.; Mauri, F. Electronic and Vibrational Properties of $TiSe_2$ in the Charge-Density-Wave Phase from First Principles. *Phys. Rev. B - Condens. Matter Mater. Phys.* **2015**, *92*, 094107.

(81) Cazzaniga, M.; Cercellier, H.; Holzmann, M.; Monney, C.; Aebi, P.; Onida, G.; Olevano, V. Ab Initio Many-Body Effects in $TiSe_2$: A Possible Excitonic Insulator Scenario from GW Band-Shape Renormalization. *Phys. Rev. B - Condens. Matter Mater. Phys.* **2012**, *85*, 195111.

Chapter IX

(1) Hemminger, John (University of California, I. *Directing Matter and Energy: Five Challenges for Science and the Imagination A Report from the Basic Energy Sciences Advisory Committee*; 2007.

(2) Carroll, F. A. *Perspectives on Structure and Mechanism in Organic Chemistry - Felix A. Carroll - Google Books*, Second Edi.; John Wiley & Sons, Inc.: Hoboken, 2010.

(3) Mayr, H.; Ofial, A. R. The Reactivity–Selectivity Principle: An Imperishable Myth in Organic Chemistry. *Angew. Chemie Int. Ed.* **2006**, *45*, 1844–1854.

(4) Smith, M. B.; March, J. *March's Advanced Organic Chemistry*; John Wiley & Sons, Inc.: Hoboken, NJ, USA, 2006.

(5) Fischer, P. The Design, Synthesis and Application of Stereochemical and Directional Peptide Isomers: A Critical Review. *Curr. Protein Pept. Sci.* **2005**, *4*, 339–356.

(6) Lu, Z.; Gan, J. Analysis, Toxicity, Occurrence and Biodegradation of Nonylphenol Isomers: A Review. *Environment International*. Elsevier Ltd December 1, 2014, pp 334–345.

(7) A. Molnár, G.; Kun, S.; Sélley, E.; Kertész, M.; Szélig, L.; Csontos, C.; Böddi, K.; Bogár, L.; Miseta, A.; Wittmann, I. Role of Tyrosine Isomers in Acute and Chronic Diseases Leading to Oxidative Stress - A Review. *Curr. Med. Chem.* **2016**, *23*, 667–685.

(8) Van Zyl, E. F. A Survey of Reported Synthesis of Methaqualone and Some Positional and Structural Isomers. *Forensic Sci. Int.* **2001**, *122*, 142–149.

(9) Bender, R.; Braunstein, P.; Bedien, A.; Ellis, P. D.; Huggins, B.; Harvey, P. D.; Sappa, E.; Tiripicchio, A. Synthetic, Structural, Spectroscopic, and Theoretical Studies of Structural Isomers of the Cluster $Pt_3(\mu\text{-}PPh_2)_3Ph(PPh_3)_2$. A Unique Example of Core Isomerism in Phosphine Phosphido-Rich Clusters. *Inorg. Chem.* **1996**, *35*, 1223–1234.

(10) Neeleshwar, S.; Chen, C. L.; Tsai, C. B.; Chen, Y. Y.; Chen, C. C.; Shyu, S. G.; Seehra, M. S. Size-Dependent Properties of CdSe Quantum Dots. *Phys. Rev. B - Condens. Matter Mater. Phys.* **2005**, *71*, 201307.

(11) Nguyen, T. P.; Sohn, W.; Oh, J. H.; Jang, H. W.; Kim, S. Y. Size-Dependent Properties of Two-Dimensional MoS_2 and WS_2. *J. Phys. Chem. C* **2016**, *120*, 10078–10085.

(12) Alivisatos, A. P. Semiconductor Clusters, Nanocrystals, and Quantum Dots. *Science.* **1996**, *271*, 933–937.

(13) Kan, S.; Mokari, T.; Rothenberg, E.; Banin, U. Synthesis and Size-Dependent Properties of Zinc-Blende Semiconductor Quantum Rods. *Nature Materials*. 2003, 155–158.

(14) Asta, M.; Foiles, S.; Quong, A. First-Principles Calculations of Bulk and Interfacial Thermodynamic Properties for Fcc-Based Al-Sc Alloys. *Phys. Rev. B - Condens. Matter Mater. Phys.* **1998**, *57* (18), 11265–11275.

(15) Merrill, D. R.; Sutherland, D. R.; Ditto, J. J.; Moore, D. B.; Falmbigl, M.; Medlin, D. L.; Johnson, D. C. The Synthesis of $[(PbSe)_{1+\delta}]_m(TiSe_2)_n[(SnSe_2)_{1+\gamma}]_m(TiSe_2)_n$ Heterostructures with Designed Nanoarchitectures by Self Assembly of Amorphous Precursors. *Nanoscale* **2016**, *8*.

(16) Wood, S. R.; Merrill, D. R.; Mitchson, G.; Lygo, A. C.; Bauers, S. R.; Hamann, D. M.; Sutherland, D. R.; Ditto, J.; Johnson, D. C. Modulation Doping in Metastable Heterostructures via Kinetically Controlled Substitution. *Chem. Mater.* **2017**, *29*, 773–779.

(17) Novoselov, K. S.; Geim, A. K.; Morozov, S. V; Jiang, D.; Zhang, Y.; Dubonos, S. V; Grigorieva, I. V; Firsov, A. A.; Novoselov, K. S. Electric Field Effect in Atomically Thin Carbon Films. *Science.* **2007**, *306*, 183–191.

(18) Lu, J.; Nagase, S.; Zhang, S.; Peng, L. Strongly Size-Dependent Electronic Properties in C_{60}-Encapsulated Zigzag Nanotubes and Lower Size Limit of Carbon Nanopeapods. *Phys. Rev. B - Condens. Matter Mater. Phys.* **2003**, *68*, 121402.

(19) Moreels, I.; Lambert, K.; Smeets, D.; De Muynck, D.; Nollet, T.; Martins, J. C.; Vanhaecke, F.; Vantomme, A.; Delerue, C.; Allan, G.; et al. Size-Dependent Optical Properties of Colloidal PbS Quantum Dots. *ACS Nano* **2009**, *3*, 3023–3030.

(20) Lopez, R.; Feldman, L. C.; Haglund, R. F. Size-Dependent Optical Properties of VO_2 Nanoparticle Arrays. *Phys. Rev. Lett.* **2004**, *93*, 177403.

(21) Park, T. J.; Papaefthymiou, G. C.; Viescas, A. J.; Moodenbaugh, A. R.; Wong, S. S. Size-Dependent Magnetic Properties of Single-Crystalline Multiferroic $BiFeO_3$ Nanoparticles. *Nano Lett.* **2007**, *7*, 766–772.

(22) Seo, W. S.; Jo, H. H.; Lee, K.; Kim, B.; Oh, S. J.; Park, J. T. Size-Dependent Magnetic Properties of Colloidal Mn_3O_4 and MnO Nanoparticles. *Angew. Chemie Int. Ed.* **2004**, *43*, 1115–1117.

(23) Göhler, F.; Hamann, D. M.; Rösch, N.; Wolff, S.; Logan, J. T.; Fischer, R.; Speck, F.; Johnson, D. C.; Seyller, T. Electronic Structure of Designed $[(SnSe)_{1+\delta}]_m[TiSe_2]_2$ Heterostructure Thin Films with Tunable Layering Sequence. *J. Mater. Res.* **2019**, *34* (12), 1965–1975.

(24) Hamann, D. M.; Lygo, A. C.; Esters, M.; Merrill, D. R.; Ditto, J.; Sutherland, D. R.; Bauers, S. R.; Johnson, D. C. Structural Changes as a Function of Thickness in $[(SnSe)_{1+\delta}]_m TiSe_2$ Heterostructures. *ACS Nano* **2018**, *12* (2), 1285–1295.

(25) Hamann, D. M.; Merrill, D. R.; Bauers, S. R.; Mitchson, G.; Ditto, J.; Rudin, S. P.; Johnson, D. C. Long-Range Order in $[(SnSe)_{1.2}]_1[TiSe_2]_1$ Prepared from Designed Precursors. *Inorg. Chem.* **2017**, *56*, 3499–3505.

(26) Merrill, D. R.; Moore, D. B.; Ditto, J.; Sutherland, D. R.; Falmbigl, M.; Winkler, M.; Pernau, H.-F.; Johnson, D. C. The Synthesis, Structure, and Electrical Characterization of $(SnSe)_{1.2}TiSe_2$. *Eur. J. Inorg. Chem.* **2015**, *2015*, 83–91.

(27) Song, Y. J.; Kim, M. J.; Jung, W. G.; Kim, B.-J.; Rhyee, J.-S. Superconducting Properties of the Misfit-Layer Compound $(SnSe)_{1.18}(TiSe_2)_2$. *Phys. status solidi.* **2016**, *253*, 1517–1522.

(28) Atkins, R.; Wilson, J.; Zschack, P.; Grosse, C.; Neumann, W.; Johnson, D. C. Synthesis of $[(SnSe)_{1.15}]_m(TaSe_2)_n$ Ferecrystals: Structurally Tunable Metallic Compounds. *Chem. Mater.* **2012**, *24*, 4594–4599.

(29) Johnson, D. C. Controlled Synthesis of New Compounds Using Modulated Elemental Reactants. *Curr. Opin. Solid State Mater. Sci.* **1998**, *3*, 159–167.

(30) Esters, M. Deposition Software for the Inficon IC6 Deposition Controller https://github.com/marcoesters/deposition_ic6.

(31) Le Bail, A.; Duroy, H.; Fourquet, J. L. Ab-Initio Structure Determination of $LiSbWO_6$ by X-Ray Powder Diffraction. *Mater. Res. Bull.* **1988**, *23*, 447–452.

(32) Phung, T.; Jensen, J.; Jonshon, D.; Donovan, J.; McBurnett, B. Determination of the Composition of Ultra-Thin Ni-Si Films on Si: Constrained Modeling of Electron Probe Microanalysis and X-ray Reflectivity Data. *X-Ray Spectrom.* **2008**, *37*, 608–614.

(33) Hamann, D. M.; Bardgett, D.; Cordova, D. L. M.; Maynard, L. A.; Hadland, E. C.; Lygo, A. C.; Wood, S. R.; Esters, M.; Johnson, D. C. Sub-Monolayer Accuracy in Determining the Number of Atoms per Unit Area in Ultrathin Films Using X-Ray Fluorescence. *Chem. Mater.* **2018**, *30* (18), 6209–6216.

(34) Schaffer, M.; Schaffer, B.; Ramasse, Q. Sample Preparation for Atomic-Resolution STEM at Low Voltages by FIB. *Ultramicroscopy* **2012**, *114*, 62–71.

(35) van der PAUW, L. J. A Method of Measuring Specific Restivity and Hall Effect of Discs of Arbitrary Shape. *Philips Reserach Reports* **1958**, *13*, 1-9.

(36) Chwang, R.; Smith, B. J.; Crowell, C. R. Contact Size Effects on the van Der Pauw Method for Resistivity and Hall Coefficient Measurement. *Solid State Electron.* **1974**, *17* (12), 1217–1227.

(37) Ramadan, A. A.; Gould, R. D.; Ashour, A. On the Van Der Pauw Method of Resistivity Measurements. *Thin Solid Films* **1994**, *239* (2), 272–275.

(38) Merrill, D. R.; Moore, D. B.; Ditto, J.; Sutherland, D. R.; Falmbigl, M.; Winkler, M.; Pernau, H.-F.; Johnson, D. C. The Synthesis, Structure, and Electrical Characterization of $(SnSe)_{1.2}TiSe_2$. *Eur. J. Inorg. Chem.* **2015**, *2015*, 83–91.

(39) Bauers, S. R.; Ditto, J.; Moore, D. B.; Johnson, D. C. Structure–Property Relationships in Non-Epitaxial Chalcogenide Heterostructures: The Role of Interface Density on Charge Exchange. *Nanoscale* **2016**, *8*, 14665–14672.

(40) Lygo, A. C.; Hamann, D. M.; Moore, D. B.; Merrill, D. R.; Ditto, J.; Esters, M.; Orlowicz, J.; Wood, S. R.; Johnson, D. C. Kinetically Controlled Formation and Decomposition of Metastable $[(BiSe)_{1+\delta}]_m[TiSe_2]_m$ Compounds. *J. Am. Chem. Soc.* **2018**, *140* (9), 3385–3393.

(41) Moore, D. B.; Stolt, M. J.; Atkins, R.; Sitts, L.; Jones, Z.; Disch, S.; Matt, B.; Johnson, D. C. Structural and Electrical Properties of $(PbSe)_{1.16}TiSe_2$. *Emerg. Mater. Res.* **2012**, *1*, 292–298.

(42) Bauers, S. R.; Moore, D. B.; Ditto, J.; Johnson, D. C. Phase Width of Kinetically Stable $([PbSe]_{1+\delta})_1(TiSe_2)_1$ Ferecrystals and the Effect of Precuror Compostion on Electrical Properties. *J. Alloys Compd.* **2015**, *645*, 118–124.

(43) Merrill, D. R.; Sutherland, D. R.; Ditto, J.; Bauers, S. R.; Falmbigl, M.; Medlin, D. L.; Johnson, D. C. Kinetically Controlled Site-Specific Substitutions in Higher-Order Heterostructures. *Chem. Mater.* **2015**, *27*, 4066–4072.

(44) Di Salvo, F. J.; Moncton, D. E.; Waszczak, J. V. Electronic Properties and Superlattice Formation in Semimetal $TiSe_2$. *Phys. Rev. B* **1976**, *14*, 4321.

(45) Chattopadhyay, T.; Pannetier, J.; Von Schnering, H. G. Neutron Diffraction Study of the Structural Phase Transition in SnS and SnSe. *J. Phys. Chem. Solids* **1986**, *47*, 879–885.

(46) Wiedemeier, H.; von Schnering, H. G. Refinement of the Structures of GeS, GeSe, SnS and SnSe. *Zeitschrift für Krist.* **1978**, *148*, 295–303.

(47) Schnering, H. G. von; Wiedemeier, H. The High Temperature Structure of β-SnS and β-SnSe and the B16-to-B33 Type λ-Transition Path. *Zeitschrift für Krist. - Cryst. Mater.* **1981**, *156*, 143–150.

(48) Atkins, R.; Wilson, J.; Zschack, P.; Grosse, C.; Neumann, W.; Johnson, D. C. Synthesis of $[(SnSe)_{1.15}]_m((TaSe_2)_n$ Ferecrystals: Structurally Tunable Metallic Compounds. *Chem. Mater.* **2012**, *24*, 4594–4599.

(49) Beekman, M.; Disch, S.; Rouvimov, S.; Kasinathan, D.; Koepernik, K.; Rosner, H.; Zschack, P.; Neumann, W. S.; Johnson, D. C. Controlling Size-Induced Phase Transformations Using Chemically Designed Nanolaminates. *Angew. Chemie - Int. Ed.* **2013**, *52*, 13211–13214.

(50) Alemayehu, M. B.; Falmbigl, M.; Ta, K.; Grosse, C.; Westover, R. D.; Bauers, S. R.; Fischer, S. F.; Johnson, D. C. Structural and Electrical Properties of $([SnSe]_{1+??})_m(NbSe_2)_1$ Compounds: Single NbSe2 Layers Separated by Increasing Thickness of SnSe. *Chem. Mater.* **2015**, *27*, 867–875.

(51) Falmbigl, M.; Fiedler, A.; Atkins, R. E.; Fischer, S. F.; Johnson, D. C. Suppressing a Charge Density Wave by Changing Dimensionality in the Ferecrystalline Compounds $([SnSe]_{1.15})_1(VSe_2)_n$ with n = 1, 2, 3, 4. *Nano Lett.* **2015**, *15*, 943–948.

(52) Wiedemeier, H.; von Schnering, H. G. Refinement of the Structures of GeS, GeSe, SnS and SnSe. *Zeitschrift fUr Krist.* **1978**, *148*, 295–303.

Chapter X

(1) A.K. Geim and I.V. Grigorieva: Van der Waals heterostructures. *Nature* **2013** *499,419*.

(2) A.C. Ferrari, F. Bonaccorso, V. Fal'ko, K.S. Novoselov, S. Roche, P. Bøggild, S. Borini, F.H.L. Koppens, V. Palermo, N. Pugno, J. A. Garrido, R. Sordan, A. Bianco, L. Ballerini, M. Prato, E. Lidorikis, J. Kivioja, C. Marinelli, T. Ryhänen, A. Morpurgo, J.N. Coleman, V. Nicolosi, L. Colombo, A. Fert, M. Garcia- Hernandez, A. Bachtold, G.F. Schneider, F. Guinea, C. Dekker, M. Barbone, Z. Sun, C. Galiotis, A.N. Grigorenko, G. Konstantatos, A. Kis, M. Katsnelson, L. Vandersypen, A. Loiseau, V. Morandi, D. Neumaier, E. Treossi, V. Pellegrini, M. Polini, A. Tredicucci, G.M. Williams, B.H. Hong, J-H. Ahn, J.M. Kim, H. Zirath, B.J. van Wees, H. van der Zant, L. Occhipinti, A.D. Matteo, I.A. Kinloch, T. Seyller, E. Quesnel, X. Feng, K. Teo, N. Rupesinghe, P. Hakonen, S.R.T. Neil, Q. Tannock, T. Löfwander, and J. Kinaret: Science and technology roadmap for graphene, related two-dimensional crystals, and hybrid systems. *Nanoscale* **2015** *7, 4598*.

(3) A. Kuc, T. Heine, and A. Kis: Electronic properties of transition-metal dichalcogenides. *MRS Bull.* **2015** *40, 577*.

(4) J.A. Robinson: Growing vertical in the flatland. *ACS Nano.* **2016,** *10, 42*.

(5) K.S. Novoselov, V.I. Fal'ko, L. Colombo, P.R. Gellert, M. G. Schwab, and K. Kim: A roadmap for graphene. *Nature* **2012** *490, 192.*

(6) C.R. Dean, A.F. Young, I. Meric, C. Lee, L. Wang, S. Sorgenfrei, K. Watanabe, T. Taniguchi, P. Kim, K.L. Shepard, and J. Hone: Boron nitride substrates for high-quality graphene electronics. Nat. *Nanotechnol.* **2010**, *5, 722*.

(7) A.S. Mayorov, R.V. Gorbachev, S.V. Morozov, L. Britnell, R. Jalil, L.A. Ponomarenko, P. Blake, K.S. Novoselov, K. Watanabe, T. Taniguchi, and A.K. Geim: Micrometer-scale ballistic transport in encapsulated graphene at room temperature. *Nano Lett.* **2011** *11, 2396*.

(8) C. Grosse, M.B. Alemayehu, A. Mogilatenko, O. Chiatti, D. C. Johnson, and S.F. Fischer: Superconducting tin selenide/niobiumdiselenide ferecrystals. Cryst. Res. Technol. *52,* **2017**, *1700126*.

(9) K. Kang, K-H. Lee, Y. Han, H. Gao, S. Xie, D.A. Muller, and J. Park: Layer-by-layer assembly of two-dimensional materials into wafer-scale heterostructures. *Nature,* **2017**, *550, 229* (2017).

(10) G. Wiegers: Misfit layer compounds: Structures and physical properties. *Prog. Solid State Chem.* **1993**, *24, 1.*

(11) J. Rouxel, A. Meerschaut, and G. Wiegers: Chalcogenide misfit layer compounds. *J. Alloys Compd.* **1995**, *229, 144*.

(12) D. Merrill, D. Moore, S. Bauers, M. Falmbigl, and D. Johnson: Misfit layer compounds and ferecrystals: Model systems for thermoelectric nanocomposites. *Materials* **2015**, *8, 2000*.

(13) F. Withers, O.D. Pozo-Zamudio, A. Mishchenko, A.P. Rooney, A. Gholinia, K. Watanabe, T. Taniguchi, S.J. Haigh, A.K. Geim, A.I. Tartakovskii, and K.S. Novoselov: Light-emitting diodes by band-structure engineering in van der Waals heterostructures. *Nat. Mater.* **2015**, *14, 301* (2015).

(14) K.S. Novoselov, A. Mishchenko, A. Carvalho, and A.H.C. Neto: 2D materials and van der Waals heterostructures. *Science.* **2016**, *353.*

(15) Y. Liu, N.O. Weiss, X. Duan, H-C. Cheng, Y. Huang, and X. Duan: Van der Waals heterostructures and devices. *Nat. Rev. Mater. 1, 16042*.

(16) M. Esters, M.B. Alemayehu, Z. Jones, N.T. Nguyen, M. D. Anderson, C. Grosse, S.F. Fischer, and D.C. Johnson: Synthesis of inorganic structural isomers by diffusion-constrained self-assembly of designed precursors: A novel type of isomerism. *Angew. Chem., Int. Ed.* **2015**, *54, 1130*.

(17) R. Westover, R.A. Atkins, M. Falmbigl, J.J. Ditto, and D. C. Johnson: Self-assembly of designed precursors: A route to crystallographically aligned new materials with controlled nanoarchitecture. *J. Solid State Chem.* **2016** *236, 173.*

(18) M. Beekman, C.L. Heideman, and D.C. Johnson: Ferecrystals: Non-epitaxial layered intergrowths. *Semicond. Sci. Technol.* 2014, *29, 064012.*

(19) C. Wan, Y. Wang, N. Wang, and K. Koumoto: Low-thermal-conductivity $(MS)_{1+x}(TiS_2)_2$ (M = Pb, Bi, Sn) misfit layer compounds for bulk thermoelectric materials. *Materials.* **2010**, *3, 2606*.

(20) D.R. Merrill, D.B. Moore, J. Ditto, D.R. Sutherland, M. Falmbigl, M. Winkler, H-F. Pernau, and D.C. Johnson: The synthesis, structure, and electrical characterization of $(SnSe)_{1.2}(TiSe)_2$. *Eur. J. Inorg. Chem.* **2015**, 83.

(21) Z. Li, S.R. Bauers, N. Poudel, D. Hamann, X. Wang, D.S. Choi, K. Esfarjani, L. Shi, D.C. Johnson, and S.B. Cronin: Cross-plane Seebeck coefficient measurement of misfit layered compounds $(SnSe)_n(TiSe_2)_n$ (n = 1, 3, 4, 5). *Nano Lett.* **2017** *17, 1978*.

(22) D.M. Hamann, D.R. Merrill, S.R. Bauers, G. Mitchson, J. Ditto, S. P. Rudin, and D.C. Johnson: Long-range order in $[(SnSe)_{1.2}]_1[TiSe_2]_1$ prepared from designed precursors. *Inorg. Chem.* **2017**, *56, 3499*.

(23) D.M. Hamann, A.C. Lygo, M. Esters, D.R. Merrill, J. Ditto, D. R. Sutherland, S.R. Bauers, and D.C. Johnson: Structural changes as a function of thickness in $[(SnSe)_{1+\delta}]_mTiSe_2$ heterostructures. *ACS Nano.* **2018**, *12, 1285.*

(24) E. Morosan, H.W. Zandbergen, B.S. Dennis, J.W.G. Bos, Y. Onose, T. Klimczuk, A.P. Ramirez, N.P. Ong, and R.J. Cava: Superconductivity in Cu_xTiSe_2. *Nat. Phys.* **2006**, *2, 544*.

(25) E. Morosan, K.E. Wagner, L.L. Zhao, Y. Hor, A.J. Williams, J. Tao, Y. Zhu, and R.J. Cava: Multiple electronic transitions and superconductivity in Pd_xTiSe_2. *Phys. Rev. B.* **2010**, *81, 094524*.

(26) F. Gőhler, G. Mitchson, M.B. Alemayehu, F. Speck, M. Wanke, D.C. Johnson, and T. Seyller: Charge transfer in $(PbSe)_{1+\delta}(NbSe_2)_2$ and $(SnSe)_{1+\delta}(NbSe_2)_2$ ferecrystals investigated by photoelectron spectroscopy. *J. Phys.: Condens. Matter 30*, **2018**, *055001*.

(27) D.C. Johnson: Controlled synthesis of new compounds using modulated elemental reactants. *Curr. Opin. Solid State Mater. Sci.* **1998**, *3,159*

(28) D.M. Hamann, D. Bardgett, D. L. M. Cordova, L.A. Maynard, E. C. Hadland, A.C. Lygo, S.R. Wood, M. Esters, and D.C. Johnson: Sub-monolayer accuracy in determining the number of atoms per unit area in ultrathin films using X-ray fluorescence. *Chem. Mater.* **2018**, *30, 6209*.

(29) D.B. Moore, L. Sitts, M.J. Stolt, M. Beekman, and D.C. Johnson: Characterization of nonstoichiometric $Ti_{1+x}Se_2$ prepared by the method of modulated elemental reactants. *J. Electron. Mater.* **2013**, *42, 1647*.

(30) J. Chen, D.M. Hamann, D. Choi, N. Poudel, L. Shen, L. Shi, D. C. Johnson, and S. Cronin: Enhanced cross-plane thermoelectric transport of rotationally disordered SnSe2 via Se-vapor annealing. *Nano Lett.* **2018**, *18, 6876* (2018).

(31) L. Makinistian and E.A. Albanesi: On the band gap location and core spectra of orthorhombic IV–VI compounds SnS and SnSe. *Phys. Status Solidi B.* **2009**, *246, 183* (2009).

(32) J.C.E. Rasch, T. Stemmler, B. Mu̇ller, L. Dudy, and R. Manzke: 1T-$TiSe_2$: Semimetal or semiconductor? *Phys. Rev. Lett.* **2008**, *101, 237602*

(33) S. Doniach and M. Sunjic: Many-electron singularity in X-ray photoemission and X-ray line spectra from metals. *J. Phys. C: Solid State Phys.* **1970**, *3, 285.*

(34) G.D. Mahan: Collective excitations in X-ray spectra of metals. *Phys. Rev. B.* **1975**, *11, 4814*.

(35) A.S. Shkvarin, Y.M. Yarmoshenko, N.A. Skorikov, M. V. Yablonskikh, A.I. Merentsov, E.G. Shkvarina, and A.N. Titov: Electronic structure of titanium dichalcogenides TiX_2 (X = S, Se, Te). *J. Exp. Theor. Phys.* **2012**, *114, 150.*

(36) D.A. Shirley: High-resolution X-ray photoemission spectrum of the valence bands of gold. *Phys. Rev. B.* **1972**, *5, 4709*.

(37) T. Ohta, A. Bostwick, J.L. McChesney, T. Seyller, K. Horn, and E. Rotenberg: Interlayer interaction and electronic screening in multilayer graphene investigated with angle-resolved photoemission spectroscopy. *Phys. Rev. Lett.* **2007**, *98, 206802*.

(38) A. Bostwick, T. Ohta, J.L. McChesney, K.V. Emtsev, T. Seyller, K. Horn, and E. Rotenberg: Symmetry breaking in few layer graphene films. *New J. Phys.* **2007**, *9, 385.*

(39) K.V. Emtsev, F. Speck, T. Seyller, L. Ley, and J.D. Riley: Interaction, growth, and ordering of epitaxial graphene on SiC

{0001} surfaces: A comparative photoelectron spectroscopy study. *Phys. Rev. B.* **2008**, *77, 155303*.

(40) J. Brandt, L. Kipp, M. Skibowski, E. Krasovskii, W. Schattke, E. Spiecker, C. Dieker, and W. Jäger: Charge transfer in misfit layered compounds. *Surf. Sci.* **2003**, *532, 705*.

(41) R. Shalvoy, G. Fisher, and P. Stiles: X-ray photoemission studies of the valence bands of nine IV–VI compounds. *Phys. Rev. B.* **1977**, *15, 2021*.

(42) N. Giang, Q. Xu, Y.S. Hor, A.J. Williams, S.E. Dutton, H. W. Zandbergen, and R.J. Cava: Superconductivity at 2.3 K in the misfit compound$(PbSe)_{1.16}(TiSe_2)_2$. *Phys. Rev. B.* **2010**, *82, 024503*.

(43) D.B. Moore, M. Beekman, S. Disch, P. Zschack, I. Häusler, W. Neumann, and D.C. Johnson: Synthesis, structure, and properties of turbostratically disordered $(PbSe)_{1.18}(TiSe_2)_2$. *Chem. Mater.* **2013**, *25, 2404*.

(44) U.A. Schröder, M. Petrovic, T. Gerber, A.J. Martínez-Galera, E. Granäs, M.A. Arman, C. Herbig, J. Schnadt, M. Kralj, J. Knudsen, and T. Michely: Core level shifts of intercalated graphene. *2D Mater.* **2017**, *4, 015013*.

(45) M. Esters: Deposition software for the Inficon IC6 deposition controller (2018). Available at: https://github.com/marcoesters/deposition_ic6 (accessed December 04, 2018)

Chapter XI

(1) Carroll, F. A. *Perspectives on Structure and Mechanism in Organic Chemistry - Felix A. Carroll - Google Books*, Second Ed.; John Wiley & Sons, Inc.: Hoboken, 2010.

(2) Mayr, H.; Ofial, A. R. The Reactivity–Selectivity Principle: An Imperishable Myth in Organic Chemistry. *Angew. Chemie Int. Ed.* **2006**, *45*, 1844–1854.

(3) Smith, M. B.; March, J. *March's Advanced Organic Chemistry*; John Wiley & Sons, Inc.: Hoboken, NJ, USA, 2006.

(4) Fischer, P. The Design, Synthesis and Application of Stereochemical and Directional Peptide Isomers: A Critical Review. *Curr. Protein Pept. Sci.* **2005**, *4*, 339–356.

(5) Lu, Z.; Gan, J. Analysis, Toxicity, Occurrence and Biodegradation of Nonylphenol Isomers: A Review. *Environment International*. Elsevier Ltd December 1, 2014, pp 334–345.

(6) A. Molnár, G.; Kun, S.; Sélley, E.; Kertész, M.; Szélig, L.; Csontos, C.; Böddi, K.; Bogár, L.; Miseta, A.; Wittmann, I. Role of Tyrosine Isomers in Acute and Chronic Diseases Leading to Oxidative Stress - A Review. *Curr. Med. Chem.* **2016**, *23*, 667–685.

(7) Van Zyl, E. F. A Survey of Reported Synthesis of Methaqualone and Some Positional and Structural Isomers. *Forensic Sci. Int.* **2001**, *122*, 142–149.

(8) Bender, R.; Braunstein, P.; Bedien, A.; Ellis, P. D.; Huggins, B.; Harvey, P. D.; Sappa, E.; Tiripicchio, A. Synthetic, Structural, Spectroscopic, and Theoretical Studies of Structural Isomers of the Cluster $Pt_3(\mu\text{-}PPh_2)_3Ph(PPh_3)_2$. A Unique Example of Core Isomerism in Phosphine Phosphido-Rich Clusters. *Inorg. Chem.* **1996**, *35* (5), 1223–1234.

(9) Ooyama, Y.; Kagawa, Y.; Harima, Y. Synthesis and Solid-State Fluorescence Properties of Structural Isomers of Novel Benzofuro[2,3-c]Oxazolocarbazole-Type Fluorescent Dyes. *European J. Org. Chem.* **2007**, *2007* (22), 3613–3621.

(10) Futschek, T.; Marsman, M.; Hafner, J. Structural and magnetic isomers of small Pd and Rh clusters: An ab initio density functional study https://iopscience.iop.org/article/10.1088/0953-8984/17/38/001/meta (accessed Apr 23, 2020).

(11) Kesanli, B.; Fettinger, J.; Eichhorn, B. The Closo-$[Sn_9M(CO)_3]_4^-$ Zintl Ion Clusters Where M=Cr, Mo, W: Two Structural Isomers and Their Dynamic Behavior. *Chem. – A Eur. J.* **2001**, *7* (24), 5277–5285.

(12) Wiener, H. Correlation of Heats of Isomerization, and Differences in Heats of Vaporization of Isomers, Among the Paraffin Hydrocarbons. *J. Am. Chem. Soc.* **1947**, *69*, 2636–2638.

(13) Wiener, H. Structural Determination of Paraffin Boiling Points. *J. Am. Chem. Soc.* **1947**, *69*, 17–20.

(14) Wang, Z.; Herbinet, O.; Cheng, Z.; Husson, B.; Fournet, R.; Qi, F.; Battin-Leclerc, F. Experimental Investigation of the Low Temperature Oxidation of the Five Isomers of Hexane. *J. Phys. Chem. A* **2014**, *118*, 5573–5594.

(15) Zhang, K.; Banyon, C.; Burke, U.; Kukkadapu, G.; Wagnon, S. W.; Mehl, M.; Curran, H. J.; Westbrook, C. K.; Pitz, W. J. An Experimental and Kinetic Modeling Study of the Oxidation of Hexane Isomers: Developing Consistent Reaction Rate Rules for Alkanes. *Combust. Flame* **2019**, *206*, 123–137.

(16) Lucius, R.; Mayr, H. Konstante Selektivitätsbeziehungen Bei Additionsreaktionen von Carbanionen. *Angew. Chemie* **2000**, *112* , 2086–2089.

(17) Lucius, R.; Loos, R.; Mayr, H. Kinetische Untersuchungen von Carbokation-Carbanion-Kombinationen: Schlüssel Zu Einem Allgemeinen Modell Polarer Organischer Reaktivität. *Angew. Chemie* **2002**, *114*, 97–102.

(18) Lemek, T.; Mayr, H. Electrophilicity Parameters for Benzylidenemalononitriles. *J. Org. Chem.* **2003**, *68*, 6880–6886.

(19) Hoffmann, R. Building Bridges Between Inorganic and Organic Chemistry (Nobel Lecture). *Angew. Chemie Int. Ed. English* **1982**, *21*, 711–724.

(20) Gopinath, C. S.; Hegde, S. G.; Ramaswamy, A. V.; Mahapatra, S. Photoemission Studies of Polymorphic $CaCO_3$ Materials. *Mater. Res. Bull.* **2002**, *37*, 1323–1332.

(21) Boulos, R. A.; Zhang, F.; Tjandra, E. S.; Martin, A. D.; Spagnoli, D.; Raston, C. L. Spinning up the Polymorphs of Calcium Carbonate. *Sci. Rep.* **2014**, *4*, 1–6.

(22) Gammage, R. B.; Glasson, D. R. The Effect of Grinding on the Polymorphs of Calcium Carbonate. *J. Colloid Interface Sci.* **1976**, *55*, 396–401.

(23) Kitamura, M.; Konno, H.; Yasui, A.; Masuoka, H. Controlling Factors and Mechanism of Reactive Crystallization of Calcium Carbonate Polymorphs from Calcium Hydroxide Suspensions. *J. Cryst. Growth* **2002**, *236*, 323–332.

(24) Stein, A.; Keller, S. W.; Mallouk, T. E. Turning down the Heat: Design and Mechanism in Solid-State Synthesis. *Science* **1993**, *259*, 1558–1564.

(25) Disalvo, F. J. Solid-State Chemistry: A a Rediscovered Chemical Frontier. *Science* **1990**, *247*, 649–655.

(26) Shoemaker, D. P.; Hu, Y.-J.; Chung, D. Y.; Halder, G. J.; Chupas, P. J.; Soderholm, L.; Mitchell, J. F.; Kanatzidis, M. G. In Situ Studies of a Platform for Metastable Inorganic Crystal Growth and Materials Discovery. *Proc. Natl. Acad. Sci. U. S. A.* **2014**, *111*, 10922–10927.

(27) Jansen, M. A Concept for Synthesis Planning in Solid-State Chemistry. *Angew. Chemie - Int. Ed.* **2002**, *41*, 3746–3766.

(28) Hemminger, John (University of California, I. *Directing Matter and Energy: Five Challenges for Science and the Imagination A Report from the Basic Energy Sciences Advisory Committee*; 2007.

(29) Lin, Q.; Smeller, M.; Heideman, C. L.; Zschack, P.; Koyano, M.; Anderson, M. D.; Kykyneshi, R.; Keszler, D. A.; Anderson, I. M.; Johnson, D. C. Rational Synthesis and Characterization of a New Family of Low Thermal Conductivity Misfit Layer Compounds $[(PbSe)_{0.99}]_m(WSe_2)_n$. *Chem. Mater.* **2010**, *22*, 1002–1009.

(30) Bauers, S.; Ditto, J.; Moore, D. B.; Johnson, D. C. Structure-Property Relationships in Non-Epitaxial Chalcogenide Heterostructures: The Role of Interface Density on Charge Exchange. *Nanoscale* **2016**, *8*, 14665–14672.

(31) Bauers, S. R.; Moore, D. B.; Ditto, J.; Johnson, D. C. Phase Width of Kinetically Stable $([PbSe]_{1+\delta})_1(TiSe_2)_1$ Ferecrystals and the Effect of Precuror Compostion on Electrical Properties. *J. Alloys Compd.* **2015**, *645*, 118–124.

(32) Merrill, D.; Moore, D.; Bauers, S.; Falmbigl, M.; Johnson, D. Misfit Layer Compounds and Ferecrystals: Model Systems for Thermoelectric Nanocomposites. *Materials (Basel).* **2015**, *8*, 2000–2029.

(33) Moore, D. B.; Beekman, M.; Zschack, P.; Johnson, D. C. Synthesis of Four New Members of the $(PbSe)_{1.16}(TiSe_2)_n$ (n = 1, 2, 3, and 4) Family of Ferecrystals. In *2011 11th IEEE International Conference on Nanotechnology*; IEEE, 2011; pp 1363–1366.

(34) Moore, D. B.; Beekman, M.; Disch, S.; Zschack, P.; Häusler, I.; Neumann, W.; Johnson, D. C. Synthesis, Structure, and Properties of Turbostratically Disordered $(PbSe)_{1.18}(TiSe_2)_2$. *Chem. Mater.* **2013**, *25*, 2404–2409.

(35) Bauers, S. R.; Merrill, D. R.; Moore, D. B.; Johnson, D. C. Carrier Dilution in $TiSe_2$ Based Intergrowth Compounds for Enhanced Thermoelectric Performance. *J. Mater. Chem. C* **2015**, *3*, 10451–10458.

(36) Hamann, D. M.; Bardgett, D.; Cordova, D. L. M.; Maynard, L. A.; Hadland, E. C.; Lygo, A. C.; Wood, S. R.; Esters, M.; Johnson, D. C. Sub-Monolayer Accuracy in Determining the Number of Atoms per Unit Area in Ultrathin Films Using X-Ray Fluorescence. *Chem. Mater.* **2018**, *30* (18), 6209–6216.

(37) Schaffer, M.; Schaffer, B.; Ramasse, Q. Sample Preparation for Atomic-Resolution STEM at Low Voltages by FIB. *Ultramicroscopy* **2012**, *114*, 62–71.

(38) Weirich, T. E.; Pottgen, R.; Simon, A. Crystal Structure of Dititanium Monoselenide, Ti_2Se. *Zeitschrift für Krist. - Cryst. Mater.* **1996**, *211* (12), 928.

(39) Moore, D. B.; Stolt, M. J.; Atkins, R.; Sitts, L.; Jones, Z.; Disch, S.; Beekman, M.; Johnson, D. C. Structural and Electrical Properties of $(PbSe)_{1.16}TiSe_2$. *Emerg. Mater. Res.* **2012**, *1*, 292–298.

Chapter XII

(1) Kraschinski, S.; Herzog, S.; Bensch, W. Low Temperature Synthesis of Chromium Tellurides Using Superlattice Reactants: Crystallisation of Layered $CrTe_3$ at 100°C and the Decomposition into Cr_2Te_3. *Solid State Sci.* **2002**, *4* (10), 1237–1243.

(2) Herzog, S.; Kraschinski, S.; Bensch, W. The Reactivity of Cr-Te Superlattice Reactants and of Co-Deposited Cr-Te Films: Studies within-Situ X-Ray Diffractometry. *Zeitschrift für Anorg. und Allg. Chemie* **2003**, *629* (10), 1825–1832.

(3) Malte Behrens; Ragnar Kiebach, and; Bensch*, W.; and, D. H.; Jäger, W. Synthesis of Thin Cr_3Se_4 Films from Modulated Elemental Reactants via Two Amorphous Intermediates: A Detailed Examination of the Reaction Mechanism. **2006**.

(4) Regus, M.; Kuhn, G.; Polesya, S.; Mankovsky, S.; Alemayehu, M.; Stolt, M.; Johnson, D. C.; Ebert, H.; Bensch, W. Experimental and Theoretical Investigation of the New, Metastable Compound Cr_3Sb. *Zeitschrift für Krist. - Cryst. Mater.* **2014**, *229* (7), 505–515.

(5) Fukuto, M.; Hornbostel, M. D.; Johnson, D. C. Use of Superlattice Structure To Control Reaction Mechanism: Kinetics and Energetics of Nb_5Se_4 Formation. *J. Am. Chem. Soc.* **1994**, *116* (20), 9136–9140.

(6) Regus, M.; Mankovsky, S.; Polesya, S.; Kuhn, G.; Ditto, J.; Schürmann, U.; Jacquot, A.; Bartholomé, K.; Näther, C.; Winkler, M.; et al. Characterization of Cr-Rich Cr-Sb Multilayer Films: Syntheses of a New Metastable Phase Using Modulated Elemental Reactants. *J. Solid State Chem.* **2015**, *230*, 254–265.

(7) König, J. D.; Winkler, M.; Buller, S.; Bensch, W.; Schürmann, U.; Kienle, L.; Böttner, H. Bi_2Te_3-Sb_2Te_3 Superlattices Grown by Nanoalloying. *J. Electron. Mater.* **2011**, *40*, 1266–1270.

(8) Novet, T.; Johnson, D. C. New Synthetic Approach to Extended Solids: Selective Synthesis of Iron Silicides via the Amorphous State. *J. Am. Chem. Soc.* **1991**, *113*, 3398–3403.

(9) Sun, W.; Dacek, S. T.; Ong, S. P.; Hautier, G.; Jain, A.; Richards, W. D.; Gamst, A. C.; Persson, K. A.; Ceder, G. The Thermodynamic Scale of Inorganic Crystalline Metastability. *Sci. Adv.* **2016**, *2*, e1600225–e1600225.

(10) Oyelaran, O.; Novet, T.; Johnson, C. D.; Johnson, D. C. Controlling Solid-State Reaction Pathways: Composition Dependence in the Nucleation Energy of InSe. *J. Am. Chem. Soc.* **1996**, *118*, 2422–2426.

(11) Joshua R. Williams; Mark Johnson, and Johnson, D. C. Composition Dependence of the Nucleation Energy of Iron Antimonides from Modulated Elemental Reactants. **2001**.

(12) Joshua R. Williams; Mark B. Johnson, and Johnson, D. C. Suppression of Binary Nucleation in Amorphous La−Fe−Sb Mixtures. **2003**.

(13) Hornbostel, M. D.; Hyer, E. J.; Thiel, J.; Johnson, D. C. Rational Synthesis of Metastable Skutterudite Compounds Using Multilayer Precursors. *J. Am. Chem. Soc.* **1997**, *119*, 2665–2668.

(14) Heimbrodt, W.; Goede, O.; Tschentscher, I.; Weinhold, V.; Klimakow, A.; Pohl, U.; Jacobs, K.; Hoffmann, N. Optical Study of Octahedrally and Tetrahedrally Coordinated MnSe. *Phys. B Condens. Matter* **1993**, *185*, 357–361.

(15) Tomasini, P.; Haidoux, A.; Tédenac, J. C.; Maurin, M. Methylpentacarbonylmanganese as Organometallic Precursor for the Epitaxial Growth of Manganese Selenide Heterostructures. *J. Cryst. Growth* **1998**, *193*, 572–576.

(16) Decker, D. L.; Wild, R. L. Optical Properties of a−MnSe. *Phys. Rev. B* **1971**, *4*, 3425–3437.

(17) Peng, Q.; Dong, Y.; Deng, Z.; Kou, H.; Gao, S.; Li, Y. Selective Synthesis and Magnetic Properties of α-MnSe and $MnSe_2$ Uniform Microcrystals. *J. Phys. Chem. B.* **2002,** 106, 9261.

(18) Chun, H.J.; Lee, J.Y.; Kim, D.S.; Yoon, S.W.; Kang, J.H.; Park, J. Morphology-Tuned Growth of α-MnSe One-Dimensional Nanostructures. *J. Phys. Chem. C.* **2006,** 111, 519-525.

(19) Wang, L.; Chen, L.; Luo, T.; Bao, K.; Qian, Y. A Facile Method to the Cube-like $MnSe_2$ Microcrystallites via a Hydrothermal Process. *Solid State Commun.* **2006**, *138* (2), 72–75.

(20) Wu, M.; Xiong, Y.; Jiang, N.; Ning, M.; Chen, Q. Hydrothermal Preparation of α-MnSe and $MnSe_2$ Nanorods. *J. Cryst. Growth* **2004**, *262* (1–4), 567–571.

(21) Qin, T.; Lu, J.; Wei, S.; Qi, P.; Peng, Y.; Yang, Z.; Qian, Y. α-MnSe Crystallites through Solvothermal Reaction in Ethylenediamine. *Inorg. Chem. Commun.* **2002**, *5* (5), 369–371.

(22) Norris, D. J.; Yao, N.; and, F. T. C.; Kennedy, T. A. High-Quality Manganese-Doped ZnSe Nanocrystals. *Nano Lett.* **2000**, 1, 3-7.

(23) Levy, L.; Feltin, N.; Ingert, D.; Pileni, M. P. Three Dimensionally Diluted Magnetic Semiconductor Clusters $Cd_{1-y}Mn_yS$ with a Range of Sizes and Compositions: Dependence of Spectroscopic Properties on the Synthesis Mode. *J. Phys. Chem. C.* **1997**, 101, 9153-9160.

(24) Suyver, J. F.; Wuister, S. F.; Kelly, J. J.; Meijerink, A. Synthesis and Photoluminescence of Nanocrystalline ZnS:Mn^{2+}. **2001**.

(25) Metha, J. M.; Riewald, P. G.; Vlack, L. H. The System MnSe-MnS. *J. Am. Ceram. Soc.* **1967**, *50*, 164–164.

(26) Elliott, N. The Crystal Structure of Manganese Diselenide and Manganese Ditelluride. *J. Am. Chem. Soc.* **1937**, *59*, 1958–1962.

(27) H. Schnaase. Kristallstruktur Der Manganosulfide Und Ihrer Mischkristalle Mit Zinksulfid Und Cadmiumsulfid. *Z. Phys. Chem. B* **1933**, *20*, 89.

(28) Baroni, A. No Title. *Z. Krist.* **1938**, No. A99, 336.

(29) Zeppenfeld, A. C.; Fiddler, S. L.; Ham, W. K.; Klopfenstein, B. J.; Page, C. J. Variation of Layer Spacing in Self-Assembled Hafnium-1,10-Decanediylbis(Phosphonate) Multilayers As Determined by Ellipsometry and Grazing Angle X-Ray Diffraction. *J. Am. Chem. Soc.* **1994**, *116* (20), 9158–9165.

(30) Vanyarkho, V.G.; Zlomanov, V.P; Novoselova, A.V.; Fokin, V. N. Investigation of The Lead Selenide-Manganese Selenide System. *Inorg. Mater.* **1969**, *5* (10), 1440–1443.

(31) Fister, L.; Johnson, D. C. Controlling Solid-State Reaction Mechanisms Using Diffusion Length in Ultrathin-Film Superlattice Composites. *J. Am. Chem. Soc.* **1992**, *114*, 4639–4644.

(32) Hamann, D. M.; Bardgett, D.; Cordova, D. L. M.; Maynard, L. A.; Hadland, E. C.; Lygo, A. C.; Wood, S. R.; Esters, M.; Johnson, D. C. Sub-Monolayer Accuracy in Determining the Number of Atoms per Unit Area in Ultrathin Films Using X-Ray Fluorescence. *Chem. Mater.* **2018**, *30* (18), 6209–6216.

Chapter XIII

(1) Geim, A. K.; Grigorieva, I. V. Van Der Waals Heterostructures. *Nature* **2013**, *499*, 419–425.

(2) Reyren, N.; Thiel, S.; Caviglia, A. D.; Fitting Kourkoutis, L.; Hammerl, G.; Richter, C.; Schneider, C. W.; Kopp, T.; Rüetschi, A. S.; Jaccard, D.; et al. Superconducting Interfaces between Insulating Oxides. *Science.* **2007**, *317* (5842), 1196–1199.

(3) Lee, J. S.; Xie, Y. W.; Sato, H. K.; Bell, C.; Hikita, Y.; Hwang, H. Y.; Kao, C. C. Titanium Dxy Ferromagnetism at the $LaAlO_3/SrTiO_3$ Interface. *Nat. Mater.* **2013**, *12*, 703–706.

(4) Brinkman, A.; Huijben, M.; Van Zalk, M.; Huijben, J.; Zeitler, U.; Maan, J. C.; Van Der Wiel, W. G.; Rijnders, G.; Blank, D. H. A.; Hilgenkamp, H. Magnetic Effects at the Interface between Non-Magnetic Oxides. *Nat. Mater.* **2007**, *6*, 493–496.

(5) Dikin, D. A.; Mehta, M.; Bark, C. W.; Folkman, C. M.; Eom, C. B.; Chandrasekhar, V. Coexistence of Superconductivity and Ferromagnetism in Two Dimensions. *Phys. Rev. Lett.* **2011**, *107*.

(6) Knez, I.; Du, R. R.; Sullivan, G. Evidence for Helical Edge Modes in Inverted InAs/GaSb Quantum Wells. *Phys. Rev. Lett.* **2011**, *107*.

(7) Georgiou, T.; Jalil, R.; Belle, B. D.; Britnell, L.; Gorbachev, R. V.; Morozov, S. V.; Kim, Y. J.; Gholinia, A.; Haigh, S. J.; Makarovsky, O.; et al. Vertical Field-Effect Transistor Based on Graphene-WS_2 Heterostructures for Flexible and Transparent Electronics. *Nat. Nanotechnol.* **2013**, *8*, 100–103.

(8) Ponomarenko, L. A.; Geim, A. K.; Zhukov, A. A.; Jalil, R.; Morozov, S. V.; Novoselov, K. S.; Grigorieva, I. V.; Hill, E. H.; Cheianov, V. V.; Fal'Ko, V. I.; et al. Tunable Metal-Insulator Transition in Double-Layer Graphene Heterostructures. *Nat. Phys.* **2011**, *7*, 958–961.

(9) Narayan, A.; Bhutani, A.; Rubeck, S.; Eckstein, J. N.; Shoemaker, D. P.; Wagner, L. K. Computational and Experimental Investigation for New Transition Metal Selenides and Sulfides: The Importance of Experimental Verification for Stability. *Phys. Rev. B* **2016**, *94*, 045105.

(10) Saal, J. E.; Kirklin, S.; Aykol, M.; Meredig, B.; Wolverton, C. Materials Design and Discovery with High-Throughput Density Functional Theory: The Open Quantum Materials Database (OQMD). *JOM* **2013**, *65*, 1501–1509.

(11) Curtarolo, S.; Hart, G. L. W.; Nardelli, M. B.; Mingo, N.; Sanvito, S.; Levy, O. The High-Throughput Highway to Computational Materials Design. *Nat. Mater.* **2013**, *12*, 191–201.

(12) Wu, J.; Liu, F.; Sasase, M.; Ienaga, K.; Obata, Y.; Yukawa, R.; Horiba, K.; Kumigashira, H.; Okuma, S.; Inoshita, T.; et al. Natural van Der Waals Heterostructural Single Crystals with Both Magnetic and Topological Properties. *Sci. Adv.* **2019**, *5*, eaax9989.

(13) Ruan, H.; Huang, Y.; Chen, Y.; Zhuge, F. Emerging Artificial Two-Dimensional van Der Waals Heterostructures for Optoelectronics. In *Nanosystems [Working Title]*; IntechOpen, 2019.

(14) Liu, C.; Chen, H.; Hou, X.; Zhang, H.; Han, J.; Jiang, Y. G.; Zeng, X.; Zhang, D. W.; Zhou, P. Small Footprint Transistor Architecture for Photoswitching Logic and in Situ Memory. *Nat. Nanotechnol.* **2019**, *14*, 662–667.

(15) Kashiwabara, Y.; Nakano, M.; Nakagawa, Y.; Wang, Y.; Matsuoka, H.; Iwasa, Y. Electrical Conduction at the Interface between Insulating van Der Waals Materials. *Adv. Funct. Mater.* **2019**, *29*, 1900354.

(16) Zereshki, P.; Wei, Y.; Long, R.; Zhao, H. Layer-Coupled States Facilitate Ultrafast Charge Transfer in a Transition Metal Dichalcogenide Trilayer Heterostructure. *J. Phys. Chem. Lett.* **2018**, *9*, 5970–5978.

(17) Ye, L.; Wang, P.; Luo, W.; Gong, F.; Liao, L.; Liu, T.; Tong, L.; Zang, J.; Xu, J.; Hu, W. Highly Polarization Sensitive Infrared Photodetector Based on Black Phosphorus-on-WSe_2 Photogate Vertical Heterostructure. *Nano Energy* **2017**, *37*, 53–60.

(18) Lalmi, B.; Oughaddou, H.; Enriquez, H.; Kara, A.; Vizzini, Ś.; Ealet, B.; Aufray, B. Epitaxial Growth of a Silicene Sheet. *Appl. Phys. Lett.* **2010**, *97* (22).

(19) Meng, L.; Wang, Y.; Zhang, L.; Du, S.; Wu, R.; Li, L.; Zhang, Y.; Li, G.; Zhou, H.; Hofer, W. A.; et al. Buckled Silicene Formation on Ir(111). *Nano Lett.* **2013**, *13*, 685–690.

(20) Fleurence, A.; Friedlein, R.; Ozaki, T.; Kawai, H.; Wang, Y.; Yamada-Takamura, Y. Experimental Evidence for Epitaxial Silicene on Diboride Thin Films. *Phys. Rev. Lett.* **2012**, *108*.

(21) Gao, S.; Lin, Y.; Jiao, X.; Sun, Y.; Luo, Q.; Zhang, W.; Li, D.; Yang, J.; Xie, Y. Partially Oxidized Atomic Cobalt Layers for Carbon Dioxide Electroreduction to Liquid Fuel. *Nature.* **2016**, *529*, 68–71.

(22) Liu, H.; Tang, H.; Fang, M.; Si, W.; Zhang, Q.; Huang, Z.; Gu, L.; Pan, W.; Yao, J.; Nan, C.; et al. 2D Metals by Repeated Size Reduction. *Adv. Mater.* **2016**, *28*, 8170–8176.

(23) Zhao, J.; Deng, Q.; Bachmatiuk, A.; Sandeep, G.; Popov, A.; Eckert, J.; Rümmeli, M. H. Free-Standing Single-Atom-Thick Iron Membranes Suspended in Graphene Pores. *Science.* **2014**, *343*, 1228–1232.

(24) Fan, Z.; Huang, X.; Han, Y.; Bosman, M.; Wang, Q.; Zhu, Y.; Liu, Q.; Li, B.; Zeng, Z.; Wu, J.; et al. Surface Modification-Induced Phase Transformation of Hexagonal Close-Packed Gold Square Sheets. *Nat. Commun.* **2015**, *6*.

(25) Fan, Z.; Bosman, M.; Huang, X.; Huang, D.; Yu, Y.; Ong, K. P.; Akimov, Y. A.; Wu, L.; Li, B.; Wu, J.; et al. Stabilization of 4H Hexagonal Phase in Gold Nanoribbons. *Nat. Commun.* **2015**, *6*.

(26) Rudin, S. P.; Johnson, D. C. Density Functional Theory Calculations of the Turbostratically Disordered Compound $[(SnSe)_{1+y}]_m(VSe_2)_n$. *Phys. Rev. B* **2015**, *91*, 144203.

(27) Rudin, S. P. A Density Functional Theory Calculations-Based Approach That Predicts Layered Materials with Emergent Structures. **2016**.

(28) Johnson, D. C. Controlled Synthesis of New Compounds Using Modulated Elemental Reactants. *Curr. Opin. Solid State Mater. Sci.* **1998**, *3*, 159–167.

(29) Noh, M.; Thiel, J.; Johnson, D. C. Synthesis of Crystalline Superlattices by Controlled Crystallization of Modulated Reactants. *Science.* **1995**, *270* (5239), 1181–1184.

(30) Noh, M.; Johnson, C.D.; Hornbostel, M.D.; Thiel, J.; Johnson, D. C. Control of Reaction Pathway and the Nanostructure of Final Products through the Design of Modulated Elemental Reactants. **1996**.

(31) Novet, T.; Johnson, D. C. New Synthetic Approach to Extended Solids: Selective Synthesis of Iron Silicides via the Amorphous State. *J. Am. Chem. Soc.* **1991**, *113*, 3398–3403.

(32) Kresse, G.; Furthmüller, J. Efficient Iterative Schemes for Ab Initio Total-Energy Calculations Using a Plane-Wave Basis Set. *Phys. Rev. B* **1996**, *54*, 11169–11186.

(33) Kresse, G.; Furthmüller, J. Efficiency of Ab-Initio Total Energy Calculations for Metals and Semiconductors Using a Plane-Wave Basis Set. *Comput. Mater. Sci.* **1996**, *6*, 15–50.

(34) Kresse, G.; Joubert, D. From Ultrasoft Pseudopotentials to the Projector Augmented-Wave Method. *Phys. Rev. B* **1999**, *59*, 1758–1775.

(35) Perdew, J. P.; Burke, K.; Ernzerhof, M. Generalized Gradient Approximation Made Simple. *Phys. Rev. Lett.* **1996**, *77*, 3865–3868.

(36) Methfessel, M.; Paxton, A. T. High-Precision Sampling for Brillouin-Zone Integration in Metals. *Phys. Rev. B* **1989**, *40*, 3616–3621.

(37) Tkatchenko, A.; Scheffler, M. Accurate Molecular Van Der Waals Interactions from Ground-State Electron Density and Free-Atom Reference Data. *Phys. Rev. Lett.* **2009**, *102*, 073005.

(38) Esters, M. Deposition Software for the Inficon IC6 Deposition Controller https://github.com/marcoesters/deposition_ic6.

(39) Hamann, D. M.; Bardgett, D.; Cordova, D. L. M.; Maynard, L. A.; Hadland, E. C.; Lygo, A. C.; Wood, S. R.; Esters, M.; Johnson, D. C. Sub-Monolayer Accuracy in Determining the Number of Atoms per Unit Area in Ultrathin Films Using X-Ray Fluorescence. *Chem. Mater.* **2018**, *30*, 6209–6216.

(40) Lu, P.; Zhou, L.; Kramer, M. J.; Smith, D. J. Atomic-Scale Chemical Imaging and Quantification of Metallic Alloy Structures by Energy-Dispersive X-Ray Spectroscopy. *Sci. Rep.* **2015**, *4*, 3945.

(41) Hamann, D. M.; Merrill, D. R.; Bauers, S. R.; Mitchson, G.; Ditto, J.; Rudin, S. P.; Johnson, D. C. Long-Range Order in $[(SnSe)_{1.2}]_1[TiSe_2]_1$ Prepared from Designed Precursors. *Inorg. Chem.* **2017**, *56*, 3499–3505.

(42) Hite, O. K.; Falmbigl, M.; Alemayehu, M. B.; Esters, M.; Wood, S. R.; Johnson, D. C. Charge Density Wave Transition in $(PbSe)_{1+\delta}(VSe_2)_n$ Compounds with n = 1, 2, and 3. *Chem. Mater.* **2017**, *29* (13), 5646–5653.

(43) Cordova, D. L. M.; Fender, S. S.; Kam, T. M.; Seyd, J.; Albrecht, M.; Lu, P.; Fischer, R.; Johnson, D. C. Designed Synthesis and Structure–Property Relationships of Kinetically Stable $[(PbSe)_{1+\delta}]_m(VSe_2)_1$ (m = 1, 2, 3, 4) Heterostructures. *Chem. Mater.* **2019**, acs.chemmater.9b02826.

(44) Anderson, M. D.; Heideman, C. L.; Lin, Q.; Smeller, M.; Kokenyesi, R.; Herzing, A. A.; Anderson, I. M.; Keszler, D. A.; Zschack, P.; Johnson, D. C. Size-Dependent Structural Distortions in One-Dimensional Nanostructures. *Angew. Chemie Int. Ed.* **2013**, *52*, 1982–1985.

(45) Moore, D. B.; Stolt, M. J.; Atkins, R.; Sitts, L.; Jones, Z.; Disch, S.; Beekman, M.; Johnson, D. C. Structural and Electrical Properties of $(PbSe)_{1.16}$ $TiSe_2$. *Emerg. Mater. Res.* **2012**, *1*, 292–298.

(46) Alemayehu, M. B.; Mitchson, G.; Ditto, J.; Hanken, B. E.; Asta, M.; Johnson, D. C. Charge Transfer between PbSe and $NbSe_2$ in $[(PbSe)_{1.14}]_m$ $(NbSe_2)_1$ Ferecrystalline Compounds. *Chem. Mater.* **2014**, *26*, 1859–1866.

(47) Thompson, A. H.; Silbernagel, B. G. *Correlated Magnetic and Transport Properties in the Charge-Density-Wave States of VSe_2*; 1979; Vol. 8.

(48) Tang, W.; Sanville, E.; Henkelman, G. A Grid-Based Bader Analysis Algorithm without Lattice Bias. *J. Phys. Condens. Matter* **2009**, *21*.

(49) Cotton, F. A.; Wilkison, G. No Title. In *Advanced Inorganic Chemistry*; Wiley: New York, 1980; pp 627–628.

(50) Nagaosa, N.; Sinova, J.; Onoda, S.; MacDonald, A. H.; Ong, N. P. Anomalous Hall Effect. *Rev. Mod. Phys.* **2010**, *82*, 1539–1592.

Appendix D

(1) Le Bail, A.; Duroy, H.; Fourquet, J. L. Ab-Initio Structure Determination of $LiSbWO_6$ by X-Ray Powder Diffraction. *Mater. Res. Bull.* **1988**, *23*, 447–452.

(2) Roisnel, T.; Rodríquez-Carvajal, J. WinPLOTR: A Windows Tool for Powder Diffraction Pattern Analysis. *Mater. Sci. Forum* **2001**, *378–381*, 118–123.

(3) Rodríguez-Carvajal, J. Recent Advances in Magnetic Structure Determination by Neutron Powder Diffraction. *Phys. B Condens. Matter* **1993**, *192*, 55–69.